CISM COURSES AND LECTURES NO. 462
INTERNATIONAL CENTRE FOR MECHANICAL SCIENCES

CHEMO-MECHANICAL COUPLINGS IN POROUS MEDIA GEOMECHANICS AND BIOMECHANICS

EDITED BY

BENJAMIN LORET
JACQUES M. HUYGHE

Springer-Verlag Wien GmbH

CISM COURSES AND LECTURES

The series presents lecture notes, monographs, edited works and proceedings in the field of Mechanics, Engineering, Computer Science and Applied Mathematics.
Purpose of the series is to make known in the international scientific and technical community results obtained in some of the activities organized by CISM, the International Centre for Mechanical Sciences.

INTERNATIONAL CENTRE FOR MECHANICAL SCIENCES

COURSES AND LECTURES - No. 462

CHEMO-MECHANICAL COUPLINGS IN POROUS MEDIA GEOMECHANICS AND BIOMECHANICS

EDITED BY

BENJAMIN LORET
INSTITUT NATIONAL POLYTECHNIQUE DE GRENOBLE

JACQUES M. HUYGHE
EINDHOVEN UNIVERSITY OF TECHNOLOGY

Springer-Verlag Wien GmbH

The publication of this volume was co-sponsored and co-financed by the UNESCO Venice Office - Regional Bureau for Science in Europe (ROSTE) and its content corresponds to a CISM Advanced Course supported by the same UNESCO Regional Bureau.

This volume contains 190 illustrations

Originally published by Springer-Verlag Wien New York in 2004
SPIN 10995044

In order to make this volume available as economically and as rapidly as possible the authors' typescripts have been reproduced in their original forms. This method unfortunately has its typographical limitations but it is hoped that they in no way distract the reader.

ISBN 978-3-211-21323-0 ISBN 978-3-7091-2778-0 (eBook)
DOI 10.1007/978-3-7091-2778-0

PREFACE

The CISM course on Chemo-Mechanical Couplings In Porous Media - Geomechanics and Biomechanics was held in Udine, June 23-27, 2003.

The objective of the course is to gather a floor of experimentalists, modelers and engineers interested in different physical, chemical, mechanical and transport aspects of

biological tissues, namely cornea, articular cartilage and intervertebral disc, and

chemically active geological materials, mainly clays and shales.

The focus is on the couplings between the electro-chemical and the mechanical aspects involved in swelling and chemical consolidation. Particular emphasis is laid on the influence of these phenomena on the mechanical properties and on the transport properties, with a view towards engineering applications, such as

- slope stability of chemically active clays;

- use of clays as barriers to store municipal and nuclear wastes,

and

- understanding of pathologies, of natural or artificial repairs, consequences of surgery;

- development of adequate prostheses, and

- of artificial muscles via electro-active polymers of biological and industrial interests, such as polymer gels.

The mechanical behaviour of swelling tissues and clays is affected by a variety of physical and chemical phenomena occurring at different scales. These are for clays:

- the nano-scale behaviour of water and ions in the interplatelet space;

- the micro-structural evolution of clusters, free water and its solutes, and air;

- the macro-scale behaviour of the continuum viewed as a multiphase multi-species medium.

There are many similarities between the swelling of clays and of biological tissues: in both cases, electro-chemo-mechanical couplings are keys to the phenomena involved. In clays, water is adsorbed to and desorbed from negatively charged clay platelets, which act as anion repulsors. In articular cartilage and cornea, the negatively charged proteoglycans are responsible for maintaining the tissue hydrated and inflated; the mechanical response involves also different kinds of water. The exchange of ions is a strongly regulated process, and, in the cornea,

ionic pumps spend a great deal of energy in living bodies to maintain physiological concentrations.

Applications in geo-environmental and geotechnical technology, including nuclear and hazardous waste isolation, oil recovery, engineering geology, geochemistry, hydrology, and in many others uses of clays are addressed directly or implied in the lecture notes collected in this volume. Analysis and control of long term effects of surgery and mechanical performance of prostheses may benefit from the modeling of irreversibilities that are of utmost importance in geological materials. On the other hand, understanding the self-regulation mechanisms of biological tissues may be helpful in the design of efficient engineering materials.

The course is multidisciplinary. Lectures are of diverse types: laboratory and field experiments, constitutive modeling at micro- and macro-scales, computational methods at nano-scales, finite element simulations of laboratory tests.

The course and lecture notes are intended mainly to Ph'D students, researchers and engineers

- *in geomechanics with interest in soil remediation, environmental problems; modeling, laboratory testing and field investigation;*
- *in petroleum engineering with interest in wellbore stability;*
- *in biomechanics with interest in tissue engineering, articular cartilage and cornea, prosthesis design and mechanical aspects of surgery;*
- *in physics and nano-scale computations of fluid-solid interactions in capillaries of porous media (clays, biological media).*

Overall, the course represents an effort to booster the cross-fertilization of ideas and methods, and to increase the permeability between domains, that in both the academic and industrial worlds, may benefit from one another.

Benjamin Loret and Jacques M. Huyghe

CONTENTS

Influence of Pore Fluid Composition on Volume Change Behaviour of Clays Exposed to the Same Fluid as the Pore Fluid

Caterina Di Maio

Dipartimento di Strutture, Geotecnica, Geologia applicata all'Ingegneria, Università della Basilicata, Italy

Abstract. This paper reports experimental results relative to the influence of pore fluid composition on volume change behaviour of four different clayey soils: the Ponza bentonite, a commercial kaolin, the Bisaccia and the Marino clays. Oedometer tests were carried out on dry materials and on the materials reconstituted with distilled water, concentrated NaCl solutions and a non polar fluid (cyclohexane). The influence of ethanol was analysed only in the case of the Bisaccia clay. All the tests were carried out by exposing the soils to the same fluid as the pore fluid. The results show that the materials prepared with cyclohexane behave similarly to the dry ones and they both are less compressible than the materials prepared with aqueous solutions. The coefficient of consolidation increases dramatically and swelling is negligible in the whole considered stress range. Volume change parameters strongly depend on the dielectric constant of the pore fluid.

1 Introduction

It is well known that the volume change behaviour of clays is greatly influenced by mineral composition. The influence is particularly strong when the pore fluid is distilled water, as shown by Figure 1 which compares the compression and swelling curves of the Ponza bentonite and a commercial kaolin prepared with and immersed in distilled water. As expected, the behaviour of the two clays – reconstituted at about the liquid limit - is very different. In particular, kaolin compression and swelling curves are more similar to those of a loose sand than to those of the other clay.

The influence of pore fluid composition depends on the type of soil. In the case of very active montmorillonite, experimental results show that compressibility and swelling decrease with increasing pore liquid ionic force, or with decreasing dielectric constant (Bolt, 1956, Kenney, 1967; Kinsky et al., 1971; Olson and Mesri, 1970; Mesri and Olson, 1971; Sridharan, 1991; Mitchell, 1993; Di Maio, 1996b). Changes in compressibility and swelling caused by pore fluid composition variations can be almost the same as those caused by mineral composition variations. In particular, the compression curve of the Ponza bentonite reconstituted with saturated salt solutions is more similar to that of kaolin than to that of the water-saturated bentonite (Figure 2). Depending on the particular value of its specific surface, kaolinite may *or may not be influenced by pore fluid* composition. Sridharan and Ventakappa Rao (1973) found that kaolinite may undergo consolidation as an effect of an increase in the dielectric

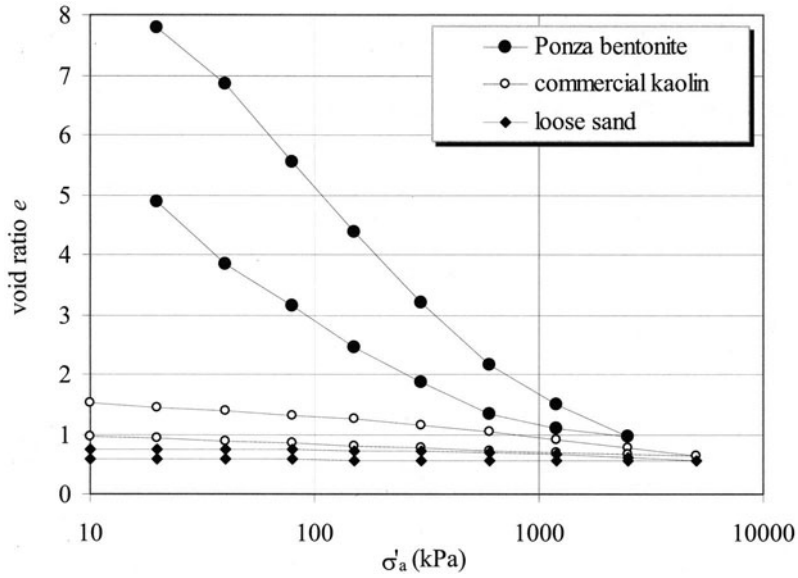

Figure 1. Oedometer compression and swelling curves of water – saturated Ponza bentonite, commercial kaolin and sand (Di Maio et al., 2003).

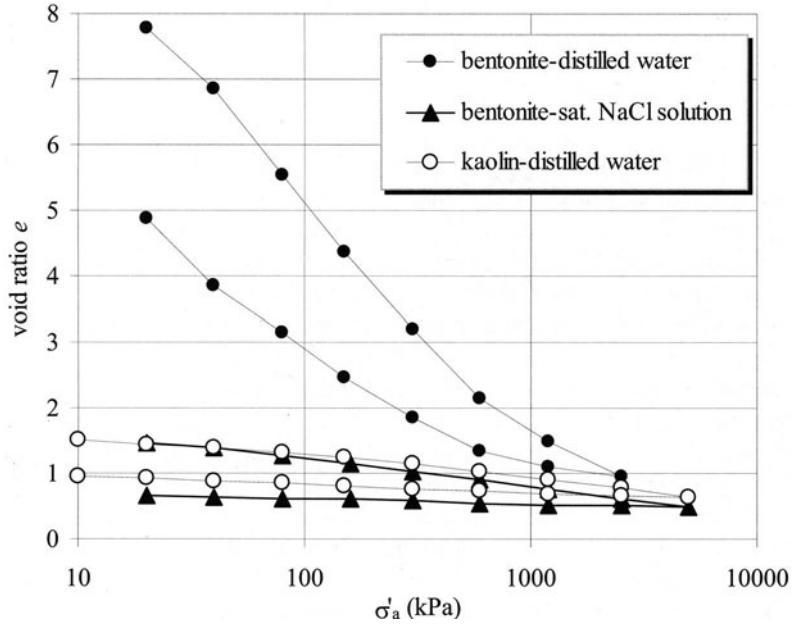

Figure 2. Oedometer compression and swelling curves of kaolin and Ponza bentonite reconstituted with and immersed in distilled water and saturated NaCl solution (Di Maio et al., 2003).

constant of the pore fluid. The Authors hypothesized that kaolin volume changes are related to the interparticle forces which control particle sliding. If the ionic strength of pore fluid decreases, or if the dielectric constant increases, the resistance to particle movements decreases, thus allowing a reduction in porosity. Chen et al. (2000) observed that the compression index of kaolin varies with the dielectric constant D of the pore organic fluid similarly to the Hamaker constant, and it exhibits a minimum at about D = 24.

Generally, results relative to materials prepared with aqueous ion solutions are explained, at least qualitatively, in terms of diffuse double layer models. The effects of organic non polar solvents - attributed to the suppression of the diffuse double layer - are often analysed in terms of the pore fluid dielectric constant. The purpose of this paper is to compare directly the influence of extreme types of fluids (water, air, concentrated salt solutions, non-polar organic fluids) on different types of soils. To this aim the materials were reconstituted at about their maximum porosity and the results were analysed with reference to a unique parameter: the pore fluid static dielectric constant. The Ponza bentonite and the commercial kaolin, since they are mainly composed of Na-montmorillonite and kaolinite respectively, represent extreme types of clay soils. In order to analyse the influence of the smectitic component on natural soil behaviour, two clays with different smectite percentages, the Bisaccia and the Marino clays, were also tested.

2 Materials

Particle size distribution curves of the tested soils are reported by Figure 3. Table 1 reports mineral composition determined by X-ray powder diffraction analysis, using Cu-Kα radiation, and the liquid limit evaluated by means of the fall cone test on the powdered soils prepared with distilled water.

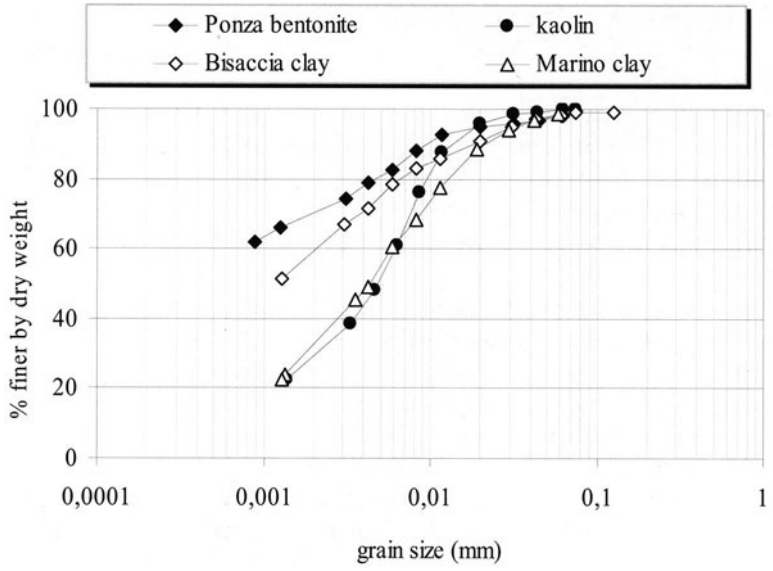

Figure 3. Grain size distribution curves.

Table 1. Specific weight G_s, liquid limit w_L, mineral percentages.

	G_s	w_L (%)	kaolinite %	illite %	smectite %	
Ponza bentonite	2.77	390	20	-	70 -80	-
Bisaccia clay	2.78	110	10	20	30	Clorite 10% Quartz 15% Calcite 10% Feldspars 5%
kaolin	2.63	50	75 - 80	8 - 10	<5	Quartz and feldspars 10%
Marino clay	2.75	50	30	10	Mixed layer 10	chlorite 10% quartz 30%-40%

The limit water content was evaluated also by mixing the soils with NaCl solutions at various concentrations. The results show (Figure 4) that w_L decreases with increasing salt solution molarity, with the exception of the commercial kaolin which seems to be unaffected by pore fluid composition.

Water retention properties were evaluated more accurately by settling tests carried out following Sridharan & Prakash (1998). Several suspensions were prepared by mixing 25 g dry material with different quantities of distilled water or saturated NaCl solution, and they were left to settle. For any initial water content of the suspension w_i, water retention capability w_f of the Bisaccia clay in the concentrated salt solution is much lower than in distilled water, consistently with the fall cone test results (Figure 5). On the contrary, water retention capability of kaolin in the salt solution is higher than in distilled water. So, pore liquid composition influences the kaolin behaviour, and the type of influence is opposite to that on the smectitic clay, as found by Sridharan & Ventakappa Rao (1973).

The difference in the type of influence is shown also by Figure 6, which reports two photographs relative to the Ponza bentonite and the commercial kaolin at about four years from the beginning of sedimentation tests. The samples were prepared with 40 g/l dry clay. The material on the left of each photograph sedimented in distilled water, whereas the material on the right hand side in a saturated NaCl solution. It can be observed that, in the case of the Ponza bentonite, the sediment volume decreases with increasing pore solution concentration whereas it increases in the case of kaolin. Time trend of consolidation too is strongly dependent on pore fluid composition, as shown by Figure 7 which reports the average void ratio of the sedimentting Bisaccia clay in distilled water and in a 1 M NaCl solution. The material consolidates in a few minutes in a concentrated salt solution, whereas, in distilled water, after 4 years from the beginning of the test, it has not reached the equilibrium yet!

The limit water contents of the Ponza and Bisaccia clays were evaluated also with cyclohexane and ethanol. For the Bisaccia clay also with dimethylsulfoxide, a fluid whose dielectric constant is equal to that of saturated NaCl solution. The obtained values, together with those obtained with the aqueous solutions, seem to be well correlated to the static dielectric constant D of the pore fluid (Figure 8). In particular, it is worth noting that w_L of the Bisaccia clay

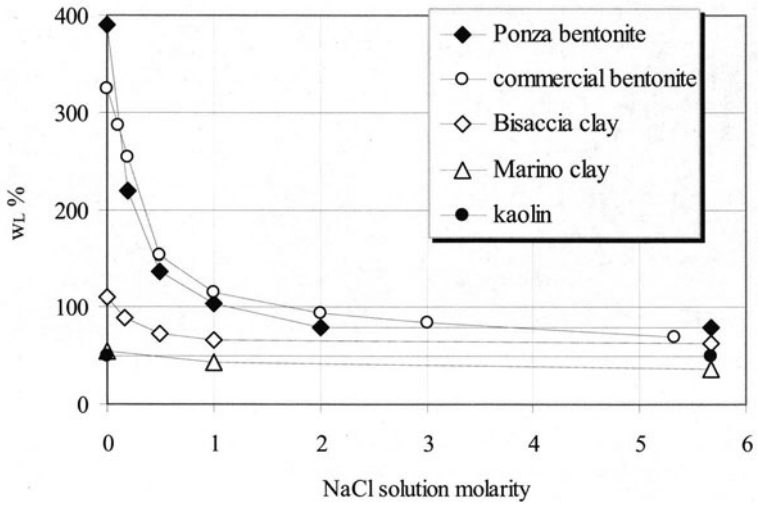

Figure 4. Liquid limit w_L against pore solution molarity. The limit, determined by fall cone test, is defined as the weight of water divided by the weight of solid (without salt).

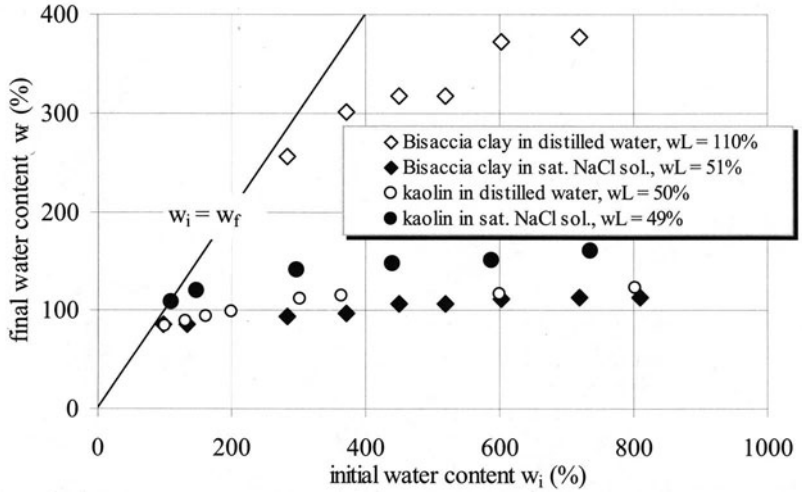

Figure 5. Equilibrium water content of the sediment volume w_f against initial water content of the suspension w_i.

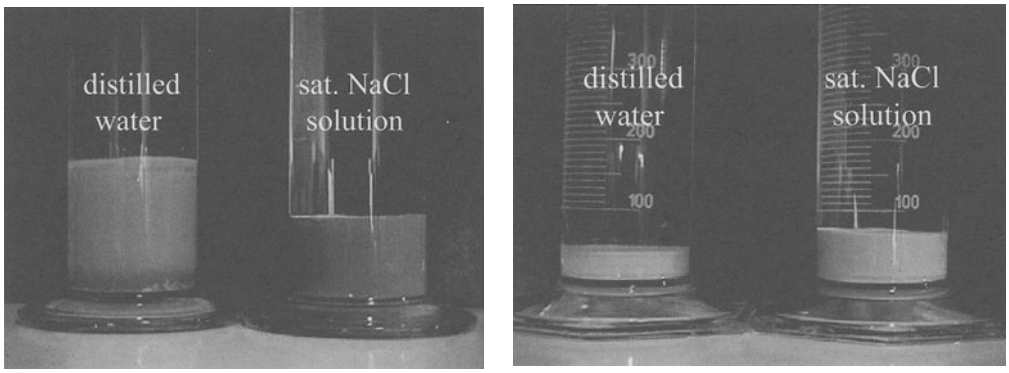

Figure 6. Sediment volume of the Ponza bentonite (on the left) and of the commercial kaolin (on the right) in distilled water and in a saturated salt solution, about four years after the beginning of the test.

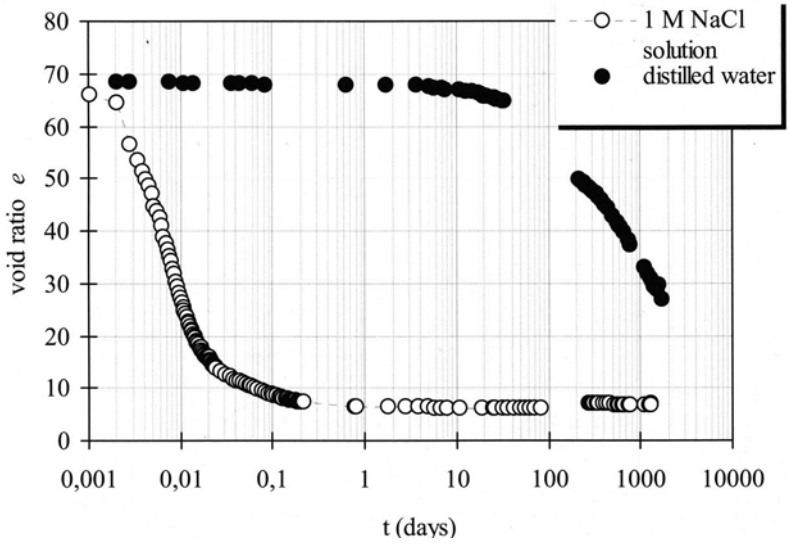

Figure 7. Average void ratio against time for the Bisaccia clay sedimenting in distilled water and in 1 M NaCl solution.

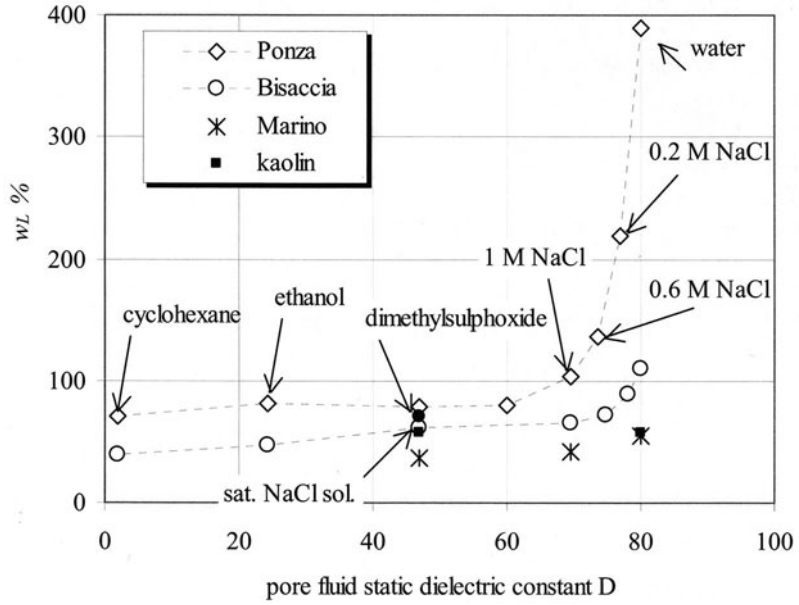

Figure 8. Liquid limit against pore fluid static dielectric constant.

reconstituted with saturated NaCl solution is very close to w_L of the material prepared with dimethylsulfoxide.

The intrinsic compressibility $C_c^* = e^*_{100} - e^*_{1000}$ (with e^*_{100} and e^*_{1000} the intrinsic void ratios at σ'_a = 100 kPa and 1000 kPa respectively) varies almost linearly with the void ratio e_L at the liquid limit (Burland, 1990). So, the results reported by Figure 8 suggest that an analogous dependence on pore fluid dielectric constant will be shown by the compression index.

3 Methods

Compressibility was evaluated by means of fixed-ring oedometer tests on specimens submerged in the same fluid as the pore fluid. Four sets of materials were reconstituted with four different fluids. The first set consisted of the natural soils reconstituted by mixing the air-dried powders with distilled water. The second set was constituted by the air-dried powdered materials mixed with NaCl solutions at various concentrations. Also in this case, the initial solution content was equal to - or higher than - the liquid limit evaluated with the same solution. For the Ponza bentonite and the Bisaccia clay reconstituted with water or with aqueous ionic solutions, the liquid limit state was verified to be a reference state. In fact the compression curves relative to several different initial solution contents higher than w_L were found to converge at low values of σ'_a (Figure 9). Another set of tests was carried out on the materials saturated with cyclohexane, an organic non polar fluid whose static dielectric constant is D = 2.0 at 20°C. The powdered soils

were oven-dried at 105°C for three days. In this case it was impossible to test the materials for fluid contents higher than the liquid limit because self-weight consolidation rapidly occurred. So, the materials were rapidly mixed with the maximum liquid content at which apparently there was no self-weight consolidation. They were placed in consolidation cells, immersed in cyclohexane, and the cells were sealed. The last set of tests was carried out on "dry" specimens. The materials, dried at 105°C for 3 days, were prepared in thin layers, with an initial void ratio close to that of the materials prepared with cyclohexane.

The specimens - 2 cm thick - were loaded and subsequently unloaded by steps, doubling and halving respectively the external load. Only in the case of the Bisaccia clay reconstituted with distilled water, a great tendency of the material to extrude required smaller axial stress increments. Each load was sustained long enough for the completion of primary compression or swelling and the development of secondary volume strains.

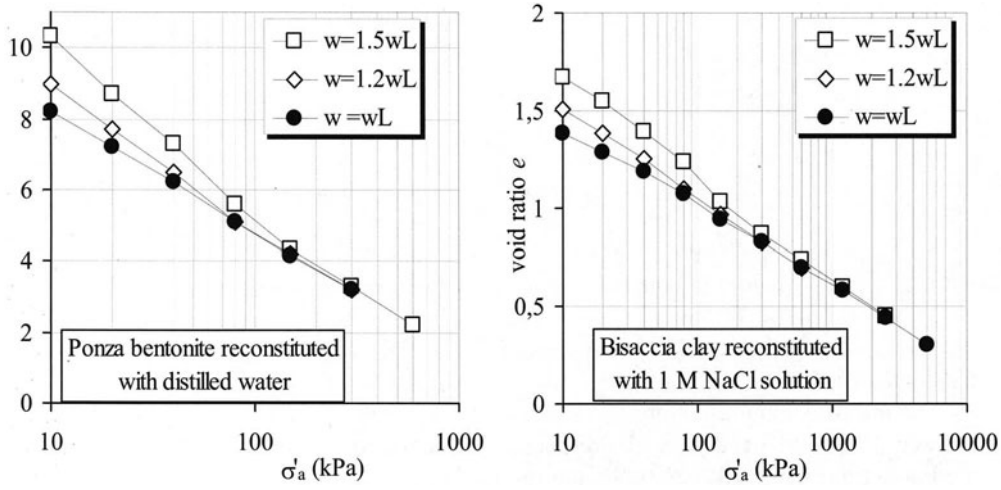

Figure 9. Compression lines for initial liquid contents higher than the liquid limit.

4 Results

The comparison of the effects of different types of pore fluids is reported by Figure 10.a for the Ponza bentonite. The figure reports the oedometer compression and swelling curves of a specimen reconstituted with distilled water, of a specimen reconstituted with a saturated NaCl solution, one prepared with cyclohexane and the curves relative to dry material. The figure shows that:

a. at a given initial void ratio the behaviour of the material prepared with cyclohexane is very similar to that of the dry material. It is worth noting that the two pore fluids have similar static dielectric constant;
b. the compression curves of both cyclohexane-saturated and dry materials intersect the normal compression lines of the material reconstituted with aqueous solutions, clearly indicating an increase in shear resistance at the particles' contacts;

c. swelling is noticeable in water, it is much lower in the solution and practically negligible for the material in cyclohexane and for dry material.

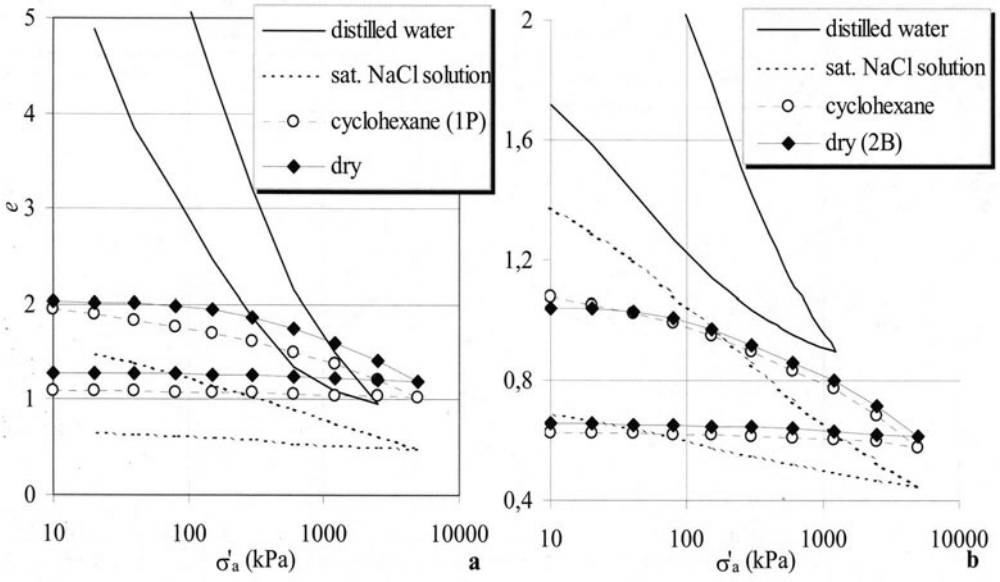

Figure 10. Comparison among oedometer curves relative to the Ponza bentonite (a) and the Bisaccia clay (b) dry, and reconstituted with distilled water, saturated NaCl solution and cyclohexane.

A behaviour qualitatively similar to that of the Ponza bentonite is exhibited by the Bisaccia and Marino clays (Figures 10.b and 11.a respectively), with the effects decreasing as the smectitic percentage decreases. Contrarily to the other materials, the slope of the compression curve of kaolin reconstituted with cyclohexane is slightly higher than that obtained by using aqueous solutions (Figure 11.b).

The differences are best seen in Figure 12 which reports the compression index C_c - evaluated for an increment of axial stress from 150 kPa to 300 kPa - against static dielectric constants of the considered pore fluids. It can be observed that the dependence of C_c on D is very strong. Furthermore, it can be observed that differences among the different materials become noticeable for values of D higher than about 70. Analogous trend can be observed for the swelling index C_s (Figure 13). Figure 14, which reports C_c* against e_L for the considered soils reconstituted with water, with the NaCl solutions and with organic solvents, compares these results to those reported by Burland (1990) and to the line $C_c^* = 0{,}256e_L - 0{,}04$ found by the Author as the best fit regression line to data reported in the literature. The point relative to the Ponza bentonite reconstituted with distilled water has not been reported because it is out of the range of validity of the relation (which holds for $0.6 < e_L < 4.5$), and in fact it would lie well above the regression line. The figure shows that there is a good agreement among data obtained by mixing different materials with distilled water and those obtained by mixing the same material with other pore fluids. So, the state of the materials at the liquid limit can be considered

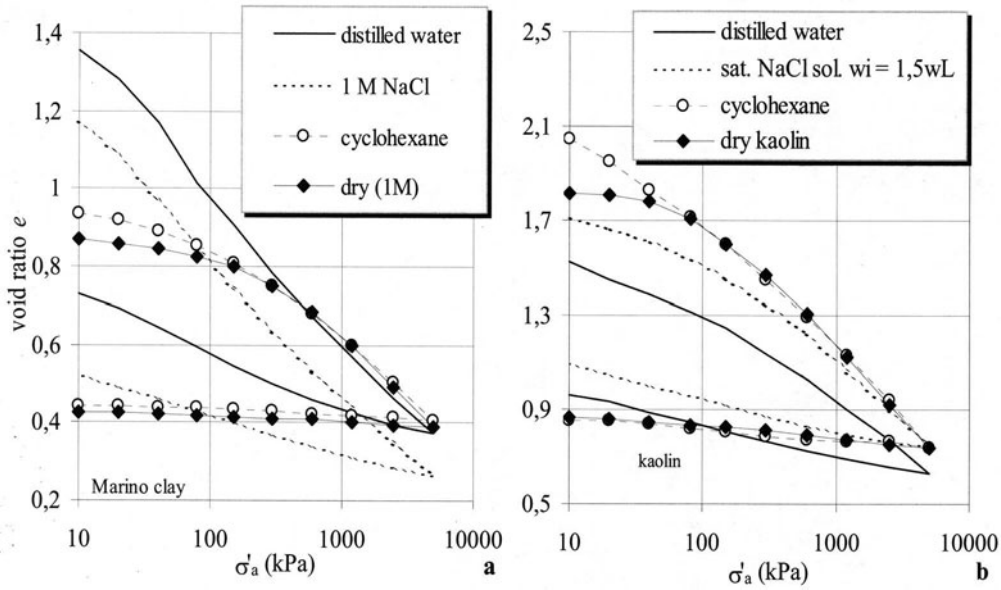

Figure 11. Comparison among oedometer curves relative to the Marino clay (a) and the commercial kaolin (b) dry, and reconstituted with distilled water, concentrated NaCl solution and cyclohexane.

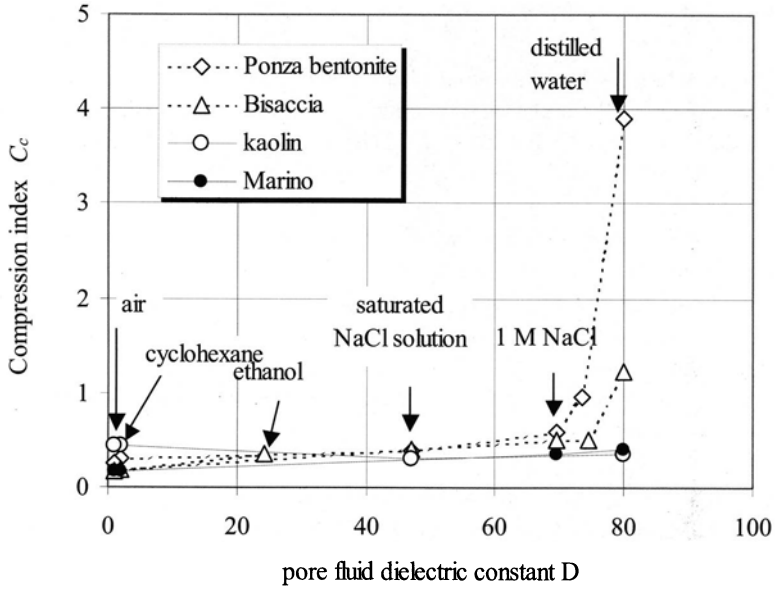

Figure 12. Compression index evaluated in the range 150 kPa - 300 kPa against pore fluid static dielectric constant.

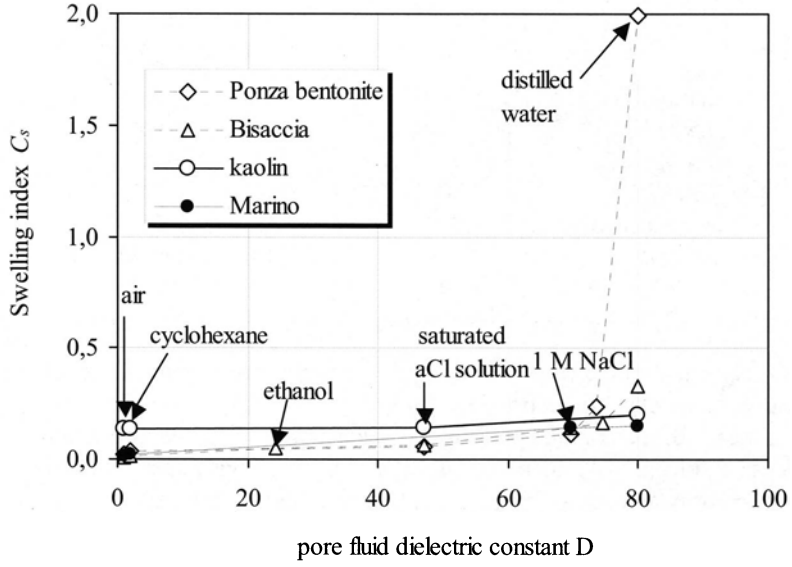

Figure 13. Swelling index C_s in the range 150 kPa - 300 kPa against pore fluid static dielectric constant.

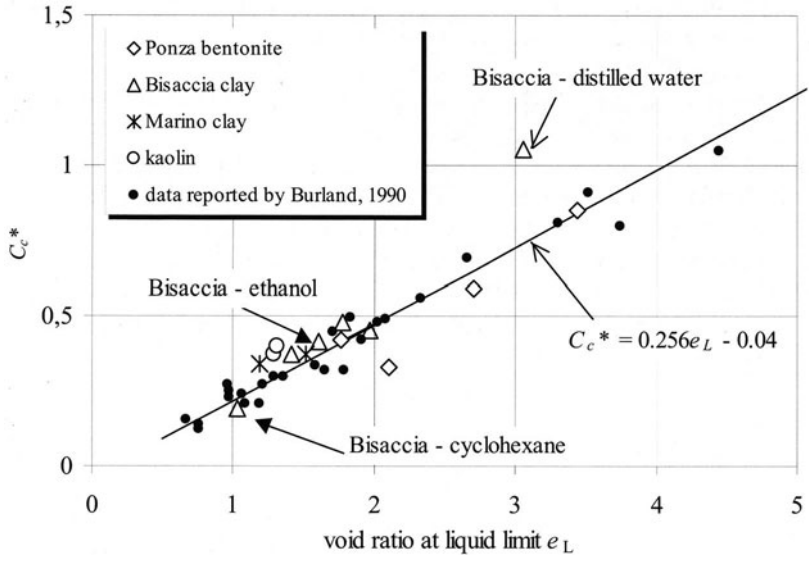

Figure 14. Intrinsic compression index $C_c^* = e^*_{100} - e^*_{1000}$ against void ratio e_L at the liquid limit.

Table 2. Intrinsic compression index $C_c^* = e^*_{100} - e^*_{1000}$ against void ratio e_L at the liquid limit.

	Ponza bentonite		Bisaccia clay	
	e_L	C_c^*	e_L	C_c^*
distilled water	10.8	3.80	3.06	1.05
0.5 M NaCl			1.97	0.45
0.6 M NaCl	3.43	0.85		
1 M NaCl	2.70	0.59	1.77	0.48
sat. NaCl solution	1.77	0.42	1.41	0.37
ethanol			1.61	0.42
cyclohexane	2.09	0.33	1.03	0.19

as a reference state also in the case of pore liquids different from water. Data relative to Ponza bentonite and Bisaccia clay are reported by Table 2.

A high influence of mineral and pore fluid composition is observed also on time trend of volume change. The influence of mineral composition is best seen on water-saturated materials. The coefficients of consolidation c_v and swelling c_s - determined on the experimental curves of displacements by the log-time method based on the Terzaghi model - are reported against axial stress in Figures 15 and 16 respectively for the extreme types of soils, bentonite and kaolin, and for their mixtures at various percentages. For bentonite contents equal to 50% and 80%, the curves are very close to that of 100% bentonite; furthermore, c_v decreases with axial stress increasing. For bentonite percentages equal to or lower than 20%, c_v and c_s increase with decreasing bentonite content, as expected on the basis of previous experimental results (among others: Yin, 1999), and increase with axial stress. The results obtained for the Bisaccia and Marino clays show that the values of c_v and c_s are close to those relative to the bentonite – kaolin mixtures containing similar percentages of montmorillonite (Di Maio et al. 2003).

The influence of pore solution concentration on c_v and c_s is noticeable in all the considered stress range (Figure 17). The difference between the material reconstituted with distilled water and that reconstituted with 1 M NaCl solution is of about two orders of magnitude in the case of the Ponza bentonite, lower for the Marino clay. The Bisaccia clay behaves similarly to the Ponza bentonite, whereas no influence was found for kaolin. For all the materials prepared with the organic fluid, consolidation occurred in a few seconds. Only under the highest stress levels for the Ponza and Bisaccia clays c_v could be determined by the *log-time* method, and a value of 0.015 cm^2/sec was obtained. This value is much higher than that obtained for the materials reconstituted with aqueous solutions.

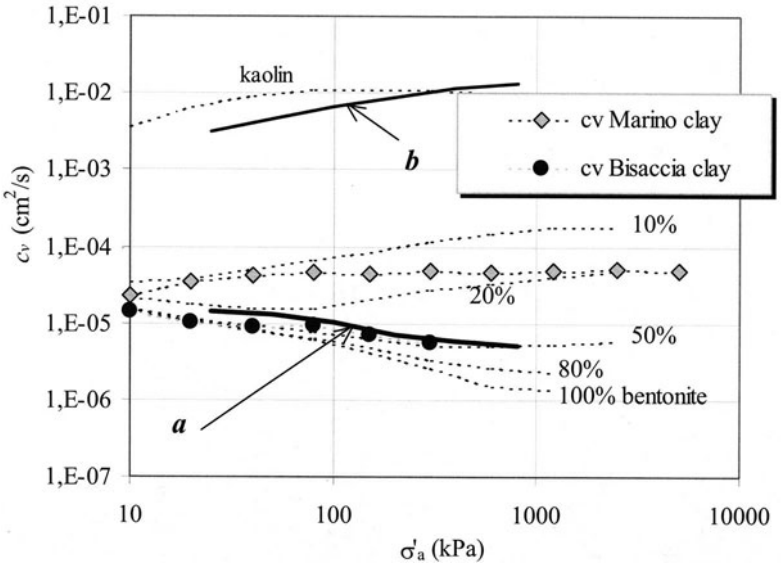

Figure 15. One-dimensional coefficient of consolidation c_v against axial stress for bentonite-kaolin mixtures reconstituted with distilled water and for the Bisaccia and Marino clays. Curves **a** and **b** were determined by Robinson and Allam (1998) for a montmorillonite and a kaolinite respectively.

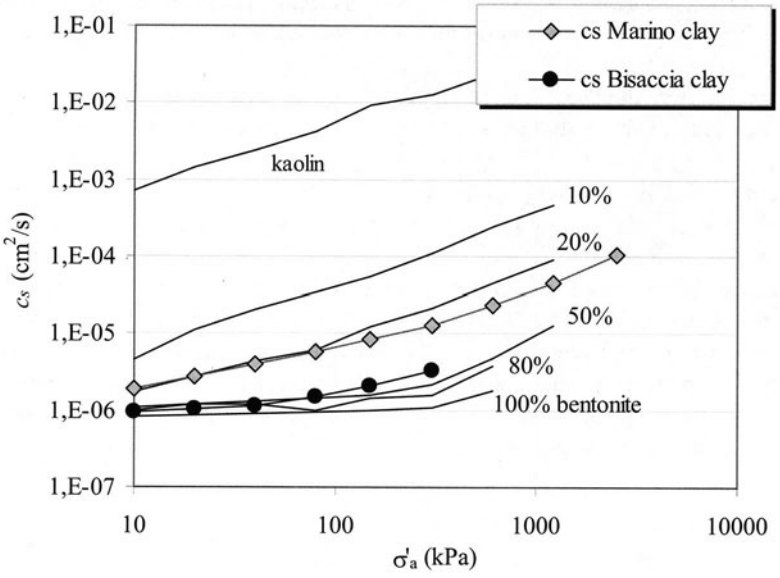

Figure 16. One-dimensional coefficient of consolidation c_s against axial stress for bentonite-kaolin mixtures reconstituted with distilled water and for the Bisaccia and Marino clays.

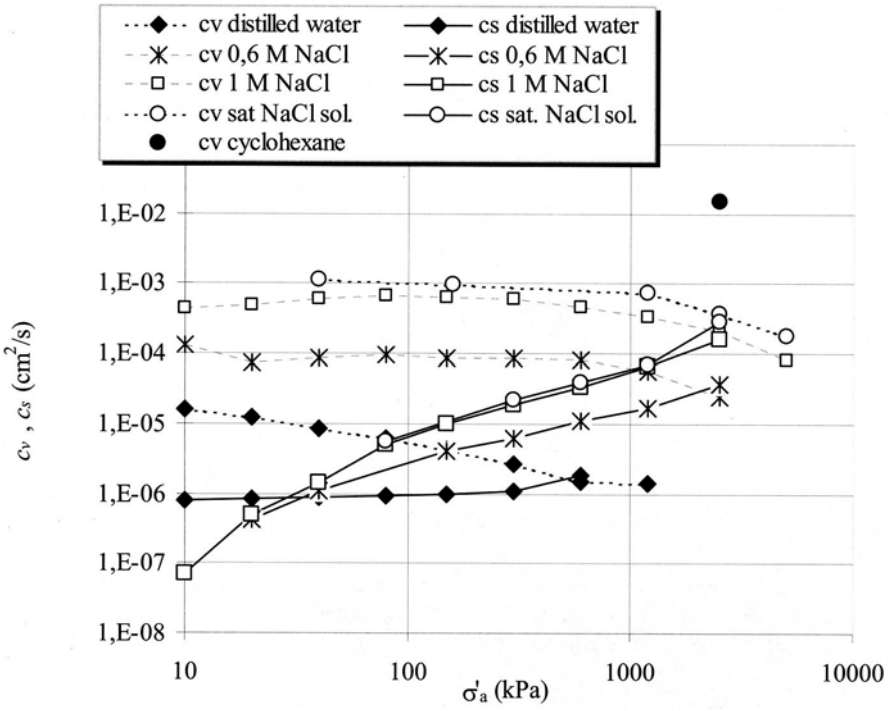

Figure 17. One-dimensional coefficients of consolidation c_v and swelling c_s against axial stress for the Ponza bentonite reconstituted with distilled water, with NaCl solutions and cyclohexane.

Under the hypothesis of the Terzaghi model of one-dimensional consolidation, a first approximate value of the hydraulic conductivity k in the axial direction can be obtained from the relation $c_v = kE_{ed}/\gamma_w$. Figure 18 reports k against void ratio for the considered soils and for mixtures bentonite-kaolin with a given percentage of bentonite. As expected, differences up to four degrees of magnitude are found between kaolin and bentonite; 10% bentonite is sufficient to cause large decrease in permeability with respect to kaolin; the values obtained for the Bisaccia clay and for the Marino clay are very close to those obtained for the artificial mixtures with a similar percentage of montmorillonite. It is interesting to observe that variations due to pore fluid are of the same order of magnitude as those due to mineral composition and grain size. In the case of the Ponza bentonite reconstituted with cyclohexane, the value of k is practically equal to that obtained for kaolin at the same void ratio (Figure 19). Furthermore, analogous variations are found in terms of intrinsic permeability.

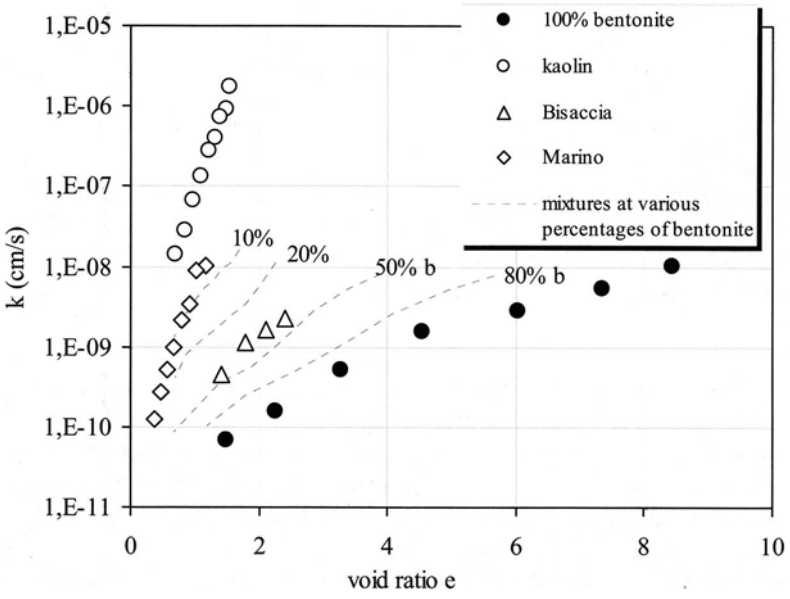

Figure 18. Hydraulic conductivity against void ratio of bentonite-kaolin mixtures and of the Bisaccia and Marino clays reconstituted with distilled water.

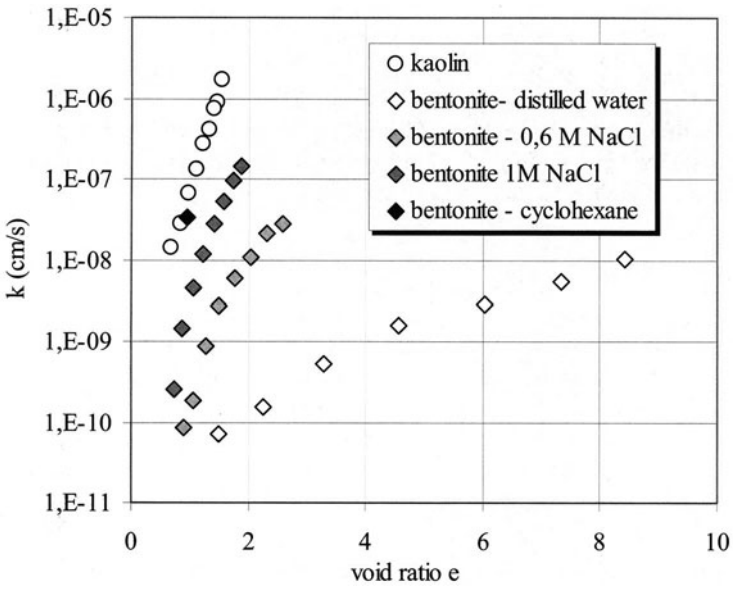

Figure 19. Hydraulic conductivity of the Ponza bentonite with different types of pore fluids.

5 Conclusions

Oedometric compression experiments are presented with different basic skeleton minerals, different smectite contents, and finally different pore fluids. Compressibility and unloading moduli in one -dimensional strain states, as well as the initial void ratio, are the study focus. The results show that:

a) Volume change behaviour of artificial mixtures and natural soils reconstituted with distilled water is strongly influenced by mineral composition and, in particular, by the smectite fraction. The influence depends on the stress level. With increasing axial stress, the influence on compression and swelling indices decreases, whereas it increases on the coefficients of consolidation and swelling.

b) An increase in pore solution concentration makes the materials compressibility decrease and the coefficients of consolidation and swelling increase, with the exception of c_s at low stress levels and for high smectite content. The differences among the different materials reduce greatly.

c) The materials prepared with cyclohexane behave more similarly to the dry ones than to those prepared with aqueous solutions. Compressibility is much lower, the coefficient of consolidation increases dramatically and swelling is negligible in the whole considered stress range.

d) The great differences in behaviour among different clayey soils are essentially due to their different interaction with water or with high dielectric constant fluid.

Further experimentation with fluids different from water but with the same dielectric constant - or with dielectric constant higher than 80 - is now under examination in order to complete the analysis.

Acknowledgements

The Authors wish to thank Dr. Giovanni Mongelli who performed X-ray diffraction analysis, Dr. Rossella Coviello for her help in performing some of the tests and Dr. A. Brancucci who evaluated the specific surface As.

References

Abdullah, W., Al-Zou'bi, M. S., and Alshibi, K. A. (1997). On physicochemical aspects of compacted clay compressibility. *Canadian Geotechnical Journal*, vol. 34, pp. 551 – 559.

Barbour, S. L. (1987). Osmotic flow and volume changes in clay soils. *Ph.D. Thesis*, Dept. of Civil Engineering, University of Saskatchewan, Saskatoon, Canada.

Barbour, S. L., and Fredlund, D. G. (1989). Mechanisms of osmotic flow and volume change in clay soils. *Canadian Geotechnical Journal*, vol. XXVI, pp. 551-562.

Bolt, G. H. (1956). Physico-chemical analysis of the compressibility of pure clays. *Géotechnique*, vol. VI, n.2, pp. 86-93.

Burland, J. B. (1990). On the compressibility and shear strength of natural clays. *Géotechnique*, vol. XL, n. 3, pp. 329 - 378.

Chen, J., Anandarajah, A., and Inyang, H. (2000). Pore Fluid Properties and Compressibility of Kaolinite. *ASCE J. Geotechnical and GeoEnvironmental Engineering*, 126, n. 9, p. 798 – 807.

Di Maio, C. (1996a). The influence of pore fluid composition on the residual shear strength of some natural clayey soils. *VII International Symposium on Landslides*, vol. II, pp. 1189 -1194.

Di Maio, C. (1996b). Exposure of bentonite to salt solution: osmotic and mechanical effects. *Géotechnique*, vol. XLVI, n. 4, pp. 695 - 707.

Di Maio, C. (1998). Discussion on Exposure of bentonite to salt solution: osmotic and mechanical effects. *Géotechnique*, vol XVVIII, No. 3, 433 - 436.

Di Maio, C., and Onorati R. (2000a). Swelling behaviour of active clays: the case of an overconsolidated, marine origin clay. *Proceedings of the VIII International Symposium on landslide*, Cardiff, Vol. 1, 469 – 474.

Di Maio, C. and Onorati, R. (2000b). Osmotic softening of overconsolidated clays. *Proceedings of the International Conference on Geotechnical & Geological Engineering*, Melbourne.

Di Maio, C., Santoli, L. and Schiamone, P. (2003). Volume change behaviour of clays: the influence of mineral composition, pore fluid composition and stress state. *Mechanics of materials*, in press

Lupini, J. F., Skinner, A. E., and Vaughan, P. R. (1981). The drained residual shear strength of cohesive soils. *Géotechnique* 31, No.2, pp. 181-213.

Marcial, D., Delage, P. and Cui, Y. J. (2001). Effect of exchangeable cations on the compressibility of bentonite clays. *Proc. Of the international workshop Chemo-mechanical coupling in clays – from nano-scale to Engineering Applications*. Balkema, The Netherlands, pp. 177 – 187.

Mesri, G., and Olson, R. E. (1971). Consolidation characteristics of montmorillonite. *Géotechnique*, vol. XXI, n. 4, pp. 341-352.

Mesri, G., Ullrich, C. R. and Choi, Y. K. (1978). The rate of swelling of overconsolidated clays subject to unloading. *Géotechnique*, vol. XXVIII, n. 3, pp. 281-307.

Mitchell, J. K. (1993). Fundamentals of soil behaviour. 2nd ed. John Wiley & Sons, Inc.

Olson, R. E., and Mesri, G. (1970). Mechanisms controlling the compressibility of clays. *J. Am. Soc. Civ. Engrs.* Vol. 96, 1853 – 1878.

Robinson, R. G., and Allam, M. M. (1998). Effect of mineralogy on coefficient of consolidation. *Clays and clay Minerals*. 46 (5) pp.596 – 600.

Sridharan, A., and Ventakappa, Rao G. (1973). Mechanisms controlling volume change of saturated clays and the role of the effective stress concept. *Géotechnique*, vol. XXIII, n. 3, pp. 359-382.

Sridharan, A., Rao, S. M., and Murthy, N. S. (1986a). Compressibility behaviour of homoionized bentonites. *Géotechnique*, vol. XXXVI, pp. 551-564.

Sridharan, A., Rao, S. M., and Murthy, N. S. (1986b). Liquid limit of Montmorillonite soils. *ASTM, Geotech. Test. Jl.*, vol. IX, pp. 156-159.

Sridharan, A., and Prakash, K. (1998). Characteristic water contents of a fine-grained soil-water system. *Géotechnique*, vol. 48, No.3, 337-346.

Sridharan, A. (1991). Engineering behaviour of fine grained soils. *Indian Geotechnical Journal*, vol. XXI, n. 1, pp. 1-136.

Sridharan, A. (2001). Engineering behaviour of clays: Influence of mineralogy. *Proc. Of the international workshop Chemo-mechanical coupling in clays – from nano-scale to Engineering Applications*. Balkema, The Netherlands, pp. 3 – 28.

Yin, J. H. (1999). Properties and behaviour of Hong Kong marine deposits with different clay contents. *Canadian Geotechnical Journal*, vol. 36, pp. 1085 – 1095.

Consolidation, Swelling and Swelling Pressure Induced by Exposure of Clay Soils to Fluids Different from the Pore Fluid

Caterina Di Maio

Dipartimento di Strutture, Geotecnica, Geologia Applicata all'Ingegneria, Università della Basilicata, Italy

Abstract. This paper reports experimental results relative to volume changes caused by exposure of clay soils to fluids different from the pore fluid. Furthermore it reports some results relative to the influence of pore fluid composition on the swelling pressure of an active smectitic clay. The experimentation on volume change behaviour was carried out on several clay soils with different grain size distribution and mineral composition. The results show that exposure of water saturated Ponza bentonite to NaCl, KCl and $CaCl_2$ solutions causes consolidation. At high void ratio, pores and fissures form. On re-exposure to water, Na^+ effects are reversible and the material swells noticeably. On the contrary, Ca^{2+} and K^+ make swelling potential decrease greatly because they substitute Na^+ as counterions. Under low values of axial stress and high void ratio, potassium and calcium effects can be reverted by exposing the material to concentrated NaCl solutions. The effects of exposure to electrolytes of soils with a smectite content between 10 % and 30 % - such as Bisaccia, Gela and Marino clays - are lower than those on the Ponza bentonite, however they are noticeable. Furthermore, depending on axial stresses, type of solution and on types of exchangeable cations, swelling caused by subsequent exposure to distilled water can be lower or higher than previous consolidation. The commercial kaolin, the Potenza and the Villa d'Agri clays undergo small consolidation as an effect of exposure to the salt solution and further large consolidation because of subsequent exposure to water. The Milazzo clay undergoes swelling because of exposure to NaCl solution. The results relative to volume change can be interpreted qualitatively in terms of double layer processes, ion exchange and initial fabric. Results relative to swelling pressure show that Bolt's model interprets satisfactory the behaviour of the Bisaccia clay reconstituted with a concentrated salt solution and exposed to distilled water. As expected, the model interprets only qualitatively the behaviour of the material exposed to concentrated salt solutions.

1 Introduction

Exposure of active clays such as smectites to fluids with ion concentration higher or – in the case of organic fluids – dielectric constant lower than that of the pore fluid, can cause volume decrease (Mitchell et al., 1973; Barbour and Fredlund 1989; Sridharan, 1991; Di Maio, 1996a; 1996b). During the chemically induced volume change, fissures and cracks can open and permeability can increase greatly, notwithstanding the overall volume decrease (Barbour, 1987). This process can occur in clay barriers of waste disposal systems as an effect of the

interaction with leachates. It often occurs in bentonite layers used as "impermeable" protection to retaining walls, probably as an effect of chemical interaction with concrete calcium ions.

On exposure to water, active clays exhibit tendency to swell. Chemically induced swelling depends on the composition of the clay, on the composition of the pore fluid, on void ratio and stress level. At low stress level, swelling caused by exposure to water of clays reconstituted with a concentrated salt solution can be extraordinarily high. Some experimental results relative to marine origin clay shales show that interaction with rain water is the most probable cause of the large difference in water content and shear strength between the upper layer, which is often a few meters thick, and the underlying material (Di Maio and Onorati, 2000a; 2000b).

Swelling pressure can be defined as the pressure required to keep a soil element at constant volume, when hydraulic or chemical conditions are such as to induce a tendency to volume increase. In actual applications, swelling pressure is a very important parameter for the design of structures interacting with swelling soils and rocks. It must be evaluated in order to prevent damage to tunnels and to any stiff support of excavation surfaces, as well as in order to design safe shallow foundations, both in the case they are designed to resist differential movements and in the case they are designed to adjust to them by means of flexible construction (Abduljauwad et al., 1998). Furthermore, in order to prevent opening of cracks and fissures, high swelling pressure must be a property of materials constituting impermeable barriers. Exposure to a fluid whose ionic force is lower or whose dielectric constant is higher than that of the pore fluid is among the possible causes of high swelling pressure.

This paper reports experimental results relative to volume changes caused by exposure of clay soils of different composition to fluids different from the pore fluid. Some results relative to the influence of pore fluid composition on swelling pressure are also reported.

2 Materials and Methods

The experimentation was carried out on several different soils. The Ponza bentonite, Bisaccia and Marino clays, and the commercial kaolin are described in the companion paper on the influence of pore fluid composition on volume change behaviour of clays exposed to the same fluid as the pore fluid. Besides these soils, a very active commercial bentonite was also tested, with a clay fraction higher than that of the Ponza bentonite (Figure 1). Some tests were carried out on the Gela, Villa D'Agri, Milazzo and Potenza soils. The liquid limits of the four latter soils are: 149 %, 53 %, 58 % and 30 % respectively; their clay fractions: 73 %, 38 %, 45 %, 25 %. The liquid limit of the commercial bentonite was evaluated by mixing the air-dried powder with different salt solutions at various concentrations and with HCl solutions at various pH. The results show that w_L decreases dramatically with the molarity of all the considered solutions (Figure 2). $MgCl_2$ and $CaCl_2$ solutions effects seem to be higher than those of NaCl and KCl solutions. It is interesting to observe that HCl effects are similar to those of the first two solutions up to 0.32 M which corresponds to pH = 0.5.

Reconstituted materials were prepared by mixing the powdered soils with a given fluid to a slurry at about the liquid limit. Volume change response of exposure to fluids different from the pore fluid was evaluated in the course of fixed-ring oedometer tests. The specimens (2 cm thick) were first consolidated to fixed axial stress, doubling the pressure for successive loads. Subsequently they were exposed to a given fluid by replacing the cell fluid. Swelling pressure was evaluated by using Geonor continuous oedometer swelling equipment in a strained controlled manner, and by means of conventional oedometers with controlled axial load.

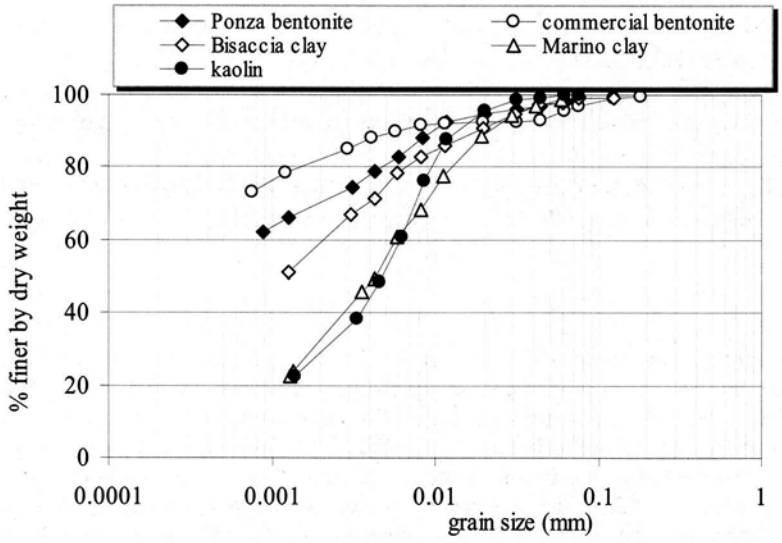

Figure 1. Grain size distribution curves of the commercial bentonite and of the other materials.

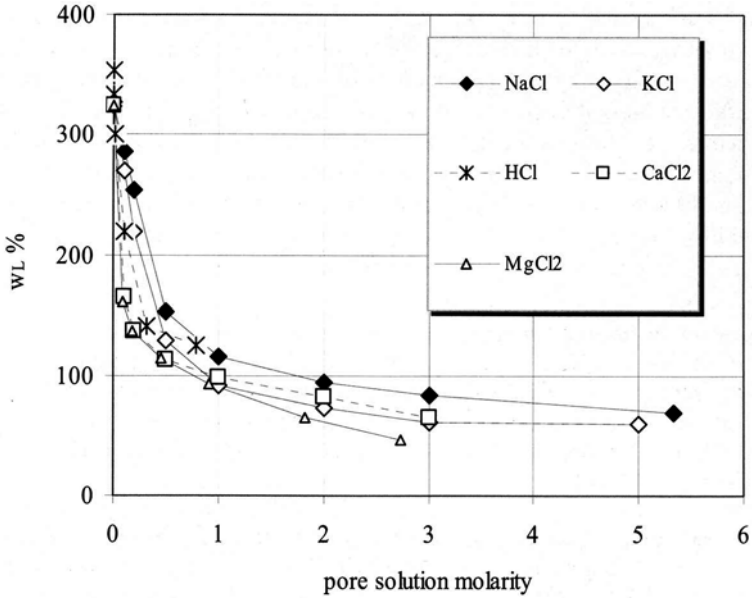

Figure 2. Liquid limit w_L of the commercial bentonite against molarity of pore solutions.

3 Chemically induced volume changes

The results relative to the Ponza bentonite are easier to interpret than those relative to the other considered soils. In fact, since it is a practically pure Na-montmorillonite, exposure to NaCl solutions doesn't cause that negligible ion exchange and thus it is possible to analyse separately the influence of pore solution concentration. The behaviour of the other natural soils is more complex because their clay minerals are heteroionic and exposure to a salt solution generally causes also ion exchange.
So, the results relative to the Ponza bentonite and some results relative to the commercial bentonite will be analysed first, and then those relative to the other soils.

3.1 Bentonite

3.1.1 Exposure to salt solutions. The technical literature reports several experimental results relative to the effects of such exposure (among others: Barbour and Fredlund, 1989; Di Maio, 1996a; 1996b; 1998). As an example, Figure 3 reports compressive volumetric strains against time for a specimen of the Ponza bentonite prepared with water at the liquid limit. The curve on the left represents consolidation for an increment of axial stress from 20 kPa to 40 kPa. Once the equilibrium had been reached, the cell water was substituted by a saturated NaCl solution. This substitution produced further consolidation, represented by the curve on the right of the arrow. Pore pressure measurements showed that this compression occurred under constant Terzaghi's effective stresses; so, in terms of void ratio e against $log\ \sigma'_a$, it is a straight line normal to the abscissa. As axial stress increases and initial void ratio decreases, consolidation caused by exposure to the salt solution decreases (Figure 4).

Effects analogous to those caused by NaCl solution are caused also by other salt solutions (Figure 5) or by other fluids with more complex composition (Figure 6). In order to observe directly the process occurring during chemically induced consolidation, a specimen was mounted in a transparent oedometer and observed during exposure to a 1 M $CuSO_4$ solution. During the chemical consolidation, the specimen shrank and large pores and fissures were observed to form (Figure 7). This process was observed in laboratory under values of axial stress lower than 80 kPa on normally consolidated Ponza bentonite. Obviously, such an effect makes permeability increase greatly. For higher stresses, the phenomenon does not occur, at least at a macroscopic level, and at least in times of laboratory tests.

3.1.2 Re-exposure to distilled water. In order to test the reversibility of salt effects, when equilibrium was reached under the new conditions imposed by the electrolytes, the specimens which had been previously exposed to salt solutions, were re-exposed to distilled water. Such exposure caused noticeable swelling of the material which had been previously exposed to NaCl solution. On the contrary, it caused much lower effects on the materials which had been exposed to KCl and $CaCl_2$ solutions.

Figure 8 refers to a water saturated specimen of the Ponza bentonite that had been previously consolidated in oedometer at 40 kPa, and then exposed alternately to salt solutions and to water. After seven cycles of exposure to a saturated NaCl solution and to water, the specimen was exposed to a saturated KCl solution. Under these new conditions, exposure to water, which followed the chemical consolidation, caused a much lower swelling than during the previous

cycles. Analogous swelling behaviour was exhibited in the second cycle of exposure to KCl solution and then to water. Afterwards, the specimen was exposed to a saturated NaCl solution

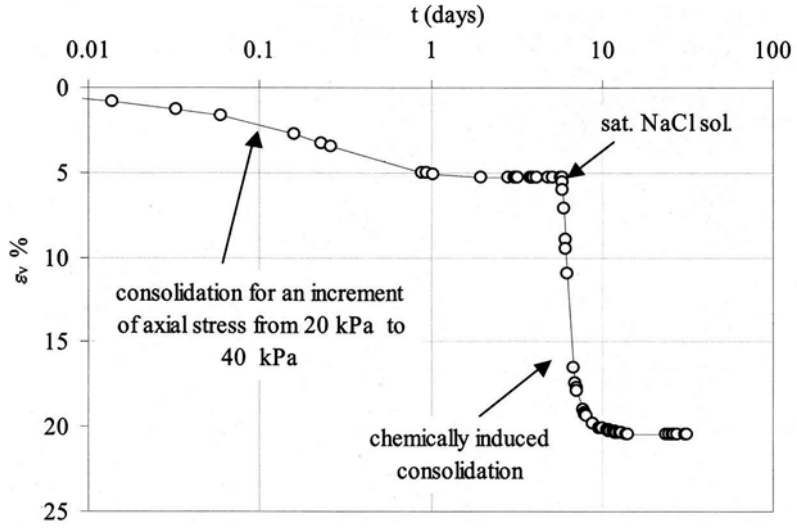

Figure 3. Mechanical consolidation and consolidation caused by exposure of the Ponza bentonite to a saturated NaCl solution.

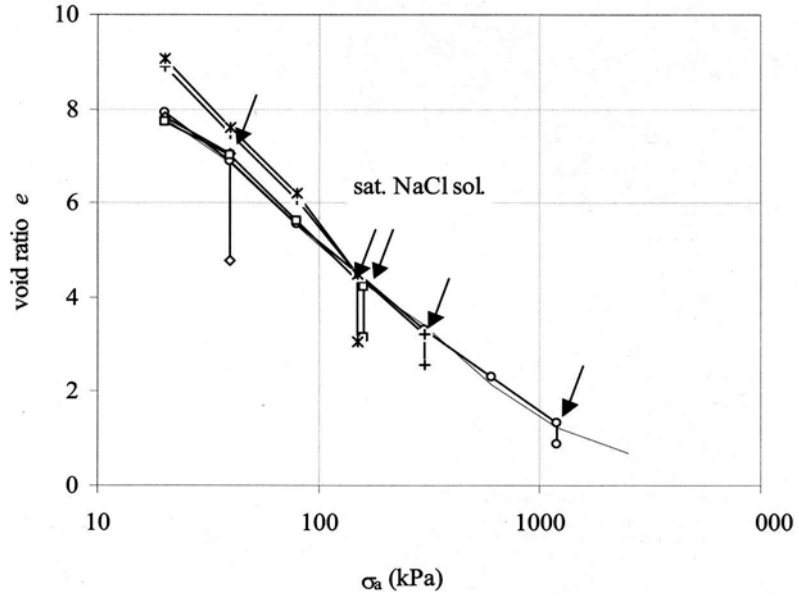

Figure 4. One-dimensional compression curves of the Ponza bentonite reconstituted with distilled water, initially compressed while submerged in water, and subsequently exposed to a saturated NaCl solution.

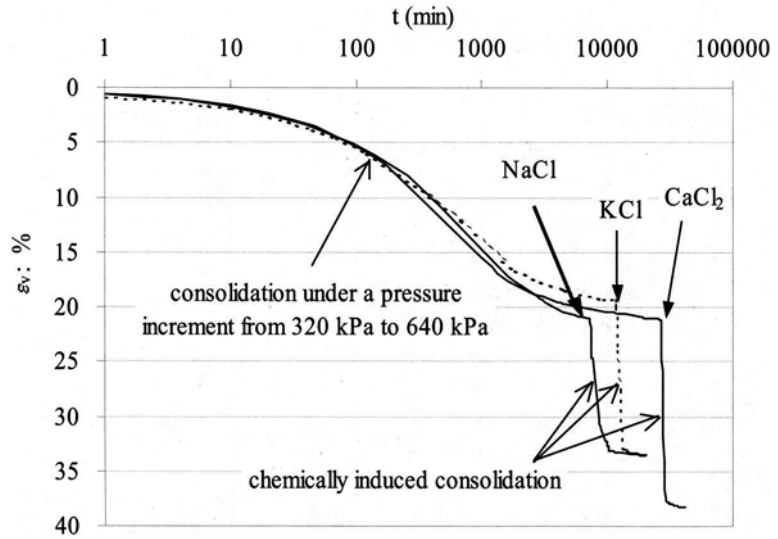

Figure 5. Consolidation of the Ponza bentonite caused by exposure to saturated NaCl, KCl and $CaCl_2$ solutions.

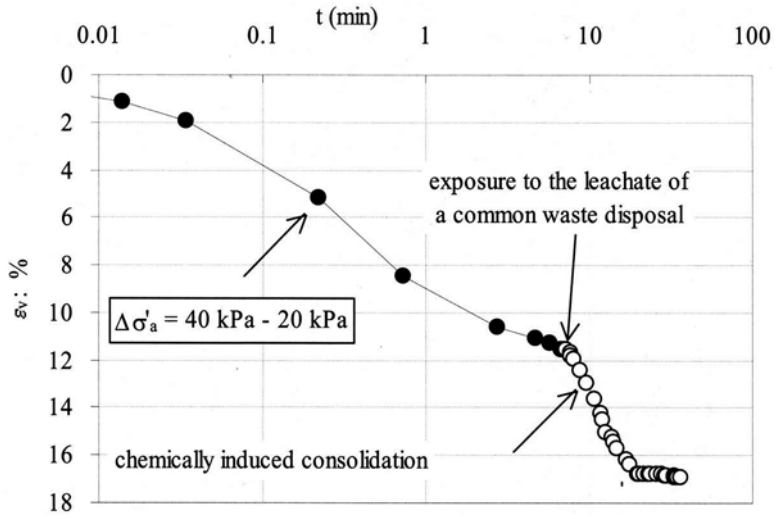

Figure 6. Consolidation of the Ponza bentonite caused by exposure to a common waste disposal leachate.

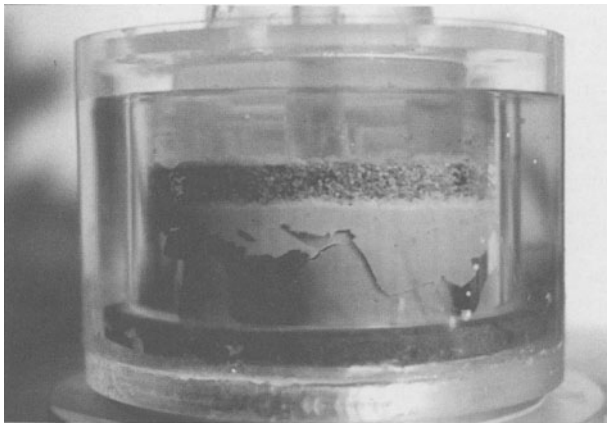

Figure 7. Ponza bentonite after exposure to a 1 M $CuSO_4$ solution.

and then to water. The latter exposure caused a very large osmotic swelling, close to that obtained before using KCl, thus showing that K^+ effects can be reverted by imposing appropriate conditions. Analogous behaviour was manifested by the material after exposure to $CaCl_2$. Exposure to water after the osmotic consolidation did not cause any volume increase. Subsequent exposure to a saturated NaCl solution caused a further small consolidation, and the following exposure to water caused large swelling. This behaviour, which can be reasonably considered as an indirect evidence of the occurrence of ion exchange, has been observed also on other smectitic soils.

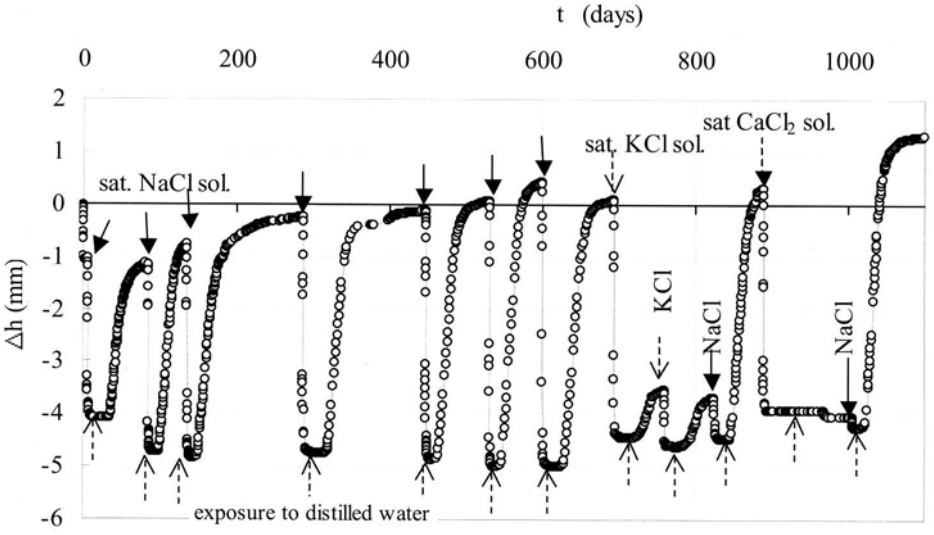

Figure 8. Consolidation caused by exposure to salt solutions and swelling caused by exposure to distilled water of a specimen of Ponza bentonite reconstituted with distilled water (Di Maio, 1998).

3.1.3 Influence of stress level and stress history. Figure 9 refers to two specimens of the Ponza bentonite reconstituted with distilled water. The specimens were one-dimensionally consolidated under axial stresses equal to 40 kPa and 960 kPa respectively. At equilibrium, they were exposed to a concentrated NaCl solution. Such exposure caused volume decrease. At equilibrium, the specimens were exposed to distilled water: this caused swelling. The figure shows that osmotic consolidation decreases with axial stress increasing (i.e. with void ratio decreasing). Furthermore, swelling is practically equal to the previous chemically induced consolidation at low axial stress, it is lower under higher values of axial stress.

However, if the material that undergoes osmotic consolidation at the higher external axial stresses is unloaded and then re-exposed to distilled water, swelling becomes such as to reach the swelling curve of the water-saturated material. This is shown by Figure 10 which reports the results of oedometer tests on four specimens of the Ponza bentonite. Specimen *a* was reconstituted with distilled water at about the liquid limit and immersed in distilled water. Specimen *b* was reconstituted with a saturated NaCl solution at the liquid limit evaluated with the same solution and immersed in it. Specimens *c* and *d* were prepared as specimen *a* and, after consolidation at 1500 kPa and 40 kPa respectively, they were exposed to a saturated NaCl solution, by simply replacing the cell fluid. Such exposure caused consolidation represented by straight lines normal to the abscissa. At equilibrium the specimens were loaded and then unloaded. After swelling at 40 kPa and at 20 kPa respectively, specimens *c* and *d* were exposed to distilled water again. This produced an increase in void ratio which made the specimens reach the swelling curve of specimen *a*. It is interesting to observe the behaviour of specimens with different load history. Figure 11 reports the results relative to a specimen of the Ponza bentonite which was exposed to the saturated NaCl solution under low void ratio, while on a re-compression curve. It was loaded up to 1200 kPa, unloaded until 10 kPa and then reloaded. At 300 kPa the specimen was exposed to a saturated NaCl solution and this caused consolidation. At the end of consolidation, the specimen was exposed to distilled water and water was continuously renewed in order to remove ions which could have diffused from the pore solution. In this case, swelling was practically equal to previous consolidation.

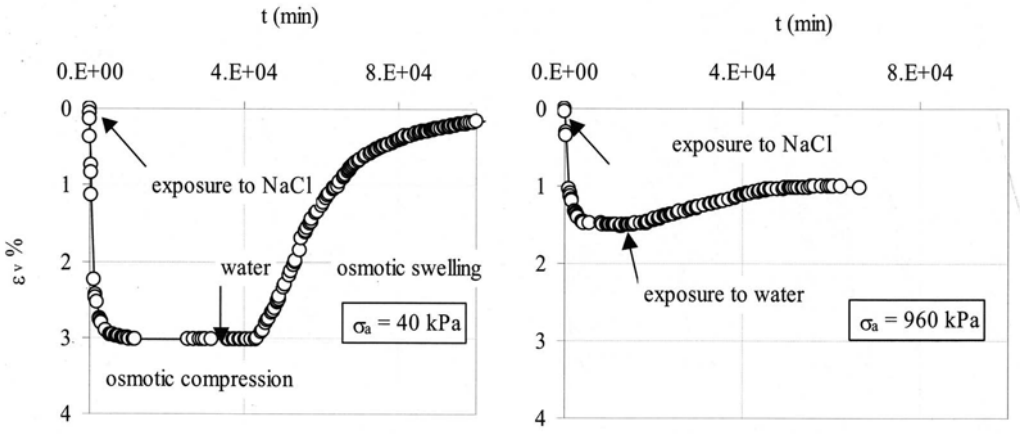

Figure 9. Consolidation caused by exposure to salt solutions and swelling caused by exposure to distilled water of a specimen of the Ponza bentonite reconstituted with distilled water.

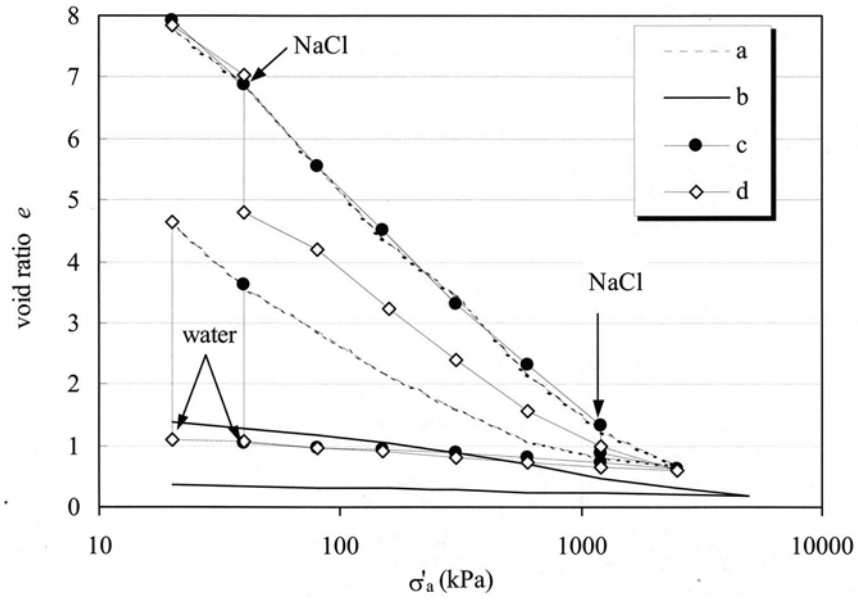

Figure 10. Consolidation caused by exposure to saturated NaCl solution and swelling caused by exposure to distilled water of the Ponza bentonite (Di Maio, 1996).

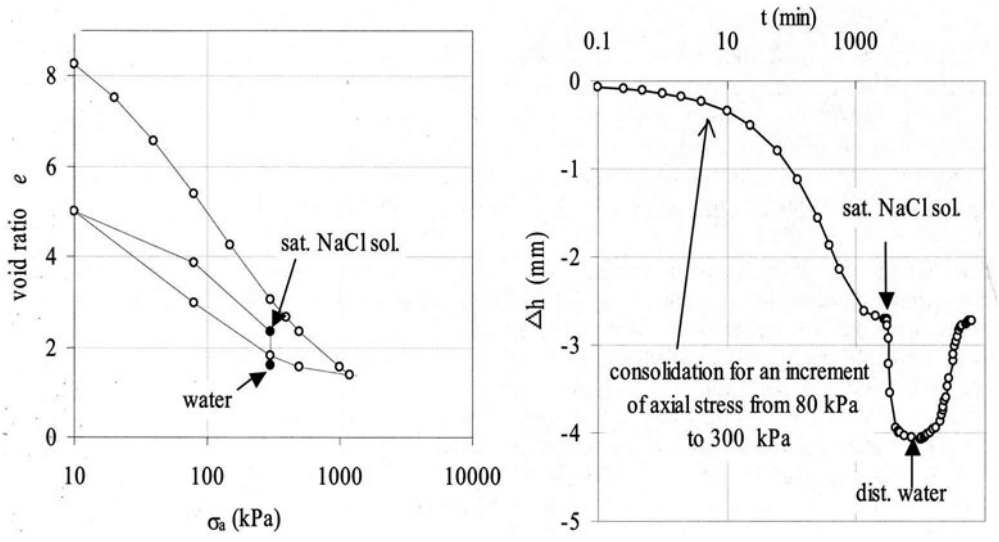

Figure 11. Consolidation caused by exposure to the electrolyte and swelling caused by exposure to water.

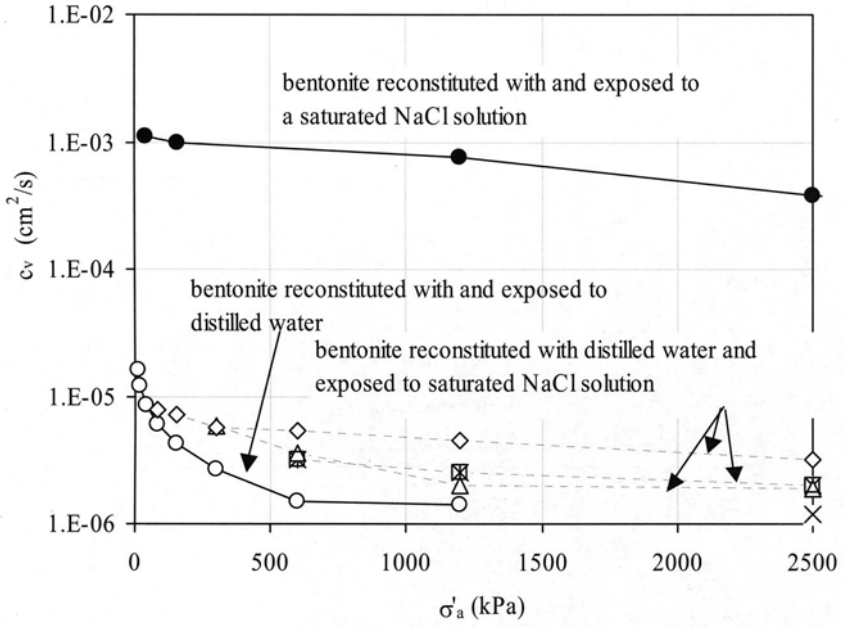

Figure 12. Coefficient of consolidation against axial stress for the Ponza bentonite reconstituted with water or saturated NaCl solution, and for the material reconstituted with water and subsequently exposed to the solution

Exposure to saturated salt solution causes noticeable consolidation, however the equilibrium condition doesn't reach the compression curve of the material prepared directly with the solution, clearly indicating a strong role of initial fabric. The influence of initial fabric is very strong also on the coefficient of consolidation. In fact, the coefficient of consolidation after exposure to the salt solutions is close to that of the material in water and it is very different from that of the material prepared directly with the solution (Figure 12).

3.1.4 Influence of ion concentration. A set of water saturated specimens of the Ponza bentonite was consolidated to 80 kPa and, at the end of mechanical consolidation, each specimen was exposed to a NaCl solution at a given molarity. Figure 13, which reports the results in terms of volumetric strains against the solution molarity, shows that chemical consolidation increases with increasing ion concentration. The largest variations occur in the range 0 – 0.5 M.

After consolidation due to exposure to the salt solutions, the specimens were re-exposed to distilled water. Figure 13 reports the results in terms of absolute values of volumetric strains $|\varepsilon_s|$ during swelling. The comparison with volumetric strains due to previous consolidation shows that the difference between consolidation and swelling slightly increases with increasing solution molarity.

The influence of ion concentration has been analysed also with reference to HCl solutions. Four specimens of the commercial bentonite were reconstituted with distilled water at the liquid limit, compressed up to 80 kPa while submerged in distilled water. At the end of mechanical

consolidation, three specimens were exposed to HCl solutions at pH = 4; 2 and 0.5 respectively. The solution at pH = 4 did not cause but a slight tendency to swell followed by a negligible consolidation. With pH decreasing, both volume change and rate of consolidation increase (Figure 14). The test relative to pH = 0.5 was interrupted after about 3 days because some iron element of the apparatus started to be corroded. pH = 0.5 corresponds to 0.3 M HCl. The comparison with the consolidation curve obtained for the fourth specimen which was exposed to a 0.3 M NaCl solution shows that, at this molarity, HCl effects are higher than those of NaCl.

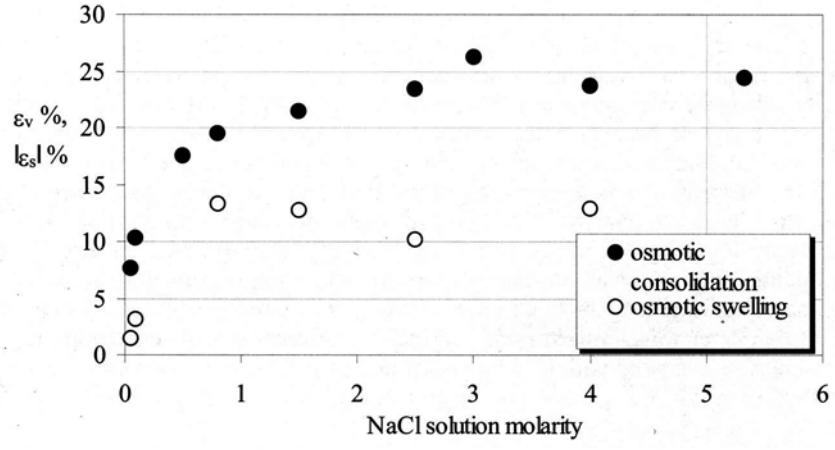

Figure 13. Volumetric strains of the Ponza bentonite caused by exposure to NaCl solutions.

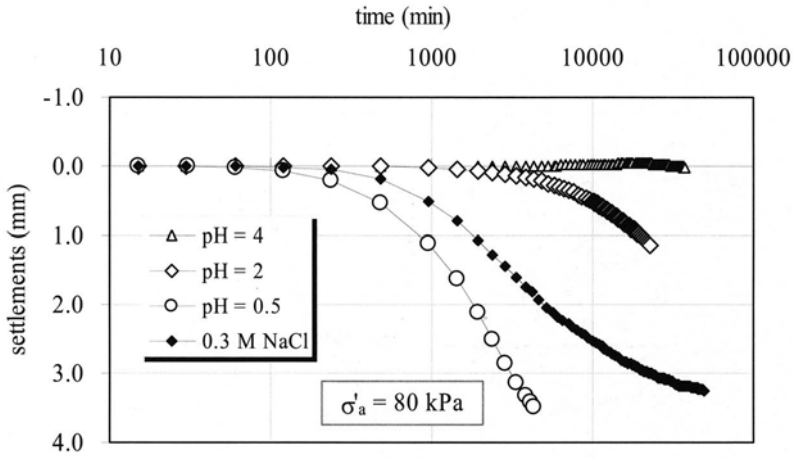

Figure 14. Consolidation of the commercial bentonite caused by HCl solutions at different pH and by 0.3 M NaCl solution.

3.2 Natural soils

Let's consider now the effects produced by exposure to salt solutions of natural soils with a clay fraction lower than that of the Ponza bentonite, with different clay minerals and different types of exchangeable cations.

Some specimens of the considered soils were reconstituted at about the liquid limit with distilled water and, after consolidation at 40 kPa, they were exposed to a saturated NaCl solution, by simply replacing the cell water. Exposure to the electrolyte produced noticeable volume decrease of the Bisaccia and Gela clays (Figure 15); smaller volume decrease for the Marino clay (Figure 16); negligible effects on the Villa d'Agri and Potenza clays (Figure 17) and on the commercial kaolin (Figure 18). At equilibrium, the cell solution was replaced by distilled water. Continuous water renewal produced swelling of the Bisaccia and Gela clays slightly higher than the previous consolidation. In the case of the Marino clay, swelling was much higher than consolidation. So, this specimen was exposed to NaCl solution again and, at the end of consolidation, to distilled water. During this second cycle, consolidation caused by exposure to the electrolyte was higher than in the first cycle and subsequent swelling due to exposure to distilled water was practically equal to the previous consolidation. The Potenza and the Villa d'Agri clays behaved differently from the above materials. They underwent small consolidation after exposure to the salt solution and a larger consolidation after the subsequent exposure to water (Figure 17), as in the case of the commercial kaolin (Figure 18). The behaviour of this latter was similar to that reported by Sridharan and Ventakappa Rao (1973) for a kaolin that was prepared with CCl_4 and that underwent osmotic consolidation because of an inward flow of water, that is, because of an increase in the dielectric constant of the pore fluid.

Once equilibrium after exposure to water was attained, the Bisaccia, Gela and Marino clays were exposed to saturated KCl solution (Figures 15, 16 and 17). This exposure produced a consolidation similar to that previously produced by NaCl. Then the specimens were exposed to distilled water again. The continuous water renewal produced swelling which, as expected, was much smaller than consolidation.

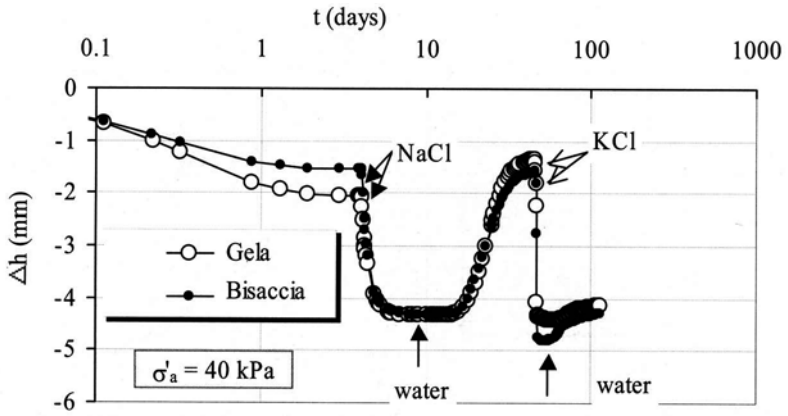

Figure 15. Consolidation of the Bisaccia and Gela clays caused by exposure to saturated NaCl and KCl solutions and swelling caused by exposure to distilled water.

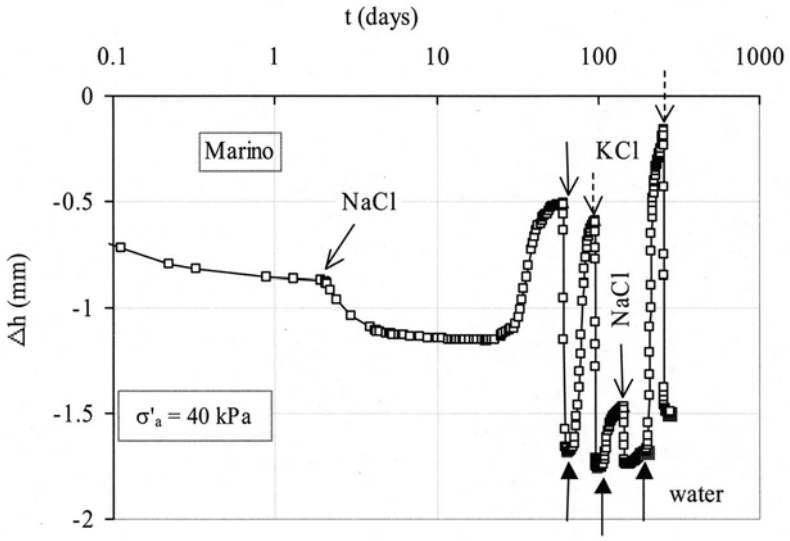

Figure 16. Consolidation of the Marino clay caused by exposure to saturated NaCl and KCl solutions and swelling caused by exposure to distilled water.

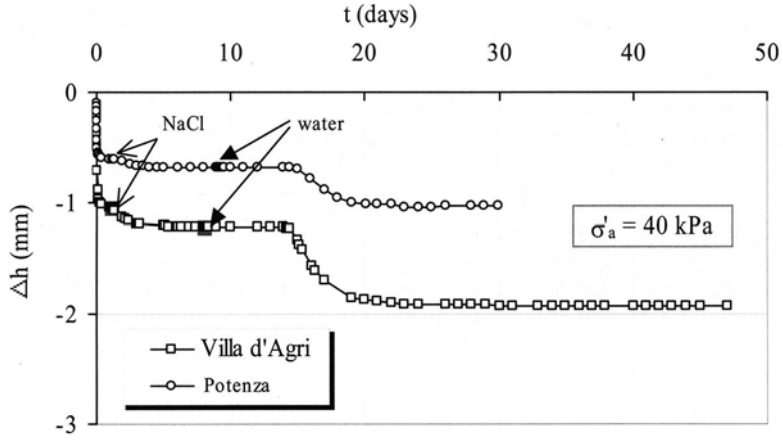

Figure 17. Consolidation of the Potenza and Villa d'Agri clays caused by exposure to saturated NaCl solution and then to distilled water.

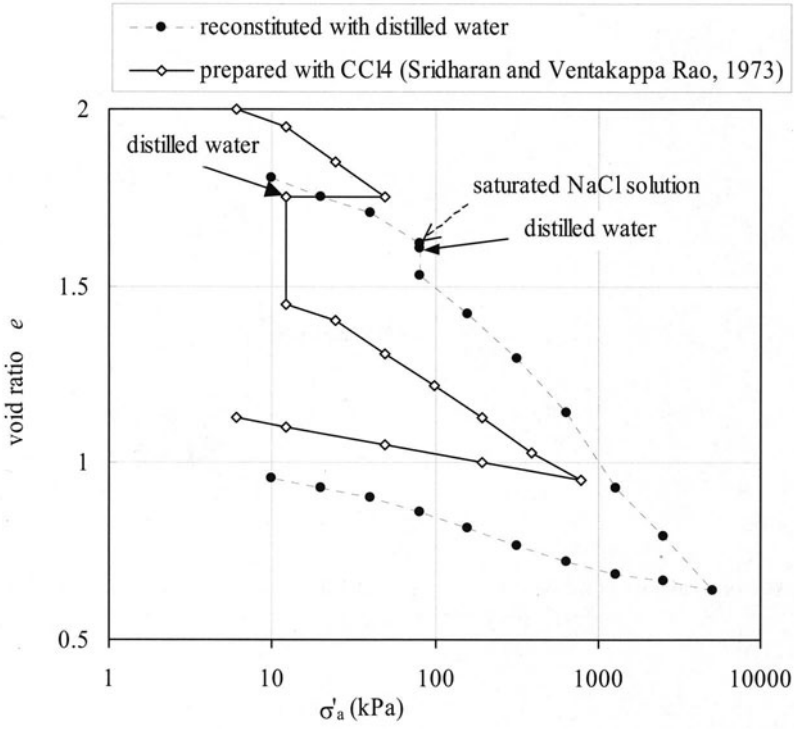

Figure 18. Consolidation of kaolin caused by exposure to saturated NaCl solution and further consolidation due to exposure to distilled water.

Other reconstituted specimens of the Bisaccia and Gela clays were exposed to concentrated salt solutions during normal compression and subsequently to distilled water during unloading. Figure 19 shows the results obtained for two specimens of the Bisaccia clay reconstituted with water at about the liquid limit and initially immersed in water. One of them was tested in the conventional way, the other was consolidated to 40 kPa and subsequently exposed to a saturated NaCl solution. This exposure produced consolidation represented by the straight line normal to the abscissa. In the subsequent compression, the specimen exhibited lower compressibility than the water-saturated specimen. Swelling due to unloading was practically negligible. Once equilibrium at 40 kPa had been reached, the specimen was exposed to water which was continuously renewed: this caused swelling. Subsequent unloading produced further noticeable swelling. Differently from the Ponza bentonite, void ratio after exposure to distilled water of the material which had interacted with the electrolyte was much higher than that of the material which had never interacted with it. Results obtained for other specimens show that the swelling curve subsequent to exposure to distilled water is unique. A series of specimens was reconstituted with 1 M NaCl solution. The specimens were initially compressed while submerged in the same solution, then they were exposed to distilled water under different values of axial stress while in the unloading phase. On subsequent unloading, carried out

during exposure to distilled water, the swelling curves of the different materials were practically coincident (Figure 20).

Figure 21 shows the results relative to the Gela clay exposed to saturated solutions of NaCl and KCl. It can be seen that on re-exposure to distilled water, the specimen which had been previously exposed to NaCl swells much more than the specimen exposed to distilled water for the whole duration of the test. On the contrary, the specimen which had been exposed to KCl swells similarly.

The Marino clay underwent tests slightly different from those carried out on the other clays. Two specimens were prepared with and immersed in distilled water. They were loaded up to 5000 kPa, afterwards, specimen *a* was unloaded conventionally, while specimen *b*, once at equilibrium at 500 kPa, was exposed to a 35g/l NaCl solution (average NaCl concentration in sea water). Such exposure produced negligible consolidation, because of the low values of the actual void ratio. However, it caused a decrease in C_S on subsequent unloading (Figure 22).

Exposure to concentrated salt solutions doesn't always cause consolidation, as shown by Figure 23 relative to the Milazzo soil. The clay underwent small swelling because of exposure to water subsequent to consolidation induced by KCl. However, the subsequent exposure to NaCl produced consolidation first, and then noticeable swelling. As it will be discussed in the 5th paragraph, this behaviour is probably the effect of two processes: counterion substitution and delayed ion diffusion into the intra-aggregates' pores.

The materials prepared with cyclohexane behave very similar to dry materials, and the compression curves of both cyclohexane-saturated and dry materials intersect the normal compression lines of the material reconstituted with aqueous solutions, clearly indicating an increase in shear resistance at the particles' contacts. When a dry material is exposed to an aqueous salt solution, two phenomena can occur simultaneously: hydration of clay particles and double layer formation, and decrease of shearing resistance at particles' contacts. If the first phenomenon prevails, then the material swells. On the contrary, if the latter phenomenon prevails, then the material compresses. In the case of the Bisaccia clay (Figure 24), exposure to a saturated NaCl solution causes swelling if the material is exposed when the condition

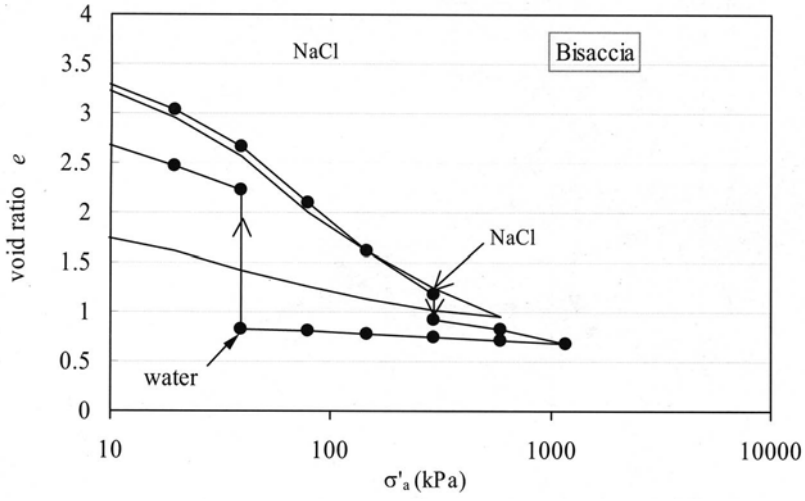

Figure 19. Consolidation of the Bisaccia clay caused by exposure to saturated NaCl solution and swelling caused by exposure to distilled water.

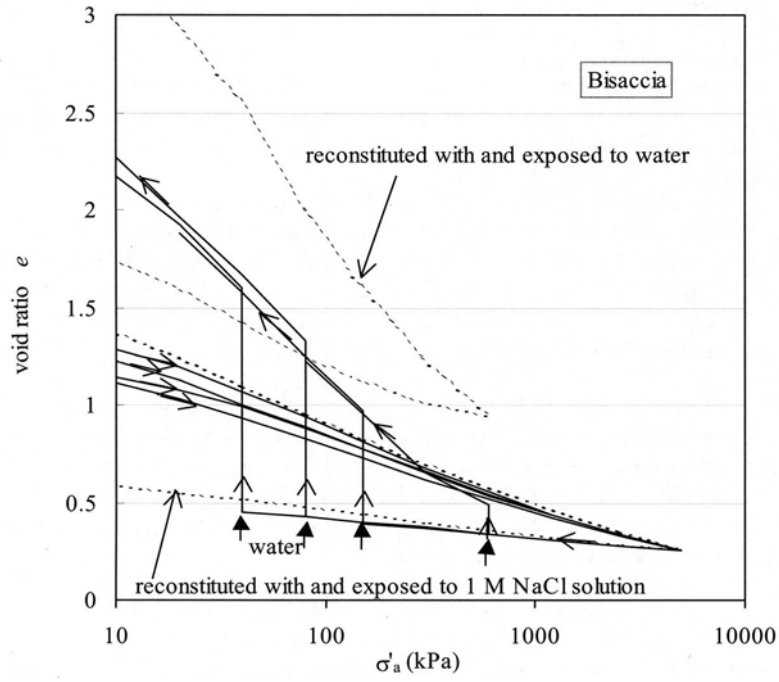

Figure 20. Effects of exposure to distilled water at several different axial stresses on the unload-ding curve of the Bisaccia clay reconstituted with 1 M NaCl solution.

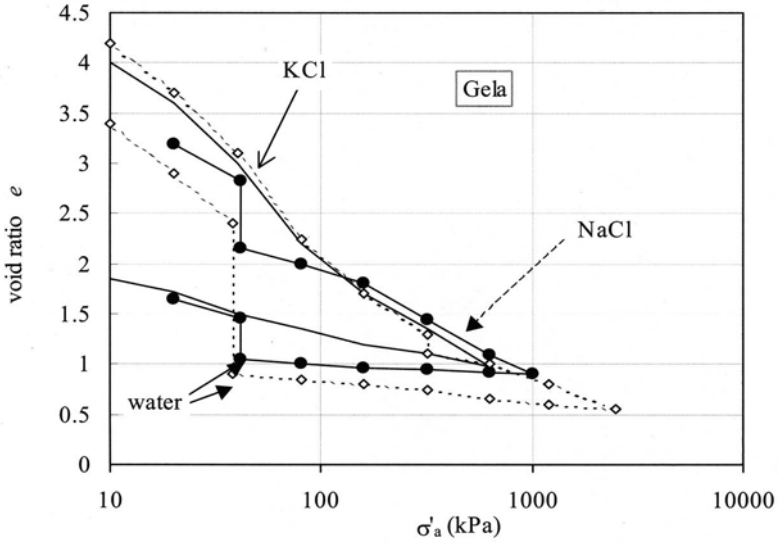

Figure 21. Consolidation caused by exposure to saturated solutions of NaCl and KCl and swelling caused by exposure to distilled water of the Gela clay.

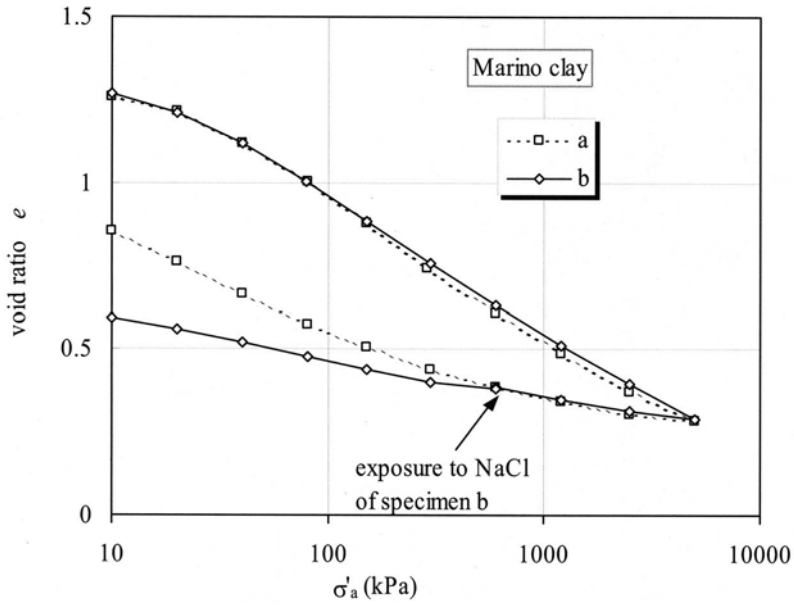

Figure 22. Effects of exposure to a saturated NaCl solution on the swelling behaviour of the Marino clay reconstituted with distilled water.

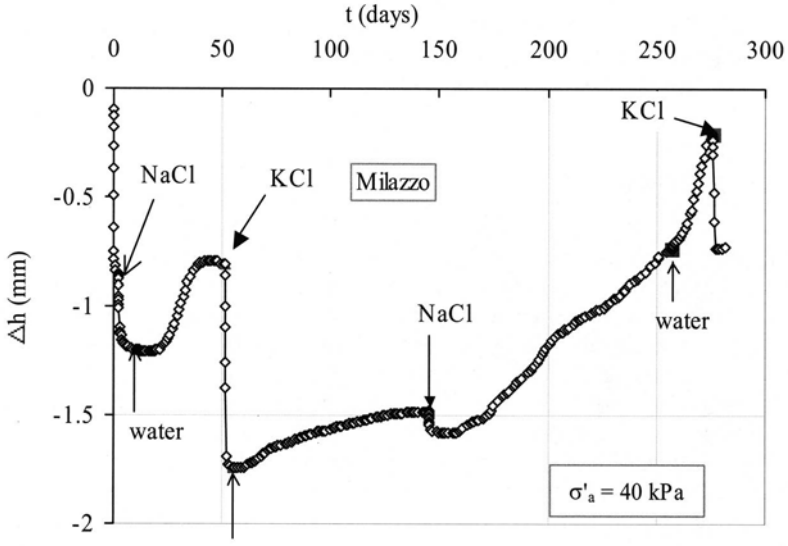

Figure 23. Consolidation of the Milazzo clay caused by exposure to saturated NaCl and KCl solutions and swelling caused by exposure to distilled water and to the NaCl solution.

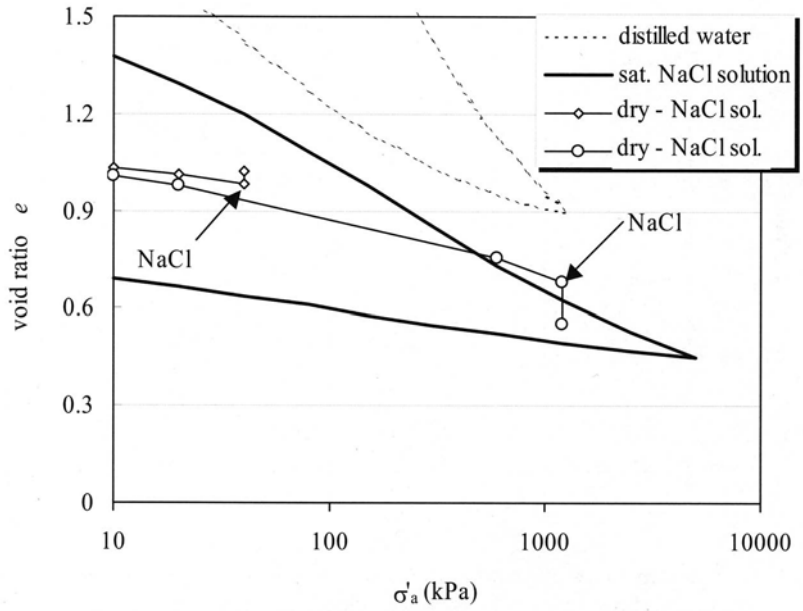

Figure 24. Effects of exposure of dry Bisaccia clay to saturated NaCl solution.

in terms of void ratio and axial stress lies on the left of the intersection. The material consolidates if its conditions before exposure to the solution are on the right of the intersection. So, in this case, the decrease in shearing resistance is the prevailing phenomenon.

3.3 Undisturbed materials

The behaviour of undisturbed materials is greatly influenced by the composition of the fluid to which they are exposed. Figure 25 refers to an undisturbed specimen of the Bisaccia clay. The specimen was immersed in water and was loaded by increments up to 8000 kPa. Afterwards it was exposed to a saturated NaCl solution and, after consolidation, it was exposed to distilled water again, water being continuously renewed. After small swelling, the specimen was unloaded until 1200 kPa (it can be seen that the swelling curve has a trend similar to that obtained for reconstituted specimens and it shows an increase of C_S with OCR). Under an axial stress of 1200 kPa, the specimen was exposed to a saturated NaCl solution (the consequent consolidation is represented by line CD). Afterwards it was unloaded until 600 kPa and, once equilibrium was reached, it was exposed to water, which was continuously renewed. This exposure produced the osmotic swelling represented by the straight line EF. On subsequent unloading, the swelling curve took on the same trend as it had before the exposure to the solution. Under an axial stress of 40 kPa, a noticeable extrusion made it necessary to suspend the test. As in the case of reconstituted specimens, swelling was strongly reduced

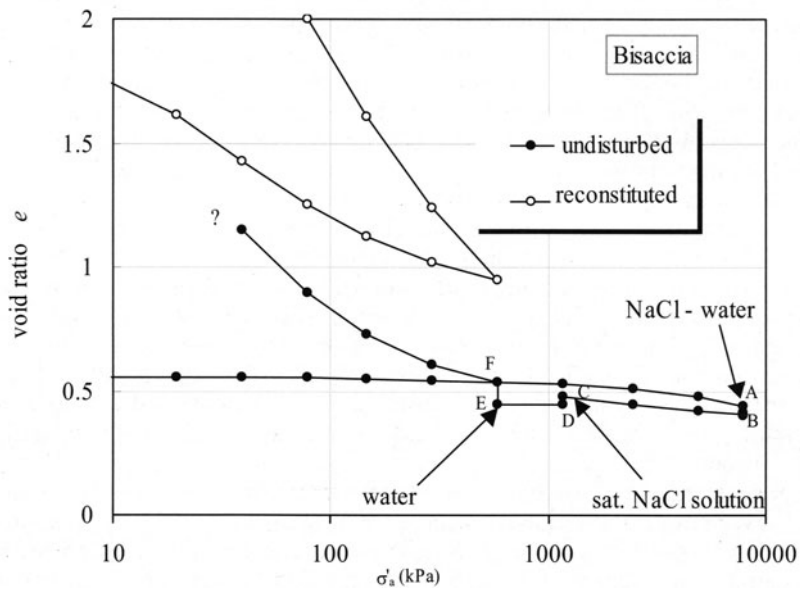

Figure 25. One-dimensional compression and swelling curves of the Bisaccia clay reconstituted with and immersed in distilled water, and of the undisturbed material exposed alternately to distilled water and saturated NaCl solution (Di Maio and Fenelli, 1997).

by exposure to the electrolyte: only the subsequent exposure to water allowed for noticeable swelling.

Figure 26 reports the oedometer curves of two couples of undisturbed specimens of the Bisaccia clay, coming from two different samples: C1, taken at about 2.5 m from the ground level , and C5bis, taken at about 21 m. A specimen of each couple underwent oedometer test in a bath of 1 M NaCl solution, and the other in a bath of distilled water. It can be seen that the specimens exposed to water experienced much higher swelling than those exposed to the NaCl solution. In particular, exposure to distilled water allowed specimen C5bis to reach void ratio close to that of the undisturbed material close to the ground surface. A first simplified analysis of the *in situ* conditions seems to show that the high water content of the upper soil was probably achieved by a similar type of swelling caused by exposure of the marine origin clay to rainwater (Di Maio and Onorati, 2000a; 2000c).

4 Swelling pressure

Swelling pressure was evaluated by means of a continuous swelling equipment which works in strain controlled manner, and by means of conventional oedometers with controlled axial load. Both reconstituted and undisturbed materials were tested (Di Maio, 2001).

Figure 27 reports the results relative to the Bisaccia clay reconstituted with a 1 M NaCl solution and compressed in the triaxial cell to p'_{max} = 230 kPa. A specimen was exposed to distilled water in the course of swelling pressure measurement and the other to the salt solution. The figure shows a large difference between the equilibrium values. Furthermore, the time of the process is highly dependent on the composition of both the pore liquid and the

liquid the clay is exposed to. In particular, the time required by the specimen prepared with and exposed to the salt solution is much shorter than that relative to the specimen exposed to water. The procedure used in reconstituting the former specimen was such as to minimise ion exchange and ion diffusion. So, in this case, the time required to reach equilibrium is intrinsic to the process. In the case of the specimen reconstituted with the salt solution and exposed to distilled water, it seems reasonable to hypothesise that the process length is due to slow ion diffusion from the pores to the cell water caused by ion concentration gradients. As ions diffuse, the repulsive interparticle forces increase and, consequently, swelling pressure increases.

The influence of the composition of the liquid the clay is exposed to is even stronger in the case of the undisturbed material, as shown by Figure 28 which reports swelling pressure against time for two undisturbed specimens of a sample taken at a depth of 21 m below ground level. The specimen immersed in a bath of distilled water exhibited a value of swelling pressure as high as 930 kPa. On the contrary, the specimen exposed to 1 M NaCl solution reached a value of about 60 kPa. Under the conditions indicated by the arrow, the cell solution of the latter specimen was substituted with distilled water. This caused a large increase in swelling pressure. It is worth noting that such an increase is due only to variations in physicochemical conditions.

Swelling pressure can be considered as the difference between the osmotic pressure in the central plane between two particles and the osmotic pressure in the equilibrium bulk solution. An equation that allows for the evaluation of osmotic pressure in terms which are convenient for geotechnical purposes was derived for saturated clay by Bolt (1956), under the hypothesis of validity of the Gouy-Chapman model, parallel flat clay particles, validity of van't Hoff's relation.

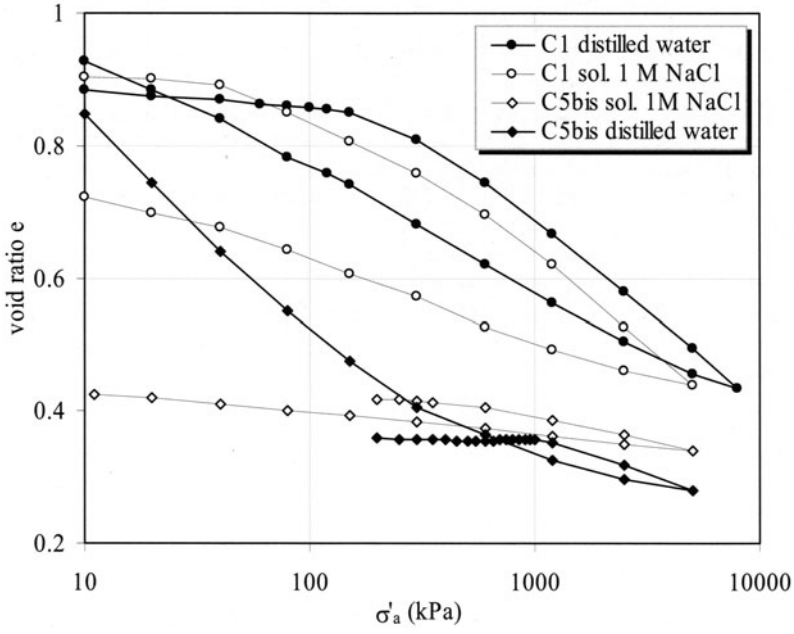

Figure 26. One-dimensional compression and swelling curves of undisturbed Bisaccia clay exposed to a concentrated NaCl solution and to distilled water.

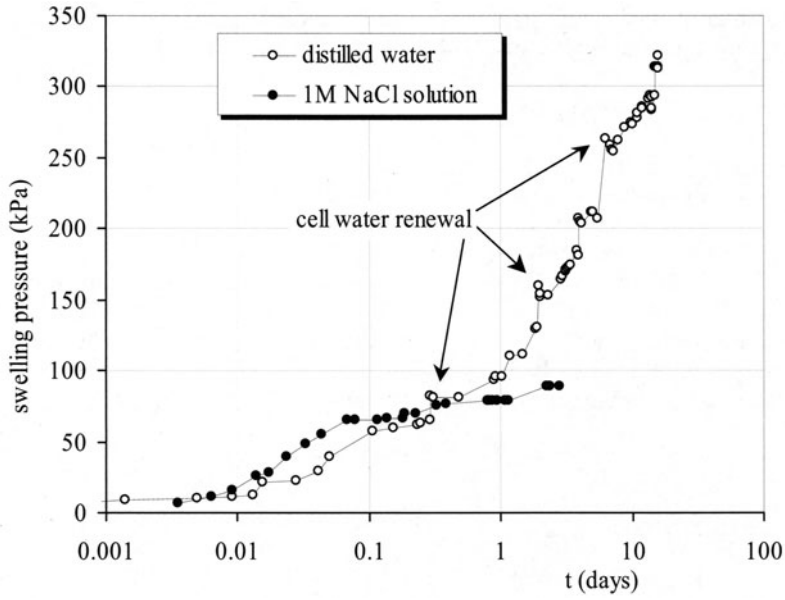

Figure 27. Swelling pressure against time for two specimens of the Bisaccia clay reconstituted with 1 M NaCl solution. A specimen was exposed to the same solution and the other to distilled water.

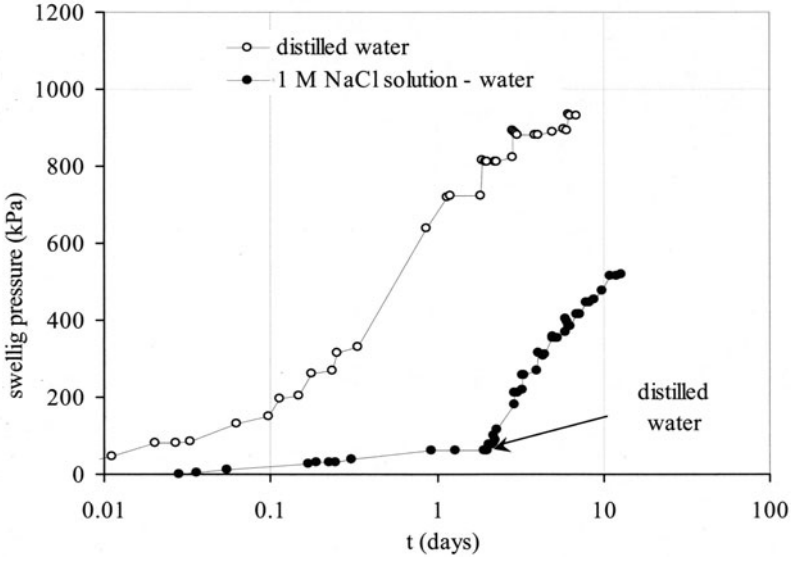

Figure 28. Swelling pressure against time for two undisturbed specimens of the Bisaccia taken at a depth of 21 m below ground level.

It is possible to relate void ratio to swelling pressure, for given values of the other parameters. The solution is highly dependent on A_s. For the considered material, A_s has been evaluated through the empirical relationship found by Farrar and Coleman (1967):

$w_L = 19 + 0.56\, A_s$

where A_s is expressed in m^2/g. It is worth noting that the values are not very different from those evaluated by an approximate method based on methylene blue adsorption (Di Maio et al. 2003). Figure 29 compares experimental data to theoretical curves. The theoretical curves are relative to 10^{-3} M, and to three values of specific surface. A_s = 114 m^2/g and A_s = 195 m^2/g are, respectively, the minimum and maximum value calculated for the undisturbed samples, and A_s = 134 m^2/g is the value calculated for the reconstituted material. For the other parameters, the following values have been considered: $\nu = 1$, $\beta = 10^{15}$ cm/mmole; $x_0 = 4/\nu$ Å (valid for montmorillonite); $G_s = 2.73$.

Notwithstanding some exceptions, theory and experiment agree (Figure 29).

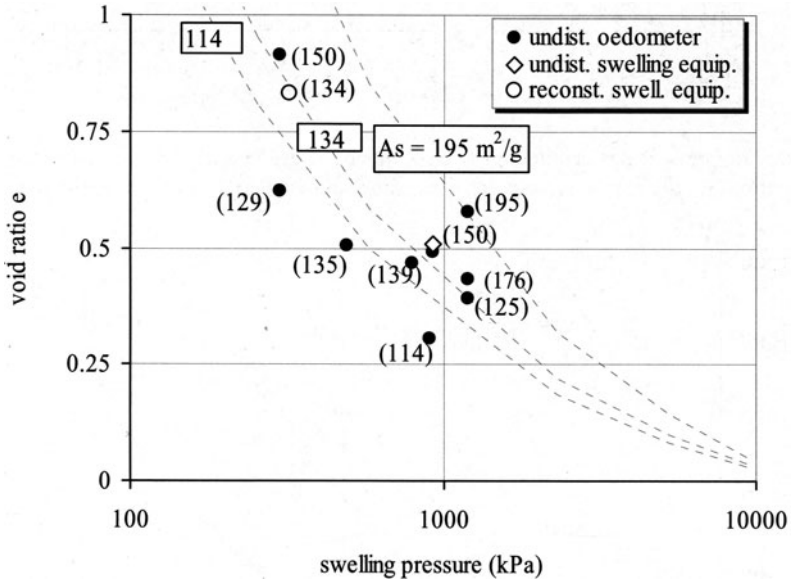

Figure 29. Comparison between experimental results and the double layer model (Di Maio, 2001).

5 Discussion and Conclusions

When a water saturated clay is exposed to a salt solution, depending on the clay porosity, electrolyte concentration and type of ions, it can behave as a semipermeable membrane that allows for the outward flow of solvent but not for the inward diffusion of solute. As described by Mitchell et al. (1973), and Barbour and Fredlund (1989), during the outward flow of water,

negative pore fluid pressures develop within the specimen, and the corresponding increase in effective stresses produces a decrease in volume. Mitchell (1991), while analysing data provided by Farrar and Coleman (1967), and by Barbour and Fredlund (1989), showed that outward osmotic water flow may be significant only in very dense, low-porosity clays and in dilute electrolytes. Conversely, the higher the void ratio and the larger the concentration of the electrolyte, the more important is ion diffusion. The results relative to the Ponza bentonite show that exposure of the water saturated specimens to the three concentrated solutions produced ion diffusion towards the pore fluid. Circumstantial evidence of this is provided by the differences found on re-exposure to water between the effects of KCl and $CaCl_2$ (irreversible) and those of NaCl (reversible). On re-exposure to water, Na^+ effects were shown to be reversible; on the contrary, where water substituted $CaCl_2$ or KCl solutions, the specimens did not undergo that a negligible swelling, even after some months of continuous water renewal.

A diffuse double layer model can explain qualitatively the observed behaviour. According to the classical diffuse double layer theory (Gouy, 1910; Chapman, 1913), the thickness of the double layer increases with ion concentration increasing. The thickness of the double layer decreases also with increasing counterion charge. The Gouy-Chapman model cannot explain the differences between Na^+ and K^+ effects because it considers ions as point charges. According to the Stern model (1924), the thickness of the double layer also decreases with decreasing hydrated ion radius. Since the radius of K^+ is smaller than that of Na^+, the thickness of a K-montmorillonite double layer is smaller than that of Na-montmorillonite.

Potassium and calcium can be replaced by sodium by exposing the clay to concentrated NaCl solutions, at least at high void ratio and low stress level (Di Maio, 1998). Several processes can account for the observed dependence on stress level, for instance diffusion itself might develop differently. In fact, as the stress level increases, aggregates of particles could form thus creating regions (intra-aggregate pores) where it would be difficult for ions to diffuse.

The behaviour of smectitic clays such as Bisaccia, Gela and Marino clays is mostly qualitatively similar to that of the Ponza bentonite, although the effects are lower because of the lower smectite content. The qualitative differences are fundamentally due to the existence of different types of counterions. For low values of axial stresses, osmotic swelling is higher than osmotic consolidation for two reasons. One reason could be that the clays' pore liquid normally contains a certain amount of ions, although they were prepared with distilled water. During exposure to distilled water these ions are removed together with those which have been made to diffuse into the pore liquid, thus allowing for a larger swelling. The other reason is that, because of its higher concentration, Na^+ could have replaced other counter-ions, for instance Ca^{2+} and K^+, thus giving the clay the possibility of a larger swelling as a consequence of exposure to water.

The commercial kaolin and the Potenza and the Villa d'Agri clays behave differently: they undergo small consolidation as an effect of exposure to the salt solution and a large consolidation because of subsequent exposure to water. Since the used kaolin is composed mainly by kaolinite and the other two clays are composed by illite and kaolinite, double layer is a small percentage of their overall water volume. So, a decrease in the double layer thickness caused by exposure to salt solutions doesn't produce noticeable volume changes. Probably, exposure to water makes resistance to particle movements decrease, thus allowing the external loads to work further and to produce porosity reduction. This mechanism was hypothesized by Sridharan and Ventakappa Rao (1973) for a kaolin that was prepared with CCl_4 and that underwent osmotic consolidation because of an inward water flow.

The Milazzo clays underwent small swelling because of exposure to water subsequent to consolidation induced by KCl. However, the subsequent exposure to NaCl produced consoli-

dation first and then noticeable swelling. This behaviour is probably due to the presence of particle aggregates. According to Barbour and Yang (1993), when a clay is exposed to a brine, ions first diffuse into the interaggregate pores. This produces consolidation. Afterwards, when ions diffuse into the intra-aggregates' pores, ion exchange can takes place. If Na^+ replaces Ca^{2+} and K^+, an increase of the double layer thickness can occur.

Results relative to swelling pressure show that the Bisaccia clay is strongly influenced by pore liquid composition and by the composition of the liquid the clay is exposed to. It is interesting to observe that, in the case of reconstituted materials, Bolt's model (1956) interprets satisfactory the behaviour of the Bisaccia clay reconstituted with a concentrated salt solution and exposed to distilled water. This probably depends on the fact that face-face particle arrangement, which is a hypothesis of the model, is obtained in salt solution for smectite. As expected, the model interprets only qualitatively the behaviour of the material exposed to concentrated salt solutions.

Acknowledgements

The author would like to thank Miss Marilena Lasco for her help in carrying out some laboratory tests.

References

Abduljauwad, S. N., Al-Sulaimani, G. J., Badunsbul I. A., and Al-Buraim, I. (1998). Laboratory and field studies of response of structures to heave of expansive clay. *Géotechnique,* Vol. 48, No. 1, pp. 103 - 121.

Barbour, S. L. (1987). Osmotic flow and volume changes in clay soils. *Ph.D. Thesis*, Dept. of Civil Engineering, University of Saskatchewan, Saskatoon, Canada.

Barbour, S. L., and Fredlund, D. G. (1989). Mechanisms of osmotic flow and volume change in clay soils. *Canadian Geotechnical Journal*, vol. XXVI, pp. 551-562.

Barbour S. L., Yang N. (1993). A review of the influence of clay-brine interactions on the geotechnical properties of Ca-montmorillonitic clayey soils from western Canada. *Can. Geotech. J.*, vol. XXX, pp.920 - 934.

Bolt, G. H. (1956). Physico-chemical analysis of the compressibility of pure clays. *Géotechnique*, vol. VI, n.2, pp. 86-93.

Chapman, D. L. (1913). A contribution to the theory of electrocapillarity. *Phil. Magazine*, Vol. 25, No. 6, pp. 475-481.

Di Maio, C. (1996). Exposure of bentonite to salt solution: osmotic and mechanical effects. *Géotechnique*, vol. XLVI, n. 4, pp. 695 - 707.

Di Maio, C., and Fenelli, G.B. (1997). Influenza delle interazioni chimico-fisiche sulla deformabilità di alcuni terreni argillosi. *Rivista Italiana di Geotecnica*, anno XXXI, No. 1, 695-707.

Di Maio, C. (1998). Discussion on Exposure of bentonite to salt solution: osmotic and mechanical effects. *Géotechnique*, vol XVVIII, No. 3, 433 - 436.

Di Maio, C., and Onorati, R. (2000a). Swelling behaviour of active clays: the case of an overconsolidated, marine origin clay. *Proceedings of the VIII International Symposium on landslide*, Cardiff, Vol. 1, 469 – 474.

Di Maio, C., and Onorati, R. (2000b). Osmotic softening of overconsolidated clays. *Proceedings of the International Conference on Geotechnical & Geological Engineering*, Melbourne.

Di Maio, C. (2001). Swelling pressure of clayey soils: the influence of stress state and pore liquid composition. *Italian Geotechnical Journal*, Vol. XXXV, n. 3, 22 – 34.

Di Maio C., Santoli L. and Schiavone P. (2003). Volume change behaviour of clays: the influence of mineral composition, pore fluid composition and stress state. *Mechanics of materials*, in press.

Farrar, D. M., and Coleman, J. D. (1967). The correlation of surface area with other properties of nineteen British clay soils. *Journal of Soil Science*, Vol. 18, No. 1, pp.118 – 124.

Gouy, G. (1910). Charge électrique à la surface d'un electrolyte. *J. Phys.* (Paris) Vol. IV, No. 9, pp. 457– 468.

Mesri, G., and Olson, R. E. (1971). Consolidation characteristics of montmorillonite. *Géotechnique*, vol. XXI, n. 4, pp. 341-352.

Mitchell, J. K., Greenberg, J. A., and Witherspoon, P. A. (1973). Chemico-osmotic effects in fine-grained soils. *J. Soil Mech. Fdn Div. Am. Soc. Civ. Engrs.* 99, SM4, 307 – 322.

Mitchell, J. K. (1991). Conduction phenomena: from theory to geotechnical practice. *Géotechnique*, vol. XLIV, n. 3, pp. 299-340.

Mitchell, J. K. (1993). Fundamentals of soil behaviour. 2nd ed. John Wiley & Sons, Inc.

Sridharan, A., and Ventakappa Rao, G. (1973). Mechanisms controlling volume change of saturated clays and the role of the effective stress concept. *Géotechnique*, vol. XXIII, n. 3, pp. 359-382.

Sridharan, A. (1991). Engineering behaviour of fine grained soils. *Indian Geotechnical Journal*, vol. XXI, n. 1, pp. 1-136.

Stern, O. (1924). Zur Theorie der electrolytischen Doppelschict. *Z. Elecktrochemie*, Vol. 30, pp. 508 – 516.

Yin, J. H. (1999). Properties and behaviour of Hong Kong marine deposits with different clay contents. *Canadian Geotechnical Journal*, vol. 36, pp. 1085 – 1095.

Shear Strength of Clays and Clayey Soils: the Influence of Pore Fluid Composition

Caterina Di Maio

Dipartimento di Strutture, Geotecnica, Geologia applicata all'Ingegneria, Università della Basilicata, Italy

Abstract. This paper reports experimental results relative to the influence of pore fluid composition on the peak shear strength of the Bisaccia clay and on the residual shear strength of several different clayey soils: the Ponza bentonite, commercial bentonite and kaolin, Bisaccia, Gela and Marino clays. Triaxial tests were carried out on the Bisaccia clay reconstituted with distilled water and with a 1 M NaCl solution. Direct shear and ring shear tests were carried out on dry materials and on the materials reconstituted with distilled water, NaCl solutions at various concentrations, cyclohexane. Some tests were carried out by using KCl solutions, ethanol and ethylene glycol. The results show that pore fluid composition influences greatly both the peak and residual shear strength of smectitic soils, even when the clay fraction is very low. The residual friction angle is about 5° in distilled water, 15° in concentrated NaCl solution, and varies between 30° and 35° for materials dry or prepared with cyclohexane. The residual friction angle is strongly correlated to the static dielectric constant of the pore fluid.

1 Introduction

Shear strength of pure clays is strongly influenced by pore fluid composition (among others: Kenney, 1967; Mesri and Olson, 1970; Sridharan, 1991; Mitchell, 1993, Di Maio, 1996a, 1996b). Furthermore shear strength of natural soils depends on clay fraction and clay composition. In particular, soils with clay fraction c.f. > 50% exhibit values of the residual shear strength equal to those of their clay part (Lupini et al., 1981). For 25%<c.f.<50% results are extremely scattered and strongly influenced by mineral and pore fluid composition. If the clay component is constituted by minerals with high specific surface such as montmorillonite, and the pore fluid is constituted by distilled water, then 25% - 30% c.f. is sufficient to make the residual strength of a composite soil equal to that of its clay part (Di Maio and Fenelli, 1994). Di Maio (1996a) reported data relative to some natural clays containing different percentages of montmorillonite, reconstituted with distilled water and with saturated NaCl solution, showing that the clays exhibit almost the same values of residual shear strength as the Ponza bentonite - which is a practically pure montmorillonite - both in distilled water and in the salt solution.

Natural state pore fluid is often a compound solution, hence the use of distilled water for laboratory tests would be not appropriate. Anson and Hawkins (1998) briefly discussed the implication for slope stability analysis of using deionised water in laboratory tests, suggesting

that the difference between results calculated by back analysis and those obtained in laboratory could be due, at least in part, to the use of deionised water. Besides its practical importance, an analysis of the influence of pore fluid composition on shear strength is very important for the elucidation of the shearing mechanism.

Generally, in the study of the influence of pore fluid composition on the behaviour of the different types of soils, the effects of ionic aqueous solutions and those of organic solvents are analysed separately. The purpose of this paper is to systematically examine shear strength response of different soils at pore fluid variations, comparing the influence of "extreme" types of pore fluids: water, salt solutions at various concentrations, organic solvents with different dielectric constants and air.

2 Materials and Methods

The experimentation was carried out on the Ponza bentonite, Bisaccia, Gela and Marino clays, a commercial kaolin provided by Igma srl (Sassuolo, Italy) and a commercial bentonite provided by Laviosa Chimica Mineraria SpA (Livorno, Italy). Particle size distribution curves of the tested soils are reported by the companion papers on this volume. The same papers report mineral composition, liquid limit evaluated by mixing the soils with NaCl solutions at various concentrations, the liquid limit of the Ponza and Bisaccia clays evaluated also with cyclohexane, ethanol and dimethylsulfoxide. The liquid limit of the commercial bentonite was evaluated with different solutions including HCl solutions at various pH.

Peak shear strength was evaluated by means of common triaxial CU tests carried out on normally consolidated specimens of the Bisaccia clay reconstituted with distilled water and with 1 M NaCl solution. The tests were carried out with constant cell pressure and with the axial stress increased in a strain controlled manner, at a rate of 0.03 mm/min.

Residual shear strength was determined by use of the conventional Casagrande box and by the Bishop ring shear apparatus. In the first case, for each value of axial stress, the specimens were sheared back and forth until the minimum strength was obtained. For both cases, rates of displacement in the range 0.001 – 0.005 were adopted. Various pore fluids were used: water, salt solutions at various concentrations and three organic solvents: cyclohexane, ethanol and ethylene glycol. Dry materials were also tested.

3 Results

3.1 Shear strength of normally consolidated Bisaccia clay

The influence of pore fluid composition on the peak strength value of normally consolidated material was determined only for the Bisaccia clay. It is known that the intrinsic compression line of this material is strongly dependent on the pore liquid composition. Figure 1 reports the one-dimensional curves of void ratio against effective axial stress for the material reconstituted with and exposed to distilled water and for the material reconstituted with and exposed to a 1 M NaCl solution. Points A^I represent the equilibrium conditions after isotropic normal consolidation for three water-saturated specimens, and points B^I for solution-saturated specimens. These specimens underwent CU tests. The results of the tests, in terms of $q' = \sigma'_a - \sigma'_r$ against $p' = (\sigma'_a + 2\sigma'_r)/3$, show that the specimens reconstituted with the salt solution are characterised by much higher values of shear strength than the specimens reconstituted with distilled water (Figure 2).

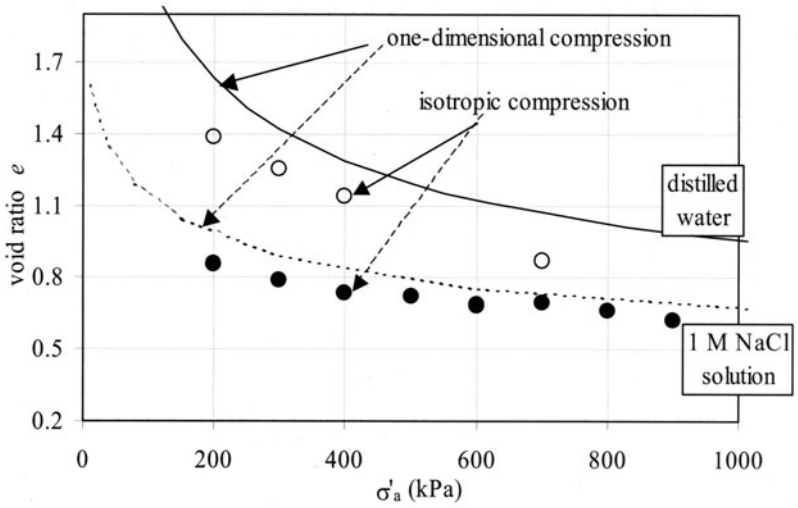

Figure 1. Intrinsic one-dimensional compression lines of the Bisaccia clay reconstituted with water and with a 1 M NaCl solution, and isotropic compression points of specimens which underwent triaxial tests.

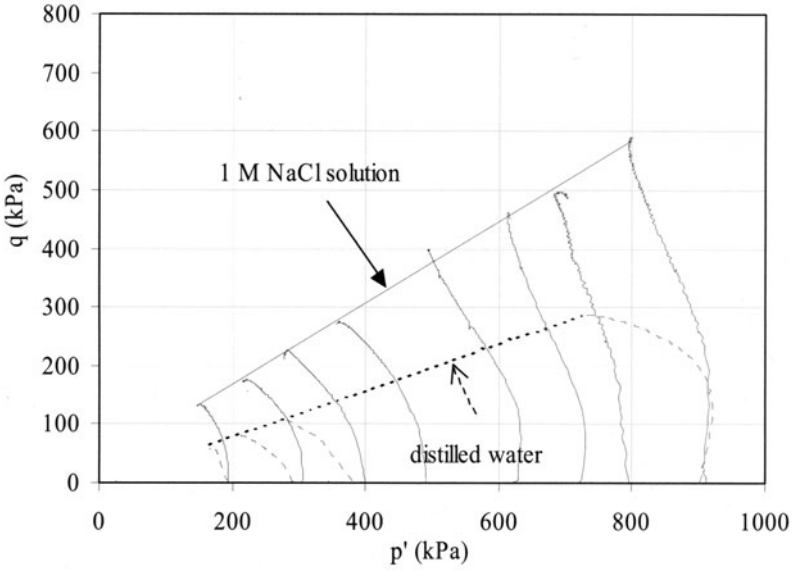

Figure 2. CU triaxial tests on normally consolidated specimens of the Bisaccia clay.

Other tests were carried out in order to evaluate the influence on shear strength of the type of test and of the composition of the fluid of the hydraulic circuits. Figure 3 compares the results of CU tests to those of CD tests carried out on specimens reconstituted with 1 M NaCl solution. The hydraulic circuits of the triaxial cell and the porous stones were saturated with distilled water. It can be observed that shear strength determined by CU tests is higher than that determined by CD tests. It is reasonable to hypothesise that, in the case of the CD test, ions of the pore solution could have diffused towards external water, so making shear strength decrease. This process could not occur in the case of the CU test. As a matter of fact, when the hydraulic circuits of the triaxial cell and the porous stones are saturated with the same solution as the pore solution, the differences between the two types of tests decrease greatly, as shown by Figure 4 which compares the results of CU and CD tests which were carried out by saturating circuits and porous stones with a 1 M NaCl solution. The specimens, reconstituted with the same solution, were consolidated to 800 kPa, and afterwards each of them was unloaded to a given value of p'. At equilibrium, some specimens were sheared in drained conditions, with a rate of axial displacement of 0.0015 mm/min, and some others in undrained conditions at a rate of 0.03 mm/min. It can be observed that, in this case, the two types of tests furnish similar results.

Peak values of strength are influenced by the different initial void ratios of the material reconstituted with the two different fluids. In order to minimize the influence of initial fabric, it is convenient to refer to the residual shear strength which is known to be independent of it.

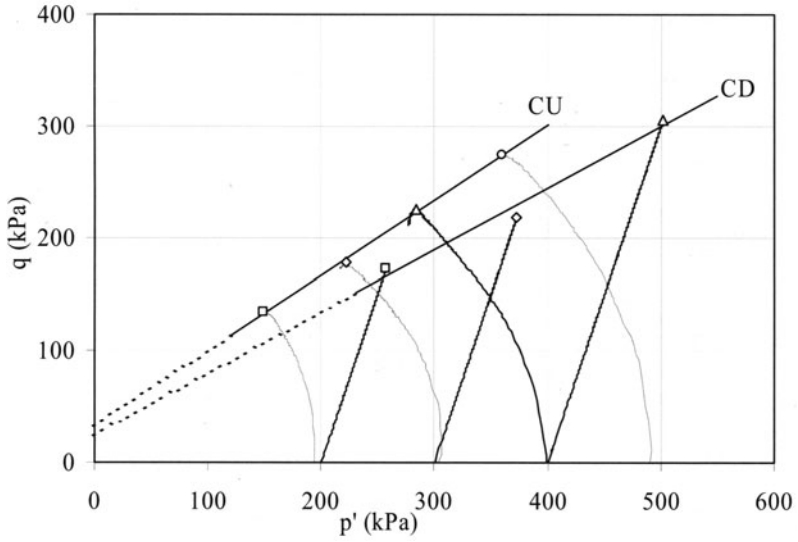

Figure 3. Results of CU and CD triaxial tests carried out on normally consolidated Bisaccia clay exposed to distilled water (Di Maio and Onorati, 2000b).

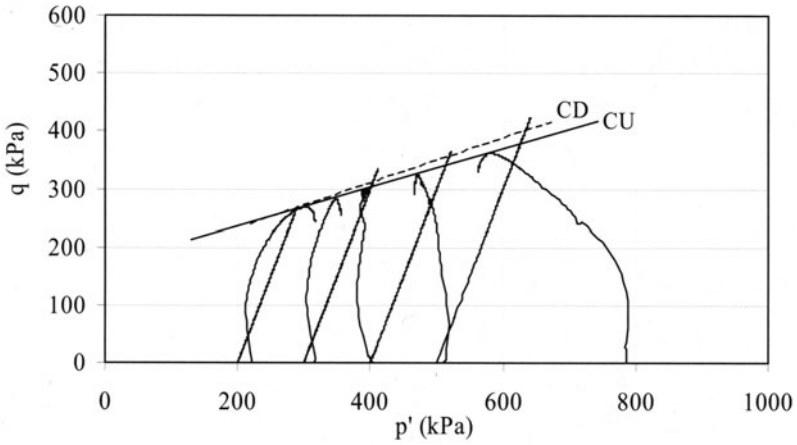

Figure 4. Results of CU and CD tests on the Bisaccia clay reconstituted with and exposed to 1 M NaCl solution (Di Maio and Onorati, 2000b).

3.2 Residual shear strength

The materials were reconstituted with distilled water and initially sheared while immersed in distilled water. In these conditions, the residual shear strength of all the considered materials was found to be very close to that of the Ponza bentonite and lower than that of the commercial kaolin (Figure 5). Once the residual shear strength had been reached, the cell water was replaced by a saturated NaCl solution. This replacement did not cause any effect on kaolin behaviour, whereas it caused a strong increase in the other soils' shear strength. In particular, the Bisaccia and Gela clays residual shear strengths are close to that of the Ponza bentonite, whereas the Marino clay strength is close to that of the commercial kaolin. It seems reasonable to hypothesise that the Marino clay behaviour depends on its low smectite content (about 10% in dry weight). When the pore fluid is distilled water, the volume of the smectite component is sufficient to influence shear strength, whereas, in the case of the concentrated salt solution, the smectite volume decreases greatly and kaolinite particles probably interact directly.

For all the considered soils, the residual shear strength obtained after exposure of water saturated materials to a saturated salt solution is equal to that obtained for the materials prepared directly with the solution and submerged in it (Di Maio, 1996a; 1996b).

The influence of NaCl solution concentration on residual shear strength was determined on specimens reconstituted with NaCl solutions at given concentrations and exposed to the same solutions. The results show that as ion concentration increases, residual shear strength of smectitic soils increases (Figure 6). The largest variations occur in the range 0 - 0.5 M, and only negligible variations occur between 0.5 M and saturation. It is worth noting that the point at 0.1 M in Figure 6 was obtained for a specimen of the Bisaccia clay reconstituted with a solution similar to the natural pore solution which had been previously analysed. The corresponding shear strength, although much lower than the maximum, is higher than that obtained with distilled water.

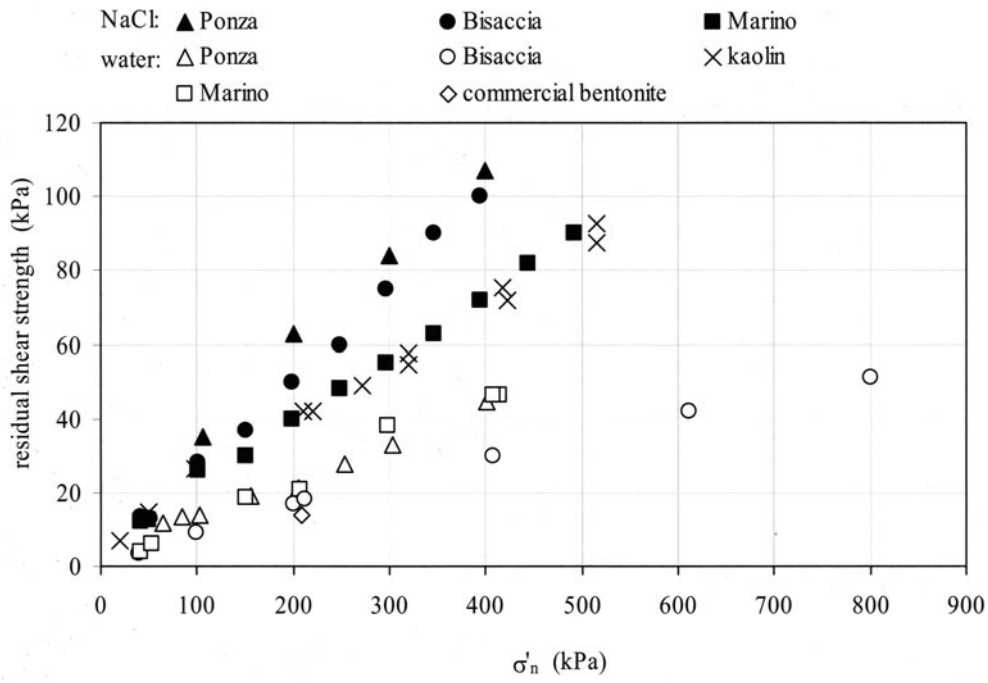

Figure 5. Residual shear strength against normal stress for the materials prepared with and exposed to distilled water and for the same materials after exposure to a saturated NaCl solution (Di Maio, 1996a).

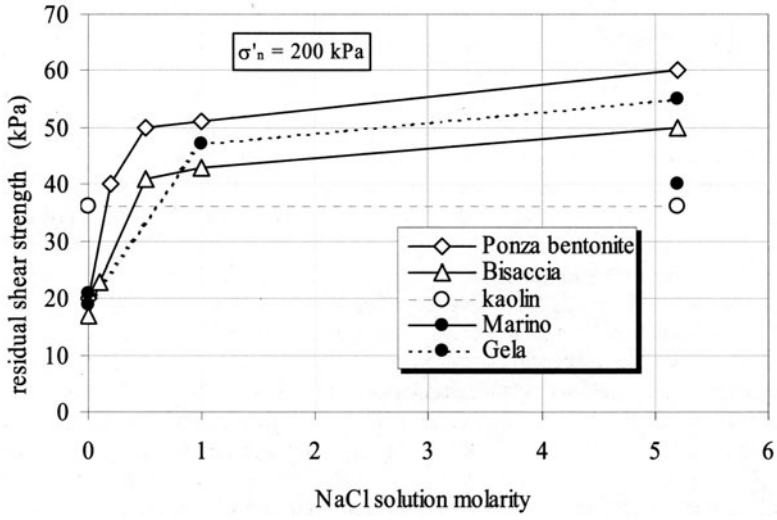

Figure 6. Residual shear strength under σ'_n = 200 kPa against NaCl solution molarity.

KCl effects on the residual shear strength of the considered materials are slightly higher than

those exerted by NaCl, as shown by Figure 7 for the Bisaccia clay. Also the results relative to the Ponza bentonite show that the effects of K^+ are slightly higher than those of Na^+ (Di Maio, 1996b).

Although the residual shear strength of smectitic soils increases dramatically as ion concentration increases, it is much lower than that the materials can exhibit with other pore fluids. This is shown by further experimental results of direct shear tests and ring shear tests carried out on dry materials and on the materials prepared with, and exposed to, organic fluids with low dielectric constants. Testing is very difficult in these conditions and results rather dispersed. Apparently, the irregularity of the shear surface is one of the main causes of the dispersion. So, often the tests were interrupted and the specimens were cut manually in order to ensure the flatness of the shear surface. Moreover, at the end of the test, the shear surface was carefully observed and only the results relative to specimens with a regular planar surface were considered in the analysis. Figure 8 reports the results obtained for a specimen of the dry Bisaccia clay tested in the Bishop ring shear apparatus under three different values of normal stress, at a rate of 0.001 mm/min. In the course of the test, the specimen was exposed to ethanol and sheared further. The exposure caused a noticeable decrease in strength with respect to the dry material.
This latter, in turn, behaved very similarly to the material prepared with and immersed in a non polar organic fluid, cyclohexane, whose dielectric constant D=2 is very close to that of air. The cohesion intercept being null, it is possible to interpret the results in terms of residual friction angle φ'_r. The strength parameter is about 30° for the Bisaccia clay prepared with cyclohexane or dry, about 24° for the material prepared with ethanol, 15° for the material reconstituted with 1 M NaCl solution, about 5° in water!

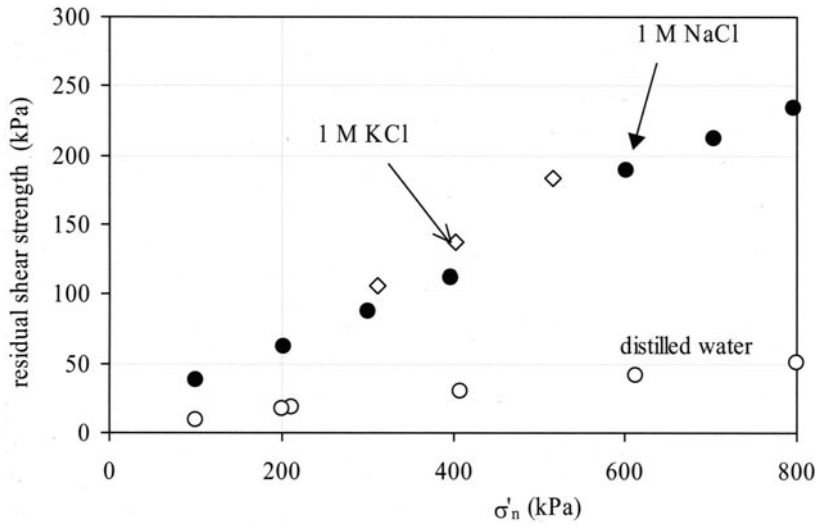

Figure 7. Residual shear strength against axial stress for the Bisaccia clay reconstituted with water, 1 M NaCl and 1 M KCl solutions.

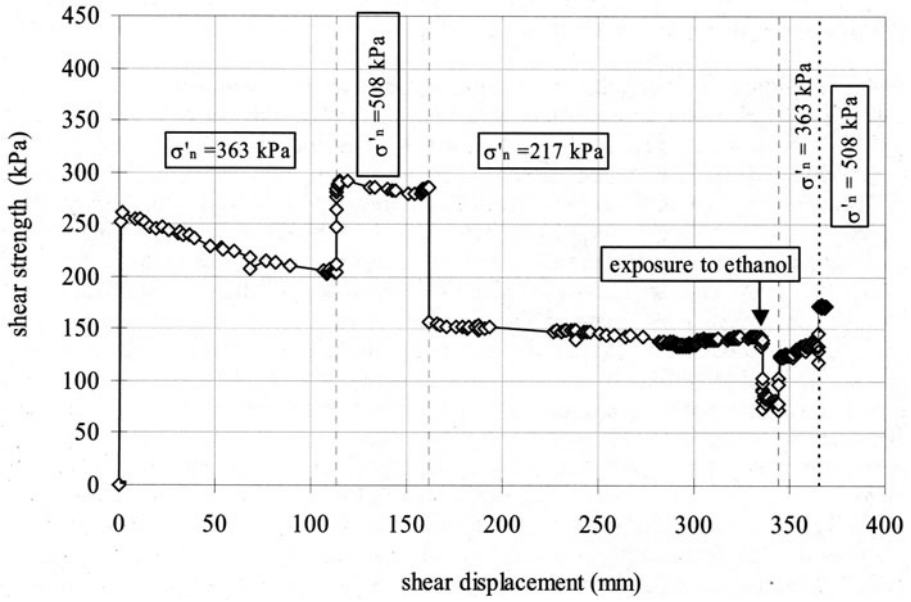

Figure 8. Shear strength against shear displacement for a dry specimen of the Bisaccia clay which was exposed to ethanol in the course of the test.

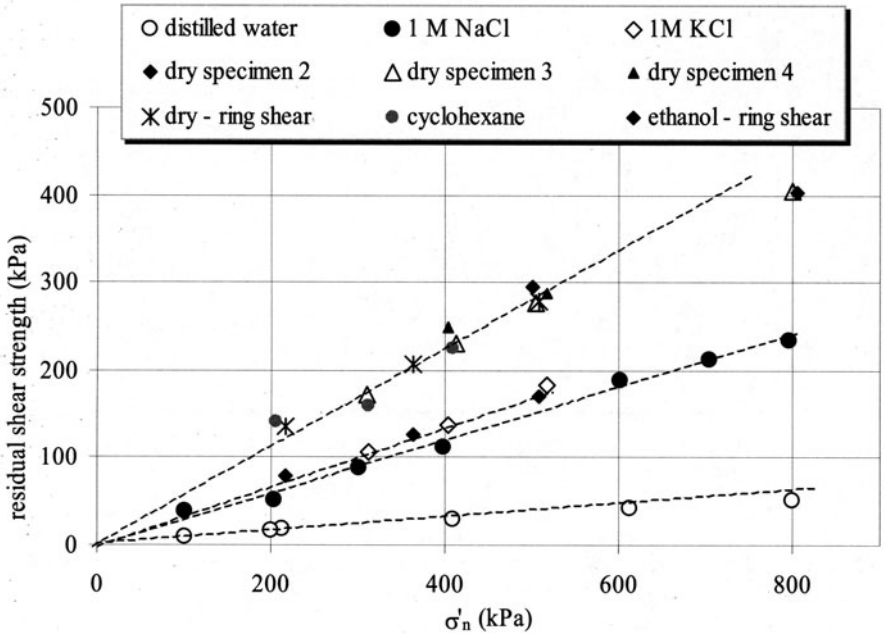

Figure 9. Residual shear strength against normal stress for the Bisaccia clay with different pore fluids.

An analogous experimentation was carried out on the Ponza bentonite. The results show that the influence of pore fluid composition is very similar to that observed on the Bisaccia clay (Figure 10).

The increase in strength caused by an increase in pore solution concentration probably depends also on the lower void ratio of the materials prepared with the electrolyte. Under the considered stress level, void ratio of the material, either dry or in cyclohexane, is equal or higher than that in the saturated salt solution. So, the increase in shear strength reasonably depends on a particular particle aggregation or on an increase in shear resistance at the particles' contacts. Such an increase can be caused by an increase in electrodynamic attraction forces. These forces are complex functions of the dielectric constant of the pore fluid as well as of the solid skeleton. The dielectric constant, in turn, is a function of the frequency of electromagnetic fluctuations. However, to a first approximate analysis, all data can be analysed with reference to the pore fluid static dielectric constant. Figure 11, shows that the ratio τ_r/σ'_n decreases with pore fluid static dielectric constant increasing. The figure reports also the result relative to the Bisaccia clay exposed to ethylene glycol. It can be observed that this result is consistent with the others in terms of dielectric constant.

In this first experimentation, both aqueous ion solutions and organic solvents were used for D < 75 and the results relative to the two types of fluids seem to be comparable. However, only aqueous ion solutions were used for D higher than about 75. Further experimentation is now under consideration with organic fluids with D > 75 in order to understand whether the results relative to organic fluids can be compared to those of salt solutions also when these latter are dilute.

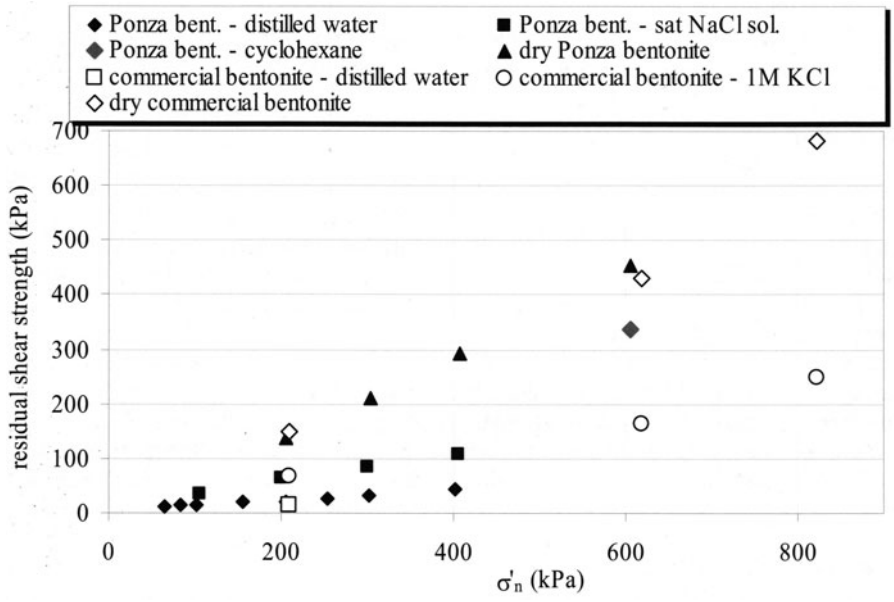

Figure 10. Residual shear strength against normal stress for the Ponza bentonite and the commercial bentonite prepared with different types of pore fluid.

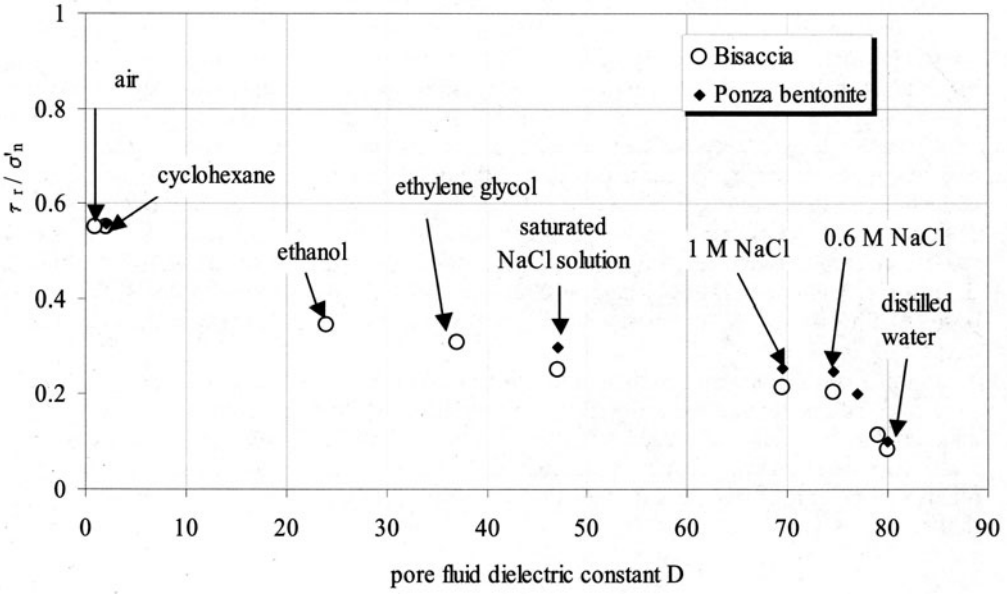

Figure 11. Ratio τ_r/σ'_n against pore fluid static dielectric constant for the Bisaccia and the Ponza clays prepared with different types of pore fluid.

4 Conclusions

This paper compares the influence of "extreme" types of pore fluids: water, concentrated salt solutions, organic solvents and air on several different soils. The results show that, with the exception of the used kaolin, the other considered soils are noticeably influenced by pore fluid composition. It is worth noting that soils containing small smectite percentages, such as the Marino clay, exhibit the same residual shear strength as the Ponza bentonite which is a practically pure montmorillonite.

The residual friction angle of smectitic soils is about 5° in distilled water, 15° in concentrated NaCl solution, and varies between 30° and 35° for materials dry or prepared with cyclohexane. Furthermore, it is strongly correlated to the static dielectric constant of the pore fluid.

Pore fluid in nature is generally a dilute composite solution. The results reported in this paper show that the largest variations of the residual shear strength of smectitic soils prepared with NaCl solutions occur in the range 0 – 0.5 M. In particular, the residual shear strength evaluated on the Bisaccia clay prepared with a solution similar to its natural pore solution is noticeably higher than that obtained with distilled water.

Most of the clays we deal with formed in marine environment. In order to understand their behaviour, it is important to take into account their original intrinsic properties which can be only determined by using concentrated salt solutions. For instance, the comparison between results obtained by using distilled water and those obtained by using concentrated NaCl solutions gives an idea of the variations which would have occurred - and that can still occur - in marine origin

clays as an effect of exposure to rainwater (Di Maio and Onorati, 2000a; 2000b; 2000c).

Acknowledgements

The Author would like to thank Dr. Rossella Coviello for her help in carrying out some of the tests.

References

Anandarajah, A., and Zhao, D. (2000). Triaxial Behavior of Kaolinite in Different Pore Fluids. *J. of Geotechnical and GeoEnvironmental Engineering*, 126, n. 2, p. 148 – 156.

Anson, R. W. W., and Hawkins, A. B. (1998). The effect of calcium ions in pore water on the residual shear strength of kaolinite and sodium montmorillonite. *Géotechnique*, vol. XLVIII, n. 6, pp. 787 - 800.

Di Maio, C., and Fenelli, G.B. (1994). Residual strength of kaolin and bentonite: the influence of their constituent pore fluid. *Géotechnique*, vol. XLIV, n. 2, pp. 217 - 226.

Di Maio, C. (1996a). The influence of pore fluid composition on the residual shear strength of some natural clayey soils. *VII International Symposium on Landslides*, vol. II, pp. 1189 -1194.

Di Maio, C. (1996b). Exposure of bentonite to salt solution: osmotic and mechanical effects. *Géotechnique*, vol. XLVI, n. 4, pp. 695 - 707.

Di Maio, C., and Onorati, R. (2000a). Swelling behaviour of active clays: the case of an overconsolidated, marine origin clay. *Proceedings of the VIII International Symposium on landslide*, Cardiff, Vol. 1, 469 – 474.

Di Maio, C., and Onorati, R. (2000b). Influence of pore liquid composition on the shear strength of an active clay. *Proceedings of the VIII International Symposium on landslide,* Cardiff, Vol. 1, 463 – 468.

Di Maio, C., and Onorati, R. (2000c). Osmotic softening of overconsolidated clays. *Proceedings of the International Conference on Geotechnical & Geological Engineering*, Melbourne.

Kenney, T. C. (1967). The influence of mineralogical composition on the residual strength of natural soils. *Proc. Geotech. Conf. on Shear Properties of Natural Soils and Rocks*, Oslo, vol.I, pp. 123-129.

Lupini, J. F., Skinner, A. E., and Vaughan, P. R. (1981). The drained residual shear strength of cohesive soils. *Géotechnique* 31, No.2, pp. 181-213.

Mesri, G., and Olson, R. E. (1970). Shear strength of montmorillonite. *Géotechnique*, vol. XX, n. 3, pp. 261-270.

Mitchell, J. K. (1993). Fundamentals of soil behaviour. 2nd ed. John Wiley & Sons, Inc.

Moore, C. A., and Mitchell, J.K. (1974). Electromagnetic forces and soil strength. *Géotechnique*, vol. XXIV, n.4, pp. 627 – 640.

Sridharan, A. (1991). Engineering behaviour of fine grained soils. *Indian Geotechnical Journal*, vol. XXI, n. 1, pp. 1-136

Swelling media: concepts and applications

Jacques M. Huyghe and Peter H. M. Bovendeerd
Department of Biomedical Engineering,
Eindhoven University of Technology, Eindhoven, The Netherlands

Abstract This document deals with applications of mixture theory to the mechanics of porous media, with particular reference to living tissues, ionised media and finite deformation. The theory is built from first principles and the presentation is worked out for first year master students. References to experimental work and to applications are included.

1 Water: a medium in which biology thrieves

There is no biological tissue which is not a mixture. By mixture we mean a composition of different components - either miscible or immiscible - which move relative to one another. This relative motion is vital to every living organism. The human body is a structure that renews itself continually. In five years time every molecule of a human body is replaced. To allow this fast pace of repair, diffusion and convection of waste materials and nutrients are essential. A mayor component of biological tissues is water. The fast pace of renewal of tissues is possible thanks to many factors, one of which being the relative motion of solid, water and solutes within cells and tissues. The high water content ensures easy diffusion of solutes. The description of this motion is obtained by considering the behaviour of the total tissue as the sum of the behaviours of the individual components of which the tissue is constructed, extended with terms that describe the interaction between the different components. This is what we call mixture theory. The application of mixture is by no means restricted to biology. engineering, several types of mixtures exist: only gasses, only fluids, gasses and fluids (e.g. multiple phase flows), or fluids and solids (flow through porous media). *The theory of mixtures* describes these types of systems. Because the theory of mixtures and its application to porous media have applications to subjects very different from biological tissues, these notes are relevant for geomechanics, polymer scientists, petroleum engineers and civil engineers as well.

2 The composition of biological tissues

The cell is the elementary building block of living organisms. The cells of multiple-celled organisms are arranged in tissues to make it possible for the organisms to function effectively. One can distinguish 4 types of tissue [Guyton and Hall, 1993]: neural tissue, epithelial tissue, muscle tissue, and connective and supportive tissue. In this book we will consider the mechanical function of a selection of tissues. All tissues show a multiple-component structure, consisting of a solid, in which at least one fluid is trapped. The fluid is generally distributed over functionally distinct compartments: intracellular, extracellular, lymphatic system, arterial system, venous system, capillary compartment. The fluid within each compartment has diffusing constituents whithin it, which play a key role in many physiological processes. As an example we illustrate this in the intervertebral disc (figure 1). The solid mainly consists of collagen structures, elastine fibers and ionised large molecules, the proteoglycans. The fluid consists of water, in which several substances are disolved, from low-molecular ions, larger molecules (e.g. albumine). The proteoglycans are constructed of glycosaminoglycans, linear polysaccharides consisting of long strings of disaccharides (figure 2). Due to their size (molecular weight 1-3 million), the proteoglycans are tangled up in a fiberstructure. Furthermore they contain negatively charged hydroxyl-, carboxyl-, and sulphate groups, which makes them strongly hydrophylic. They are able to bind a water mass up to 50 times their own weight.

Depending on the properties of the solid component we speak of *hard tissues* or *soft tissues*. The hard tissues (bones, teeth) usually have small deformations and show a linear relation between the stress and strain. Because of their elastic moduli generally higher

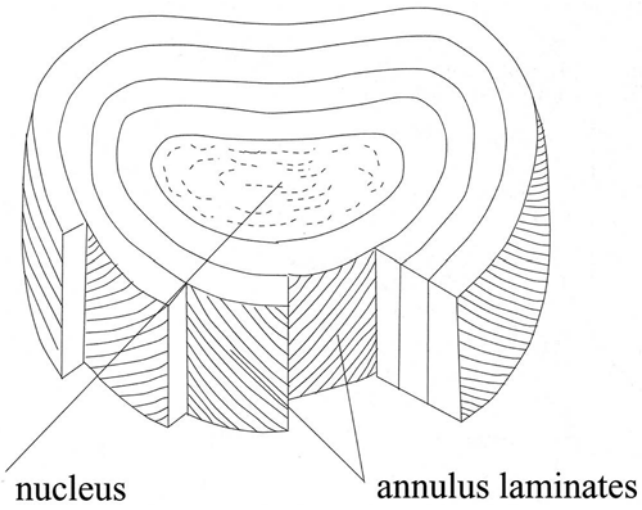

Figure 1. The intervertebral disc : laminar structure of the anulus enclosing the nucleus

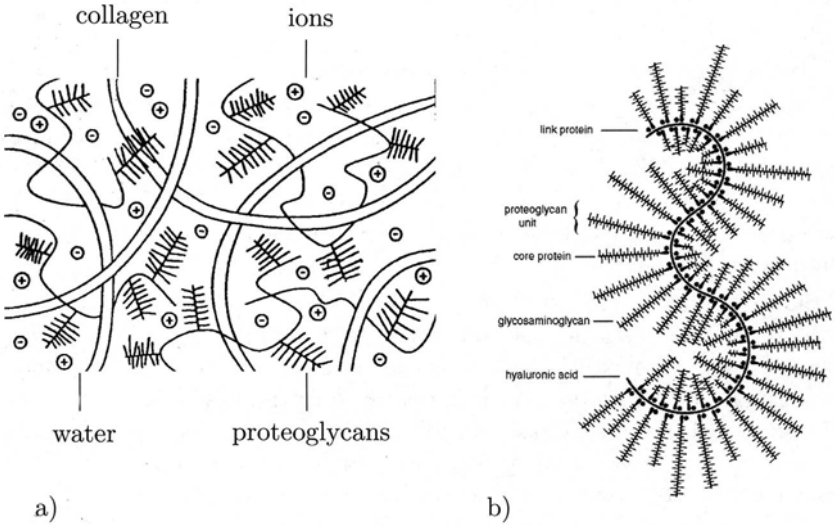

Figure 2. Schematic view of a) the structure of tissue from the intervertebral disc and b) the proteoglycan-molecule. From de Heus (1994).

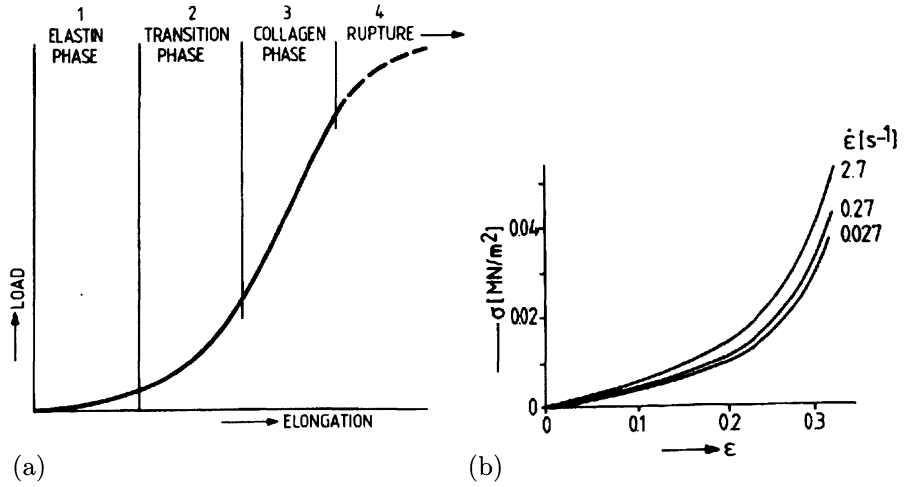

Figure 3. (a) a typical uniaxial force-length relation for soft biological tissues; (b) uniaxial stress-strain relation for aorta-tissue from a sinus of Valsalva for different strain rates. From Sauren et al. (1983).

than the bulk modulus of water, incompressible elasticity or poroelasticity does not apply to hard tissues. The compressibility of water, and even the intinsic compressibility of the solid play an important role in the overall mechanical response.

The soft tissues deform already fiercely under normal physiological circumstances. Strains of 10% up to 100% are easily obtained. The most important solid components in soft tissues are *elastine* and *collagen*. Elastine is an protein that has linear elastic behaviour up to strains of 60% with a Young's modulus of about 1MPa Fung (1993). Collagen fibers consist of tropocollagen molecules. Such a tropocollagen molecule consists of a helix of three polypeptide chains.

Collagen is about 10^3 times as stiff as elastine. The Young's modulus is about 1000 Mpa Fung (1993). For small loads a network of unstretched, undulating collagen fibers between a network of stretched elastine fibers is found. This structure gives the tissue its low stiffness for small deformations. With increasing deformation more and more collagen fibers will be stretched, which causes an increase in the stiffness. Therefore the stress-strain relation is strongly *non-linear*, which for example can be seen from figure 3. A functional consequence is that the collagen network behaves like a protection against large deformations. The mentioned stiffnesses only apply for extension, because the elastine and collagen fibers buckle easily in compression. A compression load is initially transduced by the liquid component in the tissue.

Biological materials behave anisotropically at fiber level due to the fiber construction. This means that the mechanical properties are orientation dependent. Because the fibers are unevenly oriented, these tissues also respond anisotropically on a macroscopic level.

Visco-elasticity is typical for biological tissues. This visco-elasticity expresses itself for example in the strain rate dependence of the stress-strain relation (figure 3). For cyclic loading we find a hysteresis loop in the stress-strain diagram. The stress-strain curve during loading is higher than the unloading curve. Before we established that the non-linear anisotropic behaviour mainly can be ascribed to the solid component of the tissue. The viscous effect can not be localised that easily. It can be present intrinsically in the solid, but it can also be originating from the viscous liquid component. There is experimental evidence that most of the viscosity stems from micromotion of the fluid.

3 The mechano-electrochemical behaviour of biological tissues

Osmotic forces are probably equally important in tissues as viscosity and elasticity. Osmosis ensures that the fiber network of the tissue functions under tensile prestresssing and the fluid saturating the network is under pressure. This vital to the correct functioning of the tissue as aquous solution typically resist compression and fibers resist tension. To illustrate the typical mechano-electrochemical response of tissue, we consider a *swelling and consolidation experiment.* The composition of the tissue as shown in figure 2 causes a response as well as to mechanical (forces and displacements) as to chemical loads (variations of concentration). It is convenient to group the different components of the tissue to describe the response. We consider four components: the negatively charged solid component, consisting of fibers and fixed proteoglycans, the neutral liquid component, the positively charged cations and the negatively charged anions.

The experimental setup is shown in figure 4. The specimen is, precisely fitting, closed in between the walls of the container, piston and a porous filter. The filter makes it possible for the fluid to flow out of the specimen. The resistance to flow in the filter is much smaller than in the specimen. The specimen can be mechanically loaded, using the piston (pressure on the material). A chemical load is applied as a stepwise change in the salt concentration in the fluid flowing through the filter. The response of the tissue to the load is measured in terms of variation of the height of the specimen. The experiment starts with a conditioning phase (a), during which the specimen reaches an equilibrium for a known load. Next, the concentration of the ionic solution is decreased (b). This leads to swelling of the specimen. This is the result of a combination of osmotic, diffusion and convective effects. The concentration gradient between specimen and filter causes (i) an outflux of ions out of the specimen, and (ii) an influx of water into the specimen. Because the specimen has to be electrically neutral, an outflow of ions is limited and therefore an permanent inflow of fluid occurs. In this case we speak of *Donnan osmosis.* The swelling is caused by electrostatic effects. The finally attained condition represents an equilibrium between the swelling pressure in the fluid related to osmotic an electrical effects, and the stress in the solid component, related to the strains in the solid.

In phase (c) the pressure created by the piston is increased incrementally. If we consider both the fluid and solid as incompressible, the increased load is at first carried by the liquid component only. At the bottom of the specimen a large pressure gradient

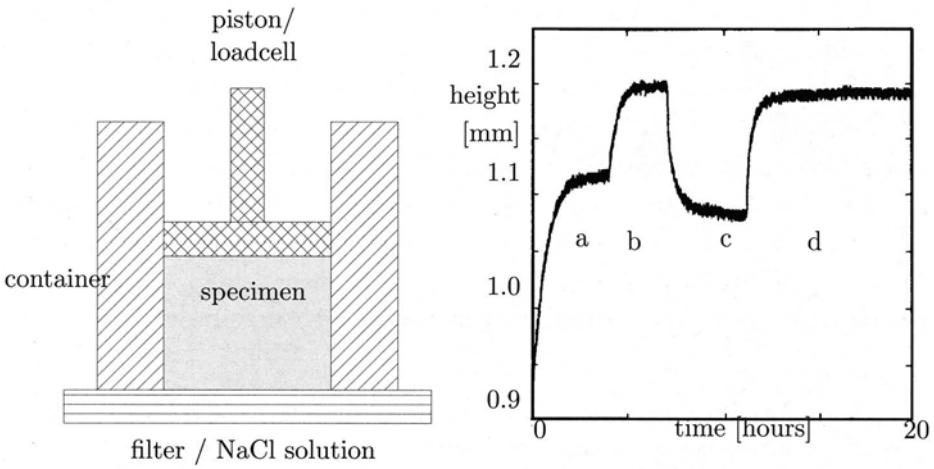

a) b)

Figure 4. The swelling and consolidation experiment: a) the experimental setup; b) the measured variation in height of the specimen in a typical experiment, consisting of a conditioning phase a (salt concentration 0.6 M, pistonpressure 0.08 MPa), a swelling phase b (0.2 M, 0.08 MPa), a consolidation phase c (0.2 M, 0.2 MPa), and a control phase d (0.2 M, 0.08 MPa). From Snijders (1994).

arises, which causes an outflux of fluid. An effect of this outflux is that the piston will lower. The deformation of the specimen causes a stress in the solid component that gradually will take over the load from the liquid.

Finally, in phase (d) the boundary conditions of phase (a) is re-established. The extent to which the equilibrium in phase (d) fits that of phase (a) is an indication for the quality of the experiment. Considering the amount of time the experiment requires this is highly recommandable.

The osmotic pressure causing the swelling here in this experiment by lowering the external concentration, is the procedure through which the body generates stiffness, even in soft tissues, and appears as a solid, while its main constituent is water. The smooth look of a young skin is a result of the pre-tension in the solid substance, as a consequence of the swelling pressure correlated with the presence of water binding molecule structures beneath the skin. The dissappearance of this smooth skin during our lives is to great extent connected to a decrease of the water binding ability of the tissues, as is the ageing of the human body in general. The amount of water decreases during our lives from 75% in a new born to 50% in our last years. Joint disorders are also a consequence of damage of the proteoglycan networks in the cartilage.

Beside biological tissues some engineering materials show the same swelling behaviour. Synthetic hydrogels swell in a similar manner. They are, among others, used for soft contact lenses, diapers, controlled drug delivery and to hold water in desert sands. In figure 5 the results are presented of a swelling and consolidation experiment, carried out upon

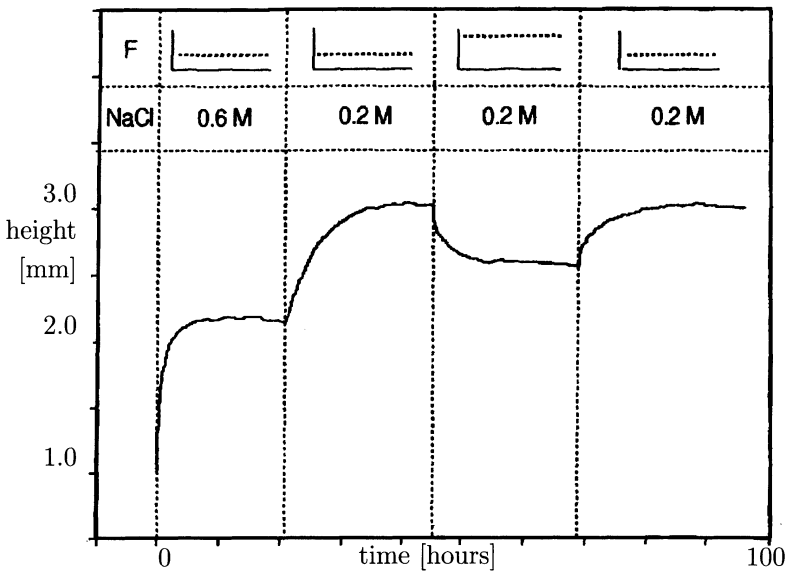

Figure 5. Swelling/consolidation test of an acrylacid-acrylamidecopolymergel processed in a polyurethane foam.

a copolymerised synthetic foam. This material imitates some features of cartilaginous material de Heus (1994). It is designed to do experiments in well controlled circumstances. The results of these experiments are used to validate some aspects of the theory of mixtures on biological tissues, as presented during this course.

The swelling behaviour of clays is important for the ceramics industry. In soil mechanics swelling clays are considered the worst manageable soil for civil engineering projects.

4 Kinematics and stress of 1-component mixtures

4.1 Kinematics

Kinematics describes the displacement and deformation of continua. We identify an arbitrary point in the continuum with *material coordinates* $\{\xi_1, \xi_2, \xi_3\}$. We put these coordinates in a column:

$$\{\xi_1, \xi_2, \xi_3\}^T \tag{4.1}$$

in which the superscript ^{T} represents the transposed. The *momentary positioning vector* $\boldsymbol{x}$ of a particle can be written as a function of the material coordinate ξ_i and the time t:

$$\boldsymbol{x} = \boldsymbol{\chi}(\xi_i, t) \tag{4.2}$$

It is often convenient to identify the points in the continuum with their position $\boldsymbol{x}_0$ in a *state of reference*, e.g. the state at time t_0:

$$\boldsymbol{x}_0 = \boldsymbol{\chi}(\xi_i, t_0) \tag{4.3}$$

We can therefore consider the momentary position $\boldsymbol{x}$ of a point as a function of the position in the state of reference:

$$\boldsymbol{x} = \boldsymbol{X}(\boldsymbol{x}_0, t) \tag{4.4}$$

If the positions of the points in the continuum can be followed, than also changes of these positions can be identified. These variations can reveal itself in changes of the distance between two points, or changes of the angles between line pieces. The size of these changes can be determined with the *deformation tensor*, which will be derived below.

Consider two neighbouring points with material coordinates ξ and $\xi_i + d\xi_i$, that are in the state of reference at positions $\boldsymbol{x}_0$ and $\boldsymbol{x}_0 + d\boldsymbol{x}_0$. In the momentary state, these points are situated at the positions $\boldsymbol{x}$ en $\boldsymbol{x} + d\boldsymbol{x}$.

The projection of the difference vector $d\boldsymbol{x}_0$ in the state of reference on the difference vector $d\boldsymbol{x}$ in the momentary state is the *deformation tensor* $\boldsymbol{F}$:

$$d\boldsymbol{x} = \boldsymbol{F} \cdot d\boldsymbol{x}_0 \tag{4.5}$$

in which $\boldsymbol{F}$ can be determined using:

$$\boldsymbol{F} = (\boldsymbol{\nabla}_0 \boldsymbol{x})^c \tag{4.6}$$

In this formulation $\boldsymbol{\nabla}_0$ represents the gradient operator correlated to the state of reference, while the superscript ^{c} indicates the conjugated. Now, consider an infinitesimal cube of matter that has a volume dV_0 in the state of reference. The momentary volume dV, obtained after deformation $\boldsymbol{F}$, is:

$$dV = \det(\boldsymbol{F})\, dV_0 \tag{4.7}$$

Often, the volumetric variation factor is also used:

$$J = dV/dV_0 = \det(\boldsymbol{F}) \tag{4.8}$$

The deformation tensor $\boldsymbol{F}$ describes the variations in volume and shape as well as the rigid rotation of the material. We are mainly interested in the variations of volume and shape, because these cause the stresses in the material. To describe this pure deformation we can use the *right Cauchy-Green strain tensor* $\boldsymbol{C}$, defined as:

$$\boldsymbol{C} = \boldsymbol{F}^c \cdot \boldsymbol{F} \tag{4.9}$$

The tensor $\boldsymbol{C}$ describes the elongation and shear. In the state of reference the right Cauchy-Green strain tensor $\boldsymbol{C}$ is equal to the unit tensor $\boldsymbol{I}$. For a description of the constitutive behaviour of materials it is most convenient to use a strain tensor that is equal to the zero tensor, $\boldsymbol{O}$, in the state of reference like the *Green-Lagrange strain tensor* $\boldsymbol{E}$:

$$\boldsymbol{E} = \frac{1}{2}(\boldsymbol{C} - \boldsymbol{I}) \tag{4.10}$$

Let us now consider the changes in position and deformation in time. The *velocity* $\boldsymbol{v}$ of a material point is defined as the material time derivative of a momentary position vector of the point:

$$\boldsymbol{v} = \dot{\boldsymbol{x}} = \dot{\boldsymbol{\chi}}(\xi_i, t) = \left.\frac{\partial \boldsymbol{\chi}(\xi_i, t)}{\partial t}\right|_{\xi_i} \tag{4.11}$$

This means that changes of the position are observed, while we are connected to one particle ($\bar{\xi}$ is constant). For the velocity $d\dot{\boldsymbol{x}}$, with which a line element $d\boldsymbol{x}$ variates in size and direction, the momentary deformation rate, can be derived:

$$d\dot{\boldsymbol{x}} = \dot{\boldsymbol{F}} \cdot \boldsymbol{F}^{-1} \cdot d\boldsymbol{x} = (\boldsymbol{D} + \boldsymbol{\Omega}) \cdot d\boldsymbol{x} \tag{4.12}$$

in which the *deformation rate tensor* $\boldsymbol{D}$ and the *rotational rate tensor* $\boldsymbol{\Omega}$ are defined as:

$$\boldsymbol{D} = \frac{1}{2}\left\{\dot{\boldsymbol{F}} \cdot \boldsymbol{F}^{-1} + (\dot{\boldsymbol{F}} \cdot \boldsymbol{F}^{-1})^c\right\} = \frac{1}{2}\left\{(\boldsymbol{\nabla v})^c + (\boldsymbol{\nabla v})\right\} \tag{4.13}$$

$$\boldsymbol{\Omega} = \frac{1}{2}\left\{\dot{\boldsymbol{F}} \cdot \boldsymbol{F}^{-1} - (\dot{\boldsymbol{F}} \cdot \boldsymbol{F}^{-1})^c\right\} = \frac{1}{2}\left\{(\boldsymbol{\nabla v})^c - (\boldsymbol{\nabla v})\right\} \tag{4.14}$$

in which the identitiy $\dot{\boldsymbol{F}} \cdot \boldsymbol{F}^{-1} = (\boldsymbol{\nabla v})^c$ is used. For the velocity, with which the momentary volume of the material changes, applies:

$$\dot{J} = J\, tr\boldsymbol{D} \tag{4.15}$$

The next expression can be deduced for the material time derivative of the Green-Lagrange strain tensor:

$$\dot{\boldsymbol{E}} = \boldsymbol{F}^c \cdot \boldsymbol{D} \cdot \boldsymbol{F} \tag{4.16}$$

4.2 Stress

The deformation, as described above, is usually caused by forces. These forces will often be applied on the surface of the continuum. It is common to relate the magnitude of the force to the size of the surface.

Now, consider a infinitesimal area with a normal vector $\boldsymbol{n}_0$ and surface dA_0. After applying a force $d\boldsymbol{f}$ this area deforms according to a deformation tensor $\boldsymbol{F}$, where the deformed area gets a normal vector $\boldsymbol{n}$ and a surface area dA. We define a *stress vector* $\boldsymbol{t}$ as force per unit surface area $\boldsymbol{t} = d\boldsymbol{f}/dA$. The local state of stress in the material now is given by the *Cauchy stress tensor* $\boldsymbol{\sigma}$, that projects the normal vector $\boldsymbol{n}$ upon the stress vector $\boldsymbol{t}$ in the momentary state:

$$\boldsymbol{t} = \boldsymbol{\sigma} \cdot \boldsymbol{n} \tag{4.17}$$

This equation is a definition of the Cauchy stress tensor. The stress $\boldsymbol{\sigma}$ in general depends on the deformation of the material. For an incompressible material the stress is determined by the deformation (and its time and spatial derivatives) except for a constant hydrostatic contribution $-p\boldsymbol{I}$, where p represents this *hydrodynamic pressure*. This can be shown by loading such a material on all sides by a single hydrostatic pressure. This load will not cause any deformation. The stress nevertheless has to increase to reach an equilibrium at the boundaries. In other words, a part of the stress in the material is independent of the state of deformation. It is convenient to subdivide the stress tensor $\boldsymbol{\sigma}$ in a hydrostatic part $-p\boldsymbol{I}$ and a deviatoric part $\boldsymbol{\sigma}^d$:

$$\boldsymbol{\sigma} = -p\,\boldsymbol{I} + \boldsymbol{\sigma}^d \tag{4.18}$$

The constitutive relation of the stresses depend on the mechanical properties of the material. This constitutive relation, has to be objective, which means that it is not allowed to change during rigid rotations. In a later chapter, we will show that when using the Green-Lagrange strain tensor as a strain quantity, it is convenient to use the *Piola-Kirchhoff stress tensor* , $\boldsymbol{P}$, as a stress quantity, based on objectivity. This stress tensor is defined as:

$$\boldsymbol{P} = \det(\boldsymbol{F})\,\boldsymbol{F}^{-1} \cdot \boldsymbol{\sigma} \cdot \boldsymbol{F}^{-c} \tag{4.19}$$

5 Conservation of mass, balance of momentum and balance of moment of momentum of one-component mixtures

5.1 Conservation of mass

We consider an arbitrary, but fixed part of space with volume V and outer surface A. The matter in this volume has a *density* ρ. Conservation of mass requires, that the variation of mass of this volume matches the mass flow per unit of time through the surface A,

$$\frac{\partial}{\partial t}\int_V \rho\, dV = -\int_A \rho \boldsymbol{v} \cdot \boldsymbol{n}\, dA \tag{5.1}$$

in which $\boldsymbol{n}$ is the outer normal unit vector. Applying Gauss' theorem and swapping of the time derivative and the integral gives

$$\int_V \left(\frac{\partial \rho}{\partial t} + \boldsymbol{\nabla} \cdot (\rho \boldsymbol{v}) \right) dV = 0 \tag{5.2}$$

Because the volume V is arbitrary, the integrant has to be zero in every point in space. This results for the *local conservation of mass* into:

$$\frac{\partial \rho}{\partial t} + \boldsymbol{\nabla} \cdot (\rho \boldsymbol{v}) = 0 \tag{5.3}$$

or

$$\dot{\rho} + \rho \boldsymbol{\nabla} \cdot \boldsymbol{v} = 0 \tag{5.4}$$

in which the *material time derivative* is used:

$$\dot{\rho} = \frac{D\rho}{Dt} = \frac{\partial \rho}{\partial t} + \boldsymbol{v} \cdot \boldsymbol{\nabla} \rho \tag{5.5}$$

5.2 Balance of momentum

Again we consider an arbitrary, but fixed part of space with volume V and a surface A.

The impuls per unit volume is equal to $\rho \boldsymbol{v}$. Fully analogously to the previous derivation, we now consider transport of impuls $\rho \boldsymbol{v}$ instead of mass ρ. The variation of momentum in a volume per unit of time is equal to:

$$\frac{\partial}{\partial t} \int_V \rho \boldsymbol{v} \, dV + \int_A (\rho \boldsymbol{v}) \boldsymbol{v} \cdot \boldsymbol{n} \, dA \tag{5.6}$$

According to the balance of momentum this momentum variation is equal to the resulting force that works on the matter in V. Generally this force consists of a *volume force* $\boldsymbol{q}$ per unit of mass and a *surface force* $\boldsymbol{t}$ per unit of surface area. According to the balance of momentum we find:

$$\frac{\partial}{\partial t} \int_V \rho \boldsymbol{v} \, dV + \int_A (\rho \boldsymbol{v}) \boldsymbol{v} \cdot \boldsymbol{n} \, dA = \int_V \rho \boldsymbol{q} \, dV + \int_A \boldsymbol{t} \, dA \tag{5.7}$$

The last term of this equation is written as:

$$\int_A \boldsymbol{t} \, dA = \int_A \boldsymbol{\sigma} \cdot \boldsymbol{n} \, dA = \int_V \boldsymbol{\nabla} \cdot \boldsymbol{\sigma}^c \, dV \tag{5.8}$$

If we apply Gauss' theorem to the second term of (5.7) also, we obtain *local balance of momentum*, using (5.4):

$$\rho \dot{\boldsymbol{v}} = \boldsymbol{\nabla} \cdot \boldsymbol{\sigma}^c + \rho \boldsymbol{q} \tag{5.9}$$

5.3 Balance of moment of momentum

According to the balance of moment of momentum the variation of the moment of momentum in a volume V is equal to the transport of moment of momentum through the surface area A added to the moment of forces, that work on the volume. The moments

of momentum are considered with respect to a fixed point O. This is written in integral form:

$$\frac{\partial}{\partial t}\int_V \boldsymbol{x}\times\rho\boldsymbol{v}\,dV = -\int_A(\boldsymbol{x}\times\rho\boldsymbol{v})\boldsymbol{v}\cdot\boldsymbol{n}\,dA + \int_V \boldsymbol{x}\times\rho\boldsymbol{q}\,dV + \int_A \boldsymbol{x}\times\boldsymbol{t}\,dA \tag{5.10}$$

This equation holds for *non-polar continua*, continua in which no spread moments are present. Through laborious deduction the *local balance of moment of momentum* is derived:

$$\boldsymbol{\sigma} = \boldsymbol{\sigma}^c \tag{5.11}$$

a simple result, which shows that $\boldsymbol{\sigma}$ is symmetric.

6 Thermodynamics of one-component mixtures

6.1 The first law of thermodynamics

The first law of thermodynamics is the *law of conservation of energy*. It says that the *heat* dQ added to a system can be used to increase an *internal energy* U of the system with an amount dU, to increase the *macroscopic kinetic energy* K of the system with an amount dK, and/or to increase the *work* done by the system with dW_s:

$$dQ = dU + dK + dW_s \tag{6.1}$$

If the first law is used for a continuum it is more convenient to consider the work $dW = -dW_s$ that is applied to the continuum. Furthermore we will consider the changes per unit of time, to write (6.1) as:

$$\dot{K} + \dot{U} = \dot{W} + \dot{Q} \tag{6.2}$$

We consider the part of space again with volume V and surface area A. The *kinetic energy* K of the continuum is:

$$K = \int_V \tfrac{1}{2}\rho\boldsymbol{v}\cdot\boldsymbol{v}\,dV \tag{6.3}$$

The variations in kinetic energy of the continuum per unit of time, $\dot{K}$, is:

$$\dot{K} = \frac{\partial}{\partial t}\int_V \tfrac{1}{2}\rho\boldsymbol{v}\cdot\boldsymbol{v}\,dV + \int_A(\tfrac{1}{2}\rho\boldsymbol{v}\cdot\boldsymbol{v})\boldsymbol{v}\cdot\boldsymbol{n}\,dA \tag{6.4}$$

The *internal energy* U of the matter in V, is:

$$U = \int_V \rho\tilde{U}\,dV \tag{6.5}$$

in which $\tilde{U}$ indicates the *specific* internal energy, or the internal energy per unit mass. In this course we will indicate specific quantities with a tilde ($\tilde{}$) on top of every symbol. The variations of the internal energy per unit of time $\dot{U}$ can be written as:

$$\dot{U} = \frac{\partial}{\partial t}\int_V \rho\tilde{U}\, dV + \int_A (\rho\tilde{U})\boldsymbol{v}\cdot\boldsymbol{n}\, dA \tag{6.6}$$

The applied load consists of a volume load $\boldsymbol{q}$ and a surface load $\boldsymbol{t}$. The power that is provided the load is:

$$\dot{W} = \int_V \rho\boldsymbol{q}\cdot\boldsymbol{v}\, dV + \int_A \boldsymbol{t}\cdot\boldsymbol{v}\, dA \tag{6.7}$$

We will now specify the heat added to the system more accurately. We consider heat supply through internal *heat sources*, that produce an amount of heat $\tilde{r}$ per unit of time per unit of mass and heat drainage through the surface caused by a *heat flux density vector* $\boldsymbol{h}$. The heat added per unit of time now yields:

$$\dot{Q} = \int_V \rho\tilde{r}\, dV - \int_A \boldsymbol{h}\cdot\boldsymbol{n}\, dA \tag{6.8}$$

Application of the first law (6.2) now yields:

$$\begin{aligned}\frac{\partial}{\partial t}\int_V \rho(\tilde{U}+\tfrac{1}{2}\boldsymbol{v}\cdot\boldsymbol{v})\, dV &= -\int_A \rho\left(\tilde{U}+\tfrac{1}{2}\boldsymbol{v}\cdot\boldsymbol{v}\right)\boldsymbol{v}\cdot\boldsymbol{n}\, dA \\ &+ \int_V \rho\boldsymbol{q}\cdot\boldsymbol{v}\, dV + \int_A \boldsymbol{t}\cdot\boldsymbol{v}\, dA \\ &+ \int_V \rho\tilde{r}\, dV - \int_A \boldsymbol{h}\cdot\boldsymbol{n}\, dA \end{aligned} \tag{6.9}$$

The local form of this law follows from Gauss' theorem. The last term of (6.7) is thereby transformed into:

$$\begin{aligned}\int_A \boldsymbol{t}\cdot\boldsymbol{v}\, dA &= \int_V \boldsymbol{\nabla}\cdot(\boldsymbol{\sigma}^c\cdot\boldsymbol{v})\, dV \\ &= \int_V \{(\boldsymbol{\nabla}\cdot\boldsymbol{\sigma}^c)\cdot\boldsymbol{v} + \sigma : (\boldsymbol{\nabla}\boldsymbol{v})^c\}\, dV \\ &= \int_V \{(\boldsymbol{\nabla}\cdot\boldsymbol{\sigma}^c)\cdot\boldsymbol{v} + \sigma : \boldsymbol{D}\}\, dV \end{aligned} \tag{6.10}$$

The last transition is justified, because the Cauchy stress tensor $\boldsymbol{\sigma}$ is symmetric. If we use the balance of mass (5.4) and the balance of momentum (5.9), we find the *local law*

macrostate	number of microstates
$n = 5$	1
$n = 4$	25
$n = 3$	100
$n = 2$	100
$n = 1$	25
$n = 0$	1

Table 1. The number of microstates is a measure of the entropy of the macrostates

for conservation of energy:

$$\rho\dot{\tilde{U}} = \rho\tilde{r} - \boldsymbol{\nabla}\cdot\boldsymbol{h} + \boldsymbol{\sigma} : \boldsymbol{D} \tag{6.11}$$

Using (4.16) and (4.19) we obtain:

$$\rho\dot{\tilde{U}} = \rho\tilde{r} - \boldsymbol{\nabla}\cdot\boldsymbol{h} + \frac{1}{J}\boldsymbol{P} : \dot{\boldsymbol{E}} \tag{6.12}$$

6.2 The second law of thermodynamics

Considering the original formulation of the second law, by Clausius in 1850, heat doesn't flow from a cold system to a warm system spontaneously. A more general formulation states that systems always show the tendency to transit from an ordered to an unordered state. The very existence of the second law is linked to the choice in continuum mechanics to describe a system of a limited number of independent variables. Because of this limitation, this macroscopic description of the system is inherently incomplete. In other words, there are many, many microstates which lead to the same macrostate. The precise definition of disorderliness or entropy (S) in statistical physica has little relevance to the subject of mixture theory of such and will therefore not be dealt with in detail. It suffies to say that the entropy of a system is related to the number of microstates, that leads to the same macrostate. A simple example illustrates this clearly. Consider a set of 5 red beads and 5 blue beads, which fit into a box with 5 spaces on the left and 5 spaces on the right. A microstate is defined by which colour is in which space. The macrostate is defined by a single variable: the number of red beads in the 5 spaces on the left. Macrostate n corresponds to $(\frac{5*..*n+1}{(5-n)!})^2$ microstates: When beads are moved around in the box, there is more chance to have the system moving towards state $n = 2$ or $n = 3$ than towards $n = 0$ or $n = 5$, simply because there are more ways to be in state $n = 2$ or $n = 3$ than $n = 0$ or $n = 5$. This is what the second law of thermodynamics is all about. The second law is almost a tautology. The box naturally moves to the more entropy states $n = 2$ or $n = 3$. In the real problem of continuum mechanics we have billions of particles within each representative elementary volume, resulting in many more microstates for each macrostate. This makes it virtually impossible for entropy to move down. For a closed system we have,

$$dS \geq 0 \tag{6.13}$$

Table 2. Balance laws for non-polar continua

quantity	balance law
mass	$\dot{\rho} + \rho \boldsymbol{\nabla} \cdot \boldsymbol{v} = 0$
momentum	$\rho \dot{\boldsymbol{v}} = \boldsymbol{\nabla} \cdot \boldsymbol{\sigma} + \rho \boldsymbol{q}$
moment of momentum	$\boldsymbol{\sigma} = \boldsymbol{\sigma}^c$
energy	$\rho \dot{\tilde{U}} = \rho \tilde{r} - \boldsymbol{\nabla} \cdot \boldsymbol{h} + \boldsymbol{\sigma} : \boldsymbol{D}$
entropy	$\rho \dot{\tilde{S}} \geq \frac{\rho \tilde{r}}{T} - \boldsymbol{\nabla} \cdot \left(\frac{\boldsymbol{h}}{T} \right)$

Entropy is the amount of knowledge of the system which is locking in the macroscopic description of the system in continuum mechanics terms. It is defined as a measure of the number of microstates which correspond to any microstate. The more microstates correspond to a macrostate, the less knowledge of the details of the system we gain from the macroscopic continuum knowledge, and therefore the higher the entropy. For an open system, the generated entropy is the change in entropy of the system minus the externally supplied entropy $\frac{dQ}{T}$:

$$dS - \frac{dQ}{T} \geq 0 \tag{6.14}$$

If the '='-sign in (6.14) counts, we speak of a *reversible* process, if the '>'-sign counts, the process is *irreversible*. Actually, (6.14) forms the thermodynamic definition of entropy. We will write (6.14) again for a part of space with volume V and surface area A. If we consider the variations per unit of time, we find, using (6.8):

$$\frac{\partial}{\partial t} \int_V \rho \tilde{S} \, dV + \int_A \rho \tilde{S} \boldsymbol{v} \cdot \boldsymbol{n} \, dA \geq \int_V \frac{\rho \tilde{r}}{T} \, dV - \int_A \frac{\boldsymbol{h}}{T} \cdot \boldsymbol{n} \, dA \tag{6.15}$$

in which the specific entropy $\tilde{S}$ is defined as the entropy per unit mass. For the local form follows:

$$\rho \dot{\tilde{S}} \geq \frac{\rho \tilde{r}}{T} - \boldsymbol{\nabla} \cdot \left(\frac{\boldsymbol{h}}{T} \right) \tag{6.16}$$

This form is also known as the *Clausius-Duhem-equation.*

7 Thermodynamic potentials

In this paragraph we will consider the amount of energy of a continua. The energy per unit mass, the specific energy, is also called the *thermodynamic potential.*

7.1 Ideal media

In the traditional application area of thermodynamics, gasses are often considered. These gasses are regarded as an *ideal medium*, which means, a medium in which the state of stress can be characterized with a *hydrostatic pressure* p. For the work done by the system dW_s applies:

$$dW_s = pdV \tag{7.1}$$

in which dV is the change of volume of the medium. Furthermore, the macroscopic kinetic energy K is neglected, as to write the first law (6.1) as:

$$dQ = dU + pdV \tag{7.2}$$

which converts for a reversible process into:

$$dU = TdS - pdV \tag{7.3}$$

We can make a transition from the global to the local form again by working with specific quantities.

$$d\tilde{U} = Td\tilde{S} - pd\tilde{V} \tag{7.4}$$

in which $\tilde{V} = 1/\rho$ represents the volume per unit mass. If we now consider the specific internal energy $\tilde{U}$ as a function of the independent variables $\tilde{S}$ and $\tilde{V}$:

$$\tilde{U} = \tilde{U}(\tilde{S}, \tilde{V}) \tag{7.5}$$

and we determine the total differential of $\tilde{U}$,

$$d\tilde{U} = \left(\frac{\partial \tilde{U}}{\partial \tilde{S}}\right)_{\tilde{V}} d\tilde{S} + \left(\frac{\partial \tilde{U}}{\partial \tilde{V}}\right)_{\tilde{S}} d\tilde{V} \tag{7.6}$$

we can derive from (7.4) and (7.6) that:

$$T = \left(\frac{\partial \tilde{U}}{\partial \tilde{S}}\right)_{\tilde{V}} \tag{7.7}$$

$$p = -\left(\frac{\partial \tilde{U}}{\partial \tilde{V}}\right)_{\tilde{S}} \tag{7.8}$$

From equation (7.6) it turns out that the internal energy doesn't change for a thermodynamic process with which the specific entropy $\tilde{S}$ and the specific volume $\tilde{V}$ remain constant. Therefore it is convenient for such *isentropic, isochoric* processes to use the potential $\tilde{U}$. We call $\tilde{S}$ and $\tilde{V}$ the *characteristic variables*, corresponding to the potential $\tilde{U}$.

For *isentropic, isobaric* processes it is more convenient to use another potential, the *specific enthalpy* $\tilde{H}$, defined as:

$$\tilde{H} = \tilde{U} + p\tilde{V} \tag{7.9}$$

In a reversible process we can write the total differential of $\tilde{H}$, using (7.4).

$$d\tilde{H} = Td\tilde{S} + \tilde{V}dp \tag{7.10}$$

Obviously we can consider the enthalpy $\tilde{H}$ as a function of the characteristic variables $\tilde{S}$ and p: $\tilde{H} = \tilde{H}(\tilde{S}, p)$. It can also be derived that:

$$T = \left(\frac{\partial \tilde{H}}{\partial \tilde{S}}\right)_p \tag{7.11}$$

$$\tilde{V} = \left(\frac{\partial \tilde{H}}{\partial p}\right)_{\tilde{S}} \tag{7.12}$$

For *isothermal, isochoric* processes we use the third thermodynamic potential, the *specific Helmholtz free energy*, defined as:

$$\tilde{F} = \tilde{U} - T\tilde{S} \tag{7.13}$$

for which we can derive that:

$$d\tilde{F} = d\tilde{U} - Td\tilde{S} - \tilde{S}dT = -\tilde{S}dT - pd\tilde{V} \tag{7.14}$$

and

$$\tilde{S} = -\left(\frac{\partial F}{\partial T}\right)_{\tilde{V}} \tag{7.15}$$

$$p = -\left(\frac{\partial F}{\partial \tilde{V}}\right)_T \tag{7.16}$$

In some cases it is recommendable to assume a thermodynamic potential that has the temperature as well as the pressure as the characteristic quantities. This potential is called the *specific Gibbs free energy* $\tilde{G} = \tilde{G}(p, T)$, and is defined as:

$$\tilde{G} = \tilde{H} - T\tilde{S} \tag{7.17}$$

For the variation $d\tilde{G}$ of $\tilde{G}$ the next total differential applies:

$$d\tilde{G} = d\tilde{H} - Td\tilde{S} - \tilde{S}dT = \tilde{V}dp - \tilde{S}dT \tag{7.18}$$

in which (7.10) is used. Following the already known manner, we can derive that:

$$\tilde{V} = \left(\frac{\partial \tilde{G}}{\partial p}\right)_T \tag{7.19}$$

$$\tilde{S} = -\left(\frac{\partial \tilde{G}}{\partial T}\right)_p \tag{7.20}$$

Table 3. Thermodynamic potentials for ideal media.

name	definition	total differential
internal energy	$\tilde{U}$	$d\tilde{U} = Td\tilde{S} - pd\tilde{V}$
enthalpy	$\tilde{H} = \tilde{U} + p\tilde{V}$	$d\tilde{H} = Td\tilde{S} + \tilde{V}dp$
Helmholtz free energy	$\tilde{F} = \tilde{U} - T\tilde{S}$	$d\tilde{F} = -\tilde{S}dT - pd\tilde{V}$
Gibbs free energy	$\tilde{G} = \tilde{H} - T\tilde{S}$	$d\tilde{G} = -\tilde{S}dT + \tilde{V}dp$

For isobaric, isothermal, reversible processes holds:

$$(d\tilde{G})_{p,T,rev} = 0 \tag{7.21}$$

For the *irreversible* case it can be derived that:

$$(d\tilde{G})_{p,T,irrev} < 0 \tag{7.22}$$

An arbitrary isobare, isothermal process goes therefore in the direction of a decreasing Gibbs free energy untill an equilibrium is reached, for which applies:

$$(d^2\tilde{G})_{p,T,equilibrium} > 0 \tag{7.23}$$

We will use these properties of the Gibbs free energy later.

In the text above, two examples of a *free energy* have come up. From (7.13) and (7.17) it appears that such a free energy is defined by reducing another measure of energy with $T\tilde{S}$. This term $T\tilde{S}$ represents that part of the specific energy, that cannot be released from the matter by some process of conversion, because of the second law. When we use the word 'energy' in daily life we mean free energy, energy that can readily be used. When we say 'energy' crisis, we mean free energy crisis. When we say 'law of conservation of energy' we mean, law of conservation of internal energy.

7.2 Non-ideal media

In general the state of stress in a continuum is not hydrostatic. In this paragraph we will describe state functions for a more general state of stress. According to the local balance of energy (6.12) and (6.16), the variations of the specific internal energy $\tilde{U}$ in time are, for reversible processes:

$$\rho\dot{\tilde{U}} = \rho T\dot{\tilde{S}} + \frac{1}{J}\boldsymbol{P} : \dot{\boldsymbol{E}} - \frac{1}{T}\boldsymbol{h}\cdot\boldsymbol{\nabla}T \tag{7.24}$$

We will now restrict ourselves to continua in which no temperature gradients are present. If we consider the variations independent of time, it follows, that:

$$d\tilde{U} = Td\tilde{S} + \frac{1}{\rho_0}\boldsymbol{P} : d\boldsymbol{E} \tag{7.25}$$

If we match this expression with the corresponding expression for ideal media (7.4), we see that the transition to general media can be attained by the next substitution:

$$-p\, d\tilde{V} \longrightarrow \frac{1}{\rho_0} \boldsymbol{P} : d\boldsymbol{E} \tag{7.26}$$

Fysically, both terms represent an infinitesimal amount of work, that is produced by the surface forces per unit of deformed volume. We see in (7.25) that the specific internal energy is a function of $\tilde{S}$ and $\boldsymbol{E}$:

$$\tilde{U} = \tilde{U}(\tilde{S}, \boldsymbol{E}) \tag{7.27}$$

Differentiating this relation yields:

$$d\tilde{U} = \left(\frac{\partial \tilde{U}}{\partial \tilde{S}}\right)_{\boldsymbol{E}} d\tilde{S} + \left(\frac{\partial \tilde{U}}{\partial \boldsymbol{E}}\right)_{\tilde{S}} : d\boldsymbol{E} \tag{7.28}$$

Comparing (7.28) with (7.25) shows that:

$$T = \left(\frac{\partial \tilde{U}}{\partial \tilde{S}}\right)_{\boldsymbol{E}} \tag{7.29}$$

$$\boldsymbol{P} = \rho_0 \left(\frac{\partial \tilde{U}}{\partial \boldsymbol{E}}\right)_{\tilde{S}} \tag{7.30}$$

Extension of (7.13), the total differential for the *specific Helmholtz free energy* $\tilde{F}$, for general media, yields,

$$d\tilde{F} = -\tilde{S}\, dT + \frac{1}{\rho_0} \boldsymbol{P} : d\boldsymbol{E} \tag{7.31}$$

from which it can be shown that:

$$\boldsymbol{P} = \rho_0 \left(\frac{\partial \tilde{F}}{\partial \boldsymbol{E}}\right)_{T} \tag{7.32}$$

$$\tilde{S} = -\left(\frac{\partial \tilde{F}}{\partial T}\right)_{\boldsymbol{E}} \tag{7.33}$$

The total differential of the *specific Gibbs free energy* $\tilde{G}$ (7.18) we extend in an analogue way,

$$d\tilde{G} = -\tilde{S}\, dT - \frac{1}{\rho_0} \boldsymbol{E} : d\boldsymbol{P} \tag{7.34}$$

from which we see that:

$$\tilde{S} = -\left(\frac{\partial \tilde{G}}{\partial T}\right)_{\boldsymbol{P}} \tag{7.35}$$

$$\boldsymbol{E} = \rho_0 \left(\frac{\partial \tilde{G}}{\partial \boldsymbol{P}}\right)_{T} \tag{7.36}$$

Table 4. Thermodynamic potentials.

name	definition	total differential
internal energy	$\tilde{U}$	$d\tilde{U} = Td\tilde{S} + \frac{1}{\rho_0}\boldsymbol{P} : d\boldsymbol{E}$
enthalpy	$\tilde{H} = \tilde{U} - \frac{1}{\rho_0}\boldsymbol{P} : \boldsymbol{E}$	$d\tilde{H} = Td\tilde{S} - \frac{1}{\rho_0}\boldsymbol{E} : d\boldsymbol{P}$
Helmholtz free energy	$\tilde{F} = \tilde{U} - T\tilde{S}$	$d\tilde{F} = -\tilde{S}dT + \frac{1}{\rho_0}\boldsymbol{P} : d\boldsymbol{E}$
Gibbs free energy	$\tilde{G} = \tilde{H} - T\tilde{S}$	$d\tilde{G} = -\tilde{S}dT - \frac{1}{\rho_0}\boldsymbol{E} : d\boldsymbol{P}$

The extensive form of the enthalpy $\tilde{H}$ can also derived this way. The result is shown in table 4.

8 The second law and constitutive behaviour

To trace the mechanical state of a continuum, constitutive equations for the material behaviour are also needed as well as the corresponding initial and boundary conditions. For the choice of the constitutive equations several limitations apply. The next topics have to be satisfied [Schreurs, 1993; Oomens, 1993d]:

- definiteness;
- objectivity;
- thermodynamic permissibility;
- equipresence.

The third demand implies that the constitutive equations have to be chosen such, that the entropy-inequality (6.16) is satisfied for all possible states and variations of state of the continuum. This means that restrictions can be obtained using the second law for a general form of the constitutive equations, that describe the material behaviour. We will use this demand frequently during this course. Equipresence demands that all dependent variables depend on all independent variables unless the third demand makes this impossible. To illustrate this, we will apply this routine first for the simple case of a 1-component mixture.

First we eliminate the term $\rho\tilde{r}$ from expression (6.16), using (6.12) for the first law, which results in:

$$\rho(T\dot{\tilde{S}} - \dot{\tilde{U}}) + \boldsymbol{\sigma} : \boldsymbol{D} + T\boldsymbol{h} \cdot \boldsymbol{\nabla}\left(\frac{1}{T}\right) \geq 0 \tag{8.1}$$

Transition to the specific Helmholtz free energy $\tilde{F}$ (7.13) yields:

$$-\rho(\dot{\tilde{F}} + \dot{T}\tilde{S}) + \boldsymbol{\sigma} : \boldsymbol{D} + T\boldsymbol{h} \cdot \boldsymbol{\nabla}\left(\frac{1}{T}\right) \geq 0 \tag{8.2}$$

We now assume the following:

- the material is incompressible;
- volume forces and forces of inertia are neglected;
- the temperature of the continuum is constant in time and space.

The last demand holds the assumption that the source term $\tilde{r}$ is chosen such that temperature remains constant. Therefore this equation will not be considered any further. Our final choice for the constitutive behaviour has to satisfy the following second law,

$$-\rho\dot{\tilde{F}} + \boldsymbol{\sigma} : \boldsymbol{D} \geq 0 \tag{8.3}$$

with additional conditions, the balance of mass and momentum:

$$\boldsymbol{\nabla} \cdot \boldsymbol{v} = 0 \tag{8.4}$$

$$\boldsymbol{\nabla} \cdot \boldsymbol{\sigma} = \boldsymbol{0} \tag{8.5}$$

One way of processing of these subsidiary conditions is *substitution*, where a variable in a side condition is first isolated and then eliminated from the main equation. The amount of equations as well as the amount of unknowns decreases. If the isolation of a variable is impossible or inconvenient, a subsidiary condition can be accounted using a *Lagrange-multiplier*. The subsidiary condition is written as an equation in which al terms are moved to the left. The right hand side of the equation is zero. The left hand side of this equation, multiplied by a Lagrange-multiplier, is added to the inequality. Because the amount of unknowns increases in this situation, the method of substitution is preferable, if at all applicable.

In this case we chose nevertheless to account the incompressibility condition using a Lagrange-multiplier λ:

$$-\rho\dot{\tilde{F}} + \boldsymbol{\sigma} : \boldsymbol{D} + \lambda\boldsymbol{\nabla} \cdot \boldsymbol{v} \geq 0 \tag{8.6}$$

which can also be written as:

$$-\rho\dot{\tilde{F}} + (\boldsymbol{\sigma} + \lambda\boldsymbol{I}) : \boldsymbol{D} \geq 0 \tag{8.7}$$

The balance laws (8.4) and (8.5) are equivalent to 4 scalar equations with 9 (6 stresses and 3 velocities) unknown variables. We need therefore 5 additional equations. Since balance laws are no more available we need at least 5 constitutive equations. We choose the quantities $\tilde{F}$ and $\boldsymbol{\sigma}+\lambda\boldsymbol{I}$ as dependent variables that depend on independent variables through constitutive relationships. These relationshipas are equivalent to 7 scalar equations (1 for $\tilde{F}$ and 6 for $\boldsymbol{\sigma} + \lambda\boldsymbol{I}$). They provide the 5 missing equations plus 2 equations to compensate for the law quantities $\tilde{F}$ and λ. Then the set of equations is closed.

We chose the Green-Lagrange strain, $\boldsymbol{E}$, as an independent variable. Such choice equates to an assumption of elasticity. Using the principle of *equipresence* we have to make all dependent variables function of all independent variables. In this simple case, it means:

$$\tilde{F} = \tilde{F}(\boldsymbol{E}) \tag{8.8}$$

$$\boldsymbol{\sigma} + \lambda\boldsymbol{I} = \boldsymbol{F} \cdot \sigma^*(\boldsymbol{E}) \cdot \boldsymbol{F}^c \tag{8.9}$$

The pre and post multiplication with $\boldsymbol{F}$ ensures that the constitutive function $\boldsymbol{\sigma}^*$ is objective. The choice of dependent and independent variables doesn't result from theory, but is based on physical insight. The number of dependent variables should be such as to ensure that the final set of equations is closed i.e. the number of unknowns should equal the number of equations. Finally, the extent to which the resulting constitutive equations describes the observed experimental behaviour of the continuum, is a justification for the choice. Substitution of the expressions (8.8) and (8.9) in (8.7) yields:

$$\boldsymbol{F} \cdot \left(-\rho \frac{\partial \tilde{F}}{\partial \boldsymbol{E}} + \boldsymbol{\sigma}^* \right) \cdot \boldsymbol{F}^c : \boldsymbol{D} \geq 0 \tag{8.10}$$

This expression has to apply for arbitrary values of $\boldsymbol{D}$. Because the factor with which $\boldsymbol{D}$ is multiplied, is dependent of $\boldsymbol{D}$ we can satisfy (8.10) by setting this factor to zero. This means that the entropy-production is equal to zero, which is in agreement with our assumption of elastic material behaviour.

Filling of expression (8.9) for $\boldsymbol{\sigma}^*$ yields:

$$\boldsymbol{\sigma} = \rho \boldsymbol{F} \cdot \frac{\partial \tilde{F}}{\partial \boldsymbol{E}} \cdot \boldsymbol{F}^c - \lambda \boldsymbol{I} \tag{8.11}$$

Let's compare this expression with (4.18). We find that the Lagrange-multiplier can physically be interpreted as the *hydrodynamic pressure* p. The deviatoric stress $\boldsymbol{\sigma}^d$ can be written as:

$$\boldsymbol{\sigma}^d = \rho \boldsymbol{F} \cdot \frac{\partial \tilde{F}}{\partial \boldsymbol{E}} \cdot \boldsymbol{F}^c \tag{8.12}$$

If we now switch to the *second Piola-Kirchhoff stress tensor* $\boldsymbol{P}$, based upon $\boldsymbol{\sigma}^d$, we can also write:

$$\boldsymbol{P} = \det(\boldsymbol{F})\, \boldsymbol{F}^{-1} \cdot \boldsymbol{\sigma}^d \cdot \boldsymbol{F}^{-c} = \rho_0 \frac{\partial \tilde{F}}{\partial \boldsymbol{E}} \tag{8.13}$$

where $\rho/\rho_0 = \det(\boldsymbol{F})$ is used. The elastic behaviour of biological materials is often described with a *strain energy density function* or the *elastic potential* , and indicated with the symbol W. This yields:

$$\boldsymbol{P} = \frac{\partial W}{\partial \boldsymbol{E}} \tag{8.14}$$

We can interpret this W as $\rho_0 \tilde{F}$, the amount of Helmholtz free energy per unit volume.

9 Quantities in mixture theories

Let's consider a general mixture of ν components. Microscopically, only one component is present at a certain moment at a certain place in space. Furthermore, the composition of the mixture will differs in general from one spot to the other. In the theory of mixtures we try not to describe the behaviour of every seperate particle. We use a continuum approach instead, in which we spread the properties of the components over a representative volume unit (RVU) ΔV. This volume has to be big enough to provide a good continuum representation of the quantities on microscopic level, but also small enough to avoid averaging of macroscopic variations. If the RVU is displaced through every possible position in the mixture and the average quantities are ascribed to the position of the centre of the RVU, we can determine the average quantities as a function of the position in the mixture (figure 6). A consequence of the averaging concept is that every component, that is present in the mixture, occupies every position $\boldsymbol{x}$ in that mixture. We express the amount of component α in terms of mass m^α or moles n^α. In the theory of mixtures we usually take the *apparent density* ρ of the components, concerned with the RVU, V, and the present amount of mass, m^α, in it:

$$\rho^\alpha = \frac{m^\alpha}{V}, \qquad \alpha = 1, \ldots, \nu \tag{9.1}$$

If component α is immiscible with other components, the volume of component α is indicated with V^α. The real *intrinsic density* ρ_i^α of the components of immiscible components is then:

$$\rho_i^\alpha = \frac{m^\alpha}{V^\alpha}, \qquad \alpha = 1, \ldots, \nu \tag{9.2}$$

We define the *volume fraction* ϕ^α of an immiscible component as:

$$\phi^\alpha = \frac{V^\alpha}{V}, \qquad \alpha = 1, \ldots, \nu \tag{9.3}$$

in which V^α is the volume occupied by component α within volume V. It will be obvious that:

$$\sum_{\alpha=1}^{\nu} \phi^\alpha = 1 \tag{9.4}$$

and

$$\rho^\alpha = \phi^\alpha \rho_i^\alpha, \qquad \alpha = 1, \ldots, \nu \tag{9.5}$$

We define the density ρ of the whole mixture as:

$$\rho = \sum_{\alpha=1}^{\nu} \rho^\alpha \tag{9.6}$$

10 Kinematics and stress in mixtures

10.1 Kinematics

We consider the mixture of ν components again. The collection of material points ξ of a component α ($\alpha = 1, \ldots, \nu$) is indicated with B^α. These points occupy an area $\aleph^\alpha$

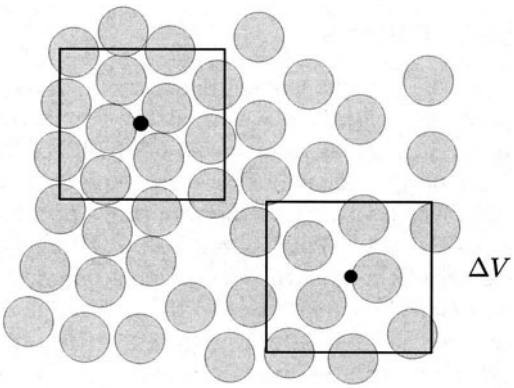

Figure 6. Illustration of the averaging procedure for a mixture of a solid and a fluid.

in the three-dimensional space at time t:

$$\aleph^\alpha(t) = \{\boldsymbol{x}^\alpha = \boldsymbol{\chi}^\alpha(\underset{\sim}{\xi}^\alpha, t) \,|\, \forall \underset{\sim}{\xi}^\alpha \in B^\alpha\}. \tag{10.1}$$

The areas $\aleph^\alpha$ $(\alpha = 1, \ldots, \nu)$ coincide according to the theory of mixtures and every position $\boldsymbol{x}$ is occupied by particles of every single component at the same time. Therefore, the following holds:

$$\boldsymbol{x}(t) = \boldsymbol{x}^1(t) = \boldsymbol{x}^2(t) = \ldots = \boldsymbol{x}^\alpha(t) = \ldots = \boldsymbol{x}^\nu(t) \tag{10.2}$$

We can now define a *deformation tensor* $\boldsymbol{F}^\alpha$ per component:

$$\boldsymbol{F}^\alpha = (\boldsymbol{\nabla}_0^\alpha \boldsymbol{x}^\alpha)^c. \tag{10.3}$$

In this equation the symbol $\boldsymbol{\nabla}_0^\alpha$ represents the gradient operator concerning the state of reference of component α. We define the *Green-Lagrange strain tensor* $\boldsymbol{E}^\alpha$ with respect to component α as:

$$\boldsymbol{E}^\alpha = \frac{1}{2}\left\{(\boldsymbol{F}^\alpha)^c \cdot \boldsymbol{F}^\alpha - \boldsymbol{I}\right\}. \tag{10.4}$$

The velocity $\boldsymbol{v}^\alpha$ of a material point from component α is defined as:

$$\boldsymbol{v}^\alpha = \left.\frac{\partial \boldsymbol{\chi}^\alpha(\underset{\sim}{\xi}^\alpha, t)}{\partial t}\right|_{\underset{\sim}{\xi}^\alpha}. \tag{10.5}$$

We define the velocity of the whole mixture $\boldsymbol{v}$ as the mass weighed average of the velocities of the components:

$$\boldsymbol{v}(\boldsymbol{x}, t) = \frac{1}{\rho}\sum_{\alpha=1}^{\nu} \rho^\alpha \boldsymbol{v}^\alpha(\boldsymbol{x}, t) \tag{10.6}$$

We can point several velocities in every point of the continuum. Therefore several material time derivatives are defined. Let's consider a quantity a^α, a quantity a connected to the component α. We now define two material time derivatives of a^α:

$$\dot{a}^\alpha = \frac{Da^\alpha}{Dt} = \frac{\partial a^\alpha}{\partial t} + \boldsymbol{v} \cdot \boldsymbol{\nabla} a^\alpha \tag{10.7}$$

$$\grave{a}^\alpha = \frac{D^\alpha a^\alpha}{Dt} = \frac{\partial a^\alpha}{\partial t} + \boldsymbol{v}^\alpha \cdot \boldsymbol{\nabla} a^\alpha \tag{10.8}$$

Using time derivative $\dot{a}^\alpha$ we move with the average velocity of the mixture, while we move with the component α if we use $\grave{a}^\alpha$.

We define the *deformation velocity tensor* $\boldsymbol{D}^\alpha$ and the *rotational velocity tensor* $\boldsymbol{\Omega}^\alpha$ as:

$$\boldsymbol{D}^\alpha = \frac{1}{2}\left\{\grave{\boldsymbol{F}}^\alpha \cdot (\boldsymbol{F}^\alpha)^{-1} + (\grave{\boldsymbol{F}}^\alpha \cdot (\boldsymbol{F}^\alpha)^{-1})^c\right\} \tag{10.9}$$

$$\boldsymbol{\Omega}^\alpha = \frac{1}{2}\left\{\grave{\boldsymbol{F}}^\alpha \cdot (\boldsymbol{F}^\alpha)^{-1} - (\grave{\boldsymbol{F}}^\alpha \cdot (\boldsymbol{F}^\alpha)^{-1})^c\right\} \tag{10.10}$$

In these definitions we take the material time derivative of the deformation tensor $\boldsymbol{F}^\alpha$ while we move with component α.

Finally we define the velocity $\boldsymbol{u}^\alpha$ of component α with respect to the velocity of the mixture as:

$$\boldsymbol{u}^\alpha = \boldsymbol{v}^\alpha - \boldsymbol{v}. \tag{10.11}$$

10.2 Stress

Let's consider a small surface with normal unit vector $\boldsymbol{n}_0$ and surface area A_0 in this mixture. We can subdivide a force $\boldsymbol{f}$, that works on this surface, in several contributions $\boldsymbol{f}^\alpha$, working on each of the components α in the mixture. As a result of the force $\boldsymbol{f}$ the surface deforms, during which it gets a normal unit vector $\boldsymbol{n}$ and a surface area A. We now define the *partial stress vector* $\boldsymbol{t}^\alpha$ as the force working on component α, divided by the *total* surface area:

$$\boldsymbol{t}^\alpha = \frac{\boldsymbol{f}^\alpha}{A} \tag{10.12}$$

For the choice of size of the averaging surface A the same considerations apply as for the averaging volume V. Analoguously to (4.17) we now define the *partial Cauchy stress tensor* $\boldsymbol{\sigma}^\alpha$:

$$\boldsymbol{t}^\alpha = \boldsymbol{\sigma}^\alpha \cdot \boldsymbol{n}. \tag{10.13}$$

The tensor $\boldsymbol{\sigma}^\alpha$ projects the normal unit vector $\boldsymbol{n}$ of a surface to the *partial stress vector* $\boldsymbol{t}^\alpha$, that represents the force that is applied per unit of surface area of the mixture of component α.

11 Balance of mass, momentum and moment of momentum in mixtures

11.1 Balance of mass

We consider an arbitrary volume V in space with surface area A. The balance of mass for component α reads in integral form:

$$\frac{\partial}{\partial t}\int_V \rho^\alpha \, dV = -\int_A \rho^\alpha \boldsymbol{v}^\alpha \cdot \boldsymbol{n} \, dA + \int_V \hat{c}^\alpha \, dV. \tag{11.1}$$

This equation is equal to (5.1), with an extra source term added that accounts for the variation in mass of component α with respect to interactions with other components. The quantity $\hat{c}^\alpha$ is defined as the rate of mass transfer from component α to other components changes per unit volume of mixture. We can think of phase-changes (mass-exchange between liquid and vapour), variation of ionisation (mass-exchange between the ion-component and the solid phase), or chemical reactions. Applying Gauss' theorem yields the *local form of the balance of mass per component* α:

$$\frac{\partial \rho^\alpha}{\partial t} + \boldsymbol{\nabla} \cdot (\rho^\alpha \boldsymbol{v}^\alpha) = \hat{c}^\alpha. \tag{11.2}$$

The exchange of mass between the mutual components may not influence the total mass:

$$\sum_{\alpha=1}^{\nu} \int_V \hat{c}^\alpha \, dV = 0. \tag{11.3}$$

At a local level this results in the *local balance of mass for the whole mixture*:

$$\sum_{\alpha=1}^{\nu} \hat{c}^\alpha = 0. \tag{11.4}$$

11.2 Balance of momentum

We consider the arbitrary, but fixed part of space with volume V and surface area A again. In integral form the balance of momentum for component α is given by:

$$\begin{aligned}\frac{\partial}{\partial t}\int_V \rho^\alpha \boldsymbol{v}^\alpha \, dV = &-\int_A (\rho^\alpha \boldsymbol{v}^\alpha)\boldsymbol{v}^\alpha \cdot \boldsymbol{n} \, dA \\ &+ \int_V \rho^\alpha \boldsymbol{q}^\alpha \, dV + \int_A \boldsymbol{t}^\alpha \, dA + \int_V (\hat{\boldsymbol{p}}^\alpha + \hat{c}^\alpha \boldsymbol{v}^\alpha) \, dV.\end{aligned} \tag{11.5}$$

We recognize the integral form for one-phase materials again (5.7), completed with an interaction-term. The volume force that works upon α is indicated with $\boldsymbol{q}^\alpha$. The term in $\boldsymbol{t}^\alpha$ represents the force per unit surface area mixture on component α. Based on

(10.12) a contribution of the surface forces has to be calculated by integrating the partial stress vectors $\boldsymbol{t}^\alpha$ over the surface of the mixture A. In the interaction term the volume force $\hat{\boldsymbol{p}}^\alpha$ represents the momentum transfered from other components to component α , counted per unit volume mixture and per unit of time. Transition of momentum occurs for example in friction forces, that are a result of relative movement of the components. The term $\hat{c}^\alpha \boldsymbol{v}^\alpha$ represents momentum transfer associated with the exchange of mass $\hat{c}^\alpha$. It is assumed that the added mass of component α gets the same velocity as the already present mass of component α. Using Gauss' theorem we find the *local form of the balance of momentum per component* α again:

$$\rho^\alpha \left\{ \frac{\partial \boldsymbol{v}^\alpha}{\partial t} + \boldsymbol{v}^\alpha \cdot \boldsymbol{\nabla} \boldsymbol{v}^\alpha \right\} = \rho^\alpha \dot{\boldsymbol{v}}^\alpha = \boldsymbol{\nabla} \cdot (\boldsymbol{\sigma}^\alpha)^c + \rho^\alpha \boldsymbol{q}^\alpha + \hat{\boldsymbol{p}}^\alpha, \tag{11.6}$$

in which $\boldsymbol{\sigma}^\alpha$ represents the partial Cauchy stress tensor. The term $\hat{c}^\alpha \boldsymbol{v}^\alpha$ doesn't show up again in this equation, because we used the balance of mass (11.2). For the total mixture applies that the net conversion of momentum with respect to the interaction terms has to be zero, so the *local balance of momentum for the total mixture* holds:

$$\sum_{\alpha=1}^{\nu} (\hat{c}^\alpha \boldsymbol{v}^\alpha + \hat{\boldsymbol{p}}^\alpha) = \boldsymbol{0}. \tag{11.7}$$

11.3 Balance of moment of momentum

The integral form of the balance of momentum for component α is:

$$\begin{aligned} \frac{\partial}{\partial t} \int_V \boldsymbol{x}^\alpha \times \rho^\alpha \boldsymbol{v}^\alpha \, dV &= - \int_A (\boldsymbol{x}^\alpha \times \rho^\alpha \boldsymbol{v}^\alpha) \boldsymbol{v}^\alpha \cdot \boldsymbol{n} \, dA \\ &+ \int_V \boldsymbol{x}^\alpha \times \rho^\alpha \boldsymbol{q}^\alpha \, dV + \int_A \boldsymbol{x}^\alpha \times \boldsymbol{t}^\alpha \, dA \\ &+ \int_V (\boldsymbol{x}^\alpha \times (\hat{c}^\alpha \boldsymbol{v}^\alpha + \hat{\boldsymbol{p}}^\alpha) + \hat{\boldsymbol{m}}^\alpha) \, dV \end{aligned} \tag{11.8}$$

The last term accounts for the transfer of the moment of momentum from other components to component α. The term $\boldsymbol{x}^\alpha \times (\hat{c}^\alpha \boldsymbol{v}^\alpha + \hat{\boldsymbol{p}}^\alpha)$ is the moment of momentum transfer associated with the momentum interaction $(\hat{c}^\alpha \boldsymbol{v}^\alpha + \hat{\boldsymbol{p}}^\alpha)$. The term $\hat{\boldsymbol{m}}^\alpha$ represents the direct moment of momentum transfer to component α by the other components, counted per unit of volume mixture and per unit of time. An example of such direct moment of momentum interaction is the case of friction forces transfered from fluid to solid in flow through helical pore structure with preferential helicity. The local form of the balance of moment of momentum is:

$$\hat{\boldsymbol{M}}^\alpha = (\boldsymbol{\sigma}^\alpha)^c - \boldsymbol{\sigma}^\alpha \tag{11.9}$$

in which $\hat{\boldsymbol{M}}^\alpha$ is the anti-symmetric tensor corresponding to the axial vector $\hat{\boldsymbol{m}}^\alpha$, defined such that for all vectors $\boldsymbol{a}$ applies:

$$\hat{\boldsymbol{m}}^\alpha \times \boldsymbol{a} = \hat{\boldsymbol{M}}^\alpha \cdot \boldsymbol{a} \tag{11.10}$$

The reader is referred to specialized literature for the proof of eq.(11.9). At this moment we consider $\hat{\boldsymbol{M}}^{\alpha}$ as a quantity, analoguous to the terms $\hat{c}^{\alpha}$ and $\hat{\boldsymbol{p}}^{\alpha}$.

12 Thermodynamics in mixture theory

12.1 The first law

We formulate the first law of thermodynamics for a component α in the mixture as the first law for a one component continuum (6.9), completed with an interaction term :

$$\begin{aligned}
&\frac{\partial}{\partial t}\int_V \rho^{\alpha}\left(\tilde{U}^{\alpha}+\tfrac{1}{2}\boldsymbol{v}^{\alpha}\cdot\boldsymbol{v}^{\alpha}\right)\,dV = \\
&-\int_A \rho^{\alpha}\left(\tilde{U}^{\alpha}+\tfrac{1}{2}\boldsymbol{v}^{\alpha}\cdot\boldsymbol{v}^{\alpha}\right)\boldsymbol{v}^{\alpha}\cdot\boldsymbol{n}\,dA+\int_V \rho^{\alpha}\boldsymbol{q}^{\alpha}\cdot\boldsymbol{v}^{\alpha}\,dV \\
&+\int_A \boldsymbol{t}^{\alpha}\cdot\boldsymbol{v}^{\alpha}\,dA+\int_V \rho^{\alpha}\tilde{r}^{\alpha}\,dV-\int_A \boldsymbol{h}^{\alpha}\cdot\boldsymbol{n}\,dA+\int_V \hat{e}^{\alpha}\,dV \\
&+\int_V \left(\boldsymbol{v}^{\alpha}\cdot\hat{\boldsymbol{p}}^{\alpha}+\tfrac{1}{2}\boldsymbol{\Omega}^{\alpha}:\hat{\boldsymbol{M}}^{\alpha}+\hat{c}^{\alpha}(\tilde{U}^{\alpha}+\tfrac{1}{2}\boldsymbol{v}^{\alpha}\cdot\boldsymbol{v}^{\alpha})\right)\,dV, \qquad (12.1)
\end{aligned}$$

in which $\tilde{U}^{\alpha}$ represents the specific internal energy of component α, $\boldsymbol{h}^{\alpha}$ represents the heat flux density vector for component α and $\tilde{r}^{\alpha}$ represents the specific heat supply to component α by heat sources. In the second of these term the symbol $\hat{e}^{\alpha}$ represents the direct energy transfer from the other components to component α, calculated per unit volume mixture and per unit of time. The last term represents the energy supply caused by interaction effects with respect to the exchange of mass $\hat{c}^{\alpha}$, the exchange of momentum $\hat{\boldsymbol{p}}^{\alpha}$ and the exchange of moment of momentum $\hat{\boldsymbol{M}}^{\alpha}$. Using Gauss' theorem and the balance of mass, momentum and moment of momentum the *local form of the balance of energy per component* α is derived:

$$\rho\dot{\tilde{U}}^{\alpha}=\rho^{\alpha}\tilde{r}^{\alpha}-\boldsymbol{\nabla}\cdot\boldsymbol{h}^{\alpha}+\boldsymbol{\sigma}^{\alpha}:\boldsymbol{D}^{\alpha}+\hat{e}^{\alpha}. \qquad (12.2)$$

Equation (6.11) shows that only the term $\hat{e}^{\alpha}$ is added in the mixture. In analogy to the other balance laws, we demand that the balance of energy for the components is consistent with the *balance of energy for the total mixture*:

$$\sum_{\alpha=1}^{\nu}\left(\hat{e}^{\alpha}+\boldsymbol{u}^{\alpha}\cdot\hat{\boldsymbol{p}}^{\alpha}+\hat{c}^{\alpha}(\tilde{U}^{\alpha}+\tfrac{1}{2}\boldsymbol{u}^{\alpha}\cdot\boldsymbol{u}^{\alpha})\right)=0. \qquad (12.3)$$

Notice that the velocities $\boldsymbol{u}^{\alpha}$, defined in (10.11), are found in this equation, i.e. the component velocities with respect to the mixture velocity.

12.2 The second law

The second law of thermodynamics, as formulated in (6.14), describes thermodynamic properties of a system. For a mixture it isn't clear how the system has to be defined: is

the system formed by the total mixture or forms every component a system on its own? In the last case the entropy production per component has to be greater or equal to zero. In the first case this demand applies for the total mixture, and there can be components for which the entropy production is less than zero. We formulate the second law for the whole mixture as this is the only restriction which is agreed upon by the whole scientific community. Starting from (6.16), we postulate the *local form of the second law for the whole mixture*:

$$\sum_{\alpha=1}^{\nu} \left\{ \rho^\alpha \hat{\tilde{S}}^\alpha - \frac{\rho^\alpha \tilde{r}^\alpha}{T^\alpha} + \boldsymbol{\nabla} \cdot \left(\frac{\boldsymbol{h}^\alpha}{T^\alpha} \right) + \hat{c}^\alpha \tilde{S}^\alpha \right\} \geq 0. \tag{12.4}$$

in which $\tilde{S}^\alpha$ is the specific entropy of component α, and T^α is the temperature of component α. The term $\sum \hat{c}^\alpha \tilde{S}^\alpha$ discounts the interaction between the components again. If we eliminate the term $\rho^\alpha \tilde{r}^\alpha$ using the balance of energy per component (12.2) and eliminate the term $\sum \hat{e}^\alpha$ using the balance of energy for the total mixture (12.3), it follows that:

$$\sum_{\alpha=1}^{\nu} \left\{ \rho^\alpha \hat{\tilde{S}}^\alpha - \frac{\rho^\alpha \hat{\tilde{U}}^\alpha}{T^\alpha} + \frac{\boldsymbol{\sigma}^\alpha : \boldsymbol{D}^\alpha}{T^\alpha} - \frac{\hat{\boldsymbol{p}}^\alpha \cdot \boldsymbol{u}^\alpha}{T^\alpha} + \boldsymbol{h}^\alpha \cdot \boldsymbol{\nabla} \left(\frac{1}{T^\alpha} \right) - \frac{\hat{c}^\alpha}{T^\alpha} (\tilde{U}^\alpha + \tfrac{1}{2} \boldsymbol{u}^\alpha \cdot \boldsymbol{u}^\alpha + T^\alpha \tilde{S}^\alpha) \right\} \geq 0. \tag{12.5}$$

If we finally define the Helmholtz free energy per unit mass for component α as,

$$\tilde{F}^\alpha = \tilde{U}^\alpha - T^\alpha \tilde{S}^\alpha, \tag{12.6}$$

we can divert (12.5) into:

$$\sum_{\alpha=1}^{\nu} \frac{1}{T^\alpha} \left\{ -\rho^\alpha (\hat{\tilde{F}}^\alpha - \tilde{S}^\alpha \hat{T}^\alpha) + \boldsymbol{\sigma}^\alpha : \boldsymbol{D}^\alpha + \hat{\boldsymbol{p}}^\alpha \cdot \boldsymbol{u}^\alpha - T^\alpha \boldsymbol{h}^\alpha \cdot \boldsymbol{\nabla} \left(\frac{1}{T^\alpha} \right) - \hat{c}^\alpha (\tilde{F}^\alpha + \tfrac{1}{2} \boldsymbol{u}^\alpha \cdot \boldsymbol{u}^\alpha) \right\} \geq 0. \tag{12.7}$$

13 Thermodynamic potentials in mixture theory

13.1 Partial quantities

The total mass of a mixture is equal to the sum of the masses of the components of which the mixture consists. The total volume V of a mixture is generally not equal to the sum of the component volumina:

$$V \neq \sum_{\alpha=1}^{\nu} V^\alpha. \tag{13.1}$$

This is caused, because the interaction between molecules of the same constituent is generally different from that between molecules of different constituent. To account the

Table 5. Balance laws for mixtures.

quantities		balance law for component (c) and mixture (m)
mass	c	$\dot{\rho}^\alpha + \rho^\alpha \boldsymbol{\nabla} \cdot \boldsymbol{v}^\alpha = \hat{c}^\alpha$
	m	$\sum \hat{c}^\alpha = 0$
momentum	c	$\rho^\alpha \dot{\boldsymbol{v}}^\alpha = \boldsymbol{\nabla} \cdot (\boldsymbol{\sigma}^\alpha)^c + \rho^\alpha \boldsymbol{q}^\alpha + \hat{\boldsymbol{p}}^\alpha$
	m	$\sum (\hat{c}^\alpha \boldsymbol{v}^\alpha + \hat{\boldsymbol{p}}^\alpha) = \boldsymbol{0}$
moment of momentum	c	$\boldsymbol{\sigma}^\alpha - (\boldsymbol{\sigma}^\alpha)^c = \hat{\boldsymbol{M}}^\alpha$
energy	c	$\rho \dot{\tilde{U}}^\alpha = \rho^\alpha \tilde{r}^\alpha - \boldsymbol{\nabla} \cdot \boldsymbol{h}^\alpha + \boldsymbol{\sigma}^\alpha : \boldsymbol{D}^\alpha + \hat{e}^\alpha$
	m	$\sum \left\{ \hat{e}^\alpha + \boldsymbol{u}^\alpha \cdot \hat{\boldsymbol{p}}^\alpha + \hat{c}^\alpha (\tilde{U}^\alpha + \frac{1}{2} \boldsymbol{u}^\alpha \cdot \boldsymbol{u}^\alpha) \right\} = 0$
entropy	m	$\sum \left\{ \rho^\alpha \tilde{S}^\alpha - \frac{\rho^\alpha \tilde{r}^\alpha}{T^\alpha} + \boldsymbol{\nabla} \cdot \left(\frac{\boldsymbol{h}^\alpha}{T^\alpha} \right) + \hat{c}^\alpha \tilde{S}^\alpha \right\} \geq 0.$

independence of mixture composition *partial quantities* are used. We define the *partial* molar volume $\bar{V}^\alpha$ of component α as:

$$\bar{V}^\alpha = \left(\frac{\partial V}{\partial n^\alpha} \right)_{p,T,n^\beta,\beta \neq \alpha}, \qquad \alpha = 1, \ldots, \nu \tag{13.2}$$

So, $\bar{V}^\alpha$ represents the increase of the volume of a mixture as a result of adding a little amount of component α, figured per mol of the added component. Furthermore, the thermodynamic state of the mixture, here characterized by p and T, has to stay constant, as well as the composition of the mixture. If $\bar{V}^\alpha$ is independent of the composition of the mixture, then integration of (13.2), yields:

$$V = \sum_{\alpha=1}^{\nu} n^\alpha \bar{V}^\alpha. \tag{13.3}$$

Generally the partial volume of a component in a mixture is not equal to the molar volume of the pure component. If this ís the case, we say the mixture is ideal.

13.2 Ideal media

Also for mixtures we can define potentials (Katchalsky en Curran, 1965). We will restrict ourselves to an ideal mixture of ν components, in which an amount n^α moles

of every component α is present. In the former chapter it turned out that for an ideal medium the Gibbs free energy G is a function of the pressure p and the temperature T. In the mixture, G is also a function of the mixture composition:

$$G = G(T, p, n^1, \ldots, n^\nu) \tag{13.4}$$

For variations dG the following differential applies:

$$\begin{aligned} dG &= \left(\frac{\partial G}{\partial T}\right)_{p,n^\alpha} dT + \left(\frac{\partial G}{\partial p}\right)_{T,n^\alpha} dp \\ &+ \sum_{\alpha=1}^{\nu} \left(\frac{\partial G}{\partial n^\alpha}\right)_{p,T,n^\beta,\beta\neq\alpha} dn^\alpha \end{aligned} \tag{13.5}$$

We now define the *partial molar Gibbs free energy* $\bar{G}^\alpha$ of a component α in a mixture as:

$$\bar{G}^\alpha = \left(\frac{\partial G}{\partial n^\alpha}\right)_{p,T,n^\beta,\beta\neq\alpha} \tag{13.6}$$

We can consider $\bar{G}^\alpha$ as an increase in free energy of the mixture if we add one mole of component α to that mixture. The partial molar Gibbs free energy is usually called the *chemical potential* μ^α:

$$\mu^\alpha = \bar{G}^\alpha = \left(\frac{\partial G}{\partial n^\alpha}\right)_{p,T,n^\beta,\beta\neq\alpha} \tag{13.7}$$

Now (13.5) can be diverted into:

$$dG = \left(\frac{\partial G}{\partial T}\right)_{p,n^\alpha} dT + \left(\frac{\partial G}{\partial p}\right)_{T,n^\alpha} dp + \sum_{\alpha=1}^{\nu} \mu^\alpha dn^\alpha \tag{13.8}$$

The part of the chemical potential in thermodynamics is comparable with that of the potential energy in mechanics. To illustrate this statement, let's consider a process – for a constant temperature and pressure – in which an amount dn^α of component α is converted from state A to state B. The variation dG in Gibbs free energy then reads:

$$dG = (\mu_B^\alpha - \mu_A^\alpha) dn^\alpha. \tag{13.9}$$

According to (7.22) the convertion from A to B will initiate spontaneously if dG is negative, i.e. if $\mu_A^\alpha > \mu_B^\alpha$. If $\mu_A^\alpha < \mu_B^\alpha$, the process will go in the opposite direction. In equilibrium $dG = 0$ applies, such that $\mu_A^\alpha = \mu_B^\alpha$. The chemical potential therefore indicates in what direction the process will go. We will see in chapter 5 that we can describe processes like osmosis well using the chemical potential.

13.3 Non-ideal media

For mixtures of ideal media we could characterize the state of stress per component with the total pressure of the mixture p and the mixture composition $n^1, \ldots, n^\nu$ (13.4), because these quantities fix the partial pressures p^α totally. For mixtures of non-ideal

media the state of stress has to be described with a whole stress tensor $\boldsymbol{\sigma}^\alpha$, that cannot be derived unambiguously from the total mixture stress $\boldsymbol{\sigma}$ and the mixture composition. Therefore we have to make G explicitly dependent on all component stresses. Starting from (7.34) we characterize the state of stress per component with the second Piola-Kirchhoff stress tensor $\boldsymbol{P}^\alpha$.

For mixtures of ideal media, like gasses, it is in addition usual to express the amount of a component in moles, indicated with n^α. For non-ideal media it is sometimes more convenient to convert to masses m^α. The Gibbs free energy G for mixtures of non-ideal media can therefore be written as:

$$G = G(T, \boldsymbol{P}^1, \ldots, \boldsymbol{P}^\nu, m^1, \ldots, m^\nu) \tag{13.10}$$

For the variation of the Gibbs free energy after adding a small amount of component α, counted per unit mass, now applies:

$$\tilde{\mu}^\alpha = \left(\frac{\partial G}{\partial m^\alpha}\right)_{T, P^1, \ldots, P^\nu, m^\beta, \beta \neq \alpha} \tag{13.11}$$

We call $\tilde{\mu}^\alpha$ the *specific chemical potential* of component α.

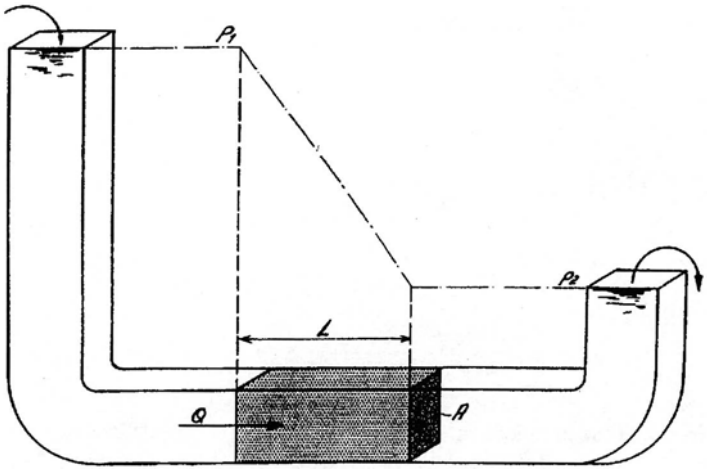

Figure 7. Darcy's experiment

14 The concepts of two-component mixtures

14.1 Permeability

The French engineer Darcy initiated a number of experiments in the context of the design of fontains in the city of Dijon. These experiments aimed at quantifying the permeation of water through sand beds Darcy (1856) (Darcy, 1856). In the experiments water saturated cylindrical sand samples were subjected to a constant pressure gradient. The flow through the specimens was measured for varying pressure difference, cross-sections and lengths of the specimens. (figuur 7). These experiments showed that the flow is proportional to the pressure difference $p_1 - p_2$ and the cross-section A of the sample and inversely proportional to the length L of the sample:

$$Q = \frac{K(p_1 - p_2)A}{L} \tag{14.1}$$

The proportionality constant K is the *permeability.* Experiments showed that biological tissues complies with Darcy's law reasonably well (Maroudas, 1968, 1979) when the fluid is a physiological salt solution. In soil mechanics Darcy's law has been shown valid for sand and coarse lime. For clays a conclusive experiment has never been done. When different Newtonian fluids are used in the same sand samples, the permeability of the sample has been shown to be inversely proportional to the viscosity of the fluid. The permeability depends on the size and the structure of the pores of the sample also. If the sample is compressed, the permeability drops. Different relationships between permeability and fluid volume fraction are proposed in the literature. In very deformable porous media, like soft biological tissues, only the viscous forces of the flowing liquid is sufficient to cause compression of the porous medium and thus a reduction of the permeability.

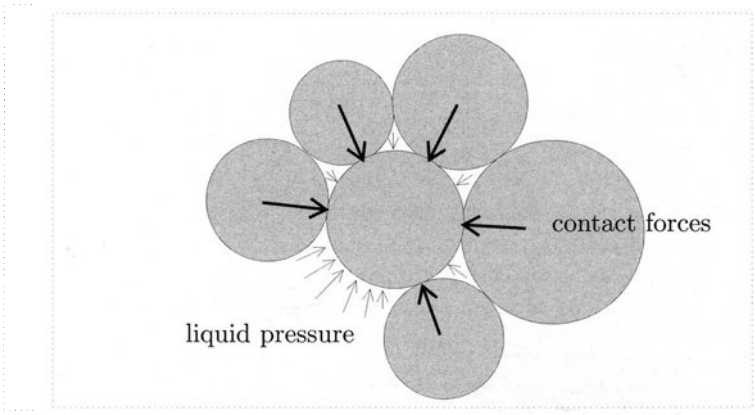

Figure 8. The mechanical stress in a fluid solid mixture.

14.2 Effective stress

Consider a mixture of an incompressible solid and an incompressible liquid (figure 8). We assume that the solid is composed of grains - to focus the attention and without loss of generality. The dimensions of the grains and the pores between the grains are small relative to the macroscopic dimensions of the material. Every grain is subject to two types of external load: (1) the liquid pressure (2) the contact forces with neighbouring grains. The liquid pressure is an isotropic load which cannot result into deformation of the grains as they are incompressible. Only the contact forces with neighbouring grains result into a stress field in the grains and thus deformation of the solid skeleton. The latter stress field, averaged over a large number of grains and measured per unit mixture surface is the effective stress. The effective stress in a mixture of an incompressible solid and an incompressible liquid is that part of the stress that causes deformation. The total stress $\boldsymbol{\sigma}$ is given by the sum of the effective stress $\boldsymbol{\sigma}_e$ and the hydrostatic pressure $-p\boldsymbol{I}$:

$$\boldsymbol{\sigma} = \boldsymbol{\sigma}_e - p\boldsymbol{I} \tag{14.2}$$

In this example we assumed that only the pressure of the liquid contributes to the total stress. In principle every component - and therefore also the liquid component - can contribute to the effective stress in a mixture. Therefore it is wrong to consider (14.2) a division of the stress in an effective stress caused by the solid and a pressure caused by the liquid. In general both components contribute to both terms. In soilb and rock mechanics, the fields from which the effective stress concept originates, the effective stress is often called the grain stress, because for lots of soil mixtures contribution of the liquid to the the effective stress is negligible.

In the former chapter we saw that in the more recent theory of mixtures, it is common practise to subdivide the total stress in a mixture in partial stresses, in analogy to the much older concept of partial pressure from the kinetic theory of gasses. These partial stresses can be associated with every individual component. For the porous medium this means:

$$\boldsymbol{\sigma} = \boldsymbol{\sigma}^s + \boldsymbol{\sigma}^f \tag{14.3}$$

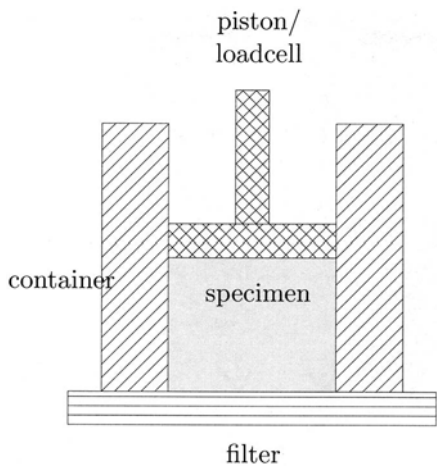

Figure 9. Setup for a one dimensional consolidation test.

The stress-strain relation becomes a relation between the effective stress and the pressure in a porous medium. Notice that in force equilibrium the total stress appears.

15 Theory of consolidation of Terzaghi

During this presentation of porous media mechanics the historical development will be followed, because that is the easiest way to comprehend it.

One of the major enemies of civil engineering is the phenomenon consolidation. After constructing a big builing or a bridge the foundation of the construction appears to sink several inches into the ground. As long as this sinking is distributed homogeneously over the total area of the foundation consequences are not yet disastrous. If there is differential sinking, the consequences can be catastrophic. Cracks in the construction, leakage in case of a dam or pulling a building out of position (tower of Pisa). Consolidation can usually be attributed to the construction pushing the fluid beneath the foundation aside. Therefore, this problem can only be studied with porous media mechanics.

The problem of consolidation has been studied by Terzaghi in the nineteen twenties. Terzaghi restricted himself to a one dimensional consolidation, in which the liquid flow and the displacement of the solid occur in only on direction. This situation is reasonable for a very wide foundation plate where the sideward outflow of fluid is only a local boundary effect. We can create this situation on purpose in a one dimensional consolidation experiment (figuur 9), which is often used to study cartilage.

In this experiment a cilindrical specimen is placed in a fitting rigid cilinder. The bottom of the specimen has contact with a porous filter in which the permeability is much higher than the permeability in the specimen itself. The top of the cilinder has contact with an inpermeable piston with surface area A, that is loaded with an axial force F. For an incremental increase of the force F, this force will first be intercepted by

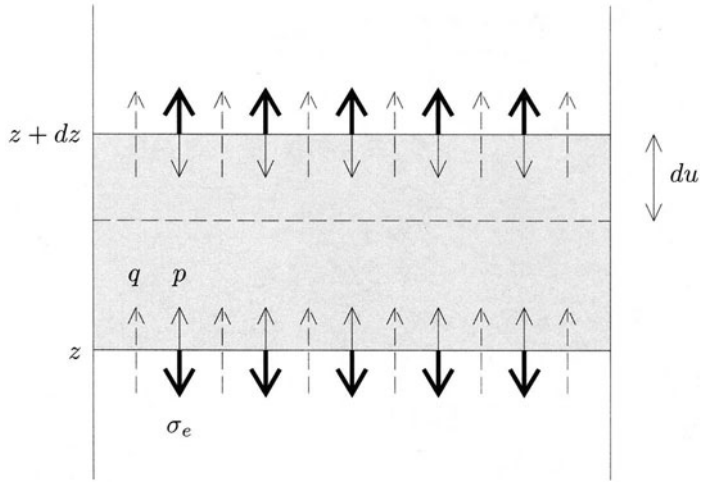

Figure 10. One dimensional consolidation of a porous medium.

the hydrostatic pressure (14.2), because no deformation of the solid has taken place yet.

$$p = \frac{F}{A} \qquad 0 < z < h, \quad t = 0^+ \tag{15.1}$$

At $z = 0$ a steep pressure gradient appears that causes the liquid to flow out of the specimen. This outflow of liquid results in a smooth downward motion of the piston. The deformation of the sample causes an effective stress within the sample that gradually will take over the load from the hydrostatic pressure.

We now consider Terzaghi's way to derive the equations that describe this process. We restrict ourselves to small deformations.

Consider a layer $[z, z + dz]$ of a one dimensional medium that is subjected to consolidation. The medium consists of a porous, incompressible, elastic solid saturated with an incompressible fluid. Analogue to (14.1) we subdivide the total stress σ in a hydrostatic pressure p, present in the liquid + solid (pressure positive, see figure 8) and an elastic stress caused by deformation σ_e, measured per unit surface area (extension positive). The liquid flux per unit mixture area is indicated with a q (z-direction positive). If we neglect the forces of inertia and the volume forces, we can write the balance of momentum as:

$$\sigma_e(z + dz) - \sigma_e(z) - p(z + dz) + p(z) = 0 \tag{15.2}$$

After dividing by dz, we find:

$$\frac{\partial \sigma_e}{\partial z} - \frac{\partial p}{\partial z} = 0 \tag{15.3}$$

Because of incompressibility the balance of mass reduces to the balance of volume:

$$du(t + dt) - du(t) - q(z)dt + q(z + dz)dt = 0 \tag{15.4}$$

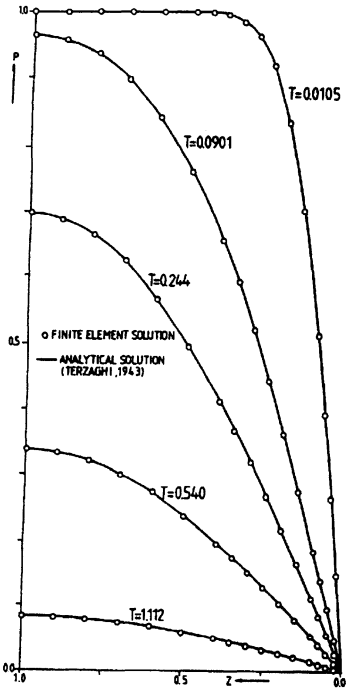

Figure 11. Dimensionless pressure P versus dimensionless position Z at different times during linear, one dimensional consolidation.

After division by $dzdt$, we find:

$$\frac{\partial^2 u}{\partial z \partial t} + \frac{\partial q}{\partial z} = 0 \tag{15.5}$$

In addition to the balance laws we need two constitutive equations. The first is the Darcy equation :

$$q = -K \frac{\partial p}{\partial z} \tag{15.6}$$

in which we consider the permeability K a constant. Substitution of (15.6) in (15.5) yields:

$$\frac{\partial^2 u}{\partial z \partial t} - \frac{\partial}{\partial z} K \frac{\partial p}{\partial z} = 0 \tag{15.7}$$

The second constitutive relation is the law of Hooke:

$$\sigma_e = H \frac{\partial u}{\partial z} \tag{15.8}$$

in which H is the compressive modulus. We consider H a constant, i.e. linear elasticity. The compressive modulus is related to the modulus of elasticity, E, and Poisson's ratio, ν, for an isotropic medium:

$$H = E \frac{1-\nu}{(1+\nu)(1-2\nu)} \tag{15.9}$$

The equations (15.3), (15.5), (15.6) and (15.8) form a complete set of partial differential equations (check this!). Integration of equation (15.3) yields:

$$\sigma(z,t) - p(z,t) = -p_0(t) \tag{15.10}$$

with $p_0(t)$ the top load. For a classical consolidation test the top load is a step function. After applying this step the function is constant in time, so:

$$\frac{\partial \sigma_e}{\partial t} - \frac{\partial p}{\partial t} = 0 \qquad for \qquad t > t_0 \tag{15.11}$$

Substitution of (15.8) in (15.11), yields

$$H\frac{\partial^2 u}{\partial z \partial t} - \frac{\partial p}{\partial t} = 0 \qquad for \qquad t > t_0 \tag{15.12}$$

Substitution of (15.12) and (15.6) in (15.5) yields the consolidation equation of Terzaghi:

$$\frac{\partial p}{\partial t} - KH\frac{\partial^2 p}{\partial z^2} = 0 \tag{15.13}$$

Notice the analogy with the diffusion equation. The characteristic time that is needed to start the consolidation process of a porous layer with thickness Δz, permeability K and compressive modulus H, follows from (15.13):

$$\frac{\Delta p}{\Delta t} = KH\frac{\Delta p}{(\Delta z)^2} \tag{15.14}$$

or:

$$\Delta t = \frac{(\Delta z)^2}{KH} \tag{15.15}$$

The consolidation time t is therefore inversely proportional to the permeability K and the stiffness H, and proportional to the square of the thickness of the layer Δz. The analytical solution for the consolidation equation (15.10) for a specimen with thickness h holds:

$$P = \sum_{n=0}^{\infty} \frac{2}{M} \sin MZ e^{-M^2 T} \tag{15.16}$$

with

$$P = \frac{p}{p_0} \tag{15.17}$$

$$M = \frac{\pi}{2}(2n+1) \tag{15.18}$$

$$Z = \frac{z}{h} \tag{15.19}$$

$$T = \frac{KHt}{h^2} \tag{15.20}$$

Notice that for $T > 1$ the consolidation process of the specimen is largely completed (zie figuur 11).

16 Mixture description of saturated porous media

We shall derive equations applicable to the behaviour of elastic incompressible fluid saturated porous media from mixture theory.

16.1 Assumptions

We consider the porous medium as a two-component mixture, composed of a solid (superscript s) and a fluid component (superscript f). We can rewrite equation (9.4) as:

$$\phi^s + \phi^f = 1. \tag{16.1}$$

Eq. (16.1) is the saturation condition. We assume that no mass-exchange occurs between the components. Each component is assumed incompressible :

$$\rho_i^\alpha = \frac{\rho^\alpha}{\phi^\alpha} = constant, \qquad \alpha = s, f. \tag{16.2}$$

The apparent densities ρ^α however do change as a function of time. We consider processes which are sufficiently slow so as to ensure that inertia forces are negligible. Volume forces are neglected as well. We assume that all components have the same temperature and no gradients in temperature are present either in time or space.

16.2 Conservation laws

Conservation of mass In the absence of mass exchange the local law of conservation of mass (11.1) of component α reduces to :

$$\frac{\partial \rho^\alpha}{\partial t} + \boldsymbol{\nabla} \cdot (\rho^\alpha \boldsymbol{v}^\alpha) = 0, \qquad \alpha = s, f. \tag{16.3}$$

Using (9.5) and (16.2) we can rewrite (16.3) :

$$\frac{\partial \phi^\alpha}{\partial t} + \boldsymbol{\nabla} \cdot (\phi^\alpha \boldsymbol{v}^\alpha) = 0, \qquad \alpha = s, f. \tag{16.4}$$

Summation of the eqs. (16.4) yields the local mass balance of the mixture :

$$\boldsymbol{\nabla} \cdot (\phi^s \boldsymbol{v}^s) + \boldsymbol{\nabla} \cdot (\phi^f \boldsymbol{v}^f) = 0, \tag{16.5}$$

or :

$$\boldsymbol{\nabla} \cdot \boldsymbol{v}^s + \boldsymbol{\nabla} \cdot \left(\phi^f (\boldsymbol{v}^f - \boldsymbol{v}^s)\right) = 0. \tag{16.6}$$

The first term of (16.6) represents the rate of volume increase of a unit volume of mixture. The second term represents the fluid flux from this unit volume. Eq. (16.6) states that every volume-increase or decrease of the mixture is associated with an equal amount of in- or outflux of liquid. At this point it is useful to refer current descriptors of the mixture with respect to an initial state of the porous solid. As is usual in continuum mechanics, we define the deformation gradient tensor $\boldsymbol{F}$ mapping an infinitesimal material line segment in the initial state onto the corresponding infinitesimal line segment in the current state.

The relative volume change from the initial to the current state is the determinant of the deformation gradient tensor $J = det\boldsymbol{F}$. If we introduce volume fractions

$$\Phi^\alpha = J\phi^\alpha \tag{16.7}$$

per unit initial volume, we can rewrite the mass balance equation (16.4) as follows:

$$\frac{D^s\Phi^\alpha}{Dt} + J\boldsymbol{\nabla}\cdot[\phi^\alpha(\boldsymbol{v}^\alpha - \boldsymbol{v}^s)] = 0 \tag{16.8}$$

when using the identity (4.15):

$$\frac{D^s}{Dt}J = J\boldsymbol{\nabla}\cdot\boldsymbol{v}^s \tag{16.9}$$

Conservation of momentum Considering the assumptions staed earlier momentum balance (11.6) reduces to :

$$\boldsymbol{\nabla}\cdot(\boldsymbol{\sigma}^\alpha)^c + \hat{\boldsymbol{p}}^\alpha = \boldsymbol{0}, \qquad \alpha = s, f. \tag{16.10}$$

The momentum interaction $\hat{\boldsymbol{p}}^\alpha$ arises e.g., as a consequence of friction between the fluid and the solid. We assume no moment of momentum interaction between fluid and solid. Therefore we tacitly assumed the symmetry of the partial Cauchy stress tensor in (16.10). Summation of the equations (16.10) yields the local momentum balance for the mixture as a whole :

$$\boldsymbol{\nabla}\cdot\boldsymbol{\sigma}^s + \boldsymbol{\nabla}\cdot\boldsymbol{\sigma}^f = \boldsymbol{\nabla}\cdot\boldsymbol{\sigma} = \boldsymbol{0}, \tag{16.11}$$

if we use :

$$\hat{\boldsymbol{p}}^s + \hat{\boldsymbol{p}}^f = \boldsymbol{0}, \tag{16.12}$$

The entropy inequality The local form of the entropy inequality (12.7) applied to the mixture as a whole, reduces to:

$$\sum_{\alpha=s,f}\left(-\rho^\alpha\dot{\tilde{F}}^\alpha + \boldsymbol{\sigma}^\alpha : \boldsymbol{D}^\alpha - \hat{\boldsymbol{p}}^\alpha\cdot\boldsymbol{u}^\alpha\right) \geq 0. \tag{16.13}$$

We introduce the strain energy function

$$W = J\sum_{\alpha=s,f}\rho^\alpha\tilde{F}^\alpha = J\sum_{\alpha=s,f}\psi^\alpha \tag{16.14}$$

as the Helmholtz free energy of a mixture volume which in the initial state of the solid equals unity. ψ^α is the Helmholz free energy of constituent α per unit mixture volume. Rewriting the inequality (16.13) for the entropy production per initial mixture volume - i.e. we multiply inequality (16.13) by the relative volume change J - we find:

$$-\frac{D^s}{Dt}W + J\boldsymbol{\sigma} : \boldsymbol{\nabla}\boldsymbol{v}^s + J\boldsymbol{\nabla}\cdot[(\boldsymbol{v}^f - \boldsymbol{v}^s)\cdot\boldsymbol{\sigma}^f - (\boldsymbol{v}^f - \boldsymbol{v}^s)\psi^f] \geq 0. \tag{16.15}$$

16.3 Constitutive restrictions

In analogy to section 8, we use the entropy inequality to derive constitutive restrictions for the mixture. The entropy inequality should hold for an arbitrary state of the mixture, complying with the balance laws and with incompressibility. There are two ways to comply with these restrictions. One is substitution of the restriction into the inequality, resulting in elimination of a field variable. The other is by introduction of a Lagrange multiplier. The mass balance of the mixture (16.6) is accounted for by means of a Lagrange multiplier. Other balance laws and the incompressibility conditions (16.2) are accounted for by means of substitution. From the inequality 16.15 we see that the apparent density and the momentum interaction $\hat{\boldsymbol{p}}^\alpha$ is already eliminated from the inequality. In other words the conditions of incompressibility and the momentum balance of the constituents have already been substituted into the second law. The divergence of the partial stress tensor of the solid $\boldsymbol{\nabla} \cdot \boldsymbol{\sigma}^s$ and the heat supplies r^α also are absent from 16.15. Thus the momentum balance of the mixture and the energy balance have already been substituted in the second law. Therefore, restrictions still to be fulfilled are the mass balances of the constituents (16.3) and mass balance of the mixture (16.6). The latter is substituted by means of a Lagrange multiplier p:

$$\begin{aligned} &-\frac{D^s}{Dt}W + J\boldsymbol{\sigma}_e : \boldsymbol{\nabla}\boldsymbol{v}^s \\ &+J[\boldsymbol{\sigma}^f + (p\phi^f - \psi^f)\boldsymbol{I}] : \boldsymbol{\nabla}(\boldsymbol{v}^f - \boldsymbol{v}^s) \\ &+J(\boldsymbol{v}^f - \boldsymbol{v}^s) \cdot (-\boldsymbol{\nabla}\psi^f + p\boldsymbol{\nabla}n^f + \boldsymbol{\nabla} \cdot \boldsymbol{\sigma}^f) \geq 0. \end{aligned} \tag{16.16}$$

in which the effective stress $\boldsymbol{\sigma}_e$ is defined as

$$\boldsymbol{\sigma}_e = \boldsymbol{\sigma} + p\boldsymbol{I} \tag{16.17}$$

Choice of independent and dependent variables We choose as dependent variables the dynamic variables appearing in inequality 16.16 : W, ψ^f, $\boldsymbol{\sigma}_e$, $\boldsymbol{\sigma}^f + p\phi^f\boldsymbol{I}$, $\boldsymbol{\nabla} \cdot \boldsymbol{\sigma}^f + p\boldsymbol{\nabla}\phi^f$. Their number should equate the number unknown variables appearing in the balance equations minus the number of balance equations. The number of independent variables should be as small as possible to describe the state of the tissue well. Their choice is a key assumption of the continuum theory and is based on insight in the physical phenomena involved in the behaviour of the material. If the independent variables include only variables describing the local state of the tissue (e.g. $\boldsymbol{E}$), the theory is a local theory. If the independent variables include variables describing the state of the tissue some distance away from the point of consideration (e.g. $\boldsymbol{\nabla}\boldsymbol{E}$), the theory is a non-local theory. Throughout this book we consider only local dependent variables. We choose as independent variables the kinematic variables : the Green strain of the solid $\boldsymbol{E}^s$, the fluid volume fraction Φ^f and the fluid velocity relative to the solid $\boldsymbol{v}^f - \boldsymbol{v}^s$. For reasons of objectivity we need to transform all the vectors and tensors among the dependent and independent variables back to the initial state. This yields for the constitutive relationships:

$$W = W(\boldsymbol{E}^s, \Phi^f, \boldsymbol{v}^{fs}),$$

$$\begin{aligned} \psi^f &= \psi^f(\boldsymbol{E}^s, \Phi^f, \boldsymbol{v}^{fs}), \\ \boldsymbol{\sigma}_e &= \boldsymbol{F} \cdot \boldsymbol{S}_e(\boldsymbol{E}^s, \Phi^f, \boldsymbol{v}^{fs}) \cdot \boldsymbol{F}^c, \\ \boldsymbol{\sigma}^f - \phi^f p \boldsymbol{I} &= \boldsymbol{F} \cdot \boldsymbol{S}^f(\boldsymbol{E}^s, \Phi^f, \boldsymbol{v}^{fs}) \cdot \boldsymbol{F}^c \\ \hat{\boldsymbol{p}}^f - p \boldsymbol{\nabla} \phi^f &= \boldsymbol{F} \cdot \hat{\boldsymbol{P}}^f(\boldsymbol{E}^s, \Phi^f, \boldsymbol{v}^{fs}) \end{aligned} \tag{16.18}$$

with

$$\boldsymbol{v}^{fs} = \boldsymbol{F}^{-1} \cdot (\boldsymbol{v}^f - \boldsymbol{v}^s) \tag{16.19}$$

The principle of equipresence requires that all dependent variables appear in each of the constitutive relationships. The choice of the independent variables is paramount for the form of the constitutive relationships that are derived. E.g., including for the solid Green strain only and no measure of strain rate, implies elasticity of the solid. In mixture mechanics it is also important to realise that each of the variables is an averaged value of a physical quantity over an averaging volume. It may seem surprising that the shear rate of the fluid is not included in the list of independent variables, although the viscosity of the fluid is absolutely essential for the behaviour of the mixture. The reason for this is that in a porous medium the shear rate at one side of the pore has a sign opposite to the shear rate at the other side of the pore. The expectation value of the shear rate in a representative elementary volume is therefore the shear rate of the solid, i.e. a generally very low value, not representative for the dissipation in the fluid. It is therefore more obvious to use the fluid velocity relative to the solid as a macroscopic measure of the microvalues of the shear rate. The fluid volume fraction Φ^f is not independent of the Green strain because of incompressibility :

$$\Phi^f = \det \boldsymbol{F} - 1 + \phi_0^f = \sqrt{\det(2\boldsymbol{E}^s + \boldsymbol{I})} - 1 + \phi_0^f \tag{16.20}$$

Because of the strong non-linearity of equation (16.20), elimination of one of the variables is tedious. In fact, the way we deal with the interdependence of these two variables is by means of the Lagrange multiplier p. The condition 16.6 is in fact a differentated form of eq. (16.20). This legitimises the use of $\boldsymbol{E}^s$ and Φ^f as independent variables.

Constitutive relationships Applying the chain rule for time differentiation of W :

$$\frac{D^s W}{Dt} = \frac{\partial W}{\partial \boldsymbol{E}^s} : \frac{D^s \boldsymbol{E}^s}{Dt} + \frac{\partial W}{\partial N^f} \frac{D^s N^f}{Dt} + \frac{\partial W}{\partial \boldsymbol{v}^{fs}} \tag{16.21}$$

and substituting the mass balance of the constituents (16.8) for the elimination of $\frac{D^s N^f}{Dt}$ from the inequality 16.16 :

$$\begin{aligned} &(J\boldsymbol{\sigma}_e - \boldsymbol{F} \cdot \frac{\partial W}{\partial \boldsymbol{E}} \cdot \boldsymbol{F}^c) : \boldsymbol{\nabla} \boldsymbol{v}^s + \\ &\frac{\partial W}{\partial \boldsymbol{v}^{fs}} \cdot \frac{D^s}{Dt} \boldsymbol{v}^{fs} \\ &+J[\boldsymbol{\sigma}^f + (\mu^f \phi^f - \psi^f)\boldsymbol{I}] : \boldsymbol{\nabla}(\boldsymbol{v}^f - \boldsymbol{v}^s) \\ &+J(\boldsymbol{v}^f - \boldsymbol{v}^s) \cdot (-\boldsymbol{\nabla} \psi^f + \mu^f \boldsymbol{\nabla} phi^f + \boldsymbol{\nabla} \cdot \boldsymbol{\sigma}^f) \geq 0. \end{aligned} \tag{16.22}$$

in which μ^f is the chemical potential of the fluid:

$$\mu^f = \frac{\partial W}{\partial N^f} + p \tag{16.23}$$

Eq. (16.22) should be true for any value of the state variables. Close inspection of the choice of independent variables and the inequality (16.22), reveals that the first term of (16.22) is linear in the solid velocity gradient $\boldsymbol{\nabla v}^s$, the second term linear in $\frac{D^s}{Dt}\boldsymbol{v}^{fs}$ and the third term linear in the relative velocity gradients $\boldsymbol{\nabla}(\boldsymbol{v}^f - \boldsymbol{v}^s)$. Therefore, by a standard argument, we find:

$$\boldsymbol{\sigma}_e = \frac{1}{J}\boldsymbol{F} \cdot \frac{\partial W}{\partial \boldsymbol{E}} \cdot \boldsymbol{F}^c \tag{16.24}$$

$$\frac{\partial W}{\partial \boldsymbol{v}^{fs}} = \boldsymbol{0} \tag{16.25}$$

$$\boldsymbol{\sigma}^f = (\psi^f - \mu^f \phi^f)\boldsymbol{I} \tag{16.26}$$

leaving as inequality:

$$J(\boldsymbol{v}^f - \boldsymbol{v}^s) \cdot (-\boldsymbol{\nabla}\psi^f + \mu^f \boldsymbol{\nabla} phi^f + \boldsymbol{\nabla} \cdot \boldsymbol{\sigma}^f) \geq 0. \tag{16.27}$$

Eq. (16.24) indicates that the effective stress of the mixture can be derived from a strain energy function W which represents the free energy of the mixture. Eq. (16.25) shows that the strain energy function cannot depend on the relative velocity of fluid versus solid. Thus, the effective stress of a biphasic medium can be derived from a regular strain energy function, which physically has the same meaning as in single phase media . According to eq. (16.26) the partial stress of the fluid and the ions are scalars. Transforming the relative velocities to their Lagrangian equivalents, we find in stead of (16.27):

$$\boldsymbol{v}^{fs} \cdot [-\boldsymbol{\nabla}_0\psi^f + \mu^f \boldsymbol{\nabla}_0\phi^f + \boldsymbol{\nabla}_0 \cdot \boldsymbol{\sigma}^f] \geq 0. \tag{16.28}$$

in which $\boldsymbol{\nabla}_0 = \boldsymbol{F}^c \cdot \boldsymbol{\nabla}$ is the gradient operator with respect to the initial configuration. Note that as $\mu^f \boldsymbol{\nabla}_0\phi^f + \boldsymbol{\nabla}_0 \cdot \boldsymbol{\sigma}^f$ depends on $\boldsymbol{v}^{fs}$ according to the constituive relationships (16.18), the lefthandside of inequality (16.28) is not a linear function of $\boldsymbol{v}^{fs}$ and therefore it is incorrect to equate the factor $-\boldsymbol{\nabla}_0\psi^f + \mu^f \boldsymbol{\nabla}_0\phi^f + \boldsymbol{\nabla}_0 \cdot \boldsymbol{\sigma}^f$ to zero. From a physical point of view it is obvious that unlike the elastic deformation of the solid the flow of fluid relative the solid results in an entropy production. If we assume that the system is not too far from equilibrium, we can express the dissipation (16.28) associated with relative flow of fluid and ions as a quadratic function of the relative velocities:

$$-\boldsymbol{\nabla}_0\psi^f + \mu^f \boldsymbol{\nabla}_0\phi^f + \boldsymbol{\nabla}_0 \cdot \boldsymbol{\sigma}^f = \boldsymbol{B} \cdot \boldsymbol{v}^{fs} \tag{16.29}$$

$\boldsymbol{B}$ is a semi-positive definite matrix of frictional coefficients. Substituting eq. (16.26) into eq. (16.29) yields the Lagrangian form of Darcy's law :

$$-\phi^f \boldsymbol{\nabla}_0 \mu^f = \boldsymbol{B} \cdot \boldsymbol{v}^{fs} \tag{16.30}$$

The constitutive behaviour of the fluid-solid mixture is thus described by a strain energy function W and frictional tensor $\boldsymbol{B}$. From the strain energy function we derive both the effective stress and the chemical potential of the fluid.

16.4 Physical interpretation of the constitutive variables

Comparing eq. (16.17) with eq. (14.2) reveals that the Lagrange multiplier p should be interpreted as the hydrostatic pressure in fluid.

$$\nabla \cdot \boldsymbol{\sigma}_e - \nabla p = \mathbf{0}. \tag{16.31}$$

If we define the permeability tensor $\boldsymbol{K}$ as:

$$\boldsymbol{K} = (\phi^f)^2 \boldsymbol{B}^{-1} \tag{16.32}$$

eq. (16.30) becomes:

$$\phi^f(\boldsymbol{v}^f - \boldsymbol{v}^s) = -\boldsymbol{K} \cdot \nabla(p + \frac{\partial W}{\partial \Phi^f}). \tag{16.33}$$

Eq. (16.33) is the threedimensional form of Darcy's law (15.6). The difference between the chemical potential μ^f and the pressure p is the matric potential. The matric potential accounts for adsorption and capillary forces. It can be quantified experimentally using capillary rising heights. In Terzaghi's consolidation theory the matric potentisal is neglected, not because it is negligible in absolute terms but because its gradient is negligible in an homogenous medium with limited variation of fluid volume fraction and coarse pore structure.

16.5 Resulting equations

The resulting equations are: Momentum balance of the mixture:

$$\nabla \cdot \boldsymbol{\sigma}_e - \nabla p = \mathbf{0} \tag{16.34}$$

Mass balance of the mixture:

$$\nabla \cdot \boldsymbol{v}^s - \nabla \cdot (\phi^f(\boldsymbol{v}^f - \boldsymbol{v}^s)) = 0 \tag{16.35}$$

Darcy's law:

$$\boldsymbol{v}^f - \boldsymbol{v}^s = \phi^f \boldsymbol{B}^{-1} \cdot \nabla \mu^f \tag{16.36}$$

Stress-strain relationship:

$$\boldsymbol{\sigma}_e = (\det \boldsymbol{F})^{-1} \boldsymbol{F} \cdot \frac{\partial W}{\partial \boldsymbol{E}^s} \cdot \boldsymbol{F}^c, \tag{16.37}$$

Constitutive law for the chemical potential of the fluid:

$$\mu^f = p + \frac{\partial W}{\partial \Phi^f} \tag{16.38}$$

The total stress in the mixture is composed of an effective stress and a hydrodynamic pressure: $\boldsymbol{\sigma} = \boldsymbol{\sigma}_e - p\boldsymbol{I}$. The effective stress $\boldsymbol{\sigma}_e$ is derived from the strain energy function of the mixture W. In eq. (16.38) $\boldsymbol{F}$ is the deformation gradient tensor of the solid and $\boldsymbol{E}^s$ the Green strain tensor of the solid. The strain energy W in a function of the solid

strain $\boldsymbol{E}$. In one dimensional space eq. (16.34) reduces to eq. (15.3) from Terzaghi's confined compression theory.

Dynamic boundary conditions are:

$$[(\boldsymbol{\sigma}_e - p\boldsymbol{I}) \cdot \boldsymbol{n}] = \boldsymbol{0} \tag{16.39}$$

with $\boldsymbol{n}$ the outer normal along the boundary and the square brackets represent the difference between the value at either side of the boundary.

$$[\overline{V}^f \mu^f] = 0, \tag{16.40}$$

with as a special case the evaporation boundary condition:

$$\overline{V}^f \mu^f = RTln\frac{p^d}{p_s^d} \tag{16.41}$$

Eq. (16.40) and eq. (16.41) enforces continuity of molar chemical potential. Discontinuity of chemical potential would lead to an infinite fluid flux which is physically impossible. For this reason we can claim that even if the material properties are sharply discontinuous the chemical potential should be continuous. This is not true for the pressure p. E.g. at the interface between a sand layer and a clay layer the pressure is not continuous, at least if capillary effects are not neglected. Similarly interstititial pressure along the surface of the skin is not equal to atmospheric pressure. We use the molar chemical potential in stead of the volumetric chemical potential because the volumetric chemical potential can be used only for incompressible media. Although the medium we consider is incompressible, the medium outside the boundary need not be incompressible as is the case for evaporation. Kinematic boundary conditions are:

$$[\boldsymbol{u}] = \boldsymbol{0} \tag{16.42}$$

$$[(\boldsymbol{v}^f - \boldsymbol{v}^s) \cdot \boldsymbol{n}] = 0 \tag{16.43}$$

17 Conclusion

We derived the equations, that describe the behaviour of a porous medium, in two different ways. The traditional approach of Terzaghi has the advantage that we know the fysical meaning of the used parameters from the start. It is a disadvantage is that we have little insight in the assumptions that we - often unconsciously - took. For example, it appears from the resulting equation, which was derived using the theory of mixtures, that we neglected the capillar forces.

In the second approach, using the theory of mixtures, all effects are taken into account, and simplifications have to be done explicitly. It is done by neglecting the terms from the balance laws or by the choice of the independent variables. This approach is also suitable for generalisation to mixtures with more components, like we will see in chapter 6. A disadvantage of this approach is the complexity of the derivation.

18 Solutions

18.1 Mixtures of ideal gasses

We first consider a pure ideal gas. We start with (7.18) for the total differential of the Gibbs free energy, now written for a total amount of gas. For a constant temperature applies:

$$dG = Vdp \tag{18.1}$$

If we now increase the pressure of the gas from p_0 to p, the variation of the Gibbs free energy ΔG is written:

$$\Delta G = G - G_0 = \int_{G_0}^{G} dG = \int_{p_0}^{p} V dp \tag{18.2}$$

For an ideal gas applies:

$$pV = nRT \tag{18.3}$$

in which R represents the universal gas constant ($8.314\ J \cdot K^{-1} \cdot \mathrm{mol}^{-1}$) and n is the amount of gas in moles. Substitution of (18.3) into (18.2) yields after integration:

$$G - G_0 = nRT \ln \frac{p}{p_0} \tag{18.4}$$

This equation shows the Gibbs free energy of a gas with respect to the state of reference (p_0, G_0). For the chemical potential of the gas it follows that:

$$\bar{\mu} = \bar{\mu}_0 + RT \ln \frac{p}{p_0} \tag{18.5}$$

Let's consider a *mixture of ideal gasses*. We take an amount n^I of gas I and an amount n^{II} of a gas II. Both gasses are subjected to a reference pressure p_0, and have the volumes V^I and V^{II}. During mixing of these gasses an ideal mixture with volume V and pressure p is created, for which:

$$V = V^I + V^{II} \tag{18.6}$$

$$p = p_0 \tag{18.7}$$

The *partial pressures* p^I and p^{II} of the gasses in the mixture measure:

$$p^I = x^I p_0 \qquad p^{II} = x^{II} p_0, \tag{18.8}$$

in which the molar fractions x of the components are defined as:

$$x^I = \frac{n^I}{n^I + n^{II}}, \qquad x^{II} = \frac{n^{II}}{n^I + n^{II}} \tag{18.9}$$

Substitution of the pressures from (18.8) into (18.5) now yields for the chemical potential of the gasses:

$$\bar{\mu}^I = \bar{\mu}_0^I + RT \ln x^I, \qquad \bar{\mu}^{II} = \bar{\mu}_0^{II} + RT \ln x^{II} \tag{18.10}$$

We know that the mixing process as described above occurs spontaneously. We can also see this by calculating the *mixing-energy*. The total Gibbs free energy before mixing amounts:

$$G_{voor} = n^I \bar{\mu}_0^I + n^{II} \bar{\mu}_0^{II} \tag{18.11}$$

For the total Gibbs free energy after mixing applies:

$$G_{na} = n^I \{\bar{\mu}_0^I + RT \ln x^I\} + n^{II} \{\bar{\mu}_0^{II} + RT \ln x^{II}\} \tag{18.12}$$

We can now derive for the mixture energy ΔG_{meng}:

$$\begin{aligned} \Delta G_{meng} &= G_{na} - G_{voor} \\ &= (n^I + n^{II}) RT \{x^I ln x^I + x^{II} ln x^{II}\} \end{aligned} \tag{18.13}$$

Because x^I as well as x^{II} are smaller than 1, $\Delta G_{meng} < 0$, which means that the mixing process occurs indeed spontaneously.

18.2 Non-electrolytic solutions

From the former we saw that for mixtures of ideal gasses the chemical potential depends on the composition of the mixture following (18.10). In general the chemical potential for mixtures of ideal media depends on the pressure p and the temperature T. We now define an *ideal mixture* as a mixture in which the following relation applies for the chemical potential of the components α:

$$\bar{\mu}^\alpha(p, T, x^\alpha) = \bar{\mu}_0^\alpha(p, T) + RT \ln x^\alpha \tag{18.14}$$

We therefore assume that $\bar{\mu}^\alpha$ depends the same way on the composition of the mixture as a mixture of ideal gasses does. For a mixture of ideal gasses we found the concentration dependency through the partial pressures of the gasses. In definition (18.14) we take the pressure dependency separately into account in the term $\bar{\mu}_0^\alpha(p, T)$. If the mixture has an equilibrium, we know that for every component:

$$\boldsymbol{\nabla} \bar{\mu}^\alpha = \mathbf{0}. \tag{18.15}$$

If all components move freely through the mixture, this means, using (18.14), that there are no gradients in concentration. If this free movement is hampered, a concentration gradient generally will be present in the equilibrium.

This last situation is demonstrated in the experiment, shown in figure 12. In the right compartment there is a solution of n^e moles of a substance e, for example a protein, in n^w moles of a solvent w, for example water. In the solution the protein consists of neutral particles. In the left compartment only the solvent is present, water. The compartments are separated by a semi-permeable membrane, that only allows transport of water. Therefore equation 18.15 applies across the membrane for water, but not for the protein.

Initially there is no hydrostatic pressure difference between both compartments. For the chemical potential of the water applies:

$$\bar{\mu}_l^w = \bar{\mu}_0^w + RT \ln x_l^w = \bar{\mu}_0^w \qquad (because\ x_l^w = 1) \tag{18.16}$$

$$\bar{\mu}_r^w = \bar{\mu}_0^w + RT \ln x_r^w < \bar{\mu}_0^w \qquad (because\ x_r^w < 1) \tag{18.17}$$

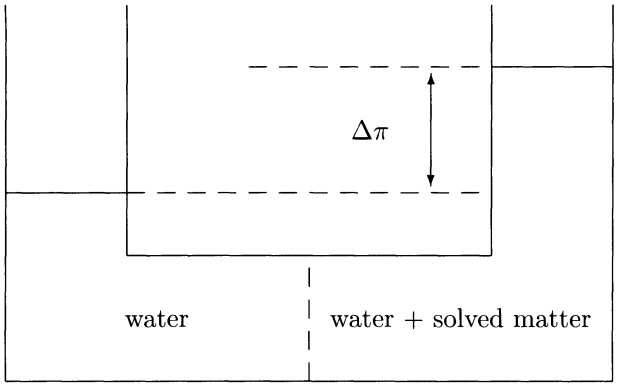

Figure 12. Illustration of the phenomenon osmotic pressure.

in which we indicate the chemical potential of the water with $\bar{\mu}^w$, in the left (index 1) and the right (index r) compartment and in pure (index 0) state. The chemical potential of the water therefore appears to be lower on the right hand side than that on the left hand side. This difference causes a net transport of water from the left to the right, which results in a hydrostatic pressure difference. The net transport reaches an equilibrium, as soon as the chemical potentials on the left and on the right are equal. In this equilibrium the hydrostatic pressure difference is equal to $\Delta\pi$, the *osmotic pressure difference*. We calculate the size of the osmotic pressure difference. The total differential of the Gibbs free energy G (13.8) is:

$$dG = \left(\frac{\partial G}{\partial T}\right)_{p,n^\alpha} dT + \left(\frac{\partial G}{\partial p}\right)_{T,n^\alpha} dp + \sum_{\alpha=1}^{\nu} \bar{\mu}^\alpha dn^\alpha, \tag{18.18}$$

in which the chemical potential $\bar{\mu}^\alpha$ is defined as:

$$\bar{\mu}^\alpha = \bar{G}^\alpha = \left(\frac{\partial G}{\partial n^\alpha}\right)_{p,T,n^\beta,\beta\neq\alpha}. \tag{18.19}$$

In analogy to (7.19) and (7.20) we now state for the volume V and the entropy S of the mixture:

$$V = \left(\frac{\partial G}{\partial p}\right)_{T,n^\alpha} \tag{18.20}$$

$$S = -\left(\frac{\partial G}{\partial T}\right)_{p,n^\alpha} \tag{18.21}$$

The partial derivative of the chemical potential with respect to the pressure is:

$$\begin{aligned}\left(\frac{\partial \bar{\mu}^\alpha}{\partial p}\right)_{T,n^\alpha} &= \left(\frac{\partial}{\partial p}\left(\frac{\partial G}{\partial n^\alpha}\right)_{p,T,n^\beta,\beta\neq\alpha}\right)_{T,n^\alpha} \\ &= \left(\frac{\partial}{\partial n^\alpha}\left(\frac{\partial G}{\partial p}\right)_{T,n^\alpha}\right)_{p,T,n^\beta,\beta\neq\alpha},\end{aligned} \tag{18.22}$$

which can be rewritten, using (18.20), into:

$$\left(\frac{\partial \bar{\mu}^{\alpha}}{\partial p}\right)_{T,n^{\alpha}} = \left(\frac{\partial V}{\partial n^{\alpha}}\right)_{T,p,n^{\beta},\beta\neq\alpha} = \bar{V}^{\alpha} \tag{18.23}$$

in which $\bar{V}^{\alpha}$ is the partial molar volume of the component α in the mixture. Applied to the water-component in the situation of figure 12, we find:

$$\left(\frac{\partial \bar{\mu}^{w}}{\partial p}\right)_{T,n^{w},n^{e}} = \bar{V}^{w} = \bar{V}_0^{w} \tag{18.24}$$

The last '='-sign can be justified for a *dilute solution*, in which the partial molar volume of the water is equal to that of pure water. We determine the difference in chemical potential of the water in both compartments, as a result of the pressure difference $p_r - p_l$, through integration of (18.24), considering that the partial molar volume of the water is independent of the pressure:

$$\bar{\mu}_r^{w} - \bar{\mu}_l^{w} = \int_{p_l}^{p_r} \bar{V}_0^{w} dp = \bar{V}_0^{w}(p_r - p_l) \tag{18.25}$$

In equilibrium the chemical potential of the water left and right is the same:

$$\bar{\mu}_l^{w} = \bar{\mu}_r^{w} = \bar{\mu}_0^{w} + RT \ln x_r^{w} + \bar{V}_0^{w}(p_r - p_l) \tag{18.26}$$

Because $\bar{\mu}_l^{w} = \bar{\mu}_0^{w}$, the osmotic pressure difference $\Delta\pi$ is:

$$\Delta\pi = p_r - p_l = -\frac{RT}{\bar{V}_0^{w}} \ln x_r^{w} \tag{18.27}$$

It is usual to relate the osmotic pressure to the concentration of the solution, the protein. For this, we use:

$$\ln x^{w} = \ln(1 - x^{e}) \approx -x^{e} = -\frac{n^{e}}{n^{w} + n^{e}} \approx -\frac{n^{e}}{n^{w}} \tag{18.28}$$

and the following expression for the volume V of the solution:

$$V = n^{w}\bar{V}^{w} + n^{e}\bar{V}^{e} \approx n^{w}\bar{V}_0^{w}. \tag{18.29}$$

Substitution of these relations in (18.27) yields:

$$\Delta\pi = \frac{n^{e}}{V} RT = c^{e} RT, \tag{18.30}$$

in which the *concentration* c^{e} is expressed in moles·m^{-3}. This relation has also been discovered empirically by *Van't Hoff*, indicating that the basic assumption for an ideal mixture, defined in (18.14), applies for dilute solutions. We define the osmotic pressure of a solution as:

$$\pi = -\frac{RT}{\bar{V}_0^{w}} \ln x^{w}, \tag{18.31}$$

which is well approximated by van 't Hoff's equation in a dilute solution:

$$\pi = c\,RT. \tag{18.32}$$

in which c is the concentration of the solved substances. Further, we specify expression (18.14) for the chemical potential of a component α, using (18.26):

$$\bar{\mu}^\alpha = \bar{\mu}_0^\alpha(T) + RT \ln x^\alpha + p\bar{V}^\alpha. \tag{18.33}$$

with particularly for water:

$$\bar{\mu}^w = \bar{\mu}_0^w(T) + RT \ln x^w + \bar{V}_0^w p = \bar{\mu}_0^w(T) + \bar{V}_0^w(p - \pi) \tag{18.34}$$

In other words, the chemical potential consists of a pressure dependent part (the pressure potential) and a concentration-dependent part (the osmotic potential) for isothermal conditions. Deviations of the ideal situations are taken into account using the so called *activity coefficient* γ^α. The molar fraction x^α is corrected to an 'active molar fraction', or *activity* a^α:

$$a^\alpha = \gamma^\alpha x^\alpha, \tag{18.35}$$

The expression for the chemical potential then becomes:

$$\bar{\mu}^\alpha = \bar{\mu}_0^\alpha(T) + RT \ln a^\alpha + p\bar{V}^\alpha. \tag{18.36}$$

18.3 Elektrolytic solutions

In biology we often have to deal with solutions of ionized high-molecular proteins. In this paragraph we will consider solutions of a protein, (component e) and a low-molecular salt (component z) in water (component w). We will indicate the protein with PX_z. We assume that in a solution of this protein an equilibrium will be established in which a protein molecule falls apart in a high molecular negative ion P^{z-} and z small positive ions X^+:

$$PX_z \rightleftharpoons P^{z-} + zX^+. \tag{18.37}$$

In general there are also ions present of a low-molecular electrolyte in such a protein solution, indicated with MZ. We assume that a solution of this electrolyte results in monovalent positive and negative ions:

$$MX \rightleftharpoons M^- + X^+. \tag{18.38}$$

In this situation the M^-- and the X^+-ion are called the 'co-ion' and the 'counter-ion' respectively.

Since the time constant, corresponding to the establishment of a local electrostatic equilibrium, is very short, we can assume that at every moment electroneutrality applies.

The electrochemical potential of an ionic component In the former the chemical potential of a component α was defined as the partial molar Gibbs free energy. This means that we considered the change of the Gibbs free energy if we added one mole of

component α to the mixture, during wich we kept the amounts of the other components constant. For a solution of an electrolyte, for example the salt MZ, the movement of cations or anions is not exclusively controled by the chemical potential, as was the case for the water in the porous medium in chapter 4. Reason for this is, that the charged particle is also sensitive for an electric-potential field. One mole of a monovalent ion has a charge equal to the constant of Faraday, F. The force that works on an ion in an electric-potential field ξ is:

$$F\nabla\xi \tag{18.39}$$

Therefore, we do not use the chemical potential for an ionic component but the electro-chemical potential, of which the gradient does not only contain the mechanical and chemical forces, but also the electric forces:

$$\bar{\mu}^\alpha = \bar{\mu}_0^\alpha + RTlna^\alpha + p\bar{V}^\alpha + z^\alpha F\xi \quad \alpha = +,- \tag{18.40}$$

Here, z^α is the valence of the ion, from which it follows that for a salt in water the chemical potential is:

$$\bar{\mu}^z = \bar{\mu}_0^z + RT\ln a^z + p\bar{V}^z, \tag{18.41}$$

We see that the *activity of the salt* is,

$$a^z = a^+a^-, \tag{18.42}$$

that the reference-potential is,

$$\bar{\mu}_0^z = \bar{\mu}_0^+ + \bar{\mu}_0^-, \tag{18.43}$$

and that the partial molar volume is,

$$\bar{V}^z = \bar{V}^+ + \bar{V}^-. \tag{18.44}$$

We now define the activity coefficients for the ions γ^+ and γ^-, in analogy to (18.35), as:

$$a^+ = \gamma^+x^+, \qquad a^- = \gamma^-x^-, \tag{18.45}$$

in which x^+ and x^- represent the (equal) molar fractions of the anion and the cation. We can now derive the activity of the salt a^z:

$$a^z = \gamma^+x^+\gamma^-x^- = (\gamma^\pm x)^2, \tag{18.46}$$

in which we defined the *average activity coefficient* of the salt $\gamma^\pm$ as:

$$\gamma^\pm = (\gamma^+\gamma^-)^{1/2}, \tag{18.47}$$

and used $x^+ = x^- = x$. The activity coefficients can be determined experimentally from electro-chemical experiments. A theoretical foundation of the relations above is provided for strongly diluted solutions by Debye and Hückel in 1923. In this course we consider the relations as empirical ones. It is obvious that the relations for the chemical potential of a salt as mentioned above do not apply for a pair of ions, present in a porous medium with fixed charges, because in that case the co-ionic charge and the counter-ionic charge do not neutralize one another and therefore one cannot speak of a salt (=electric neutral molecule) in a solution.

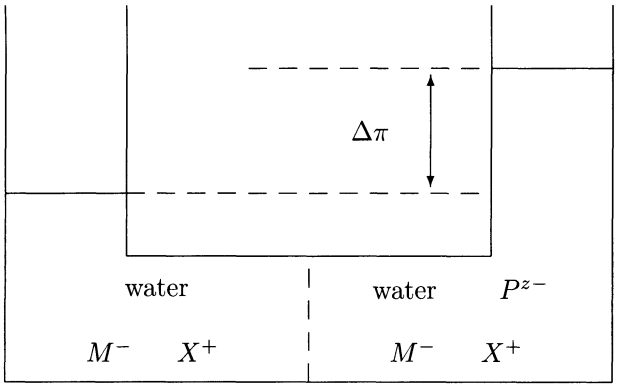

Figure 13. Illustration of the Donnan-effect.

The Donnan-effect The Donnan-effect occurs in a saturated electrically charged porous solid. We consider two neighbouring points in the charged porous medium. Between these two points there is a difference in fixed charge concentration. The two points are now considered to be two containers, between which water and ions (M^- en X^+) can move freely. The fixed charges (P^{z-}), however, cannot move from one container to the other. In other words, the containers communicate through a semi-permeable medium (figure 13). To fix our thoughts and without loss of generality, we assume that the left container has no fixed charge. An equilibrium is established, in which no net transport of particles through the membrane takes place. This equilibrium is characterized by the condition, that the (electro)-chemical potential for substances, that are able to pass the medium freely, is equal in the left as well as the right container:

$$\bar{\mu}_l^w = \bar{\mu}_r^w \tag{18.48}$$

$$\bar{\mu}_l^\alpha = \bar{\mu}_r^\alpha \quad \alpha = +, - \tag{18.49}$$

Using (18.36) we can write these relations as:

$$\bar{\mu}_0^w + RT \ln a_l^w + p_l \bar{V}^w = \bar{\mu}_0^w + RT \ln a_r^w + p_r \bar{V}^w, \tag{18.50}$$

$$\bar{\mu}_0^\alpha + RT \ln a_l^\alpha + p_l \bar{V}^\alpha + z^\alpha F \xi_l = \bar{\mu}_0^\alpha + RT \ln a_r^\alpha + p_r \bar{V}^\alpha + z^\alpha F \xi_r \quad \alpha = +, -. \tag{18.51}$$

Now, we first consider the ionic equilibrium. As the solution is dilute, the contribution $p\bar{V}^\alpha$ is negligible with respect to the term $RT \ln a^\alpha$. With this the summation of (18.51), for $\alpha = +, -$, reduces to the condition:

$$a_l^+ a_l^- = a_r^+ a_r^- \tag{18.52}$$

Using (18.46) this leads, after conversion to concentrations, to:

$$(\gamma^\pm)_l^2 c_l^+ c_l^- = (\gamma^\pm)_r^2 c_r^+ c_r^- \tag{18.53}$$

Beside this condition, the condition of electroneutrality for the solution in the left as well as the right compartment should be kept. Deviation from electroneutrality would lead to - relative strong - electric forces, restoring electroneutrality almost immediately. Therefore:

$$c_l^+ = c_l^- \tag{18.54}$$

$$c_r^+ = c_r^- + zc_r^e, \tag{18.55}$$

in which c^e is the concentration of the macromolecule to which z fixed charges are attached. For the concentrations of M^-- and X^+-ions in the left and right compartment a combination of (18.53) – (18.55) yields:

$$c_r^- = \frac{1}{2}\left(zc_r^e + \sqrt{(zc_r^e)^2 + \frac{(\gamma_l^\pm)^2(c_l^-)^2}{(\gamma_r^\pm)^2}}\right) \tag{18.56}$$

$$c_r^- = \frac{1}{2}\left(-zc_r^e + \sqrt{(zc_r^e)^2 + \frac{(\gamma_l^\pm)^2(c_l^-)^2}{(\gamma_r^\pm)^2}}\right) \tag{18.57}$$

In a dilute solution we are allowed to equate the activity coefficients $\gamma_l^\pm$ and $\gamma_r^\pm$. We now see that the concentration c^+ of the X^+-ions is different between left and right, as is the concentration c^- of the M^--ions. This difference in concentration is called the *Donnan-effect*. We also see, that the Donnan-effect decreases for an increasing salt concentration.

The osmotic pressure difference between the left and the right compartment $\Delta\pi$ can now be determined from the equilibrium for the water. Therefore, we rewrite (18.51) as:

$$\Delta\pi = p_r - p_l = -\frac{RT}{\bar{V}^w}\ln\frac{a_r^w}{a_l^w}, \tag{18.58}$$

If we suppose that the activity coefficients for water are equal left and right, we can switch to molar fractions:

$$x_l^w = \frac{c_l^w}{c_l^w + c_l^+ + c_l^-} = 1 - \frac{c_l^+ + c_l^-}{c_l^w + c_l^+ + c_l^-} \tag{18.59}$$

$$x_r^w = \frac{c_r^w}{c_r^w + c_r^+ + c_r^- + c_r^e} = 1 - \frac{c_r^+ + c_r^- + c_r^e}{c_r^w + c_r^+ + c_r^- + c_r^e} \tag{18.60}$$

Because the water concentration is much higher than the other concentrations, we can use the first order approximation $\ln(1+x) \approx x$ and we will find:

$$\frac{\Delta\pi\bar{V}^w}{RT} = \frac{c_r^+ + c_r^- + c_r^e}{c_r^w} - \frac{c_l^+ + c_l^-}{c_l^w}, \tag{18.61}$$

This expression can be simplified further, because $c_l^w \approx c_r^w = 1/\bar{V}^w \approx 1/\bar{V}_0^w$, which gives:

$$\Delta\pi = RT(c_r^+ - c_l^+ + c_r^- - c_l^- + c_r^e) \tag{18.62}$$

In many cases the valence z of the protein is very high and therefore the contribution of the protein concentration c^e is neglectable, compared to the concentrations of the small ions. If we define the osmotic pressure, in this case, as:

$$\pi = RT(c^+ + c^-) \tag{18.63}$$

we find the former expression for the osmotic pressure difference back. In the non-ideal situation equation 18.63 is extended with an osmotic coefficient Γ:

$$\pi = \Gamma RT(c^+ + c^-) \tag{18.64}$$

From equation (18.51) also the Donnan-potential difference between the left and right compartment follows:

$$\xi_r - \xi_l = \frac{RT}{F} ln \frac{a_l^+}{a_r^+} = \frac{RT}{F} ln \frac{a_r^-}{a_l^-} \tag{18.65}$$

Donnan osmosis in biological tissues The semi-permeable membrane exists in many forms in nature: for example as a cell membrane, as a layer endothelial cells (covering the inner side of blood vessels), or as elastic lamina (a layer that is found in the wall of arteries). The transmembrane potential observed across the membrane of a living cell is a Donnan-potential. However, one should realize that many biological tissues function as a semipermeable medium leading to the Donnan-effect (and to osmosis) as a continuous osmotic pressure gradient across the tissue. Therefore the Donnan-effect occurs in, for example, cartilage, where the huge, ionized proteoglycan molecules are tangled in a network of collagen and elastine fibers. The charge of the proteoglycan molecules is caused by the negative carboxyl groups (COO^-) and sulphate groups (SO_3^-). It will be clear from the former, that not the concentration of big molecules c^e, but the concentration of negatively combined charge zc^e, is an important characteristic quantity of the material. This concentration is often called *fixed charge density* c^{fc}. We come across several small ions in biological tissues like Na^+, K^+, Ca^{2+} en Cl^-.

For studying the properties of biological tissues, synthetic model materials are developed, consisting of ionised polymer chains (de Heus, 1994). The Donnan-osmotic effect can be used to determine the fixed charge density c^{fc} in these materials. The model material ('the right compartment') is therefore exposed to an external solution of a known concentration ('the left compartment'), after which the osmotic pressure in the material is measured. In figure 14 the measured osmotic pressure is plotted against the external salt concentration. From a combination of the relations (18.53) – (18.57) and (18.62) we can eliminate the concentration of free ions in the model material, which will result in:

$$\Delta\pi = RT\{c^{fc^2} + 4f^2c^2\}^{1/2} - 2cRT, \tag{18.66}$$

in which $c = c_l^+ = c_l^-$ is the (known) concentration of ions in the external solution, and f is a short notation for the relation between the activity of salt in the external solution and that in the material $f = \gamma_l^{\pm}/\gamma_r^{\pm}$. We have to realize, that several approximations have been introduced when deriving expression (18.62). A more elaborate derivation leads to:

$$\Delta\pi = \Phi RT(c^{fc^2} + 4f^2c^2)^{1/2} - 2\Phi^* cRT, \tag{18.67}$$

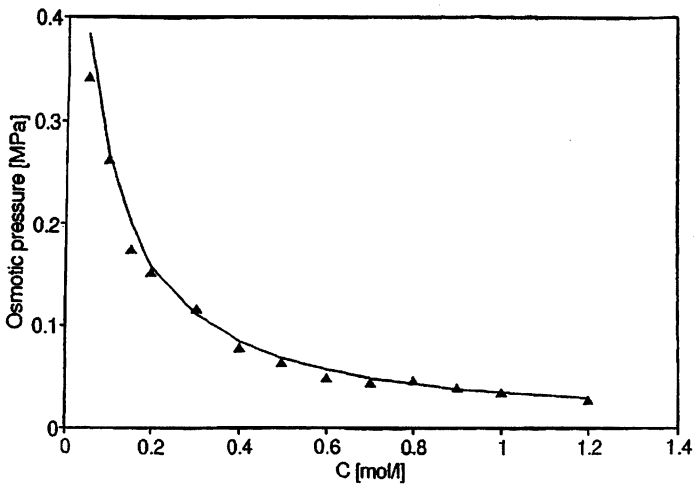

Figure 14. Measured relation between the osmotic pressure and external salt concentration (△) in a synthetic material. The drawn line represents relation (18.67), with parameter values $\Phi = \Phi^* = 0.93$, $f = 1$ and $c^{fc} = 0.24 \cdot 10^3 \text{mol}\cdot\text{m}^{-3}$.

with *osmotic coefficients* Φ and Φ^*. The unknowns in this relation can be determined by fitting the experimental data. From figure 14, we see that the relation between the measured concentration and the osmotic pressure can be described well using relation (18.67).

18.4 Chemical potential and mass transport

In the former it is stated, that the direction in which thermodynamic processes go, is dependent of differences in chemical potential. We will now specify this statement for the flow of a dissolved substance in a solution. The 'derivation' is meant to give better insight and not to be mathematically precise.

As an introduction we consider a simple one dimensional system, characterized by a mass m and a friction coefficient k, to which a force $\boldsymbol{f}$ is applied, that is related to a potential $\bar{\mu}$. The system model for such a system reads:

$$\boldsymbol{f} = \boldsymbol{\nabla}\bar{\mu} = m\boldsymbol{a} + k\boldsymbol{v}, \tag{18.68}$$

in which $\boldsymbol{v}$ and $\boldsymbol{a}$ are the velocity and the acceleration of the system. Some time after the force is applied to the system a stationary state will be established, in which the acceleration equals zero, so the velocity $\boldsymbol{v}$ is proportional to the gradient of the potential $\bar{\mu}$:

$$\boldsymbol{v} = \frac{1}{k}\boldsymbol{\nabla}\bar{\mu} \tag{18.69}$$

Similarly the flow of a constituent α in a solution can also be considered. If we state again, that the friction term is linear in velocity, we find:

$$\boldsymbol{v}^\alpha = \boldsymbol{L}^\alpha \cdot \boldsymbol{\nabla}\bar{\mu}^\alpha, \tag{18.70}$$

in which $\boldsymbol{L}^{\alpha}$ is a second order tensor. Substitution of expression (18.33) for the chemical potential yields:

$$\boldsymbol{v}^{\alpha} = \boldsymbol{D}^{\alpha} \cdot \boldsymbol{\nabla} x^{\alpha} + \boldsymbol{K}^{\alpha} \cdot \boldsymbol{\nabla} p \tag{18.71}$$

If a pressure gradient is absent, we recognize the *law of Fick* for diffusion of constituents caused by a concentration gradient. In the absence of a concentration gradient the equation reduces to the *law of Darcy* for flow of a fluid through a porous medium caused by the influence of a pressure gradient. The tensor $\boldsymbol{K}^{\alpha}$ therefore represents a *permeability tensor*, while $\boldsymbol{D}^{\alpha}$ is a *diffusion tensor*. If we deal with an isotropic system, these tensors reduce to $K^{\alpha}\,\boldsymbol{I}$ and $D^{\alpha}\,\boldsymbol{I}$, respectively.

19 Quadriphasic mixture theory

19.1 Introduction

In chapter 4 we presented a biphasic model of biological tissue. This model basically assumes that the tissue is a sponge saturated with a viscous fluid. Anyone who has worked with biological tissue will agree there is something realistic about this, although many body fluids look more like a gel than a fluid. This is true, e.g., for intracellular fluid, interstitial fluid and for synovial fluid. Part of those fluids are bound by hygroscopic macromolecules and are not free to move as assumed in biphasic mixture theory. Cartilaginous tissue is a tissue in which this gel property is dramatic. The pressure in the intervertebral disk of an unloaded spine, e.g., exceeds 0.1 MPa showing that strong forces are attracting fluid in the disk. If the disks of the spine were biphasic, they would very soon loose their fluid content (= 60 to 90 % of their volume), cause the spine to shorten under its daily load and be unable to perform their function. In fact hygroscopic macromolecular networks ensure that the fluid component of biological tissue remains under compression and the fibrous solid remains under tension irrespective of the loads applied on the tissue. The functionality of this lies in the inability of fibers to take up compression and the fluid to take up uni- or biaxial tensile loads. The physiological relevance of the hydrophylic nature of the solid component of biological tissues is clearly illustrated by the close correlation between water content of the human body and age. Maintenance of youthfulness is closely associated with the maintenance of hydrophylic nature of macromolecular networks within the tissue. Smoothness of skin is achieved by tensile prestressing the skin. Loss of fluid content of cutaneous and subcutaneous structures necessarily implies wrinkling of the skin. The load bearing capacity of cartilage strongly depends on the gellike fluid inside the cartilage layer to transform the compressive load into a tensile fibre stress. In the literature, finite deformation formulations are found in Huyghe and Janssen (1997) in the isothermal case, in Huyghe and Janssen (1999) in the non-isothermal case, in Huyghe (1999) for a dual porosity model. Some experimental work aiming at verifying some aspects of the theory are found in Frijns et al. (1997) for intervertebral disk, in Lanir et al. (1998) for hydrogel, in Huyghe et al. (2003) for a dual porosity model of intervertebral disk in Huyghe et al. (2002b,a) for electro-osmosis experiments. An efficient numerical scheme to deal with isothermal finite deformation of single porosity gels is give by van Loon et al. (2003).

19.2 Basic assumptions

. We distinguish a solid (superscript s), a fluid (superscript f) , a cationic component (superscript $+$) and an anionic component (superscript $-$). As is usual in porous media mechanics we consider trapped fluid (e.g. intracellular fluid) to belong to the solid because the fluid is not free to move. Part of the solid is assumed to be ionised. In case of cartilage or intervertebral disk this might be the proteoglycan network which is negatively charged (they contain COO^- en SO_3^-). The fixed charge density c^{fc} is expressed per unit volume of fluid. The cationic component is assumed to consist of only one monovalent cation (e.g. Na^+) with molar mass M^+, molar volume $\bar{V}^+$ and concentration c^+ per unit fluid volume. The anionic component is assumed to consist

of only one monovalent anion (e.g. Cl^-) with molar mass M^-, molar volume $\bar{V}^-$ and concentration c^- per unit fluid volume. We assume all phases intrinsically incompressible, i.e. the intrinsic density

$$\rho_i^\alpha = \frac{\rho^\alpha}{\phi^\alpha}, \qquad \alpha = s, f, +, - \tag{19.1}$$

is constant.

19.3 Conservation laws

Excluding mass transfer between phases, the mass balance of each phase is then written as:

$$\frac{\partial \phi^\alpha}{\partial t} + \nabla \cdot (\phi^\alpha \boldsymbol{v}^\alpha) = 0, \qquad \alpha = s, f, +, - \tag{19.2}$$

in which ϕ^α is the volume fraction and $\boldsymbol{v}^\alpha$ the velocity of phase α. As we assume saturation, we find

$$\phi^s + \phi^f + \phi^+ + \phi^- = 1 \tag{19.3}$$

Differentiation of equation (19.3) and substitution of the mass balance equations (19.2) yields the differentiated from of the saturation condition:

$$\nabla \cdot \boldsymbol{v}^s + \sum_{\beta=f,+,-} \nabla \cdot \left(\phi^\beta (\boldsymbol{v}^\beta - \boldsymbol{v}^s)\right) = 0 \tag{19.4}$$

In analogy to chapter 4, we refer current descriptors of the mixture with respect to an initial state of the porous solid. If we introduce volume fractions

$$\Phi^\alpha = J\phi^\alpha \tag{19.5}$$

per unit initial volume, we can rewrite the mass balance equation (19.2) as follows:

$$\frac{D^s \Phi^\alpha}{Dt} + J\nabla \cdot [\phi^\alpha (\boldsymbol{v}^\alpha - \boldsymbol{v}^s)] = 0 \tag{19.6}$$

The electroneutrality condition requires :

$$C^- = C^+ + C^{fc} \tag{19.7}$$

in which C^β is the current molar concentration per unit initial mixture volume:

$$C^\beta = J\phi^f c^\beta \quad \beta = +, -, fc \tag{19.8}$$

As the fixed charges are linked to the solid, we know that

$$\frac{D^s C^{fc}}{Dt} = 0 \tag{19.9}$$

Differentiation of (19.7) with respect to time yields:

$$\frac{D^s C^-}{Dt} = \frac{D^s C^+}{Dt} \tag{19.10}$$

or, after substitution of eq. (19.6),

$$\frac{1}{\overline{V}^{+}}\boldsymbol{\nabla}\cdot[\phi^{+}(\boldsymbol{v}^{+}-\boldsymbol{v}^{s})]=\frac{1}{\overline{V}^{-}}\boldsymbol{\nabla}\cdot[\phi^{-}(\boldsymbol{v}^{-}-\boldsymbol{v}^{s})] \tag{19.11}$$

in which $\overline{V}^{\beta}$ are the partial molar volumes of the ions.Neglecting body forces and inertia, the momentum balance takes the form:

$$\boldsymbol{\nabla}\cdot\boldsymbol{\sigma}^{\alpha}+\boldsymbol{\pi}^{\alpha}=\mathbf{0}, \qquad \alpha=s,f,+,- \tag{19.12}$$

which after summation over the four phases, yields:

$$\boldsymbol{\nabla}\cdot\boldsymbol{\sigma}=\boldsymbol{\nabla}\cdot\boldsymbol{\sigma}^{s}+\boldsymbol{\nabla}\cdot\boldsymbol{\sigma}^{f}+\boldsymbol{\nabla}\cdot\boldsymbol{\sigma}^{+}+\boldsymbol{\nabla}\cdot\boldsymbol{\sigma}^{-}=\mathbf{0} \tag{19.13}$$

if use is made of the balance condition:

$$\boldsymbol{\pi}^{s}+\boldsymbol{\pi}^{f}+\boldsymbol{\pi}^{+}+\boldsymbol{\pi}^{-}=\mathbf{0} \tag{19.14}$$

$\boldsymbol{\sigma}^{\alpha}$ is the partial stress tensor of constituent α, $\boldsymbol{\pi}^{\alpha}$ is the momentum interaction with constituents other than α. Balance of moment of momentum requires that the stress tensor $\boldsymbol{\sigma}$ be symmetric. If no moment of momentum interaction between components occurs, the partial stresses $\boldsymbol{\sigma}^{\alpha}$ also are symmetric. In this paper we assume all partial stresses to be symmetric. Under isothermal and incompressible conditions, the entropy inequality for a unit volume of mixture reads:

$$\sum_{\alpha=s,f,+,-}\left(-\phi^{\alpha}\frac{D^{\alpha}\Psi^{\alpha}}{Dt}+\boldsymbol{\sigma}^{\alpha}:\boldsymbol{D}^{\alpha}-\boldsymbol{\pi}^{\alpha}\cdot\boldsymbol{v}^{\alpha}\right)\geq 0. \tag{19.15}$$

in which Ψ^{α} is the Helmholtz free energy of constituent α per unit volume constituent. We introduce the strain energy function

$$W=J\sum_{\alpha=s,f,+,-}\phi^{\alpha}\Psi^{\alpha}=J\sum_{\alpha=s,f,+,-}\psi^{\alpha} \tag{19.16}$$

as the Helmholtz free energy of a mixture volume which in the initial state of the solid equals unity. ψ^{α} is the Helmholz free energy of constituent α per unit mixture volume. Rewriting the inequality (19.15) for the entropy production per initial mixture volume - i.e. we multiply inequality (19.15) by the relative volume change J - we find:

$$\begin{aligned}&-\frac{D^{s}}{Dt}W+J\boldsymbol{\sigma}:\boldsymbol{\nabla}\boldsymbol{v}^{s}\\&+J\boldsymbol{\nabla}\cdot\sum_{\beta=f,+,-}[(\boldsymbol{v}^{\beta}-\boldsymbol{v}^{s})\cdot\boldsymbol{\sigma}^{\beta}-(\boldsymbol{v}^{\beta}-\boldsymbol{v}^{s})\psi^{\beta}]\geq 0.\end{aligned} \tag{19.17}$$

The entropy inequality should hold for an arbitrary state of the mixture, complying with the balance laws, incompressibility, saturation and electroneutrality. There are two ways to comply with these restrictions. One is substitution of the restriction into the inequality,

resulting in elimination of a field variable. The other is by introduction of a Lagrange multiplier. The balance laws and the incompressibility condition (19.1) are accounted for by means of substitution. The differentiated forms of the saturation condition (19.4) and of the electroneutrality (19.11) are accounted for by means of a Lagrange multiplier. From the inequality 19.17 we see that the apparent density and the momentum interaction π is already eliminated from the inequality. In other words the conditions of incompressibility and the momentum balance have already been substituted into the second law. Therefore, restrictions still be fulfilled are the mass balances, saturation and the electroneutrality. The differentiated form of the saturation condition (19.4) is substituted by means of a Lagrange multiplier p:

$$\begin{aligned}
&-\frac{D^s}{Dt}W + J\boldsymbol{\sigma}^{eff} : \boldsymbol{\nabla}\boldsymbol{v}^s \\
&+J\sum_{\beta=f,+,-}[\boldsymbol{\sigma}^\beta + (p\phi^\beta - \psi^\beta)\boldsymbol{I}] : \boldsymbol{\nabla}(\boldsymbol{v}^\beta - \boldsymbol{v}^s) \\
&+J\sum_{\beta=f,+,-}(\boldsymbol{v}^\beta - \boldsymbol{v}^s)\cdot(-\boldsymbol{\nabla}\psi^\beta + p\boldsymbol{\nabla}\phi^\beta + \boldsymbol{\nabla}\cdot\boldsymbol{\sigma}^\beta) \geq 0.
\end{aligned} \tag{19.18}$$

in which the effective stress $\boldsymbol{\sigma}^{eff}$ is defined as

$$\boldsymbol{\sigma}^{eff} = \boldsymbol{\sigma} + p\boldsymbol{I} \tag{19.19}$$

Introducing the restriction (19.11) into inequality (19.18) by means of a Lagrange multiplier λ, yields:

$$\begin{aligned}
&-\frac{D^s}{Dt}W + J\boldsymbol{\sigma}^{eff} : \boldsymbol{\nabla}\boldsymbol{v}^s \\
&+J\sum_{\beta=f,+,-}[\boldsymbol{\sigma}^\beta + ((p + \frac{z^\beta\lambda}{\overline{V}^\beta})\phi^\beta - \psi^\beta)\boldsymbol{I}] : \boldsymbol{\nabla}(\boldsymbol{v}^\beta - \boldsymbol{v}^s) \\
&+J\sum_{\beta=f,+,-}(\boldsymbol{v}^\beta - \boldsymbol{v}^s)\cdot \\
&[-\boldsymbol{\nabla}\psi^\beta + (p + \frac{z^\beta\lambda}{\overline{V}^\beta})\boldsymbol{\nabla}\phi^\beta + \boldsymbol{\nabla}\cdot\boldsymbol{\sigma}^\beta] \geq 0.
\end{aligned} \tag{19.20}$$

in which z^β is the valence of constituent β. We choose as independent variables the Green strain $\boldsymbol{E}$, the Lagrangian form of the volume fractions of the fluid and the ions Φ^β, and of the relative velocities $\boldsymbol{v}^{\beta s} = \boldsymbol{F}^{-1}\cdot(\boldsymbol{v}^\beta - \boldsymbol{v}^s)$, $\beta = f,+,-$. We apply the principle of equipresence, i.e. all dependent variables depend on all independent variables, unless the entropy inequality requires otherwise. We apply the chain rule for time differentiation of W:

$$\begin{aligned}
&(J\boldsymbol{\sigma}^{eff} - \boldsymbol{F}\cdot\frac{\partial W}{\partial \boldsymbol{E}}\cdot\boldsymbol{F}^c) : \boldsymbol{\nabla}\boldsymbol{v}^s + \\
&\sum_{\beta=f,+,-}\{\frac{\partial W}{\partial \boldsymbol{v}^{\beta s}}\cdot\frac{D^s}{Dt}\boldsymbol{v}^{\beta s}
\end{aligned}$$

$$+J[\boldsymbol{\sigma}^{\beta}+(\mu^{\beta}\phi^{\beta}-\psi^{\beta})\boldsymbol{I}]:\boldsymbol{\nabla}(\boldsymbol{v}^{\beta}-\boldsymbol{v}^{s}) \\ +J(\boldsymbol{v}^{\beta}-\boldsymbol{v}^{s})\cdot(-\boldsymbol{\nabla}\psi^{\beta}+\mu^{\beta}\boldsymbol{\nabla}\phi^{\beta}+\boldsymbol{\nabla}\cdot\boldsymbol{\sigma}^{\beta})\}\geq 0. \tag{19.21}$$

in which μ^{β} are the electrochemical potentials of fluid and ions:

$$\begin{aligned}\mu^{f}&=\frac{\partial W}{\partial\Phi^{f}}+p\\ \mu^{+}&=\frac{\partial W}{\partial\Phi^{+}}+p+\frac{\lambda}{\overline{V}^{+}}\\ \mu^{-}&=\frac{\partial W}{\partial\Phi^{-}}+p-\frac{\lambda}{\overline{V}^{-}}\end{aligned} \tag{19.22}$$

Comparison of the above equations to the classical equations of electrochemistry (18.36-18.40) indicates that the Lagrange multiplier p can be interpreted as the fluid pressure and λ as the electrical potential of the medium multiplied by the constant of Faraday. Eq. (19.21) should be true for any value of the state variables. Close inspection of the choice of independent variables and the inequality (19.21), reveals that the first term of (19.21) is linear in the solid velocity gradient $\boldsymbol{\nabla}\boldsymbol{v}^{s}$, the second term linear in $\frac{D^{s}}{Dt}\boldsymbol{v}^{\beta s}$ and the third term linear in the relative velocity gradients $\boldsymbol{\nabla}(\boldsymbol{v}^{\beta}-\boldsymbol{v}^{s})$. Therefore, by a standard argument, we find:

$$\boldsymbol{\sigma}^{eff}=\frac{1}{J}\boldsymbol{F}\cdot\frac{\partial W}{\partial\boldsymbol{E}}\cdot\boldsymbol{F}^{c} \tag{19.23}$$

$$\frac{\partial W}{\partial\boldsymbol{v}^{\beta s}}=\boldsymbol{0} \tag{19.24}$$

$$\boldsymbol{\sigma}^{\beta}=(\psi^{\beta}-\mu^{\beta}\phi^{\beta})\boldsymbol{I} \tag{19.25}$$

leaving as inequality:

$$\sum_{\beta=f,+,-}J(\boldsymbol{v}^{\beta}-\boldsymbol{v}^{s})\cdot(-\boldsymbol{\nabla}\psi^{\beta}+\mu^{\beta}\boldsymbol{\nabla}\phi^{\beta}+\boldsymbol{\nabla}\cdot\boldsymbol{\sigma}^{\beta})\geq 0. \tag{19.26}$$

Eq. (19.23) indicates that the effective stress of the mixture can be derived from a strain energy function W which represents the free energy of the mixture. Eq. (19.24) shows that the strain energy function cannot depend on the relative velocities. Thus, the effective stress of a quadriphasic medium can be derived from a regular strain energy function, which physically has the same meaning as in single phase or biphasic media, but which can depend on both strain and ion concentrations in the medium. According to eq. (19.25) the partial stress of the fluid and the ions are scalars. Transforming the relative velocities to their Lagrangian equivalents, we find in stead of (19.26):

$$\sum_{\beta=f,+,-}\boldsymbol{v}^{\beta s}\cdot[-\boldsymbol{\nabla}_{0}\psi^{\beta}+\mu^{\beta}\boldsymbol{\nabla}_{0}\phi^{\beta}+\boldsymbol{\nabla}_{0}\cdot\boldsymbol{\sigma}^{\beta}]\geq 0. \tag{19.27}$$

in which $\boldsymbol{\nabla}_{0}=\boldsymbol{F}^{c}\cdot\boldsymbol{\nabla}$ is the gradient operator with respect to the initial configuration. If we assume that the system is not too far from equilibrium, we can express the dissipation

(19.27) associated with relative flow of fluid and ions as a quadratic function of the relative velocities:

$$-\nabla_0\psi^\beta + \mu^\beta\nabla_0\phi^\beta + \nabla_0\cdot\boldsymbol{\sigma}^\beta = \sum_{\gamma=f,+,-} \boldsymbol{B}^{\beta\gamma}\cdot\boldsymbol{v}^{\gamma s} \tag{19.28}$$

$\boldsymbol{B}^{\beta\gamma}$ is a positive definite matrix of frictional coefficients. Substituting eq. (19.25) into eq. (19.28) yields Lagrangian forms of the classical equations of irreversible thermodynamics:

$$-\phi^\beta\nabla_0\mu^\beta = \sum_{\gamma=f,+,-} \boldsymbol{B}^{\beta\gamma}\cdot\boldsymbol{v}^{\gamma s} \tag{19.29}$$

The next sections illustrate that from the above equations several well-known physical theories can be derived.

19.4 Diffusion Potential

The electric flux through the mixture is

$$\boldsymbol{i} = F\sum_{\gamma=f,+,-} \frac{\phi^\gamma z^\gamma}{\overline{V}^\gamma}\boldsymbol{v}^{\gamma s} \tag{19.30}$$

$\boldsymbol{i}$ is defined as the current electric flux through a surface of the mixture which initially equalled a unit surface. If use is made of (19.29), we find

$$\boldsymbol{i} = -F\sum_{\gamma=f,+,-} z^\gamma \sum_{\beta=f,+,-} \boldsymbol{L}^{\beta\gamma}\cdot\overline{V}^\beta\nabla_0\mu^\beta \tag{19.31}$$

in which $\boldsymbol{L}^{\beta\gamma}$ are the conductances:

$$\boldsymbol{L}^{\beta\gamma} = \frac{\phi^\gamma\phi^\beta(\boldsymbol{B}^{-1})^{\beta\gamma}}{\overline{V}^\beta\overline{V}^\gamma} \tag{19.32}$$

$\boldsymbol{B}^{-1}$ is the inverse of the matrix of tensors $[\boldsymbol{B}^\beta\gamma]_{\beta,\gamma=f,+,-}$ used in eqs. (19.28-19.29). Substituting the standard expressions for the electrochemical potentials into eq. (19.31), we find:

$$\boldsymbol{i} = \left(-F\sum_{\gamma=f,+,-} z^\gamma \sum_{\beta=f,+,-} \boldsymbol{L}^{\beta\gamma}\cdot(\overline{V}^\beta\nabla_0 p + RT\nabla_0 lna^\beta)\right)$$
$$-\boldsymbol{L}_e\cdot\nabla_0\xi \tag{19.33}$$

with

$$\boldsymbol{L}_e = F^2\sum_{\gamma=f,+,-}\sum_{\beta=f,+,-} z^\gamma z^\beta\boldsymbol{L}^{\beta\gamma} \tag{19.34}$$

the electrical conductance. At uniform temperature and pressure, when $\boldsymbol{i} = \boldsymbol{0}$, the electrical potential gradient is given by:

$$-\nabla_0\xi = RT\sum_{\beta=f,+,-} \boldsymbol{T}^\beta\cdot\nabla_0 lna^\beta \tag{19.35}$$

with $\boldsymbol{T}^{\beta}$ the reduced electrical transport tensor of component β:

$$\boldsymbol{T}^{\beta} = F\boldsymbol{L}_e^{-1} \cdot \sum_{\gamma=f,+,-} z^{\gamma}\boldsymbol{L}^{\beta\gamma} \tag{19.36}$$

in analogy to the reduced electrical transport number introduced by Staverman Staverman (1952): An integrated form of (19.35) is

$$\xi_2 - \xi_1 = -RT \int_1^2 \sum_{\beta=f,+,-} [\boldsymbol{n}_0 ds_0 \cdot \boldsymbol{T}^{\beta} \cdot \boldsymbol{\nabla}_0 lna^{\beta}] \tag{19.37}$$

in which $\boldsymbol{n}_0 ds_0$ is an infinitesimal segment of the path from 1 to 2, transformed back to the initial configuration. In the special case of a onedimensional non-deforming medium (19.37) is the classic isothermal diffusion potential derived by Nernst Nernst (1888),Nernst (1889) and later by Staverman Staverman (1952). Note that the uncharged water is also included in the summation.

19.5 Electrokinetic Relationships

The volume flux through the mixture is, in its Lagrangian form:

$$\boldsymbol{j} = \sum_{\gamma=f,+,-} \phi^{\gamma}\boldsymbol{v}^{\gamma s} \tag{19.38}$$

or, if use is made of (19.29) and (19.32), we find

$$\boldsymbol{j} = -\sum_{\gamma=f,+,-} \overline{V}^{\gamma} \sum_{\beta=f,+,-} \boldsymbol{L}^{\beta\gamma} \cdot \overline{V}^{\beta} \boldsymbol{\nabla}_0 \mu^{\beta} \tag{19.39}$$

Substituting the standard expressions for the electrochemical potentials into eq. (19.39), we find:

$$\boldsymbol{j} = -\sum_{\gamma=f,+,-} \overline{V}^{\gamma} \sum_{\beta=f,+,-} \boldsymbol{L}^{\beta\gamma} \cdot (Fz^{\beta}\boldsymbol{\nabla}_0\xi + RT\boldsymbol{\nabla}_0 lna^{\beta}) - \boldsymbol{L}_p \cdot \boldsymbol{\nabla}_0 p \tag{19.40}$$

with

$$\boldsymbol{L}_p = \sum_{\gamma=f,+,-} \sum_{\beta=f,+,-} \overline{V}^{\gamma}\overline{V}^{\beta}\boldsymbol{L}^{\beta\gamma} \tag{19.41}$$

If no gradients in chemical activities are assumed, eqs. (19.33) and (19.40) reduce to electrokinetic relationships:

$$\boldsymbol{j} = -\boldsymbol{L}^{p} \cdot \boldsymbol{\nabla}_0 p - \boldsymbol{L}^{pe} \cdot \boldsymbol{\nabla}_0 \xi \tag{19.42}$$

$$\boldsymbol{i} = -\boldsymbol{L}^{pe} \cdot \boldsymbol{\nabla}_0 p - \boldsymbol{L}^{e} \cdot \boldsymbol{\nabla}_0 \xi \tag{19.43}$$

in which

$$\boldsymbol{L}^{pe} = F \sum_{\gamma=f,+,-} \sum_{\beta=f,+,-} \overline{V}^{\gamma} z^{\beta} \boldsymbol{L}^{\beta\gamma} \tag{19.44}$$

As a result of the symmetry of the eqs. (19.42) and (19.43), a threedimensional form of the four Saxen's relations can be found: one connecting streaming current to electro-osmotic pressure,

$$(j)_{\nabla_0\xi=\mathbf{0}} \cdot (\nabla_0 p)_{j=\mathbf{0}} = (i)_{\nabla_0\xi=\mathbf{0}} \cdot (\nabla_0 \xi)_{j=\mathbf{0}} \tag{19.45}$$

one connecting streaming potential and electro-osmotic flow,

$$(j)_{\nabla_0 p=\mathbf{0}} \cdot (\nabla_0 p)_{i=\mathbf{0}} = (i)_{\nabla_0 p=\mathbf{0}} \cdot (\nabla_0 \xi)_{i=\mathbf{0}} \tag{19.46}$$

one connecting second streaming potential and second electro-osmotic pressure

$$(j)_{i=\mathbf{0}} \cdot (\nabla_0 p)_{j=\mathbf{0}} = (i)_{j=\mathbf{0}} \cdot (\nabla_0 \xi)_{i=\mathbf{0}} \tag{19.47}$$

one connecting second streaming current and second electro-osmotic flow,

$$(j)_{\nabla_0 p=\mathbf{0}} \cdot (\nabla_0 p)_{\nabla_0\xi=\mathbf{0}} = (i)_{\nabla_0\xi=\mathbf{0}} \cdot (\nabla_0 \xi)_{\nabla_0 p=\mathbf{0}} \tag{19.48}$$

19.6 Reconstruction of the biphasic theory of chapter 4

The bophasic theory from chapter 4 Biot (1972) is obtained from the previous by skipping all the term relating to the presence of fixed charges and ions. Conservation of mass follows from (19.4):

$$\nabla \cdot \boldsymbol{v}^s + \nabla \cdot \left(\phi^f (\boldsymbol{v}^f - \boldsymbol{v}^s)\right) = 0 \tag{19.49}$$

Conservation of momentum is obtained by substitution of eq. (19.19) into eq. (19.13):

$$\nabla \cdot \boldsymbol{\sigma}^{eff} - \nabla p = \mathbf{0} \tag{19.50}$$

while the stress-strain relationship is given by (19.23)

$$\boldsymbol{\sigma}^{eff} = \frac{1}{J}\boldsymbol{F} \cdot \frac{\partial W}{\partial \boldsymbol{E}} \cdot \boldsymbol{F}^c \tag{19.51}$$

in which the strain energy function W depends only on local deformation. Darcy's law follows from eqs. (19.29) and (19.22):

$$\phi^f \boldsymbol{v}^{fs} = -\boldsymbol{K} \cdot \nabla_0 (p + \frac{\partial W}{\partial \Phi^f}) \tag{19.52}$$

in which the term $\frac{\partial W}{\partial \Phi^f}$ is interpreted for immiscible mixtures as the matric potential. Equations (19.49-19.52) are the biphasic equations derived in chapter 4.

19.7 Recapitulation

The equations In short, the quadriphasic equations are as follows:
The momentum balance of the mixture (19.13) inwhich we substitute eq. (19.19) :

$$\nabla \cdot \boldsymbol{\sigma}_e - \nabla p = \mathbf{0} \tag{19.53}$$

The mass balance of the mixture (19.4) :

$$\boldsymbol{\nabla} \cdot \boldsymbol{v}^s - \boldsymbol{\nabla} \cdot \phi^f (\boldsymbol{v}^f - \boldsymbol{v}^s) = 0 \tag{19.54}$$

The mass balance of the ionic constituents (19.6):

$$\frac{D^s \Phi^\alpha}{Dt} + J \boldsymbol{\nabla} \cdot [\phi^\alpha (\boldsymbol{v}^\alpha - \boldsymbol{v}^s)] = 0 \quad \alpha = +, - \tag{19.55}$$

The reversible constitutive relationships (19.23) :

$$\boldsymbol{\sigma}_e = (\det \boldsymbol{F})^{-1} \boldsymbol{F} \cdot \frac{\partial W}{\partial \boldsymbol{E}^s} \cdot \boldsymbol{F}^c \tag{19.56}$$

and (19.22)

$$\begin{aligned} \mu^f &= \frac{\partial W}{\partial \Phi^f} + p \\ \mu^+ &= \frac{\partial W}{\partial \Phi^+} + p + \frac{\lambda}{V^+} \\ \mu^- &= \frac{\partial W}{\partial \Phi^-} + p - \frac{\lambda}{V^-} \end{aligned} \tag{19.57}$$

The dissipative constitutive relationships, containing Darcy's law and Fick's law (19.29) :

$$-\phi^\beta \boldsymbol{\nabla}_0 \mu^\beta = \sum_{\gamma=f,+,-} \boldsymbol{B}^{\beta\gamma} \cdot \boldsymbol{v}^{\gamma s} \tag{19.58}$$

The incompressibility of the solid :

$$(1 - \phi^f) \det \boldsymbol{F} = 1 - \phi_0^f \tag{19.59}$$

The fixation of the fixed charges to the solid (19.9) :

$$\phi^f c^{fc} \det \boldsymbol{F} = \phi_0^f c_0^{fc} \tag{19.60}$$

The reversible constitutive relationships are described by one function : the strain energy function W. The dissipative constitutive relationships are described by a symmetric semi-positive definite matrix $\boldsymbol{B}$. W depends on the deformation of the solid, the volume fraction of the fluid Φ^f, cations Φ^+ and anions Φ^-. Equation (19.54) says that the volume change of the porous solid, expressed as the divergence of the solid velocity $\boldsymbol{v}^s$, is caused by in or outflow of fluid. This flux depends in turn on the gradients of chemical potential of the fluid, and of the electrochemical potentials of the ions according to eq. (19.58).

Equations (19.55) are the mass balance of cations and anions, in which the relative ionic velocities $\boldsymbol{v}^\alpha - \boldsymbol{v}^s = \boldsymbol{F} \cdot \boldsymbol{v}^{\alpha s}$ are expressed as a function of gradients of (electro)chemical potentials by eqs. (19.58) .

Boundary conditions As for single-phase materials momentum balance of the boundary is compulsory :

$$[(\boldsymbol{\sigma}_e - p\boldsymbol{I}) \cdot \boldsymbol{n}] = \boldsymbol{0} \tag{19.61}$$

with $\boldsymbol{n}$ de outer normal along the boundary. From eqs (19.58) we can infer that the following jump conditions should hold along the boundary :

$$[\bar{V}^f \mu^f] = 0 \tag{19.62}$$

$$[\bar{V}^+ \mu^+] = 0 \tag{19.63}$$

$$[\bar{V}^- \mu^-] = 0 \tag{19.64}$$

because the fluxes across the boundary cannot be infinite .

19.8 Example of a constitutive relationship

We take the example of a material complying with linear isotropic elasticity and Donnan-osmosis (figure 5.3). In this case the strain energy function W takes the form :

$$\begin{aligned} W = \quad & {\mu_O}^f N^f + {\mu_0}^+ N^+ + {\mu_0}^- N^- - RT\Gamma \left(\tfrac{N^+}{\bar{V}^+} + \tfrac{N^-}{\bar{V}^-} \right) ln(N^f) + \\ & + RT \tfrac{N^+}{\bar{V}^+} \left(ln \tfrac{f^+ N^+}{\bar{V}^+} - 1 \right) + \\ & + RT \tfrac{N^-}{\bar{V}^-} \left(ln \tfrac{f^- N^-}{\bar{V}^-} - 1 \right) + \tfrac{\lambda_s}{2} tr\boldsymbol{E} tr\boldsymbol{E} + \mu_s \boldsymbol{E} : \boldsymbol{E} \end{aligned} \tag{19.65}$$

in which Γ is the osmotic coefficient, f^+ the activity coefficient of the cations, f^- the activity coefficient of the anions, λ_s and μ_s the Lamé constants. From eqs. (19.56) and (19.57) we derive expressions for the stress and the (electro)chemical potentials :

$$\boldsymbol{\sigma}_e = \tfrac{1}{J} \boldsymbol{F} \cdot (\lambda_s \boldsymbol{I} tr\boldsymbol{E} + 2\mu \boldsymbol{E}) \cdot \boldsymbol{F}^c \tag{19.66}$$

$$\mu^f = {\mu_0}^f(T) + p - RT\Gamma(c^+ + c^-) \tag{19.67}$$

$$\mu^+ = {\mu_0}^+(T) + p + \tfrac{RT}{\bar{V}^+} ln \tfrac{f^+ N^+}{\bar{V}^+ (N^f)^\Gamma} + \tfrac{\lambda}{\bar{V}^+} \tag{19.68}$$

$$\mu^- = {\mu_0}^-(T) + p + \tfrac{RT}{\bar{V}^-} ln \tfrac{f^- N^-}{\bar{V}^- (N^f)^\Gamma} - \tfrac{\lambda}{\bar{V}^-} \tag{19.69}$$

In eq. (19.67) we identify the chemical potential in the same way as in chapter 5. It is the difference between the mechanical pressure p and the osmotic pressure pi given by eq. (18.65). The eqs. (19.68-19.69) are consistent with the expression (18.41) for the limiting case of a dilute solution ($\Gamma \rightarrow 1$ and $f^\beta \rightarrow 1$).

Bibliography

M A Biot. Theory of finite deformations of porous solids. *Indiana University Mathematics J*, 21(7):597–620, 1972.

H.P.G. Darcy. *Les fontaines publiques de la ville de Dijon.* Delmont, Paris, France, 1856.

H J de Heus. *Verification of mathematical models describing soft charged hydrated tissue behaviour.* PhD dissertation, Eindhoven University of Technology, Department of Mechanical Engineering, Dec 1994.

A.J.H. Frijns, J.M. Huyghe, and J.D. Janssen. A validation of the quadriphasic mixture theory for intervertebral disc tissue. *Int. J. Eng. Sci.*, 35:1419–1429, 1997.

Y.C. Fung. *Biomechanics: Mechanical properties of living tissues.* Springer Verlag, New York, USA, 1993.

J. M. Huyghe, C.F. Janssen, Y. Lanir, C.C. van Donkelaar, A. Maroudas, and D.H. van Campen. Experimental measurement of elctrical conductivity and electro-osmotic permeability of ionised porous media. In W. Ehlers and J. Bluhm, editors, *Porous media: theoretical, experimental and numerical applications*, pages 295–313. Springer Verlag, Berlin, Germany, 2002a.

J.M. Huyghe. Intra-extrafibrillar mixture formulation of soft charged hydrated tissues. *Journal of Theoretical and Applied mechanics*, 37(3):519–536, 1999.

J.M. Huyghe, G.B. Houben, M.R. Drost, and C.C. van Donkelaar. An ionised/non-ionised dual porosity model of intervertebral disc tissue: experimental quantification of parameters. *Biomechanics and modelling in mechanobiology*, 2:3–19, 2003.

J.M. Huyghe, C.F. Janssen, C.C. van Donkelaar, and Y. Lanir. Measuring principles of frictional coefficients in cartilaginous tissues and its substitutes. *Biorheology*, 39: 47–53, 2002b.

J.M. Huyghe and J.D. Janssen. Quadriphasic mechanics of swelling incompressible porous media. *Int. J. Eng. Sci.*, 35:793–802, 1997.

J.M. Huyghe and J.D. Janssen. Thermo-chemo-electro-mechanical formulation of saturated charged porous solids. *Transport in Porous Media*, 34:129–141, 1999.

A. Katchalsky and P.F. Curran. *Nonequilibrium thermodynamics in biophysics.* Harvard University Press, Cambridge, Ma, U.S.A., 1965.

Y. Lanir, J. Seybold, R. Schneiderman, and J. M. Huyghe. Partition and diffusion of sodium and chloride ions in soft charged foam : the effect of external salt concentration and mechanical deformation. *Tissue Engineering*, 4(4):365–378, 1998.

A Maroudas. *Physicochemical properties of articular cartilage*, chapter 4, pages 215–290. In: M A R Freeman, ed. Adult articular cartilage. 2nd ed. Tunbridge Wells, Kent, UK: Pitman medical, 1979.

A. Maroudas and P.G. Bullough. Permeability of articular cartilage. *Nature*, 219:1260–1261, 1968.

W. Nernst. Zur kinetik der in loesung befindlichen koerper. *Z. Phys. Chem.*, 2:613–637, 1888.

W. Nernst. Die electromotorische wirksamkeit der jonen. *Z. Phys. Chem.*, 4:129–181, 1889.

A.A.H.J. Sauren, M.C. van Hout, A.A. van Steenhoven, F.E. Veldpaus, and J.D. Janssen. The mechanical properties of porcine aortic valve tissues. *J. Biomech.*, 16:327–337, 1983.

H Snijders. *A triphasic model of the intervertebral disc.* PhD dissertation, University of Maastricht, The Netherlands, Department of Health Sciences, 1994.

A. J. Staverman. Non-equilibrium thermodynamics of membrane processes. *Trans. Faraday Soc.*, 48:176–185, 1952.

R. van Loon, J.M. Huyghe, M.W. Wijlaars, and F.P.T. Baaijens. 3d fe implementation of an incompressible quadriphasic mixture model. *Int. J. Numer. Meth. Engng.*, 2003. in press.

Chemo-Mechanical Interactions in Geological and Biological Materials: examples

Benjamin Loret [*], Alessandro Gajo [†] and Fernando M. Simões[‡]

[*] Laboratoire Sols, Solides, Structures, Institut National Polytechnique de Grenoble, France
[†] Dipartimento di Ingegneria Meccanica e Strutturale, Università di Trento, Trento, Italia
[‡] Departamento de Engenharia Civil, Instituto Superior Técnico, Lisboa, Portugal

Abstract Examples of chemo-mechanical couplings are presented briefly. First, the notion of a semi-impermeable membrane is introduced together with the concept of osmosis. Chemical contraction and swelling are illustrated in chemically sensitive clays and articular cartilages. The heart muscle provides a prominent instance of electro-chemo-mechanical coupling. Reverse couplings play an important role in the engineering of soft tissues. Microstructural aspects of the chemically sensitive materials highlight the ubiquitous electric charges that promote the couplings.

1 Introduction

Chemo-mechanical couplings occur in many engineering and biological fields. A typical instance is swelling that has relevance in clays, soft tissues and polymer inter alia.

Swelling is an important property of soils being exploited or fought, or engineered in a variety of circumstances, from laying foundations, to setting hydraulic or contamination barriers, to petroleum drilling. Swelling may cause a non-uniform soil heave, resulting in damage of over-structures, or weakening of bore walls in petroleum drillings. On the other hand, swelling of bentonite is taken advantage of to build barriers to water flow, or contaminant transport in hazardous and nuclear waste disposal technologies.

Swelling of soils is generally understood to be driven by capillary forces and/or by chemical gradients. The former one, termed *matric swelling*, occurs when soil is unsaturated. The latter one, termed *chemical swelling*, is characteristic of so called expansive clays, rich in mineral smectite, and occurs when there exists a positive difference in concentration of certain species in the soil and in the water in contact with the soil. Typically, these species are metallic ions (Na^+, K^+, Ca^{2+}, etc...).

Gels are also highly susceptible of swelling. Gels are aqueous environments that contain soluble components, e.g. metallic ions, and insoluble structural molecules. The articular cartilage, and the corneal stroma, are instances of *extracellular* biological gels in which the structural molecules are located outside the cells, and so form the extracellular matrix. In contrast, the muscle is an *intracellular* gel in which the myosin filament has a diameter comparable to that of collagen in articular cartilage.

Swelling in non-ionic polymers is traditionally traced to the volume exclusion concept, according to which in a very dilute solution in a good solvent each molecule tends to

exclude all others from the volume it occupies, Flory [1953]. In ionic polymers, electrical repulsion between fixed charges provides another source of swelling. The presence of mobile ions, due to electroneutrality, shields these repulsive forces, but is not sufficient to make them vanish, unless at very high concentrations, referred to as hypertonic state.

Electro-chemo-mechanical couplings are also exploited by engineers. For example, electro-migration is used to remediate soils polluted by heavy metals, electro-osmosis to consolidate soils.

In biological tissues, couplings arise as processes to maintain a certain equilibrium: swelling of articular cartilages opposes the water depletion that would occur due to mechanical compression. In some instances, they are driving processes: the cardiac function is a typical process of electro-chemo-mechanical coupling. A common feature to most, if not all, these examples is the presence of *fixed electric charges* that play a key role in promoting the couplings.

Reverse couplings, e.g. mechano-electric feedback, are less studied. They appear nevertheless to be at work in many instances of the development of biological organs. Indeed, while in vitro cultures of engineered soft tissues are able to induce cell proliferation, the mechanical properties of the tissues are not satisfactory. *Mechanobiology* aims at defining mechanical loading programmes that improve these properties.

2 A Semi-Permeable Membrane and the Osmotic Effect

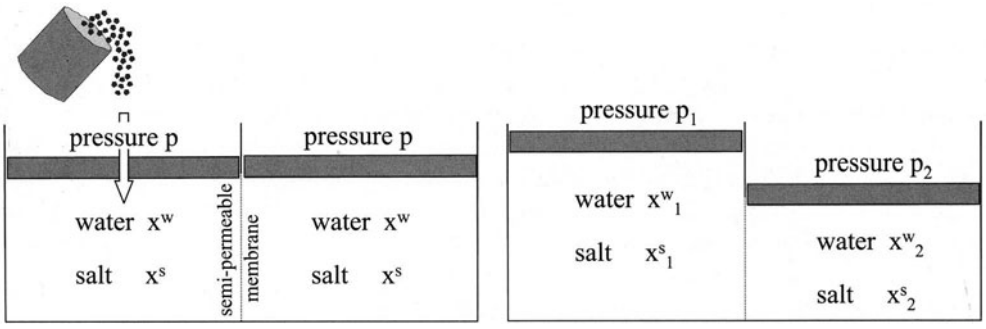

Figure 1 A membrane permeable to water only separates a bucket in two parts. Initially, the chemical content and load is identical on both sides. Addition of solute in side 1 triggers a transfer of water from side 2 to side 1 and the applied load required by equilibrium is larger in side 1.

This first example introduces the notion of chemical potential as a vehicle to explain the concept of osmosis.

Consider a bucket separated in two parts by a membrane impermeable to solute [1].

[1] Unlike the usual presentation which uses a thin U-shaped tube, gravity is neglected here and the mechanical loads are applied by external agents. In the usual presentation, the external load on both sides of the tube is the atmospheric pressure and the difference of pressures gives

Initially, the two sides of the membrane, numbered 1 and 2, have identical chemical content, water w and solute s, and are submitted to the same external pressure p. At any time, the molar fractions satisfy the identities $x_1^w + x_1^s = 1$ and $x_2^w + x_2^s = 1$.

The *mechanical potential* of water at pressure p and molar fraction x^w is [2]

$$g^w = v^w p + RT \ln x^w, \tag{2.1}$$

with v^w molar volume of water, R is the universal gas constant and T the absolute temperature. Since only water can transfer through the membrane, chemo-mechanical *equilibrium* along the membrane is phrased in terms of the chemical potential of water only. The initial concentration of solute is very small, so that:

$$\text{Initial equilibrium}: \quad p_1 = p_2, \ x_1^w = x_2^w \sim 1, \ x_1^s = x_2^s \sim 0. \tag{2.2}$$

Salt is then added on side 1:

$$\text{Add solute}: \quad \Delta x_1^s > 0 \ \Rightarrow \Delta x_1^w = -\Delta x_1^s < 0. \tag{2.3}$$

The short term rate of mass transfer of water through the membrane is assumed to be governed by the following law defined by a constant $k > 0$ representative of the permeability of the membrane to water (motivation for and generalization of this law will be addressed be later),

$$\begin{aligned} \text{Law of transfer}: \quad \dot{m}_1^w &= k\,(\Delta g_2^w - \Delta g_1^w) \\ &= k\,(\ 0\ -(-RT\,\Delta x_1^s)\ ) \quad \text{instantaneously.} \end{aligned} \tag{2.4}$$

Consequently, we have

Rule 1: *flow is directed towards the region of higher solute concentration.*

The final equilibrium, corresponding to a vanishing flow through the membrane, occurs when

$$g_1^w \sim v^w p_1 - RT\, x_1^s \ = \ g_2^w \sim v^w p_2 - RT\, x_2^s \tag{2.5}$$

This result is encapsulated as

Rule 2 or van't Hoff law: *pressure is higher where solute concentration is higher, namely*

$$p_1 - p_2 = RT\,(x_1^s - x_2^s)/v^w > 0. \tag{2.6}$$

Hence, osmotic effect generates a counterflow to usual Darcy flow. The chemical potential may be phrased in terms of concentration, e.g. $c^s = x^s/v^w$, instead of molar fraction. The *osmotic pressure* is defined as

$$\pi = RT\, c^s\,. \tag{2.7}$$

rise to different elevations of water on the two sides of the tube.

[2] In this section, we use mole-based chemical potentials following the usual convention of textbooks of physical chemistry.

So far, the membrane was assumed to be completely impermeable to solute. More generally, the permeability of the membrane for the solute can be introduced via the *reflection coefficient* or *osmotic efficiency* ω (hence ω is a property of both the membrane and the solute). The osmotic efficiency varies between 0 and 1, and is equal to 0 for a completely permeant solute and to 1 for an non-permeant solute (as assumed above). Then the law of transfer of water has to be modified. For that purpose, we need the chemical potential of the solute. An approximative expression for dilute solution is

$$g^s \simeq RT \ln x^s. \tag{2.8}$$

Then, noting $k_{ws} = k_w\,(1-\omega)$, the general mass transfer law is

$$\begin{aligned} \dot{m}_1^w &= k_w(\Delta g_2^w - \Delta g_1^w) + k_{ws}(\Delta g_2^s - \Delta g_1^s)\,, \\ &= k_w\, v^w \Big(\Delta p_1 - \Delta p_2 - \omega\,(\Delta \pi_1 - \Delta \pi_2)\Big)\,. \end{aligned} \tag{2.9}$$

Therefore, for any non completely permeant solute, i.e. $\omega \neq 0$, one should exert a pressure differential, proportional to the osmotic coefficient, to reach a steady state, that is to stop water flow:

$$\Delta p_1 - \Delta p_2 = \omega(\Delta \pi_1 - \Delta \pi_2)\,. \tag{2.10}$$

The law of transfer for the solute involves its diffusional properties through the membrane,

$$\begin{aligned} \dot{m}_1^s &= k_{sw}(\Delta g_2^w - \Delta g_1^w) + k_s(\Delta g_2^s - \Delta g_1^s)\,, \\ &= k_{sw}\, v^w \Big(\Delta p_1 - \Delta p_2 - Y\,(\Delta \pi_1 - \Delta \pi_2)\Big)\,. \end{aligned} \tag{2.11}$$

For a non-permeant solute, $\omega = 1$ and, in addition, $Y \equiv 1 - k_s/c^s\, k_{sw}$ has to be finite.

Complete equilibrium is defined by the equality of the chemical potentials of both water and salt, and more generally of all (even partially) permeant species.

We have seen that osmosis requires a membrane to develop. Crucially, membranes are selective. A species is endowed with a transfer time. An infinite transfer time practically prevents a species to cross the membrane. Transfer times depend, inter alia, on the size, polarity, molar mass of the species. Membranes may be well defined objects, natural like the ones that limit cells or engineered, for example clay barriers to prevent leakage of pollutants. They may also be fictitious: in cartilage, steric considerations prevent macromolecules to enter the space defined by collagen fibers.

3 Influence of the Pore Composition in Clays and Soft Tissues

3.1 Chemical Consolidation and Swelling in Clays

Ionic strength in homoionic clays. Swelling of clayey soils is an important factor in their engineering, but the accurate prediction of its amount and its consequences have been eluding engineers for several decades. *Chemical swelling* here will cover both *crystalline swelling* due to absorption of water into interlamellar space and *osmotic swelling*

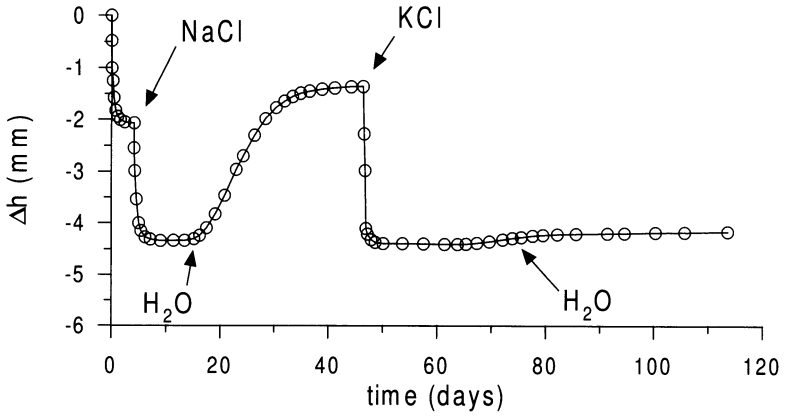

(a) Experimental data on Bisaccia clay, Di Maio and Fenelli (1997).

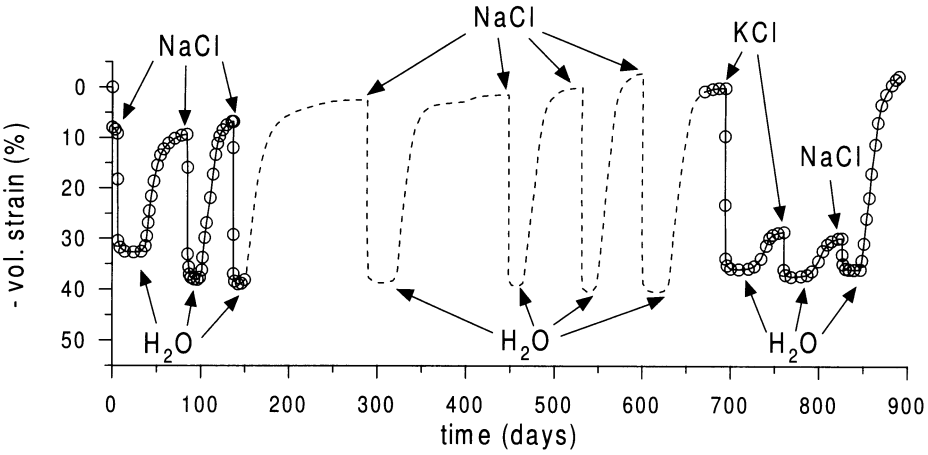

(b) Experimental data on Ponza bentonite, Di Maio (1998).

Figure 2 Successive replacements of pore solution by NaCl and KCl saturated solutions during oedometric tests at constant vertical stress of 40 kPa. Evolution of (a) the settlement and (b) the volumetric strain. Increase of salt concentration implies chemical consolidation, and KCl stiffens more the clays than NaCl. The stiffening effect due to cation exchange seems mostly reversible. Replacement of cations initially present in Ponza bentonite by cations Na^+ is slow, progressive and requires several cycles to get steady.

due to adsorption of water to the external surface of clay particles, and no distinction will be made between adsorbed and absorbed water.

Montmorillonites are particularly sensitive to the composition of their pore water. Figure 2-(a) shows the time evolution of the vertical settlement in a oedometric test. The sample is in contact with a reservoir of controlled chemical composition. Initially the reservoir is distilled water (dw). The sample is first mechanically compressed by the

application of an instantaneous load and this results in a *mechanically induced consolidation* which tends to stabilize in few days. Next, while the load is kept unchanged, the water of the reservoir is NaCl-saturated. A significant *chemically induced consolidation* develops. The consolidation time is of about the same duration as for mechanical consolidation. When the reservoir chemistry is refreshed, the sample undergoes a volume expansion, termed *chemical swelling*, that requires a few weeks to stabilize.

The resulting volume change upon the chemical cycle turns out here to be positive (expansion). In general, it is the result of mechanisms which might compete or cooperate:

- cations are attracted by the *negatively charged clay clusters*, they are hydrated, and this gives rise to absorbed water.
- the cations initially present around clusters may be 'displaced' by other ions which have a higher affinity for the clay charge. Later, in the context of the theory of mixtures, we shall use the terms 'transfer' and 'exchange' rather than 'displacement'. Ion exchange may result in an expansion or contraction;
- as a result of the osmotic effect, absorbed water in between clay platelets is desorbed when the salt concentration in pore water increases, the overall stiffness of the clay is increased, and this results in volume decrease. The converse occurs when pore water is desalinized.
- plastic contraction may develop, especially at large mechanical stress.

Ionic replacements in clays. The *reversible* or *irreversible* character of the material response to a chemical loading is thus difficult to be defined because it involves a number of physical aspects, as well as microstructural features of the clays.

Reversibility can be assumed as a first rough approximation. Let us illustrate this statement by an example.

Figure 2-(a) shows that saturation of the fresh reservoir by KCl results in about the same consolidation as that induced by NaCl. However, later refreshment of the reservoir implies a very small swelling. The phenomenon is due to displacement of ions Na^+ by ions K^+, and this stiffens considerably the material behaviour, as advocated in the model developed in the Chapter 'Constitutive Equations for Heteroionic Clays'.

To recover approximately the initial volume, a complete symmetric chemical cycle should be performed, that is dw NaCl - dw KCl dw - NaCl dw, as confirmed by Figure 2-(b).

The latter figure shows that a number of cycles dw NaCl dw are necessary to reach steady state. This might be traced to the fact that the transfer times of ions is long with respect to the time scale of the chemical cycles.

3.2 Modification of the Electrolyte Circulating an Articular Cartilage

Homoionic cartilage. The articular cartilage is a porous medium that provides normal compliance so as to minimize friction at joints. A key constituent are the negatively charged proteoglycans (PG's). The skeleton of cartilage is formed by collagen fibers who resist both the external loads and the chemical pressure exerted by PG's.

The latter depends much on the repulsive forces between PG's, which are themselves function of the ionic content of the electrolyte, in communication with the synovial fluid, that circulates the cartilage. The macroscopic outcome of these nanoscale interactions is a compressive stress that decreases when the electrolyte changes from distilled water to a salt-saturated solution, Figure 3.

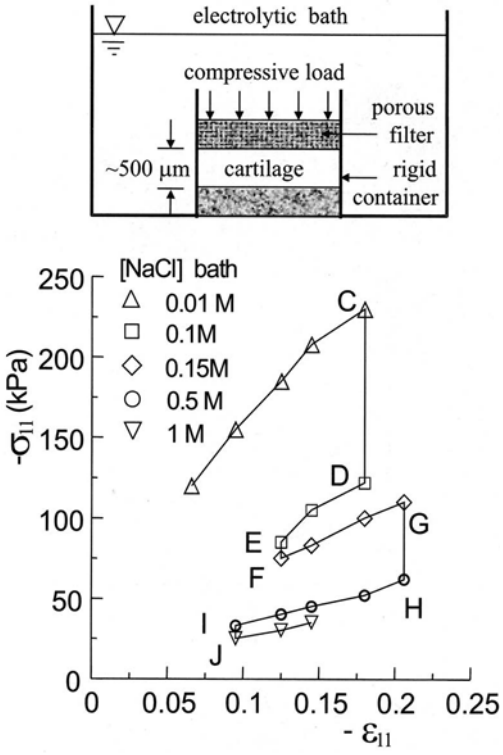

Figure 3 Confined compression test on bovine articular cartilage by Eisenberg and Grodzinsky [1985]. The sample is in contact with a bath of controlled salinity. Sufficient time is left after each modification of the bath salinity to reach steady state. The complex loading path involves successive confined compression, at fixed bath salinity, and increase in bath salinity at fixed strain. *Shielding* of negative charges of proteoglycans by salt reduces the repulsive forces and the overall compressive stress. The apparent moduli are thus maximum when the salt concentration of the electrolyte is minimal, and minimal when the salt concentration of the electrolyte is maximal.

Ionic replacements in an articular cartilage. Owens et al. [1991] have performed uniaxial traction tests on specimens of bovine articular cartilage, harvested from the superficial zone of the medial patello-femoral groove, parallel to the split-line orientation. Pre-equilibration is performed at constant axial tensile strain of 5%, relative to the largest free swelling strain, under distilled water. The bath chemistry is then modified as indicated by Figure 4. Data show that shielding by calcium is more important than by sodium. On the other hand, the hypertonic state is universal: the nature of ions matter in the shielding process at low to moderate salinities only.

Consequently, in articular cartilages like in clays, what matters is not an overall salinity of the electrolyte including all ions, but the concentration of each ionic species itself.

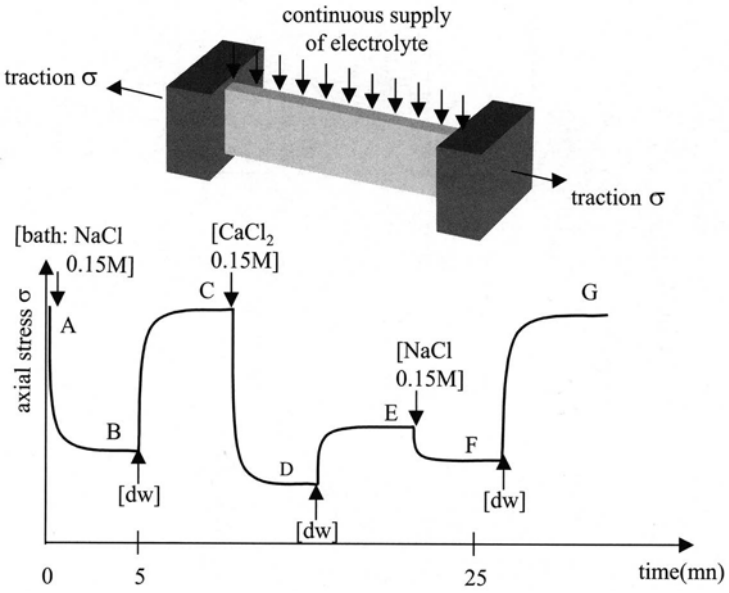

Figure 4 Uniaxial traction experiment on bovine articular cartilage by Owens et al. [1991]. At a given axial strain of 5% counted from isotropic free swelling, the bath chemistry is modified instantaneously at the instants denoted by an arrow. Sufficient time is left however for equilibrium to be reached before further modifications.
The presence of proteoglycans in the cartilage gives rise to a certain chemical pressure p^{eff}. For this strain, the chemical pressure p^{eff} is maximal for a fresh bath and decreases as salinity increases. The collagen fibers resist the external load and the pressure p^{eff} by stretching. Since the strain is given (in fact in the axial direction only), decrease of p^{eff} implies the external load to decrease as well. The reverse phenomenon occurs when the water of the bath is refreshed. The difference in response to the two salts can be traced to the fact that the chemical pressure due to calcium ions is smaller than to sodium ions, if it is assumed that initially only sodium ions exist in the cartilage, Simões and Loret [2003].

4 The Heart Muscle, and Cell Electrophysiology

The human heart beats about 87 times per minute. Functionally, each beat involves a passive stage (intake of blood) and an active stage (expulsion of blood). For the organ itself, the process is crudely as follows:

- step 1: *electrical conduction*: the sino-atrial node, which has a larger eigenfrequency than the other parts of the heart, is the cardiac pacemaker. It sends a signal that travels through a dedicated net: the signal reaches first the atria, and next, through the His bundle and the Purkinje net, it circulates the ventricles, from the endocardium to the epicardium: the epicardium has received the electrical impulsion after about 200 msec;
- step 2: *action potential and calcium release*: the electrical signal induces a depolarizing current across the membrane of the cardiac cell (the myocyte) which gives rise to the action potential: the resting potential difference of -90 mV increases temporarily, a small amount of plasmic ions Na^+ enters the cell through dedicated channels, and this intake in turns produces a huge modification of the internal repartition of ions Ca^2+, the latter being temporarily released from the sarcoplasmic reticulum;
- step 3: *establishment of cross-bridges and force development*: calcium is used immediately: binding to the low affinity site of Troponin C, calcium induces a change of conformation of the tropomyosin that makes possible myosin heads to establish a *bond* with actin sites: this is the relative sliding of the myosin and actin filaments that develops a force.

The time course of the process for human muscles is shown in Figure 4 of the Chapter 'Transfer through Membranes and Generalized Diffusion'.

Cell electrophysiology models aim at describing the many currents and cytoplasmic fluxes that develop, e.g. Figure 5. Some of these currents and fluxes are driven by ionic pumps, that require energy. The biological energy unit ATP is produced by the metabolism. In fact, the proportion of energy used by ionic pumps is small with respect to that necessary to ensure the bond of the myosin head on the actin sites for force development. Many models of muscle behaviour use the *cross-bridge theory* of Huxley as a basic ingredient.

It is important to highlight that this description corresponds to

- an electro-chemical coupling, i.e. the electrical current induces a change of ionic concentrations in the cardiomyocytes, followed by
- a chemo-mechanical coupling, i.e. the temporary increase of calcium concentration allows a relative motion of the myosin and actin filaments that implies force development.

But none of these two steps involves a priori a feedback, that is

- neither a mechano-chemical effect, i.e. the force developed by the muscle does not influence the chemical intra- or extra-cellular concentrations.

- nor a chemo-electrical feedback, that is the electrical current created by the ions moving in and out of the cells does not modify the electric signal originated from the sino-atrial node.

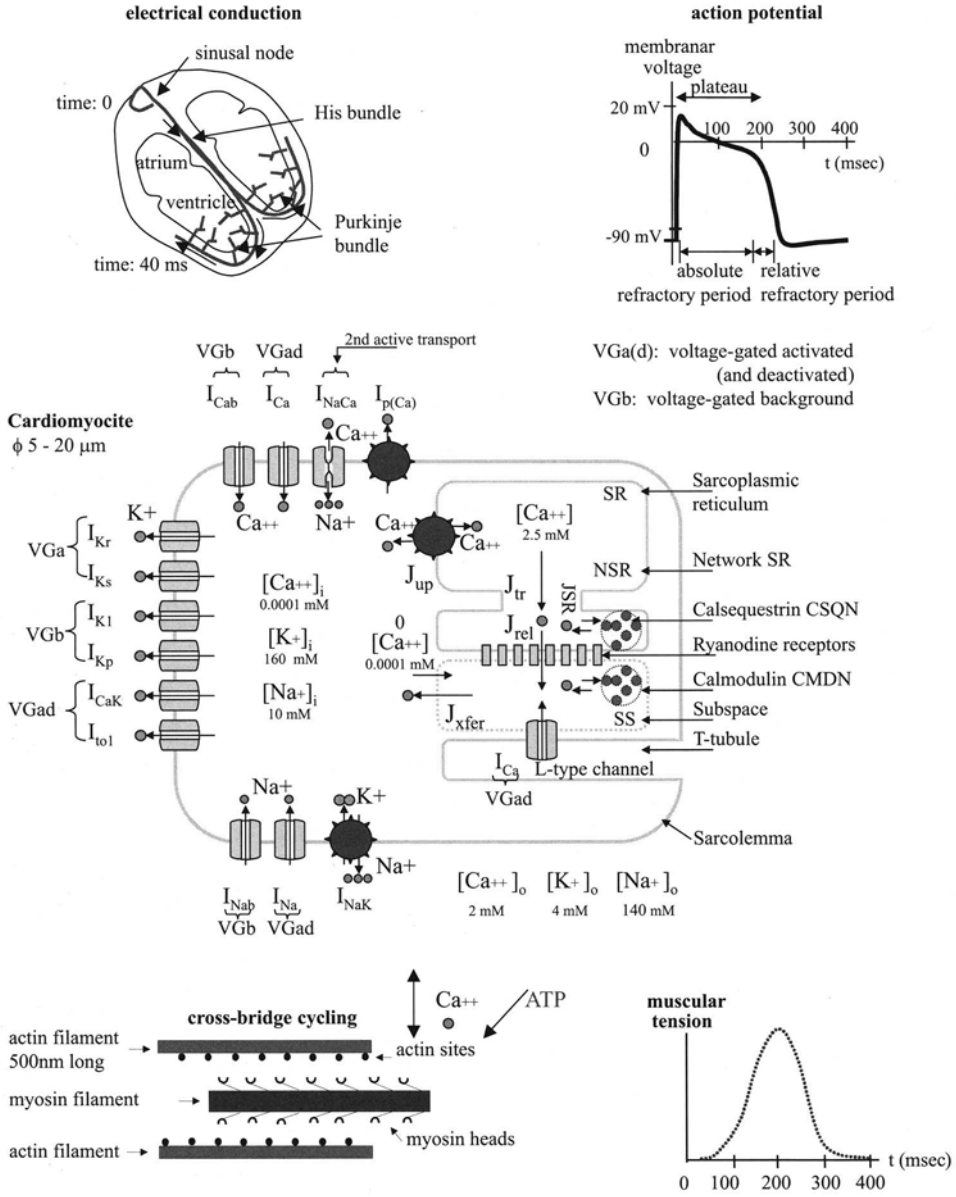

Figure 5 Sketch of the successive steps of a cardiac period. The signal starts from the sinusal node and reaches quickly the endocardium and then the pericardium. It gives rise to a potential difference across the cell membrane, which in turn triggers complex current between the cytoplasm and the extracellular milieu as well as intracellular fluxes. The main effect is a temporary release of calcium which is necessary to ensure cross-bridge cycling and force development. The central sketch illustrates the membranar currents and intracellular fluxes in the cardiomyocyte electrophysiology model of Winslow et al. [1999].

However, due to some physiological observations, e.g. commotio cordis, there has been recently a renewed interest in so-called stretch-activated ionic channels, through which mechanics impacts directly on ionic currents. We will come to implicate another type of mechano-chemical feedback in Section 7.1 in view of mechanical tests on muscle fibers.

5 Electrokinetic Remediation

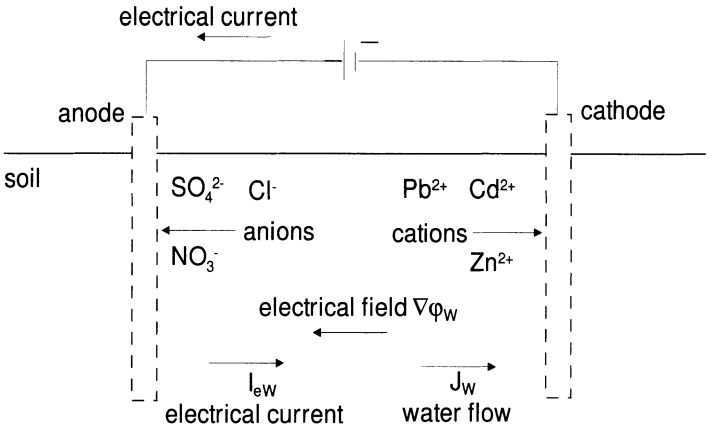

Figure 6 Sketch of electrokinetic remediation. By convention, the electrical current in the circuit flows in the direction opposite to electrons. By *electromigration*, cations move towards the cathode and anions move towards the anode with velocities depending on individual *ionic mobilities*. *Electro-osmosis* implies a water flow towards the cathode, when the acidity is not too high, i.e. electrical charge of clay below isoelectric point. For higher acidity, a reverse osmotic flow occurs.

Electrokinetics has been used in environmental applications in various directions that take advantage, enhance or decrease some properties of clays and clayey soils: to assess and optimize the impermeability of barriers to contaminants, to extract pollutants from contaminated soils, to inject nutrients in order to enhance bioremediation of some wastes, or to inject chemicals that improve the mechanical properties.

Electrokinetic remediation aims at removing heavy metals (lead, cadmium, chromium, copper, strontium, ...) from several types of clays, including kaolinites and montmorillonites, as well as organic pollutants dissolved in contaminated soils (acetic acid, phenol, gasoline, hydrocarbons, ...). For example, Acar et al. [1994] present results that illustrate the efficiency of the method to extract cadmium from saturated kaolinites, while the data reported by Eykholt and Daniel [1994] concern removal of copper also from kaolinites. A review of experimental results up to 1990 is presented by Acar [1992].

The modeling of electrokinetic remediation processes has so far mainly assumed a rigid

solid skeleton. Advection of contaminants by water flow is accounted, but models differ in the way they include ionic mobility of the various species present in the pore fluid, and in the number of electrochemical reactions included. A terminology has emerged that precises the key physical properties triggered. *Electro-osmosis* denotes the process of transport of water induced by a gradient of electrical potential through low permeability soils. In the context of soil remediation, it can used to remove soluble electrically neutral species, Figure 6. It has applications in the improvement of barriers to contaminants: solutes moved by advection to the cathode region can be contained. *Electro-migration* on the other hand addresses the removal of ionic species from fine-grained soils.

Pamukcu and Wittle [1992] compare the removal efficiency of soils in the extraction of Cd^{2+}, Cu^{2+} and other metals. They observe that kaolinites have the highest removal efficiency and montmorillonites the lowest, that is low activity and low ionic strength promote removal.

Experiments consider contaminant concentrations, of e.g. Cu^{2+} and Pb^{2+}, usually lower than 5-10 mg/g of soil and the electrical current density is about 0.3-0.5 A/m^2. Higher concentrations, pollutant up to 10% of dry weight, require current density of up to 10 A/m^2, Alshawabkeh et al. [2002]. Note that higher concentrations enroll more electromigration than electro-osmosis.

In order to improve the efficiency of remediation processes, enhancement techniques are tested, like addition of acid at cathode to desorb cations, addition of EDTA (ethylene-diamine-tetra-acetate) that enhances complexation of desorbed cations, use of semi-permeable membranes close to cathode (to prevent migration of hydroxyl ions towards the anode), and optimization of the position of electrodes. Indeed, there are two keys to successful electrokinetic remediation of metal contaminated soils: first to extract the cations from solid phase, second to keep the desorbed cations in fluid phase so as to move them to electrodes either by electromigration to cathode or by electro-osmosis when complexated. Of course, addition of acid is of theoretical help in both steps, but the quantity required increases prohibitively for soils with high buffer capacity. The *buffer capacity* of a system is defined as the amount of strong acid that causes this system to have a pH change of one unit. In addition, acids are hazardous substances. That is one of the reason of the use of a strong anionic complexing agent by Yeung et al. [1996].

Alternative substances, like polyphosphates, are used to increase the negative charge of clays for specific purposes, e.g. enhance the adsorption of heavy metals.

6 Structural Description and the Electrical Charge

6.1 Basics of Clay Mineralogy

The clay particles are not electrically neutral due to uncompensated lateral termination sites in kaolinites and *isomorphous substitutions*, Figure 8.

Isomorphous substitution, particle charge. Typically, when two ions have non-hydrated sizes that do not differ by more than 15% and valences by more than unity, they can exchange in the clay sheets: this phenomenon, called *isomorphous substitution*, leaves the clay with a fixed negative charge.

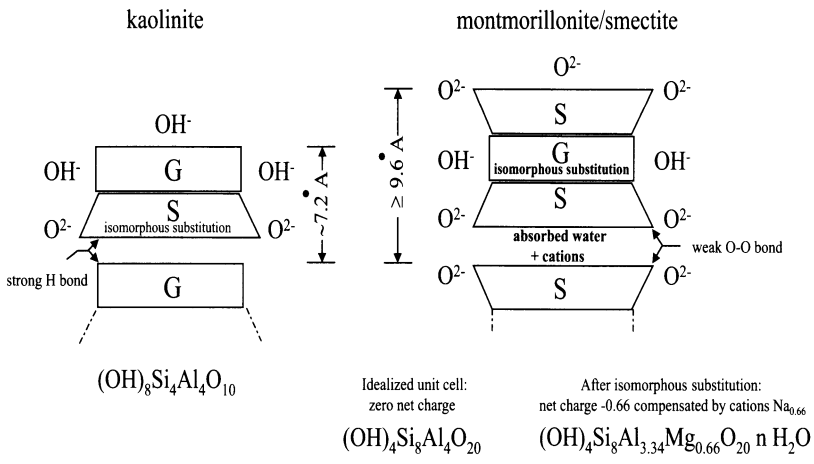

Figure 8 Idealized structures of kaolinites and smectites. The mineral structure consists of tetrahedral:octahedral (1:1) stackings for kaolinites and tetrahedral:octahedral:tetrahedral(2:1) stackings for montmorillonites. In the latter, the bonds between the structural units are weak, so that layers of absorbed waters and cations may enter the interlayer spaces and produce swelling. At neutral pH, the *cation exchange capacity* is about 3-15 meq/100 gm for kaolinites and much larger for smectites, 80-150 meq/100 gm, Figure 10. Tetrahedral sheets consist of Si^{4+} at the center with O^{2-} at the vertices. Octahedral gibbsite and brucite sheets consist of Al^{3+} and of Mg^{2+} respectively, surrounded by OH^{-}.

The net charge of these idealized structures is zero. However, a number of substitutions occur in actual structures, so-called isomorphous substitutions, that overall induce a negative net charge. Starting from the uncharged pyrophyllite $Al_2(OH)_2Si_4O_{10}$, typically for montmorillonites, Mg^{2+} atoms replace one over six Al^{3+} atoms, which implies a negative charge of -0.66 per cell, which is compensated by exchangeable cations which are admitted in the interlayers: as they are hydrated, their absorption/desorption induce significative volume changes. Beidellite is obtained by replacement of silicon atoms Si^{4+} by aluminum atoms starting from pyrophyllite as well. On the other hand, for kaolinites, the substitutions are less important, typically one Al^{3+} replacing one over 400 Si^{4+}. Since there is no interlayer separation in kaolinites, ions that balance the charge can only adsorb to the exterior edges and faces. Because the hydroxyl ions are present on egdes and faces, kaolinites are very sensitive to changes of pH, and they are positively charged at low pH below the isoelectric point, and negatively charged at moderate to high pH above the isoelectric point, Figure 10. Montmorillonites and illites, whose charge is due to isomorphous substitution, are sometimes called *fixed charge clays*. Kaolinites whose surface charge is due to broken bonds along the edges of the sheets are called *variable charge clays*. Illites are 2:1 materials but the interlayers are bonded by K^{+} and they do not swell. In fact, only 5-10% of the negative charge on 2:1 layer silicates is pH dependent whereas 50% or more of the charge developed on kaolinites can be pH dependent.

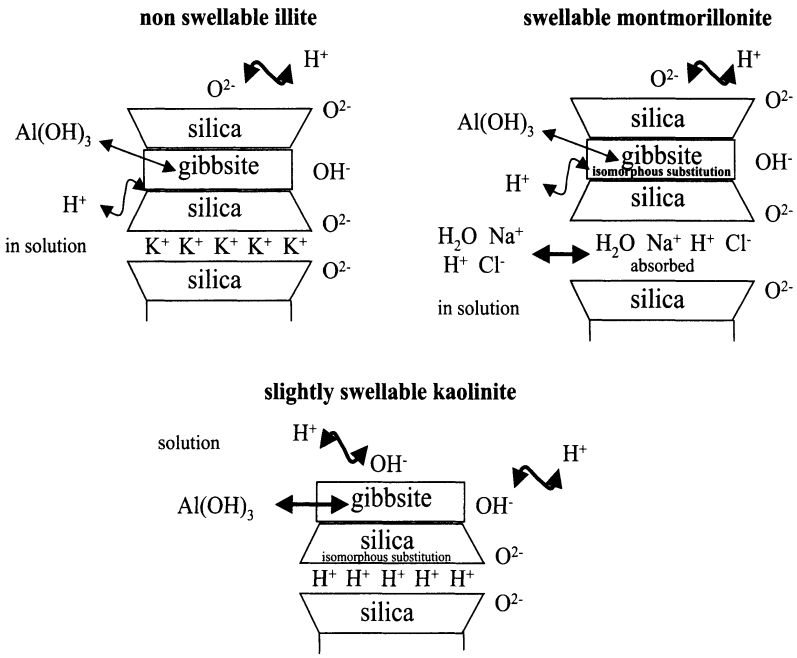

Figure 9 The nature and amount of ions that adsorb on the surface of clay sheets, or absorb in the interlayer space, depend on the clay type. At extreme pH, the clay mineral, and consequently the electrical charge, may be modified for clays sensitive to pH like kaolinites. The thickness of the arrows is proportional to the intensity of the exchange.
Literature indicates that the hydrogen ions can replace other exchangeable cations, even of higher valence. The H^+ ions can also fix to the hydroxyl groups XOH of the mineral, or to the oxygen termination sites, $XOH + H^+ \rightleftharpoons XOH_2^+$, $XO^- + H^+ \rightleftharpoons XOH$.

Montmorillonite silica layers are weakly bonded and they are therefore subject to swelling, a volume increase due to the absorption of hydrated ions in the interlayers, Figure 8. Since at usual pH, the clay surface is negatively charged, the above ions are cations, that absorb (resp. desorb to) from the water phase. Common exchangeable cations are Ca^{2+}, Mg^{2+}, H^+, K^+, NH_4^+, Na^+, and common exchangeable anions SO^{2-}, Cl^-, PO_4^{3-}, NO_4^-. The ability of a clay to exchange cations (resp. anions) is characterized by its *cation exchange capacity* (resp. *anion retention capacity*).

There are several measures of electrical charges in clays, depending on the volume in which charges are counted. In any event, all structural charges within and on the minerals as well as adsorbed H^+ are included. When the volume is limited by the Stern layer (the Stern layer consists of tightly bound cations surrounding the clay surface), the transition pH between a negative and a positive overall charge is termed *point of zero electrical charge*. When the reference volume extends further to the plane of shear between solid and fluid, as in the definition of the ζ-potential, the total, or net, charge changes sign, together with the ζ-potential, at the pH called *isoelectric point*. *The point*

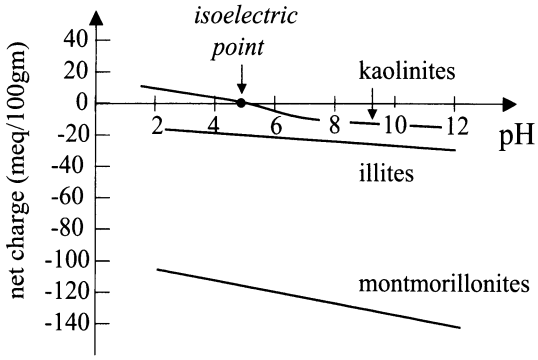

Figure 10 Qualitative evolution of the electric charge of clays as a function of pH, gathering information from literature. The electric charge is measured in different units, e.g. Q_p in meq/100 gm of clay=centimole/kg, or σ_p in Coulomb/m^2. These two quantities are related through the specific surface s in m^2/kg and Faraday's constant F = 96487 Coulomb/mole by $\sigma_p = Q_p\,\mathrm{F}/s$. The valence ζ is equal to $10^{-5}\,Q_p\,m^M$ where m^M is the molar mass of the clay in gm. The specific surface s is about $10{\times}10^3$ to $20{\times}10^3$ m^2/kg for kaolinites, $65{\times}10^3$ to $100{\times}10^3$ m^2/kg for illites, $700{\times}10^3$ to $840{\times}10^3$ m^2/kg for montmorillonites. So for a montmorillonite of molar mass m^M =382 gm, an electric charge Q_p = -100 meq/100 gm=1 mole/kg is equivalent to $\sigma_p = -0.125$ Coulomb/m^2 and to $\zeta = -0.382$.

of zero net proton charge corresponds to the pH where the variable charge vanishes.

Structural change due to pH. In an electrokinetic process, as they move away from the anode, hydrogen ions H^+ in the electrolyte solution extract cations absorbed in the clay clusters: desorbed into the electrolyte, these cations will be attracted to the cathode where they can be disposed of. The basic property in force is that, at pH 7 or higher, the clay particles are negatively charged on their surface. So in a superficial view, cations H^+ are much more likely to absorb to the clay clusters than anions OH^-, which are a priori electrically repulsed. Said otherwise, acid solutions are able to dissolve metallic cations; decreasing the pH=-log $[H]^+$, i.e. acidification of the soil, improves desorption of heavy metals from clays and solubilize them in pore fluid, while precipitation of metallic cations occurs as the pH increases.

At pH 7 or higher, clay minerals have hydroxyl OH^- termination sites on their edges and faces. As pH increases, the dissociation/deprotonation Me-OH $\rightarrow$ Me-O^-+H^+, or Me-OH^-+OH^- $\rightarrow$ Me-O^{2-}+H_2O, that makes the charge more negative, is favored (Me is a metal, e.g. Si). On the other hand, as pH decreases, fixation of H^+/protonation, makes the overall charge of clay particle less negative, and even positive. In fact, fixation of H^+ on these sites, Me-OH^-+H^+ $\rightarrow$ Me-HOH, further weakens internal bonds and leads to the release in the solution (dissolution) of multivalent ions, which become exchangeable, and possibly might further precipitate. Small radius multivalent ions, like Al^{3+}, play a prominent role here in reducing the absorbed water content for several reasons. First, they require less volume and, second, the repulsive electrical forces that would be due to

three monovalent cations vanish. Not surprisingly, Chen et al. [2000] observe that increase of the valence of cations of the pore electrolyte, namely successively NaCl, $CaCl_2$ and $AlCl_3$, leads to higher and higher compaction.

Alternatively, protons might only replace a univalent cation which is released into solution, so called *hydrolysis*, e.g. K-silicate + H^+OH^- $\longrightarrow$ H-silicate + K^+OH^-.

Note that kaolinites are said to be more sensitive to pH than montmorillonites because the former have OH^- termination sites on the octahedral faces and edges while OH^- termination sites exist on the edges only for the latter, see Figures 8, 9. The faces are negatively charged at any pH. The edges contain silica and alumina and their charge is positive at low pH and negative at high pH. Montmorillonites and illites, whose negative charge is due to isomorphous substitutions, are actually sometimes called *fixed charge clays* while kaolinites whose negative charge is due to broken bonds are known as *variable charge clays*. At low pH, the charge of the latter become positive. A direct consequence is that contaminant cations, like Pb^{2+}, are more easily extracted/desorbed from kaolinites than from illites at low pH. Cation exchange for illites is practically independent of pH, in contrast to kaolinites. Therefore, for soil remediation processes, acidification is not an efficient technique for illites.

On the other hand, montmorillonites are very active clays in the sense that change of pore liquid composition implies large volume changes at constant load. Kaolinites are much less affected by pore liquid composition.

Figure 10 shows a qualitative variation of the electric charge of clays with pH. Clearly, the material properties that depend directly on the clay charge, e.g. the ζ-potential, the electro-osmotic coefficient, are thus pH-dependent, strongly for kaolinites but quite moderately for illites and montmorillonites.

Clay clusters, absorption. Fundamental to understanding and modeling of chemically driven swelling of expansive clays are their microstructure and organization of their pore space and water. For smectites, this microstructure is dominated by clusters of parallel arranged platelets of clay mineral separated by 10-20 Å interlamellar pores filled with few one-molecule layers of water, called interlayer water, or internal absorbed water. This water has properties, such as density, or viscosity, slightly different from those of free water. Interlayer water does not flow, even when subjected to high hydraulic gradients, and it deforms together with the solid part of clusters. Clusters are enveloped by external adsorbed water, up to seven molecular diameter in thickness. For Montmorillonites, clusters of width 1 to 10μm may contain from 5 to 15 three-layer units and up to 1000 units in compacted clays. Clusters in kaolinites have width from 0.1 to 4μm, and thickness usually from 0.05 to 0.1μm=60 to 120 two-layer units.

Ordinarily, clusters are separated by pores with the characteristic size of the order of 1 micrometer and more. Water that resides in such pores is called free water. Indeed, this water can be displaced by ordinary hydraulic gradients.

Swelling of compacted clays develops in two distinct regimes. During swelling at the lowest water contents, called *crystalline swelling*, interlamellar space *ad*sorbs water, until it is filled with three or four molecular water layers. After the interlamellar space has been saturated with this amount of water, water starts to *ad*sorb to the external surfaces of clay particles, producing *osmotic swelling*. However, the model presented hereafter

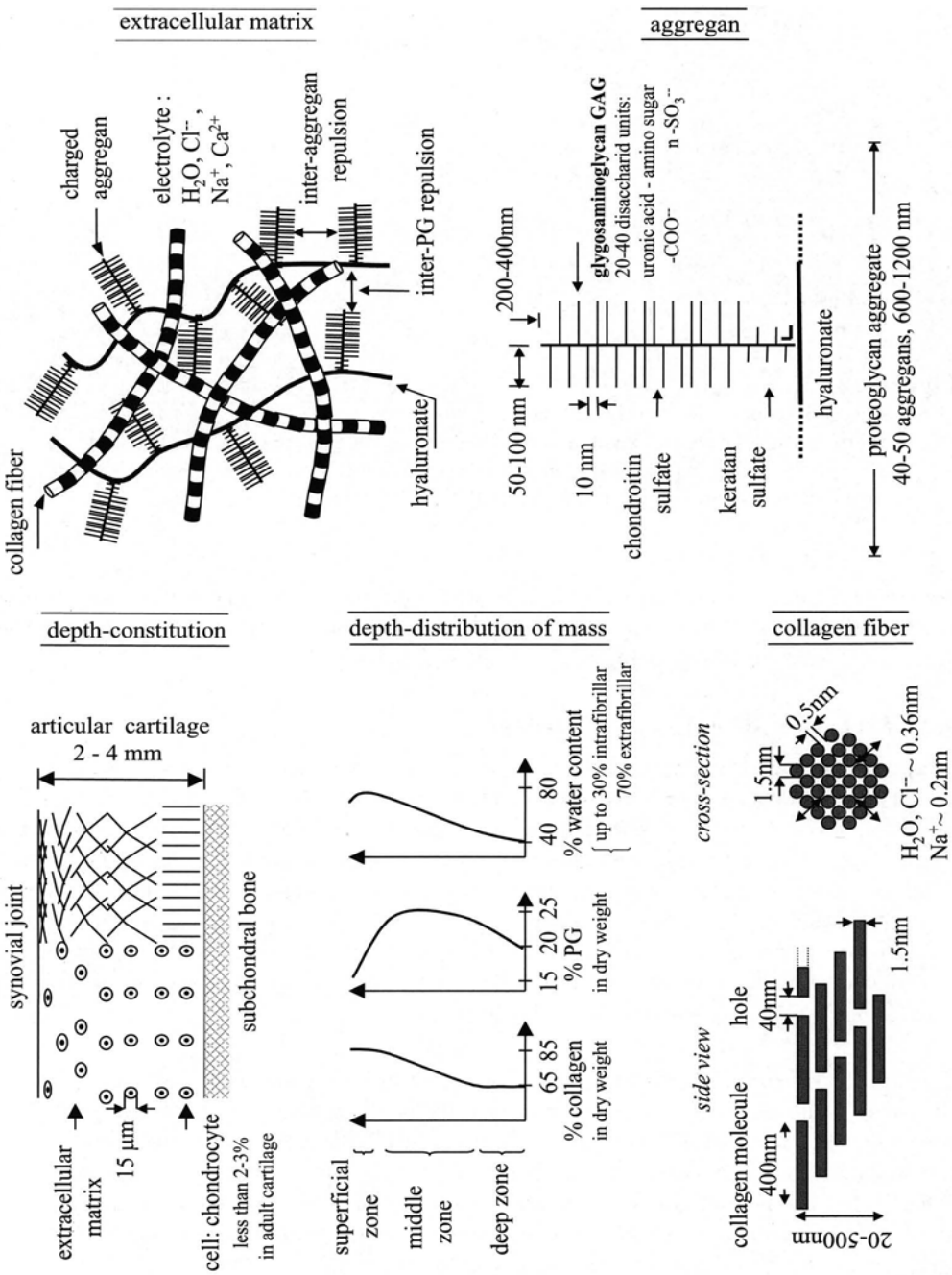

Figure 11 The main components of articular cartilages are:
- the collagen fibers that resist external tensile loads and chemical pressure;
- an electrolyte with water as solvent and dissolved dissociated salts NaCl and $CaCl_2$;
- the negatively charged proteoglycans (PG's).

The mass-distribution in depth is taken from Mow and Guo [2002].

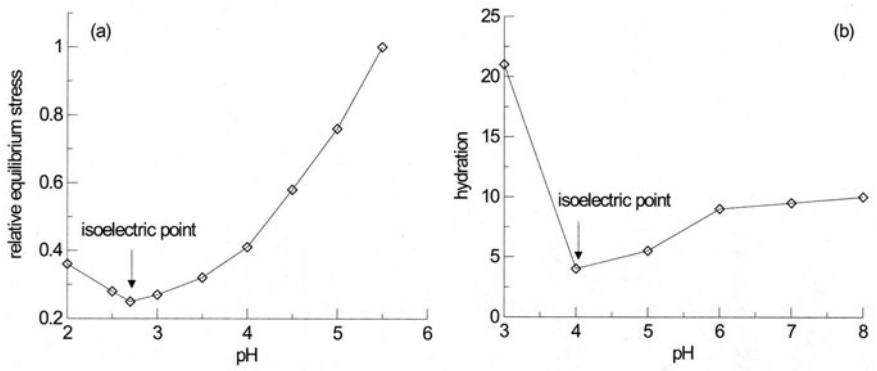

Figure 12 pH affects the electric charge, and therefore the electrostatic repulsion. At the isoelectric point, the electric charge is presumably zero. (a): axial stress in a uniaxial traction test relative to its value in distilled water, data on bovine articular cartilage from Grodzinsky et al. [1981]; (b): relative hydration (≡wet weight/dry weight - 1), data on bovine cornea from Huang and Meek [1999].

does not pretend to address such details, and we shall gather crystalline and osmotic swelling under the term *chemical swelling* and make no distinction between *adsorbed* and *absorbed* water, both being parts of the solid phase.

6.2 Structure of Articular Cartilage

The negatively charged proteoglycans. The proteoglycans are responsible for the swelling behaviour as they repulse themselves and originate a 'chemical' pressure. The repulsion force is however shielded by the presence of ions: in the hypertonic state (high ionic concentration), the repulsive force is minimum and the structure tends to collapse. The proteoglycans are macromolecules of molar mass 2×10^6 gm, with *effective* concentration (=concentration×valence), of 0.1 to 0.2 M. Their mass consists for 85% in glycosaminoglycans (GAG's) and for 15% in proteins, Figure 11. GAG's contain 80% of chondroitin sulfates of charge -2 and 20% of keratan sulfate of charge -1, so that the valence of PG's varies from -6000 to -8000.

The effect of pH in articular cartilage and corneal stroma. As pH decreases, the ions H^+ fix onto the proteoglycans and decrease its electric charge. At given ionic concentration, the electrical repulsion between PG's decreases and therefore so does the macroscopic chemical pressure, Figure 12-(a). Note that however the picture is complicated by the fact that, at low, and high pH, the collagen becomes charged, while, at physiological pH, it contains nearly equal numbers of amino and carboxyl groups, NH_3^+ and COO^-, and hence it has almost no net charge.

The corneal stroma presents many structural similarities with the articular cartilage. The collagen fibers form lamellae whose orientation aims at maximizing the transparency of the cornea. The stroma has an innate tendency to swell without limit, because the

crosslinks between collagen fibers are not strong enough to oppose the chemical pressure, unlike in cartilage. However, a too large hydration tends to generate inhomogeneous repartition of the absorbed water and to form 'lakes', that decrease the transparency. The later is ensured by endothelial pumps that drive bicarbonate ions HCO_3^+ out of the cornea, thus maintaining ionic strength and hydration to acceptable levels. The phenomena are pH dependent, Figure 12-(b).

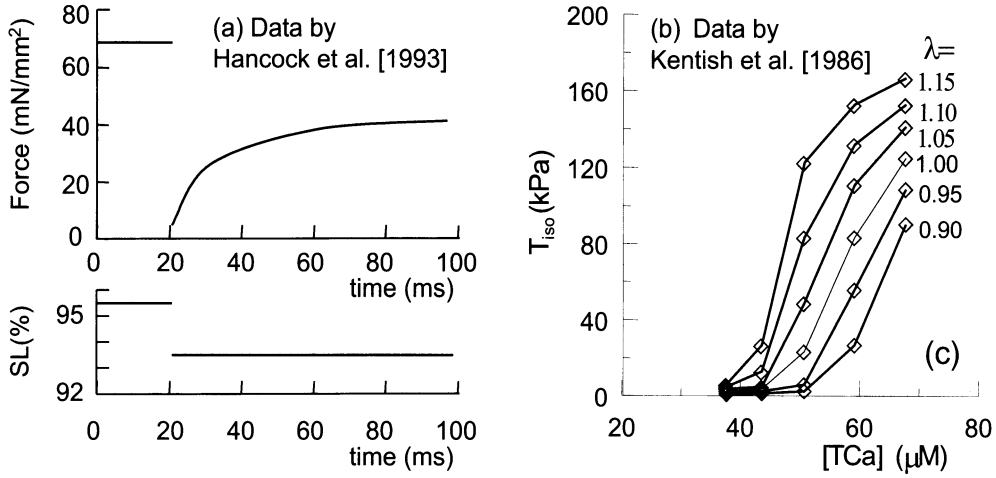

Figure 7 (a) Upon rapid muscle shortening, the tension is suddendly reduced but it does not recover its value after transients are wiped off, even if the elastic correction is applied. (b) The increase of the isometric tension with the concentration of calcium binded to Troponin C is 'length-modulated'.

7 Reverse Couplings

The above examples address essentially the effects of the chemical composition on the mechanical properties. Conversely, the mechanical environment may influence the evolution of the chemical composition in time. As an example, consider the influence of confinement on the breaktrough time of a diffusion process. Here are others examples.

7.1 Mechano-Electric Feedback in the Heart Muscle

Commotio cordis and stretch-gated ionic channels. Stretch-activated ionic channels located on the membrane of cardiac cells (SAC's) are still subject to debate because they have not been cloned in adult mammalian myocytes but observed in cultured cells and in young cells. Interest in these channels has been renewed due to their link to *commotio cordis* which is observed in young adults, because they may originate arrythmias and fibrillation. The Oxford group has contributed to suggest models and stress the physiological importance of the phenomemon. Commotio cordis is characterized by a projectile impacting the chest and leading to sudden cardiac death, but without creating

material damage. In fact, the dangerosity of such impacts depends much on the precise time during the heart beat at which they occur: they are much more dangerous if applied during diastole.

Quite generally, SAC's are thought/aimed to contribute to depolarize cell membrane, essentially during diastole, alter/prolongate action potential, raise the rest potential, increase the active force, and induce premature ventricular excitations and arrhythmias.

In practice, SAC's just create another additional current I to be added to the list of membranar currents. They are controlled by some representative of the stretch of the muscle fibers. Stretch λ, or increase of sarcomere length SL, is believed to increase the electric conductance. Several models, ion-*in*sensitive or ion-sensitive, have been proposed. A general expression has the form $I = g(\lambda)\,(V - E_r)$ where E_r is the reverse potential. For $V < E_r$, this model indicates an inward/depolarizing current, while the opposite applies for $V > E_r$. That is, the maximum potential is lowered while the rest potential is increased, and the descending branch of the voltage is modified/raised if the reverse potential is sufficiently high.

Stretch-activated channels participate to the mechano-electric feedback. However, there has been doubt that stretch itself, or only, is responsible for phenomena that can be traced to belong to this kind of effect. Indeed, strain-rate, or tension, are other candidates to enter the game.

Rate-dependent cell electrophysiology. Upon rapid shortening, the isometric tension $\mathrm{T_{iso}}$ of muscle fibers decreases, and, after the transient effects have been wiped off, it returns to a lower value, Figure 7-(a). This *force deficit* phenomenon, is attributed to an increased (rate of) Ca-detachment from Troponin C. Note that this force deficit is too large to be due only to an elastic parallel contribution. That elastic component is on the other hand sufficient to define the force at its steady state for instantaneous (re-)stretching. This means that a *force recovery* phenomenon does not exist during (re-)stretching.

One way to describe the force deficit phenomenon is to make the cell-electrophysiology model dependent on the rate of stretch, or on the tension transients represented by the ratio $\mathrm{T/T_{iso}}$ of the tension over its isometric value. Hunter et al. [1998] modify the kinetics of the $\mathrm{Ca^{2+}}$ binded to Troponin C,

$$\frac{d[\mathrm{TCa}]}{dt} = k_{+1}\,\mathrm{Ca}_i^{2+}\Big([\mathrm{TCa}]_{\max} - [\mathrm{TCa}]\Big) - k_{-1}\,[\mathrm{TCa}], \tag{7.1}$$

with Ca_i^{2+} the cytoplasmic calcium concentration, k_{+1} and k_{-1} the rates of attachment and detachment of calcium on Troponin C. They make the rate of detachment $k_{-1} = k_{-1}^0\,(1 - T/\mathrm{T_{iso}}/\gamma_T)$, with $\gamma_T > 0$, to increase as the tension T decreases, so that a lower concentration [TCa] induces a lower isometric tension, Figure 7-(b).

7.2 Mechanobiology and Engineered Cartilages

Immature articular cartilage contains vessels that circulate nutrients. On the other hand, adult articular cartilage is aneural, avascular and alymphatic. Nutrients from the synovial joint are transported by the extracellular fluid through diffusion and convec-

tion. Therefore the self-healing capacities of adult articular cartilage are practically nil. One method to treat damaged cartilage consists in removing the damaged part and in implanting biodegradable cell-polymer constructs. Engineered cartilages are cultured on scaffolds of agarose or alginate gels. Agarose and alginate gels are chosen because, polymerized, they display an open three-dimensional lattice structure that is prone to fix cells. Once in place, artificial cartilage proliferates reasonably well, but the issue is that its mechanical properties are lower than those of native cartilage. Recent studies have shown that the mechanical conditions to which chondrocytes are subject in vivo and in vitro affect the synthesis and degradation of the extracellular matrix (ECM), see Figure 11. In fact, the chondrocytes are much more compliant than the ECM, about 1000 times according to Guilak et al. [1999], so that the ECM deformation carries over to chondrocytes.

Although experiments tend to quantify the variations in the rates of stimulation and inhibition of cartilage synthesis, the numbers should be taken with care. Indeed, the depth-distribution of strain in a cartilage layer submitted to compression at its top surface is highly inhomogeneous. Strains are much larger near the surface, and thus the percentage of tissue undergoing mechanical stimuli strongly depends on the layer thickness. These heterogeneities on the other hand may imply that there are optimal geometries for the loaded cultures. The biological environment should also be controlled, e.g. hypoxic conditions are also known to stimulate regeneration of cartilage.

Special bioreactors have been developed to apply unconfined compression on cartilage cultures. The following points have been highlighted, Buschmann et al. [1992][1995], Mauck et al. [2000]:

- static (prolongated) compression has a detrimental influence on the synthesis of the ECM;
- dynamic (time variable) compression on the other hand contributes to matrix synthesis. The actual efficiency of dynamic compression depends on the frequency and on the details of the loading programme (amplitude, mean value, ...).

Unconfined compression, which is accompanied by lateral tension, is assumed to corresponds better to the in vivo state of stress. On the other hand, the loading programmes are highly arbitrary, and, in particular, the pros and cons of strain- over stress-controlled loadings are not elucidated. Therefore there are plenty degrees of freedom for optimization.

Mauck et al. [2000] loaded dynamically disks about 1 mm thick with a strain amplitude of 10%, at a frequency of 1 Hz, 3 times 1 hour on, 1 hour off, 5 days a week during 4 weeks. At the end of this period, the modulus is increased sixfold over unloaded disks. They also observed an increase in glycosaminoglycans (GAG) and hydroxyproline (measurements use [^{35}S]sulfate and [^{3}H]proline radiolabel incorporation). However, the GAG content showed a peak at week 3, and further studies showed that it is later substantially reduced. On the other hand, Buschmann et al. [1992] observed, on agarose-seeded calf chondrocytes, an increase of GAG until day 70. Another conclusion of the studies of Mauck et al. [2000] is that agarose gels are more prone than alginate gels to improve the mechanical properties and matrix proliferation.

Interestingly enough, static compression seems to simply delay, not prevent, the stimulating effects of insulin-like growth factor 1 (IGF-1), suggesting that the modes of action

of these two factors are independent, Grodzinsky et al. [2000]. Transforming growth factor β (TGF-β) triggers also growth and differentiation, but is less efficient than IGF-1, Laurencin et al. [1999].

One possible way in which mechanics stimulates biological synthesis is by generation of *advective flow* that particularly enhances the transport of large soluble molecules (e.g. growth factors) that are thus more accessible to the chondrocytes and their immediate neighborhood, Garcia et al. [1996].

A second mode in which mechanics acts is by *altering the metabolism*. Deforming the chondrocytes and their organelles modifies intracellular signaling and communication between cells. On one hand, dynamic unconfined compression affects the *gene transcription* phase, by increasing the expression of aggrecan and type II collagen mRNA, Ragan et al. [1999]. On the other hand, deformation of organelles may alter, slow down, the post-transcription *metabolic pathways* that involve different organelles that deliver type II collagen and the various pieces of the proteoglycans, Hascall et al. [1991]. Elements that may decrease the density of electrical charges of the glycosaminoglycans are of particular relevance: indeed, the *effective* concentration of proteoglycans is a key parameter in their mechanical interactions.

The effects of shear-stress have also been tested. Lee et al. [2002] observe that fluid-induced shear-stress (1.64 Pa) application on human chondrocytes during periods of 2 to 24 hours increases more than twofold production of nitric oxide (NO), an intra- and extracellular messenger present at increased levels in osteoarthritis, and inhibits aggrecan and type II collagen mRNA levels, by about a third.

These observations confirm the alternative point of view, that cartilage degeneration and ossification are stimulated by shear stress but inhibited by dynamic compression, Carter and Wong [1990].

Bibliography

Acar Y.B. (1992). Electrokinetic soil processing. A review of the state of the art. In *Grouting, Soil Improvement and Geosynthetics*, edited by R.H. Borden, R.D. Holtz and I. Juran. American Society of Civil Engineeers, New York, Geotechnical Special Publication No 30, 2, 1420-1432.

Acar Y.B., Hamed J., Alshawabkeh A.N. and R.J. Gale (1994). Removal of cadmium (II) from saturated kaolinite by application of electric current. *Géotechnique*, 44, 239-254.

Alshawabkeh A.N., Oszu-Acar E., Gale R.J. and S.K. Puppala (2002). Remediation of soils contaminated with tetraethyl lead by electrical fields. preprint.

Buschmann M.D., Gluzband Y.A., Grodzinsky A.J., Kimura J.H. and E.B. Hunziker (1992). Chondrocytes in agarose culture synthesize a mechanically functional extracellular matrix. *J. of Orthopaedic Research*, 10, 745-758.

Buschmann M.D., Gluzband Y.A., Grodzinsky A.J., Kimura J.H. and E.B. Hunziker (1995). Mechanical compression modulates matrix biosynthesis in chondrocyte/agarose culture. *J. Cell Science*, 108, 1497-1508.

Carter D.R. and M. Wong (1990). Mechanical stresses in joint morphogenesis and maintenance. In *Biomechanics of Diarthrodial Joints*, Mow V.C., Ratcliffe A. and S.L.-Y. Woo eds., New York, Springer, 155-174.

Chen J., Anandarajah A. and H. Inyang (2000). Pore fluid properties and compressibility of kaolinite. *J. of Geotechnical Engng. Div.*, Transactions of the ASCE, 126(9), 798-807.

Di Maio C. (1998). Discussion on 'Exposure of bentonite to salt solution: osmotic and mechanical effects'. *Géotechnique*, 48(3), 433-436.

Di Maio C. and G. Fenelli (1997). Influenza delle interazioni chimico-fisiche sulla deformabilità di alcuni terreni argillosi. *Rivista Italiana di Geotecnica*, 1, 695-707.

Eisenberg S.R. and A.J. Grodzinsky (1985). Swelling of articular cartilage and other connective tissues: electromechanical forces. *J. of Orthopaedic Research*, 3, 148-159.

Eykholt G.R. and D.E. Daniel (1994). Impact of system chemistry on electro-osmosis in contaminated soil. *J. of Geotechnical Engng. Div.*, Transactions of the ASCE, 120, 797-815.

Flory P.J. (1953). *Principles of Polymer Chemistry*. Cornell University Press, Ithaca, New York.

Garcia A.M., Frank E.H., Grimshaw P.E. and A.J. Grodzinsky (1996) Contribution of fluid convection and electrical migration to transport in cartilage: relevance to loading. *Archives Biochemistry Biophysics*, 333, 317-325.

Grodzinsky A.J., Levenston M.E., Jin M. and E.H. Frank (2000) Cartilage Tissue Remodeling in Response to Mechanical Forces, *Annual Review of Biomedical Engng.*, 2, 691-713.

Grodzinsky A., Roth V., Myers E., Grossman W. and V.C. Mow (1981) The significance of electromechanical and osmotic forces in the nonequilibrium swelling behavior of articular cartilage in tension. *J. of Biomech. Engng.*, Transactions of the ASME, 103, 221-231.

Guilak F., Jones W.R., Ting-Beall H.P. and G.M. Lee (1999) The deformation behavior and mechanical properties of chondrocytes in articular cartilage. *Osteoarthritis Cartilage*, 7, 59-70.

Hancock W.O., Martyn D.A. and L.L. Huntsman (1993). Ca^{2+} and segment length dependence of isometric force kinetics in intact ferret cardiac muscle. *Circulation Research*, 73(4), 603-610.

Hascall V.C., Heinegard D.K. and T.N. Wight (1991). Proteoglycans: metabolism and pathology. In *Cell Biology of ExtraCellular Matrix*, Hay E.D. ed., Plenum Press, New York, 149-175.

Huang Y. and K.M. Meek (1999) Swelling studies on the cornea and sclera: The effects of pH and ionic strength., *Biophysical J.*, 77, 1655-1665.

Hunter P.J., McCulloch A.D. and H.E.D.J. ter Keurs (1998). Modelling the mechanical properties of cardiac muscle. *Progress Biophysics Molecular Biology*, 69, 289-331.

Kentish J.C., ter Keurs H.E.D.J., Ricciardi L., Bucx J.J.J. and M.I.M. Noble (1986). Comparison between the sarcomere length-force relations of intact and skinned trabeculae from rat right ventricle. *Circulation Research*, 58-6, 755-768.

Laurencin C.T., Ambrosio A.M.A., Borden M.D. and J.A. Cooper Jr. (1999). Tissue Engineering: Orthopaedic Applications. *Annual Review of Biomedical Engng.*, 1, 19-46.

Lee M.S., Trindade C.D., Ikenoue T., Schurman D.J., Goodman S.B. and R. Lane Smith (2002). Effects of shera stress on nitric oxide and matrix protein gene expression in human osteoathritic chondrocytes in vitro. *J. of Orthopaedic Research*, 20, 556-561.

Mauck R.L., Soltz M.A., Wang C.C.B., Wong D.D., Chao P.H., Valhmu W.B., Hung C.T. and G.A. Ateshian (2000). Functional tissue engineering of articular cartilage through dynamic loading of chondrocyte-seeded agarose gels. *J. of Biomech. Engng.*, Transactions of the ASME, 122, 252-260.

Mow V.C. and X.E. Guo (2002). Mechano-electrochemical properties of articular cartilage: their inhomogeneities and anisotropies. *Annual Review of Biomedical Engng.*, 4, 175-209.

Owens J.M., Lai W.M. and V.C. Mow (1991). Biomechanical effects due to Na^{+}-Ca^{2+} exchange in articular cartilage. *Transactions of the Orthopaedic Research Society*, 37th Annual Meeting, March 4-7, Anaheim, California, p. 360.

Pamukcu S. and J.K. Wittle (1992). Electrokinetic removal of selected heavy metals from soil. *Environmental Progress*, 11(3), 241-250, American Institute of Chemical Engineers

Ragan P.M., Badger A.M., Cook M., Chin V.I, Gowen M., Grodzinsky A.J. and M.W. Lark (1999). Down-regulation of chondrocyte aggregan and type II collagne gene expression correlates with increases in static compression magnitude and duration. *J. of Orthopaedic Research*, 17, 836-842.

Simões F.M. and B. Loret (2003). Mechanical effects of ionic replacements in articular cartilage. submitted for publication.

Winslow R.L., Rice J.J., Jafri S., Marban E. and B. O'Rourke (1999). Mechanisms of altered excitation-contraction coupling in canine tachycardia-induced heart failure. II Model studies. *Circulation Resarch*, 84, 571-586.

Yeung A.T., Hsu C. and R.M. Menon (1996). EDTA-enhanced electro-kinetic extraction of lead. *J. of Geotechnical Engng. Div.*, Transactions of the ASCE, 122(8), 666-673.

Multi-Phase Multi-Species Mixtures

Benjamin Loret * and Alessandro Gajo †

* Laboratoire Sols, Solides, Structures, Institut National Polytechnique de Grenoble, France
† Dipartimento di Ingegneria Meccanica e Strutturale, Università di Trento, Trento, Italia

Abstract The notion of phases in a mixture theory is presented. Three examples are provided to illustrate the versatility of the framework to different physical contexts. Next, emphasis is laid on chemically active saturated clays in a two-phase framework. The phases and the species they contain are endowed with geometrical, mass, stress and strain properties. The solid phase contains clay particles, absorbed water and dissolved ions, Na^+, K^+ and Cl^-. The fluid phase, or pore water, contains free water and the same ionic species. Water and ions can transfer between the two phases. In addition, they diffuse through the porous medium. A global understanding of all phenomena, mass transfer, diffusion/advection and deformation is provided.

1 Definition of Phases

For a porous medium where a single fluid diffuses through the solid skeleton, the definition of phases is unambiguous: the solid phase contains a single species, namely the solid particles, and the fluid phase contains also a single species, the fluid, e.g. water.

If the fluid contains dissolved species, these species will be considered a priori to be part of the fluid phase.

Species (or constituents) have their own intrinsic physical, mechanical, thermal, electrical properties. However, these properties must be reconsidered when the species are viewed as part of the mixture. Indeed the references with respect to which these properties are defined have to be specified. For example, the *intrinsic* density is defined as the ratio of the mass over the volume occupied by that mass. But, when dealing with all species simultaneously, it is instrumental to refer to the volume occupied by the whole mixture, and one then obtains an *apparent* density. In the same vein, it is important to refrain to endow the porous medium with properties averaged over the species it contains. For example, even if all species are incompressible, the porous medium may change volume if matter can be exchanged with the exterior. More generally, a distinction should be made between *averaged* quantities and *macroscopic* quantities. Only the latter enter the constitutive behaviour of the homogenized porous medium, a possible confusion coming from the fact that for certain quantities averaged quantities are indeed also macroscopic quantities.

For swellable materials, the definition of phases is not unambiguous. Segregating species into phases allows to highlight certain physical aspects, see e.g. Figure 1. As

it will appear later, species *diffuse* within their phase, essentially according to Fick's law, although couplings may give rise to additional diffusive forces. On the other hand, species *transfer* from one phase to the other according to transfer laws, which are similar to physico-chemical reactions.

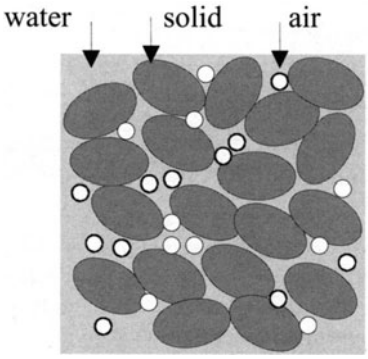

representative elementary volume:
at any point,
I find either solid
or water
or air

a) spatially heterogeneous material

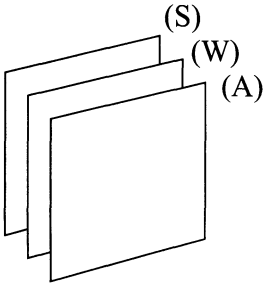

local representation:
the three phases overlap, and
they appear in proportion
of their volume fractions

solid phase	water phase	air phase	← phases
solid particles	water	dry air	← species or
		vapour saturated air	constituents

b) locally homogeneous three-phase mixture

Figure 1 Idealization by the mixture theory of a heterogeneous material containing solid particles, water, dry air and vapour saturated air into three phases. The real material is spatially heterogeneous, i.e. at a given point, a single species is present. The mixture theory smooths this spatially discontinuous representation. At any point in space, any species k appears in proportion to its volume fraction. Within a phase, species *diffuse*. Across phases, species *transfer*.

The examples below taken from our own works illustrate these general considerations. Attention is drawn to two points:

- the notion of a fictitious membrane surrounding the phases. A membrane is species-

selective, its physical raisons d'être are plenty. For example, it might be used to mimic electrical repulsion, or as a sieve against molecules whose size is larger than admissible;

- the motivations that dictate the choice of the phase to which the fixed charges are attached.

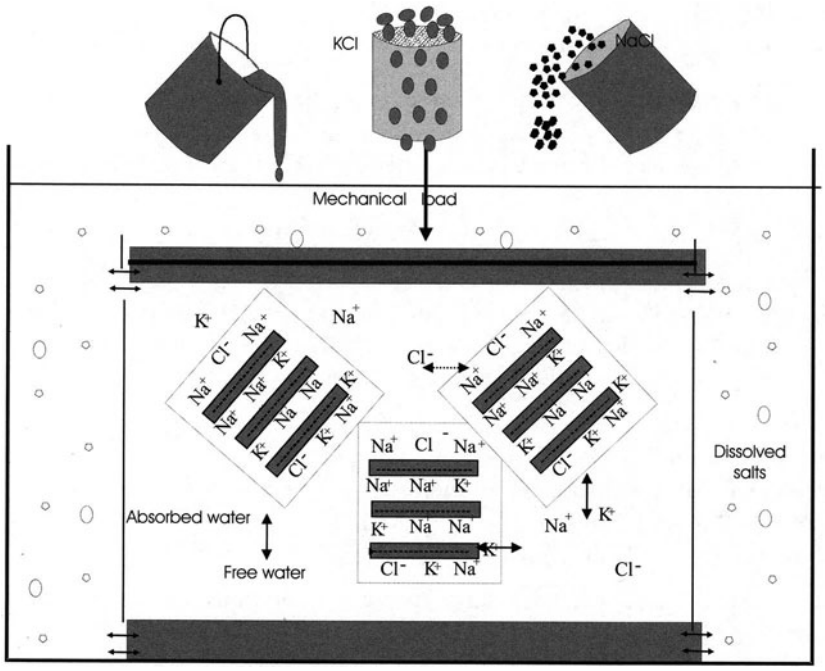

Figure 2 Schematic of a chemo-mechanical experiment on a heteroionic clay. The pore water is in contact with a large reservoir whose chemical composition is controlled. In the sample submitted to a variable mechanical load in terms of stress or strain, the solid phase (clay clusters structured by negatively charged particles with attached absorbed water and ions) is in contact with the fluid phase (pore water with dissolved salts). Water and ions absorbed in the solid phase are exchanged/transferred with their counterparts in pore water depending on their respective contents and on mechanical conditions. The membrane around the solid phase prevents the sole clay particles from being exchanged. Only species of the fluid phase exchange with the exterior.

1.1 Phases in Heteroionic Clays

Heteroionic clays are considered as a two-phase porous medium, Gajo et al. [2002], Gajo and Loret [2003]b, Loret et al. [2003]. Each phase is composed of several species, Figure 2:

- the *solid phase* S contains five species

$$\left\{\begin{array}{lll} \text{clay particles} & \text{denoted by the symbol} & c \\ \text{absorbed and adsorbed water} & & w \\ \text{ions sodium, potassium, chloride} & & \mathrm{Na}^+,\ \mathrm{K}^+,\ \mathrm{Cl}^- \end{array}\right. \tag{1.1}$$

- the *fluid phase* W contains four species

$$\left\{\begin{array}{lll} \text{pore water} & \text{denoted by the symbol} & w \\ \text{ions sodium, potassium, chloride} & & \mathrm{Na}^+,\ \mathrm{K}^+,\ \mathrm{Cl}^- \end{array}\right. \tag{1.2}$$

The clay clusters are surrounded by a fictitious membrane which is a priori impermeable to clay particles only: clay suspensions are out of the realm of this study. Thus the mass of clay in the solid phase, obtained by aggregation of clay clusters, is constant,

$$m_{cS} = \text{constant}\,. \tag{1.3}$$

However, the membrane can serve, directly or indirectly, e.g. via electroneutrality, as a filter or barrier to specific ions. A species in a phase is referred by two indices, the index of the species and the index of the phase in that order, as in (1.3). We shall introduce several sets of species with specific properties, namely:

- species in the solid phase $S = \{w, \mathrm{Na}^+, \mathrm{K}^+, \mathrm{Cl}^-, c\}$;
- species in the fluid phase $W = \{w, \mathrm{Na}^+, \mathrm{K}^+, \mathrm{Cl}^-\}$;
- species that can cross the membrane, $S^{\leftrightarrow} = W^{\leftrightarrow} = W = \{w, \mathrm{Na}^+, \mathrm{K}^+, \mathrm{Cl}^-\}$;
- cations in the solid phase $S^+ = \{\mathrm{Na}^+, \mathrm{K}^+\}$;
- ionic species in the fluid phase, $W^{\pm} = \{\mathrm{Na}^+, \mathrm{K}^+, \mathrm{Cl}^-\}$;

The main assumptions which underly the two-phase multi-species model follow the *strongly interacting* model of Bataille and Kestin [1977], namely,

(H1) Mass balance is required for each species. Mass balance for each phase is obtained via mass balances of the species it contains.

(H2) Momentum balance is required for the mixture as whole. Species in the fluid phase are endowed with their own velocities so as to allow them to diffuse in their phase, with electrical effects, and satisfy their own balance of momentum.

(H3) The velocity of any species in the solid phase is that of the latter, $\mathbf{v}_{kS} = \mathbf{v}_S$, $\forall k \in S$, and therefore their balance of momentum is not required explicitly, but accounted for by the balance of momentum of the mixture. Water and ions of the solid phase *transfer* to and from the fluid phase.

(H4) In the fluid phase, pressure is assumed to be uniform across all species, $p_{kW} = p_W$, $\forall k \in W$. In contrast, absorbed species in the solid phase are endowed, through specific constitutive equations, with their own intrinsic pressure.

(H5) Electroneutrality is required in each phase separately. In the solid phase, negatively charged clay particles require the presence of the cations.

In the solid phase, the pressures attributed to the phase and to the species in that phase are not set equal a priori. At variance with other analyses, we make a distinction between

absorbed cations which are kinematically tied to the clay particles (H3) and cations in the fluid phases which are endowed with their own velocities (H4).

Assumptions (H1)-(H2) are compatible with the usual finite element alternatives which consist in

- either imposing the balance of momentum of the whole mixture and the balance of mass of the fluid phase (or some equivalent scalar condition), the solid displacement and fluid pressure being part of the primary unknowns;
- or imposing the balances of momentum of both solid and fluid phases, the fluid displacement replacing the fluid pressure as a primary unknown.

Of course the presence of ionic species and electrical effects increase the list of primary variables and associated field equations.

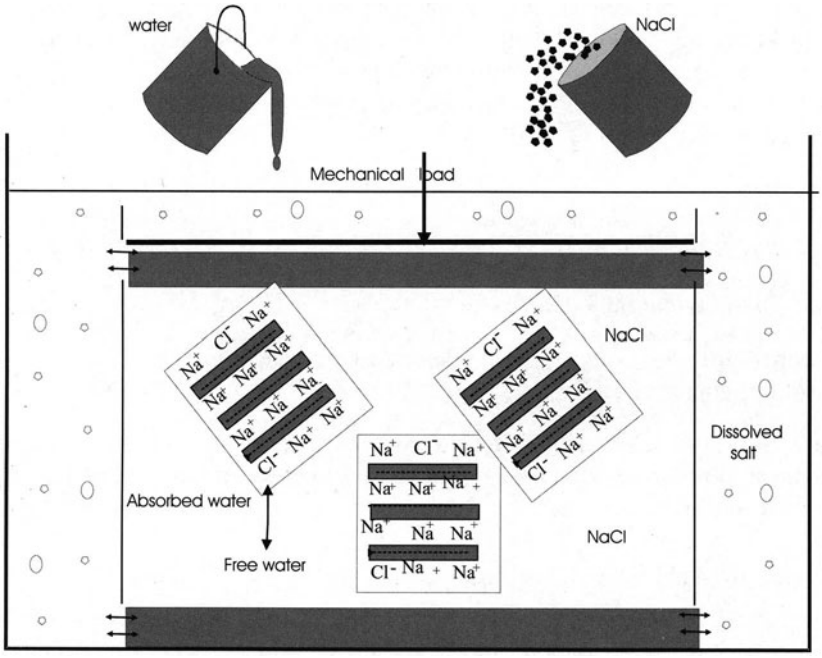

Figure 3 Same as Figure 2 but for a *homoionic* Na-clay in contact with a reservoir loaded with NaCl. Since anions are unlikely to be attracted by the negatively charged clay platelets, electroneutrality practically prevents cations Na^+ to be exchanged between the solid and fluid phases. Therefore the sole species to be exchanged between the phases is water. Only species of the fluid phase exchange with the exterior.

1.2 Phases in Homoionic Clays and Clays with Organic Pollutants

Homoionic clays are assumed to contain a single type of cations, say cations sodium Na^+, both in the electrolyte and around the clay platelets, Figure 3. Like for heteroionic

clays, their chemo-mechanical behaviour has been considered in a two-phase framework in Loret et al. [2002], Gajo and Loret [2003]a.

The clay clusters are surrounded by a fictitious membrane which is a priori impermeable to clay particles and to ionic species. Only water can exchange between the two phases. Indeed, a cation Na^+ can exchange between the two phases only if it is accompanied by an anion Cl^- if electroneutrality is to be satisfied in both solid and fluid phases. But the negatively charged clay particles tend to repulse anions. Therefore, exchange of Na^+ is considered to be prevented.

Moreover, the model developed in Loret et al. [2002], Gajo and Loret [2003]a introduces another simplification so as to disregard electrical effects: the salt dissolved in the fluid phase is considered *undissociated*, that is the ions Na^+ and Cl^- do not appear any longer, and the single solute is the salt s=NaCl. At variance with this approach, sodium chloride has been considered to be completely dissociated in the analysis of articular cartilage of Loret and Simões [2003]. This assumption of complete dissociation has also been adopted in the analysis of heteroionic clays.

Thus, the phases for homoionic clays are defined as follows:
- the *solid phase* S contains four species

$$\begin{cases} \text{clay particles} & \text{denoted by the symbol} \quad c \\ \text{absorbed and adsorbed water} & \quad w \\ \text{ions sodium, chloride} & \quad Na^+,\ Cl^- \end{cases} \tag{1.4}$$

- the *fluid phase* W contains two species

$$\begin{cases} \text{pore water} & \text{denoted by the symbol} \quad w \\ \text{sodium chloride salt} & \quad s = \text{NaCl} \end{cases} \tag{1.5}$$

Note that, more generally, the framework applies as it is to clays in which ions other than sodium and chloride ions are present in the vicinity of clay platelets, in as far as they do not leave the solid phase.

1.3 Phases in Articular Cartilage

A kinematical criterion classifies species according to their velocities. On the other hand, in Loret and Simões [2003] and Simões and Loret [2003], the definition of the phases of articular cartilage is mechanically motivated. Cartilage is viewed as a three-phase, multi-species, porous medium:

- the *solid phase* S contains the collagen fibers denoted by the symbol c.
- the *intrafibrillar fluid phase* I contains intrafibrillar water w, ions sodium Na^+ and calcium Ca^{2+} and ions chloride Cl^-.
- the *extrafibrillar fluid phase* E contains proteoglycans PGs, extrafibrillar water, mobile and non-mobile cations sodium and calcium, and anions chloride.

The main assumptions which underly the three-phase multi-species model differ from their counterparts for heteroionic and homoionic two-phase clays for two reasons: first because the solid skeleton has been isolated (note however that is a minor point), second, because the fixed charges are now located in a fluid phase that exchanges with the exterior. The assumptions (H1) to (H5) for clays listed in Sect. 1.1 become:

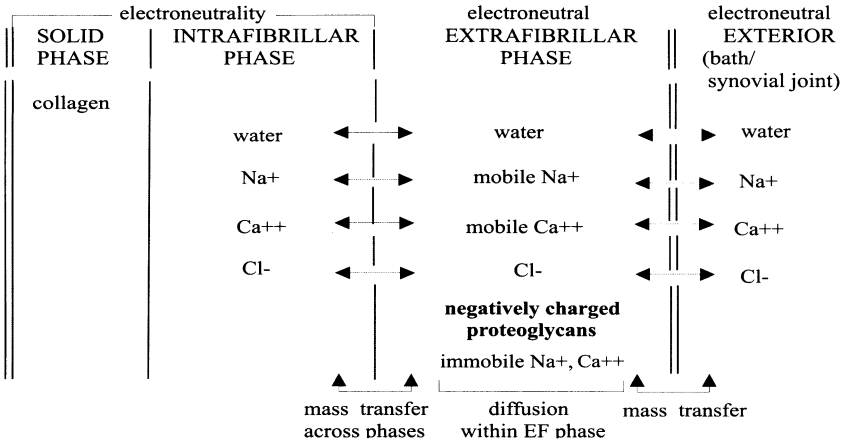

Figure 4 Articular cartilage is partitioned in three phases, one solid phase and two fluid phases. Each fluid phase contains several species. Some of these species are mobile, at least partially: water and ions can enter and leave the intrafibrillar space defined by collagen fibrils. Proteoglycans which are macromolecules are too large to be admitted into that space, at least in absence of osteo-arthritis. Water and ions can also be exchanged between the extrafibrillar phase and the exterior.

(H1) The mass balance is required for each species. Mass balance for each phase is obtained via mass balances of the species it contains.

(H2) Momentum balance is required for the mixture as a whole. Water and mobile ions in the extrafibrillar phase are endowed with their own velocities so as to allow the latter to diffuse in their phase, possibly with electrical effects, and satisfy their own balance of momentum.

(H3) The velocity of any species in the intrafibrillar phase is that of the solid phase, i.e. of collagen, $\mathbf{v}_{kI} = \mathbf{v}_S$, $\forall k \in I$. The velocities of the proteoglycans, and of non-mobile cations of the extrafibrillar phase, which do not diffuse through the cartilage are also equal to $\mathbf{v}_S$. Therefore, the balance of momentum of the above species is not required explicitly, but accounted for by the balance of momentum of the mixture as a whole. Note that the assumption on velocity does not hinder exchange of water and ions between the two fluid phases, this exchange being viewed as a *mass transfer* and not as a diffusion process.

(H4) In the intrafibrillar phase, the pressure in water and ions is assumed to be uniform, while, in the extrafibrillar phase, species are endowed a priori, through specific constitutive equations, with their own intrinsic pressure.

(H5) Electroneutrality is required for the extrafibrillar phase alone, and for the solid and intrafibrillar fluid phases together.

A more accurate description would split intrafibrillar water in mobile and non-mobile parts. Actually, part of the intrafibrillar water seems to be bound to collagen fibrils, Maroudas et al. [1991], Torzilli [1985]. However, the splitting of water into two intrafibrillar subspecies is not necessary: neither from the mechanical point of view since the

non-mobile water can be seen as water whose exchange requires higher energy, nor from the diffusion point of view since their common velocity is that of the collagen, that is of the solid phase.

On the other hand, a certain minimal concentration of cations is required to ensure electroneutrality of the extrafibrillar phase. Therefore, a diffusion analysis should endow mobile cations with a velocity independent of that of their non-mobile counterparts, which, like the proteoglycans, move with the velocity of the solid phase. The use of a mass-averaged velocity for all cations as in Lai et al. [1991], their eqn. (14), does not recognize this point. Thus cations in the extrafibrillar space are partitioned into a mobile part and a non-mobile part. Exchanges of water and ions occur between the fluid phases, but only the extrafibrillar phase communicates with the exterior, Figure 4.

As already mentioned, the definition of phases in articular cartilage is not unambiguous, because the mechanical, chemical and electrical roles of proteoglycans may dictate contradictory choices. In fact, if the phase criterion was kinematically based (that is on velocity), PG would be classified as part of the solid phase. However, its osmotic effect is important, not so much because of its concentration or molar fraction itself, but because of its effective charge and the latter should be involved in the electroneutrality condition of the extrafibrillar phase. One way to go around this issue is to consider a single electroneutrality condition, as in Lai et al. [1991] or Levenston et al. [1998]. However, topological considerations seem to dictate electroneutrality separately for collagen and extrafibrillar water. That aspect might turn important when the collagen becomes electrically charged, at non neutral pH.

Fixed charges: in the solid phase or in the fluid phase? According to a kinematic criterion, fixed charges would be part of the solid phase. On the other hand, their mechanical effects are related to their concentration with respect to the volume of extrafibrillar water.

Some key differences between the two options are listed below:

1. *Fixed charges in the solid phase.* This is the option taken in the modeling of expansive clays in Loret et al. [2002], Gajo et al. [2002]. Let us consider the chemo-mechanical equilibrium of a clay with an external reservoir. The solid phase is surrounded by a membrane, and jumps of specific quantities occur between the solid phase and the fluid phase, but there are no jumps of pore pressure or concentration between the water phase and the reservoir.

   Further, the electro-osmotic coefficient and the osmotic coefficient are not constraint by compatibility conditions. Thus they have to be provided by additional constitutive equations, Gajo and Loret [2003]ab, Loret et al. [2003]. Note that, in that situation, the osmotic efficiency is an important ingredient to be considered *within* the constitutive equations of generalized diffusion.

2. *Fixed charges in the fluid phase.* Then the electro-osmotic coefficient can be related directly to the fixed charge, Simões and Loret [2003], and the constitutive equations of generalized diffusion do not display explicitly the 'osmotic pressure' π. This is however not critical, because the pressure term in the chemical potential of water depends on chemistry (and strain) so that an osmotic efficiency re-appears. Indeed,

in contrast to the situation in clays where the pressure in the water phase was uniform over species, this is no longer the case for cartilage, and the pressure term in the chemical potential of water has to be postulated by constitutive equations, e.g. Loret and Simões [2003]. As another consequence of the presence of the fixed charge in the extrafibrillar phase, the pore pressure, concentrations and electrical field undergo a jump across the interface that separates the cartilage and a bath, even at equilibrium. This is because now the membrane is surrounding the whole material.

3. *Structure of the chemo-mechanical model.* The presence of the fixed charges in a fluid phase promotes the introduction of the chemo-mechanical effects in the form of an *effective stress*, which modifies Terzaghi effective stress. On the other hand, when the fixed charges are part of the solid phase, their effects are viewed more as modifying the stiffness of the material.

2 The Pieces of the Puzzle

2.1 Geometry, Volume and Mass

One of the principal tasks in building a theory of deformable porous media is to link the change of pore space to the mass of pore liquid flowing in or out of the representative volume element. This description is more complex when reactions take place, resulting in generation or disappearance of mass. We shall define below different measures of mass changes and volume changes that will be used in the constitutive and field equations.

Let N_{kK} be the mole number of the species k of phase K and $N_K = \sum_{k\in K} N_{kK}$ the number of moles in that phase. The *molar fraction* x_{kK} of the species k is defined by the relative ratio of the species k within its phase,

$$x_{kK} = \frac{N_{kK}}{N_K} \quad \text{with} \quad \sum_{k\in K} x_{kK} = 1\,, \quad K = S, W. \tag{2.1}$$

Let the initial volume of the porous medium be V_0 and let $V = V(t)$ be its current volume. The current volume of the species k of phase K is denoted by V_{kK} and the current volume of phase K by V_K. Then the *volume fraction* of the species k of phase K is defined as $n_{kK} = V_{kK}/V$ while the volume fraction of phase K is $n_K = V_K/V = \sum_{k\in K} n_{kK}$ and $n_S + n_W = 1$. On the other hand, *volume contents* $v_{kK} = V_{kK}/V_0 = n_{kK}\,V/V_0$ for the species k of phase K and $v_K = V_K/V_0 = n_K\,V/V_0$ for the phase K refer to the initial total volume V_0. The *mass contents* m_{kK} per unit initial volume V_0 of the species k of phase K [unit kg/m^3], and m_K of the phase K, are obtained from the volume contents v_{kK} and *intrinsic* mass densities ρ_k (the summation over mute indices does *not* apply):

$$m_{kK} = \frac{M_{kK}}{V_0} = \frac{N_{kK}\,m_k^{(\mathrm{M})}}{V_0} = \rho_k\,v_{kK}\,, \quad m_K = \frac{M_K}{V_0} = \sum_{k\in K} m_{kK}\,. \tag{2.2}$$

For incompressible species, the mass- and volume-contents are one and the same variables, and, although transfer and constitutive equations are phrased in terms of mass-contents, the use of volume-contents may occasionally simplify the notations.

The *apparent* density of the species k in the porous medium, namely $\rho^{kK} = n_{kK}\,\rho_k$, and the *apparent* density of the phase K, namely $\rho^K = \sum_{k\in K}\rho^{kK}$, refer to the volume of the porous medium. With (2.2), the molar fractions x_{kK} can be expressed in terms of the mass-contents

$$x_{kK} = \frac{m_{kK}/m_k^{(\mathrm{M})}}{\sum_{l\in K} m_{lK}/m_l^{(\mathrm{M})}}\,. \tag{2.3}$$

The molar volume $v_k^{(\mathrm{M})}$ and molar mass $m_k^{(\mathrm{M})}$ of the species k are linked by the intrinsic density ρ_k, namely $m_k^{(\mathrm{M})} = \rho_k\, v_k^{(\mathrm{M})}$. Note that the density of any species is assumed to be one and the same in both solid and fluid phases. The *molar volume* of the fluid phase is $v_W^{(\mathrm{M})} = \sum_{k\in W} x_{kW}\, v_k^{(\mathrm{M})}$.

We will also need the non-dimensional concentration c_{kW} which is the volume fraction referred to the fluid phase rather than to the porous medium, namely for any $k \in W$, [1]

$$c_{kW} = \frac{\text{volume of species } k \text{ of fluid phase}}{\text{volume of fluid phase}} = \frac{V_{kW}}{V_W} = \frac{n_{kW}}{n_W} = \frac{v_{kW}}{n_W}\,\frac{V_0}{V} = \frac{v_k^{(\mathrm{M})}}{v_W^{(\mathrm{M})}}\,x_{kW}\,, \tag{2.4}$$

and therefore $\sum_{k\in W} c_{kW} = 1$.

Under standard conditions of temperature and pressure, the maximum mass of NaCl dissolved in one liter of distilled water is 360 gm, that is 6.15 moles, since $m_{\mathrm{Na}}^{(\mathrm{M})} = 23\,\mathrm{gm}$ and $m_{\mathrm{Cl}}^{(\mathrm{M})} = 35.5\,\mathrm{gm}$, corresponding to the molar fraction $x_{\mathrm{NaW}}^{\mathrm{sat}} = 0.091$, i.e. $x_{wW}^{\mathrm{Na-sat}} = 0.819$. The molar volume of dissolved salt varies from $17.6\,\mathrm{cm}^3$ at low molarity of 0.25 mole/liter to $21.3\,\mathrm{cm}^3$ at high molarity of 5.142 mole/liter. Here, we admit a fixed value of $v_{\mathrm{NaCl}}^{(\mathrm{M})}{=}20\,\mathrm{cm}^3$. The molar volume of the fluid phase varies from $18\,\mathrm{cm}^3$ for distilled water to $0.9 \times 18 + 0.1 \times v_{\mathrm{NaCl}}^{(\mathrm{M})}{=}18.2\,\mathrm{cm}^3$, which gives a saturated salt concentration $c_{\mathrm{NaW}}^{\mathrm{sat}} = 0.10$, or equivalently $c_{\mathrm{NaW}}^{\mathrm{sat}}/v_{\mathrm{NaCl}}^{(\mathrm{M})}$ equal to 5 moles, or also 115 gm of Na^+ per liter of solution ($\equiv$ fluid phase). The maximum mass of KCl dissolved in one liter of distilled water is 342 gm, that is 4.58 moles, since $m_{\mathrm{K}}^{(\mathrm{M})} = 39.1\,\mathrm{gm}$. Admitting also a molar volume of dissolved salt of $v_{\mathrm{KCl}}^{(\mathrm{M})}{=}20\ \mathrm{cm}^3$, the above figures become $x_{\mathrm{KW}}^{\mathrm{sat}} = 0.071$, i.e. $x_{wW}^{\mathrm{K-sat}} = 0.858$, $v_W^{(\mathrm{M})}{=}18.15\,\mathrm{cm}^3$, $c_{\mathrm{KW}}^{\mathrm{sat}} = 0.078$, or equivalenty $c_{\mathrm{KW}}^{\mathrm{sat}}/v_{\mathrm{KCl}}^{(\mathrm{M})}$ equal to 3.91 moles, or 153 gm of K^+ per liter of solution. If the salts were dissolved together, the above saturated values would vary.

2.2 Energy and Electro-Chemical Potentials

A key entity that accounts for the chemical properties of species k of phase K is the *electro-chemical potential* which can be mass-based and denoted μ_{kK}^{ec} [unit $\mathrm{m}^2/\mathrm{sec}^2$], or mole-based and denoted $g_{kK}^{(\mathrm{ec})}$ [unit $\mathrm{m}^2{\times}\mathrm{kg}/\mathrm{sec}^2/\mathrm{mole}$], that is

$$g_{kK}^{(\mathrm{ec})} = m_k^{(\mathrm{M})}\,\mu_{kK}^{(\mathrm{ec})}\,. \tag{2.5}$$

The incremental work done by the total stress $\boldsymbol{\sigma}$ in the incremental strain $\delta\boldsymbol{\epsilon}$ of the solid phase and by the electro-chemical potentials μ_{kK}^{ec} during the addition of mass δm_{kK}

[1] Traditional analyses make use of the concentration measured in mole/volume of solution, that is of $c_{kW}/v_k^{(\mathrm{M})}$, or in mass/volume of solution, that is $\rho_k\, c_{kW}$.

of the species k to the phase K (or by the electro-chemical potentials $g^{\rm ec}_{kK}$ during the addition of δN_{kK} moles) can be cast in either form

$$\delta\Psi = \boldsymbol{\sigma} : \delta\boldsymbol{\epsilon} + \sum_{k,K} \mu^{\rm ec}_{kK}\, \delta m_{kK} \quad \Leftrightarrow \quad \delta\Psi = \boldsymbol{\sigma} : \delta\boldsymbol{\epsilon} + \sum_{k,K} g^{\rm ec}_{kK}\, \frac{\delta N_{kK}}{V_0}\,. \tag{2.6}$$

Summation extends only to species that transfer, i.e. $k \in S^{\leftrightarrow} = W^{\leftrightarrow} = W$ and K=S, W. In particular, the contribution due to the clay particles vanishes due to (1.3).

The constitutive equations will be phrased in terms of mass-based (electro-)chemical potentials, with the mass-contents as independent variables. However, only mole-based free enthalpies of formation are available. Therefore, use will be made of the entities best appropriate to the context.

The classical formula of the chemical potential of the species k in the fluid phase W, e.g. Haase [1990], chap. 2-5, Kestin [1968], chap. 21, identifies a purely mechanical contribution which involves

- the intrinsic pressure of the fluid phase p_W,
- the intrinsic density ρ_k or molar volume of the species $v^{(\rm M)}_k$,

and a chemical contribution phrased in terms of the molar fraction x_{kW}. For charged species in presence of the electrical potential ϕ^K [unit Volt=kg×m^2/sec^3/A], the electro-chemical potentials involve in addition an electrical contribution. Moreover, soluble species develop a configurational energetic property measured by their free enthalpy of formation g^0_{kW}. As for the species within the solid phase S, the mechanical contribution to the electro-chemical potential of species k is assumed to involve its intrinsic mean-stress p_{kS} to be defined by constitutive relations. In integral form,

$$m^{(\rm M)}_k\, \mu^{\rm ec}_{kK} = g^{\rm ec}_{kK} = g^0_{kK} + \int v^{(\rm M)}_k\, dp'_{kK} + RT\, {\rm Ln}\, x_{kK} + \zeta_k\, {\rm F}\, \phi^K\,, \tag{2.7}$$

with $p_{kW} = p_W$, $k \in W$. The integration above is performed from a reference state, say ($p_{kK} = 0$, $x_{kW} = 1$, $\phi^K = 0$), to the current state. Therefore, g^0_{kK} serves as the mole-based value of the chemical potential in the reference state. In these formulas, $R = 8.31451$ J/mole/°K is the universal gas constant, and T(°K) the absolute temperature. The electrical contribution to the chemical potentials is introduced through the valence ζ_k and Faraday's equivalent charge F=Avogadro number × charge of an electron= 96487 Coulomb/mole (1 Coulomb=1 A×sec). By convention, $\zeta_w = 0$.

2.3 Electroneutrality

Two additional phase entities of physical importance in electrolytes are the electrical density and the electrical current density. The latter definition is deferred to Sect. 3.1.

In phase K, the *electrical density* $I_{{\rm e}K}$ [unit Coulomb/m^3] can be expressed in terms, inter alia, of mole numbers, or molar fractions, mass-contents,

$$I_{{\rm e}K} = \frac{\rm F}{V} \sum_{k\in K} \zeta_k\, N_{kK} = {\rm F}\, \frac{N_K}{V} \sum_{k\in K} \zeta_k\, x_{kK} = {\rm F}\, \frac{V_0}{V} \sum_{k\in K} \zeta_k\, \frac{m_{kK}}{m^{(\rm M)}_k}\,, \tag{2.8}$$

and, in addition, for the fluid phase, in terms of concentrations as

$$I_{eW} = n_W \sum_{k\in W} \zeta_k \frac{c_{kW}}{v_k^{(\mathrm{M})}} . \tag{2.9}$$

The fulfillment of *electroneutrality* in phase K is simply $I_{eK} = 0$. The solid and fluid phases are assumed to be electrically neutral, individually. Typical relaxation times below which departure from electroneutrality might be of concern are much smaller than any event of interest in the present study, so that indeed electroneutrality can be considered to hold at any time [2]. On the other hand, transfer times between phases are magnitudes larger than the electrical relaxation time, and therefore electroneutrality becomes established for each phase independently.

Let us now comment two direct consequences of electroneutrality.

The electroneutrality condition sets a minimal admissible value for the molar fractions of the absorbed cations, especially when the pore solution is distilled water: then at equilibrium, the molar fraction of absorbed water overweights the other molar fractions. However, electroneutrality implies

$$N_{\mathrm{Na}S} + N_{\mathrm{K}S} = -\zeta_c\, N_{cS} + N_{\mathrm{Cl}S} > 0 \;\Leftrightarrow\; X \equiv x_{\mathrm{Na}S} + x_{\mathrm{K}S} = -\zeta_c\, x_{cS} + x_{\mathrm{Cl}S} > 0\,, \tag{2.10}$$

where the actual valences of the ionic species $\zeta_{\mathrm{Na}} = \zeta_{\mathrm{K}} = -\zeta_{\mathrm{Cl}} = 1$ have been used. Therefore, in the plane $(x_{\mathrm{Na}S},\, x_{\mathrm{K}S})$, the triangle defined by the points $(0,0)$, $(X,0)$ and $(0,X)$ is inaccessible, see Figure 2 of Gajo et al. [2002].

As another consequence of electroneutrality in each phase, the mass-content of anions chloride is no longer an independent variable and it can be eliminated in favor of the mass-contents of the cations,

$$\delta N_{\mathrm{Cl}K} = \delta N_{\mathrm{Na}K} + \delta N_{\mathrm{K}K} \Leftrightarrow \frac{\delta m_{\mathrm{Cl}K}}{m_{\mathrm{Cl}}^{(\mathrm{M})}} = \frac{\delta m_{\mathrm{Na}K}}{m_{\mathrm{Na}}^{(\mathrm{M})}} + \frac{\delta m_{\mathrm{K}K}}{m_{\mathrm{K}}^{(\mathrm{M})}}, \quad K = S,\, W. \tag{2.11}$$

Note however that the above differential relation is correct in the solid phase only if the electrical charge is fixed. It has to be modified when pH varies.

Thus the incremental energy (2.6) can be recast in terms of chemical potentials of water and salts s_1=NaCl and s_2=KCl conjugated respectively to the mass-contents of water and cations sodium and potassium,

$$\delta\Psi = \boldsymbol{\sigma} : \delta\boldsymbol{\epsilon} + \sum_{K=S,W} \mu_{wK}\, \delta m_{wK} + \mu_{\mathrm{s}_1 K}\, \delta m_{\mathrm{Na}K} + \mu_{\mathrm{s}_2 K}\, \delta m_{\mathrm{K}K}\,. \tag{2.12}$$

The entities $\mu_{\mathrm{s}_i K}$, $i = 1, 2$, can be viewed as the chemical potentials of the dissociated salts in phase K, namely in accordance with (2.7),

$$\mu_{\mathrm{s}_1 K} = \frac{p_{\mathrm{s}_1 K}}{\rho_{\mathrm{s}_1}} + \frac{RT}{m_{\mathrm{Na}}^{(\mathrm{M})}} \mathrm{Ln}\, x_{\mathrm{Na}K}\, x_{\mathrm{Cl}K}\,, \quad \mu_{\mathrm{s}_2 K} = \frac{p_{\mathrm{s}_2 K}}{\rho_{\mathrm{s}_2}} + \frac{RT}{m_{\mathrm{K}}^{(\mathrm{M})}} \mathrm{Ln}\, x_{\mathrm{K}K}\, x_{\mathrm{Cl}K}\,, \tag{2.13}$$

[2] The motions of ions close to the fixed charges disturb the electrical fields. The conduction process reaches a steady state in a characteristic time equal to the ratio of the dielectric constant ϵ over the electric conductivity of the solvent σ_e. For water, $\epsilon = 80\,\epsilon_0$ with $\epsilon_0 = 8.8542 \times 10^{-12}$ $\mathrm{C}^2/\mathrm{J/m}$ the permittivity of the vacuum and, for fine grained soils, σ_e depends strongly on ionic concentration and takes values from 0.01 to 1 Siemens. Therefore electroneutrality can be considered to hold for times greater than $10^{-9} - 10^{-7}$ sec.

where $p_{s_i W}$, $i = 1, 2$, is equal to p_W, the pore water pressure, while $p_{s_i S}$ is to be obtained by constitutive equations, and ρ_{s_1}, ρ_{s_2} are defined implicitly by the relations,

$$v^{(M)}_{NaCl} = \frac{m^{(M)}_{Na}}{\rho_{s_1}} = v^{(M)}_{Na} + v^{(M)}_{Cl}, \quad v^{(M)}_{KCl} = \frac{m^{(M)}_{K}}{\rho_{s_2}} = v^{(M)}_{K} + v^{(M)}_{Cl}. \tag{2.14}$$

Consequently, the electrical fields do not work and they do not enter the elastic constitutive equations, that can be phrased in terms of chemical potentials, rather than electro-chemical potentials.

2.4 Incompressibility constraint

A situation of particular interest arises when all species are incompressible, $\delta\rho_k = 0\,,\ \forall k$. Then, there exists a relation between the generalized strain variables $\{\boldsymbol{\epsilon}, v_W, \{v_{kS} = m_{kS}/\rho_k, k \in S^{\leftrightarrow}\}\}$. Indeed, the volume change is then equal to the sum of the changes of volume of all species. This relation will be used to express the volume change of the fluid phase as

$$\delta v_W = \delta \operatorname{tr} \boldsymbol{\epsilon} - \sum_{k \in S^{\leftrightarrow}} \delta v_{kS}\,. \tag{2.15}$$

3 The Global Picture: Deformation, Mass Transfer, Diffusion and Electrical Flow

The mass balance equations will be written for all the species in the fluid phase but water, and for the fluid phase as a whole. To simplify the analysis, the species are assumed to be incompressible. Balance of momentum will be required for the mixture as whole.

3.1 Mass-, volume-fluxes and electrical current density

Balance equations are phrased in terms of several fluxes. Because of the incompressibility of the species, mass fluxes and volume fluxes can be viewed as entities that differ only by their units. The *mass flux* $\mathbf{M}_{kK}$ and the associated *volume flux* $\mathbf{J}_{kK}$ of the species k of phase K through the solid skeleton are defined as,

$$\mathbf{M}_{kK} = \rho_k\, \mathbf{J}_{kK} = \rho^{kK}\, (\mathbf{v}_{kK} - \mathbf{v}_S)\,. \tag{3.1}$$

Of course, due to assumption (H3), only the fluxes of the species in the fluid phase are not zero. The sum of the fluxes $\mathbf{J}_{kW}$ provides the volume averaged flux $\mathbf{J}_W$ of fluid phase through the solid skeleton,

$$\mathbf{J}_W = \sum_{k \in W} n_{kW}\, (\mathbf{v}_{kW} - \mathbf{v}_S). \tag{3.2}$$

The diffusive flow of a species with respect to water in the fluid phase is denoted as $\mathbf{J}^{\mathrm{d}}_{kW}$,

$$\mathbf{J}^{\mathrm{d}}_{kW} = n_{kW}\, (\mathbf{v}_{kW} - \mathbf{v}_{wW})\,. \tag{3.3}$$

The *electrical current density* $\mathbf{I}_{eK}$ in phase K [unit A/m^2] is defined as the sum of constituent velocities weighted by their valences and molar densities,

$$\mathbf{I}_{eK} = \mathrm{F} \sum_{k \in K} \zeta_k \frac{N_{kK}}{V} \mathbf{v}_{kK} \,. \tag{3.4}$$

On comparing $(2.8)_2$ and (3.4), a uniform velocity for all species of a phase satisfying electroneutrality is seen to be a sufficient condition for the electrical current density to vanish in that phase, therefore $\mathbf{I}_{eS} = \mathbf{0}$. If electroneutrality is assumed in fluid phase, $\mathbf{I}_{eW}$ may be viewed as a sum of either interphase or diffusive fluxes, namely

$$\mathbf{I}_{eW} = \mathrm{F} \sum_{k \in W} \frac{\zeta_k}{v_k^{(\mathrm{M})}} \mathbf{J}_{kW} = \mathrm{F} \sum_{k \in W} \frac{\zeta_k}{v_k^{(\mathrm{M})}} \mathbf{J}^{\mathrm{d}}_{kW} \,. \tag{3.5}$$

3.2 Balance equations

Balances of masses. The change of mass of a species is due a priori to both *transfer*, i.e. a physico-chemical reaction, and *diffusion*. In practice, the changes in the species of the solid phase are purely reactive, and they are due to transfer through the membrane, between the solid and fluid phases, of water and ionic species. On the other hand, the species of the fluid phase may also undergo mass changes by exchanges (diffusion) with the outside, i.e.

$$\frac{\delta\, m_{kK}}{\delta t} = \begin{cases} \hat{\rho}^{kS}, & K = S \\ \hat{\rho}^{kW} - \operatorname{div} \mathbf{M}_{kW}, & K = W \end{cases} \tag{3.6}$$

so that

$$\frac{\delta\, m_{kW}}{\delta\, t} = -\frac{\delta\, m_{kS}}{\delta\, t} - \operatorname{div}\, \mathbf{M}_{kW}\,, \quad k \in W. \tag{3.7}$$

Here the symbol $\delta\,/\delta t$ means derivative following the solid phase, and $\hat{\rho}^{kK}$ is the *rate of transfer* of mass density towards the species k of phase K. The implied balance of mass of the species k in fluid phase is due to the fact that the transfer concerns individual species, that is $\hat{\rho}^{kS} + \hat{\rho}^{kW} = 0$, $k \in S^{\leftrightarrows} = W^{\leftrightarrows}$. It may be phrased in terms of the concentration c_{kW}, eqn (2.4), and of the rate of n_W given by eqn (A9) of Gajo and Loret [2003]a, namely, neglecting the spatial heterogeneity of ρ_k,

$$n_W \frac{\delta\, c_{kW}}{\delta\, t} + c_{kW} \operatorname{div} \mathbf{v}_S + \operatorname{div} \mathbf{J}_{kW} + \sum_{l \in S^{\leftrightarrows}} (I_{kl} - c_{kW}) \frac{\delta\, v_{lS}}{\delta\, t} = 0, \quad k \in W. \tag{3.8}$$

Eqn (3.8) indicates that the change of salt concentration is due to change of volume of solid skeleton, diffusion of species through the porous medium, and transfer of all species between the two phases, with appropriate weights and signs.

As another consequence of (3.7), if electroneutrality is assumed in both the solid and fluid phases, $\mathbf{I}_{eW}$ defined by (3.4), or (3.5), is divergence free,

$$\operatorname{div} \mathbf{I}_{eW} = 0\,. \tag{3.9}$$

For incompressible species, the change of volume of the solid skeleton (i.e. porous medium) is equal and opposite to the volume change of the fluid phase that diffuses through this solid skeleton,

$$\text{div } \mathbf{v}_S + \text{div } \mathbf{J}_W = 0. \tag{3.10}$$

Balance of momentum. Under quasi-static loading and with the sole gravity $\mathbf{g}$ with intensity g as body force, the balance of momentum of the porous medium as a whole writes, e.g. Eringen and Ingram [1965],

$$\text{div } \boldsymbol{\sigma} + \rho \mathbf{g} = \mathbf{0}, \tag{3.11}$$

where ρ is the density of the porous medium, i.e. $\rho = \sum_{k,K} \rho^{kK} = \sum_K \rho^K$.

3.3 The Clausius-Duhem Inequality

In the absence of thermal effects, starting from the statements of balance of mass for each species, and of momentum and energy for the phases, the Clausius-Duhem inequality for the mixture as a whole can be cast as the sum of three contributions of mechanical, transfer and diffusion natures. Thus these contributions will be required to be positive individually,

$$\left\{ \begin{array}{l} \text{Deformation:} \\ \delta D_1 = -\delta\Psi + \boldsymbol{\sigma} : \delta\boldsymbol{\epsilon} + \displaystyle\sum_{k,K} \mu_{kK}^{(\mathrm{ec})}\, \delta m_{kK} \geq 0\,, \\ \text{Mass transfer across phases:} \\ \delta D_2 = -\displaystyle\sum_{k \in S^{\mapsto}} (\mu_{kS}^{(\mathrm{ec})} - \mu_{kW}^{(\mathrm{ec})})\, \delta m_{kS} \geq 0\,, \\ \text{Diffusion in the fluid phase:} \\ \delta D_3/\delta t = -\displaystyle\sum_{k \in W} (\nabla \mu_{kW}^{\mathrm{ec}} - \mathbf{b}_{kW} + d^{kW}\mathbf{v}_{kW}/dt\,) \cdot \mathbf{M}_{kW} \geq 0\,. \end{array} \right. \tag{3.12}$$

Due to phase electroneutrality, the electrical fields do not work, and this implies that δD_1 and δD_2 can be phrased equivalently in terms of electro-chemical potentials or chemical potentials. Consequently, neither the elastic constitutive relations nor the mass transfer relations depend directly on the electrical fields.

In the next chapters, the chemo-hyperelastic behaviour will be constructed in order for the first term δD_1 to exactly vanish. Satisfaction of the second and third inequalities motivates generalized transfer equations and generalized diffusion equations respectively. When only acceleration of gravity is considered, all body force densities $\mathbf{b}_{kW}$ are equal to the gravity $\mathbf{g}$, and the accelerations $d^{kW}\mathbf{v}_{kW}/dt$ are neglected.

Bibliography

Bataille, J. and J. Kestin (1977). Thermodynamics of mixtures. *J. Non-Equilib. Thermodynamics*, 2, 49-65.

Eringen, A.C. and J.D. Ingram (1965). A continuum theory for chemically reacting media -I. *Int. J. Engng. Science*, 3, 197-212.

Gajo, A., Loret, B. and T. Hueckel (2002). Electro-chemo-mechanical couplings in saturated porous media: elastic-plastic behaviour of heteroionic expansive clays. *Int. J. Solids and Structures*, 39, 4327-4362.

Gajo, A. and B. Loret (2003)a. Finite element simulations of chemo-mechanical coupling in elastic-plastic homoionic expansive clays. *Computer Methods in Applied Mechanics and Engineering*, 192(31-32), 3489-3530.

Gajo, A. and B. Loret (2003)b. Transient analysis of ionic replacements in elastic-plastic expansive clays. submitted for publication.

Haase, R. (1990). Thermodynamics of Irreversible Processes. Dover Publications, New York.

Kestin, J. (1968). A Course in Thermodynamics. Blaisdell Publishing Co., Waltham, Massachusetts.

Lai, W.M., Hou, J.S. and V.C. Mow (1991). A triphasic theory for the swelling and deformation behaviors of articular cartilage. *J. of Biomech. Engng.*, Transactions of the ASME, 113, 245-258.

Levenston, M.E., Eisenberg, S.R. and A.J. Grodzinsky (1998). A variational formulation for coupled physicochemical flows during finite deformations of charged porous media. *Int. J. Solids and Structures*, 35, 4999-5019.

Loret, B., Hueckel, T. and A. Gajo (2002). Chemo-mechanical coupling in saturated porous media: elastic-plastic behaviour of homoionic expansive clays. *Int. J. Solids and Structures*, 39, 2773-2806.

Loret, B., Gajo, A., and F.M. Simões (2003). A note on the dissipation due to generalized diffusion with electro-chemo-mechanical couplings in heteroionic clays. submitted for publication.

Loret, B. and F.M. Simões (2003). Articular cartilage with intra- and extrafibrillar waters. A chemo-mechanical model. *Mechanics of Materials*, accepted for publication.

Maroudas, A., Wachtel, E., Grushko, G., Katz, E. P. and P. Weinberg (1991). The effect of osmotic and mechanical pressures on water partitioning in articular cartilage. *Biochimica et Biophysica Acta*, 1073, 285-294.

Simões, F.M. and B. Loret (2003). Articular cartilage with intra- and extrafibrillar waters. Deformation, mass transfer and generalized diffusion. submitted for publication.

Torzilli, P.A. (1985). Influence of cartilage conformation on its equilibrium water partition. *J. of Orthopaedic Research*, 3, 473-483.

Constitutive Equations for Homoionic Clays

Benjamin Loret * and Alessandro Gajo †

* Laboratoire Sols, Solides, Structures, Institut National Polytechnique de Grenoble, France
† Dipartimento di Ingegneria Meccanica e Strutturale, Università di Trento, Trento, Italia

Abstract Exchange of matter between the clay clusters (solid phase) and pore water (fluid phase) implies changes in the thermomechanical state of the porous medium. Both elastic and elastic-plastic properties are affected. Chemical effects act reversibly on the plastic properties by increasing or decreasing the preconsolidation stress and also by changing the shear-strength. But by the same token, they also implicitly trigger or prevent plastic strains. The analysis addresses the situation where the chemical dissolved in pore water does not dissociate, excluding electrical interactions.

1 The general setting

The absorption/desorption of water (and salt) into/from the solid phase introduces a chemo-mechanical coupling. On the other hand, salt in the fluid phase does not affect directly the mechanical behaviour of the porous medium, it just flows through. Its amount is governed by an equation of mass conservation and a flow law. Therefore, to develop the chemo-mechanical constitutive equations, we will treat the fluid phase as a whole and, temporarily, ignore its chemical composition. The constitutive equations are developed for the following variables:

- two thermodynamic dual variables characterizing the mechanical state of each phase, namely $(\boldsymbol{\sigma}, \boldsymbol{\epsilon})$ for the solid phase and (p_W, v_W) for the fluid phase;
- as many thermodynamic dual variables of chemical potential-mass content as there are species that cross the membrane, namely $(\mu_{kS}, m_{kS}), k \in S^{\leftrightarrow}$.

Incompressibility of all species will reduce the number of independent variables by one.

In view of extension to the elastic-plastic behaviour, generalized elastic strains will henceforth be denoted by a superscript ^{el}. Instances are strains, volume and mass contents, number of moles. Later, these entities will be decomposed into an elastic (or reversible) part and a plastic (or irreversible) part. Given a reference state, and a process which is reversible from that reference state to the current state, the elastic part of each of above entities is by convention equal to the total entity.

We begin by recalling basic notions of elasticity and elastoplasticity in fluid-saturated soils.

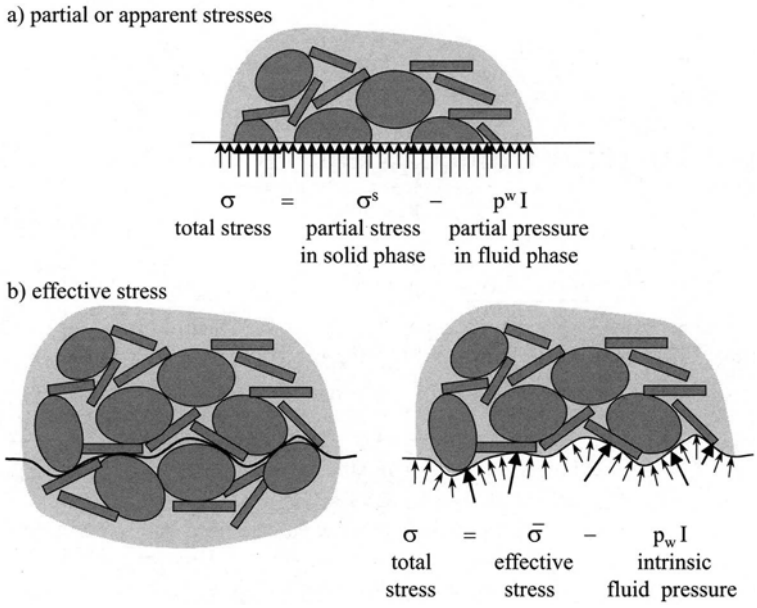

Figure 1 Apparent stresses and Terzaghi effective stress in a two-phase porous medium.

2 Elasticity and Elastoplasticity for Chemically Insensitive Soils

2.1 Total Stress, Partial Stresses and Terzaghi Effective Stress

Stresses represent forces averaged over a certain surface. When the forces acting over a species are referred to the surface defined by this very species, the resulting stresses are termed *intrinsic*. When the surface of reference is that surface defined by the mixture, the stresses are called *apparent* stresses, or *partial* stresses, Figure 1-(a). In the definition of these entities, it is tacitly assumed that surface fractions and volume fractions are identical.

In particulate media, forces between particles are most often highly localized. Suitably averaged, contact forces give rise to so-called *Terzaghi effective* stress, Figure 1-(b). Terzaghi effective stress is of utmost importance because it controls the mechanical behaviour of particulate media with rigid particles, like soils.

These two points of view provide two additive partitions of the total stress acting on the porous medium, Figure 1.

Let us introduce now the decomposition of the strain into a spherical part and a deviatoric part. Similarly, the decomposition of the total and effective stresses introduces the first invariants of the total and effective mean-stresses p, $\overline{p}$ and the deviatoric stress $\mathbf{s}$,

$$\boldsymbol{\epsilon} = \frac{1}{3}\operatorname{tr}\boldsymbol{\epsilon}\,\mathbf{I} + \operatorname{dev}\boldsymbol{\epsilon}\,, \quad \boldsymbol{\sigma} = -p\,\mathbf{I} + \mathbf{s}\,, \quad \bar{\boldsymbol{\sigma}} = -\overline{p}\,\mathbf{I} + \mathbf{s}, \quad p = -\frac{1}{3}\operatorname{tr}\boldsymbol{\sigma}, \quad \overline{p} = -\frac{1}{3}\operatorname{tr}\bar{\boldsymbol{\sigma}}\,. \tag{2.1}$$

It is also intrumental to define the following invariant measures of the deviatoric strain

and of the (effective or total) stress,

$$\epsilon_q = (2/3\,\mathrm{dev}\,\boldsymbol{\epsilon}:\mathrm{dev}\,\boldsymbol{\epsilon})^{1/2}\,, \quad q = (3/2\,\mathbf{s}:\mathbf{s})^{\frac{1}{2}}\,. \tag{2.2}$$

Although the formulation is by no means restricted to such states, the manipulations will become more familiar to Cam-Clay users if the deviatoric stress and strain are assumed to maintain fixed directions during loading, e.g. as for triaxial compression or extension paths, or more generally paths with constant Lode angle. Then the stress and strain states can be fully characterized by only two work-conjugate invariants, namely $(\overline{p},\, q)$ and $(\mathrm{tr}\,\boldsymbol{\epsilon},\, \epsilon_q)$, since then the incremental work $\bar{\boldsymbol{\sigma}}:\delta\boldsymbol{\epsilon}$ reduces to $\overline{p}\;\delta\,\mathrm{tr}\,\boldsymbol{\epsilon} + q\,\delta\epsilon_q$.

2.2 Logarithmic Poro-Elasticity

Logarithmic Elasticity for Dry Soils. Experimental data over a large range of stress show that the elastic bulk moduli of soils depend on the stress state. A usual approximation linked to the Cam-Clay models consists in assuming the volumetric elastic strain to be proportional to the logarithm of the effective mean-stress.

For chemically inert soils, the logarithmic stress based formulation starts by assuming the stored energy in the following form,

$$\mathcal{W}^{\mathrm{el}}(\overline{p},\, q) = \kappa\,\overline{p}\,\mathrm{Ln}\frac{\overline{p}}{\overline{p}_0} - \kappa\,\overline{p} + \frac{q^2}{6\,G}\,, \tag{2.3}$$

where κ and G are material constants and $\overline{p}_0$ a reference mean-stress. The strain is

$$\boldsymbol{\epsilon}^{\mathrm{el}} = \frac{\partial \mathcal{W}^{\mathrm{el}}}{\partial \bar{\boldsymbol{\sigma}}} = -\kappa\,\mathrm{Ln}\,\frac{\overline{p}}{\overline{p}_0}\,\frac{\mathbf{I}}{3} + \frac{\mathbf{s}}{2\,G}\,. \tag{2.4}$$

For non-linear elasticity, a clear difference should be made between *secant* and *tangent* moduli. More general hyperelastic relations for soils are analyzed in Loret [1985].

Poro-Elasticity for a mixture with incompressible species. When the solid particles and water are both incompressible, the incompressibility condition yields the change of volume content Δv_w from an unstrained state to be equal to the volume change of the whole mixture $\mathrm{tr}\,\boldsymbol{\epsilon}^{\mathrm{el}}$. The elastic strain, counted from the reference state $\bar{\boldsymbol{\sigma}} = -\overline{p}_0\,\mathbf{I}$, is still given in terms of effective stress by (2.4).

Poro-elastic relations with compressible constituents and an anisotropic solid skeleton are considered in e.g. Loret and Harireche [1991] and Loret et al. [2001].

2.3 Poro-Plasticity for a Mixture with Incompressible Species

When the species are all incompressible, the elasto-plastic constitutive equations may be phrased in terms of Terzaghi effective stress and of hardening/softening parameters of scalar or tensorial natures that indicate how the yield surfaces changes size, position and shape during deformation processes. These constitutive equations have the same format as if the material considered were the single phase *drained solid*.

A prototype behaviour for clays is provided by the Modified Cam-Clay Model where the yield function is elliptical and the plastic volume change $\mathrm{tr}\,\boldsymbol{\epsilon}^{\mathrm{pl}}$ serves as hardening/softening parameter,

$$f = f(\overline{p}, q, \mathrm{tr}\,\boldsymbol{\epsilon}^{\mathrm{pl}}) = \frac{q^2}{M^2\,\overline{p}} + \overline{p} - p_c\,, \tag{2.5}$$

where M is the critical state constant and $p_c = p_c(\mathrm{tr}\,\boldsymbol{\epsilon}^{\mathrm{pl}})$ is the preconsolidation stress.

3 Chemo-Elasticity

3.1 The Gibbs-Duhem relation

The chemical potentials that enter the free energy

$$\delta\Psi = \boldsymbol{\sigma} : \delta\boldsymbol{\epsilon} + \sum_{k,K} \mu_{kK}\,\delta m_{kK}\,. \tag{3.1}$$

are those associated to the species whose mass-content varies, that is all species of the fluid phase and the single species of the solid phase that can transfer to the fluid phase, namely water. In incremental form, the chemical potentials write,

$$\delta\mu_{kK} = \begin{cases} \dfrac{\delta p_W}{\rho_k} + \dfrac{RT}{m_k^{(\mathrm{M})}}\,\delta\,\mathrm{Ln}\,x_{kW}\,, & k = w, s, \\ \dfrac{\delta p_{kS}}{\rho_k} + \dfrac{RT}{m_k^{(\mathrm{M})}}\,\delta\,\mathrm{Ln}\,x_{kS}\,, & k = w\,. \end{cases} \tag{3.2}$$

For a fluid phase, the Gibbs-Duhem relation provides the fluid pressure p_W in terms of the chemical potentials of the species μ_{kW}, $k \in W$, namely Haase [1990], chap. 1-13,

$$\delta p_W = \rho_w\,c_{wW}\,\delta\mu_{wW} + \rho_s\,c_{sW}\,\delta\mu_{sW}\,, \tag{3.3}$$

This relation is easy to retrieve by forming a linear combination of the chemical potentials that eliminates the chemical contribution.

In order to define the mechanical constitutive equations of the porous medium, we will isolate the chemical effects in pore water. For that purpose, following Heidug and Wong [1996], we define the chemical energy per current unit volume of the fluid phase through its differential

$$\delta\psi_W = \mu_{wW}\,\rho_w\,\delta c_{wW} + \mu_{sW}\,\rho_s\,\delta c_{sW}\,, \tag{3.4}$$

which, via the Gibbs-Duhem relation (3.3), can be integrated, up to a constant, to

$$\psi_W = \mu_{wW}\,\rho_w\,c_{wW} + \mu_{sW}\,\rho_s\,c_{sW} - p_W\,. \tag{3.5}$$

Therefore, the explicit form of the chemical energy Ψ_W of the fluid phase per unit initial volume of porous medium writes,

$$\Psi_W = \psi_W\,\frac{V_W}{V_0} = \psi_W\,v_W = \mu_{wW}\,m_{wW} + \mu_{sW}\,m_{sW} - p_W\,v_W\,. \tag{3.6}$$

Due to the Gibbs-Duhem relation (3.3), the differential of Ψ_W simplifies to

$$\delta\Psi_W = \sum_{k\in W} \mu_{kW}\,\delta m_{kW} - p_W\,\delta v_W\,. \tag{3.7}$$

3.2 Dependent and Independent Variables

When the behaviour is elastic, the energy of the porous medium per unit initial volume $\mathcal{W}^{\,\mathrm{el}} = \Psi^{\,\mathrm{el}} - \Psi_W$ can be viewed as the elastic energy of the porous medium for which the chemical effects in the fluid phase are disregarded. This energy depends on the restricted set of independent variables $\{\boldsymbol{\epsilon}^{\mathrm{el}}, v_W^{\mathrm{el}}, m_{wS}^{\mathrm{el}}\}$[1]. Indeed, with the work definition (3.1) and the Gibbs-Duhem relation (3.3), the incremental form of the energy $\mathcal{W}^{\mathrm{el}}$ simplifies to

$$\delta\mathcal{W}^{\mathrm{el}} = \boldsymbol{\sigma} : \delta\boldsymbol{\epsilon}^{\mathrm{el}} + p_W\,\delta v_W^{\mathrm{el}} + \mu_{wS}\,\delta m_{wS}^{\mathrm{el}}\,. \tag{3.8}$$

Thus constitutive equations for the *dependent variables* $\{\boldsymbol{\sigma},\, p_W,\, \mu_{wS}\}$ in terms of the *independent variables* $\{\boldsymbol{\epsilon}^{\mathrm{el}},\, v_W^{\mathrm{el}},\, m_{wS}^{\mathrm{el}}\}$ are obtained in the format:

$$\boldsymbol{\sigma} = \frac{\partial\mathcal{W}^{\mathrm{el}}}{\partial\boldsymbol{\epsilon}^{\mathrm{el}}}\,, \quad p_W = \frac{\partial\mathcal{W}^{\mathrm{el}}}{\partial v_W^{\mathrm{el}}}\,, \quad \mu_{wS} = \frac{\partial\mathcal{W}^{\mathrm{el}}}{\partial m_{wS}^{\mathrm{el}}}\,. \tag{3.9}$$

Alternative choices in the sets of independent and dependent variables can be postulated by partial or total Legendre transforms of $\mathcal{W}^{\mathrm{el}}$, Loret et al. [2002].

3.3 Incompressible species

In the sequel, we will restrict the formulation by assuming that all species are incompressible. Moreover we require the incompressibility condition to hold in both the elastic and elastic-plastic regimes. Then the increment of elastic fluid volume content is given by the incompressibility condition in terms of the two elastic quantities $\{\boldsymbol{\epsilon}^{\mathrm{el}}, m_{wS}^{\mathrm{el}}\}$ that we shall adopt as independent variables. Hence, $\delta\mathcal{W}^{\mathrm{el}}$, eqn (3.8), becomes

$$\delta\mathcal{W}^{\mathrm{el}} = \bar{\boldsymbol{\sigma}} : \delta\boldsymbol{\epsilon}^{\mathrm{el}} + \overline{\mu}_{wS}\,\delta m_{wS}^{\mathrm{el}}\,, \tag{3.10}$$

in terms of Terzaghi effective stress $\bar{\boldsymbol{\sigma}}$ and of the effective chemical potential $\overline{\mu}_{wS}$,

$$\bar{\boldsymbol{\sigma}} = \boldsymbol{\sigma} + p_W\,\mathbf{I}\,, \quad \overline{\mu}_{wS} = \mu_{wS} - \frac{p_W}{\rho_w}\,. \tag{3.11}$$

The mass transfer is assumed not alter the density of water. Then the transfer equation considered in later chapters may be phrased identically in terms of chemical potentials or in terms of effective chemical potentials. In particular, the equilibrium of the chemical potential of water, $\mu_{wS} = \mu_{wW}$, is equivalent to the equilibrium of the effective chemical potentials, $\overline{\mu}_{wS} = \overline{\mu}_{wW}$. Remember that chemical equilibrium applies only to species

[1] Notice that only the arguments that vary during loadings are listed; for example, since the mass content in clay is constant inside the solid phase, its influence is not shown explicitly in the list of arguments although it is tacitly assumed.

that can cross the membrane. Note also that continuous equilibrium does not hinder transfer of matter.

The constitutive relations take now the form,

$$\bar{\boldsymbol{\sigma}} = \frac{\partial \mathcal{W}^{\mathrm{el}}}{\partial \boldsymbol{\epsilon}^{\mathrm{el}}}\,, \quad \overline{\mu}_{wS} = \frac{\partial \mathcal{W}^{\mathrm{el}}}{\partial m^{\mathrm{el}}_{wS}}\,. \tag{3.12}$$

Notice that, when there is only a single species present per phase as in the usual poroelasticity, that is, $\delta m^{\mathrm{el}}_{wS} = 0$, the classical relations are retrieved. Indeed, the incremental energy reduces to $\boldsymbol{\sigma} : \delta\boldsymbol{\epsilon}^{\mathrm{el}} + p_W\, \delta v^{\mathrm{el}}_W$ in the compressible case. In the incompressible case, the incremental energy is equal to $\bar{\boldsymbol{\sigma}} : \delta\boldsymbol{\epsilon}^{\mathrm{el}}$ since then the incompressibility condition is $\delta v^{\mathrm{el}}_W = \delta \mathrm{tr}\, \boldsymbol{\epsilon}^{\mathrm{el}}$ and the remaining constitutive equations $(3.12)_1$ specify the effective stress only, that is the pore pressure p_W does not enter explicitly the constitutive equations: in a boundary value problem, it is defined by boundary conditions.

3.4 Logarithmic Hyperelasticity

Bolt [1956] has provided data on the influence of the chemical composition of pore water on the isotropic rebound (unloading) curves from high stresses: in the plane ($\mathrm{Ln}\,\overline{p}$-void ratio e), they are almost linear trajectories emanating from a restricted zone with a very narrow range of void ratios. In our formulation, a constant chemical composition of the pore water is equivalent, if the pore pressure is constant, to a constant chemical potential of any species in fluid phase, and, at equilibrium, to a constant chemical potential of absorbed water. Thus, one would be lead a priori to use the effective stress and chemical potential of absorbed water as primary variables. However, the extension to electrolyte solutions is facilitated if the effective stress and the mass of absorbed water m^{el}_{wS} (or the molar fraction x^{el}_{wS} derived consistently from the latter) are considered as primary variables instead. From a practical point of view, the above mentioned unloading curves can be associated with an almost constant x^{el}_{wS} as mechanical loading, at constant chemical potential μ_{wS}, has a small influence on the chemical composition of the solid phase.

Let us consider now the purely chemical contribution to the chemo-elastic potential, namely $RT/V_0\, \varphi(x^{\mathrm{el}}_{wS})$. We require the chemical part of the chemical potential $\overline{\mu}_{wS}$ to have the classic form $(3.2)_2$, that is since $N^{\mathrm{el}}_{wS} = m^{\mathrm{el}}_{wS} V_0/m^{(\mathrm{M})}_w$, we require $\partial\varphi/\partial N^{\mathrm{el}}_{wS} = \mathrm{Ln}\, x^{\mathrm{el}}_{wS}$. Then up to a constant depending on the number of moles of solid particles N_{cS},

$$\varphi(\{x^{\mathrm{el}}_{kS}\,,\ k \in S^{\leftrightarrow}\}) = \sum_{k\in S^{\leftrightarrow}} N^{\mathrm{el}}_{kS}\, \mathrm{Ln} N^{\mathrm{el}}_{kS} - \Big(\sum_{k\in S} N^{\mathrm{el}}_{kS}\Big)\, \mathrm{Ln}\Big(\sum_{l\in S} N^{\mathrm{el}}_{lS}\Big)\,. \tag{3.13}$$

This expression holds for both homoionic and heteroionic clays with the proviso that $S^{\leftrightarrow} = \{w\}$ for homoionic clays.

We are now in the position to obtain the chemo-elastic potential in the above motivated mixed form. For that purpose, let us first define a partial Legendre transform $\mathcal{W}^{el}_M(\bar{\boldsymbol{\sigma}}, m^{\mathrm{el}}_{wS})$ of the energy $\mathcal{W}^{\mathrm{el}}$, namely

$$\delta \mathcal{W}^{\mathrm{el}}_M = \delta\left(\bar{\boldsymbol{\sigma}} : \boldsymbol{\epsilon}^{\mathrm{el}} - \mathcal{W}^{\mathrm{el}}\right) = \boldsymbol{\epsilon}^{\mathrm{el}} : \delta\bar{\boldsymbol{\sigma}} - \overline{\mu}_{kS}\, \delta m^{\mathrm{el}}_{wS}\,, \tag{3.14}$$

from which follow the constitutive relations,

$$\boldsymbol{\epsilon}^{\rm el} = \frac{\partial \mathcal{W}_M^{\rm el}}{\partial \bar{\boldsymbol{\sigma}}}\,, \quad \overline{\mu}_{wS} = -\frac{\partial \mathcal{W}_M^{\rm el}}{\partial m_{wS}^{\rm el}}\,. \tag{3.15}$$

In order to reproduce the expected elastic behaviour, Figure 2, the complete potential is taken in the format

$$\mathcal{W}_M^{\rm el}(\bar{\boldsymbol{\sigma}}, m_{wS}^{\rm el}) = -\overline{p}\,{\rm tr}\,\boldsymbol{\epsilon}_\kappa^{\rm el} + \kappa(x_{wS}^{\rm el})\,F(\overline{p},\overline{p}_\kappa) + \frac{q^2}{6\,G} - \frac{RT}{V_0}\,\varphi(x_{wS}^{\rm el})\,. \tag{3.16}$$

Here $F(\overline{p},\overline{p}_\kappa)$ is the function that introduces a logarithmic dependance in mean-stress,

$$F(\overline{p},\overline{p}_\kappa) = \overline{p}\,{\rm Ln}\,\frac{\overline{p}}{\overline{p}_\kappa} - \overline{p}\,, \quad \frac{dF}{d\overline{p}} = {\rm Ln}\,\frac{\overline{p}}{\overline{p}_\kappa}\,, \tag{3.17}$$

and ${\rm tr}\,\boldsymbol{\epsilon}_\kappa^{\rm el}$ is the value of the volume change when the effective mean-stress varies from the convergence stress $\overline{p}_\kappa$ to a small reference value $\overline{p}_0$ while the pore fluid is distilled water, Figure 2. In absence of precise experimental influence of the chemical composition of pore water on the shear modulus G, the latter will be simply assumed to be constant. Then, with the elastic potential (3.16), the elastic constitutive equations (3.15) become:

$$\left\{\begin{array}{l} \boldsymbol{\epsilon}^{\rm el} = \left({\rm tr}\,\boldsymbol{\epsilon}_\kappa^{\rm el} - \kappa(x_{wS}^{\rm el})\,{\rm Ln}\,\dfrac{\overline{p}}{\overline{p}_\kappa}\right)\dfrac{\mathbf{I}}{3} + \dfrac{\mathbf{s}}{2\,G}\,, \\ \overline{\mu}_{wS} = -F(\overline{p},\overline{p}_\kappa)\,\dfrac{d\kappa}{dm_{wS}^{\rm el}} + \dfrac{RT}{m_w^{(\rm M)}}\,{\rm Ln}\,x_{wS}^{\rm el}\,. \end{array}\right. \tag{3.18}$$

An incremental form of the elastic constitutive equations giving $(-\delta\overline{p},\ \delta q,\ \delta\overline{\mu}_{wS})$ in terms of $(\delta\,{\rm tr}\,\boldsymbol{\epsilon},\ \delta\epsilon_q^{\rm el},\ \delta m_{wS}^{\rm el})$ can be expressed via the symmetric matrix,

$$\left[\begin{array}{c} -\delta\overline{p} \\ \delta q \\ \delta\overline{\mu}_{wS} \end{array}\right] = \left[\begin{array}{ccc} B & 0 & B_w \\ 0 & 3G & 0 \\ B_w & 0 & \beta \end{array}\right] \left[\begin{array}{c} \delta{\rm tr}\,\boldsymbol{\epsilon}^{\rm el} \\ \delta\epsilon_q^{\rm el} \\ \delta m_{wS}^{\rm el} \end{array}\right]. \tag{3.19}$$

Notice that the symmetry of the constitutive matrix in (3.19) is due to the existence of the chemo-elastic potential. Moreover, since G is independent of the chemical composition of the solution, there is no coupling between shear components and the chemical variable.

The explicit expressions of the elastic matrix and the calibration of a typical interpolation function for $\kappa(x_{wS}^{\rm el})$ are provided in Loret et al. [2002], with data corresponding to distilled and salt-saturated pore water.

The format of this chemo→mechanical coupling. A comment on the format in which the chemical composition of the mixture effects the mechanical properties may be of interest at this point. The elastic coupling is completely described by the dependence of the elastic coefficient κ in the molar fraction of absorbed water. There are other

ways to induce coupling. For example, in Loret and Simões [2003], the elastic moduli are taken constant, and the chemical coupling is accounted for by the effective stress $\overline{\overline{\boldsymbol{\sigma}}} = -p^{\text{eff}}\,\mathbf{I} + \boldsymbol{\sigma}$, where the pressure p^{eff} contains a chemical contribution in addition to the pore water pressure p_W.

4 Chemo-Elasto-Plasticity

Exchange of matter between the clay cluster (solid phase) and pore water (fluid phase) implies changes in the thermomechanical state of the porous medium. Both elastic and elastic-plastic properties are affected. Chemical effects act reversibly on the plastic properties by increasing or decreasing the preconsolidation stress and also by changing the shear-strength. But by the same token, they also implicitly trigger or prevent plastic strains. Therefore chemical effects are, even qualitatively, different from thermal effects which essentially decrease the preconsolidation stress or from desaturation effects which increase this preconsolidation stress.

The terms elastic and plastic mass change are to be understood as *reversible* and *irrreversible* reactions, which can proceed in both directions or in a single direction of transfer, in agreement with the respective meanings in mechanics of solids.

We begin by providing a simplified description of experimental data, delineating the key features of the model that will be given an analytical formulation in a second step.

4.1 Experimental Observations

The main features of the typical behaviour of a Na-Montmorillonite that emanates from the oedometric tests of Di Maio [1996] on Ponza bentonite and that we intend to model are summarized below.

Mechanical loading. The specimen is in contact with a large reservoir of constant chemical composition and at atmospheric pressure, so that $p_W \sim 0$. The load is continuously varied, sufficiently slowly however in such a way that chemical equilibrium can be established at the end of each load increment. Therefore, one may assume the chemical potentials of species that can transfer to be equal, at the end of each load increment, to their known counterparts in pore water and in the water contained in the reservoir. Experiments show that the $e - \text{Ln}\,\overline{p}$ curves are nearly straight and converging to a narrow interval void ratio, Figure 2. However, the slopes of the loading and unloading curves decrease as the Na-content of the pore water increases. This trend holds whatever this content, that is from zero Na-content (distilled water) to saturated solutions. The model considers that all the loading curves meet at the common stress $\overline{p}_\lambda$, while all the unloading curves meet at the common stress $\overline{p}_\kappa$. In addition, for the simplified model, $\overline{p}_\kappa = \overline{p}_\lambda$.

Chemical loading: chemical consolidation and swelling. Under constant mechanical conditions, a chemical loading consists in varying the salt content of the pore water. When the latter increases, the void ratio decreases, and this decrease is especially large at low salt content: in fact most of the volume change occurs for Na-concentrations

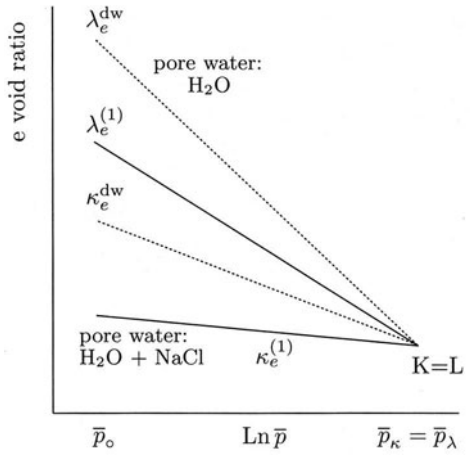

(a) A mechanical loading cycle on a sample in contact with distilled water and on another sample in contact with a saline solution.

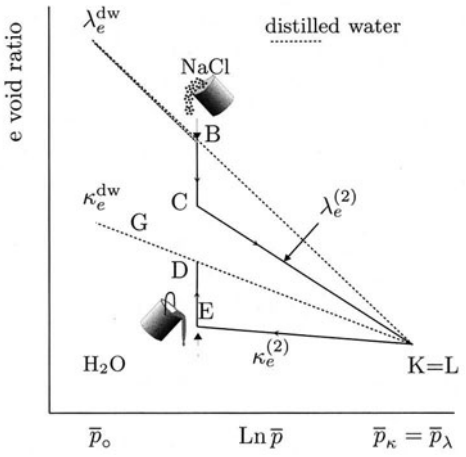

(b) Idealized mixed mechanical and chemical cycle. The purely mechanical test with distilled water as a pore fluid is shown for comparison.

Figure 2 In the simplified modeling, a sample keeps approximatively its chemical composition during a purely mechanical loading cycle and behaves like a Cam-Clay material. Chemical loading and unloading occur in an elastic regime: after a chemical cycle, the final point G is back on the initial curve, corresponding here to a sample in contact with distilled water. Increase of salt fraction up to solution saturation BC leads to *chemical consolidation* while later re-exposure to distilled water ED displays *swelling*.

between 0 and 1 mole/liter. If the Na-content of pore water is decreased, either immediately at constant stress, or after a mechanical loading path, the volume of the sample increases. Notice that these volume changes are in qualitative agreement with the osmotic effect: water desorption/absorption to clay surfaces occurs to equilibrate the salt contents in pore water and clay pockets.

Chemical softening and preconsolidation: a paradox. Mechanical loading at constant chemical composition on a normally consolidated soil corresponds clearly to an elastic-plastic behaviour. The situation is more complex for chemical loadings and unloadings. At relatively low stresses, a chemical loading cycle seems to be practically reversible while the amount of plastic contractancy increases with the applied stress, Figure 7 of Di Maio [1996].

Also, when chemical consolidation performed at a constant low stress is followed by mechanical loading, the slope is the elastic-plastic slope right from the beginning of the stress increase, so that there seems to be almost no chemical preconsolidation. The data available do not allow to unveil if this description is still correct or not at larger stresses. The above interpretation may have to account for the large void ratio of Ponza bentonite. Other tests on Bisaccia clay at smaller void ratios, Figure 7 of Di Maio and

Fenelli [1997], show in fact some chemical preconsolidation. This state of affairs, chemical softening leading to plasticity and chemical consolidation, seems somehow paradoxical. The model developed in Loret et al. [2002] is able to provide an explanation of these phenomena. In fact, we shall proceed with two levels of sophistication:

- a first conceptual model for which chemical loading and unloading are purely elastic, Figure 2-b;
- a more complete model that accounts for chemical softening and preconsolidation. In this model, chemical consolidation has first an elastic-plastic stage, possibly followed by a purely elastic stage, the relative size of the former increasing with the stress level, Figure 3 (a).

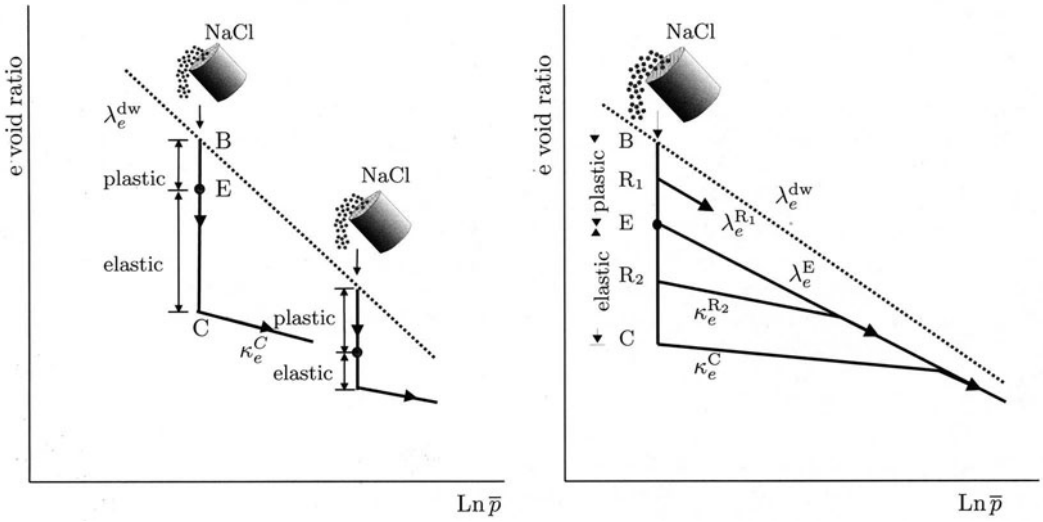

(a) During chemical loading, the relative part of the plastic stage increases with the level of the effective mean-stress. The chemical loading path BC is enlarged on Figure 3 (b).

(b) Mechanical reloading from R_1 in the plastic stage displays a plastic behaviour. Mechanical reloading from R_2 in the elastic stage displays an elastic behaviour: it reveals *chemical consolidation*.

Figure 3 Chemical loading (increase of salt concentration) occurs first plastically and later elastically. Mechanical reloading shows *preconsolidation* in the second range only.

4.2 Incremental Elastic-Plastic Relations

The *generalized strains* are endowed with an elastic part (superimposed symbol ^{el}) and a plastic part (superimposed symbol ^{pl}), namely

$$\boldsymbol{\epsilon} = \boldsymbol{\epsilon}^{\rm el} + \boldsymbol{\epsilon}^{\rm pl}\,, \quad v_W = v_W^{\rm el} + v_W^{\rm pl}\,, \quad m_{wS} = m_{wS}^{\rm el} + m_{wS}^{\rm pl}\,. \tag{4.1}$$

The flow rule. The plastic incremental flow relations are motivated by the mechanical Clausius-Duhem inequality. In fact, let us first substitute $\delta\Psi^{\rm el}$ by $\delta\mathcal{W}^{\rm el} + \delta\Psi_W^{\rm el}$ in that

inequality, and second let us use the strain decomposition (4.1). The resulting dissipation δD_1,

$$\delta D_1 = \boldsymbol{\sigma} : \delta\boldsymbol{\epsilon}^{\rm pl} + p_W \delta v_W^{pl} + \mu_{wS}\, \delta m_{wS}^{\rm pl} \geq 0\,, \tag{4.2}$$

motivates the generalized normality flow rule,

$$\delta\boldsymbol{\epsilon}^{\rm pl} = \delta\Lambda \frac{\partial g}{\partial \boldsymbol{\sigma}}\,, \quad \delta v_W^{\rm pl} = \delta\Lambda \frac{\partial g}{\partial p_W}\,, \quad \delta\, m_{wS}^{\rm pl} = \delta\Lambda \frac{\partial g}{\partial \mu_{wS}}\,, \tag{4.3}$$

where $\delta\Lambda \geq 0$ is the plastic multiplier and $g = g(\boldsymbol{\sigma}, p_W, \mu_{wS})$ the plastic potential. Henceforth, the analysis is restricted to incompressible constituents. The incompressibility constraint, that holds in both the elastic and elastic-plastic regimes, provides the increment of 'plastic' volume change of the fluid phase,

$$\delta v_W^{\rm pl} = \delta\, {\rm tr}\, \boldsymbol{\epsilon}^{\rm pl} - \delta m_{wS}^{\rm pl}/\rho_w - \delta m_{sS}^{\rm pl}/\rho_s\,. \tag{4.4}$$

The dissipation inequality (4.2) becomes

$$\delta D_1 = \bar{\boldsymbol{\sigma}} : \delta\boldsymbol{\epsilon}^{\rm pl} + \overline{\mu}_{wS}\, \delta m_{wS}^{\rm pl} = -\overline{p}\, {\rm tr}\, \delta\boldsymbol{\epsilon}^{\rm pl} + \mathbf{s} : {\rm dev}\, \delta\boldsymbol{\epsilon}^{\rm pl} + \overline{\mu}_{wS}\, \delta m_{wS}^{\rm pl} \geq 0\,. \tag{4.5}$$

If, for simplicity, one restricts the analysis to stress paths with constant Lode angles, that expression motivates the generalized normality flow rule

$${\rm tr}\, \delta\boldsymbol{\epsilon}^{\rm pl} = -\delta\Lambda \frac{\partial g}{\partial \overline{p}}\,, \quad {\rm dev}\, \delta\boldsymbol{\epsilon}^{\rm pl} = \delta\Lambda \frac{\partial g}{\partial q} \frac{3}{2} \frac{\mathbf{s}}{q} \; (\Rightarrow \delta\epsilon_q^{\rm pl} = \delta\Lambda \frac{\partial g}{\partial q}), \; \delta\, m_{wS}^{\rm pl} = \delta\Lambda \frac{\partial g}{\partial \overline{\mu}_{wS}}\,. \tag{4.6}$$

The plastic potential g and consequently the yield function f depend on the state defined by the generalized stress $\{\overline{p}, q, \overline{\mu}_{wS}\}$, and on ${\rm tr}\, \boldsymbol{\epsilon}^{\rm pl}$, which will allow hardening and softening. When plastic loading occurs, i.e. $f \geq 0$, $\delta\Lambda \geq 0$, the incremental constitutive equations can be cast in the elastic-plastic format below,

$$\begin{bmatrix} -\delta\overline{p} \\ \delta q \\ \delta\overline{\mu}_{wS} \end{bmatrix} = \begin{bmatrix} B - \frac{1}{H} g_p f_p & -\frac{1}{H} g_p f_q & B_w - \frac{1}{H} g_p f_w \\ -\frac{1}{H} g_q f_p & 3G - \frac{1}{H} g_q f_q & -\frac{1}{H} g_q f_w \\ B_w - \frac{1}{H} g_w f_p & -\frac{1}{H} g_w f_q & \beta - \frac{1}{H} g_w f_w \end{bmatrix} \begin{bmatrix} \delta{\rm tr}\, \boldsymbol{\epsilon} \\ \delta\epsilon_q \\ \delta m_{wS} \end{bmatrix}. \tag{4.7}$$

In order to specify the yield function and plastic potential, we simply extend the Modified Cam-Clay model, namely

$$f = f(\overline{p}, q, \overline{\mu}_{wS}, {\rm tr}\, \boldsymbol{\epsilon}^{\rm pl}) = \frac{q^2}{M^2\, \overline{p}} + \overline{p} - p_c\,, \tag{4.8}$$

with $M = M(\overline{\mu}_{wS})$ and $p_c = p_c(\overline{\mu}_{wS}, {\rm tr}\, \boldsymbol{\epsilon}^{\rm pl})$. Notice that the major symmetry of the elastic-plastic incremental relations holds iff the flow rule is associative, namely $f = g$.

The general expressions of the coefficients entering in (4.7), namely B, B_w, β, f_p, f_q, f_w, g_p, g_q, g_w, of the plastic modulus $H > 0$ and of the hardening modulus h are reported in Appendix C of Loret et al. [2002]. The calibrations of typical interpolation functions for the now chemically-dependent Cam-Clay coefficients $\lambda(\overline{\mu}_{wS})$ and $M = M(\overline{\mu}_{wS})$, with extreme data corresponding to distilled and salt-saturated pore water, are provided in Appendix D of the above reference.

Mechanical and chemical hardening/softening. To close the model, the influence of absorbed water on the preconsolidation stress p_c is now addressed. The more complete model is described first, as the simplified model will emerge as a particular case.

The consolidation lines[2] have a slope $\lambda(\overline{\mu}_{wS})$ and they converge at the effective mean-stress $\overline{p}_\lambda$,

$$\mathrm{tr}\,\boldsymbol{\epsilon} = \mathrm{tr}\,\boldsymbol{\epsilon}_\lambda - \lambda(\overline{\mu}_{wS})\,\mathrm{Ln}\,\frac{\overline{p}}{\overline{p}_\lambda}\,, \quad \mathrm{tr}\,\boldsymbol{\epsilon}_\lambda = -\lambda^{\mathrm{dw}}\,\mathrm{Ln}\,\frac{\overline{p}_\lambda}{\overline{p}_0}\,, \tag{4.9}$$

while the unloading curves emanate a priori from a different point $\overline{p}_\kappa$, eqn (3.18),

$$\mathrm{tr}\,\boldsymbol{\epsilon}^{\mathrm{el}} = \mathrm{tr}\,\boldsymbol{\epsilon}^{\mathrm{el}}_\kappa - \kappa(x^{\mathrm{el}}_{wS})\,\mathrm{Ln}\,\frac{\overline{p}}{\overline{p}_\kappa}\,, \quad \mathrm{tr}\,\boldsymbol{\epsilon}^{\mathrm{el}}_\kappa = -\kappa^{\mathrm{dw}}\,\mathrm{Ln}\,\frac{\overline{p}_\kappa}{\overline{p}_0}\,, \tag{4.10}$$

with $\lambda^{\mathrm{dw}} = \lambda(\overline{\mu}^{\mathrm{dw}}_{wS})$, $\kappa^{\mathrm{dw}} = \kappa(x^{\mathrm{el,dw}}_{wS})$. Combining (4.9) and (4.10) provides the preconsolidation stress p_c. In order to reduce the chemical dependance of p_c to a single parameter, namely $\overline{\mu}_{wS}$, we introduce a slight qualitative modification, expressing the chemical dependance of κ in terms of $\overline{\mu}_{wS}$, namely $\kappa = \tilde{\kappa}(\overline{\mu}_{wS})$. The resulting preconsolidation stress p_c given implicitly in the following format,

$$(\lambda - \tilde{\kappa})\,\mathrm{Ln}\,\frac{p_c}{\overline{p}_0} = -\mathrm{tr}\,\boldsymbol{\epsilon}^{\mathrm{pl}} + \Big((\lambda - \tilde{\kappa}) - (\lambda^{\mathrm{dw}} - \tilde{\kappa}^{\mathrm{dw}})\Big)\,\mathrm{Ln}\,\frac{\overline{p}_\lambda}{\overline{p}_0} + (\tilde{\kappa} - \tilde{\kappa}^{\mathrm{dw}})\,\mathrm{Ln}\,\frac{\overline{p}_\lambda}{\overline{p}_\kappa}\,, \tag{4.11}$$

with differential

$$(\lambda - \tilde{\kappa})\,\frac{\delta p_c}{p_c} = -\delta\mathrm{tr}\,\boldsymbol{\epsilon}^{\mathrm{pl}} + \mathrm{Ln}\,\frac{\overline{p}_\lambda}{p_c}\,\delta\lambda - \mathrm{Ln}\,\frac{\overline{p}_\kappa}{p_c}\,\delta\tilde{\kappa}\,, \tag{4.12}$$

appears as a generalization of the usual Cam-Clay expression.

Implicit in the above description is the assumption that plasticity occurs first during the chemical loading. This requires that the initial value of the chemical contribution to p_c, eqn (4.12), be negative. When $\overline{p}_\kappa = \overline{p}_\lambda$, this condition implies some relations between the chemical variations of $\tilde{\kappa}$ and λ, namely between the initial slopes κ_3 and λ_3. If, on the other hand, elasticity were occuring first followed by plasticity, then preconsolidation would be excluded at saturation, a situation which is not impossible a priori for some clays but that does not correspond to the experimental behaviour of Bisaccia.

The simplified model without chemical preconsolidation. When the difference $\lambda - \kappa$ is constant and the effective mean-stresses $\overline{p}_\kappa$ and $\overline{p}_\lambda$ are equal, the consolidation stress p_c does not depend on the chemical effects. Chemical loadings and unloadings are then elastic, Figure 2. Furthermore, the elastic-plastic incremental response to isotropic paths simplifies, since then f and g depend on $\overline{\mu}_{wS}$ only through p_c: $\delta q = 0$, $\delta\epsilon_q = 0$, and, for the associative Modified Cam-Clay (4.8),

$$\begin{bmatrix} -\delta\overline{p} \\ \\ \delta\overline{\mu}_{wS} \end{bmatrix} = \frac{1}{\lambda}\begin{bmatrix} B\,\kappa & B_w\,\kappa \\ \\ B_w\,\kappa & \beta\,\lambda - \dfrac{B_w^2}{B}\,(\lambda - \kappa) \end{bmatrix}\begin{bmatrix} \delta\mathrm{tr}\,\boldsymbol{\epsilon} \\ \\ \delta m_{wS} \end{bmatrix}, \tag{4.13}$$

where β, B_w and B are the elastic coefficients appearing in (3.19).

[2]The compressibility coefficients κ and λ refer to the volumetric strains while κ_e and λ_e refer to the void ratio e, e.g. $\kappa_e = (1 + e_o)\,\kappa$, with e_o initial void ratio.

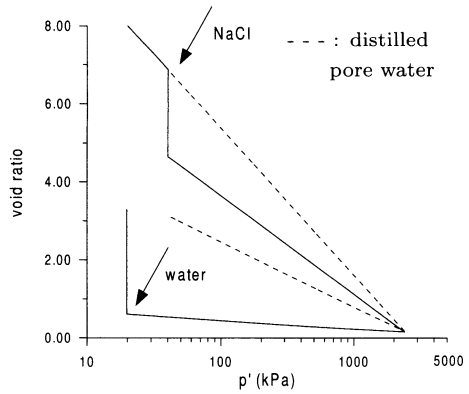

(a) Model simulations, $\kappa_3 = \lambda_3 = 1$.

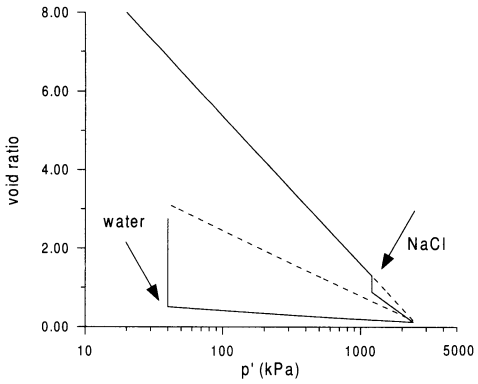

(b) Model simulations, same as (a).

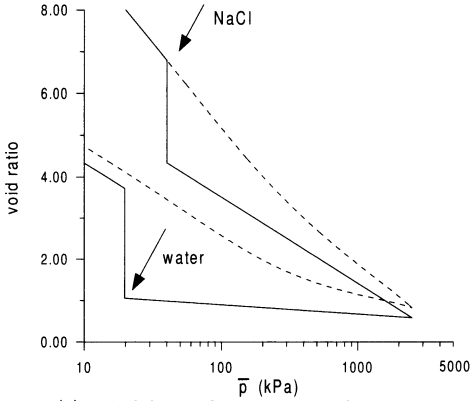

(c) Model simulations, $\kappa_3 = \lambda_3 = 6$.

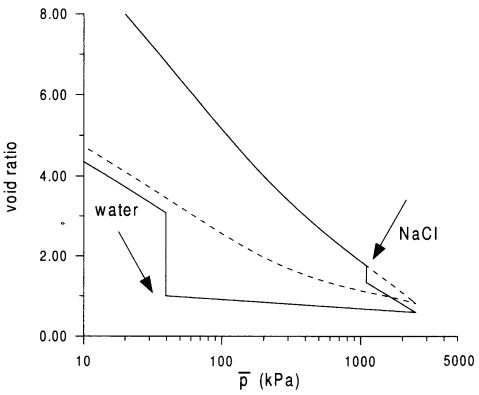

(d) Model simulations, same as (c).

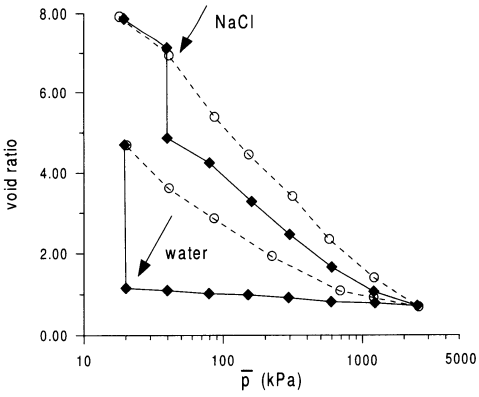

(e) Experimental data.

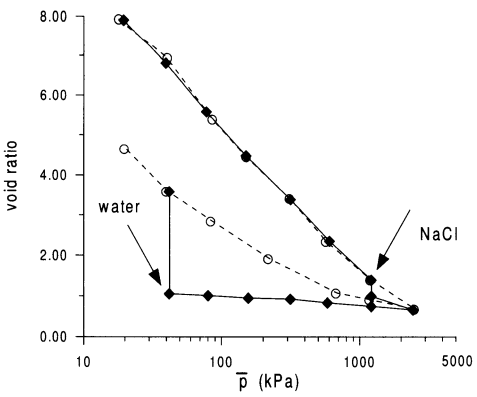

(f) Experimental data.

Figure 4 Comparison of a purely mechanical loading cycle for a specimen in contact with distilled water (dashed curve) with a mixed mechanical-chemical loading cycle for a specimen initially in contact with distilled water (solid curve). The salinity of pore water (with NaCl) is varied between its minimum value (distilled water) and its maximum value corresponding to saturation. Increase of salinity leads to **c**hemical consolidation while decrease of salinity leads to **s**welling. Model simulations (a)-(d) and experimental data (e),(f) on Ponza bentonite by Di Maio [1996], her figure 8.

5 Simulations of Mechanical, Chemical and Mixed Loading Paths

The subsequent simulations aim at quantifying the capacity of the model to capture the main features of the chemo-mechanical coupling that have been described in the previous sections. A key experimental difficulty stems from the time duration necessary to perform chemical loading for which chemical equilibrium can be considered to hold at any time. Only steady states at which the concentrations are deemed uniform throughout the specimen are considered. An order of magnitude of the duration the physico-chemical processes need to reach equilibrium can be grasped from the chemical tests at fixed mean-stresses shown in Di Maio [1996]. They refer to oedometric tests on cylindrical specimens of initial height 20mm. Chemical consolidation appears to reach equilibrium in few days, while swelling is a much slower process, requiring several weeks. The experimental data used here are assumed to represent effectively a succession of equilibrium states, i.e.

$$\overline{\mu}_{wS} = \overline{\mu}_{wW} \quad \Leftrightarrow \quad \mu_{wS} = \mu_{wW} \,. \tag{5.1}$$

The validity of the above assumptions of homogeneity and equilibrium is critically examined in a subsequent finite element analysis, Gajo and Loret [2003].

5.1 Material Parameters

The main source of data that we have used concerns clays of Southern Italy, Di Maio [1996], Di Maio and Fenelli [1997], Di Maio and Onorati [1999]. One of the clays analyzed by these authors, Ponza bentonite, is an almost pure Na-Montmorillonite which fits in the present analysis. Part of the behaviour of Bisaccia clay, a natural marine-origin clay, is also explained when it is exposed to distilled water or saline solutions of NaCl only. Most of the experimental data have been obtained in oedometric tests; however for the sake of simplification, they are used as isotropic tests for parameter calibration and subsequent simulations. The key material parameters of these clays are reported in Table 1. They have been obtained using the calibration methods described in Appendices B and D of Loret et al. [2002]. Each interpolation function for κ, λ and M uses three parameters: the values for distilled water and salt-saturated solution, and a third parameter (κ_3, ...) that indicates the rate of variation of these quantities at the immediate departure from distilled water. Initial conditions are obtained as described in Appendix E of the above reference.

The material behaviour referred to as 'Model Ponza bentonite' has been modeled using a simplified calibration, with the initial slopes κ_3 and λ_3 simply set equal to 1.

The Ponza bentonite and Bisaccia clay have been remolded using distilled water and later exposed to various saline pore solutions. The mixed Bisaccia clay has been obtained by mixing clay particles with a saline solution (1 mole/per liter of NaCl). During mechanical loading, the sample has been assumed to remain in contact with its initial pore solution; however even if it is exposed to distilled water during the mechanical loading, the duration of the triaxial test is so small that a chemical loading which involves a diffusion process has no time to take place.

Table 1. Initial conditions and material parameters

clay type	e_0	p_{c0} (kPa)	κ^{dw}	κ^{sat}	κ_3	$\overline{p}_\kappa$ (kPa)	λ^{dw} M^{dw}	λ^{sat} M^{sat}	λ_3 M_3	$\overline{p}_\lambda$ (kPa)
Ponza bentonite	8.00	20	0.081	0.011	6	1400	0.171	0.101	6	2600
Model Ponza bentonite	8.00	20	0.081	0.011	1	1400	0.180	0.121	1	2600
Bisaccia clay	3.24	10	0.044	0.009	3	700	0.129	0.094	6	700
Mixed Bisaccia clay	2.80	10	0.047	0.012	3	700	0.109 0.401	0.048 0.803	6 6	700

5.2 Simulations of Mechanical and Chemical Loadings and Unloadings

In most of the simulations, the situation where the specimen is in contact with distilled water and undergoes a purely mechanical loading has been used as a reference.

Figure 4 shows a mixed chemo-mechanical loading and unloading cycle. The mechanical load corresponds to the change of effective mean-stress while the chemical load is induced by the change of molar fraction of NaCl in pore water. Due to the elastic-plastic behaviour that takes place during increase of the salinity of pore water (chemical loading), the final void ratio after completion of the loading cycle does not reach exactly the distilled water reference although the gap is quite small (it increases at higher mean-stresses). The consolidation curves are nearly straight in the 'Model Ponza bentonite', Figure 4-(a)-(b). In fact, instead of taking an average slope over the available range of mean-stresses, we have preferred to calibrate the model from the straight part of the mechanical compression. As a consequence, the void ratio at the end of the loading process is slightly smaller than it should. On the other hand, when the chemical dependance of κ and λ is more properly calibrated from the chemical consolidation test in Figure 5, the consolidation curves tend to become less steep at large stresses, in agreement with experimental data.

5.3 Simulations of Chemical Loading Cycles

Simulations of purely chemical loading cycles at given effective mean-stress are displayed in Figure 6: plastic loading that occurs during chemical consolidation leads, at larger mean-stresses, to an increased proportion of plastic contractancy with respect to elastic swelling. This feature of the model is also displayed by experimental data.

Since we are concerned here with pointwise material properties, the time scale along the abscissa for simulated results in Figure 6 is fictitious. In order to obtain the time-evolution of the volume change of the sample, a complete initial and boundary value problem including transfer and diffusion effects has to be considered, Gajo and Loret [2003].

More details of a purely chemical loading are given on Figure 5 which complements Figure 6-(a) and serves to calibrate the initial slopes κ_3 and λ_3. The slope of the chemical consolidation versus salinity change decreases as the pore water departs from distilled water. On the other hand, increase of salinity above 1 M NaCl per liter of solution is practically without effect. Observe that the experimental slope of the chemical consolidation curve is larger than that of the swelling curve, $\lambda_3 > \kappa_3$. Although the experimental

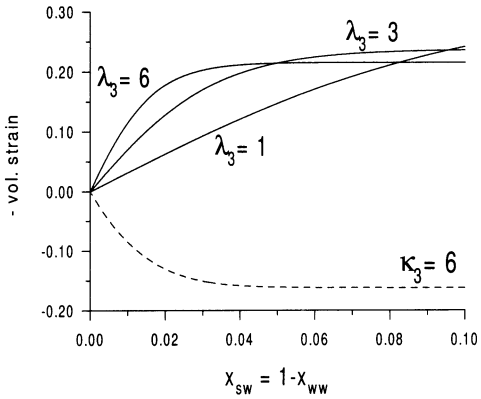

(a) Model simulations with different initial slopes κ_3 and λ_3.

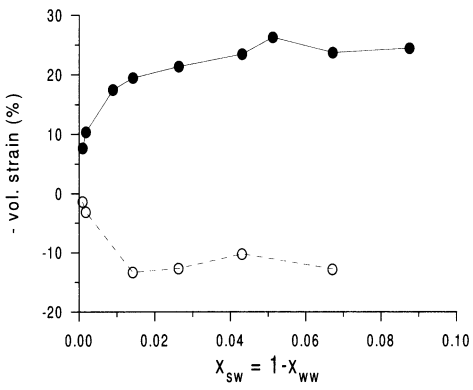

(b) Experimental data, courtesy C. Di Maio.

Figure 5 Chemical consolidation and swelling of Ponza bentonite starting from distilled water up to NaCl saturation at constant mechanical load $\overline{p} = 80\,\text{kPa}$. The essential of the contractancy occurs experimentally for NaCl concentrations smaller than 1 mole per liter, that is for molar fractions x_{sW} of NaCl inferior to 0.018. Each of the experimental points corresponds to a single experiment.

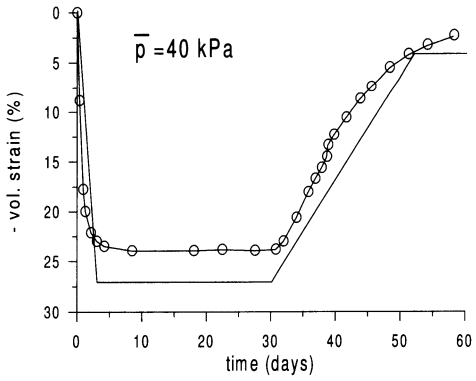

(a)

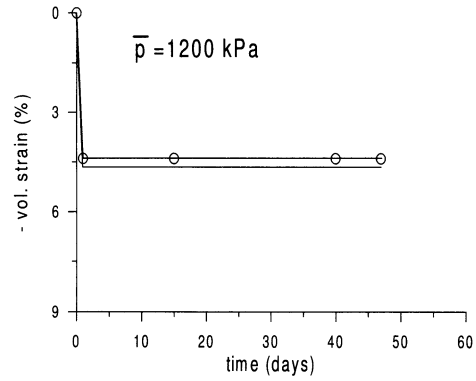

(b)

Figure 6 Chemical cycle at constant effective mean-stress. Model simulations (solid curve) versus experiments by Di Maio [1996], her figure 7, (symbols). In the model simulations, the time scale is purely fictitious. Increase of salinity of the pore solution by addition of NaCl up to saturation implies a plastic consolidation whose relative amount increases with the effective mean-stress.

loading/unloading curves are not available for Bisaccia clay, the same type of inequality is expected to lead, for that clay, to chemical preconsolidation, Figure 7.

5.4 Chemical Preconsolidation

Tests on Bisaccia clay remolded with distilled water have been partially calibrated from the purely mechanical loading cycles shown in Figure 7 corresponding to distilled and saturated pore solutions. It seems that Bisaccia clay displays a tendency to higher chemical preconsolidation than Ponza bentonite, compare the slopes at the resuming of mechanical loading on Figure 4-(e) and 7-(b). Even if $\overline{p}_\kappa = \overline{p}_\lambda$, the model can capture this feature, if $\lambda - \tilde{\kappa}$ is not a constant at varying chemical composition, eqn (4.12). Since $\kappa^{\mathrm{dw}} - \kappa^{\mathrm{sat}}$ is equal to $\lambda^{\mathrm{dw}} - \lambda^{\mathrm{sat}}$, Table 1, setting $\kappa_3 = \lambda_3$ will not produce preconsolidation, case a) in Figure 7. On the other hand, an increasing difference $\lambda_3 - \kappa_3$ implies an increasing preconsolidation, cases b) and c) in Figure 7. Indeed, the variation of p_c due to chemical effects is negative for pore solutions close to distilled water, as can be checked in eqn (4.12) with the material parameters given in Table 1. Hence plasticity occurs right at the beginning of chemical consolidation up to the point, noted E in Figure 3, where the sign of the derivative of chemical contribution to p_c changes. There the competition between the negative chemical effect, i.e. softening, and positive plastic effect, i.e. hardening, ceases because the latter is no longer required as the chemical effect becomes positive.

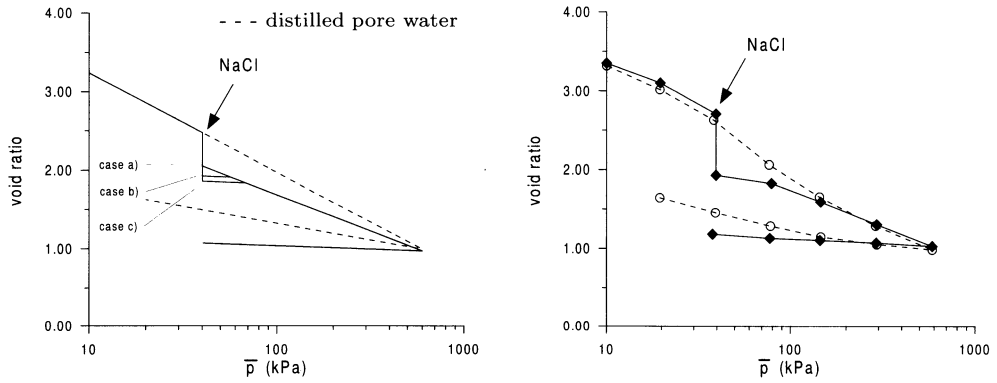

(a) Model simulations with different slopes.

(b) Experimental data.

Figure 7 Mixed chemo-mechanical loading on Bisaccia clay reconstituted with distilled water. The dashed line corresponds to distilled pore water and the solid line to a NaCl saturated pore water. Experimental data by Di Maio and Fenelli [1997], their figure 7-a. In the numerical simulations, $\kappa_3 = 3$ while three values of λ_3 are tested: a) λ_3=3; b) λ_3=6; c) λ_3=9 (see text).

5.5 Drained and Undrained Triaxial Tests

In order to clearly demonstrate that the model is not restricted to a one-dimensional setting and that it is embodied in a three-dimensional framework, normally consolidated and overconsolidated drained and undrained triaxial paths in the cylindrical apparatus have been simulated, Figures 8 and 9. The parameters are partly calibrated from the data

corresponding to mechanical loadings on Bisaccia clay remolded with a saline pore solution. The tests indicate a very strong influence of the pore water chemical composition on the friction angle φ, i.e. on the generalized Cam-Clay coefficient M equal for triaxial compression to $6\sin\varphi/(3-\sin\varphi)$: a saline pore water implies water desorption and thus increases the value of the friction angle, as already noted by Mesri and Olson [1970].

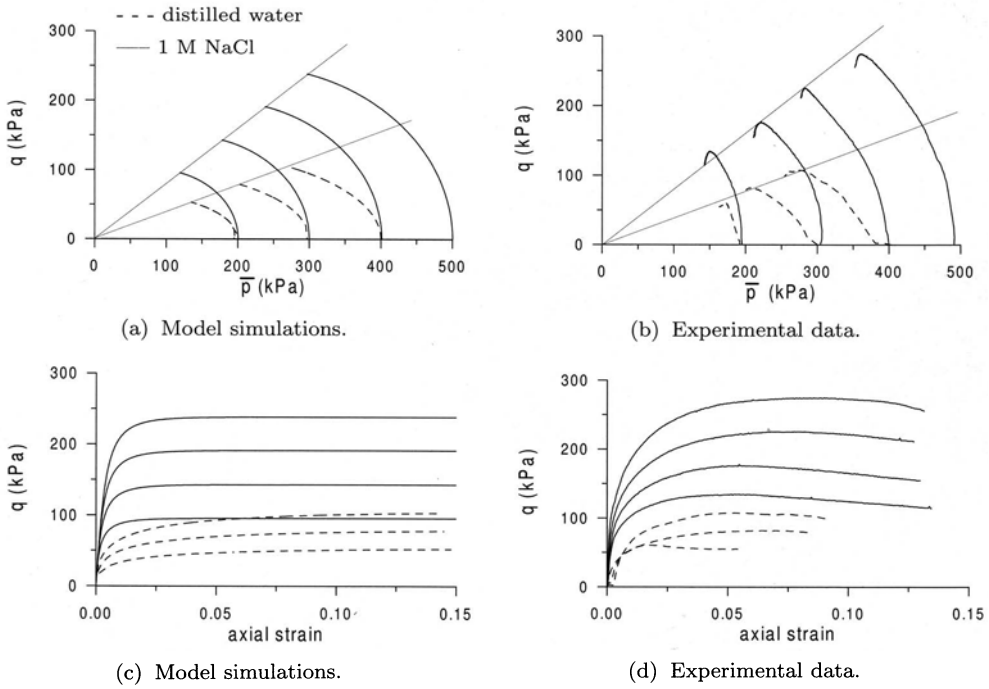

(a) Model simulations. (b) Experimental data.

(c) Model simulations. (d) Experimental data.

Figure 8 Undrained tests with different initial effective mean-stresses on normally consolidated Bisaccia clay obtained by mixing clay particles with distilled water (dashed curves) and with a 1 molar NaCl solution (solid curves). The specimen mixed with a saline pore water has an increased strength (friction angle $\varphi^{\mathrm{sat}} = 20.7°$) with respect to the specimen with distilled pore water (friction angle $\varphi^{\mathrm{dw}} = 10.8°$). Experimental data (b) by Di Maio and Onorati [1999], their figure 9, and (d) courtesy C. Di Maio.

6 Concluding Remarks

The model developed in this paper is embedded in a general three-dimensional framework that can be viewed as extending the classic elastic-plastic framework for porous media to account for chemo-mechanical couplings. Therefore, it can capitalize upon the available theoretical and computational developments in view of solving initial and boundary value problems in a multi-dimensional setting. The local inter-phase mass transfer phenomena have to be accounted for in addition to diffusion. Although analyses of instrumented in-situ cases are the ultimate goal, it is necessary in a first step to simulate laboratory

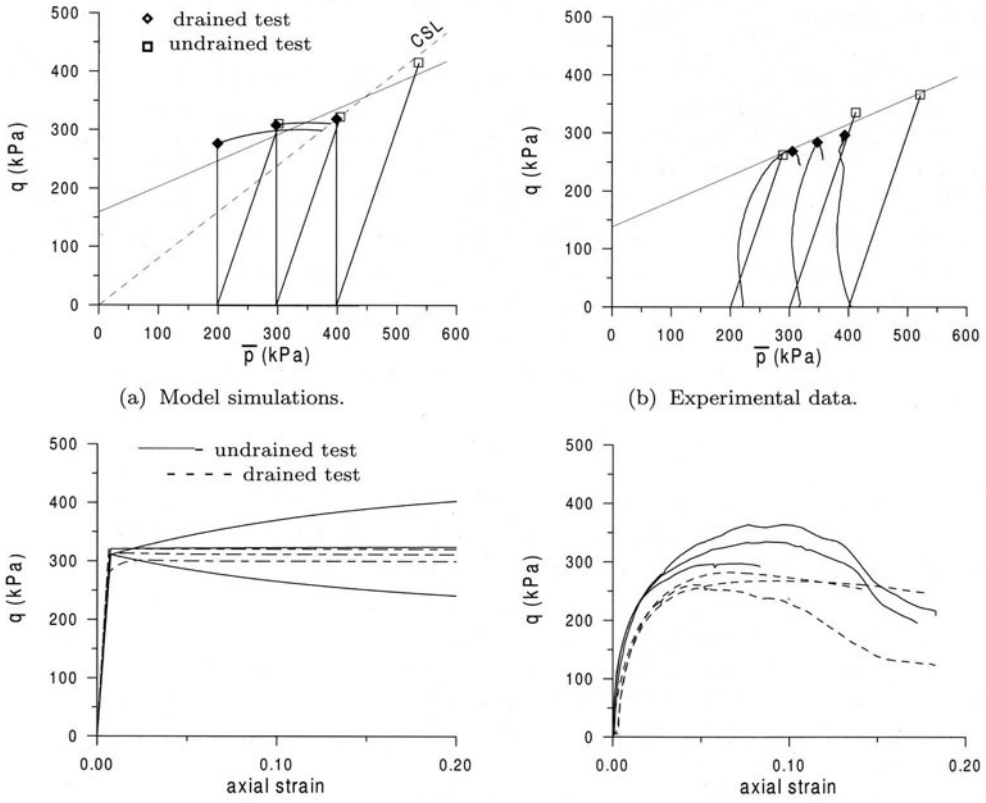

Figure 9 Drained and undrained triaxial tests with different initial effective mean-stresses on Bisaccia clay overconsolidated to 800 kPa and obtained by mixing clay particles with a 1M NaCl solution. The friction angle is $\varphi^{sat} = 20.7°$ as in the previous plot. Experimental data (b) by Di Maio and Onorati [1999], their figure 11, and (d) courtesy C. Di Maio.

tests to check the validity of certain assumptions that have been made to interpret the experimental results, e.g. assumption of chemical equilibrium and homogeneity of the chemical fields throughout the sample at the times where measurements are made. Such a companion analysis is performed in a subsequent chapter.

An extension of the framework is necessary to analyze natural clays where several cations co-exist. The electrolytic nature of the solutions requires to account for electroneutrality and replace chemical potentials by electrochemical potentials. This subject is examined in the next chapter, with finite element analysis of boundary value problems in the last chapter. On the other hand, the present formulation is thought to constitute at least a useful tentative framework to analyze the behaviour of clays submitted to non-ionic solutes, such as organic pollutants.

Bibliography

Bolt, G.H. (1956). Physico-chemical analysis of the compressibility of pure clays. *Géotechnique*, 6(2), 86-93.

Di Maio, C. (1996). Exposure of bentonite to salt solution: osmotic and mechanical effects. *Géotechnique*, 46(4), 695-707.

Di Maio, C. and G. Fenelli (1997). Influenza delle interazioni chimico-fisiche sulla deformabilità di alcuni terreni argillosi. *Rivista Italiana di Geotecnica*, 1, 695-707.

Di Maio, C. and R. Onorati (1999). Prove di laboratorio: influenza di composizione del liquido di cella. *Rendiconti del XX Convegno Nazionale di Geotecnica, Parma*, 87-94.

Gajo, A. and B. Loret (2003). Finite element simulations of chemo-mechanical coupling in elastic-plastic homoionic expansive clays. *Computer Methods in Applied Mechanics and Engineering*, 192(31-32), 3489-3530.

Haase, R. (1990). Thermodynamics of Irreversible Processes. Dover Publications, New York.

Heidug, W.K. and S.-W. Wong (1996). Hydration swelling of water-absorbing rocks: a constitutive model. *Int. J. Num. Anal. Meth. Geomechanics*, 20, 402-430.

Loret, B. (1985), On the choice of elastic parameters for sand, *Int. J. Num. Anal. Meth. Geomechanics*, 9, 285-292.

Loret, B. and O. Harireche (1991). Acceleration waves, flutter instabilities and stationary discontinuities in inelastic porous media, *J. Mechanics Physics Solids*, 39(5), 569-606.

Loret, B., Rizzi, E. and F. Zerfa (2001). Relations between drained and undrained moduli in anisotropic elastic fluid-saturated porous media, *J. Mechanics Physics Solids*, 49(11), 2593-2619.

Loret, B., Hueckel, T. and A. Gajo (2002). Chemo-mechanical coupling in saturated porous media: elastic-plastic behaviour of homoionic expansive clays. *Int. J. Solids and Structures*, 39, 2773-2806.

Loret, B. and F.S. Simões (2003). Articular cartilage with intra- and extrafibrillar waters. A chemo-mechanical model. *Mechanics of Materials*, accepted for publication.

Mesri, G. and R.E. Olson (1970). Shear-strength of Montmorillonite. *Géotechnique*, 20(3), 261-270.

Constitutive Equations for Heteroionic Clays

Alessandro Gajo [†] and Benjamin Loret [*]

[†] Dipartimento di Ingegneria Meccanica e Strutturale, Università di Trento, Trento, Italia
[*] Laboratoire Sols, Solides, Structures, Institut National Polytechnique de Grenoble, France

Abstract Chemically active saturated clays containing several cations are considered in a two-phase framework. The solid phase contains the negatively charged clay particles, absorbed water and ions. The fluid phase contains free water and ions. Electroneutrality is ensured in both phases. Water and ions can transfer between the two phases. Emphasis is laid on the electro-chemo-mechanical constitutive equations in an elastic-plastic setting. Elastic chemo-mechanical coupling is introduced through a potential, in such a way that the tangent elastic stiffness is symmetric. The elastic-plastic behaviour aims at reproducing typical experimental phenomena observed on natural clays during chemical and mixed chemo-mechanical loadings, including chemical consolidation and swelling already described in the simpler context of Na-Montmorillonite clays. Ionic replacements, e.g. Na^+ by K^+, is accompanied with important, reversible volume changes, in agreement with experimental data.

1 The general setting

Emphasis is laid in this chapter on chemically induced swelling and collapse of heteroionic clays, which constitute the majority of natural clays and a great part of engineered clays. In the previous chapter, we have addressed swelling of homoionic clays: these clays rarely occur in natural conditions, but they can be manufactured for specific industrial applications. Homoionic clays serve also as a good material model for preliminary studies.

The microstructure, and especially the organization of water in the different pore spaces, is very much the same in both homoionic and heteroionic clays; it has been detailed in Loret et al. [2002]. In both cases, swelling arises as a result of chemical or electrochemical disequilibrium of a structural unit comprising:

- an amorphous substructure of quasi-crystals (clusters) of the clay mineral platelets;
- absorbed water within the clusters and adsorbed water enveloping the substructure;
- the free pore water;
- and, critically, ions in the interplatelet space and in the free water.

The amorphous substructure of parallel platelets is conceptualized as being wrapped in a semi-permeable membrane. This membrane serves as a gate-keeper for ion and water transfer between the free pore water and the clusters including the absorbed water. Unlike in biological tissues, such a membrane is not a physical object, rather it is a separation across which the two spaces exchange species at a specific rate.

2 Chemo-Elasticity

The elastic constitutive equations are introduced in three ways, each one designed to highlight a specific idea. In contrast to the formal presentation of Section 2.2, the electroneutrality condition of the solid phase is accounted for from the start in Sections 2.3 and 2.4. The underlying key idea is that the mechanical effects of the absorbed cations Na^+ are quite different from the effects of the absorbed cations K^+. Therefore, their mass-contents, or molar fractions, have to be known at each time step.

2.1 The Gibbs-Duhem relation

The chemical potentials that enter the free energy

$$\delta\Psi = \boldsymbol{\sigma} : \delta\boldsymbol{\epsilon} + \sum_{k,K} \mu^{(\mathrm{ec})}_{kK}\, \delta m_{kK}\,, \tag{2.1}$$

are those associated to the species whose mass-content varies, that is all species of the fluid phase and the species of the solid phase that can transfer to the fluid phase,

$$m^{(\mathrm{M})}_k\, \mu^{\mathrm{ec}}_{kK} = g^{\mathrm{ec}}_{kK} = g^0_{kK} + \int v^{(\mathrm{M})}_k\, dp'_{kK} + RT\,\mathrm{Ln}\, x_{kK} + \zeta_k\, \mathrm{F}\, \phi^K\,, \tag{2.2}$$

with $p_{kW} = p_W$ for $k \in W$, and p_{kS} to be specified by constitutive equations for $k \in S$. The electrical work vanishes in (2.1) as a consequence of electroneutrality in each phase. Note that a single electroneutrality condition for the whole mixture would have the same implication in (2.1).

For an electrically neutral fluid phase, the Gibbs-Duhem relation provides the fluid pressure p_W in terms of the chemical potentials of the species μ_{kW}, $k \in W$, namely Haase [1990], chap. 1-13,

$$\delta p_W = \sum_{k\in W} c_{kW}\, \delta\mu^{\mathrm{ec}}_{kW} - \frac{I_{\mathrm{e}W}}{n_W}\, \delta\phi^W = \sum_{k\in W} c_{kW}\, \delta\mu_{kW}\,. \tag{2.3}$$

Use has been made of the electroneutrality of the fluid phase that implies the electrical work and the electrical density $I_{\mathrm{e}W}$ to vanish.

In order to define the mechanical constitutive equations of the porous medium, we will isolate the chemical effects in pore water. Proceeding exactly as for homoionic clays, we obtain the chemical energy of the fluid phase per unit initial volume of porous medium Ψ_W in explicit and differential forms as,

$$\Psi_W = \sum_{k\in W} \mu_{kW}\, m_{kW} - p_W\, v_W\,, \quad \delta\Psi_W = \sum_{k\in W} \mu_{kW}\, \delta m_{kW} - p_W\, \delta v_W\,. \tag{2.4}$$

2.2 A formal presentation

In this formal presentation, the use of the electroneutrality condition in the solid phase is deferred. All the transferable mass-contents appear on an equal footing in the free energy. Electroneutrality is finally introduced as a constraint and the electrical field appears as a lagrangian.

The elastic potential. The elastic energy of the porous medium per unit initial volume $\mathcal{W}^{\rm el} = \Psi^{\rm el} - \Psi_W$ can be viewed as the elastic energy of the porous medium for which the chemical effects in the fluid phase are disregarded. This energy depends on the restricted set of independent variables $\{\boldsymbol{\epsilon}^{\rm el}, v_W^{\rm el}, \{m_{kS}^{\rm el},\ k \in S^{\leftrightarrow}\}\}$. Indeed, with the work definition (2.1), electroneutrality of both phases and the Gibbs-Duhem relation (2.3), the incremental form of the energy $\mathcal{W}^{\rm el}$ simplifies to

$$\delta\mathcal{W}^{\rm el} = \boldsymbol{\sigma} : \delta\boldsymbol{\epsilon}^{\rm el} + p_W\, \delta v_W^{\rm el} + \sum_{k\in S^{\leftrightarrow}} \mu_{kS}\, \delta m_{kS}^{\rm el}\,. \tag{2.5}$$

Thus constitutive equations for the dependent variables $\{\boldsymbol{\sigma}, p_W, \{\mu_{kS},\ k \in S^{\leftrightarrow}\}\}$ in terms of the variables $\{\boldsymbol{\epsilon}^{\rm el}, v_W^{\rm el}, \{m_{kS}^{\rm el},\ k \in S^{\leftrightarrow}\}\}$ are obtained in the format:

$$\boldsymbol{\sigma} = \frac{\partial \mathcal{W}^{\rm el}}{\partial \boldsymbol{\epsilon}^{\rm el}}\,, \quad p_W = \frac{\partial \mathcal{W}^{\rm el}}{\partial v_W^{\rm el}}\,, \quad \mu_{kS} = \frac{\partial \mathcal{W}^{\rm el}}{\partial m_{kS}^{\rm el}}\,,\ k \in S^{\leftrightarrow}. \tag{2.6}$$

Alternative choices in the sets of independent and dependent variables can be postulated by partial or total Legendre transforms of $\mathcal{W}^{\rm el}$.

Incompressible species. In the sequel, we will restrict the formulation by assuming that all species are incompressible. Moreover we require the incompressibility condition to hold in both the elastic and elastic-plastic regimes. Then the increment of elastic fluid volume content is given by the incompressibility condition in terms of $\{\boldsymbol{\epsilon}^{\rm el}, \{m_{kS}^{\rm el},\ k \in S^{\leftrightarrow}\}\}$ that we shall adopt as independent variables. Hence, $\delta\mathcal{W}^{\rm el}$, eqn (2.5), becomes

$$\delta\mathcal{W}^{\rm el} = \bar{\boldsymbol{\sigma}} : \delta\boldsymbol{\epsilon}^{\rm el} + \sum_{k\in S^{\leftrightarrow}} \overline{\mu}_{kS}\, \delta m_{kS}^{\rm el}\,, \tag{2.7}$$

in terms of Terzaghi's effective stress $\bar{\boldsymbol{\sigma}}$ and of the effective chemical potential $\overline{\mu}_{wS}$,

$$\bar{\boldsymbol{\sigma}} = \boldsymbol{\sigma} + p_W\, \mathbf{I}\,, \quad \overline{\mu}_{kS} = \mu_{kS} - \frac{p_W}{\rho_w}\,,\ k \in S^{\leftrightarrow}. \tag{2.8}$$

The mass transfer is assumed not to alter the density of water. Then the transfer equations considered in later chapters may be phrased identically in terms of chemical potentials or in terms of effective chemical potentials. In particular, the equilibrium of the chemical potentials, i.e. $\mu_{kS} = \mu_{kW}$, $k \in S^{\leftrightarrow}$, is equivalent to the equilibrium of the effective chemical potentials, i.e. $\overline{\mu}_{kS} = \overline{\mu}_{kW}$. Note also that continuous equilibrium does not hinder transfer of matter.

The constitutive relations take now the form,

$$\bar{\boldsymbol{\sigma}} = \frac{\partial \mathcal{W}^{\rm el}}{\partial \boldsymbol{\epsilon}^{\rm el}}\,, \quad \overline{\mu}_{kS} = \frac{\partial \mathcal{W}^{\rm el}}{\partial m_{kS}^{\rm el}}\,,\ k \in S^{\leftrightarrow}\,. \tag{2.9}$$

Logarithmic Hyperelasticity. In order to introduce logarithmic elasticity, the procedure developed for homoionic clays is followed, and a mixed form is introduced through

the Legendre transform $\mathcal{W}_M^{\rm el}(\bar{\boldsymbol{\sigma}},\, \{m_{kS}^{\rm el},\ k \in S^{\leftrightarrow}\})$ of the energy $\mathcal{W}^{\rm el}(\boldsymbol{\epsilon},\, \{m_{kS}^{\rm el},\ k \in S^{\leftrightarrow}\})$. The constitutive relations then become

$$\boldsymbol{\epsilon}^{\rm el} = \frac{\partial \mathcal{W}_M^{\rm el}}{\partial \bar{\boldsymbol{\sigma}}}\,, \quad \overline{\mu}_{kS} = -\frac{\partial \mathcal{W}_M^{\rm el}}{\partial m_{kS}^{\rm el}}\,,\ k \in S^{\leftrightarrow}\,. \tag{2.10}$$

The electro-chemical potentials are finally re-introduced together with the electroneutrality condition in the solid phase, in order to produce a symmetric constitutive tangent matrix,

$$\begin{bmatrix} \delta\bar{\boldsymbol{\sigma}} \\ \delta\overline{\mu}_{wS}^{\rm ec} \\ \delta\overline{\mu}_{{\rm Na}S}^{\rm ec} \\ \delta\overline{\mu}_{{\rm K}S}^{\rm ec} \\ \delta\overline{\mu}_{{\rm Cl}S}^{\rm ec} \\ 0 \end{bmatrix} = \begin{bmatrix} & & & & & \mathbf{0} \\ & & & & & 0 \\ & & \mathrm{X} & & & \xi_{\rm Na} \\ & & & & & \xi_{\rm K} \\ & & & & & \xi_{\rm Cl} \\ \mathbf{0} & 0 & \xi_{\rm Na} & \xi_{\rm K} & \xi_{\rm Cl} & 0 \end{bmatrix} \begin{bmatrix} \delta\boldsymbol{\epsilon}^{\rm el} \\ \delta m_{wS}^{\rm el} \\ \delta m_{{\rm Na}S}^{\rm el} \\ \delta m_{{\rm K}S}^{\rm el} \\ \delta m_{{\rm Cl}S}^{\rm el} \\ \delta\phi^S \end{bmatrix}, \tag{2.11}$$

with the notation $\xi_k \equiv \zeta_k\, {\rm F}/m_k^{\rm (M)}\,,\ k \in S$.

2.3 A Method Using the Chemical Potentials of the Salts

As a more direct approach, the electroneutrality condition in the solid phase is now introduced in the energy expression so as to eliminates the mass-contents of chloride anions of the set of independent variables. The energy is then phrased in terms of the chemical potentials of salts s_1=NaCl, s_2=KCl: they are defined in the Section 2.4 of the Chapter 'Multi-Phase Multi-Species Mixtures'. For incompressible constituents, the constitutive equations for *the dependent variables* $\{\bar{\boldsymbol{\sigma}},\, \overline{\mu}_{wS},\, \overline{\mu}_{{\rm s}_1 S},\, \overline{\mu}_{{\rm s}_2 S}\}$ in terms of *the independent variables* $\{\boldsymbol{\epsilon}^{\rm el},\, m_{wS}^{\rm el},\, m_{{\rm Na}S}^{\rm el},\, m_{{\rm K}S}^{\rm el}\}$ are obtained in the format:

$$\boldsymbol{\epsilon}^{\rm el} = \frac{\partial \mathcal{W}_M^{\rm el}}{\partial \bar{\boldsymbol{\sigma}}}\,, \quad \overline{\mu}_{wS} = \frac{\partial \mathcal{W}_M^{\rm el}}{\partial m_{wS}^{\rm el}}\,, \quad \overline{\mu}_{{\rm s}_1 S} = \frac{\partial \mathcal{W}_M^{\rm el}}{\partial m_{{\rm Na}S}^{\rm el}}\,, \quad \overline{\mu}_{{\rm s}_2 S} = \frac{\partial \mathcal{W}_M^{\rm el}}{\partial m_{{\rm K}S}^{\rm el}}\,. \tag{2.12}$$

2.4 A Model Viewing Mass Transfer as a Physico-Chemical Reaction

The mass transfer between the two phases is now viewed as restricting the number of the independent variables, beyond the electroneutrality condition.

Basics of chemical reactions. Chemical equilibrium between two thermodynamic states is defined by a vanishing variation of *free enthalpy* ΔG [1] If the free enthalpy of the

[1] Basic thermodynamical measures of the state of a system with pressure p and volume V: internal energy $U = U(V,S) \Rightarrow dU = p\,dV + T\,dS$; free energy $E = E(V,T) = U - T\,S \Rightarrow dE = p\,dV - S\,dT$; enthalpy $H = H(p,S) = U - p\,V \Rightarrow dH = -V\,dp + T\,dS$; free enthalpy $G = G(p,T) = H - T\,S \Rightarrow dG = -V\,dp - S\,dT$; and for a reversible process $dQ = T\,dS$ is the heat exchange.

final state is lower than initially, $\Delta G < 0$, the reaction occurs *spontaneously* and, based on our admiration for ancient greeks, it is said exergonic. Otherwise, i.e. if $\Delta G > 0$, some form of energy should be provided for the reaction to occur and the reaction is said endergonic. In thermodynamics textbooks, the free enthalpy G is also called chemical potential because it is the chemical work that a substance can provide and it is noted μ or g, see Chapter 'Multi-Phase Multi-Species Mixtures'.

The variation of free enthalpy ΔG, at constant temperature T, is equal to $\Delta H - T\,\Delta S$, where ΔH is the variation of *enthalpy* and ΔS the variation of *entropy*. Enthalpy is a measure of heat content. Depending whether the reaction occurs with $\Delta H < 0$ or $\Delta H > 0$, it is said exothermic or endothermic. For example, the reaction $H_2{+}O_2/2{\rightarrow}H_2O$ is exothermic and $\Delta H = -287\,\mathrm{kJ/mole}$. Also, when one puts NaCl in a reservoir filled with water, the reservoir cools because it has given heat for the dissolution to occur, $\Delta H = +3.8\,\mathrm{kJ/mole}$.

Entropy is a measure of *molecular disorder*. It is larger for systems whose order is low. If during a reaction the order increases, then the associated $\Delta S < 0$ is negative. For example, the gas mixture of H_2 and O_2 has a larger entropy than water H_2O and the reaction $H_2{+}O_2/2{\rightarrow}H_2O$ has $-T\,\Delta S = 49\,\mathrm{kJ/mole}$ at $T{=}20\,^\circ\mathrm{C}$. Let us consider again the dissolution of NaCl in water. NaCl initially cristallized has a high order of organization while, when dissolved in water, the ions Na^+ and Cl^- move randomly. Therefore dissolution of NaCl in water is associated to $\Delta S > 0$. In figures, at ambient temperature, $-T\,\Delta S = -12.8\,\mathrm{kJ/mole}$.

This example of dissolution of salt in water is a bit peculiar because it is exergonic, i.e. spontaneous, $\Delta G = -9\,\mathrm{kJ/mole} < 0$, while endothermic, $\Delta H = +3.8\,\mathrm{kJ/mole} > 0$. Therefore, even if quite often $\Delta G \sim \Delta H$, *an endothermic reaction may occur spontaneously if it is (sufficiently) entropy-driven.*

Cation exchange as a chemical reaction. We now consider that the cations and adsorbed water do not affect the mechanical properties independently. We will employ constraint resulting from the chemical reaction analysis to express these relations of dependence.

At pH greater than or equal to 7, the clay platelets are negatively charged, and the amount of chlorine anions in the solid phase is certainly small. So, we may assume that the membrane surrounding clay clusters is impermeable to chloride anions, or even that the number of moles of chloride anions is negligible, $N_{\mathrm{Cl}S} \simeq 0$. Therefore, as a consequence of electroneutrality, the total number of exchangeable cations N_{ex} in the solid phase [2] turns out to be constant,

$$N^{(\mathrm{el})}_{\mathrm{Na}S} + N^{(\mathrm{el})}_{\mathrm{K}S} = N_{\mathrm{ex}} \equiv -\zeta_c\, N_{cS} = \text{ constant} > 0\,. \tag{2.13}$$

The superscript $^{(\mathrm{el})}$ is intended to imply that the relation is assumed to hold in terms of total numbers of cations, as well as in terms of the reversible change in their number. Consequently, a single variable is sufficient to describe the variation of the number of cations in the solid phase. Indeed, the cation exchange, combined with the mechanism

[2] In fact, in the present analysis, N_{ex} can be considered either as the total number of cations in the solid phase or as the number of exchangeable cations.

of water absorption into/desorption from the clay crystal, may be viewed as a chemical reaction between solid and fluid phases,

$$\overbrace{K^+}^{\text{fluid phase}} + \underbrace{Na\,X\cdot\, n\,H_2O}_{\text{solid phase}} \rightleftharpoons \underbrace{K\,X\cdot m\,H_2O}_{\text{solid phase}} + \overbrace{Na^+}^{\text{fluid phase}} + \overbrace{(n\text{-}m)\,H_2O}^{\text{fluid phase}}, \tag{2.14}$$

involving

- the cations in pore water Na^+ and K^+;
- the exchange complex $Na\,X\cdot n\,H_2O$;
- absorbed or desorbed water, and
- n and m, stoichiometric numbers of moles of interlayer water hydrating a cation.

Thus, the difference n - m corresponds to the number of moles of water (per mole of clay) removed from/added to the solid phase as a result of the cation exchange: it introduces a second variable that describes the water content of the phases. We shall assume that there are no free (non-hydrating) water molecules in the interlayer before and after the reaction. Also, we assume that external surfaces hydrate cations with the same proportion. Thus, the difference n-m can be directly expressed in terms of a variable of water content of the phases.

According to (2.14), the total and elastic changes in the numbers of moles of cations in the solid and fluid phases are linked by the following relations,

$$\delta N_{\mathrm{Na}S}^{(\mathrm{el})} = -\delta N_{\mathrm{K}S}^{(\mathrm{el})} = -\delta N_{\mathrm{Na}W}^{\mathrm{reactive}} = \delta N_{\mathrm{K}W}^{\mathrm{reactive}}. \tag{2.15}$$

Consequences for the relations between changes of (reversible) masses follow from the relation $m_{kK}^{(\mathrm{el})}{=}m_k^{(\mathrm{M})}/V_0\, N_{kK}^{(\mathrm{el})}$. The molar fractions of absorbed cations and water can be expressed in terms of the numbers of moles of cations Na^+ and of water,

$$\frac{x_{\mathrm{Na}S}^{(\mathrm{el})}}{N_{\mathrm{Na}S}^{(\mathrm{el})}} = \frac{x_{wS}^{(\mathrm{el})}}{N_{wS}^{(\mathrm{el})}} = (1-\zeta_c)\, N_{cS} + N_{wS}^{(\mathrm{el})}. \tag{2.16}$$

Notice that $x_{wS}^{(\mathrm{el})}$ depends on a single variable, namely on $N_{wS}^{(\mathrm{el})}$.

Enthalpies of hydration and dehydration and the equilibrium constant. We shall consider in particular the smectite defined by the complex $X^- = Al_3\,Si_3O_{10}(OH)_2{}^-$ for which we have specific data available. If we restrict attention to the reaction of cation exchange, setting aside the absorption/desorption of water, the so-called equilibrium constant K_{eq} can be shown to be equal to the product of two terms, the first one coming from the mechanical contribution to the chemical potentials, the second one from the contribution due to the free enthalpies of hydration/dehydration,

$$\mathrm{K_{eq}} = \frac{x_{\mathrm{K}S}^{\mathrm{el}}}{x_{\mathrm{Na}S}^{\mathrm{el}}}\,\frac{x_{\mathrm{Na}W}}{x_{\mathrm{K}W}} = \exp\left(-\frac{\Delta g^{\mathrm{mech}}}{RT}\right) \times \exp\left(-\frac{\Delta g^{\mathrm{hydr}}}{RT}\right). \tag{2.17}$$

To prove this relation, it is convenient to choose the ion number, or mass content, of the sodium as sole independent variable. Let us start from the incremental work done by

the reversible exchange of the number of the cations. In this sum, all the incremental ion numbers can be expressed in terms of $\delta N^{\rm el}_{{\rm Na}S}$, or $\delta m^{\rm el}_{{\rm Na}S}$, in view of (2.15),

$$\sum_{k\in S^+,\,K} g_{kK}\,\delta N^{\rm el}_{kK} = (\overline{A}_S - \overline{A}_W)\,\delta m^{\rm el}_{{\rm Na}S}\,, \tag{2.18}$$

where $\overline{A}_K$ is the (mass-based) effective chemical affinity of the cations in phase K,

$$m^{(\rm M)}_{\rm Na}\,\overline{A}_K = \overline{g}_{{\rm Na}K} - \overline{g}_{KK}\,, \quad K = S, W. \tag{2.19}$$

Note that the relation (2.18) can be phrased equivalently in terms of affinities but the *effective* affinities have been introduced because they come into play later on.

Hence, equilibrium of the cation exchange is found to require the mass-based effective chemical affinities to be the same in both phases,

$$\overline{A}_S - \overline{A}_W = 0. \tag{2.20}$$

The mechanical contribution $\Delta g^{\rm mech}$ to the equilibrium constant can be checked to be very small for the range of pressures of interest here, in the sense that the first term on the rhs of (2.17) is practically equal to one, Gajo et al. [2002].

The hydration contribution $\Delta g^{\rm hydr}$ in eqn (2.17) results from (2.20),

$$\Delta g^{\rm hydr} = (g^0_{{\rm K}S} - g^0_{{\rm Na}S}) - (g^0_{{\rm K}W} - g^0_{{\rm Na}W})\,. \tag{2.21}$$

Here $g^0_{{\rm K}S}$ is the free enthalpy of formation of the anhydrous part of the hydrated cluster $\mathrm{K\,X{\cdot}n\,H_2O}$, with a similar definition for $g^0_{{\rm Na}S}$. $g^0_{{\rm K}W}$ and $g^0_{{\rm Na}W}$ are the free enthalpies of solubility of the cations $\mathrm{K^+}$ and $\mathrm{Na^+}$ in pore water.

For the smectite $\mathrm{Na\,Al_3\,Si_3O_{10}(OH)_2}$ under a pressure of 1 bar and at a temperature $T = 298°\mathrm{K}$, Tardy and Duplay [1992] provide the following data for the hydration free enthalpy $\Delta g^{\rm hydr} = (-5591.1 - (-5565.9)) - (-282.5 - (-261.9)) = -4.6\,\mathrm{kJ/mole}$.

The negative sign of this quantity implies the value of $\mathrm{K_{eq}}$ to be greater than 1, in fact $\mathrm{K_{eq}} = 6.3$. It indicates that the cation exchange from left to right in (2.14) is *spontaneous*.

Elastic constitutive equations. In view of the relations (2.15), the incremental mixed elastic potential simplifies to

$$\delta\mathcal{W}^{\rm el}_M(\bar{\boldsymbol{\sigma}}, \{m^{\rm el}_{wS}, m^{\rm el}_{{\rm Na}S}\}) = \boldsymbol{\epsilon}^{\rm el} : \delta\bar{\boldsymbol{\sigma}} - \overline{\mu}_{wS}\,\delta m^{\rm el}_{wS} - \overline{A}_S\,\delta m^{\rm el}_{{\rm Na}S}\,, \tag{2.22}$$

from which follow the constitutive relations,

$$\boldsymbol{\epsilon}^{\rm el} = \frac{\partial\mathcal{W}^{\rm el}_M}{\partial\bar{\boldsymbol{\sigma}}}\,, \quad \overline{\mu}_{wS} = -\frac{\partial\mathcal{W}^{\rm el}_M}{\partial m^{\rm el}_{wS}}\,, \quad \overline{A}_S = -\frac{\partial\mathcal{W}^{\rm el}_M}{\partial m^{\rm el}_{{\rm Na}S}}\,. \tag{2.23}$$

The elastic constitutive equations are thus completely defined as soon as the potential $\mathcal{W}^{\rm el}_M$ is given. To obtain logarithmic elasticity, we take

$$\mathcal{W}^{\rm el}_M(\bar{\boldsymbol{\sigma}}, \{m^{\rm el}_{kS}\,,\, k \in S^{\leftrightarrow}\}) = -\sum_{k\in S^{\leftrightarrow}} \mu^0_{kS}\,m^{\rm el}_{kS} - \bar{p}\,\mathrm{tr}\,\boldsymbol{\epsilon}^{\rm el}_\kappa + \kappa\,F(\bar{p}, \bar{p}_\kappa) + \frac{q^2}{6\,G} - \frac{RT}{V_0}\,\varphi\,. \tag{2.24}$$

The purely chemical term φ and the function F are given in the analysis of homoionic clays. There are however two main differences with respect to homoionic clays:

- the enthalpies of formation of the cations, $\mu^0_{kS} = g^0_{kS}/m^{(\mathrm{M})}_k$, $k \in S^+$, give rise to an equilibrium constant different from one;
- the elastic coefficient κ depends on the set $\{x^{\mathrm{el}}_{kS},\ k \in S^+ \cup \{w\}\}$.

The chemo-elastic potential exhibited in (2.24) specializes the hyperelastic constitutive equations to:

$$\left\{\begin{array}{l} \boldsymbol{\epsilon}^{\mathrm{el}} = \left(\mathrm{tr}\,\boldsymbol{\epsilon}^{\mathrm{el}}_{\kappa} - \kappa\,\mathrm{Ln}\dfrac{\overline{p}}{\overline{p}_{\kappa}}\right)\dfrac{\mathbf{I}}{3} + \dfrac{\mathbf{s}}{2\,G}\,, \\ \overline{\mu}_{wS} = \mu^0_{wS} - F(\overline{p},\overline{p}_{\kappa})\,\dfrac{\partial\kappa}{\partial m^{\mathrm{el}}_{wS}} + \dfrac{RT}{m^{(\mathrm{M})}_w}\,\mathrm{Ln}\,x^{\mathrm{el}}_{wS}\,, \\ \overline{A}_S = A^0_S - F(\overline{p},\overline{p}_{\kappa})\left(\dfrac{\partial\kappa}{\partial m^{\mathrm{el}}_{\mathrm{Na}S}} - \dfrac{m^{(\mathrm{M})}_{\mathrm{K}}}{m^{(\mathrm{M})}_{\mathrm{Na}}}\,\dfrac{\partial\kappa}{\partial m^{\mathrm{el}}_{\mathrm{K}S}}\right) + \dfrac{RT}{m^{(\mathrm{M})}_{\mathrm{Na}}}\,\mathrm{Ln}\,\dfrac{x^{\mathrm{el}}_{\mathrm{Na}S}}{x^{\mathrm{el}}_{\mathrm{K}S}}. \end{array}\right. \tag{2.25}$$

To complete the formulation, the explicit expression of κ is provided. It is defined by a double interpolation between two sets of extreme situations, where the molar fraction of one cation overweights the other in both phases. The procedure is as follows:

- in reference to Figure 1, we consider states on the Na-plane and κ is noted κ_{Na}. We measure $\kappa^{\mathrm{dw}}_{\mathrm{Na}}$ and $\kappa^{\mathrm{sat}}_{\mathrm{Na}}$ corresponding respectively to distilled water and NaCl-saturated solution. The chemical effect on κ_{Na} is introduced through a first interpolation based on $x_{\mathrm{Na}S}$, between these two situations, involving a third coefficient $\kappa_{3\mathrm{Na}}$ which indicates the rate of variation of κ close to the distilled water limit;
- the same procedure is followed on the K-plane to obtain the coefficients $\kappa^{\mathrm{dw}}_{\mathrm{K}}$, $\kappa^{\mathrm{sat}}_{\mathrm{K}}$ and $\kappa_{3\mathrm{K}}$;
- a final interpolation is defined between the two reference planes, namely Na-plane and K-plane, based on the relative numbers of moles of the cations sodium and potassium.

The mass-content of cations potassium is given in terms of the mass-content of cations sodium by (2.16). The incremental form of the elastic constitutive equations is then defined by a symmetric 4×4 matrix, given in explicit form in Gajo et al. [2002],

$$\begin{bmatrix} -\delta\overline{p} \\ \delta q \\ \delta\overline{\mu}_{wS} \\ \delta\overline{A}_S \end{bmatrix} = \begin{bmatrix} B & 0 & B_{pw} & B_{p\mathrm{Na}} \\ 0 & 3G & 0 & 0 \\ B_{wp} & 0 & \beta_{ww} & \beta_{w\mathrm{Na}} \\ B_{\mathrm{Na}\,p} & 0 & \beta_{\mathrm{Na}\,w} & \beta_{\mathrm{Na\ Na}} \end{bmatrix} \begin{bmatrix} \delta\mathrm{tr}\,\boldsymbol{\epsilon}^{\mathrm{el}} \\ \delta\epsilon^{\mathrm{el}}_q \\ \delta m^{\mathrm{el}}_{wS} \\ \delta m^{\mathrm{el}}_{\mathrm{Na}S} \end{bmatrix}. \tag{2.26}$$

3 Chemo-Elasto-Plasticity

The analysis presented in the previous chapter was devoted to clays which contain essentially one cation, like the Ponza bentonite studied by Di Maio [1996] which is an Na-Montmorillonite. The presence of several cations not only requires to account explicitly for electroneutrality but it also produces new aspects in the behaviour, as the

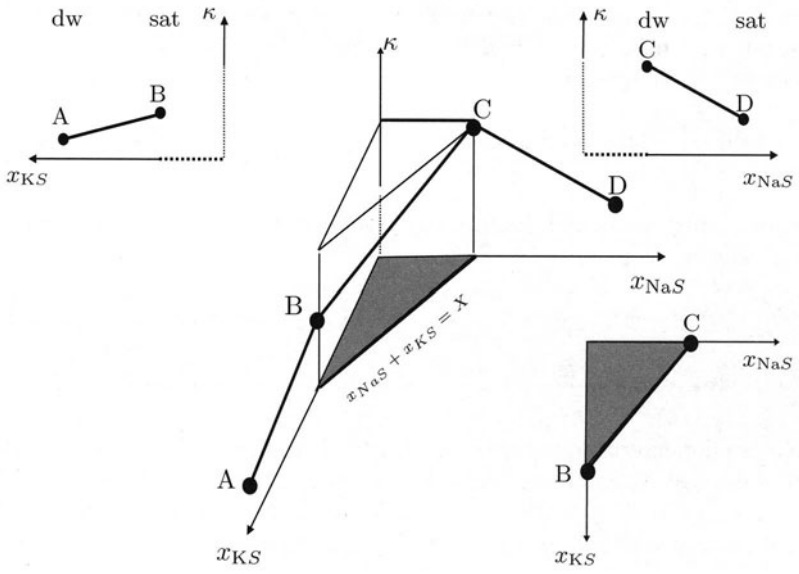

Figure 1 Due to electroneutrality, the molar fractions of the cations are excluded from a triangular zone adjacent to the origin. The elastic coefficient κ is interpolated from the elastic molar fractions of the cations, taking the Na-plane and K-plane as references.

relative contents of the two cations vary, as a consequence of the chemical composition of the pore water. These aspects have been introduced in the elastic behaviour through κ-dependence in the molar fractions of the cations. On the other hand, experimental data available so far in the literature do not reveal effects on the plastic behaviour typical of the presence of several cations. Therefore, the elastic-plastic model will follow the same trend as for Na-Montmorillonites, to within the important fact that the relative contents of the cations will be kept trace of.

The flow rule. The superscript $^{\mathrm{pl}}$ denotes the plastic contribution to a generalized strain, for example,

$$\boldsymbol{\epsilon} = \boldsymbol{\epsilon}^{\mathrm{el}} + \boldsymbol{\epsilon}^{\mathrm{pl}}\,, \quad m_{kS} = m_{kS}^{\mathrm{el}} + m_{kS}^{\mathrm{pl}}\,, \quad k \in S^{\leftrightarrow}. \tag{3.1}$$

According to the reactive model, the total number of cations in the solid phase is a constant for electroneutrality to be satisfied, eqn (2.13). Since this relation is assumed to hold for purely elastic processes, it should do as well for elastic-plastic processes. Therefore the plastic, or irreversible, numbers of cations in the solid phase denoted by the superimposed $^{\mathrm{pl}}$ satisfy

$$\delta N_{\mathrm{Na}S}^{\mathrm{pl}} + \delta N_{\mathrm{K}S}^{\mathrm{pl}} = 0, \quad \delta N_{\mathrm{Cl}S}^{\mathrm{pl}} = 0\,. \tag{3.2}$$

The inequality dissipation becomes,

$$\delta D_1 = -\overline{p}\,\mathrm{tr}\,\delta\boldsymbol{\epsilon}^{\mathrm{pl}} + \mathbf{s} : \mathrm{dev}\,\delta\boldsymbol{\epsilon}^{\mathrm{pl}} + \overline{\mu}_{wS}\,\delta m_{wS}^{\mathrm{pl}} + \overline{A}_S\,\delta m_{\mathrm{Na}S}^{\mathrm{pl}} \geq 0\,. \tag{3.3}$$

For simplicity, the stress dependence of the plastic potential g is restricted to the two first invariants $\overline{p}$ and q, i.e. $g = g(\overline{p}, q, \overline{\mu}_{wS}, \overline{A}_S)$. Then the expression (3.3) motivates the generalized normality flow rule

$$\operatorname{tr}\delta\boldsymbol{\epsilon}^{\mathrm{pl}} = -\delta\Lambda\,\frac{\partial g}{\partial \overline{p}}\,,\quad \operatorname{dev}\delta\boldsymbol{\epsilon}^{\mathrm{pl}} = \delta\Lambda\,\frac{\partial g}{\partial q}\,\frac{3}{2}\frac{\mathbf{s}}{q}\,,\quad \delta\, m^{\mathrm{pl}}_{wS} = \delta\Lambda\,\frac{\partial g}{\partial \overline{\mu}_{wS}}\,,\quad \delta\, m^{\mathrm{pl}}_{\mathrm{Na}S} = \delta\Lambda\,\frac{\partial g}{\partial \overline{A}_S}\,. \tag{3.4}$$

Mechanical and chemical hardening/softening. The volume change varies linearly as a function of $\operatorname{Ln}\overline{p}$,

$$\begin{aligned} \operatorname{tr}\boldsymbol{\epsilon}^{\mathrm{el}} &= \operatorname{tr}\boldsymbol{\epsilon}^{\mathrm{el}}_{\kappa} - \tilde{\kappa}\operatorname{Ln}\frac{\overline{p}}{\overline{p}_{\kappa}}\,, \quad \operatorname{tr}\boldsymbol{\epsilon}^{\mathrm{el}}_{\kappa} = -\kappa^{\mathrm{dw}}\operatorname{Ln}\frac{\overline{p}_{\kappa}}{\overline{p}_0}\,, \quad \text{for elastic unloading,} \\ \operatorname{tr}\boldsymbol{\epsilon} &= \operatorname{tr}\boldsymbol{\epsilon}_{\lambda} - \lambda\operatorname{Ln}\frac{\overline{p}}{\overline{p}_{\lambda}}\,, \quad \operatorname{tr}\boldsymbol{\epsilon}_{\lambda} = -\lambda^{\mathrm{dw}}\operatorname{Ln}\frac{\overline{p}_{\lambda}}{\overline{p}_0}\,, \quad \text{for plastic loading,} \end{aligned} \tag{3.5}$$

but the slopes depend on chemistry via the chemical potential of absorbed water and the chemical affinity of Na in the solid phase, i.e. $\tilde{\kappa}$, λ, λ^{dw} and $\tilde{\kappa}^{\mathrm{dw}}$ depend on $\{\overline{\mu}_{wS}, \overline{A}_S\}$. The dependence $\tilde{\kappa} = \tilde{\kappa}(\overline{\mu}_{wS}, \overline{A}_S)$ is introduced to simplify formally the rate equations.

The resulting preconsolidation stress p_c, with differential

$$(\lambda - \tilde{\kappa})\,\frac{\delta p_c}{p_c} = -\delta\operatorname{tr}\boldsymbol{\epsilon}^{\mathrm{pl}} + \operatorname{Ln}\frac{\overline{p}_{\lambda}}{p_c}\,\delta\lambda - \operatorname{Ln}\frac{\overline{p}_{\kappa}}{p_c}\,\delta\tilde{\kappa}\,, \tag{3.6}$$

appears as a modification of the usual Cam-Clay expression.

The yield function f has the same arguments as g plus $\operatorname{tr}\boldsymbol{\epsilon}^{\mathrm{pl}}$ which allows for hardening and softening, for example when the yield function and plastic potential are of the Modified Cam-Clay type, namely

$$f = f(\overline{p}, q, \overline{\mu}_{wS}, \overline{A}_S, \operatorname{tr}\boldsymbol{\epsilon}^{\mathrm{pl}}) = \frac{q^2}{M^2\,\overline{p}} + \overline{p} - p_c\,, \tag{3.7}$$

with $M = M(\overline{\mu}_{wS}, \overline{A}_S)$ and $p_c = p_c(\overline{\mu}_{wS}, \overline{A}_S, \operatorname{tr}\boldsymbol{\epsilon}^{\mathrm{pl}})$. The interpolation functions for λ and M in terms of $\{\overline{\mu}_{wS}, \overline{A}_S\}$ follows essentially the same spirit as for the elastic coefficient κ, Appendices A and C of Gajo et al. [2002].

Incremental elastic-plastic relations. The incremental elastic-plastic relations can be cast in the following matrix form:

$$\begin{bmatrix} -\delta\overline{p} \\ \delta q \\ \delta\overline{\mu}_{wS} \\ \delta\overline{A}_S \end{bmatrix} = \begin{bmatrix} B^{\mathrm{ep}}_{\overline{p}\overline{p}} & B^{\mathrm{ep}}_{\overline{p}q} & B^{\mathrm{ep}}_{\overline{p}w} & B^{\mathrm{ep}}_{\overline{p}\mathrm{Na}} \\ B^{\mathrm{ep}}_{q\overline{p}} & B^{\mathrm{ep}}_{qq} & B^{\mathrm{ep}}_{qw} & B^{\mathrm{ep}}_{q\mathrm{Na}} \\ B^{\mathrm{ep}}_{w\overline{p}} & B^{\mathrm{ep}}_{wq} & B^{\mathrm{ep}}_{ww} & B^{\mathrm{ep}}_{w\mathrm{Na}} \\ B^{\mathrm{ep}}_{\mathrm{Na}\,\overline{p}} & B^{\mathrm{ep}}_{\mathrm{Na}\,q} & B^{\mathrm{ep}}_{\mathrm{Na}\,w} & B^{\mathrm{ep}}_{\mathrm{Na}\,\mathrm{Na}} \end{bmatrix} \begin{bmatrix} \delta\operatorname{tr}\boldsymbol{\epsilon} \\ \delta\epsilon_q \\ \delta m_{wS} \\ \delta m_{\mathrm{Na}S} \end{bmatrix}. \tag{3.8}$$

The incremental moduli B^{ep}_{kl} classically differ from their elastic counterparts B_{kl} read from (2.26) by a dyadic product, namely:

$$B^{\mathrm{ep}}_{kl} = B_{kl} - \frac{1}{H}\,g_k\,f_l\,, \quad k, l \in \{\overline{p}, q, w, \mathrm{Na}\}. \tag{3.9}$$

The coefficients f_k, g_k, $k \in \{\overline{p}, q, w, \mathrm{Na}\}$ that enter the elastic-plastic stiffness (3.8) are obtained by the consistency condition $\delta f = 0$.

The major symmetry of the elastic-plastic incremental relations holds iff the flow rule is associative, namely $f = g$.

4 Simulations of Chemo-Mechanical Processes

The subsequent simulations aim at quantifying the ability of the model using the concept of chemical reaction to capture the main features of the chemo-mechanical couplings. The experimental data used here are assumed to represent effectively a succession of equilibrium states, that is $\overline{\mu}_{wS} = \overline{\mu}_{wW}$, $\overline{A}_S = \overline{A}_W$.

Material parameters. The behaviour of Ponza bentonite, an Na-montmorillonite clay, is explained by the one-salt model exposed in the chapter on homoionic clays. Part of the behaviour of Bisaccia clay, a natural marine-origin clay, is explained by this model as well when it is exposed to distilled water or saline solutions of NaCl only. However, when chemical loading involves another salt, it is necessary to have a finer description of the solid phase. In line with the present modeling, Bisaccia clay will be considered to contain two essential cations, Na^+ and K^+. The available and guessed material parameters of these clays are reported in Tables 1, 2 and 3. In addition, the equilibrium constant K_{eq} has been taken equal to 5.

Table 1. Initial conditions and other physical data

Material	e_0	p_{c0}(kPa)	N_{cS}	N_{wS}	$N_{\mathrm{Na}S}$	$N_{\mathrm{K}S}$	N_{wW}	$1 - x_{wW}$	ζ_c
Bisaccia clay	3.30	10	1570	21100	278	245	21100	10^{-6}	-0.33
Ponza bentonite	8.00	40	1570	21100	491.4	317.9	81446	10^{-6}	-0.33

Table 2. Elastic parameters

Material	$\kappa_{\mathrm{Na}}^{\mathrm{dw}}$	$\kappa_{\mathrm{Na}}^{\mathrm{sat}}$	$\kappa_{3\mathrm{Na}}$	$\kappa_{\mathrm{K}}^{\mathrm{dw}}$	$\kappa_{\mathrm{K}}^{\mathrm{sat}}$	$\kappa_{3\mathrm{K}}$	$\overline{p}_\kappa$(kPa)
Bisaccia clay	0.120	0.010	3.5	0.013	0.005	3.5	800
Ponza bentonite	0.081	0.011	6.0	0.020	0.014	6.0	1400

Table 3. Plastic parameters

Material	$\lambda_{\mathrm{Na}}^{\mathrm{dw}}$	$\lambda_{\mathrm{Na}}^{\mathrm{sat}}$	$\lambda_{3\mathrm{Na}}$	$\lambda_{\mathrm{K}}^{\mathrm{dw}}$	$\lambda_{\mathrm{K}}^{\mathrm{sat}}$	$\lambda_{3\mathrm{Na}}$	$\overline{p}_\lambda$(kPa)
Bisaccia clay	0.200	0.090	6.0	0.093	0.085	6.0	800
Ponza bentonite	0.171	0.101	6.0	0.110	0.104	6.0	2600

The Ponza bentonite and Bisaccia clay have been remolded using distilled water and later exposed to various saline pore solutions. During mechanical loading, the samples are assumed to remain in contact with their initial pore solution; however even if they are exposed to distilled water during the mechanical loading, the duration of the mechanical test is so small that a chemical loading which involves a diffusion process has no time to take place.

At 20°K, water saturation by the sole NaCl is reached for $x^{\rm sat}_{{\rm Na}W}$=0.091, and water saturation by the sole KCl is $x^{\rm sat}_{{\rm K}W}$=0.078. Saturation in presence of the two salts is not experienced in the simulations reported here.

In fact, not all the measurable quantities listed in Table 1 are available. Practically, the identification procedure is skewed by the fact that there are many more data in or close to the Na-plane than to the K-plane. The presence of cations K^+ in the solid phase stiffens the mechanical behaviour, i.e. it reduces significantly the coefficients κ and λ.

In the analysis of homoionic clays, it was observed that chemical loading and unloading at constant stress are purely elastic processes if the difference $\lambda - \tilde{\kappa}$ is constant while the limit mean-stresses $\overline{p}_\kappa$ and $\overline{p}_\lambda$ are equal. In fact, this follows from (3.6) which then simplifies to

$$(\lambda - \tilde{\kappa})\,\frac{\delta p_c}{p_c} = -\delta {\rm tr}\,\boldsymbol{\epsilon}^{\rm pl} + {\rm Ln}\,\frac{\overline{p}_\lambda}{p_c}\,\delta(\lambda - \tilde{\kappa}). \tag{4.1}$$

Clearly, for $\lambda - \tilde{\kappa}$ constant, the preconsolidation stress is not affected by changes of the chemical state. However, some experiments by Di Maio [1996] show that chemical loading cycles are accompanied with irreversible strains, whose intensity increases with the mean-stress level. Consequently, $\lambda - \tilde{\kappa}$ should depend in general on the chemical state, which for homoionic clays, is defined by the chemical potential of water $\overline{\mu}_{wS}$. The chemical affinity of the cations is expected to be involved as well for heteroionic clays.

It has been shown in Gajo et al. [2002] that only the chemical potential of absorbed water influences p_c, if the material coefficients satisfy the following restrictions,

$$\lambda^{\rm sat}_{\rm Na} - \kappa^{\rm sat}_{\rm Na} = \lambda^{\rm sat}_{\rm K} - \kappa^{\rm sat}_{\rm K},\quad \lambda^{\rm dw}_{\rm Na} - \kappa^{\rm dw}_{\rm Na} = \lambda^{\rm dw}_{\rm K} - \kappa^{\rm dw}_{\rm K},\quad \lambda_{\rm 3Na} = \lambda_{\rm 3K} = \kappa_{\rm 3Na} = \kappa_{\rm 3K}\,. \tag{4.2}$$

Chemical loadings and unloadings at constant effective stress are elastic, that is, there is no chemical influence any longer on p_c, if $\overline{p}_\lambda$=$\overline{p}_\kappa$ and if in addition,

$$\lambda^{\rm sat}_{\rm Na} - \kappa^{\rm sat}_{\rm Na} = \lambda^{\rm sat}_{\rm K} - \kappa^{\rm sat}_{\rm K} = \lambda^{\rm dw}_{\rm Na} - \kappa^{\rm dw}_{\rm Na} = \lambda^{\rm dw}_{\rm K} - \kappa^{\rm dw}_{\rm K}. \tag{4.3}$$

However, the values of $\kappa_{\rm 3Na}$ and $\lambda_{\rm 3Na}$, which can be identified as chemical consolidation/swelling slopes, were shown to be distinct for Bisaccia Clay in the analysis of homoionic clays. On the other hand, in absence of available data, we shall accept the constraints above which require that these slopes are the same on the Na- and K-planes of Figure 1. In addition, we do not have specific data that allow to explore the intensity of plasticity for paths at constant chemical affinity and at constant chemical potential of water respectively. Therefore, we shall accept that the distance between the elastic and plastic coefficients is a constant in the Na- and K-planes, and that this constant is the same in these two planes as indicated by the first set of equalities in (4.3).

For Ponza bentonite, the identification procedure of homoionic clays provides parameters on the Na-plane that verify the related constraints dictated by (4.3). The parameters in the K-plane are chosen in order that all the relations in (4.3) be satisfied. However, plasticity during purely chemical loadings can occur if the limit stresses $\overline{p}_\kappa$ and $\overline{p}_\lambda$ are not equal.

The first set of equalities in (4.3) leaves a single value to be ascribed for the parameters in the K-plane, say $\lambda^{\rm dw}_{\rm K}$. After the initial state corresponding to distilled water has been obtained in the solid phase, the parameter $\lambda^{\rm dw}_{\rm K}$ can be calculated using the interpolation rules since the corresponding elastic-plastic slope is available.

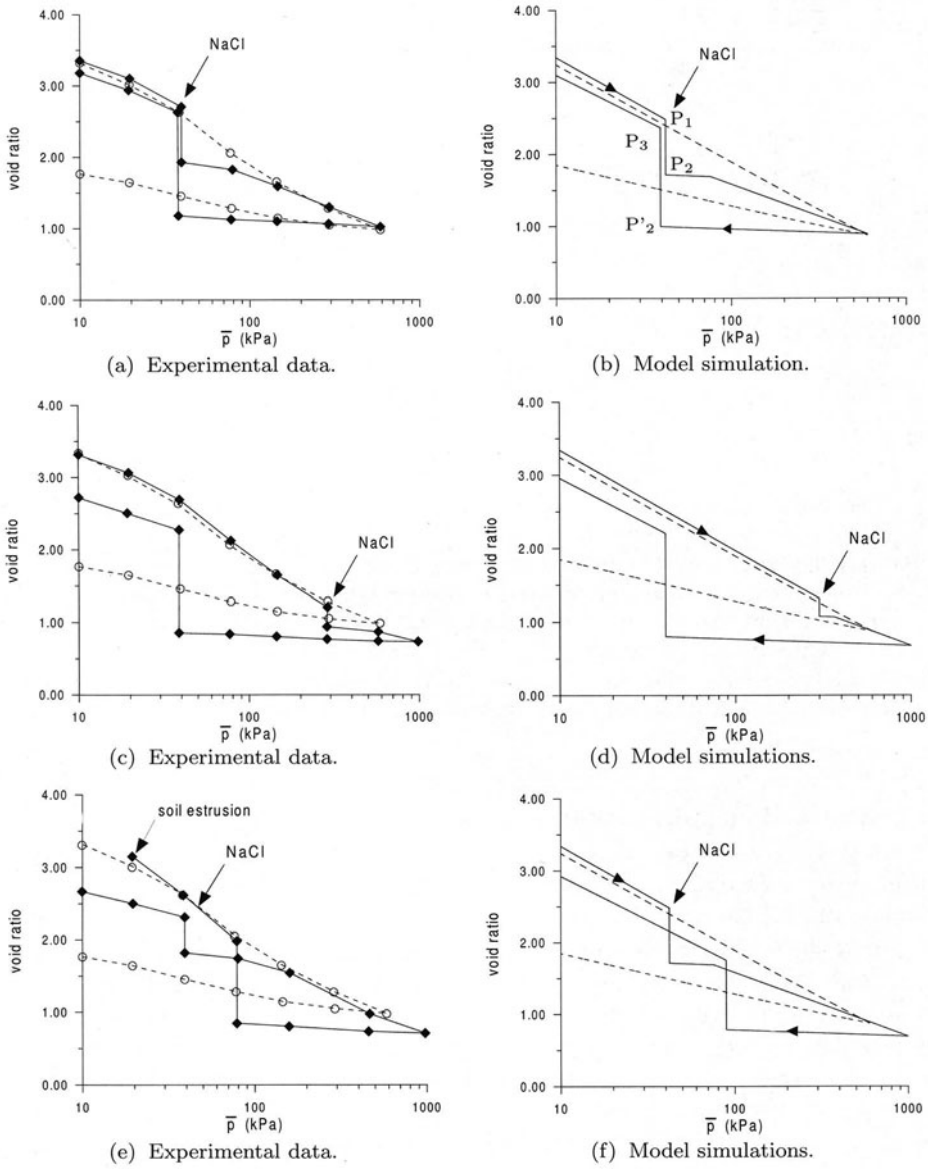

Figure 2 Mechanical load cycle on Bisaccia clay exposed to distilled water (dashed curve). Chemo-mechanical loading cycles with replacement of the distilled water solution by a NaCl-saturated solution, later replaced itself by the distilled water solution (solid curve). The three sets of data and simulations differ by the mean-stresses at which chemical loading and unloading are performed. Replacement of preexisting cations K^+ in the clay cluster by cations Na^+ implies that swelling is larger than chemical consolidation as explained by the increase of mechanical coefficients shown in Fig. 3-(a). Experimental data by Di Maio and Fenelli [1997].

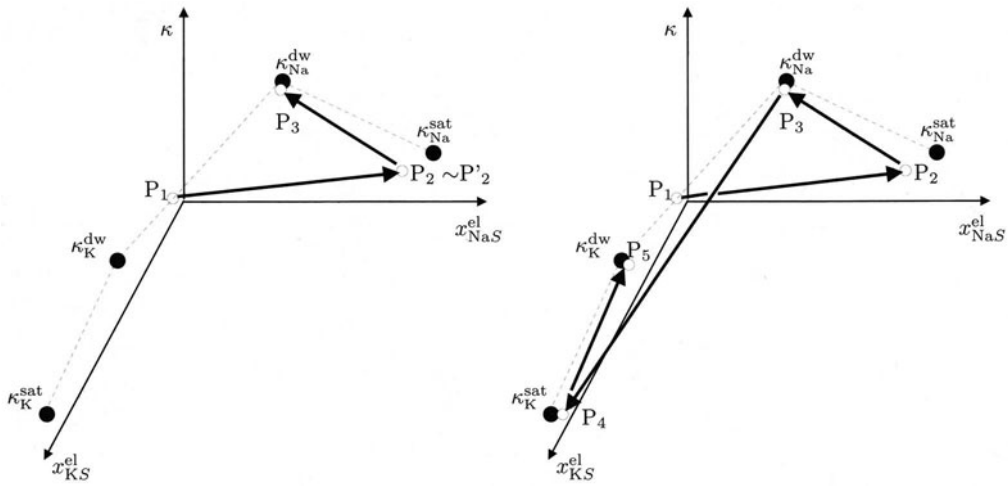

(a) Chemo-mechanical loading of Figure 2 (b) Chemical loading of Figure 4

Figure 3 Qualitative evolution of the elastic coefficient κ during the chemical loadings described by Figure 2 and Figure 4. The initial state, Point P_1, is located on the line of minimal cation content which ensures electroneutrality for a distilled pore water, see Figure 1. The subsequent changes of the chemical content of pore water leads to changes in the solid phase which are accompanied with variations of κ, Points P_2 to P_5. As a general rule, both coefficients κ and λ are much smaller on the K-plane than on the Na-plane.

Mechanical and chemical loading cycles. In order to highlight the strong effects of chemical loading, the evolution of the void ratio for the specimen which is in contact with distilled water and undergoes a purely mechanical loading is used as a reference, marked by dashed curves in Figure 2.

Figure 2 shows mixed chemo-mechanical loading and unloading cycles. Since $\lambda - \tilde{\kappa}$ is not constant, chemical loading leads first to a change, in fact a decrease, of the preconsolidation stress p_c, a phenomenon that can be referred to as *chemical softening*. Thus plasticity occurs to compensate for this negative effect and to maintain the preconsolidation stress equal to the applied stress, up to a point from which the chemical influence on p_c becomes positive, i.e. p_c increases due to the increase of Na^+ in solid phase, leading to *chemical hardening* and preconsolidation, Fig. 6-(a). Plasticity gives rise to an increased chemical consolidation. During chemical unloading, the swelling is partly elastic and partly elastic-plastic, as can be checked from Fig. 6-(b). The volume change is larger than during chemical consolidation, and in this respect the behaviour of Bisaccia clay is quite distinct from that of Ponza bentonite. Indeed for the latter, the void ratio at the end of swelling practically returns to the dashed curve of the purely mechanical cycle, see Figure 6 in Loret et al. [2002]. The reason of this different behaviour is due to the presence of two cations in the solid phase of Bisaccia clay. The initial state contains the two cations in a certain proportion, point P_1 in Fig. 3-(a). Increase of the Na-content leads to a decrease of κ, point P_2, but later chemical unloading leads to a

value of κ larger than the initial one, point P_3, Fig. 3-(b). Mechanical loading-unloading has a small effect on the chemical composition of the solid phase, so that the state does not change significantly from the end of the chemical consolidation to the beginning of chemical swelling, i.e. $P_2 \simeq P'_2$.

The fact that κ is larger at P_3 than at P_1 is responsible for the larger swelling observed in the simulations of Fig. 2, in agreement with experimental data. On the other hand, for the Ponza bentonite studied in Loret et al. [2002], the whole process was occurring in the Na-plane of Fig. 3-(a), so that the initial and final values of κ, like their representative points P_1 and P_3, were quite close.

For the sake of simplicity, we assume that the sample is in contact with a water reservoir having a volume equal to the pore volume of the sample. Actually the volume of water surrounding a sample in an oedometric cell is usually larger than the value here assumed. The chemical loading is simulated by adding a controlled mass of NaCl salt to free and pore water. This addition induces an increase of the molar fraction x_{NaW}, which, in the initial phase of loading, is countered by the release of K^+ from absorbed water, point P_1 to point P_2 in Fig. 4-(b). This counter phenomenon is particularly important at low values of x_{NaW} and induces the curved increase of the relative weight of Na^+ in the solid phase as shown in Figure 5 from point P_1 to point P_2. In fact, one should stress that the exact experimental set up has a quantitative influence on the absorption/desorption processes. For example, increasing the ratio volume of reservoir water versus volume of pore water decreases the curvature of the path P_1 to P_2. The chemical unloading was simulated by the subtraction of masses of both NaCl and KCl from the reservoir and pore water, point P_2 to point P_3 in Figures 4-(b), 5: the idea is to mimic the frequent substitutions of reservoir water performed experimentally.

Ionic Replacements. Tests concern Bisaccia clay, Figure 4, and Ponza bentonite, Figure 7. For Bisaccia clay, the first chemical consolidation due to saturation of pore water by NaCl leads to some plasticity as described in relation to Figure 2. Also in agreement with the observations regarding that figure, the amount of contractancy due to plasticity is not sufficient to overcome the increase of κ due to the subsequent exposure to distilled water, path P_2 to P_3 in Figure 3-(b): therefore the chemical cycle results in a net dilatancy. However for Ponza clay, the initial state is much closer to the Na-plane in Figure 1. Therefore, the change of κ at the end of the chemical cycle is quite small, and consequently, the occurrence of plasticity during chemical consolidation results in a net contractancy at the end of the first cycle.

The first exposure to a KCl saturated pore water solution leads to a large decrease of κ, path P_3 to P_4 in Figure 3-(b): since $\kappa_K^{sat} - \kappa_{Na}^{dw} = -0.115$ is almost equal to $\kappa_{Na}^{sat} - \kappa_{Na}^{dw} = -0.110$, the associated decrease of volume is quite similar (to within the sign) to the volume increase due to the previous exposure to distilled pore water, Figures 4 and 7. Subsequent exposures to distilled water and KCl saturated solutions display small volume changes since the values of κ remain small as the path remains close to the K-plane in Figure 3-(b), e.g. path P_4 to P_5 associated to Figure 4.

The effect of the equilibrium constant K_{eq} is illustrated by the evolution of the relative number of cations Na^+ with respect to the total number of cations present in the solid

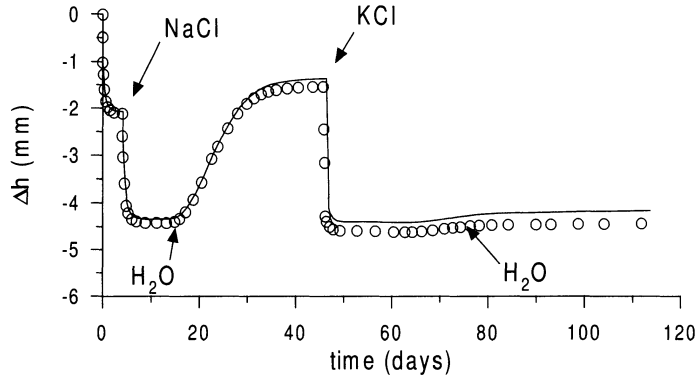

(a) Experimental data by Di Maio and Fenelli (1997).

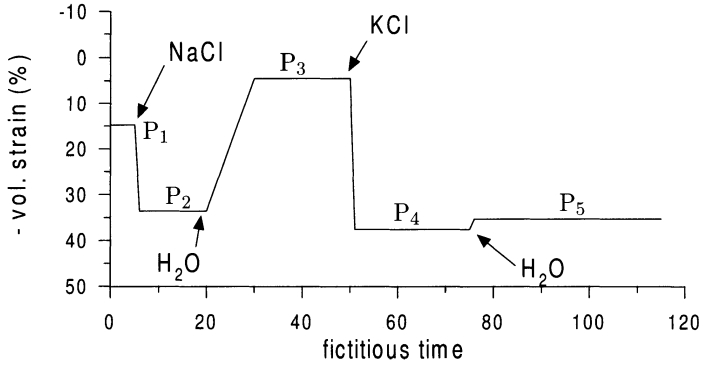

(b) Model simulations.

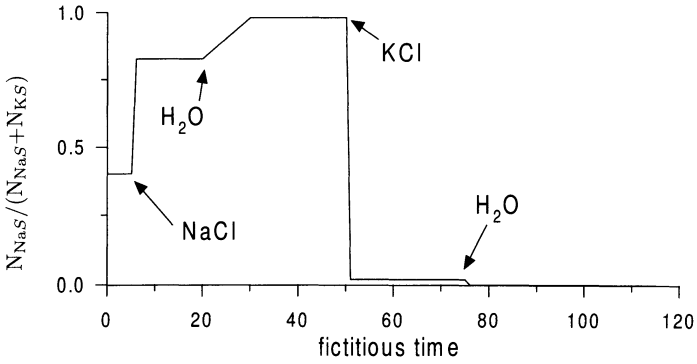

(c) Evolution of the relative number of cations Na^+ and K^+ in the solid phase.

Figure 4 Successive replacements of the pore solution in Bisaccia clay at fixed effective mean-stress $\bar{p}$=40 kPa. Pore solution is 1/ distilled water, 2/ a Na-saturated solution, 3/ distilled water, 4/ a K-saturated solution, and finally 5/ distilled water. Replacement of preexisting cations K^+ by cations Na^+ implies that the first swelling is larger than chemical consolidation, and the second swelling much smaller in agreement with Figure 1. Evolution during the process of (a) the height of the oedometer, (b) the volumetric strain, (c) the relative number of cations Na^+ in solid phase.

phase, Figures 4-(c) and 7-(c). In fact, saturation of the pore water by NaCl leads to a relative increase of cations Na^+ in the solid phase, but the percentage of cations K^+ that are not desorbed is still significant at the end of the first cycle. On the other hand, saturation of the pore water by KCl leads to almost complete desorption of the cations Na^+. This information is also readable from Figure 5 which provides in addition the quantitative evolution of the relative number of cations Na^+ with the chemical content of pore water.

Notice that the model forecasts a progressive replacement of the absorbed cations by cations Na^+ at the first stage of loading history, Figure 7-(c). However, the amplitude of the phenomenon is much smaller than experimentally observed, Figure 7-(a). One explanation might be that the initial content in absorbed cations Na^+ is smaller than assumed in the simulations.

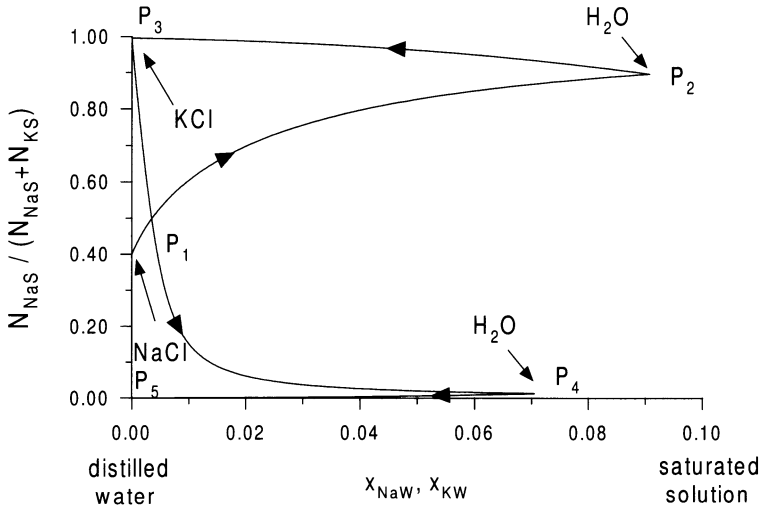

Figure 5 Evolution of the relative number of cations Na^+ in the solid phase with respect to the total number of exchangeable cations during the process on Bisaccia clay of Figure 4.

5 Constitutive Equations for Homoionic and Heteroionic Clays: Similarities and Differences

The model developed here can be viewed as extending the classic elastic-plastic framework for porous media to account for electro-chemo-mechanical couplings. Therefore, it can capitalize upon the available theoretical and computational developments in view of solving initial and boundary value problems in a multi-dimensional setting. Although analyses of instrumented in situ cases are the ultimate goal, it will be necessary in a first step to simulate laboratory tests to check the validity of certain assumptions that have been made to interpret the experimental results, e.g. assumption of chemical equilibrium and homogeneity of the chemical fields throughout the sample at the times

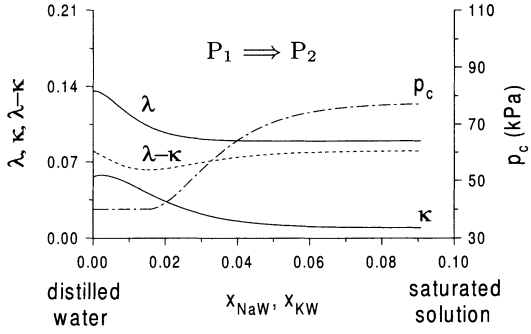

(a) Exposure to NaCl saturated solution.

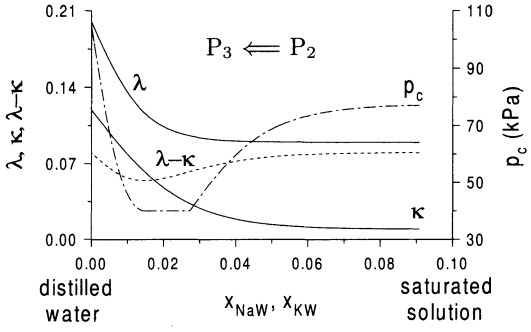

(b) Exposure to distilled water.

Figure 6 Evolution of the mechanical properties and of the preconsolidation stress p_c during the first chemical loading and unloading at constant $\overline{p} = 40\,\text{kPa}$ shown in Figure 4. The behaviour is elastic-plastic initially: plastic contractancy occurs first to compensate for chemical softening and maintain constant $p_c = \overline{p}$. Where the chemical influence on p_c is positive, it results in an elastic behaviour and preconsolidation. The subsequent exposure to water (b) shows also some plasticity (where p_c is equal to the applied $\overline{p}$) which disappears in the next cycle (not shown). The points P_1, ... P_3 refer to Figure 4.

where measurements are made. Such an analysis is presented in Gajo and Loret [2003]ab.

The present electro-chemo-mechanical constitutive model for heteroionic clays (used for two cations) reduces smoothly to the chemo-mechanical model for Na-Montmorillonite clays when the relative fraction of cations Na^+ overweights that of K^+. In fact, the present simulations of Ponza clay displays two modifications with respect to homoionic clays. There salt was not allowed to transfer from the solid phase to the fluid phase and conversely. The reason to prevent that transfer was that the model did not recognize cations and anions but only salts, e.g. NaCl, and so transfer of Na^+ in the solid phase would have brought anions Cl^- as well. Here, as for homoionic clays, the *total* amount of absorbed salts, that is cations and anions, is constant, due to the assumption of a negligible amount of chloride anions and electroneutrality. A second modifica-

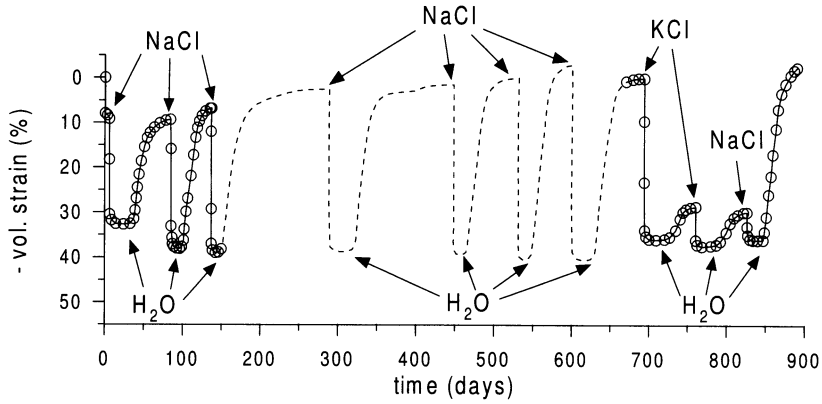

(a) Experimental data.

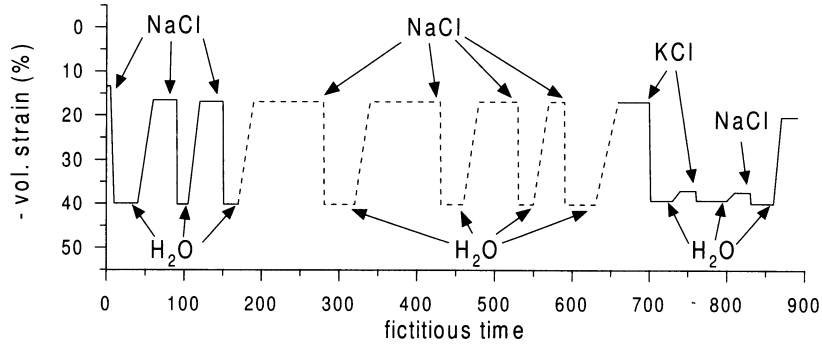

(b) Model simulations.

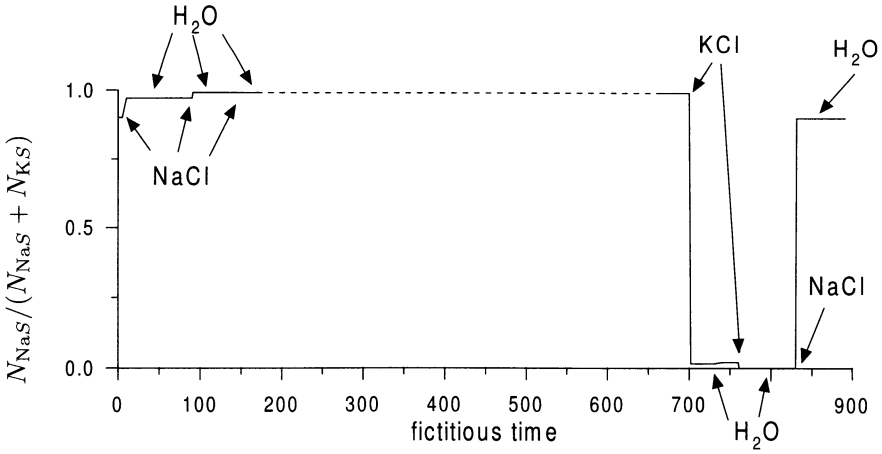

(c) Evolution of the relative number of cations Na^+ in the solid phase.

Figure 7 After equilibrium has been reached under the fixed effective mean-stress $\bar{p}=40\,\text{kPa}$, a complex chemical loading is performed consisting of successive replacements of the pore solution. Experimental data on Ponza bentonite by Di Maio [1998], her Figure 15. The presence of cations K^+ stiffens significantly the mechanical properties.

tion is that the present model recognizes that Ponza bentonite, although an essentially Na-Montmorillonite, contains also cations K^+ whose relative weight strongly matters. Therefore while the representative states of the solid phase shown in Figures 1 and 3 were *in* the Na-plane for homoionic clays, they are now, more realistically, *close* to that plane as long as pore water is distilled or contains NaCl. If another cation, like K^+, of selectivity constant greater than one with respect to Na^+ is dissolved in pore water, it transfers at a fast rate in the solid phase, e.g. Figures 5 and 7-(c), the cations Na^+ are desorbed and the representative states in Figure 3 leaves the Na-plane to get closer to the K-plane.

The data available show that cations Na^+ and, more drastically, K^+ stiffen significantly the mechanical properties κ and λ. Data from Di Maio and Onorati [1999] also show that samples in contact with a NaCl solution have a friction angle which increases with the salt content of the solution. The model presented here can incorporate the variation of friction angle due to chemical content of the solid phase through the parameter M. However, we do not have available data showing whether or not exposure of samples to KCl solutions has a still stronger effect on the friction angle than exposure to NaCl solutions. For that purpose, triaxial drained or undrained tests have to be performed.

Bibliography

Di Maio, C. (1996). Exposure of bentonite to salt solution: osmotic and mechanical effects. *Géotechnique*, 46(4), 695-707.

Di Maio, C. (1998). Discussion on 'Exposure of bentonite to salt solution: osmotic and mechanical effects'. *Géotechnique*, 48(3), 433-436.

Di Maio, C. and G. Fenelli (1997). Influenza delle interazioni chimico-fisiche sulla deformabilità di alcuni terreni argillosi. *Rivista Italiana di Geotecnica*, 1, 695-707.

Di Maio, C. and R. Onorati (1999). Prove di laboratorio: influenza di composizione del liquido di cella. *Rendiconti del XX Convegno Nazionale di Geotecnica, Parma*, 87-94.

Gajo, A., Loret, B. and T. Hueckel (2002). Electro-chemo-mechanical couplings in saturated porous media: elastic-plastic behaviour of heteroionic expansive clays. *Int. J. Solids and Structures*, 39, 4327-4362.

Gajo, A. and B. Loret (2003)a. Finite element simulations of chemo-mechanical coupling in elastic-plastic homoionic expansive clays. *Computer Methods in Applied Mechanics and Engineering*, 192(31-32), 3489-3530.

Gajo, A. and B. Loret (2003)b. Transient analysis of ionic replacements in elastic-plastic expansive clays. submitted for publication.

Haase, R. (1990). Thermodynamics of Irreversible Processes. Dover Publications, New York.

Loret, B., Hueckel, T. and A. Gajo (2002). Chemo-mechanical coupling in saturated porous media: elastic-plastic behaviour of homoionic expansive clays. *Int. J. Solids and Structures*, 39, 2773-2806.

Tardy, Y. and J. Duplay (1992). A method of estimating the Gibbs free energies of formation of hydrated and dehydrated clay minerals. *Geochimica and Cosmochimica Acta*, 56, 3007-3029.

Mass Transfer Through Membranes and Generalized Diffusion

Alessandro Gajo † and Benjamin Loret *

† Dipartimento di Ingegneria Meccanica e Strutturale, Università di Trento, Trento, Italia
* Laboratoire Sols, Solides, Structures, Institut National Polytechnique de Grenoble, France

Abstract Phases serve to isolate species. To change phases, species have to transfer across a membrane. Transfer through biological membranes involves several mechanisms that accounts inter alia on the size and polarity of the species. Dedicated carriers activate the transfer of molecules for which simple diffusion is inefficient.

Within a phase, species diffuse. In the simplest context, the diffusion of a species is to be traced to a main driving force. However, in general, several driving forces collaborate, or compete, to move particles in the diffusion process. Depending on the boundary conditions, these couplings may give rise to quite typical flows.

1 Mass Transfer Through Membranes

We have endowed phases with an external membrane, whose permeability is species-dependent. When it occurs, this transfer is characterized by a typical transfer time. We begin by a brief account on transfer across the membranes of biological cells. Our current description of the properties of the membranes around the clay platelets is more rudimentary.

1.1 Biological Membranes

Cardiac cells are limited by a membrane to which many ionic channels and signal carriers are attached. They are proteins which might change conformation to transfer, or transport (the two terms are synonymous), the information. Most of them are highly specialized and species-dedicated. The membrane behaves as a capacitor, with more negative charges in the cytoplasmic face under rest conditions. Periodic electrical signals emitted by the sinusal node and traveling through the extracellular space activate the ionic channels and other proteins so as to induce a transmembranar current and modify the rest ionic concentrations. This modification is of capital importance, because the excitation of muscles depends crucially on the intracellular concentration of Ca^{2+}.

The cardiac cell[1] is geometrically bounded by its phospholipidic membrane, about

[1] The myocardium is a *syncitium*, where cells are (electrically) linked by gap junctions which ensure a fast transmission of an electric signal. This situation can be contrasted with that of adult cartilage, where the cells, the chondrocytes, are inactive and where the extra-cellular matrix occupies a much larger volume than chondrocytes.

6 nm thick. Membranar proteins may cross completely the membrane or be attached on one side only. These proteins ensure different functions, in particular controlled transport of matter and reception and transduction of signals.

Transfer of small molecules. Small[2], apolar or polar uncharged molecules, like H_2O, O_2, N_2, urea, *diffuse* relatively quickly through the membrane. In fact, the diffusion process obeys *Fick's law* that states that the rate of transport/transfer of n moles of uncharged substances is equal in absolute value, but opposite in sign, to the gradient $d\,/dx$ of the substance in the direction of transfer times the area A over which transfer is considered times a diffusion coefficient D. If one introduces the flux J as $J = (dn/dt)/A$, then Fick's law is $dn/dt = -D\,A\,dc/dx \Leftrightarrow J = -D\,dc/dx$. For a thin membrane of width Δx, the formula applies with the differential operator $d\,/dx$ replaced by the difference operator $\Delta\,/\Delta x$, Δn (resp. Δc) denoting the difference of n (resp. c) on both sides of the membrane.

Diffusion distances are proportional to the square root of the time times the diffusion coefficient, say $\delta x \simeq \sqrt{2\,D\,\delta t}$. A molecule with $D = 10^{-5}\,\mathrm{cm}^2/\mathrm{s}$ would travel the small distance $\delta x = 1\,\mu$m very fast in $\delta t = 1$ msec but, for the longer distance $\delta x = 1$ cm, it needs an exceedingly long time $\delta t = 28$ hr.

The diffusion coefficient D is inversely proportional to the molar mass of the diffusing species to the power 1/2 to 1/3. Therefore, free diffusion becomes inefficient for larger molecules.

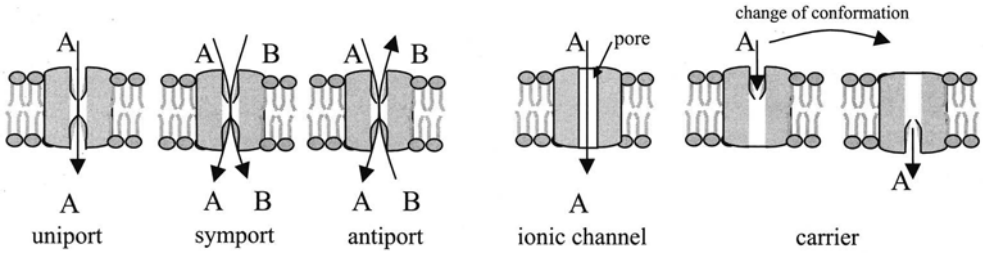

Figure 1 Various types of *passive* transfer by membranar proteins. Passive transfer of matter occurs against the concentration gradient.

Mass transfer through dedicated proteins. In fact there are other means of transfer. Larger and charged molecules can transfer through the membrane via specific proteins, which may be dedicated to a single species, or to a set of species endowed with special biochemical properties, or activated for a family of species of limited size. One distinguishes between

- *passive transfer* where the transfer is *against* the concentration gradient. Transfer of ions is performed by ionic channels which contain a channel filled by water which facilitates the diffusion process, Figure 1.

[2]Diameters of Na^+~1.96 Å, Ca^{2+}~2.20 Å, K^+~2.66 Å, H_2O~3.6 Å.

- *active transfer* that uses some form of energy and is thus able to induce a transfer *along* a concentration gradient, Figure 2.

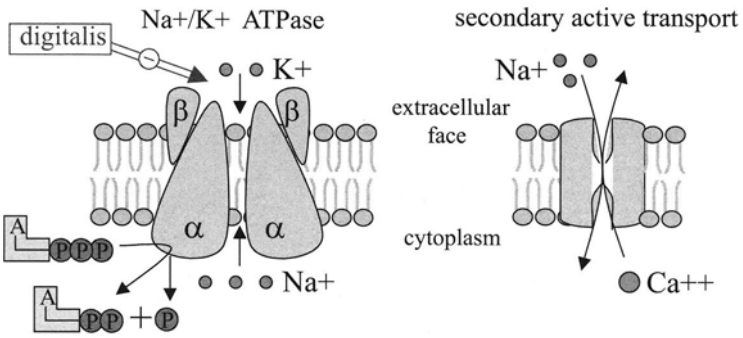

Figure 2 In active transfer, membranar carriers provide energy to exchange matter in the direction of their concentration. There are two main types of active transfer, ATP synthase and secondary active transfer.
An example of *ATP synthase*, also referred to as a ionic pump when the transported species is ionic, is the Na^+/K^+-ATPase whose energy comes from the dephosphorylation of ATP into ADP and cytosolic P_i, which releases a free enthalpy of -30 kJ/mole. This pump is electrogenic since, for each ATP, 3 Na^+ leave the cell and only 2 K^+ enter. The exchange requires a change of conformation of the protein, see Figure 1. The Na^+/K^+ pump is responsible to re-establish rest concentrations of these ions after the depolarisation process. Cardiac glycosides, such as digitalis and ouabain, inhibit the activity of the pump.
An example of *secondary active transfer* is the electrogenic Na^+-Ca^{2+} antiport that uses the energy of passive transfer of Na^+ to extrude Ca^{2+}.

Membrane receptors, second messengers and signal-transduction. A hydrophilic *signal*, or *first messenger*, can not cross the lipidic cellular membrane and reach directly the target cell. Therefore, it uses a *receptor* located on the extracellular side of the membrane that transfers the information to the internal face, a phenomemon termed *signal transduction*. Once it has reached the internal face, the signal will stimulate/activate certain enzymes that control the metabolism or trigger the transcription of specific genes.

There exist three types of receptors: receptors with a single transmembranar segment, ionic channels that are stimulated by a *ligand* that opens the channel for ions such as Na^+, K^+ and Cl^-, and receptors with seven transmembranar segments: on the cytoplasmic face, the signal is transmitted by a *G protein* to an *effector* which then modifies the concentration of specific ions or *second messengers*, Figure 3. The role of Ca^{2+} as a second messenger in muscle excitation is capital.

Membranar currents and rest potential. With respect to *non-excitable cells*, cardiac cells, cells of the nerves and cells of skeletal muscles have, in addition to channels for ions K^+, repolarization channels traversed by ions Na^+ and Ca^{2+}.

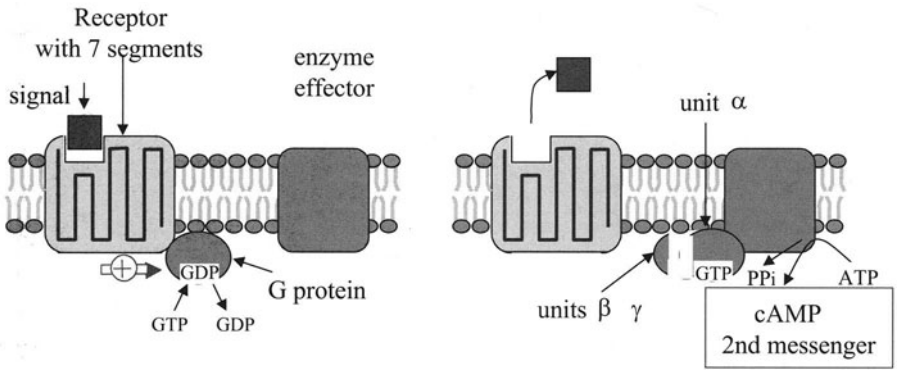

Figure 3 G proteins transfer the signal to an effector. Upon reception of the signal, the G protein becomes activated by exchange of GDP (Guanosine-DiPhosphate) against GTP. It leaves the receptor, links to the protein effector, which activates and, using metabolic energy, produces the second messenger cAMP with short life span.

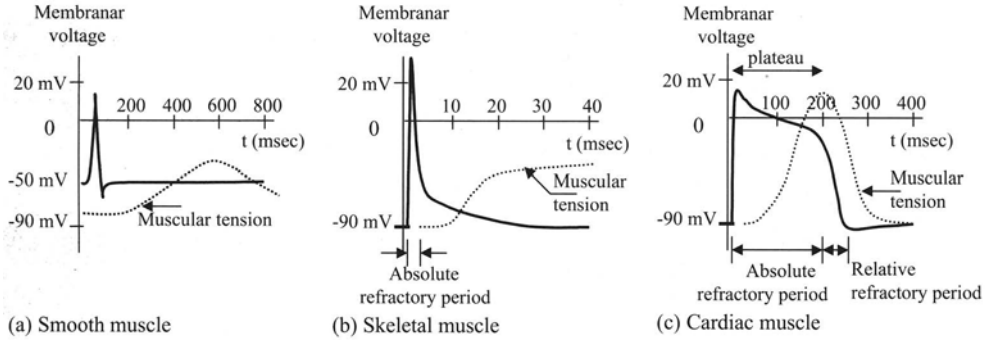

Figure 4 Response to an electrical signal of the three types of muscle cells. Note that the membranar potentials have the same magnitude but the characteristic times differ. The shapes of the muscular tension are germane to each muscle and, of course, adapted to the physiological use of the organ. The human cardiac frequency is about 87 per min, that is a period of 690 msec. Therefore, the period of quasi-rest of 690-250=440 msec makes it possible to absorb usual arrythmia and other temporary irregularities of the electrical excitation (modified from Atlas de Poche de Physiologie, Flammarion, 1992).

Moreover, *action potential*, i.e. the evolution in time of the membranar voltage, is different in cardiac cells than in nerve and skeletal muscle because different channels exist in cardiomyocytes. The binding of Ca^{2+} by Troponinc C in cardiac and skeletal muscle cells is different as well.

The differences of action potentials in smooth muscle, skeletal muscle and cardiac muscle can be appreciated from Figure 4. The plateau phase in cardiac muscle is due to special channels, L-type Ca^{2+} channels (L for long lasting), that remain open for a relatively long period. The subsequent repolarization is due to both closing of the L-type

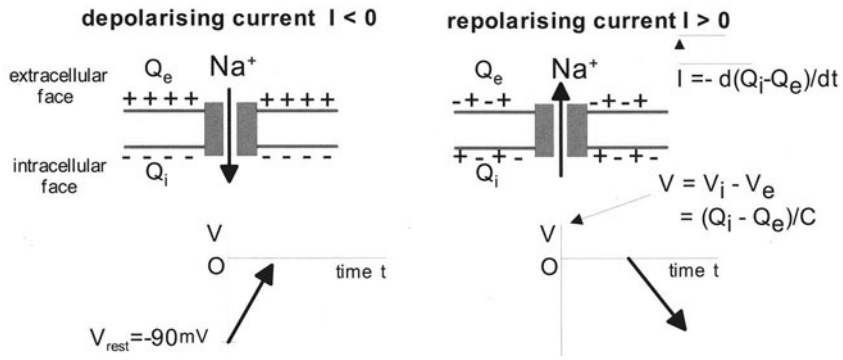

Figure 5 Sign convention for membranar currents. An outward flow of cations induces a positive current and a (re)polarisation of the membrane. At rest, the membrane has a negative potential V_{rest}, that is the intracellular/cytoplasmic face of the membrane has more negative charges than the extracellular face.

Ca^{2+} channels and opening of outward K^+ channels.

The membrane behaves as a *capacitor* of fixed capacitance C: the difference of potential between the internal and external faces is proportional to the difference of surface charges Q_i and Q_e, i.e.

$$V \equiv V_i - V_e = \frac{1}{C}(Q_i - Q_e) \rightarrow \frac{dV}{dt} = -\frac{1}{C}\, I, \quad I = -\frac{d}{dt}(Q_i - Q_e). \tag{1.1}$$

The sign convention for the current is indicated on Figure 5. The total current I is the sum of all ionic currents I_k that traverse the membrane, i.e., in practice, (1.1) is written

$$\frac{dV}{dt} = -\frac{1}{C}\sum_k I_k\,. \tag{1.2}$$

A typical current associated to a species or to a specific process I_k is itself the sum of several currents of the same type that cross channels of the same type, which might differ in certain characteristics, inaccessible to measurement, or too cumbersome to be accounted for, and whose properties are averaged. Each cardiac cell has indeed a few thousands channels which might not work in exact simultaneity.

At another scale, the one of the heart, there exist *heterogeneities* and gradients of properties for channels of a given type, that is material properties may differ in the sino-atrial node, Purkinje fiber, atrial muscle and ventricular muscle.

The numerous membranar current models used in cell-electrophysiology are of three main types: *voltage-gated*, *ligand-gated* and *stretch-gated*.

Knowing the ionic concentrations on the extracellular and cytoplasmic faces of the membrane, the rest potential is defined by the Huxley-Hodgkin-Katz formula based on

the ionic permeabilities or on the chord conductance formula based on the conductances, Sperelakis [2001].

Several cell-electrophysiology models have been developed in the last decade in view to provide a correct time-history of the cytoplasmic Ca^{2+} concentration, which plays a key role in muscle excitation, e.g. Winslow et al. [1999].

1.2 Membranes around Clay Clusters

Constitutive equations that govern the mass transfer across the fictitious membranes surrounding the clay platelets are designed primarily to satisfy the dissipation inequality. Only rough indications on the transfer times are available.

Transfer of water. In our model for homoionic clays, only water can change phase. The inequality dissipation simplifies

$$\delta D_2 = -(\mu_{wW} - \mu_{wS})\,\delta m_{wS} \geq 0\,, \tag{1.3}$$

and it is satisfied by the existence of a positive transfer coefficient, namely

$$\frac{\delta m_{wS}}{\delta t} = k_w^{\mathrm{t}}\,(\mu_{wW} - \mu_{wS})\,, \quad k_w^{\mathrm{t}} \geq 0\,. \tag{1.4}$$

The transfer equation (1.4) may be made non-dimensional by introducing a characteristic transfer time τ_w,

$$\tau_w = \frac{m_w^{(\mathrm{M})}}{RT}\,\frac{\rho_w}{k_w^{\mathrm{t}}}\,. \tag{1.5}$$

Transfer of ionic species. If two dissolved salts, say NaCl and KCl, are present in the solid and fluid phases, the electroneutrality of the solid phase implies that the inequality dissipation associated to mass transfer can be recast in a format that involves the chemical potentials of the salts,

$$\delta D_2 = -(\mu_{wS} - \mu_{wW})\,\delta m_{wS} - (\mu_{s_1S} - \mu_{s_1W})\,\delta m_{\mathrm{Na}S} - (\mu_{s_2S} - \mu_{s_2W})\,\delta m_{\mathrm{K}S} \geq 0\,. \tag{1.6}$$

This format motivates the transfer relations,

$$\frac{\delta}{\delta t}\begin{bmatrix} m_{wS} \\ m_{\mathrm{Na}S} \\ m_{\mathrm{K}S} \end{bmatrix} = -\mathbf{K}^{\mathrm{t}}\begin{bmatrix} \mu_{wS} - \mu_{wW} \\ \mu_{s_1S} - \mu_{s_1W} \\ \mu_{s_2S} - \mu_{s_2W} \end{bmatrix}. \tag{1.7}$$

Dissipation is ensured if the 3×3 transfer matrix $\mathbf{K}^{\mathrm{t}}$ is symmetric positive (semi-)definite. As a simplification, uncoupling between the mass transfers amounts to assume the transfer matrix to be diagonal. It implies that the sole chemical disequilibrium for water does not result in cation transfers, and conversely. The transfer equations then involve three characteristic transfer times which can be displayed by non-dimensionalization as in (1.5). Experimental data seem to suggest that transfer of ions is much slower than transfer of water.

Transfer of ionic species in the model for heteroionic clays. As argued in the Chapter 'Constitutive Equations for Heteroionic Clays', the amount of chloride anions in the solid phase is certainly small due to the presence of the negatively charged clay platelets. So, we may assume that the membrane is impermeable to chloride anions, or even that the number of moles of chloride anions in the solid phase is negligible, $N_{\mathrm{Cl}S} \simeq 0$. Therefore, electroneutrality of the solid phase implies $\delta N_{\mathrm{Na}S} = -\delta N_{\mathrm{K}S}$ or $\delta m_{\mathrm{Na}S}/m_{\mathrm{Na}}^{(\mathrm{M})} = -\delta m_{\mathrm{K}S}/m_{\mathrm{K}}^{(\mathrm{M})}$. The dissipation inequality associated to mass transfer then involves the difference in chemical activities, namely

$$\delta D_2 = -(\mu_{wS} - \mu_{wW})\,\delta m_{wS} - (A_S - A_W)\,\delta m_{\mathrm{Na}S} \geq 0\,. \tag{1.8}$$

The resulting transfer relations are phrased in terms of a positive (semi-)definite 2×2 matrix $\mathbf{K}^{\mathrm{t}}$,

$$\frac{\delta}{\delta t}\begin{bmatrix} m_{wS} \\ m_{\mathrm{Na}S} \end{bmatrix} = -\mathbf{K}^{\mathrm{t}}\begin{bmatrix} \mu_{wS} - \mu_{wW} \\ A_S - A_W \end{bmatrix}. \tag{1.9}$$

Uncoupling between the two mass transfers has been adopted in the finite element simulations reported in Gajo and Loret [2003]b.

2 Generalized Diffusion

2.1 Two Families of Conjugate Fluxes - Chemical Potential Gradients

In the Chapter 'Multi-Phase Multi-Species Mixtures', the dissipation inequality associated to diffusion in the fluid phase has been written in terms of mass fluxes and gradients of electro-chemical potentials. Onsager reciprocity relations may be postulated based on this set of conjugate variables. On the other hand, there are other couples of conjugate variables that might be interest to consider because they might be advantageous in the parameter identification process, or because they provide more insight into the degree of dependence of the various coefficients. To simplify the presentation, the body forces are neglected. A complete exposition is to be found in Loret et al. [2003].

Here we consider two families of conjugate variables,

$$\delta D_3/\delta t = -\mathbf{j}^T\,\mathbf{f}^{\mathrm{ec}} = -\mathcal{J}^T\,\mathcal{F} \geq 0. \tag{2.1}$$

The fluxes in the vector $\mathbf{j}$ refer to the solid,

$$\mathbf{j} = \begin{bmatrix} \mathbf{J}_{wW} \\ \mathbf{J}_{\mathrm{Na}W} \\ \mathbf{J}_{\mathrm{K}W} \\ \mathbf{J}_{\mathrm{Cl}W} \end{bmatrix}, \quad \mathbf{f}^{\mathrm{ec}} = \begin{bmatrix} \rho_w\,\nabla\mu^{\mathrm{ec}}_{wW} \\ \rho_{\mathrm{Na}}\,\nabla\mu^{\mathrm{ec}}_{\mathrm{Na}\,W} \\ \rho_{\mathrm{K}}\,\nabla\mu^{\mathrm{ec}}_{\mathrm{K}\,W} \\ \rho_{\mathrm{Cl}}\,\nabla\mu^{\mathrm{ec}}_{\mathrm{Cl}\,W} \end{bmatrix}, \tag{2.2}$$

while the fluxes in the vector $\mathcal{J}$ refer to the free water,

$$\mathcal{J}=\begin{bmatrix}\mathbf{J}_W\\ \mathbf{J}^{\mathrm{d}}_{\mathrm{Na}W}\\ \mathbf{J}^{\mathrm{d}}_{\mathrm{K}W}\\ \mathbf{J}^{\mathrm{d}}_{\mathrm{Cl}W}\\ \mathbf{I}_{\mathrm{e}W}\end{bmatrix},\quad \mathcal{F}=\begin{bmatrix}\mathbf{F}_W\\ \mathbf{F}^{\mathrm{d}}_{\mathrm{Na}W}\\ \mathbf{F}^{\mathrm{d}}_{\mathrm{K}W}\\ \mathbf{F}^{\mathrm{d}}_{\mathrm{Cl}W}\\ \mathbf{F}_{\mathrm{e}W}\end{bmatrix}=\begin{bmatrix}\nabla p_W\\ RT/v^{(\mathrm{M})}_{\mathrm{Na}}\,\nabla\mathrm{Ln}\,c_{\mathrm{Na}W}\\ RT/v^{(\mathrm{M})}_{\mathrm{K}}\,\nabla\mathrm{Ln}\,c_{\mathrm{K}W}\\ RT/v^{(\mathrm{M})}_{\mathrm{Cl}}\,\nabla\mathrm{Ln}\,c_{\mathrm{Cl}W}\\ \nabla\phi_W\end{bmatrix}. \tag{2.3}$$

The dissipation inequality is written in terms of two sets of pairs (flux, gradient) along an onsagerist format. The determination of the material parameters uses entities that mainly refer to the latter diffusive fluxes and electrical current density. However, these fluxes are linearly dependent. Therefore it is interesting to analyze another formulation that uses fluxes relative to solid and that are independent. Possible restrictions emanating from this second formulation are sought.

2.2 Generalized Diffusion Equations Based on Diffusive Fluxes

Inequality $\delta D_3 \geq 0$, eqn (2.1), is ensured by generalization of Darcy's law of seepage through the porous medium, Fick's law of diffusion of ions in the fluid phase, and electrical flow, Figure 6.

The general format. If the material behaviour is assumed isotropic, a generalized law describing flow of pore water through the solid skeleton, diffusion of ions with respect to the free water and electrical flow can be introduced in the format (the notation is formal)

$$\mathcal{J}=-\mathcal{K}\,\mathcal{F}, \tag{2.4}$$

with $\mathcal{K}$ a symmetric matrix,

$$\mathcal{K}=\begin{bmatrix} k_{WW} & k^{\mathrm{d}}_{W\mathrm{Na}} & k^{\mathrm{d}}_{W\mathrm{K}} & k^{\mathrm{d}}_{W\mathrm{Cl}} & k_{\mathrm{e}}\\ k^{\mathrm{d}}_{\mathrm{NaW}} & k^{\mathrm{d}}_{\mathrm{NaNa}} & 0 & 0 & k^{\mathrm{d}}_{\mathrm{Na\,e}}\\ k^{\mathrm{d}}_{\mathrm{KW}} & 0 & k^{\mathrm{d}}_{\mathrm{KK}} & 0 & k^{\mathrm{d}}_{\mathrm{K\,e}}\\ k^{\mathrm{d}}_{\mathrm{ClW}} & 0 & 0 & k^{\mathrm{d}}_{\mathrm{ClCl}} & k^{\mathrm{d}}_{\mathrm{Cl\,e}}\\ k_{\mathrm{e}} & k^{\mathrm{d}}_{\mathrm{e\,Na}} & k^{\mathrm{d}}_{\mathrm{e\,K}} & k^{\mathrm{d}}_{\mathrm{e\,Cl}} & \sigma_{\mathrm{e}}\end{bmatrix} \tag{2.5}$$

with components

$$\begin{cases} k_{WW}=k_{\mathrm{D}}+\dfrac{k_{\mathrm{e}}^2}{\sigma_{\mathrm{e}}},\quad k^{\mathrm{d}}_{k\mathrm{e}}=n_W\,c_{kW}\,u^*_k\,\mathrm{sgn}\,\zeta_k,\quad \sigma_{\mathrm{e}}=n_W\,\mathrm{F}\sum_{k\in W^{\pm}}|\zeta_k|\dfrac{c_{kW}}{v^{(\mathrm{M})}_k}\,u^*_k,\\ k^{\mathrm{d}}_{kW}=-\omega\,c_{kW}\,k_{\mathrm{D}}+\dfrac{k_{\mathrm{e}}}{\sigma_{\mathrm{e}}}\,k^{\mathrm{d}}_{k\mathrm{e}},\quad k^{\mathrm{d}}_{kl}=n_W\,v^{(\mathrm{M})}_k\,c_{kW}\,\dfrac{u^*_k}{\mathrm{F}\,|\zeta_k|}\,I_{kl},\quad k,l\in W^{\pm}. \end{cases} \tag{2.6}$$

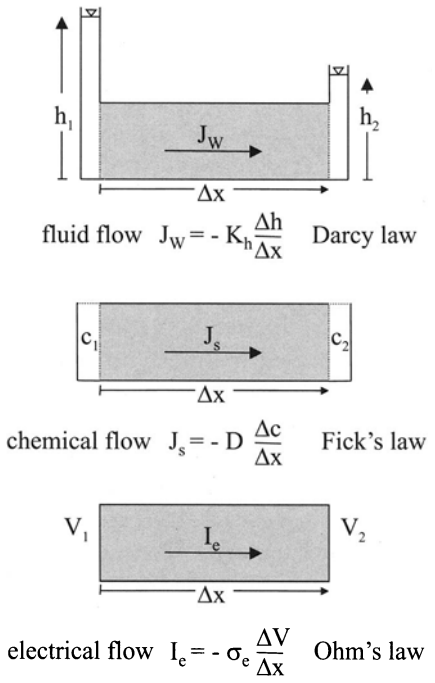

Figure 6 Sketches of uncoupled diffusional processes (modified from Mitchell [1993]).

with $k_{\mathrm{D}} = K_h/(\rho_w\, \mathrm{g}) > 0$. The format used to cast the above coefficients, their signs and the associated terminology are justified by an identification procedure in the next subsection.

Remark on the dependence of the components of $\mathcal{J}$ and $\mathcal{F}$

Note that the components $\mathbf{F}^{\mathrm{d}}_{\mathrm{Na}W}$, $\mathbf{F}^{\mathrm{d}}_{KW}$ and $\mathbf{F}^{\mathrm{d}}_{\mathrm{Cl}W}$ of the vector $\mathcal{F}$ are not linearly independent due to electroneutrality. The same situation of dependence occurs between the components of the flux $\mathcal{J}$. Indeed the electrical current density $\mathbf{I}_{\mathrm{e}W}$ is a linear combination of the diffusional fluxes $\mathbf{J}^{\mathrm{d}}_{kW}$.

The present extended format has been used because it treats all ionic components on the same footing, which has the advantage that reciprocity relations can readily be imposed. On the other hand, there exist compatibility relations between the components of the 5×5 symmetric matrix $\mathcal{K}$ that are unveiled in the identification procedure.

Identification of the diffusion coefficients. Some coefficients in the matrix $\mathcal{K}$ have been set to zero, under the apparent assumption that a concentration gradient of the ionic species k affects directly only the diffusional flux $\mathbf{J}^{\mathrm{d}}_{kW}$. In the simpler case of a single anion and a single cation, Yeung [1990] and Mitchell [1993] have indicated typical values for fine grained soils:

- $K_h \in [10^{-11}, 10^{-6}]$ [unit m/sec] is the hydraulic conductivity;
- $\omega \in [0,1]$, $k \in W^{\pm}$, is referred to as (non-dimensional) osmotic efficiency;
- $D_k^* \in [2 \times 10^{-10}, 2 \times 10^{-9}]$ [unit m^2/sec] is the coefficient of *effective* diffusion of ionic species k in soil. The effective diffusion coefficient accounts for the tortuous path that the species have to diffuse along in the porous medium and it is smaller than the diffusion coefficient of the same species in free solution;
- $\sigma_e \in [10^{-2}, 1]$ [unit siemens/m=A/Volt/m] is the bulk electrical conductivity of the soil. The bulk electrical conductivity can be viewed as weighted average in the fluid phase of the ionic mobilities. It is not constant, it assumes a very small but non zero value for quasi-distilled water and it increases with ionic saturation. It involves only properties of ions in the fluid phase, as if the path of ions were completely in fluid phase, and the solid phase, where the electrical current density vanishes, does not enter. Some empirical models include the contribution of the charged solid particles that provide a path to the electrical current parallel to that in the fluid phase: in that situation, the minimum electrical conductivity for distilled water does not vanish. Note that when the fixed charges are part of the fluid phases as in our model for articular cartilage, they naturally contribute to the electrical conductivity;
- $k_e \in [-10^{-8}, 10^{-8}]$ [unit m^2/sec/Volt] is the coefficient of electro-osmotic conductivity; it depends on the electric charge of the particles, and it is positive above the isoelectric point, and negative below;
- $u_k^* \in [3 \times 10^{-9}, 10^{-8}]$ [unit m^2/sec/Volt] is the effective ionic mobility, a diffusive property, that is: the velocity relative to water that the ionic species k can reach under an electrical potential ϕ_W is $-u_k^* \operatorname{sgn} \zeta_k \nabla \phi_W$. The sign of the electrical charge indicates that a cation is moving towards the cathode, while an anion is moving towards the anode, i.e. in the direction of increasing electrical potential. This phenomenon known as *electro-phoresis* is used to densify fine particle suspensions around the anode; densified materials are removed periodically to allow for the process of anion elimination to continue. In agreement with the usual convention, the electrical current density has a direction opposite to that of electrons. The ionic mobility is linked to the effective diffusion by Nernst-Einstein relation applied to the soil: $u_k^* = D_k^* |\zeta_k| \mathrm{F}/RT$.

The identification of k_{WW} accounts for the fact that measurement of hydraulic conductivity, at uniform ionic concentrations and preventing electrical current $\mathbf{I}_{eW}$, necessarily gives rise to a *streaming potential* $\nabla \phi_W = -k_e/\sigma_e \nabla p_W$, that is water flows against pore pressure gradient but along the streaming potential gradient. Under these experimental conditions, if the diffusional flow $\mathbf{J}_{kW}^{\mathrm{d}}$ is formally taken as $\omega\, c_{kW}\, k_{\mathrm{D}}\, \nabla p_W$, the coefficients k_{Wk}^{d} result as shown in (2.6).

The coefficient ω has been coined *osmotic efficiency*, because, in the flux of the fluid phase $\mathbf{J}_W$, it moderates the osmotic flow. This is realized by introduction of the *osmotic pressure* $\pi = RT\, c^{\pm} = 2\, RT\, c^{+}$ where c^+ is the cationic concentration (in mole/volume of solution). Let us consider the particular case of a semi-permeable membrane, that is a membrane permeable to water only, not to ionic species. The electrical current density across the membrane is thus vanishing. Therefore the diffusion equations yield

$\mathbf{J}_W = -k_D (\nabla p_W - \omega \nabla \pi)$, in which we recognize that ω weights the osmotic pressure. Separately Darcy law implies water to flow against the pressure gradient, while osmosis implies water to flow towards higher chemical concentration, hence $\omega > 0$. Consider now situations where the gradients $-\nabla p_W$ and $-\nabla \pi$ are opposite. When $-\nabla p_W$ is larger (resp. smaller) than $-\omega \nabla \pi$, water flow is towards the lower (resp. the higher) concentration region: concentration will increase in regions with high concentration and decrease in regions of low concentration, a phenomenon called *reverse osmosis*. Typically, the osmotic efficiency is largest (equal to 1) at small ionic concentration, and decreases quickly as ionic concentration increases.

An alternative interpretation emerges when one considers, no longer the flow of water, but the flux of species dissolved in the fluid phase. In the analysis of clay barriers, the osmotic coefficient ω is referred to as *reflection coefficient*.

For *electro-osmosis* where the ionic concentrations and pore pressures are uniform, water flows against the electrical potential gradient, that is towards the cathode. This water flow may lead to negative pore pressures (suction) in the cathode region, and thus initiate a consolidation process, Acar et al. [1991]. The electro-osmotic conductivity is insensitive to the pore size according to the Helmholtz-Smoluchowski theory, while the hydraulic conductivity decreases with the pore size: therefore, for fine-grained soils, an electrical field is a more efficient tool to displace water than a hydraulic gradient.

2.3 Generalized Diffusion Equations Based on Fluxes Relative to the Solid

As an alternative to the above developments, the diffusion equations might well be phrased in terms of the couple $(\mathbf{j}, \mathbf{f}^{ec})$. Onsager reciprocity relations write

$$\mathbf{j} = -\boldsymbol{\kappa}\, \mathbf{f}^{ec}, \quad \boldsymbol{\kappa} = \boldsymbol{\kappa}^T \text{ D.P.} \tag{2.7}$$

Given the non-invertible 5×5 matrix $\mathcal{K}$, one might identify the coefficients of the invertible 4×4 matrix $\boldsymbol{\kappa}$. The identification procedure is developed in Loret et al. [2003] for clays and in Simões and Loret [2003] for articular cartilages. There are conditions for this identification to be possible: they turn out to be the same as the compatibility conditions that emanate from the non-invertibility of the matrix $\mathcal{K}$.

As mentioned in the Chapter 'Multi-Phase Multi-Species Mixtures', the presence of the fixed charges in the solid phase (clays) or in the fluid phase (articular cartilages) , the electro-osmotic coefficient is provided by the identification procedure for articular cartilages while it has to be postulated by additional constitutive equations for clays. Moreover, the notion of osmotic efficiency in the diffusion equations survives only for clays, although it can be re-introduced through chemo-mechanical couplings for articular cartilages.

2.4 Additional Specific Constitutive Equations and Constraints

Since for clays the fixed charge does not belong to the fluid phase, constitutive equations for the electro-osmotic coefficient k_e and for the osmotic coefficient ω need to be provided, Loret et al. [2003]. The latter is defined as a function of the water content w and cationic concentration c^+.

Moreover, actual satisfaction of the dissipation inequality $\delta D_3 \geq 0$ requires the generalized diffusion matrices $\boldsymbol{\kappa}$ and $\mathcal{K}$ to be positive (semi-)definite . The three cases where the fluid phase contains the undissociated salt NaCl, the dissociated salt NaCl and the two dissociated salts NaCl and KCl are considered in the above reference. The actual satisfaction of the dissipation inequality requires the osmotic coefficient to be bounded. The bound has the same multiplicative format in the three cases. For the two dissociated salts NaCl and KCl,

$$\omega(c^+) \leq \overline{\omega}(c^+), \quad \text{with} \quad \overline{\omega}^2(c^+) = \frac{n_W}{RT}\frac{\rho_w\, g}{K_h}\left(\frac{1}{D^*_{\mathrm{Cl}}} + \frac{1}{2\,D^*_{\mathrm{Na}}} + \frac{1}{2\,D^*_{\mathrm{K}}}\right)^{-1}\frac{1}{c^+}, \qquad (2.8)$$

where c^+ (mole/m^3) is the total cationic concentration. This condition holds, for the simulations presented in Gajo and Loret [2003]b, as the bound $\overline{\omega}(c^+)$ defined by (2.8) is always larger than the actual osmotic efficiency $\omega(w, c^+)$, see Figure 7.

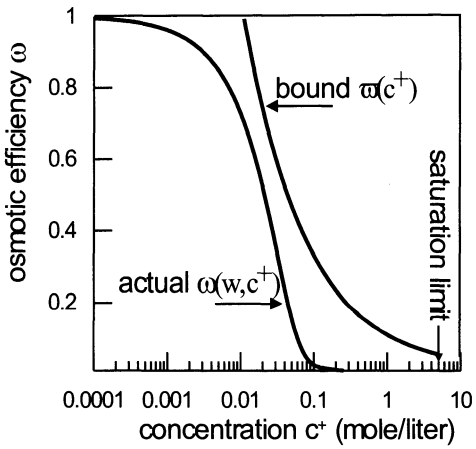

Figure 7 Actual osmotic coefficient ω as obtained from the finite element analysis and bound $\overline{\omega}$ defined in the text. Case (a), solid curve, corresponds to the undissociated salt treated in Gajo and Loret [2003]a and case (b), dashed curve, corresponds to the dissociated salt NaCl treated in Gajo and Loret [2003]b. Actual satisfaction of the dissipation inequality requires the osmotic coefficient to drop quickly as cationic concentration increases.

Bibliography

Acar, Y.B., Gale, R.J., Hamed, J. and G. Putnam (1991). Acid/base distibution in electrokinetic soil processing. *Soils Geology and Foundations, Geotechnical Engineering, Bull. Transportation Research Record*, 1288, 23-34.

Gajo, A. and B. Loret (2003)a. Finite element simulations of chemo-mechanical coupling in elastic-plastic homoionic expansive clays. *Computer Methods in Applied Mechanics and Engineering*, 192(31-32), 3489-3530.

Gajo, A. and B. Loret (2003)b. Transient analysis of ionic replacements in elastic-plastic expansive clays. submitted for publication.

Loret, B., Gajo, A., and F.M. Simões (2003). A note on the dissipation due to generalized diffusion with electro-chemo-mechanical couplings in heteroionic clays. submitted for publication.

Mitchell, J.K. (1993). Fundamentals of Soil Behavior. 2nd ed., J. Wiley & Sons, Chichester.

Simões, F.M. and B. Loret (2003). Articular cartilage with intra- and extrafibrillar waters. Deformation, mass transfer and generalized diffusion. submitted for publication.

Sperelakis, N. (2001). Origin of the cardiac resting potential. Handbook of Physiology-The cardiovascular system I-The Heart, Chapter 6, 187-267.

Winslow, R.L., Rice, J.J., Jafri, S., Marban, E. and B. O'Rourke (1999). Mechanisms of altered excitation-contraction coupling in canine tachycardia-induced heart failure. II Model studies. *Circulation Resarch*, 84, 571-586.

Yeung, A. (1990). Electrokinetic barrier to contaminant transport through compacted clay, PhD Dissertation, University of California, Berkeley, 260 pp.

Finite Element Formulation, and Simulations of Laboratory Tests

Alessandro Gajo [†] and Benjamin Loret [*]

[†] Dipartimento di Ingegneria Meccanica e Strutturale, Università di Trento, Trento, Italia
[*] Laboratoire Sols, Solides, Structures, Institut National Polytechnique de Grenoble, France

Abstract A finite element formulation is developed to simulate laboratory tests and field events where (electro-)chemo-mechanical couplings are involved. The constitutive equations sketched in the previous chapters structure the formulation, and all aspects of mechanical behaviour, mass transfer, generalized diffusion and advection are accounted for.

Simulations of laboratory experiments aim at testing the assumptions of homogeneity and chemo-mechanical equilibria used to calibrate the mechanical constitutive equations. They reveal unexpected transient aspects, and point out to the capital importance of many details of the testing apparati.

1 Scope

A finite element formulation for chemically sensitive clays is reported below. Simulations aim at highlighting transient phenomena that were not displayed by the analysis of the chemo-mechanical constitutive behaviour. Indeed, to calibrate the chemo-mechanical behaviour, data were gathered from curves obtained by the aggregation of a succession of equilibria.

The couplings of mechanics with mass transfer and generalized diffusion imply time to be involved in actual experimental and in situ processes.

The finite element formulation for homoionic clays and for heteroionic clays presented here taps on Gajo and Loret [2003]ab. Available data allow to calibrate the diffusion parameters. A parametric analysis is performed to reveal the influence of the transfer coefficients. Details on the identification of the coefficients involved in the generalized diffusion equations can be found in these references.

2 Finite Element Formulation for Homoionic Clays

The semi-discrete equations. The four primary unknowns, namely

- the solid displacement $\mathbf{u}$,
- the fluid pressure p_W,
- the concentration c_{sW} of salt in pore water, and
- the mass-content of absorbed water m_{wS},

are interpolated, within the generic element e, in terms of the nodal values through a priori specific shape functions,

$$\mathbf{u} = \mathbf{N}_u \, \mathbf{U}^e, \quad p_W = \mathbf{N}_p \, \mathbf{P}^e_W, \quad c_{sW} = \mathbf{N}_c \, \mathbf{C}^e_{sW}, \quad m_{wS} = \mathbf{N}_m \, \mathbf{M}^e_{wS} \, . \tag{2.1}$$

Multiplying the four field equations by the virtual fields $\delta\mathbf{w}$, δp, δc and δm, and integrating by parts over the body V provides the weak form of the problem:

- balance of momentum of the porous medium as a whole :

$$\int_V \nabla\,(\delta\mathbf{w}) : \boldsymbol{\sigma}\, dV - \int_V \delta\mathbf{w} \cdot (\rho\,\mathbf{g})\, dV = \int_{\partial V} \delta\mathbf{w} \cdot \boldsymbol{\sigma} \cdot \hat{\mathbf{n}}\, dS \, ,$$

- global balance of mass :

$$\int_V \delta p \,\mathrm{div}\, \mathbf{v}_S - \nabla(\delta p) \cdot \mathbf{J}_W \, dV = - \int_{\partial V} \delta p \, \mathbf{J}_W \cdot \hat{\mathbf{n}}\, dS \, ,$$

- balance of mass of salt :

$$\int_V \delta c \left(n_W \frac{\delta c_{sW}}{\delta\, t} - c_{sW} \frac{\delta v_{wS}}{\delta\, t} \right) dV + \\ + \int_V -\nabla(\delta c) \cdot \mathbf{J}^{\mathrm{d}}_{sW}\, c_{wW} + \delta c\, \mathbf{J}_W \cdot \nabla c_{sW}\, dV = - \int_{\partial V} \delta c \; c_{wW} \, \mathbf{J}^{\mathrm{d}}_{sW} \cdot \hat{\mathbf{n}}\, dS \, , \tag{2.2}$$

- mass transfer equation :

$$\int_V \delta\, m \left(\frac{1}{k^{\mathrm{t}}_w} \frac{\delta m_{wS}}{\delta\, t} - (\overline{\mu}_{wW} - \overline{\mu}_{wS}) \right) dV = 0 \, ,$$

where $\hat{\mathbf{n}}$ is the unit outward normal to the boundary ∂V.

The resulting nonlinear first-order semi-discrete equations for the unknown vector $\mathbf{X}$,

$$\mathbf{X} = [\mathbf{U} \;\; \mathbf{P}_W \;\; \mathbf{C}_{sW} \;\; \mathbf{M}_{wS}]^{\mathrm{T}}, \tag{2.3}$$

with maximum nodal length = dimension of space+3, imply the residual $\mathbf{R}$,

$$\mathbf{R} = \mathbf{F}^{\mathrm{surf}}(\mathbf{S}, \mathbf{X}) - \mathbf{F}^{\mathrm{int+grav}}\left(\mathbf{g}, \mathbf{X}, \frac{\delta \mathbf{X}}{\delta\, t}\right) - \mathbf{F}^{\mathrm{adv}}(\mathbf{X}, \frac{\delta \mathbf{X}}{\delta\, t}) = \mathbf{O}, \tag{2.4}$$

to vanish. Here $\mathbf{F}^{\mathrm{surf}}$ is the vector of surface loadings denoted collectively $\mathbf{S}$; $\mathbf{F}^{\mathrm{int+grav}}$ is the vector that contains the elastic-plastic and viscous internal forces together with the gravity forces appearing in the left-hand-side of (2.2). $\mathbf{F}^{\mathrm{adv}}$ is the sum of element advective contributions including SUPG stabilization.

Time-integration. The semi-discrete equations are integrated through a generalized midpoint scheme defined by $\alpha \in]0, 1]$, that is, at step $n+1$, the equations are enforced at time $t_{n+\alpha} = t_n + \alpha \Delta\, t$, where $\Delta t = t_{n+1} - t_n$, namely

$$\mathbf{R}_{n+\alpha} = \mathbf{F}^{\mathrm{surf}}(\mathbf{S}_{n+\alpha}, \mathbf{X}_{n+\alpha}) - \mathbf{F}^{\mathrm{int+grav}}\left(\mathbf{g}, \mathbf{X}_{n+\alpha}, \mathbf{V}_{n+\alpha}\right) - \mathbf{F}^{\mathrm{adv}}(\mathbf{X}_{n+\alpha}, \mathbf{V}_{n+\alpha}) = \mathbf{O}. \tag{2.5}$$

Generically, for $\mathbf{Z}$=$\mathbf{S}$, $\mathbf{X}$, $\mathbf{V}$,

$$\mathbf{Z}_{n+\alpha} = (1-\alpha)\mathbf{Z}_n + \alpha\, \mathbf{Z}_{n+1} \, , \tag{2.6}$$

and $\mathbf{X}_{n+1}$ and $\mathbf{V}_{n+1}$ are approximations of $\mathbf{X}(t_{n+1})$ and $(\delta\mathbf{X}/\delta t)(t_{n+1})$ respectively. The system (2.5) is solved iteratively by an explicit/implicit operator splitting, namely at iteration $i+1$,

$$\mathbf{F}_E^{\text{surf}}(\mathbf{S}_{n+\alpha}, \mathbf{X}^i_{n+\alpha}) - \mathbf{F}_I^{\text{int}}\left(\mathbf{X}^{i+1}_{n+\alpha}, \mathbf{V}^{i+1}_{n+\alpha}\right) - \mathbf{F}_E^{\text{grav}}\left(\mathbf{g}, \mathbf{X}^i_{n+\alpha}\right) - \mathbf{F}_I^{\text{adv}}(\mathbf{X}^{i+1}_{n+\alpha}, \mathbf{V}^{i+1}_{n+\alpha}) = \mathbf{O}, \tag{2.7}$$

where,

$$\begin{aligned} &- \quad \text{for } i=0: \quad \mathbf{X}^0_{n+1} = \mathbf{X}_n + (1-\alpha)\,\Delta t\,\mathbf{V}_n, \quad \mathbf{V}^0_{n+1} = \mathbf{V}_n, \\ &- \quad \text{for } i \geq 1: \quad \begin{cases} \mathbf{X}^{i+1}_{n+1} = \mathbf{X}_n + \Delta t\,\mathbf{V}^{i+1}_{n+\alpha} = \mathbf{X}^0_{n+1} + \alpha\,\Delta t\,\mathbf{V}^{i+1}_{n+1} = \mathbf{X}^i_{n+1} + s\,\Delta t\,\alpha\,\Delta\mathbf{V}, \\ \mathbf{V}^{i+1}_{n+1} = \mathbf{V}^i_{n+1} + s\,\Delta\mathbf{V}. \end{cases} \end{aligned} \tag{2.8}$$

and

$$\mathbf{X}^{i(+1)}_{n+\alpha} = (1-\alpha)\,\mathbf{X}_n + \alpha\,\mathbf{X}^{i(+1)}_{n+1}, \quad \mathbf{V}^{i+1}_{n+\alpha} = (1-\alpha)\,\mathbf{V}_n + \alpha\,\mathbf{V}^{i+1}_{n+1}. \tag{2.9}$$

The scalar $s = s^{i+1}$ is a line search parameter. The subscripts $_E$ and $_I$ denotes a partition into explicit and implicit operators, that is, for any operator $\mathbf{F}$, $\mathbf{F}_E + \mathbf{F}_I = \mathbf{F}$. The splitting shown in (2.7) is motivated by the following observations:
- the dependence of the vector of external forces on the solution is weak;
- the vector of internal forces depends linearly on the rate vector $\mathbf{V}$;
- the vector of internal forces depends nonlinearly on the solution in several ways: the elasticity is strongly non-linear, due to the dependence of the elastic coefficients on both the effective mean-stress and the chemical state. Therefore, the elastic operator will always be treated implicitly. Elastoplasticity induces another type of nonlinearity, which may be treated explicitly or implicitly.

In the examples considered in the next section, only mechanical boundary fluxes, which are independent of $\mathbf{X}$, will be non zero and the gravity will be neglected. Therefore, the scheme turns out to be completely implicit.

The Newton direction $\Delta\mathbf{V}$ corresponding to $s=1$ is obtained by insertion of the time-integrator (2.8) in the residual (2.7), linearizing and setting the result to zero,

$$\mathbf{C}^*\,(\alpha\,\Delta\mathbf{V}) = \mathbf{R}^i_{n+\alpha}. \tag{2.10}$$

The effective diffusion matrix $\mathbf{C}^*$ is expressed in terms of the diffusion matrix $\mathbf{C}$ and of the stiffness matrix $\mathbf{K}$,

$$\mathbf{C}^* = \mathbf{C} + \alpha\,\Delta t\,\mathbf{K} \quad \text{with} \quad \mathbf{C} = \frac{\partial \mathbf{F}_I}{\partial \mathbf{V}}\left(\mathbf{X}^i_{n+\alpha}\right), \quad \mathbf{K} = \frac{\partial \mathbf{F}_I}{\partial \mathbf{X}}\left(\mathbf{X}^i_{n+\alpha}\right), \tag{2.11}$$

where $\mathbf{F}_I$ is the sum of implicit operators, namely internal forces and advective forces, and it has been recognized that the derivatives of $\mathbf{F}_I$ do not depend on $\mathbf{V}$.

The element diffusion and stiffness matrices have the following block structure,

$$\mathbf{C}^e = \begin{bmatrix} \mathbf{0} & \mathbf{0} & \mathbf{0} & \mathbf{0} \\ \mathbf{C}^e_{pu} & \mathbf{0} & \mathbf{0} & \mathbf{0} \\ \mathbf{0} & \mathbf{0} & \mathbf{C}^e_{cc} & \mathbf{C}^e_{cm} \\ \mathbf{0} & \mathbf{0} & \mathbf{0} & \mathbf{C}^e_{mm} \end{bmatrix}, \quad \mathbf{K}^e = \begin{bmatrix} \mathbf{K}^e_{uu} & \mathbf{K}^e_{up} & \mathbf{0} & \mathbf{K}^e_{um} \\ \mathbf{0} & \mathbf{K}^e_{pp} & \mathbf{K}^e_{pc} & \mathbf{0} \\ \mathbf{0} & \mathbf{K}^e_{cp} & \mathbf{K}^e_{cc} & \mathbf{0} \\ \mathbf{K}^e_{mu} & \mathbf{0} & \mathbf{K}^e_{mc} & \mathbf{K}^e_{mm} \end{bmatrix}. \tag{2.12}$$

The virtual primary unknowns are discretized with the same shape functions as the actual unknowns, advection requiring a special treatment.

The finite element discretization involves quadratic solid displacements (3 nodes per element) while the other three unknowns vary linearly (2 nodes per element). The number of integration points and history points are two, for all stiffness matrices and all residuals. Plastic history is stored at the same two points.

A single mesh has been used for all tests: it involves 10 elements of length 0.4 mm in the porous stone and, in the upper half sample, 29 elements of length increasing from 0.0125 mm close to the porous stone to 0.4 mm at the center of the specimen. The qualitative accuracy of the results has been checked with a mesh twice finer.

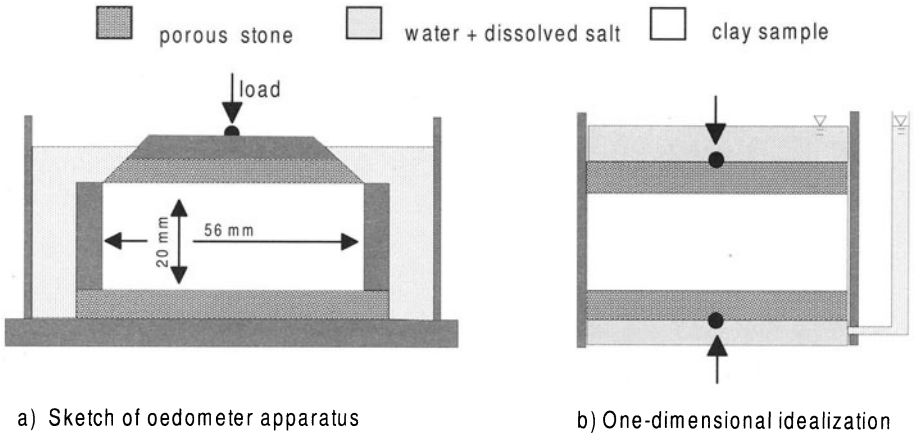

Figure 1 Schematic of an oedometer test. The sample in the oedometer apparatus undergoes instantaneous mechanical loading through a rigid porous stone. Chemical loading is performed by infiltration of a solution of controlled chemical composition through the lateral sides of the porous stone. Note that the solution is kept at atmospheric pressure. A change in composition of the solution reaches the interface porous stone/sample delayed and smoothed out. Moreover, center points receive the change in composition later than peripheral points, a). This heterogeneity is not accounted for by the one-dimensional idealization, b).

3 Chemical Consolidation and Swelling in Homoionic Clays

The oedometer apparatus: caveats. The oedometer apparatus seems ideal for a preliminary test of the validity of the constitutive equations and of the computational artillery. Indeed it provides essentially one-dimensional displacements and flows. There are however caveats.

For purely mechanical tests, load measurements may be biased by lateral friction when the sample would like to change volume. In addition, for chemo-mechanical tests, a closer look at the flow paths of pore water and salt is necessary. In fact, in the experimental setup used by Di Maio [1996] schematized in Figure 1, the porous stones at the top and

bottom of the sample are in contact on the internal side with the sample and on the external side either with the solution, or with an impervious basis. Therefore, when salt is added to the solution, it reaches first the points located at the periphery of the porous stone. Salt will then diffuse vertically and obliquely towards the sample. The change in salt concentration at the interfaces between the porous stone and the sample will not occur at the same time for all the points of these interfaces. Therefore, in view of the stubby shape of the sample (height 20mm, radius 28mm) the one-dimensional idealization is not exactly correct during chemical loading/unloading stages. No attempt was made to mimic the oblique flow path of salt at the periphery of the porous stone, nor the longer path that salt entering the porous stone on its center has to travel. The height, porosity and diffusion coefficients of porous stone have a very strong influence on the actual chemical loading rate *on* the sample: in fact the porous stone damps considerably the external changes of composition of the solution, Figure 2. This is why a parametric analysis of the effects induced by the thickness of the porous stone, a quantity that may assume various values, has to be performed.

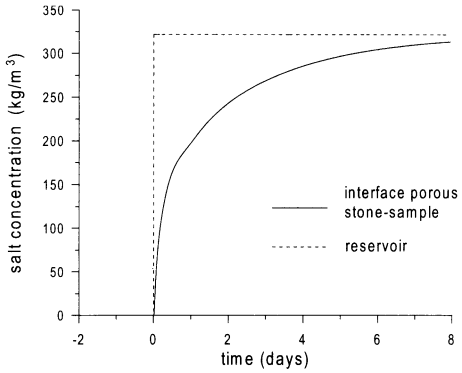

Figure 2 The instantaneous chemical loading in the reservoir is smoothed out by the porous stone. Dashed curve: salt concentration in the reservoir; solid curve: salt concentration at the interface porous stone-sample.

A quasi-static mechanical loading is transmitted instantaneously to the sample, the homogeneity of the stress state being improved by reducing the lateral friction. On the other hand, changes of chemical loading in the reservoir are not transmitted instantaneously and homogeneously over the whole sample. One might argue that the characteristics of the apparatus affect only a transient period; this would be inconsequential for a linear behaviour, it is certainly not if the transient (essentially uncontrolled) stage gives rise to irreversibilities. Consequently, while the one-dimensional idealization involves some slight approximation, the porous stone should be definitely included together with the sample in the finite element domain.

Another difficulty in the simulations comes from the fact that chemical consolidation may induce cracking: the actual computations were stopped when the stress was close to vanish.

Chemical versus mechanical consolidation/swelling. The solution in the reservoir is initially distilled water and the sample is normally consolidated with $p_{c0} = 20\,\text{kPa}$. At time t=0, a load is applied to mechanically consolidate the sample under a vertical stress equal to 40 kPa. Once a steady state has been reached, the salt concentration of the reservoir is increased instantaneously to saturation ($\equiv$ chemical consolidation). The composition is kept constant until consolidation of the sample is reached and then the salt concentration in the reservoir is instantaneously reduced to zero ($\equiv$ chemical swelling).

Figure 3 compares the evolution in time of the consolidation and swelling ratios for this purely chemical loading cycle at constant load and for a purely mechanical loading cycle, at given reservoir chemistry, in fact distilled water. The scatter in experimental data shown in Figure 3 is due to the large range of stress levels involved. The delay in osmotic consolidation is originated by the buffer effect of the inert porous stone, across which salt has first to diffuse before reaching the sample. The delay in osmotic swelling is originated by both that effect plus the key fact that the mechanical coupling, that is mainly volume expansion, occurs only when the salt concentration returns to low values, less than 1 mole/liter, as we have observed in the chapter on constitutive equations. At higher salt concentrations, the mechanical properties change little. Consolidation and swelling ratios in Figure 3 are independent, so that irreversible effects are concealed by this figure; they are shown in Figure 11.

Characteristic times. Notice that the fact that consolidation is reached does not imply that the spatial profile of salt concentration is uniform. This aspect will be stressed in the comments below.

The analysis of each stage, chemical consolidation and swelling, highlights three characteristic times, namely

- end of dissipation of negative pressures,
- end of dissipation of positive pressures (consolidation time),
- end of diffusion of salt.

These time and space inhomogeneities might be thought to induce size effect and to lead to a final inhomogeneous steady state, especially because the elastic-plastic material is sensitive to the loading paths. We observe that this is however not the case only at moderate stress levels and for the range of material properties considered which are representative of Ponza Clay.

The osmotic efficiency induces negative pore pressures. During chemical consolidation, the pore pressure profiles show strong fronts that propagate downwards, Figures 4 and 5. Higher salt concentrations in the upper part of the sample give rise to a negative pore pressure wave (which would induce an upward water flow). We have seen in the Chapter 'Mass Transfer and Generalized Diffusion' that the water flux $\mathbf{J}_W$ is equal to $-k_D\,(\nabla p_W - \omega\nabla\pi)$. Since the pressure is maintained to zero (atmospheric pressure reference) at the top of the sample, negative pressures develop on a downward propagating front, at locations where the osmotic efficiency is large because the salt concentration is small, as far as the low permeability does not allow water to move upwards fast enough

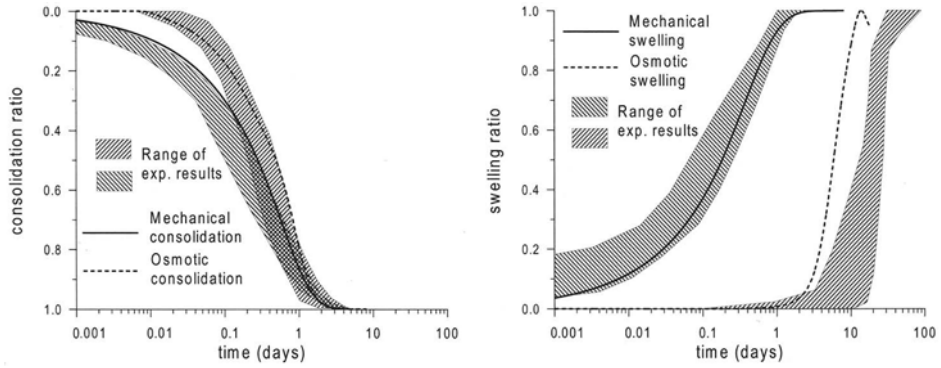

(a) Consolidation. (b) Swelling.

Figure 3 Mechanical (solid curve) and osmotic (dashed curve) consolidation and swelling ratios resulting from the computations. Dashed areas: experimental data from Di Maio [1996], her figures 9 and 10.

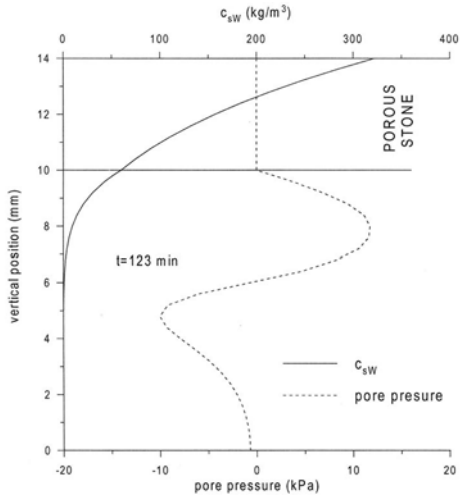

Figure 4 Spatial profiles of salt concentration and pore pressure about 2 hours after chemical loading. Downward diffusion of salt gives rise to negative pore pressures due to osmotic efficiency at small concentration. Subsequent mechanical coupling induces a downward propagating contractancy front and consequently positive pressures.

so that $\mathbf{J}_W \sim \mathbf{0}$. A contrario, a vanishing osmotic efficiency results in a quite different picture, Figure 6. As the salt concentration increases, the osmotic efficiency quickly decreases and mechanical coupling induces a volume decrease: both phenomena contribute to bring pore pressures from negative to positive values, except at the top of the sample since the reservoir is maintained at atmospheric pressure. The development of a negative

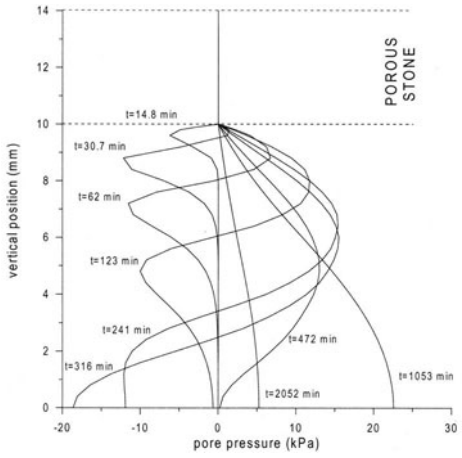

Figure 5 Evolution in time of the pore pressure profiles during chemical consolidation. A front of negative pore pressures due to osmotic efficiency propagates downwards at very small salt concentrations. A positive pore pressure front due to mechanical contraction follows at salt concentration lower than normal($\equiv$ 1 mole/liter). Later increase of salt concentration does not drive further pore pressures which dissipate.

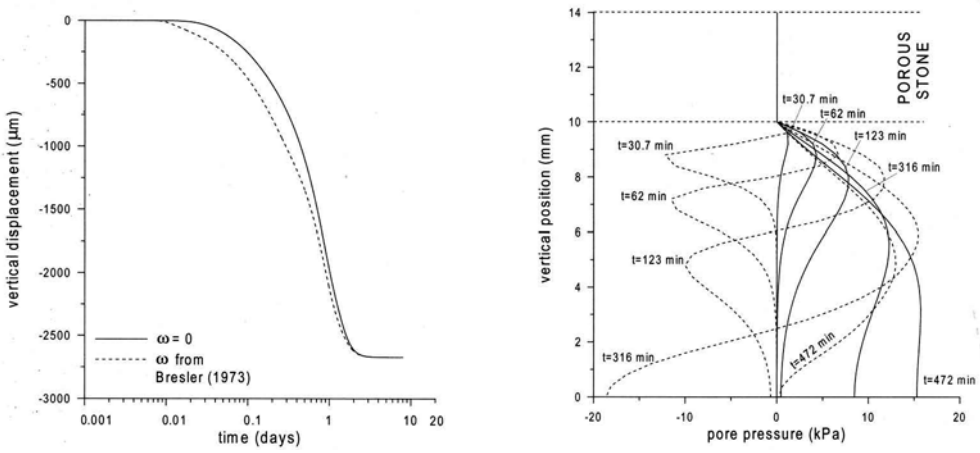

(a) Vertical displacement.

(b) Pore pressures.

Figure 6 Osmotic efficiency, by introducing cross-couplings in the diffusion law, gives rise to negative pore pressures in early times.

pore pressure front has been observed during experiments by J.C. Santamarina (private communication). These changes of sign of the pore pressures might induce ultimately non-homogeneous state variables in elastic-plastic or brittle materials. At low stress levels, circumferential cracking is expected to occur due to contractancy and vanishing

lateral effective stresses induced by the positive pore pressures.

In fact, Fernandez and Quigley [1991] mention that the application of a minimum effective stress is necessary to prevent the huge increase of hydraulic conductivity due to organic contaminant. They observe that this increase of hydraulic conductivity is due to the double layer contraction causing an increase of 'free void space' (corresponding to our void ratio $e^* = V_S/V_W$) at fairly constant value of the conventional void ratio e.

After a short transient period where osmotic efficiency is large, cross-couplings in the generalized diffusion law due to osmotic efficiency do not modify the Darcy's direction of water flow that is opposite to the pore pressure gradient, Figure 7.

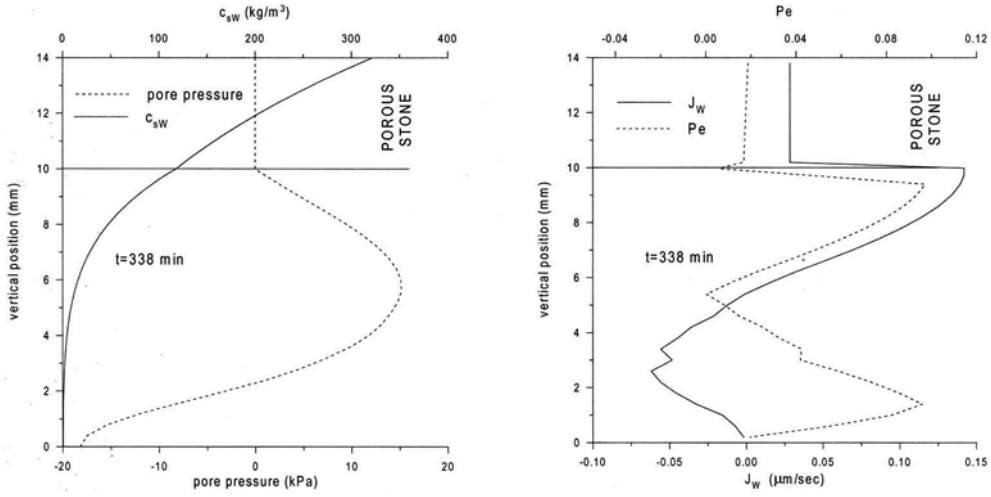

(a) Salt concentration and pore pressure. (b) Water flux $\mathbf{J}_W$ and Péclet number P_e.

Figure 7 Profiles of various quantities at time $t = 338$ mn during chemical consolidation.

The successive events. The downward history of pore pressure is faster than that of salt concentration, compare Figures 5 and 8-(a). In fact, increase of salt concentration quickly drops osmotic efficiency, and therefore the negative pressure front. The positive pressure front occurs due to mechanical coupling for salt concentration lower than 1 mole/liter: the presence of salt triggers water desorption, stiffening and shrinking of the solid skeleton and therefore increases the pore pressure. Further increase of salt concentration does not drive pore pressures any longer, since the mechanical coupling fades away. After about three days, they have dissipated and displacements stabilize, Figure 11-(a).

Salt diffusion, as controlled by the value of the effective diffusion coefficient D_s^* and affected adversely by advection, is slower and a uniform profile is reached only after eight days, Figure 8. Water desorption, due to mechanical coupling, shows virtually the same profile since the mass transfer is quasi-instantaneous. Note that salt concentration and desorbed mass show diffusive profiles, Figure 8, in agreement with the small value of the

global Péclet number $|\mathbf{v}^{\mathrm{adv}}|\, L/D_s^*$, defined by the advective velocity $\mathbf{v}^{\mathrm{adv}} \sim \mathbf{v}_{wW} - \mathbf{v}_S$ the half-height of the sample $L = 10\,\mathrm{mm}$, and the effective diffusion coefficient D_s^*, Figure 7-(b).

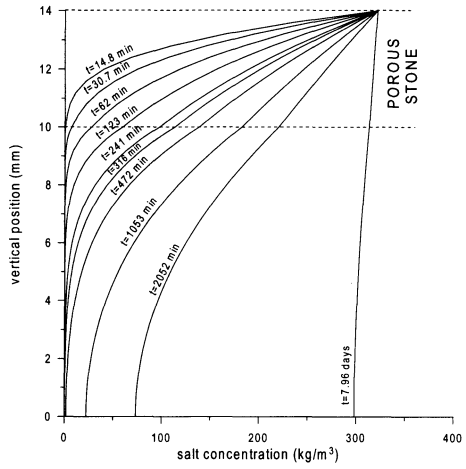

(a) Salt concentration.

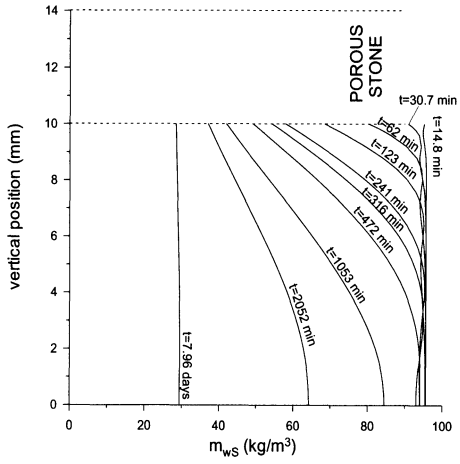

(b) Mass of absorbed water.

Figure 8 Evolution in time of the profiles of salt concentration and mass of absorbed water during chemical consolidation.

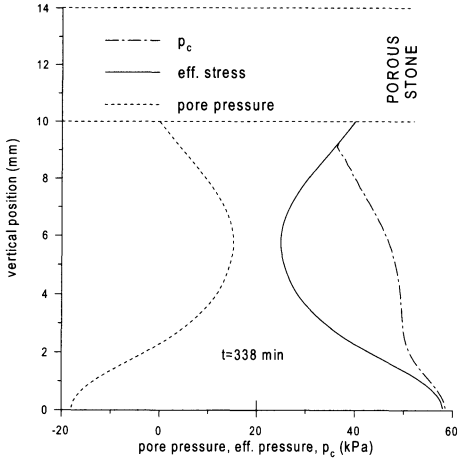

(a) Ponza bentonite, early time.

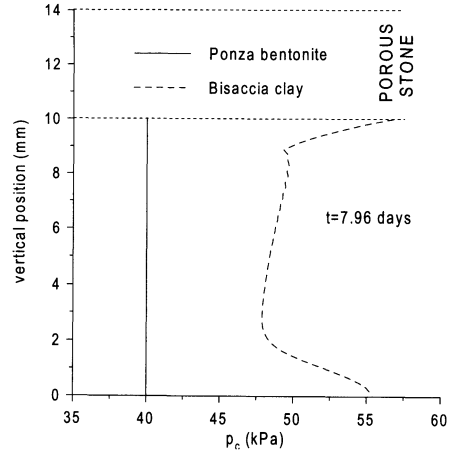

(b) Preconsolidation stress, late time.

Figure 9 Vertical profiles of effective stress, pore pressures and preconsolidation stress at an early time for Ponza bentonite (a); Comparison of preconsolidation stress at the end of the chemical consolidation process for Ponza bentonite and Bisaccia clay (b).

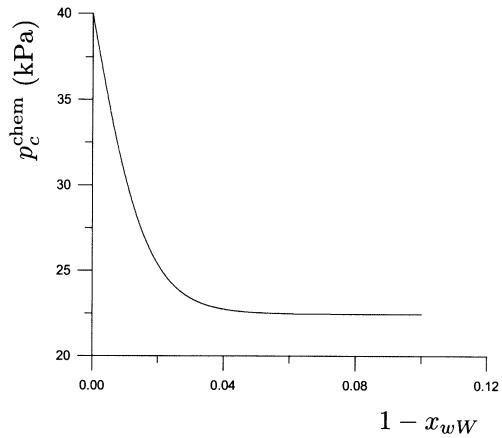

Figure 10 For Ponza bentonite, chemical softening holds, that is, the chemical effect on the preconsolidation stress p_c is always negative.

Chemo-plastic preconsolidation. During the chemical loading process, the total vertical stress is constant and equal to 40 kPa (gravity is neglected). Since the pore pressure varies from -20 kPa to +20 kPa, the effective stress $\overline{p}$ will vary as well. When the pore pressure is negative, the effective stress is larger than 40 kPa and plasticity occurs with strain-hardening. Subsequent chemical loading accompanied with increasing pore pressures, and decreasing effective stress, occurs initially elastically, Figure 9. Later, due to chemical softening, the preconsolidation stress decreases (the sole chemical softening reduces it from 40 kPa to 22 kPa at salt saturation), while the positive pore pressures dissipate, and the effective stress increases again towards 40 kPa. Starting from the porous stone interface, a plastic zone where $p_c = \overline{p}$, with p_c increasing due to strain-hardening, penetrates the sample downwards. At the end of the chemical consolidation, the preconsolidation stress p_c is uniform, Figure 9-(b): chemical softening decreases p_c, Figure 10, but strain-hardening should develop to sustain the vertical load. Depending on the model parameters, the chemical softening stage may stop at some lower salt concentration, and further chemical loading would imply chemical preconsolidation and an elastic behaviour. However, although theoretically possible because $\overline{p}_\kappa$ and $\overline{p}_\lambda$ are distinct, this is not the case: in fact the condition $\lambda_3 = \kappa_3$ is known to be non conducive to preconsolidation, see Chapter 'Constitutive Equations for Homoionic Clays' for notation and concepts.

The effects of the stress level. The figure 11 shows the time evolution of the vertical displacement of the top of the sample during chemical consolidation and swelling at constant vertical stress. For the vertical stress of 40 kPa, the strain matches well the homogeneous analysis performed in Loret et al. [2002] for both the consolidation (maximum) value and swelling (residual) value, their Figure 7-a. For the larger stress level of 320 kPa, both values are smaller than the homogeneous analysis, because then the difference in loading history with respect to the homogeneous case is more important.

Indeed, the larger effective stresses experienced in the finite element analysis lead to a smaller irreversible settlement. In fact, the final plastic state at this stress level is not homogeneous, as the large negative pressures (not shown) induce a large preconsolidation stress near the middle of the sample. The slight final overshoot of the displacement is to be linked to the final dissipation of positive pore pressures, and consequently increase of effective stress: this effect is not observed in experiments and might be an artefact of the one-dimensional idealization.

Competing events. Both characteristic times, end of dissipation of negative pore pressures first at about 8h and end of dissipation of positive pore pressures at about three days are identified on the time evolution of the displacement of the top of the sample, Figures 11-(a),(b). The transition from negative to positive pore pressures is associated, due to equilibrium, to a decrease of effective stress. There is a competition between this local mechanical trend to dilatancy which temporarily slows down the settlement and the progressive establishment of the global equilibrium (consolidation process), resulting in a sigmoidal time profile of the vertical settlement at points A in Figures 11-(a),(b). To confirm this interpretation, let us note that, when negative pore pressures are absent, e.g. for a vanishing osmotic efficiency, this sigmoidal shape does not appear, Figure 6-(a); on the other hand, when negative pore pressures are more important, the sigmoidal shape is more visible.

Once positive pore pressures have dissipated, the strain and vertical displacement stabilize even if the salt concentration has not reached a steady state, Figure 8: the reason is that, at salt concentrations larger than one mole/liter, the chemo-mechanical coupling is quite low, that is the mechanical parameters are practically independent of the chemical content, Figure 8 of Loret et al. [2002].

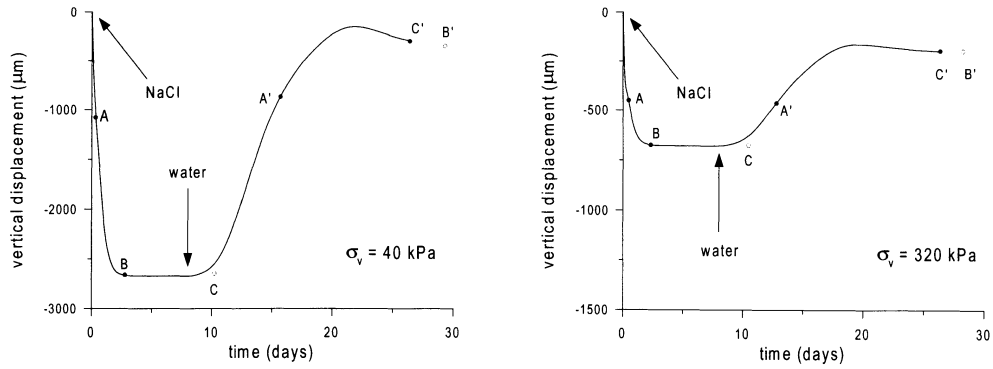

(a) Vertical stress 40 kPa.

(b) Vertical stress 320 kPa.

Figure 11 Evolution of the vertical displacement of the top of the sample during chemical consolidation and swelling. A: end of dissipation of negative pore pressures, B: end of dissipation of positive pore pressures, C: end of salt diffusion for chemical consolidation. A', B' and C' are the associated characteristic times during chemical swelling.

Sensitivity analysis. Some parameters are not directly accessible through macroscopic experiments. On another side, it is interesting to analyze the sensitivity of the results with respect to the experimental setting, e.g. geometry of the sample, properties of the porous stone, etc ... In both cases, parameters may be varied around a plausible value to detect their influences.
- *effect of permeability*: increasing the permeability yields larger negative pore pressures because the permeability enters the coupling effect due to osmotic efficiency, and therefore triggers plasticity and increases the vertical settlement;
- *effect of porous stone*: the thicker the porous stone, the smoother the chemical loading and the slower the consolidation process;
- *effect of sample height*: the taller the sample, the smaller the negative pressures, and the slower the consolidation process;
- *effect of advective transport*: during chemical loading, salt is diffusing downwards while water is flowing upwards, allowing for consolidation. Therefore neglecting advection results in slightly faster downward diffusion of salt, and slightly faster consolidation. This effect is expected to depend on Péclet number. For the parameters at hand, advective transport has an effect similar to a twofold increase of diffusion coefficient;
- *effect of transfer time* τ_w: increase of the transfer time by a factor 10^4 delays consolidation, and leads to larger negative pore pressures. The later effect is due to the fact that the chemo-mechanical trend to contractancy, which increases pore pressures, is much delayed. Notice however that these larger negative pore pressures grow after a while, and once they do, they result in larger compressive effective stresses which induce, with some delay, an increase of the rate of settlement, with a limited backwards-and-forwards excursion in the domain of positive pore pressures.

Transfer time is expected to be much larger than the mere transfer time associated to the elementary system consisting of two aligned (or oblique) plates. Note also that the existence of an internal memory effect, due here to transfer of a species between solid and fluid phases, is shared by the double porosity scheme where the transfer occurs between the two fluid phases, namely the fluids of fractures and pores.

4 Simulations of Soil Electro-Remediation with a Rigid Skeleton

The principles of electrokinetic remediation have been briefly sketched in Section 5 of the Chapter 'Examples of chemo-mechanical interactions in geological and biological materials'.

Some details on laboratory setups are provided now and emphasis is laid on the development of the acid front during the remediation process. Next, finite element simulations of a specific test using the generalized diffusion model exposed in the previous chapter are presented.

4.1 Laboratory Setups

Laboratory experimental setups use graphite passive electrodes to avoid spreading of parasite ions into the soil sample. Samples are typically prepared in horizontal cylindrical tubes, 10 to 20 cm long and 5 cm in diameter. Alshawabkeh and Acar [1996], p. 188, argue that a one-dimensional idealization is a good approximation of actual experiments. Electrodes, placed at the extremities, are endowed with reservoirs, that allow to circulate an electrolyte of controlled chemical composition. This separation between electrodes and soil avoids heating and dessication, desaturation and cracking. Reservoirs are separated from the soil by a membrane permeable to water and ions. In fact, electro-osmosis depletes water from the anode region and moves it towards the cathode: control of the electrolyte circulating in the reservoir allows to provide water at the anode and dispose of it at the cathode. Additional passive electrodes along the sample allow measurements, e.g. Eykholt and Daniel [1994].

A typical electrokinetic experiment proceeds as follows. The initial state is usually homogeneous and defined by a given concentration of cations, anions and pH. An electrical field is applied between the electrodes. The pore pressures at the electrodes are maintained at a reference value, say atmospheric pressure. Flow of water and ions is prevented on the bottom soil boundary while the upper soil boundary is kept at atmospheric pressure. Therefore a one-dimensional analysis appears as a good approximation. The boundary conditions for the ionic species at the electrodes are of two types: either the concentrations are given initially and, during the experiments, the ionic fluxes are free, or the concentrations are given in the reservoirs.

4.2 Development of an Acid Front

A significant step forward in the understanding of electrokinetic processes is due to the contribution of Acar et al. [1994]. They show that the most prominent phenomenon is the development of an acid front starting close to the anode and moving towards the cathode. An electrolytic decomposition of water in ions hydrogen and hydroxyl occurs at the electrodes, Figure 12,

$$\begin{aligned} H_2O \quad - \quad 2e^- \quad &\rightarrow \quad 1/2\,O_2 \uparrow \quad + \quad 2H^+ \qquad \text{oxidation at anode} \\ 2H_2O \quad + \quad 2e^- \quad &\rightarrow \quad H_2 \uparrow \quad + \quad 2OH^- \qquad \text{reduction at cathode} \end{aligned} \tag{4.1}$$

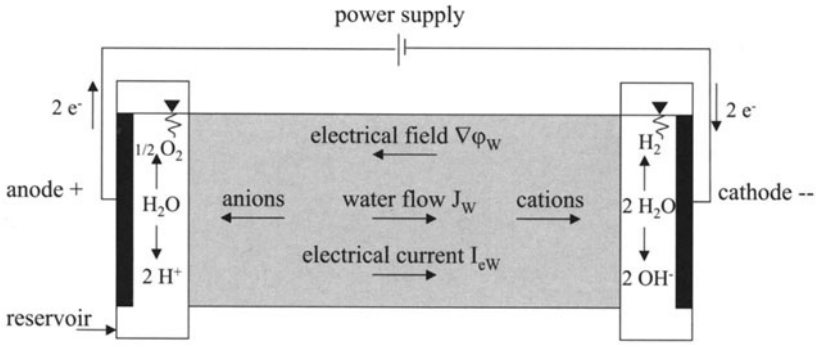

Figure 12 Schematization of the setup an elektrokinetic remediation process. An acid front due to freed hydrogen ions H^+ is created at the anode that propagates towards the cathode. A basic front due to freed hydroxyl ions OH^- is also created at the cathode that propagates towards the anode. However, the motions are not symmetric and the acid front is faster than the basic front: first, because the mobility of hydrogen ions is 1.76 higher than that of hydroxyl ions; second because electro-osmosis implies, below the isoelectric point, a water flow towards the cathode, therefore amplifying the motion of cations and opposing that of anions. However, high pH prevalent close to the cathode might jeopardize the efficiency of the process and precipitate metal hydroxides.

The mobility of these ions is high with respect to that of other ions [1] and, once generated, they move in the soil by advection of the pore fluid, fickian diffusion and migration due to electrical field. The acid front created by the motion of hydrogen ions H^+ towards the cathode and the basic front created by the motion of hydroxyl ions OH^- towards the anode are not symmetric first because the mobility of the former is much larger and second because the motion of the H^+'s (resp. OH^-) is assisted (resp. opposed) by electro-osmosis.

4.3 Finite Element Simulations

Initial and boundary conditions, and material parameters. A soil is placed in between two vertical electrodes separated by a distance L=100 mm. The soil is rigid so that there are no chemo-mechanical couplings, precipitation/dissolution is not accounted for, and there are no chemical reactions, except water auto-ionization which is instantaneous[2]

$$H_2O \leftrightarrow H^+ + OH^- . \tag{4.2}$$

[1] Some absolute ionic mobilities (unit: $10^{-8}\,m^2/s/V$): 36.25 for H^+, 20.55 for OH^-, 7.4 for NO_3^-, 8.25 for SO_4^-; effective mobilities are obtained by multiplication of absolute mobilities by tortuosity.

[2] In practice, it seems that water auto-ionization and oxidation-reduction at electrodes combine to produce the acid front, but here we account only for water-autoionization.

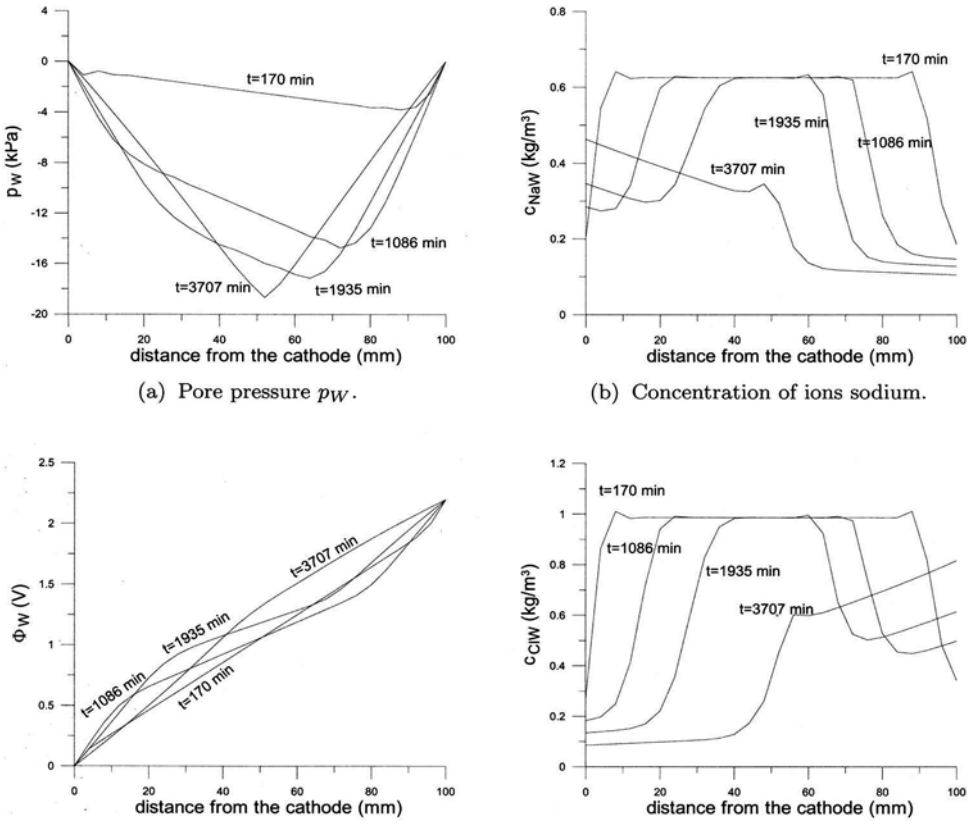

(a) Pore pressure p_W.

(b) Concentration of ions sodium.

(c) Electrical potential ϕ_W.

(d) Concentration of ions chloride.

Figure 13 Simulations of an electrokinetic remediation process on a rigid soil.

The effective diffusion coefficients D_k^*, k=Na, K, Cl, osmotic efficiency ω and tortuosity τ are given in Table 1, and the initial concentrations in Table 2. The soil is discretized by a mesh of 25 linear elements of length 4 mm. A constant difference of electrical potential $\Delta\phi_W = 2.2\,\mathrm{V}$ is imposed between the two electrodes through a linear ramp over 10 mn. The electrodes are bathed in two reservoirs kept at atmospheric pressure and water can flow freely between the soil and the reservoir. Three elements are added on each side to simulate the external reservoirs.

Initially, the concentrations of ions sodium, potassium, chloride, hydrogen and hydroxyl is uniform in the soil and in the reservoirs, but the ionic strength is lower in the latter. The motions of ions and water can be considered to be one-dimensional. The water of the reservoirs is not refreshed so that the concentrations of ionic species change during the tests, and the volume of the reservoirs comes into picture: the larger the ratio volume of reservoirs/volume of soil, the more constant stay the ionic concentrations in

the reservoirs.

Table 1. Material parameters for the electro-remediation process

n_W	K_h (m/sec)	D^*_{Na} (m^2/sec)	D^*_{K} (m^2/sec)	D^*_{Cl} (m^2/sec)	ω	τ
0.66	10^{-8}	0.8×10^{-10}	1.18×10^{-10}	1.22×10^{-10}	0	0.06

Table 2. Initial concentrations (mole/liter)

	Na^+	K^+	Cl^-	H^+	OH^-
soil	0.027186	0.0006539	0.0278399	10^{-7}	10^{-7}
reservoirs	0.00817755	0.0001716	0.00834915	10^{-7}	10^{-7}

The electro-osmotic coefficient can be expressed in terms of the ζ-potential by the Helmholtz-Smoluchowski relation $k_{\mathrm{e}} = -n_W \tau \epsilon \zeta / \eta$, which involves the dynamic viscosity of fluid phase η, its permittivity ϵ and the tortuosity of the porous medium τ. The permittivity of a substance is equal to the product of its dielectric constant D(=78.3 for distilled water at 20 °C), and of the permittivity of vacuum $\epsilon_0 = 8.8542 \times 10^{-12}\,\mathrm{C}^2/\mathrm{J/m}$. The dynamic viscosity of water has been taken equal to 0.89×10^{-3} kg/m/sec (the dynamic viscosity of distilled water at 20°C is 10^{-3} kg/m/sec).

The above formulas indicate clearly that the sign of the electro-osmotic coefficient depends on the sign of the electrical charge of the particles. Therefore, typically, k_{e} is expected to be positive for clays insensitive to pH, and positive at high pH and negative at low pH for pH-sensitive clays like kaolinites. For kaolinite beds, Eykholt and Daniel [1994] average experimental data of the zeta potential to $\zeta = -38.1 + 281 \exp(-0.48\,\mathrm{pH})$ (unit: mV). The change of sign of ζ occurs at pH=4.16, and, for pH$\geq$7, ζ varies little between -28 and -38 mV. The above pH-dependent ζ-potential has been used to obtain the results shown in Figure 13.

Results. The finite element simulations are shown in Figure 13. As expected, electro-osmosis draws water towards cathode in the vicinity of which the electro-osmotic coefficient is always positive. Suction (negative pore pressure) develops because this water flow towards cathode is not equilibrated by an equal water flow from anode. In fact the progressive acidification of the anode region reduces the electro-osmotic coefficient, and even makes it negative, so that the contribution of electro-osmosis to the water flow turns progressively towards anode. This trend is balanced by Darcy law so that a final steady suction establishes.

The resulting pore pressure field is here approximately symmetric between anode and cathode while suction is larger close to cathode in the experiments of Eykholt and Daniel [1994] and Acar and Alshawabkeh [1996]. Recall that in the present preliminary simulations, the electrical conductivity does not account for the contribution of hydrogen and hydroxyl ions.

Electromigration drives cations to cathode and anions to anode, Figure 13-(b),(d). The electric conductivity is obtained by summing up contributions from ions Na^+, K^+ and Cl^- only. The electrical field (gradient of electrical potential) does not deviate much from a constant, Figure 13-(c): its spatial profile are linked to those of the pore pressure.

Electromigration implies a pH front to develop from anode to cathode, as described by Acar et al. [1994]. The rate of advancement is of the order of 1cm/day as in the experiments of Acar and Alshawabkeh [1994].

As a final comment, note that the development of negative pressures would trigger settlements in a coupling electro-chemo-mechanical analysis (work in progress).

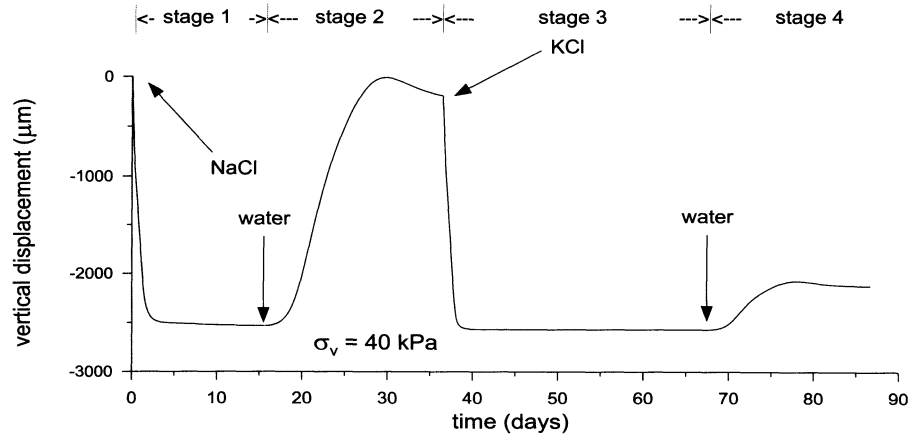

(a) Chemical loading history with a single replacement.

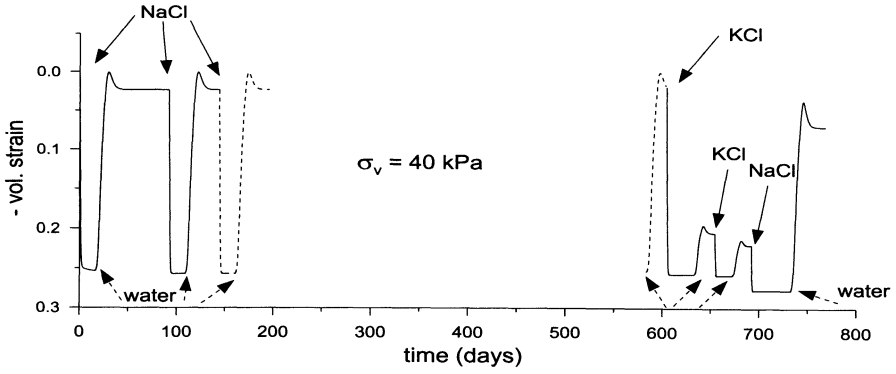

(b) More complex chemical loading histories.

Figure 14 Evolution of the settlement of the oedometer during changes of chemical composition of the reservoir at constant vertical stress. Finite element computations.

5 Simulations of Ionic Replacements

Finite element simulations of oedometric mechanical and chemical loadings on Ponza Clay considered as a heteroionic clay are presented in Gajo and Loret [2003]b. The concentrations of all ionic species present in the fluid and solid phases are obtained at each node of the mesh at each time step. The simulations aim at illustrating the dramatic differences on mechanical properties due to the presence of different ions. This point has been stressed in the Chapter 'Constitutive Equations for Heteroionic Clays'. Here time effects due to mass transfer and generalized diffusion are accounted for.

The loading process. The solution in the reservoir is initially distilled water and the sample has been normally consolidated to 40 kPa. The subsequent chemical loading programme simulated involves four stages, Figure 14-(a):

stage 1: at time t=0, the NaCl concentration of the reservoir is increased to saturation.
stage 2: the NaCl saturated solution of the reservoir is replaced by distilled water.
stage 3: the KCl concentration of the reservoir is increased to saturation.
stage 4: the KCl saturated solution of the reservoir is replaced by distilled water.

Ions K^+ and Na^+ have quite distinct mechanical effects. Initially, the mass of cations sodium in the solid phase (clay platelets) is taken five times larger than the mass of cations potassium.

The evolution of the vertical settlement during the first chemical consolidation (stage 1) and swelling (stage 2) follows essentially the same lines as when the clay is viewed as homoionic, Figure 14-(a). In particular, chemical consolidation occurs after about two days while swelling takes about two weeks to stabilize.

Dramatic differences occur when KCl is added in the reservoir. The specific ionic effect is revealed only upon stage 4 when the reservoir is refreshed. Indeed, the saturated state has been guessed to be independent of the ions present in the solid phase, so that the vertical dimensions after addition of NaCl or KCl are the same. On the other hand, the introduction of ion K^+ in the solid phase has ejected Na^+ present initially, so that the elastic and plastic compliances at the end of stage 3 are much smaller than at the end of stage 1. This result in a much smaller swelling in stage 4, as the mechanical behaviour is now controlled essentially by the ions K^+.

The exact time sequence and transfer times. Correlations of the simulations with the data by Di Maio [1998] require the transfer time for water to be much smaller than for ions.

The actual evolution of the vertical settlement depends on the time at which the chemistry of the reservoir is modified. Let us illustrate this point by an example, Figure 14-(b). After KCl loading, the reservoir is refreshed 30 days later: the resulting swelling is larger than at next cycle. This is because all the cations sodium have not been yet expulsed from the interlayers. The volume change upon swelling is thus larger than when only cations potassium are present.

A priori, two chemical loadings that differ only by the time sequence will induce different transient responses but equal steady states, if only elastic processes are involved.

However, as we have seen, the mechanical properties are strongly affected by chemistry, and plastic events might develop for one time sequence and not for the other, so that, in general, the steady states might differ as well.

Bibliography

Acar, Y.B., Hamed, J., Alshawabkeh, A.N. and R.J. Gale (1994). Removal of cadmium (II) from saturated kaolinite by application of electric current. *Géotechnique*, 44, 239-254.

Acar, Y.B. and Alshawabkeh, A.N. (1996). Elektrokinetic remediation. I: Pilot-scale tests with lead-spiked kaolinite. *J. of Geotechnical Engng. Div.*, Transactions of the ASCE, 122(3), 173-185.

Alshawabkeh, A.N. and Acar, Y.B. (1996). Elektrokinetic remediation. II: Theoretical model. *J. of Geotechnical Engng. Div.*, Transactions of the ASCE, 122(3), 186-196.

Di Maio, C. (1996). Exposure of bentonite to salt solution: osmotic and mechanical effects. *Géotechnique*, 46(4), 695-707.

Di Maio, C. (1998). Discussion on 'Exposure of bentonite to salt solution: osmotic and mechanical effects'. *Géotechnique*, 48(3), 433-436.

Eykholt, G.R. and D.E. Daniel (1994). Impact of system chemistry on electro-osmosis in contaminated soil. *J. of Geotechnical Engng. Div.*, Transactions of the ASCE, 120, 797-815.

Fernandez, F. and R.M. Quigley (1991). Controlling the destructive effects of clay-organic liquid interactions by application of effective stresses. *Canadian Geotechnical J.*, 28, 388-398.

Gajo, A. and B. Loret (2003)a. Finite element simulations of chemo-mechanical coupling in elastic-plastic homoionic expansive clays. *Computer Methods in Applied Mechanics and Engineering*, 192(31-32), 3489-3530.

Gajo, A. and B. Loret (2003)b. Transient analysis of ionic replacements in elastic-plastic expansive clays. submitted for publication.

Loret, B., Hueckel, T. and A. Gajo (2002). Chemo-mechanical coupling in saturated porous media: elastic-plastic behaviour of homoionic expansive clays. *Int. J. Solids and Structures*, 39, 2773-2806.

Swelling shales and compacting cakes

J.D.Sherwood *
* Schlumberger Cambridge Research, High Cross, Madingley Rd, Cambridge CB3 0EL, England

Abstract

Swelling clays are important to the petroleum industry because of their use in drilling fluids and because of their presence in shales through which oil wells are drilled. Models for compaction of clay filtercakes are discussed; these models incorporate chemical effects both in the equilibrium stress-strain relation and in the transport relations for water and ions. Analyses of shale swelling similarly require models both for equilibrium and for transport. A theory based upon Biot poroelasticity is applied to a wellbore geometry, and laboratory experiments are presented. Transport through a clay membrane is analysed in terms of linear relations for the fluxes of water and ions as functions of the jump in chemical potentials across the membrane, and the analysis is used to interpret experiments.

1 Introduction

Drilling for oil is an expensive, hazardous operation in which a hole is drilled through rock, perhaps for a distance of several kilometres. Rock mechanics has therefore always been a subject of interest to the petroleum industry. In some parts of the world the rocks to be drilled are strong and chemically inert, and drilling is straightforward. However, elsewhere the driller encounters shales formed from clay particles which have sedimented to the sea bed and then undergone compaction over geological timescales. Such shales have very low permeability, and are therefore capable of preventing the migration of hydrocarbons, which accumulate within the rock pores to form a petroleum reservoir. It is therefore not uncommon to find shales in the neighbourhood of petroleum reservoirs: in the North Sea many hundreds of metres of shale or shaly sand must be drilled before petroleum is reached.

Some shales swell when brought into contact with water-based drillling fluids, and in the following lectures I shall discuss the problems encountered when drilling through such shales. The reverse process, compaction, occurs when filtercakes are formed from the clay particles within drilling fluids, and this too will be discussed. Sometimes we shall restrict our attention to equilibrium properties of shales and clay compacts, but often the rate at which swelling (or compaction) occurs is important and so transport properties will also be of interest.

In general, the materials with which a petroleum engineer works are ill-characterised. It is difficult to obtain large, undamaged samples of shale for mechanical testing, and the

fluids used during drilling are far removed from the idealised suspensions often studied in academic colloid science laboratories. The analyses presented here and in the other lectures are important aids to understanding, but empirical knowledge is just as important (if not more so) to the engineer who has to plan and monitor the drilling of an oil well. To set the scene, we first describe this process.

Figure 1(i) shows a very simplified sketch of an oil well. The drill bit is connected to the surface by a cylindrical pipe (the drill string). In a vertical well such as that shown in figure 1(i), the entire drill string is rotated at the surface in order to turn the bit downhole. If the well deviates significantly from the vertical, it may be more practical to rotate only the bit, by means of a downhole motor, rather than the entire drill string. As the well increases in length, it becomes necessary to extend the drillstring by adding extra 30 foot (9.1 m) lengths of drillpipe (stands) to the drillstring.

The rock cuttings created by the drill bit have to be brought to the surface. This is done by means of a drilling fluid which fills the entire well throughout the course of drilling. The fluid (often referred to as 'mud') is pumped down the hollow drillstring and through nozzles in the drill bit, forming high-speed jets which dislodge rock cuttings. The drilling fluid then flows up the annulus between the drillstring and rock, and carries the cuttings with it. From time to time it is necessary to stop pumping (e.g. whenever an additional stand of drillpipe is added to the drillstring), and it is important that the rock cuttings within the annulus do not then sediment to the bottom of the well. It is therefore desirable that the drilling fluid possesses a yield stress, so that rock cuttings are held in suspension. Many drilling fluids are based on a suspension of bentonite (clay) particles in water. Such fluids are thixotropic, and form a gel on emerging from the region of turbulent flow close to the drill bit. They then appear to have a yield stress (at least on the engineering timescales of practical interest) which is capable of maintaining rock cuttings in suspension.

The hydrostatic pressure within a fluid-filled wellbore plays an important role in balancing the earth stresses within the surrounding rock. If the wellbore were empty, the rock would be unable to withstand these stresses and the wellbore would collapse. Earth stresses usually increase with depth more rapidly than does the hydrostatic pressure in a column of water, and the density of the drilling fluid is increased by the addition of barite particles of density 4200 kg m^{-3}. These barite particles must be maintained in suspension, so the rheology of the drilling fluid is again of importance.

The pressure within the fluid-filled pores of the rock similarly increases with depth. It is usually desirable to prevent gas or other pore fluids escaping from the rock into the wellbore during the course of drilling, and so the density of the drilling fluid is usually chosen so that the pressure within the wellbore is higher than that in the pores of the surrounding rock. This pressure difference drives a flow from the wellbore into the rock pores. Typical pore sizes are such that the liquid within the drilling fluid can enter the rock pores, but the clay particles are too large to enter, and form a filter cake on the rock-fluid interface. If the drilling fluid has been correctly designed, this filtercake has very low permeability, and controls the rate at which fluid is lost into highly permeable rocks. We shall discuss filtercake growth in §2. If the rock has very low permeability, little or no cake will form, but little fluid will be lost into the rock. Shales are often weak, so that the drilling fluid density has to be carefully controlled in order to avoid

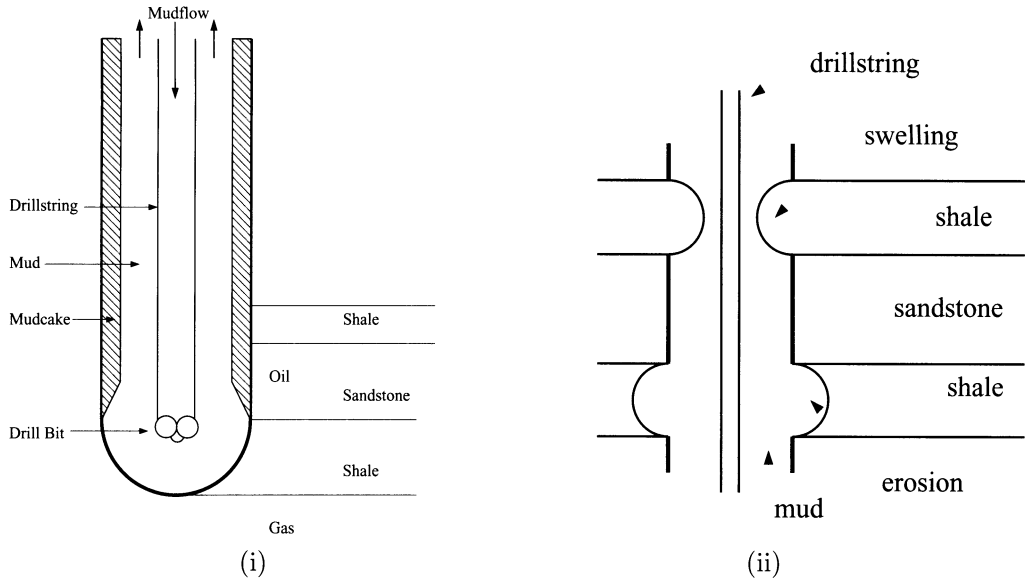

Figure 1. (i) During drilling, the drilling fluid circulates down the drillstring and up the surrounding annulus. Clay particles that are too large to enter the rock pores form a cross-flow filtercake at the surface of the rock. (ii) Swelling shales can reduce the wellbore diameter, thereby trapping the drillstring. Alternatively, the weak swollen shale can be eroded by flow within the wellbore.

mechanical instability of the wellbore, but if the low permeability shale is inert, fluid loss should not be a problem.

However, some shales swell when in contact with water-based drilling fluids. Although the initial permeability of the shale is low, the permeability of swollen shale, with high water content, is much larger. Fluid flow into the rock pores can therefore take place more rapidly than might be estimated from the initial permeability of the shale. The wellbore diameter can be reduced by swelling of the surrounding shale (figure 1(ii)), and drillstring can become stuck.

Alternatively, the swollen shale disperses in the drilling fluid and the wellbore is locally enlarged (figure 1(ii)). Drillstring can snag on the resulting roughened rock surface as the string is tripped in and out of the well. The drilling fluid becomes more viscous as a result of the large number of finely dispersed clay particles, which are not easily removed by the standard screens used to remove drilled rock cuttings. Some of the problems of drilling through shales are reviewed by Durand *et al.* (1995a,b).

Thus the drilling engineer needs to understand the behaviour of clays within both shale and drilling fluid. Shale swelling involves the irreversible breaking of cementation bonds formed between individual clay particles, and the compaction of clay particles, either in soil or in a filtercake, is not reversible. In both cases this irreversibility is poorly understood. Nevertheless, it is convenient to regard these two processes as the converse of each other.

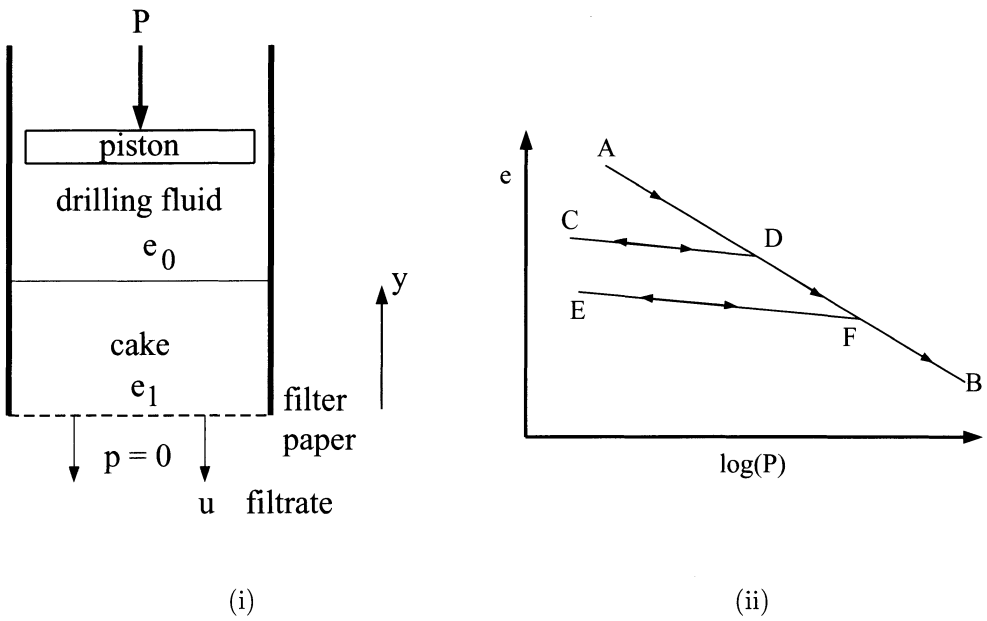

(i) (ii)

Figure 2. (i) A simple filtration test with applied pressure P. (ii) Typical compaction curves for soil, as found in standard textbooks of soil mechanics. The void ratio e is shown as a function of the applied pressure P.

We shall first discuss filtercake compaction in the absence of any chemo-mechanical couplings. We then (§3) show how such couplings play a role in both the mechanical properties of the cake and in the transport of water and ions through the cake. In §4 we discuss equilibrium models for clay swelling, based on Biot poroelasticity, and in §5 we show how these may be applied to the wellbore geometry. Finally in §6 we discuss a continuum model for flow of water and ions through clay, and use it to interpret simple laboratory experiments.

2 Filtration of a chemically inert suspension

2.1 Continuum analysis

Many models of filtration are available, and the work presented here is based on that of Philip & Smiles (1982). Applications of this theory to wellbore filtration have been reviewed by Sherwood & Meeten (1997) and by Sherwood (1997), and there is a recent review of compressive rheology by de Kretser *et al.* (2003).

We consider uniaxial filtration, as depicted in figure 2(i). Following Philip & Smiles we describe both the slurry and filter cake by means of the void ratio e, defined as

$$e = \frac{\text{volume of liquid}}{\text{volume of solid}}. \tag{2.1}$$

The volume fraction of solids, ϕ, is related to e *via* $\phi = 1/(e+1)$.

Filtration occurs sufficiently slowly that the forces acting on the particles and liquid within the cake are always in equilibrium, and we assume that gravity may be neglected. The stress within the cake may be expressed as the sum of the liquid pressure p and an additional term which we associate with the stress within the matrix of solid particles. We further divide the matrix stress into an isotropic part Ψ and a deviatoric (shear) stress Σ. The y component of the stress balance within the cake leads to an equation

$$p + \Psi + \Sigma_{yy} = \text{constant}. \tag{2.2}$$

During compaction of the cake, the matrix of solid particles is continuously yielding, and Σ_{yy} is related to the yield stress within the cake, as discussed by Meeten (1994). However, the yield stress is generally small compared with the isotropic pressure Ψ required to compact the cake, and we choose here to neglect Σ_{yy}. Its inclusion in models of uniaxial compaction is straightforward.

We assume that the void ratio e within the cake is a function of the isotropic matrix stress Ψ. Filtrate flow, at a velocity u_{rel} relative to the particles within the cake, is assumed to obey Darcy's law:

$$u_{\text{rel}} = -\frac{k(e)}{\mu}\frac{\partial p}{\partial y} \tag{2.3}$$

where μ is the viscosity of the filtrate, and the permeability k of the cake is assumed to be a function of the void ratio e. We adopt a Lagrangian coordinate m, defined by

$$m = \int_0^y [1 + e(y')]^{-1}\, \mathrm{d}y'. \tag{2.4}$$

The filtrate is assumed to be incompressible, and the evolution of void ratio e as a function of time t is given by the equation of continuity:

$$\frac{\partial e}{\partial t} = -\frac{\partial u_{\text{rel}}}{\partial m} = \frac{\partial}{\partial m} D(e) \frac{\partial e}{\partial m} \tag{2.5}$$

where

$$D(e) = -\frac{k(e)}{\mu(1+e)}\frac{\mathrm{d}\Psi}{\mathrm{d}e}. \tag{2.6}$$

Equation (2.5) is a diffusion equation, and $D(e)$ is a diffusivity. In the limit $e \to 0$ (or $P \to \infty$) we expect $k(e) \to 0$ and $\mathrm{d}\Psi/\mathrm{d}e \to \infty$: one or other of these limits will dominate and determine the behaviour of $D(e)$. It is most unlikely that $D(e)$ tends to a finite, non-zero value as $e \to 0$.

At time $t = 0$ the pressure P is applied to the upper surface of the slurry, and hence, within the cake, equation (2.2) becomes

$$p + \Psi(e) = P. \tag{2.7}$$

Initially, the slurry has void ratio e_0, and this will usually be sufficiently large (i.e. the solids volume fraction ϕ is sufficiently small) that $\Psi(e) \simeq 0$, and hence the liquid pressure

$p \simeq P$ far from the filter cake. We shall assume that P is held constant throughout the filtration process.

At the base of the cake, the filtrate is at atmospheric gauge pressure $p = 0$, and hence the matrix stress $\Psi = P$. The immediate effect of the applied pressure is therefore to compact the slurry at the base of the cake to a void ratio e_1, where

$$\Psi(e_1) = P. \tag{2.8}$$

If the volume of slurry is infinite there are solutions of (2.5) in which the cake thickness grows as $t^{1/2}$ and the filtration flux decreases as $t^{-1/2}$. Such solutions also hold during the early stages of dewatering of a finite sample of slurry, when the upper piston (see figure 2(i)) is sufficiently far from the cake. The void ratio e can be expressed as a function of a similarity variable $s = mt^{-1/2}$, and the diffusion equation (2.5) becomes

$$\frac{\mathrm{d}}{\mathrm{d}s}\left(D(e)\frac{\mathrm{d}e}{\mathrm{d}s}\right) = -\frac{s}{2}\frac{\mathrm{d}e}{\mathrm{d}s}. \tag{2.9}$$

The volume of filtrate Q collected per unit area of filter paper is given by

$$Q = St^{1/2} \tag{2.10}$$

where

$$S = \int_0^\infty (e_0 - e)\,\mathrm{d}s \tag{2.11}$$

is a desorptivity.

If the volume of slurry is finite, with $0 \leq m \leq M$, the boundary condition $u_{\mathrm{rel}} = 0$ is appropriate at the upper surface of the slurry, and hence

$$\frac{\partial p}{\partial m} = \frac{\partial \Psi}{\partial m} = 0 \qquad \text{at } m = M. \tag{2.12}$$

During the early stages of filtration, when the piston is far from the surface of the cake, the similarity solution (2.9) holds. Eventually, however, the supply of slurry above the cake becomes exhausted, and filtration ceases when all the slurry has been compacted to a void ratio e_1.

Results for $\Psi(e)$ can be obtained by squeezing a cake at a fixed pressure until filtration has ceased. The moisture content of the cake is determined by weighing the cake first when wet, and subsequently after drying. The resulting values for e_1, shown in figure 3(i), were fitted to the expression

$$e_1 = e_\infty + \left(\frac{p_1}{P + p_2}\right)^\alpha \tag{2.13}$$

with $e_\infty = 0.45$, $p_1 = 18.6$ bar, $p_2 = 0.15$ bar and $\alpha = 0.60$. Equation (2.13), with $p_2 = 0$, is of the form found by Carrier & Beckman (1984) and by Den Haan (1992). The addition of a fourth parameter p_2 markedly improves the fit to the experimental data shown in figure 3(i), but it should not be assumed that (2.13) has any fundamental

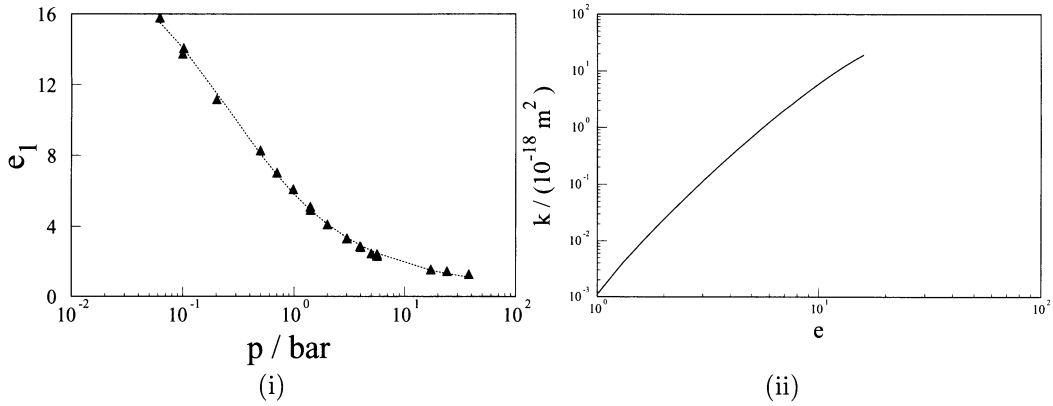

Figure 3. (i) Final void ratio e_1 as a function of applied filtration pressure P. (ii) Filtercake permeability $k(e)$ computed by means of (2.13) and (2.14).

significance, nor that it may be extrapolated beyond the range of pressures over which experiments were performed. In particular, (2.13) predicts $e_1 \to e_\infty + (p_1/p_2)^\alpha = 18.5$ as $P \to 0$, rather than $e_1 \simeq e_0 = 43.5$.

It is possible to obtain an estimate for $D(e)$ from data for S obtained over a range of pressures, as discussed by Smiles & Harvey (1973) and by Sherwood & Meeten (1997), who for a particular bentonite found

$$D(e) = C(E - e)(B - e)^{2\beta - 1} \tag{2.14}$$

where $C = 955\ \mathrm{pm^2\,s^{-1}}$, $E = 51.5$, $B = 78.8$, $\beta = 2.68$. Note that (2.14) predicts that D tends to a finite, non-zero value $CEB^{2\beta-1}$ as $e \to 0$, which is not expected from (2.6). This serves as a warning that an expression such as (2.14) should not be extrapolated beyond the range over which the experimental data were obtained.

If we combine (2.13) and (2.14) in (2.6) we may obtain an estimate of the permeability $k(e)$, as shown in figure 3(ii), but again we must remember that the results should not be extrapolated beyond the range of e over which they were obtained.

So far there has been no mention of chemo-mechanical effects. Nevertheless, the above discussion has introduced two important features, namely the mechanical properties of the compacted clay, described by $\Psi(e)$, and the transport properties of the cake, described by the permeability $k(e)$.

It is convenient to think of compaction as a re-arrangement of the clay particles. Figure 4(i) shows randomly arranged clay particles which are negatively charged over their flat surfaces, with an edge charge which varies according to pH (Van Olphen, 1977). When edges and faces are oppositely charged, it is standard to discuss a house-of-cards structure similar to that figure 4(i), though direct evidence for such an arrangement is difficult to find. After compaction, the charged faces of the clay particles are in close proximity (figure 4(ii)) and repulsions can cause swelling when the applied pressure is reduced. Such swelling in clay soils is not reversible, and uniaxial compaction/swelling

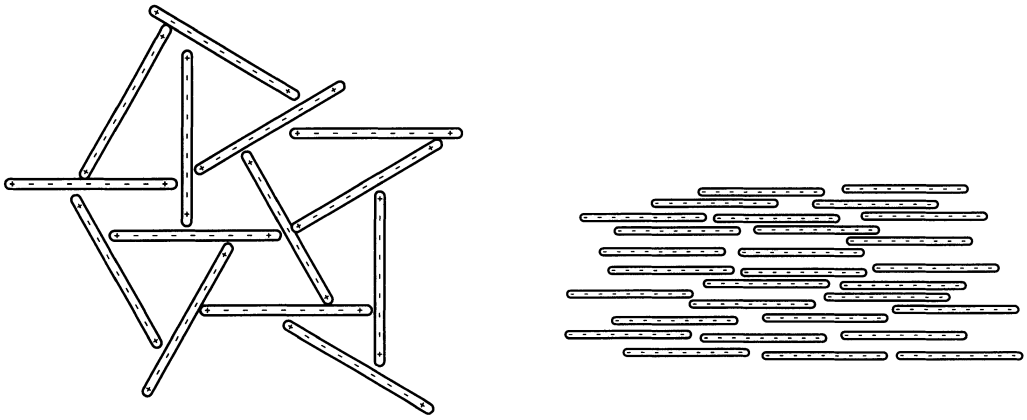

(i) (ii)

Figure 4. (i) A random house-of-cards structure for clay before compaction. (ii) After compaction, the clay particles are aligned, and repulsion can occur between charged clay surfaces.

is often represented by diagrams similar to figure 2(ii) (e.g. Atkinson & Bransby 1978). The primary compaction curve AB in figure 2(ii) is equivalent to the compaction curve of figure 3(i). However, if the compaction pressure is reduced from C swelling occurs (reversibly) over the curve CB. Explanation of this hysteriesis in terms of microscopic models of friction is not yet developed.

2.2 A simple microscopic model

Figure 5 shows an idealised 2-dimensional model of a filtercake. The clay particles are plates of thickness $2k$ and length $2L_c$, arranged in N_c layers with layer $n = 1$ adjacent to the filter paper. A pressure p_A is applied at the upper surface of the filtercake, $n = N_c$. The separation $2h_n$ between plate layers n and $n+1$ varies with n, and the void ratio is

$$e = \frac{\text{volume of fluid}}{\text{volume of solid}} = h/k. \tag{2.15}$$

The model in figure 5 is 2-dimensional: all fluxes and forces will be per unit thickness of the model in the direction normal to the surface of the page.

The path of a typical fluid particle is depicted on figure 5. The total distance travelled within the cake is $L = N_c L_c$. We can use this path-length to define the lengthscale L in the direction of flow; this leads naturally to a Lagrangian coordinate $\hat{x} = n/N_c$. The local superficial fluid velocity through the cake is Q, so that the volume flux through any one gap (e.g. A on figure 5) is $2QL_c$ and the fluid flux along any one channel (e.g. CD on figure 5) is QL_c. Assuming plane Poiseuille flow, it can be shown that the pressures acting on the two sides of any single plate lead to a downwards force F_H on the plate of magnitude

$$F_H = \frac{3L_c^3 Q\mu}{2}\left(\frac{1}{h_n^3} + \frac{1}{h_{n+1}^3}\right). \tag{2.16}$$

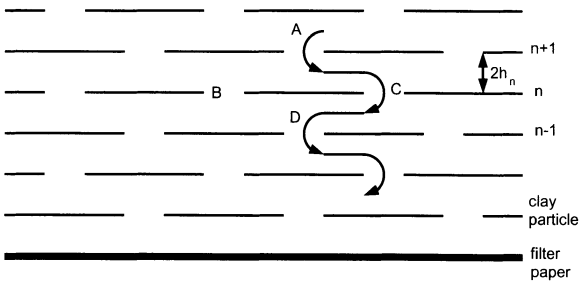

Figure 5. A simple microscopic model for a cake of clay platelets.

Colloidal forces, such as electrical double layer repulsions and contact or cementation forces, will also act upon each face of the plates. Such forces are discussed by Israelachvili (1992). In §3 we shall adopt a model based upon classical theory of electrical double layers between plane particles (e.g. Russel *et al.*, 1989). We refer the reader to recent detailed analyses of such theories (Leote de Carvalho *et al.*, 2000, Rowan & Hansen, 2002), but it is known from experiment (e.g. Powell *et al.*, 1998) and simulation (e.g. Chang *et al.*, 1998) that the predictions of the classical theory break down when there are only a few layers of water between the clay particles. Here we leave the forces unspecified and merely assume that they have strength $2L_cF_e(h)$. Since the entire process of compaction is sufficiently slow for inertia to be negligible, the force balance on one plate implies

$$\frac{3L_c^2Q\mu}{4}\left(\frac{1}{h_n^3}+\frac{1}{h_{n+1}^3}\right)=F_e(h_n)-F_e(h_{n+1}). \tag{2.17}$$

The equation of continuity for the fluid (assumed incompressible) is

$$2L_c\frac{\partial h_n}{\partial t}=L_c(Q_n-Q_{n+1}). \tag{2.18}$$

Regarding n as a continuous variable, we may combine (2.17) and (2.18) to give

$$\frac{\partial h}{\partial t}=\frac{\partial}{\partial n}\left(\frac{h^3}{3L_c^2\mu}\frac{\mathrm{d}F_e}{\mathrm{d}h}\frac{\partial h}{\partial n}\right)=\frac{\partial}{\partial n}\left(D(h)\frac{\partial h}{\partial n}\right). \tag{2.19}$$

This is a non-linear diffusion equation, and $D(h)$ plays the role of a diffusivity. The permeability of the cake is $4h^3(k+h)/3L_c^2$. Taking $L_c=10^{-7}$ m and $h=k=5\times10^{-10}$ m gives an estimated permeability $10^{-23}\,\mathrm{m}^2=10^{-11}$ Darcy, two orders of magnitude smaller than the permeabilities reported by McKelvey & Milne (1962). The pressure F_e plays the role of the matrix stress $\Psi(e)$.

The microscopic model of figure 5 can be modified to introduce non-parallel plates (Anandarajah, 2000) or particle flexibility (Sherwood & Van Damme, 1994), but any realistic representation of the permeability of a clay compact would need to be 3-dimensional.

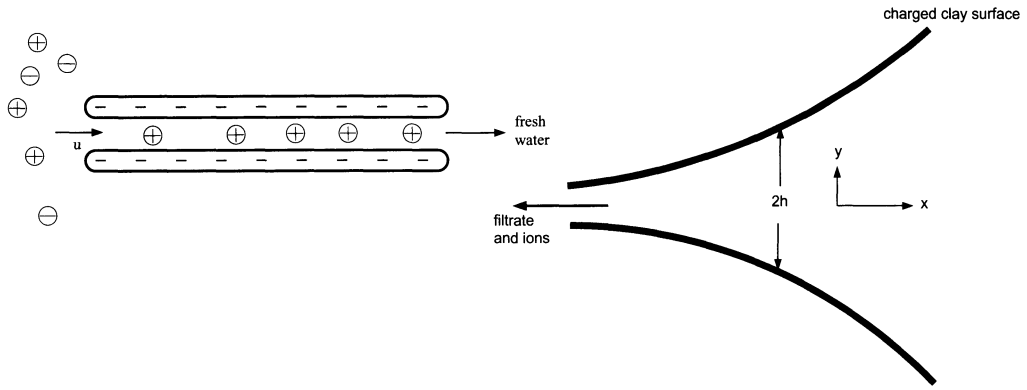

Figure 6. (i) Anions are excluded from the narrow gap between two negatively charged clay surfaces. (ii) Lubrication model of a filtercake, with clay surfaces close together at the base of the cake.

3 Filtration of clay, water and ions

We now introduce the effect ions into models of filtercake compaction. As indicated in §2, we need to consider both the equilibrium compaction of the filtercake as a function of ionic concentration, and the effect of ions upon transport within the cake.

The ionic content of a suspension of clay particles can influence both the colloidal stability of the suspension and its rheological properties. If the suspension is compacted in order to squeeze out the fluid, it is not clear (since the clay particles are charged) how the ionic content of the filtrate relates to that of the original suspension. Moreover, any non-uniformity of the ionic content within the compacting filtercake will affect the filtration process, if only because it will modify the forces between the clay particles and thereby modify the stress distribution within the cake.

Similarly, the ionic content of the pore fluid within a shale (which consists largely of clay compacted over geological timescales) can affect the properties of the shale, including the tendency of the shale to swell when brought into contact with fresh water. We shall see below that any pore fluid collected by compacting a shale sample may not represent the original *in-situ* pore fluid.

Many theoretical studies have considered the compaction to occur sufficiently slowly that the clay suspension is at all times uniform in space. We shall set down the analysis for this limit in §3.1. However, the process of filtration usually causes a concentrated, compacted cake to form between the filter membrane and the original clay suspension. The cake is non-uniform, and typical concentration profiles are given by Sherwood *et al.* (1991). It is well known that clay compacts can act as ion-exclusion membranes, because of the negative charges over the flat surfaces of the clay particles (e.g. McKelvey & Milne 1962, Jacazio *et al.* 1972, Kharaka & Berry 1973, Rieke & Chilingarian 1974). In figure 6(i) we see that cations can enter the gap between the clay particles more easily than anions. In order to maintain electrical neutrality an electric field (the streaming potential) is set up and reduces the flow of cations. The ionic content of the filtrate

which passes through the cake will therefore differ from that of the suspension above the cake. In §3.2 we discuss a model for the transport coefficients which control the motion of water and ions through the cake, and in §3.4 we present numerical results for the time-evolution of the clay- and ion-concentration profiles within the cake.

3.1 Donnan Equilibrium

A clay particle can be considered as a large, charged colloidal particle, and the theory of the Donnan equilibrium can therefore be applied to the ionic equilibrium between a clay suspension and an electrolyte. We follow the presentation due to Overbeek (1956).

Suppose a large colloidal ion, of valence Z, is confined to one side (the inside) of a membrane through which it is unable to diffuse. The molar fraction of this ion is x_z^{i} on the inside and 0 outside the membrane. Superscripts i and o will be used to denote the inside and outside, respectively. The molar fractions of the ions of the salt (assumed monovalent) are x_+ and x_-, while x_w is the molar fraction of the solvent. The partial molar volumes of the solvent, V_w, and ions, V_+, V_-, are assumed to be independent of the pressure p. The electrical potentials are ψ^{i} and ψ^{o} inside and outside the membrane.

We use the standard notation k for Boltzmann's constant, T for temperature, N_A for Avogadro's number, $R = kN_A$ for the gas constant, $F = eN_A$ for the Faraday. The symbol e, used here for the charge on a proton, has already been adopted for the void ratio (2.1), but it is unlikely that the reader will be confused. Assuming ideality, the equality of the electrochemical potentials for all species able to diffuse through the membrane requires

$$(p^{\mathrm{i}} - p^{\mathrm{o}})V_+ + F(\psi^{\mathrm{i}} - \psi^{\mathrm{o}}) = RT\ln(x_+^{\mathrm{o}}/x_+^{\mathrm{i}}) \tag{3.1}$$

$$(p^{\mathrm{i}} - p^{\mathrm{o}})V_- - F(\psi^{\mathrm{i}} - \psi^{\mathrm{o}}) = RT\ln(x_-^{\mathrm{o}}/x_-^{\mathrm{i}}) \tag{3.2}$$

$$(p^{\mathrm{i}} - p^{\mathrm{o}})V_w = RT\ln(x_w^{\mathrm{o}}/x_w^{\mathrm{i}}). \tag{3.3}$$

In addition, electroneutrality requires

$$x_+^{\mathrm{i}} - x_-^{\mathrm{i}} + Zx_z^{\mathrm{i}} = 0 \tag{3.4}$$

$$x_+^{\mathrm{o}} - x_-^{\mathrm{o}} = 0. \tag{3.5}$$

Adding (3.1) and (3.2) gives

$$\ln\frac{x_+^{\mathrm{o}}x_-^{\mathrm{o}}}{x_+^{\mathrm{i}}x_-^{\mathrm{i}}} = \frac{(p^{\mathrm{i}} - p^{\mathrm{o}})(V_+ + V_-)}{RT}. \tag{3.6}$$

When the concentration of the colloidal ion is sufficiently small, the pressure difference $p^{\mathrm{i}} - p^{\mathrm{o}}$ on the right hand side of (3.6) may be neglected, and hence

$$x_+^{\mathrm{i}}x_-^{\mathrm{i}} = x_+^{\mathrm{o}}x_-^{\mathrm{o}}. \tag{3.7}$$

The osmotic pressure difference is

$$p^{\mathrm{i}} - p^{\mathrm{o}} = \frac{RT}{V_w}\ln\frac{x_w^{\mathrm{o}}}{x_w^{\mathrm{i}}} = \frac{RT}{V_w}\ln\frac{1 - 2x^{\mathrm{o}}}{1 - x_+^{\mathrm{i}} - x_-^{\mathrm{i}} - x_z^{\mathrm{i}}} \tag{3.8}$$

$$\simeq RT(c_+^{\mathrm{i}} + c_-^{\mathrm{i}} - 2c^{\mathrm{o}} + c_z^{\mathrm{i}}), \tag{3.9}$$

where $x^{\mathrm{o}} = x^{\mathrm{o}}_{+} = x^{\mathrm{o}}_{-}$, and where c denotes a molar concentration (i.e. moles per litre of solution). We can now see that the right-hand side of (3.6) is indeed negligible as long as $x^{\mathrm{i}}_{+} + x^{\mathrm{i}}_{-} - 2x^{\mathrm{o}} + x^{\mathrm{i}}_{z} \ll 1$.

The potential difference between the inside and outside follows from (3.1) and (3.2) after neglecting the small pV terms:

$$\psi^{\mathrm{i}} - \psi^{\mathrm{o}} = \frac{RT}{F} \ln \frac{c^{\mathrm{o}}_{+}}{c^{\mathrm{i}}_{+}} = \frac{RT}{F} \ln \frac{c^{\mathrm{i}}_{-}}{c^{\mathrm{o}}_{-}}. \tag{3.10}$$

We now consider the ionic content of filtrate which is removed from the suspension by compaction. Following Bolt (1961a), Appelo (1977) and Smith (1977) we assume that the suspension is at all times uniform, and that it is in equilibrium with the fluid most recently exuded through the filter membrane. This equilibrium between filtrate and suspension is the unstirred limit, and is close to what happens when filtrate leaves the filter membrane as a series of individual droplets. Alternatively, some experiments have been performed on systems which are held in contact with a large reservoir of salt solution of known composition (Denis, 1991).

We assume that the volume V_s occupied by the solid clay particles is small, and we shall consider ionic concentrations to be averages over the pore volume V_p, rather than over the total volume $V_s + V_p$ of solid+liquid.

Let n^{i}_{+}, n^{i}_{-} and n^{i}_{z} be the total number of moles of ions and clay particles within the suspension. If the pore volume is reduced by a small amount ΔV_p, then $\Delta n^{\mathrm{i}}_{+}$, $\Delta n^{\mathrm{i}}_{-}$ ions will leave with the filtrate, which thus has concentration

$$\frac{\Delta n^{\mathrm{i}}_{+}}{\Delta V_p} = \frac{\Delta n^{\mathrm{i}}_{-}}{\Delta V_p} = c^{\mathrm{o}}. \tag{3.11}$$

Taking the limit $\Delta n^{\mathrm{i}}/\Delta V_p \to \mathrm{d}n^{\mathrm{i}}/\mathrm{d}V_p$, the equilibrium between filtrate and suspension implies, by (3.7)

$$\frac{n^{\mathrm{i}}_{+} n^{\mathrm{i}}_{-}}{V_p^2} = \left(\frac{\mathrm{d}n^{\mathrm{i}}_{+}}{\mathrm{d}V_p} \right)^2. \tag{3.12}$$

But electroneutrality requires $n^{\mathrm{i}}_{+} - n^{\mathrm{i}}_{-} + Zn^{\mathrm{i}}_{z} = 0$, and thus (3.12) can be regarded as a differential equation for n^{i}_{-} (or alternatively, for n^{i}_{+}). Assuming that Z is negative, so that $\hat{n} = -2n^{\mathrm{i}}_{-}/Zn^{\mathrm{i}}_{z} > 0$, the solution is

$$V_p/A = 1 + \hat{n} + \left((1+\hat{n})^2 - 1 \right)^{1/2} \tag{3.13}$$

where A is a constant of integration determined by the initial salt concentration and pore volume. Note that there is a pore volume $V_p = A > 0$ at which the co-ion concentration becomes zero. Further compaction will squeeze fresh water out of the suspension. The analysis assumes that filtration is sufficiently slow that the clay suspension is at all times spatially homogeneous. In practice, at all but the very slowest filtration rates a compacted filter cake will form at the filter membrane. Moreover, at low ionic concentrations transport of ions through the suspension will become slow. Thus equilibrium is unlikely to be maintained, and time dependent effects will be important.

Bolt (1961b) observed differences between experimental observations and the above analysis, and suggested that these were due to the base of the cake acting as an ion-selective mebrane. In the following sections we study the time-dependent motion of the ions within the cake, and in §3.4 we shall present numerical results (Sherwood, 1992) which support Bolt's explanation.

3.2 Transport Coefficients: a parallel plate model

Onsager's treatment of small departures from thermodynamic equilibrium associates a series of fluxes J_i with conjugate forces X_i such that the rate of entropy production may be expressed in the form $\mathrm{d}S/\mathrm{d}t = \sum_i J_i X_i$. The fluxes may then be expressed in the form

$$J_i = \sum_k L_{ik} X_k \tag{3.14}$$

where the L_{ik} are the transport coefficients. Discussions of the transport across semi-permeable membranes are given by Staverman (1952), Kedem & Katchalsky (1963) and Staverman & Smit (1975). With solvent and 2 diffusible ions, there are a total of 6 independent transport coefficients to be measured (since, by Onsager's reciprocal relations, $L_{ik} = L_{ki}$). These could be determined experimentally, but to cover all concentrations of clay and salt would require many experiments: see e.g. Kemper & Quirk (1972), Elrick *et al.* (1972) and Rolfe & Aylmore (1981). We therefore turn to a model similar to that of Gross & Osterle (1968) who considered the motion of ions in a cylindrical capillary. The transport coefficients within the capillary depended on the ionic concentrations, which were non-uniform because of electrical double layers at the capillary walls. Subsequently Jacazio *et al.* (1972) used these transport coefficients to predict salt rejection when electrolyte was passed through a clay compact.

In the next section we modify the Gross & Osterle model, changing the geometry to one in which fluid flows between two parallel charged plates (intended to represent clay particles). The model is based upon electrical double layer theory, and is therefore inappropriate when the particles are sufficiently close that double layer theory breaks down. Similarly, it does not incorporate experimentally observed ion-specific effects. Nevertheless, the relative simplicity of the model will enable us in §3.4 to consider the time-dependent problem of compaction of a clay filtercake.

The plates occupy the planes $y = \pm h(x)$. The ionic species ($i = 1, \ldots, n$) have concentration c_i, valence z_i and diffusivity D_i. The velocity $v_i = \omega_i f$ of a single ion is proportional to the applied force f, where $\omega_i = D_i/kT$ is the ionic mobility. The electrical force on an individual ion in an electric field of strength $-\nabla\phi$ is $-ez_i\nabla\phi$, and the flux of ions due to the electric field is

$$j_i = -ec_i z_i \omega_i \nabla\phi = -Fc_i z_i K_i \nabla\phi \tag{3.15}$$

where $K_i = \omega_i/N_A = D_i/RT$.

Ions are convected with the fluid velocity u, and move under the influence of electrical and thermal (diffusive) forces. The ion-flux density of the i^{th} species in the x direction is therefore

$$j_i = c_i u - K_i F z_i c_i \frac{\partial\phi}{\partial x} - D_i \frac{\partial c_i}{\partial x}. \tag{3.16}$$

We assume that there is local thermodynamic equilibrium of the ionic concentration across the width $-h < y < h$ of the slot. We write the potential as

$$\phi = \phi_0(x) + \psi(y; x) \tag{3.17}$$

and local thermal equilibrium gives an ionic concentration

$$c_i = c_i^0(x) \exp(-z_i F\psi/RT). \tag{3.18}$$

Note that there is a degree of arbitrariness in the division of ϕ into $\phi_0 + \psi$. If ψ in (3.18) is replaced by $\phi_0 + \psi$, the concentrations will be identical if $c_i^0(x)$ is replaced by $c_i^0(x) \exp(z_i F\phi_0/RT)$. We choose to adopt a convention in which $\sum_i^n z_i c_i^0(x) = 0$. Thus the potential ψ is measured relative to an electrically neutral electrolyte.

The potential satisfies the Poisson-Boltzmann equation

$$\frac{\partial^2 \psi}{\partial y^2} = -\rho/\epsilon = -F \sum z_i c_i/\epsilon \tag{3.19}$$

where ϵ is the permittivity of the suspending fluid. It is assumed that any variations in the x direction are much slower than those in the y direction, and hence derivatives $\partial/\partial x$ are negligibly small compared with $\partial/\partial y$. We adopt a condition of fixed surface charge density at the clay surface, as suggested by the experimental results of Lubetkin *et al.* (1984). Other workers (e.g. Chan *et al.*, 1984) consider that a constant surface potential may be a more appropriate boundary condition.

The dimension $2h$ of the flow channel is sufficiently small that fluid motion is at low Reynolds number, and inertia may be neglected. The fluid velocity u therefore satisfies the Stokes equation

$$-\nabla p + \mu \nabla^2 u - \sum_1^n z_i c_i F \nabla \phi = 0 \tag{3.20}$$

where p is the total pressure, μ is the fluid viscosity (assumed independent of ionic concentration), and the term in $\nabla\phi$ is an electric body force.

The slot is supposed sufficiently long, narrow and slowly varying that a lubrication analysis is appropriate. Velocities in the y direction are negligible, and the y component of (3.20) leads to

$$p - RT \sum c_i = p_0(x) \tag{3.21}$$

where $p_0(x)$, the partial pressure of the solvent, is independent of y. The x component of the Stokes equation (3.20) gives

$$\begin{aligned} \mu \frac{\partial^2 u}{\partial y^2} &= \frac{\mathrm{d}p_0}{\mathrm{d}x} + RT \sum_i \frac{\partial c_i}{\partial x} + F\left(\frac{\mathrm{d}\phi_0}{\mathrm{d}x} + \frac{\partial \psi}{\partial x}\right) \sum_i z_i c_i \\ &= \frac{\mathrm{d}p_0}{\mathrm{d}x} + RT \sum_i c_i \frac{\mathrm{d} \ln c_i^0}{\mathrm{d}x} + F \frac{\mathrm{d}\phi_0}{\mathrm{d}x} \sum_i z_i c_i. \end{aligned} \tag{3.22}$$

Note that the arbitrary choice of ϕ_0 and $c_i^0(x)$ does not affect this equation. Only the combination $kT \ln c_i + e z_i \phi$ (the electrochemical potential) is of importance. The

equation for the fluid velocity can be integrated twice to give

$$u = \frac{h^2 - y^2}{2\mu}\left(-\frac{\mathrm{d}p_0}{\mathrm{d}x}\right) - \frac{RT}{\mu}\sum_i \frac{\mathrm{d}\ln c_i^0}{\mathrm{d}x}\int_y^h \mathrm{d}y' \int_0^{y'} c_i \,\mathrm{d}y'' - \frac{F}{\mu}\frac{\mathrm{d}\phi_0}{\mathrm{d}x}\int_y^h \mathrm{d}y' \int_0^{y'} \sum_i z_i c_i \,\mathrm{d}y''. \tag{3.23}$$

A further integration over the total channel width gives the volume flux q, which we write in the form (cf. Gross & Osterle, 1968)

$$q = k_{00}\left(-\frac{\mathrm{d}p_0}{\mathrm{d}x}\right) + \sum_{i=1}^{n} k_{0i}\left(-RT\frac{\mathrm{d}\ln c_i^0}{\mathrm{d}x}\right) + k_{0,n+1}\left(-\frac{\mathrm{d}\phi_0}{\mathrm{d}x}\right). \tag{3.24}$$

The flux of each ionic species (3.16) may be written as

$$j_i = c_i u - \frac{D_i F}{RT} z_i c_i \frac{\mathrm{d}\phi_0}{\mathrm{d}x} - D_i c_i \frac{\mathrm{d}\ln c_i^0}{\mathrm{d}x}. \tag{3.25}$$

After integrating over the channel width, we obtain the total flux J_i

$$J_i = k_{i0}\left(-\frac{\mathrm{d}p_0}{\mathrm{d}x}\right) + \sum_{j=1}^{n} k_{ij}\left(-RT\frac{\mathrm{d}\ln c_j^0}{\mathrm{d}x}\right) + k_{i,n+1}\left(-\frac{\mathrm{d}\phi_0}{\mathrm{d}x}\right). \tag{3.26}$$

Finally, the total current is

$$I = \sum_i J_i z_i F. \tag{3.27}$$

Gross & Osterle (1968) took the primary fluxes to be q_0, I and the salt flux $J_s = J_1 + J_2$, a choice which leads to coefficients k_{ij} which are symmetric in i and j. The current $I = 0$ in many problems. In particular, a pressure-driven flow through a capillary will generate a potential gradient $\mathrm{d}\phi_0/\mathrm{d}x$ (the streaming potential) sufficient to reduce I to zero if there is no return path for the current.

The coefficients in the above equations (3.24) and (3.26) are

$$k_{00} = \tfrac{2}{3}h^3/\mu \tag{3.28}$$

$$k_{0i} = 2\mu^{-1}\int_0^h \mathrm{d}y \int_y^h \mathrm{d}y' \int_0^{y'} c_i \,\mathrm{d}y'' \tag{3.29}$$

$$k_{0,n+1} = 2F\mu^{-1}\int_0^h \mathrm{d}y \int_y^h \mathrm{d}y' \int_0^{y'} \sum_i z_i c_i \,\mathrm{d}y'' \tag{3.30}$$

$$k_{i0} = \mu^{-1}\int_0^h c_i(h^2 - y^2)\,\mathrm{d}y \tag{3.31}$$

$$k_{ij} = 2\mu^{-1}\int_0^h \mathrm{d}y\, c_i \int_y^h \mathrm{d}y' \int_0^{y'} c_j \,\mathrm{d}y'' + \delta_{ij}\frac{2D_j}{RT}\int_0^h c_j \,\mathrm{d}y \tag{3.32}$$

$$k_{i,n+1} = 2F\mu^{-1}\int_0^h \mathrm{d}y\, c_i \int_y^h \mathrm{d}y' \int_0^{y'} \sum_j z_j c_j \,\mathrm{d}y'' + \frac{2D_i F}{RT}\int_0^h z_i c_i \,\mathrm{d}y. \tag{3.33}$$

If we integrate the Poisson-Boltzmann equation

$$\epsilon F^{-1} \frac{\partial^2 \psi}{\partial y^2} = -\sum z_i c_i \tag{3.34}$$

we obtain

$$\int_y^h \mathrm{d}y' \int_0^{y'} \sum_i z_i c_i \, \mathrm{d}y'' = -\epsilon F^{-1} \left(\psi(h) - \psi(y)\right) \tag{3.35}$$

and this may be used to simplify the expressions for $k_{0,n+1}$ and $k_{i,n+1}$.

3.3 Non-dimensionalisation and order of magnitude estimates

We scale all potentials by $kT/e = RT/F$, and all concentrations by a typical concentration C_0. Lengths in the y direction are scaled by a typical Debye length κ^{-1}, defined by

$$\kappa^2 = \frac{C_0 F^2}{RT\epsilon}. \tag{3.36}$$

Note that this differs from the more usual definition

$$\kappa'^2 = \sum_{i=1}^{n} z_i^2 C_i F^2 / RT\epsilon. \tag{3.37}$$

Lengths in the x direction are scaled by some typical length L. Pressures are scaled by RTC_0. The volume flux q is scaled by $RTC_0/\mu\kappa^3 L$ and the ionic fluxes J_i are scaled by $RTC_0^2/\mu\kappa^3 L$, a scaling based on convection. The ionic fluxes also depend on diffusion, and hence there is an additional non-dimensional group, the Peclet number P_e, measuring the ratio of convection to diffusion. In view of the above scalings, we take

$$P_e = \frac{C_0 RT}{\mu\kappa^2 D} \tag{3.38}$$

where D is a typical ionic diffusivity. From now on, we assume that all the diffusivities D_i are identical, and equal to D. Volumes (per unit length in the z direction) scale naturally with $\kappa^{-1}L$. Combining this with the above scaling for the volume flux leads to a timescale $\mu\kappa^2 L^2/RTC_0$.

Consider now some typical order of magnitude estimates for a 0.1 mol dm^{-3} solution of NaCl in water. The ionic concentration $C_0 = 10^2$ mol m^{-3}, and at 25 °C the electrolyte has a conductivity of about 1 S m^{-1}. From (3.36) $\kappa = 0.7 \times 10^9$ m^{-1}, whereas the standard definition (3.37) of the Debye length $\kappa' = 10^9$ m^{-1}.

Taking $T = 300\ K$ and $R = 8.3$ J K^{-1} mol^{-1}, our reference pressure is $RTC_0 = 2.5 \times 10^5$ Pa $= 2.5$ bar.

The charge convected by N_A ions of valence z_i in an electric field $\nabla\phi$ is $N_A e^2 \omega_i z_i^2 \nabla\phi$, and the infinite-dilution conductivity of sodium ions at 25 °C is 5.0×10^{-3} S m^2 mol^{-1}. Hence $\omega_i = 3 \times 10^{11}$ m N^{-1} s^{-1}, and $D_i = kT\omega_i \simeq 10^{-9}$ $\mathrm{m}^2\mathrm{s}^{-1}$. The conductivities of K^+ and Cl^- are 7.3×10^{-3} S m^2 mol^{-1} and 7.6×10^{-3} S m^2 mol^{-1}, respectively, leading to somewhat higher diffusivities.

Taking the viscosity of water to be $\mu = 10^{-3}$ Pa s, we obtain a Peclet number $P_e = C_0 RT/\mu\kappa^2 D = 0.5$.

The surface charge density of montmorillonite is typically 0.1 C m^{-2} (Lubetkin *et al.*, 1984), $F = 9.6 \times 10^4$ C mol^{-1} and $\epsilon = \epsilon_r \epsilon_0$, where the permittivity of free space is $\epsilon_0 = 8.8 \times 10^{-12}$ F m^{-1} and the relative permittivity of water is $\epsilon_r \simeq 80$. This leads to a non-dimensional surface charge density $\hat{\sigma} = 7.9$. Taking the typical thickness of a clay platelet to be $2k$=1 nm we have $\hat{k} = 0.4$: this neglects any layers of water adsorbed to the surface of the clay (Norrish & Raussel-Colom, 1963).

3.4 Ionic motion in a compacting filtercake

Figure 5 shows a typical path followed by a fluid particle as it passes through a filtercake. We take this path and represent it by a single channel of varying width, as shown in figure 6(ii). Thus we ignore the sharp edges of the clay particles at which the electrical double layers may change abruptly. The effect of this approximation is unknown. Edge effects are in principle included in the homogenisation analyses of Moyne & Murad (2002), and can sometimes be important (Sherwood & Stone, 1995). We assume that all variations along the direction of flow (the $\hat{x}$ direction) are sufficiently slow that the equations of §3.2 hold locally.

The applied pressure p_A will compress the cake, and standard filtration theory is based on a matrix stress $\Psi(e)$, which gives the void ratio e as a function of the applied stress. Here, this can be based on the double layer force per unit area F_e between pairs of plates as a function of their separation $2h$. Various approximations for F_e are available, notably at separations large compared to the double layer thickness. More generally, the electrical repulsion may be obtained from (3.21), evaluating the ionic concentrations on the channel centreline $y = 0$, where the electric field normal to the charged plates is zero, while fields in the x direction are small. Thus

$$p_A = p_0 + RT \sum_i c_i(y = 0). \tag{3.39}$$

Lubetkin *et al.* (1984) found good agreement between the force F_e predicted by electrical double layer and experimental measurements at large separations $h > \kappa'^{-1}$. At smaller separations other effects, including the finite size of the ions and Van der Waals forces, become important. Philip & Smiles (1982) report filtration experiments in which the variation of the matrix stress $\Psi(e)$ with salt concentration was qualitatively (though not quantitatively) consistent with electrical double layer theory. For simplicity, we shall assume that (3.39) holds at all separations. If we wished to include an additional mechanical contribution to the matrix stress, Ψ_m, due, for example, to contact between non-parallel plates, (3.39) could be modified to give

$$p_A = p_0 + RT \sum_i c_i + \Psi_m(h). \tag{3.40}$$

We now restrict ourselves to just 2 species of monovalent ions, and set $c_1^0 = c_2^0 = c^0$. The total volumetric flow q and ion flux J_i are given by (3.24) and (3.26). However, in

the absence of current $z_1\hat{J}_1 + z_2\hat{J}_2 = 0$. This enables us to eliminate $\mathrm{d}\hat{\phi}_0/\mathrm{d}\hat{x}$ and J_2, and after non-dimensionalisation the fluxes can be simplified to

$$\hat{q} = K_{00}\left(-\frac{\partial\hat{p}_0}{\partial\hat{x}}\right) + K_{01}\left(-\frac{\partial\hat{c}^0}{\partial\hat{x}}\right) \tag{3.41}$$

$$\hat{J}_1 = K_{10}\left(-\frac{\partial\hat{p}_0}{\partial\hat{x}}\right) + K_{11}\left(-\frac{\partial\hat{c}^0}{\partial\hat{x}}\right) \tag{3.42}$$

for some set of coefficients K_{ij}. The conservation equations for the total number of ions

$$\hat{c}_i^T = 2\hat{c}_i^0\int_0^{\hat{h}}\exp(-z_i\hat{\psi})\,\mathrm{d}\hat{y} \tag{3.43}$$

and fluid volume are

$$2\frac{\partial\hat{h}}{\partial\hat{t}} = -\frac{\partial\hat{q}}{\partial\hat{x}} \quad , \quad \frac{\partial\hat{c}_1^T}{\partial\hat{t}} = -\frac{\partial\hat{J}_1}{\partial\hat{x}}. \tag{3.44}$$

We assume that the filtercake occupies the region $0 \le \hat{x} \le 1$, which is divided into gridblocks for numerical computation. The filter paper on which the cake is formed is at $\hat{x} = 0$, and the upper surface of the clay suspension is at $\hat{x} = 1$. At each time step the fluxes are computed and the change in total ionic content and fluid volume within each block are obtained. Knowing the total ionic contents c_i^T, we must obtain the concentrations c_i^0. The partial pressure of the water, $\hat{p}_0$ may then be obtained from (3.39).

Initially the clay suspension is dilute and the plates well separated: we assume an initial channel half-width $\hat{h} = \hat{h}_0 = 5$. When the pressure p_A is applied, the base of the cake is compacted. In the absence of ionic effects, the fluid pressure at the base of the cake is assumed to be atmospheric (which we take to be 0). The base of the cake is immediately compacted to a void ratio e_1 such that the matrix stress Ψ satisfies $\Psi(e_1) = p_A$. Two possible boundary conditions for the ions at the base of the cake were considered by Sherwood (1992). Here we assume that ions and water are convected out of the cake without any relative motion. The ionic concentration in the filtrate is, by (3.41) and (3.42),

$$\hat{c}_f^0 = \frac{\hat{J}_1}{\hat{q}} = \frac{K_{10}\frac{\partial\hat{p}_0}{\partial\hat{x}} + K_{11}\frac{\partial\hat{c}^0}{\partial\hat{x}}}{K_{00}\frac{\partial\hat{p}_0}{\partial\hat{x}} + K_{01}\frac{\partial\hat{c}^0}{\partial\hat{x}}}, \tag{3.45}$$

where the derivatives are evaluated at the base of the cake. There is zero flux of both fluid and ions at the upper surface $\hat{x} = 1$ of the cake.

In numerical simulations, we fix the surface charge density $\hat{\sigma} = 5$, and the initial separation between the plates $2\hat{h}_0 = 10.0$. This corresponds to a void ratio $e = \hat{h}/\hat{k} = 12.5$, somewhat lower than the typical value $e \simeq 45$ in an unweighted drilling fluid. We investigate the effect of varying the ionic Peclet number P_e and the applied filtration pressure $\hat{p}_A$.

The applied filtration pressure was in general $\hat{p}_A = 5$, which corresponds to a filtration pressure 12.5 bar. This (along with the ionic content) controls the plate spacing at the base of the cake. The plate separation at the base is typically $\hat{h} = 0.5$, corresponding to a void ratio $e = 1$.

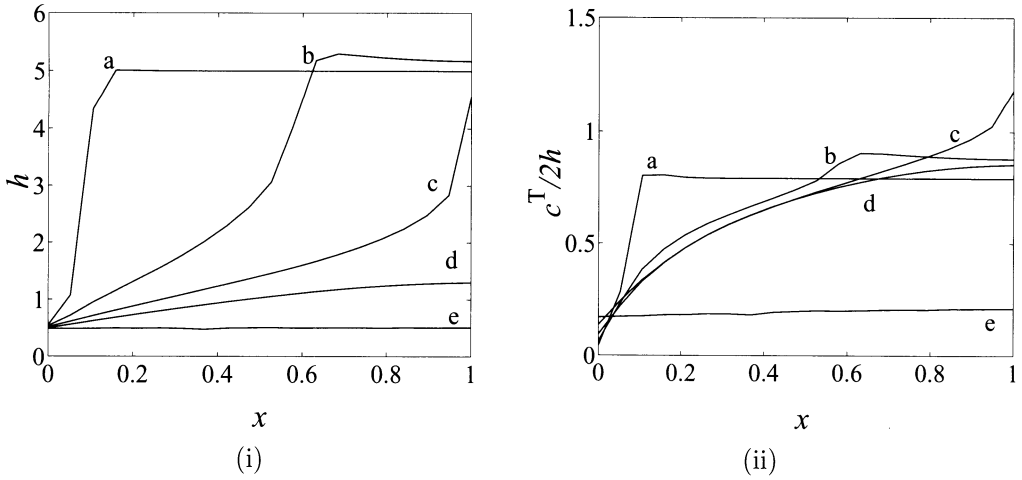

Figure 7. (i) The channel half-width $\hat{h}$ as a function of Lagrangian position $\hat{x}$ within the cake. Peclet number $P_e = 5$, applied pressure $\hat{p}_A = 5$, at time (a) $\hat{t} = 0.01$, (b) $\hat{t} = 1$, (c) $\hat{t} = 4$, (d) $\hat{t} = 6$, (e) $\hat{t} = 14$. (ii) Mean co-ion concentration $\hat{c}^T/2\hat{h}$ in the fluid, against $\hat{x}$. Pe, p_A and times as in (i).

Figure 7(i) shows the channel half-width $\hat{h}$ (proportional to the void ratio within the cake) as a function of the Lagrangian distance $\hat{x}$ from the base of the cake, for the case $P_e = 0.5$. The cake grows thicker as $\hat{t}$ increases, and eventually a uniform clay compact is formed.

Figure 7(ii) shows profiles of the mean ionic concentration $\hat{c}^T/(2\hat{h})$ within each grid-block, for the co-ions. Initially $\hat{c}^T/(2\hat{h}) = 0.76$ throughout the cake. During filtration, the compacted base of the cake acts as an ion-exclusion membrane, and the ionic content of the clay suspension above the cake increases. High ionic concentrations generate osmotic pressures, and additional water is drawn into such regions, as can be seen from the void ratio profiles of figure 7(i). In figure 7 the Peclet number $P_e = 5$. When $P_e = 0.5$ diffusion is stronger, so the ionic concentration within the suspension is almost uniform, with just a slight gradient to drive ions away from the cake and into the bulk clay suspension.

Figure 8 shows $Q = \int \hat{q}\, d\hat{t}$, the total volume of filtrate collected. If the supply of clay suspension were infinite, we would expect $Q \propto t^{1/2}$ (because of the similarity solutions discussed in §2). In the simulations, the amount of fluid is finite, and the flow of filtrate eventually ceases. In figure 8(i) we see that more filtrate is squeezed out of the cake when the imposed filtration pressure is increased, as expected. In figure 8(ii) we see that as the Peclet number decreases, ions can move more freely relative to the water and there is less resistance to the filtration process, which occurs more rapidly.

The predicted ionic concentration in the filtrate is shown on figure 9(i) as a function of the filtration pressure $\hat{p}_A$. At the higher pressures the base of the cake is more compacted, and the overlapping double layers act more effectively to impede the passage of ions,

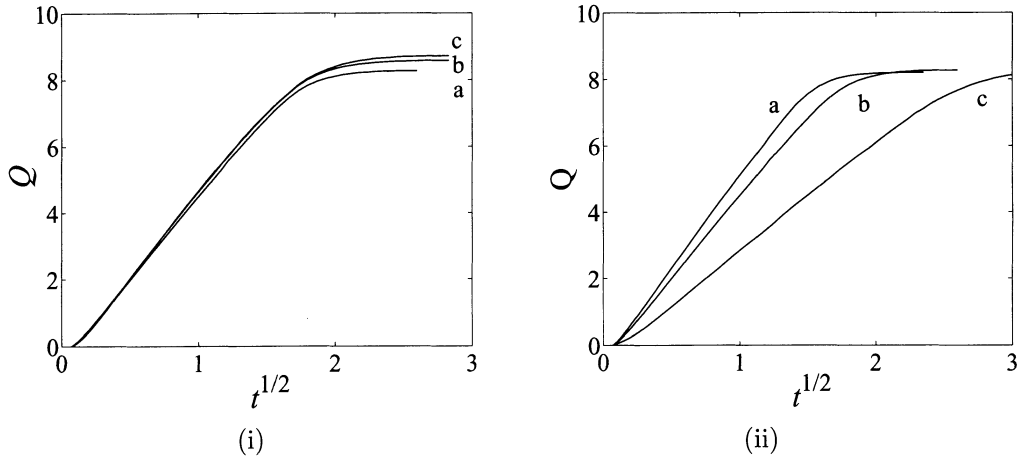

Figure 8. Total volume Q of filtrate plotted against $\hat{t}^{1/2}$. (i) $P_e = 1$, applied pressure (a) $\hat{p}_A = 5$, (b) $\hat{p}_A = 10$, (c) $\hat{p}_A = 15$. (ii) $p_A = 5$, Peclet number (a) $P_e = 0.5$, (b) $P_e = 1.0$, (c) $P_e = 5$.

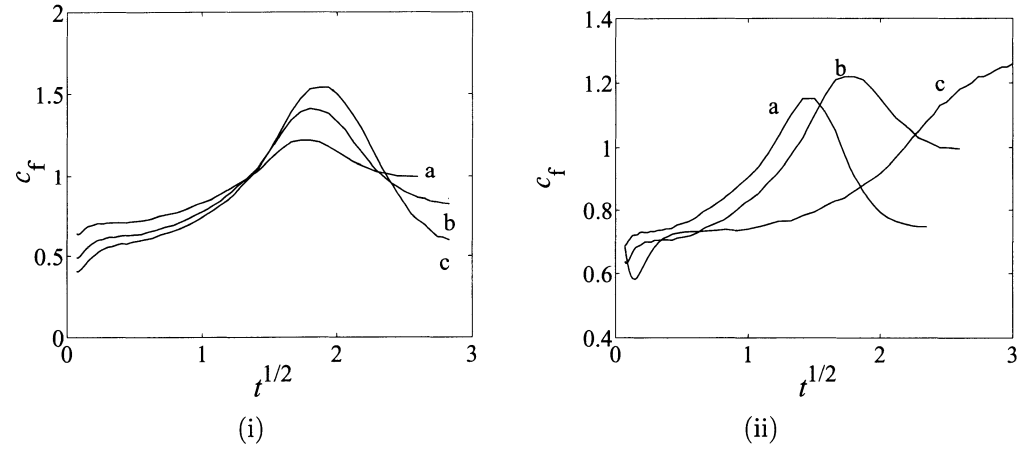

Figure 9. Ionic concentration c_f in filtrate plotted against $\hat{t}^{1/2}$. (i) $P_e = 1$, applied pressure (a) $\hat{p}_A = 5$, (b) $\hat{p}_A = 10$, (c) $\hat{p}_A = 15$. (ii) $p_A = 5$, Peclet number (a) $P_e = 0.5$, (b) $P_e = 1.0$, (c) $P_e = 5$.

which remain in the dilute suspension above the cake. When eventually all the dilute suspension is converted to cake, these ions move with the filtrate to the base of the cake and the increase in ionic concentration in the filtrate is much stronger than at lower pressures. The effect of changing the Peclet number is shown in figure 9(ii). At the end of the filtration process the ions which have collected at the top of the cake are able to diffuse to its base, and there is a peak in the ionic concentration in the filtrate.

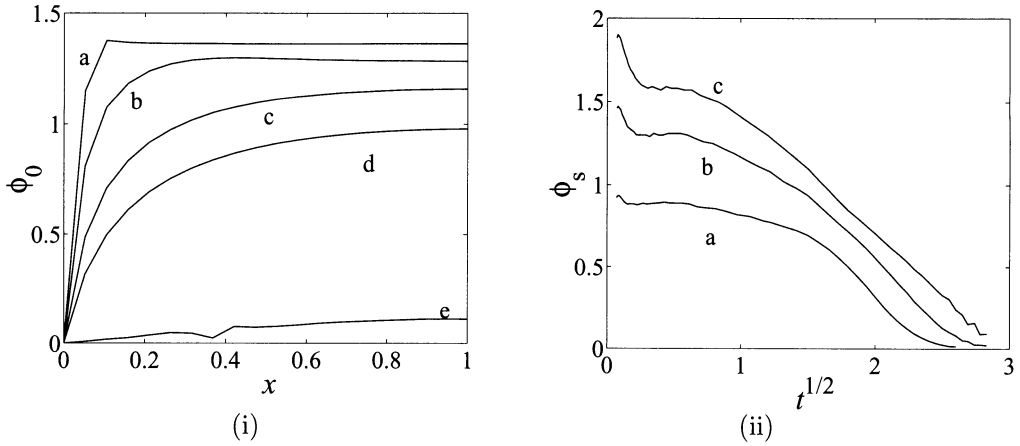

Figure 10. (i) Streaming potential $\hat{\phi}_0$ against position $\hat{x}$ within the cake. $P_e = 5$, $\hat{p}_A = 5$, and times as in figure 7. (ii) Total streaming potential $\hat{\phi}$ across the cake, plotted against $\hat{t}^{1/2}$. $P_e = 1$. Applied pressure (a) $\hat{p}_A = 5$, (b) $\hat{p}_A = 10$, (c) $\hat{p}_A = 15$.

Bolt (1961b) measured the ionic concentration of filtrate during the course of a filtration experiment, and indeed found that the ionic concentration was initially lower than that within the clay suspension. It subsequently increased and then fell. Other authors (e.g. Smith, 1977) tend to measure the mean ionic concentration of the total filtrate collected. This is initially low, and also drops immediately after each successive increase in the applied pressure, since relatively fresh water is squeezed out during the initial stage of compaction.

The potential $\hat{\phi}_0$ is shown as a function of position within the cake in figure 10(i). In the early stages of compaction, the ionic concentration at the base of the cake is identical to that in the dilute suspension of clay particles, and $\hat{\phi}_0$ can be readily interpreted as the streaming potential (Hunter, 1981). At the end of the simulation all flows of fluid and ions have stopped, and the potential $\hat{\phi}_0$ is zero everywhere, as expected. Figure 10 shows $\hat{\phi}_0 > 0$. With negatively charged surfaces, the streaming potential will be negative at the upper surface $\hat{x} = 1$ of the cake.

The total streaming potential $\hat{\phi}_s = \hat{\phi}_0(\hat{x} = 1)$ across cakes formed at 3 different pressures is plotted against $\hat{t}^{1/2}$ in figure 10(ii). If the similarity solutions of §2 were valid, $\hat{\phi}_s$ would be constant. Although the cake grows in thickness as $t^{1/2}$, the fluid velocities decrease as $t^{-1/2}$. Immediately after the initial transients have decayed, the streaming potentials at pressures $\hat{p}_A = 5$, 10 and 15 are $\hat{\phi}_s = 0.9$, 1.3 and 1.6. Thus $\hat{\phi}_s \propto \hat{p}_A^{0.5}$ over this limited range of data. Wyllie (1951) measured streaming potentials across a wide range of drilling fluid filtercakes as a function of the filtration pressure, and showed that they obeyed a relation of the form $\hat{\phi}_s = k\hat{p}_A^{\alpha}$ with α typically in the range 0.6–0.9. At a pressure differential of 500 psi (corresponding to $\hat{p}_A = 14$) the streaming potential across the cakes was typically in the range 20–30 mV corresponding to a reduced potential $0.8 < \hat{\phi}_s < 1.2$. Thus the streaming potentials predicted by the model are of

the correct order of magnitude, but exaggerate the non-linear dependence of $\hat{\phi}_s$ on the filtration pressure $\hat{p}_A$.

The simulations discussed above can be run in the reverse direction in order to model the swelling of shale. Details can be found in Sherwood (1994a). We shall not discuss this here, since we shall move on to consider in §4 macroscopic constitutive relations which describe the behaviour of shale.

4 Biot poroelasticity

When a hole (e.g. an oil well) is drilled into the Earth's crust, the stress distribution in the surrounding rock will be modified and the rock will deform. If the rock is porous, the deformation can sometimes be predicted using Biot's (1941) theory of poroelasticity (e.g. Rice & Cleary 1976, Detournay & Cheng 1988). This gives the strain $\boldsymbol{\epsilon}$ as a function both of the total stress $\boldsymbol{\sigma}$ acting on the rock, and of the pore pressure p, and was extended by Biot (1956a, 1956b, 1973) to include the effects of anisotropy, viscoelasticity, thermoelasticity and finite deformations.

In some rocks additional osmotic effects are present, and gradients in chemical potential can cause the rock to swell, leading possibly to complete disintegration. This is particularly true of shales, which consist of compacted clays. Such swelling can considerably slow the process of drilling, and is a well-known problem in the petroleum industry (e.g. Chenevert 1970, Hale *et al.* 1992). One way to avoid swelling is to use an oil-based drilling fluid, but the disposal of rock cuttings, coated with oil, can lead to environmental problems. There is therefore great interest in finding water-based drilling fluids which inhibit swelling. One route towards this is to add salts to the drilling fluid, thereby modifying its water activity and reducing the osmotic forces driving water into the shale. Reviews by Bailey *et al.* (1991, 1994a) and Durand *et al.* (1995a,b) give further details of these problems.

The deformation of shale has been modelled using Biot-like analyses based on water activity (Yew *et al.* 1990, Onaisi *et al.* 1993). However, if the pore pressure is simply replaced by the chemical potential of the water, the possibility of ion-exchange between the shale and the drilling fluid is ignored. Biot (1941) used thermodynamics in order to set the theory of poroelasticity on a sound foundation. In §4.1 we show how his analysis may be modified in order to include pore fluids which contain several chemical species. In §4.2–§4.4 we consider various examples of equilibrium between porous media and a reservoir of pore fluid.

4.1 The deformation of the shale

We follow the analysis set down by Biot (1941), with modifications (Sherwood, 1993) to include solvent (usually water) and $R-1$ other species in the pore fluid. The mass of each species per unit reference volume of the porous material is m^r (measured here in moles), and the chemical potential of each species is μ^r. The total stress σ_{ij} is taken to be positive for tensile stress i.e. an isotropic pressure p corresponds to a stress $\sigma_{ij} = -p\delta_{ij}$. The strain is ϵ_{ij}. The problem is depicted in figure 11.

Let f be the Helmholtz free energy of the complete system (i.e. rock + pore fluid) per

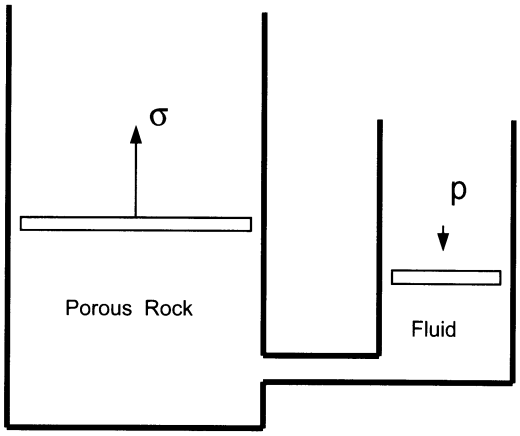

Figure 11. The system under consideration. The stress $\boldsymbol{\sigma}$ acting on the porous rock, applied in the figure by means of a piston, is arbitrary.

unit reference volume of porous material, T the temperature, and s the entropy (again, per unit reference volume). Then

$$df = \sigma_{ij} d\epsilon_{ij} + \sum_{r=1}^{R} \mu^r \, dm^r - s dT. \tag{4.1}$$

The chemical potentials of the components of a solution are conventionally written in the form

$$\mu^r = \mu_0^r + RT \ln x^r \gamma^r = \mu_0^r + RT \ln a^r, \tag{4.2}$$

where μ_0^r is the chemical potential of species r in some reference state, x^r is the partial molar fraction of species r, γ^r is the activity coefficient and $a^r = x^r \gamma^r$ is the activity of the r^{th} species. R is the gas constant and T the temperature. In an ideal solution $\gamma^r = 1$. The reference chemical potential μ_0^r is a function of pressure, and

$$\frac{\partial \mu_0^r}{\partial p} = v^r = 1/\rho^r \tag{4.3}$$

where $v^r = 1/\rho^r$ is the volume of 1 mole of the material. We shall from henceforth neglect the effect of temperature. This is appropriate for laboratory experiments, which are usually performed at constant temperature, but is harder to justify in the wellbore. Recent work on this has been reported by Ghassemi & Diek (2002). We similarly ignore the effect of electrical potential: little is known about how this varies in a wellbore during the course of swelling. A rigorous analysis, including electrical effects, is given by Huyghe & Janssen (1997) and Molenaar & Huyghe (2002).

If we now define a Helmholtz free energy associated with the solid, f_0, in the form

$$df_0 = d\left[f - \sum_r \mu^r m^r\right] = \sigma_{ij} d\epsilon_{ij} - \sum_r m^r d\mu^r \tag{4.4}$$

then df_0 is an exact differential. Taking ϵ_{ij} and the μ^r as state variables, we may obtain the Maxwell relations

$$\frac{\partial \sigma_{ij}}{\partial \mu^r} = -\frac{\partial m^r}{\partial \epsilon_{ij}} \tag{4.5}$$

and

$$\frac{\partial m^r}{\partial \mu^s} = \frac{\partial m^s}{\partial \mu^r}. \tag{4.6}$$

Hence if we look for elastic stress-strain relations, these will have the form

$$d\sigma_{ij} = C_{ijkl} d\epsilon_{kl} - \sum_r D^r_{ij} d\mu^r \tag{4.7}$$

$$dm^r = D^r_{ij} d\epsilon_{ij} + \sum_s A^{rs} d\mu^s \tag{4.8}$$

where we have used (4.5) to identify the cross-coefficients D^r_{ij} in (4.7) and (4.8), and where $A^{rs} = A^{sr}$, by (4.6). Alternatively, we may look for a Gibbs free energy, which satisfies

$$d\left[f - \sum_r \mu^r m^r - \sigma_{ij}\epsilon_{ij}\right] = -\epsilon_{ij} d\sigma_{ij} - \sum_r m^r d\mu^r. \tag{4.9}$$

Again, this is an exact differential, and so, taking σ_{ij} and μ^r as state variables,

$$\frac{\partial \epsilon_{ij}}{\partial \mu^r} = \frac{\partial m^r}{\partial \sigma_{ij}}, \tag{4.10}$$

and (4.6) holds as before. Consequently

$$d\epsilon_{ij} = S_{ijkl} d\sigma_{kl} + \sum_r Q^r_{ij} d\mu^r \tag{4.11}$$

$$dm^r = Q^r_{ij} d\sigma_{ij} + \sum_s B^{rs} d\mu^s, \tag{4.12}$$

where we have used (4.10) to identify the cross-coefficients Q^r_{ij} in (4.11) and (4.12), and $B^{rs} = B^{sr}$, by (4.6).

We shall regard the applied stress σ_{ij} and the chemical potentials μ^r as our state variables, and work with (4.11) and (4.12). We assume that the shale is in equilibrium with a fluid reservoir of known chemical composition. Thus the state variables σ_{ij} and μ^r can all be measured, as can the pressure p in the external reservoir.

Experiments on compaction of clay in contact with a large reservoir have been performed by Mesri & Olson (1971) and Denis (1991). In each experiment the composition of the reservoir fluid was held constant, and the applied stress was varied: the results give information about the S_{ijkl}. The chemical composition of the reservoir fluid was varied between one experiment and the next, either by changing from a solution of $CaCl_2$ to one of NaCl, or by changing the concentration of the salt. Observations of the degree of swelling of clay as a function of the salt concentration may also be performed on a

microscopic level, using X-ray diffraction to measure the separation between clay particles (e.g. Slade *et al.* 1991, Denis *et al.* 1991). Thus a limited amount of information is already available concerning the Q^r_{ij}.

If we apply a change in stress and merely collect all fluid which is squeezed from the shale, either in the absence of a reservoir of fluid, or without leaving sufficient time for equilibrium to be re-established, then the chemical potentials within the rock will be modified. We therefore cannot use (4.12) to determine Q_{ij} merely by analysing fluid which has been squeezed from a shale in the absence of a fluid reservoir held at constant chemical potential. This is unfortunate, as such a measurement is comparatively straightforward (Engelhart & Wolf 1963, Bolt 1961b, Rieke & Chilingarian 1974, Smith 1977).

B^{rs} represents the change in mass of the r^{th} species due either to a change in the reservoir pressure p, which leads to a change in the chemical potentials within the pore fluid because of (4.2), or due to a change in the chemical composition of the reservoir fluid. This term includes changes in the pore volume of the solid, changes due to the compressibility of the pore fluid, compositional changes which would occur even in a chemically inert rock (e.g. if the pore fluid is changed from fluid A to fluid B), and changes due to adsorption/desorption of ions from the surface of the clay particles within the shale.

The coefficients S_{ijkl}, Q^r_{ij} and B^{rs} (or C_{ijkl}, D^r_{ij} and A^{rs}) will depend not only on the chemical composition and physical properties of the solid and liquid, but also on the porosity and on the pore-size distribution. Changes in the pore size distribution will modify the mechanical properties of the solid matrix, thereby modifying the coefficients in the constitutive relation. Such changes will also modify the area of the solid/fluid interface, at which adsorption of ions, or density modification of water, could occur. The pore fluid squeezed from small pores by a step change in stress $d\sigma_{ij}$ or chemical potential $d\mu^s$ may therefore depend upon the surface area of the solid, leading to an additional dependence of the coefficients upon the pore size distribution.

The thermodynamic treatment discussed here has little to say either about the magnitudes of the coefficients S_{ijkl}, Q^r_{ij} and B^{rs}, or about how these change during the course of compaction.

4.2 A one-component pore fluid

In a one-component fluid, $x^1 = \gamma^1 = a^1 = 1$, and hence, by (4.2), $d\mu^1 = dp/\rho^1$. The response of the shale will depend only on the fluid pressure p within the reservoir and on the applied total stress σ_{ij}. If the system is isotropic, (4.11) and (4.12) simplify to

$$d\epsilon_{ij} = S_1 d\sigma_{ij} + \delta_{ij} S_2 d\sigma_{kk} + \delta_{ij} \sum_r Q^r d\mu^r \tag{4.13}$$

$$dm^r = Q^r d\sigma_{kk} + \sum_r B^{rs} d\mu^s, \tag{4.14}$$

and we see that just 4 material coefficients are required if only one chemical species is present in the pore fluid. The isotropic Biot formulation of (4.13)–(4.14) can be written

in the form (Rice & Cleary, 1976)

$$2Gd\epsilon_{ij} = d\sigma_{ij} - \frac{\nu}{1+\nu} d\sigma_{kk}\delta_{ij} + \frac{3\rho^1(\nu_u - \nu)}{B(1+\nu)(1+\nu_u)}\delta_{ij}\frac{dp}{\rho^1} \tag{4.15}$$

$$dm^1 = \frac{3\rho^1(\nu_u - \nu)}{2GB(1+\nu)(1+\nu_u)}\left[d\sigma_{kk} + 3B^{-1}dp\right]. \tag{4.16}$$

Here the four material coefficients are scalars and have been chosen to be the shear modulus G, the drained and undrained Poisson ratios ν and ν_u, and Skempton's parameter B which relates the undrained response of the pore pressure to the applied stress. Note that the cross terms of (4.15) and (4.16) satisfy the reciprocal relationship (4.10).

4.3 A chemically inert rock

We now consider the case in which there is no chemical interaction between the pore fluid and the rock. This might be appropriate for a very clean sandstone, in which the interaction between the quartz of the sandstone and the pore fluid could be ignored. A second example would be rock containing charged particles (e.g. clay particles), surrounded by thin electrical double layers, of thickness κ^{-1} much smaller than the typical pore size. The bulk of the pore fluid would be identical to any outside fluid reservoir. Compressing the rock would merely squeeze out this bulk pore fluid. In this case, when the stress acting on the rock is increased by an amount $d\sigma_{ij}$, whilst keeping the chemical potentials μ^r constant, the mass dm^r of each species which flows out of the rock will be proportional to the partial molar fraction x^r of that species in the pore fluid. Hence, from (4.12),

$$Q^r_{ij} = x^r \hat{Q}_{ij} \tag{4.17}$$

for some $\hat{Q}_{ij}$. Equation (4.17) is effectively our defininition of a chemically inert rock.

We can now consider changes in the strain of the rock, given by (4.11). The Gibbs-Duhem equation for a solution is (e.g. Everett, 1959)

$$-SdT + \rho^{-1}dp - \sum^{r} x^r d\mu^r = 0 \tag{4.18}$$

where S is the entropy, T the temperature and ρ^{-1} the molar volume. Our isothermal assumption implies $dT = 0$, and hence (4.11) simplifies to

$$d\epsilon_{ij} = S_{ijkl}d\sigma_{kl} + \hat{Q}_{ij}\frac{dp}{\rho}. \tag{4.19}$$

Thus only the pore pressure is important, and changing the composition of the pore fluid, at constant pressure, will cause no strain in the material.

4.4 A highly compacted shale

We now consider a model shale which consists of aligned clay particles, each of which is negatively charged and surrounded by an electrical double layer. The shale is assumed to have been compacted, so that the electrical double layers around each particle overlap.

The co-ions are excluded from the spaces between particles, and the pore fluid will contain just sufficient counter-ions to ensure electrical neutrality of the clay and pore fluid.

We first assume that the reservoir contains only one salt (i.e. one species of co-ion and one species of counter-ion); ion-exclusion ensures that the co-ion is absent from the shale. We apply a step increase $d\sigma_{ij}$ in the stress, whilst keeping the chemical potentials constant within the reservoir. Water will be squeezed from the shale, but no ions will emerge, since electrical neutrality must be maintained. The coefficients Q^r_{ij} in equation (4.12) will be zero for all chemical species other than water. The reciprocal relationship then implies that the corresponding coefficients Q^r_{ij} in (4.11) will be zero. Similarly, if we change the chemical potentials of the pore fluid (either by changing the pressure or the salt concentration in the external reservoir), only water will enter (or leave) the shale. Co-ions are excluded from the gaps between the clay platelets, and electrical neutrality prevents any increase in the number of counter ions. Consequently, the governing equations (4.11) and (4.12) reduce to

$$d\epsilon_{ij} = S_{ijkl}d\sigma_{kl} + Q^1_{ij}d\mu^1 \tag{4.20}$$

$$dm^1 = Q^1_{ij}d\sigma_{ij} + B^{11}d\mu^1, \tag{4.21}$$

where the superscript ^{1} refers to water. These equations are identical in form to the standard Biot equations (4.15) and (4.16), with the change in the pore pressure dp/ρ replaced by the change in the chemical potential of the water. This is the model adopted by Onaisi *et al.*, (1993), whereas Yew *et al.*, (1990) allowed for the possibility of non-linear, anisotropic swelling, using an analogy between poroelasticity and thermoelasticity.

We now suppose that there are two species of counter-ions, which we label r and s, and which have valence z^r, z^s respectively. If we apply a step increase in the stress, the *total* number of counterions within the shale will stay constant. However, it is quite possible that the degree of preferential adsorption of one ion relative to the other is a function of the applied stress. Ion r may be expelled from the shale, and replaced by ion s. Thus Q^r_{ij} and Q^s_{ij} will be non-zero. Electro-neutrality requires that

$$z^r Q^r_{ij} + z^s Q^s_{ij} = 0. \tag{4.22}$$

If we change the ionic content of the reservoir, whilst maintaining the water potential μ^1 and applied stress σ_{ij} constant, we would expect ion exchange to occur. Equation (4.11) predicts that the change in strain will be

$$d\epsilon_{ij} = Q^r_{ij}d\mu^r + Q^s_{ij}d\mu^s. \tag{4.23}$$

By the Gibbs-Duhem equation (4.18), $x^r d\mu^r + x^s d\mu^s = 0$ at constant pressure and temperature, and hence

$$d\epsilon_{ij} = Q^r_{ij}d\mu^r \left(1 + \frac{z^r x^r}{z^s x^s}\right). \tag{4.24}$$

Experiments by Mesri & Olson (1971) show that Na montmorillonite will be much more swollen than Ca montmorillonite, at the same appplied stress σ_{ij}. Thus we would expect a compacted cake of Ca montmorillonite to swell if the reservoir fluid was changed

from Ca to Na. Of course, the timescale for complete exchange to take place might be very long, especially if the cake is highly compacted.

Experiments have been reported in which shales or clay suspensions were compacted, and the salt concentration within the exudate measured (Engelhart & Wolf 1963, Bolt 1961b, Rieke & Chilingarian 1974, Smith 1977). The salt concentration within the exudate generally decreases as the clay becomes more compacted, though large increases in the applied pressure can lead to non-monotonic changes in concentration. This is thought to be due to the ion-selective properties of very compacted filtercakes formed at the outer surface of the shale (Bolt 1961a, Smith 1977, Sherwood 1992). However, none of the above authors report completely salt-free exudate, and we must conclude that the limit considered in this section is never attained in practice. The errors involved in neglecting the ions in equations (4.20) and (4.21) are unknown, but will presumably decrease as the clay becomes more compacted.

Note that the thermodynamic analysis presented above treats the shale as a black box, which is in equilibrium with a fluid reservoir. All the chemical potentials and the applied stress may in principle be determined. The analysis does not attempt to split the chemical potential of any species within the shale into a mechanical pressure and an osmotic pressure, nor does it attempt to distinguish water and ions adsorbed to the clay from those which are not.

In addition to the cases discussed above, Sherwood (1993) showed that if the shale is considered to be in Donnan equilibrium with an external reservoir of fluid, its swelling could be described by the Biot equations (4.11) and (4.12). Dormieux *et al.* (1995) showed that microscopic equations based on electrical double layer repulsions between plates could be used similarly to produce a macroscopic constitutive relation for swelling shale.

Standard Biot poroelasticity makes no predictions concerning possible fracture or failure of the shale: one could introduce a failure criterion based, for example, on strain. If the distribution of clay is inhomogeneous, fracture may be controlled solely by the clay-rich regions

The mechanical properties of the clay (e.g. S_{ijkl}) are expected to vary during the course of compaction or swelling, but have been assumed here to be reversible. It is well-known that the primary compaction of a clay suspension is not reversible when swelling is subsequently allowed to occur. However, hysteresis is very much reduced in any subsequent compaction and swelling, as long as the initial maximum compaction pressure is not exceeeded. Lubetkin *et al.* (1984) ascribed the initial irreversibility to work dissipated in breaking contacts between clay particles as they are re-arranged from some initial, random configuration to a final state in which particles lie parallel to one another. An example of such irreversibility will be given in §5.2.

5 Biot analysis of wellbore swelling

It is known in the petroleum industry that the addition of salt to an aqueous drilling fluid can reduce shale swelling. We now apply the theory of §4 to this problem. Many experiments on shale swelling have been reported, e.g. Chenevert (1970), Bol (1986), Simpson *et al.* (1989), Salisbury *et al.* (1991), Chenevert & Osisanya (1992), Bol *et al.*

(1992), Mody & Hale (1993), Onaisi *et al.* (1993), Simpson & Dearing (2000) and Mody *et al.* (2000). Here we discuss the experiments of Sherwood & Bailey (1994).

We first summarise the equations of §4 for Biot poroelasticity with chemical effects. The full analysis predicts that deformation depends on changes in the chemical potentials of both the water and ions present in the pore fluid. Yew *et al.* (1990) and Onaisi *et al.* (1993) assumed that only the chemical potential of the water is important in determining stresses around the wellbore, and we too adopt this simplifying assumption in the computations of §5.1. Such computations implicitly assume (Sherwood 1993) that the shale is a perfect ion-exclusion membrane, which it is not; for example, pore fluid squeezed from shale is not salt-free (e.g. Rieke & Chilingarian 1974), ion-transport coefficients within clay compacts are non-zero (e.g. Kharaka & Berry 1973) and ion exchange can occur (van Olphen, 1977). Real shale lies somewhere between the limit corresponding to chemically inert rock, and that corresponding to perfect ion exclusion. The experiments presented in §5.2 suggest that the ion-exclusion limit captures the main features of the observed swelling (apart from ionic transport and exchange). However, no estimates are at present available for the errors introduced by the use of this approximation when predicting the stresses around the wellbore.

We work within the linearised theory of small deformations, and adopt the notation of Rice & Cleary (1976), dropping the differential notation $\mathrm{d}\epsilon_{ij}$, and using:

$$G = \text{shear modulus} \tag{5.1}$$
$$e_{ij} = \text{strain} \tag{5.2}$$
$$\sigma_{ij} = \text{stress} \tag{5.3}$$
$$p = \text{pore pressure} \tag{5.4}$$
$$\nu_u = \text{undrained Poisson's ratio} \tag{5.5}$$
$$\nu = \text{drained Poisson's ratio} \tag{5.6}$$
$$B = \text{Skempton's parameter} \tag{5.7}$$
$$m = \text{mass of pore fluid (per unit volume of rock)} \tag{5.8}$$
$$m_0 = \text{mass of pore fluid in the reference state} \tag{5.9}$$
$$\rho_f = \text{density of the pore fluid in the reference state} \tag{5.10}$$
$$c = \kappa \left[\frac{2G(1-\nu)}{(1-2\nu)}\right]\left[\frac{B^2(1+\nu_u)^2(1-2\nu)}{9(1-\nu_u)(\nu_u-\nu)}\right] \tag{5.11}$$
$$k = \text{permeability} \tag{5.12}$$
$$\mu = \text{pore fluid viscosity} \tag{5.13}$$
$$\kappa = k/\mu \tag{5.14}$$
$$t = \text{time} \tag{5.15}$$
$$\eta = \frac{3(\nu_u-\nu)}{2B(1+\nu_u)(1-\nu)}. \tag{5.16}$$

The standard constitutive relations for a chemically inert, isotropic rock are

$$2Ge_{ij} = \sigma_{ij} - \frac{\nu}{1+\nu}\sigma_{kk}\delta_{ij} + \frac{3(\nu_u-\nu)}{B(1+\nu)(1+\nu_u)}p\delta_{ij} \tag{5.17}$$

$$m - m_0 = \frac{3\rho_f(\nu_u - \nu)}{2GB(1+\nu)(1+\nu_u)}\left[\sigma_{kk} + 3B^{-1}p\right], \tag{5.18}$$

and Darcy's law for the motion of pore fluid leads to a diffusion equation

$$c\nabla^2(\sigma_{kk} + 3B^{-1}p) = \frac{\partial}{\partial t}(\sigma_{kk} + 3B^{-1}p). \tag{5.19}$$

Note that we are adopting a sign convention in which compressive stresses are negative, and a pressure p corresponds to an isotropic stress $-p\delta_{ij}$. Stress equilibrium leads to the equation

$$\nabla^2\left[\sigma_{kk} + \frac{6(\nu_u - \nu)}{B(1-\nu)(1+\nu_u)}p\right] = 0. \tag{5.20}$$

If the porous material acts as a perfect ion exclusion membrane, only the chemical potential μ_w of the water plays a role, as discussed in §4.4. We write μ_w in the form

$$\mu_w = pV_w + RT\ln a_w + \mu_w^{\ominus} + M_w g z \tag{5.21}$$

where p is the thermodynamic pressure, V_w is the partial molar volume of water, R is the gas constant, T the temperature, and a_w is the water activity. $\mu_w^{\ominus}$ is the chemical potential in the reference state. Only differences in chemical potential will be of interest to us, and we set $\mu_w^{\ominus} = 0$. $M_w = \rho_w V_w$ is the mass of 1 mole of water, and the gravitational potential $M_w g z$ is discussed in §5.4. Clearly μ_w/V_w plays the role of a modified pressure. We shall assume (as in linearised Biot theory) that V_w varies little with pressure: this is inappropriate if V_w changes significantly over the pressure range of interest. The material coefficients in the constitutive relations would be determined by the standard drained and undrained tests, and it is therefore natural to express these coefficients using the symbols G, ν, ν_u and B (or some equivalent set of constitutive coefficients). Thus the Biot equations (5.17),(5.18) become

$$2Ge_{ij} = \sigma_{ij} - \frac{\nu}{1+\nu}\sigma_{kk}\delta_{ij} + \frac{3(\nu_u - \nu)}{B(1+\nu)(1+\nu_u)}\frac{\mu_w}{V_w}\delta_{ij} \tag{5.22}$$

$$m - m_0 = \frac{3\rho_f(\nu_u - \nu)}{2GB(1+\nu)(1+\nu_u)}\left[\sigma_{kk} + \frac{3\mu_w}{BV_w}\right], \tag{5.23}$$

together with the diffusion equation

$$c\nabla^2\left(\sigma_{kk} + \frac{3\mu_w}{BV_w}\right) = \frac{\partial}{\partial t}\left(\sigma_{kk} + \frac{3\mu_w}{BV_w}\right). \tag{5.24}$$

We see from (5.23) that the parameter B now relates the change in μ_w/V_w to the change in stress σ_{kk} in an undrained deformation, and is therefore a straightforward extension of Skempton's B, which gives the change in pore pressure p in an undrained deformation of a chemically inert system. The equation of stress equilibrium (5.20) becomes

$$\nabla^2\left[\sigma_{kk} + \frac{6(\nu_u - \nu)\mu_w}{BV_w(1-\nu)(1+\nu_u)}\right] = 0. \tag{5.25}$$

The mechanical properties of shale vary widely because of inhomogeneities and fractures; nevertheless, it is appropriate here to indicate the order-of-magnitude of the various constitutive coefficients. We might expect that the behaviour of compacted clay is not far removed from the classical soil mechanics limit, in which the water and clay are incompressible, with $\nu_u = \frac{1}{2}$ and $B = 1$. The mechanical properties of Pierre shale have been discussed by Savage & Braddock (1991) (who also considered anisotropic effects). These properties depend upon the applied stress. The average drained bulk modulus $K = 2G(1+\nu)/3(1-2\nu)$ was typically 0.4 GPa at a stress of 20 MPa. The average diffusivity measured at confining pressures of 5 MPa and 10 MPa was $c = 10^{-7}$ m^{2}s^{-1}; that at confining pressures of 20 MPa and 40 MPa was 10^{-8} m^{2}s^{-1}. The corresponding permeabilities were $k = 1.4 \times 10^{-20}$ m^2 and $k = 8.0 \times 10^{-22}$ m^2, respectively. Tests performed during drainage in the experiments of §5.2 suggest $G = 0.6$ GPa, $\nu_u = 0.44$ and $\nu = 0$ (Bailey *et al.*, 1994b). Somewhat higher values for ν have been given by Swolfs & Nichols (1987).

5.1 Plane strain analysis of swelling around a wellbore

The analysis presented here is almost identical, mathematically, to the plane-strain analyses of Rice & Cleary (1976) and of Detournay & Cheng (1988). We adopt cylindrical polar coordinates, and assume that a circular wellbore of radius b is drilled through the shale along the z axis at time $t = 0$. It is assumed that the stress within the shale prior to drilling is uniform, with components $\sigma_{zz} = \sigma_{zz}^{\infty}$ and $\sigma_{rr} = \sigma_{\theta\theta} = \sigma_{rr}^{\infty}$, and the initial chemical potential of water within the shale is $\mu_w = \mu_w^{\infty}$ everywhere. After drilling, the boundary conditions at the wellbore will be

$$\sigma_{rr} = -p_{\rm mud} \qquad r = b \tag{5.26}$$

$$\mu_w = \mu_w^{\rm mud} \tag{5.27}$$

where $p_{\rm mud}$ is the fluid pressure within the wellbore, and

$$\mu_w^{\rm mud} = V_w p_{\rm mud} + RT \ln a_w^{\rm mud} + M_w g z \tag{5.28}$$

is the chemical potential of water within the drilling fluid. The boundary conditions at infinity are

$$\sigma_{rr} \to \sigma_{rr}^{\infty} \quad , \quad \sigma_{\theta\theta} \to \sigma_{rr}^{\infty} \quad , \quad \sigma_{zz} \to \sigma_{zz}^{\infty} \quad , \quad \mu_w \to \mu_w^{\infty} \quad \text{as } r \to \infty. \tag{5.29}$$

We take as our initial, reference state the state of the rock before the well is drilled. Thus all stresses will be relative to the stress at infinity, and the chemical potential μ_w will be measured relative to μ_w^{∞}. The stress and chemical potential at the wellbore wall $r = b$ become

$$\sigma_{rr}^{w} = -p_{\rm mud} - \sigma_{rr}^{\infty} \tag{5.30}$$

$$\mu_{wb} = \mu_w^{\rm mud} - \mu_w^{\infty}. \tag{5.31}$$

Any variation of μ_{wb} with depth z is assumed to be negligibly small, and deformation of the rock around the wellbore is assumed to be plane strain, with $e_{zz} = 0$. The immediate

(undrained) change in the stress due to the creation of the wellbore is

$$\sigma_{rr} = -\sigma_{\theta\theta} = \frac{b^2}{r^2}\sigma^w_{rr}. \tag{5.32}$$

Subsequent deformation is controlled by diffusion of water into the shale. Setting

$$\Phi = \sigma_{rr} + \sigma_{\theta\theta} + \sigma_{zz} + \frac{3\mu_w}{BV_w} \tag{5.33}$$

and taking the Laplace transform

$$L(v) = \overline{v} = \int_0^\infty e^{-st} v \, \mathrm{d}t, \tag{5.34}$$

the diffusion equation (5.24) transforms to become

$$c\nabla^2\overline{\Phi} = s\overline{\Phi} - \Phi^1 \tag{5.35}$$

where $\Phi^1 = 0$ is the initial value of Φ at $t = 0$. Equation (5.35) has solution

$$\overline{\Phi} = A(s)I_0(qr) + B(s)K_0(qr) \tag{5.36}$$

where $q = (s/c)^{1/2}$, and I_0, K_0 are modified Bessel functions. We seek a solution which decays as $r \to \infty$, and hence set $A(s) = 0$.

The equation of stress equilibrium (5.25) implies that

$$\frac{\partial}{\partial r}\left[\sigma_{rr} + \sigma_{\theta\theta} + \sigma_{zz} + \frac{6(\nu_u - \nu)\mu_w}{BV_w(1-\nu)(1+\nu_u)}\right] = \frac{C_1}{r}. \tag{5.37}$$

If we assume a radial displacement $u_r = u(r;t)$ such that

$$e_{rr} = \frac{\partial u}{\partial r} \quad , \quad e_{\theta\theta} = \frac{u}{r}, \tag{5.38}$$

then it can be shown, using

$$\frac{\partial e_{zz}}{\partial r} = 0 \quad \text{and} \quad \frac{\partial \sigma_{rr}}{\partial r} + \frac{\sigma_{rr} - \sigma_{\theta\theta}}{r} = 0, \tag{5.39}$$

that the constant $C_1 = 0$. Using equations (5.36),(5.37), we obtain

$$\frac{3(1+\nu)(1-\nu_u)\overline{\mu}_w}{BV_w(1+\nu_u)(1-\nu)} = B(s)K_0(qr). \tag{5.40}$$

and the boundary condition $\mu_w = \mu_{wb}$ at $r = b$ implies

$$B(s) = \frac{3(1+\nu)(1-\nu_u)\mu_{wb}}{BV_w(1+\nu_u)(1-\nu)K_0(qb)s}. \tag{5.41}$$

Equations (5.22), (5.33), (5.37) and (5.38) lead to

$$2G\overline{u}r = -\frac{2\eta\mu_{wb}rK_1(qr)}{V_w qK_0(qb)s} + C_2(s) \tag{5.42}$$

where

$$\eta = \frac{3(\nu_u - \nu)}{2B(1+\nu_u)(1-\nu)} \tag{5.43}$$

and $C_2(s)$ is a constant of integration. The radial stress is given by

$$\overline{\sigma}_{rr} = 2G\overline{e}_{rr} + \frac{\nu\overline{\sigma}_{kk}}{1+\nu} - \frac{3(\nu_u-\nu)\overline{\mu}_w}{BV_w(1+\nu)(1+\nu_u)} \tag{5.44}$$

$$= \frac{b^2\sigma^w_{rr}}{sr^2} + \frac{2\eta\mu_{wb}}{V_w sq}\left[\frac{K_1(qr)}{rK_0(qb)} - \frac{bK_1(qb)}{r^2K_0(qb)}\right] \tag{5.45}$$

where we have set

$$C_2(s) = \frac{2\eta\mu_{wb}bK_1(qb)}{V_w sqK_0(qb)} - \frac{b^2\sigma^w_{rr}}{s} \tag{5.46}$$

in order to satisfy the stress boundary condition at the wellbore.

The tangential stress $\sigma_{\theta\theta}$ is given by

$$\overline{\sigma}_{\theta\theta} = 2G\overline{e}_{\theta\theta} + \frac{\nu\overline{\sigma}_{kk}}{1+\nu} - \frac{3(\nu_u-\nu)\overline{\mu}_w}{BV_w(1+\nu)(1+\nu_u)}$$

$$= -\frac{b^2\sigma^w_{rr}}{sr^2} + \frac{2\eta\mu_{wb}}{V_w s}\left[\frac{bK_1(qb)}{r^2qK_0(qb)} - \frac{K_1(qr)}{rqK_0(qb)} - \frac{K_0(qr)}{K_0(qb)}\right] \tag{5.47}$$

and hence

$$\overline{\sigma}_{rr} - \overline{\sigma}_{\theta\theta} = \frac{2b^2\sigma^w_{rr}}{sr^2} + \frac{2\eta\mu_{wb}}{V_w s}\left[\frac{2K_1(qr)}{rqK_0(qb)} - \frac{2bK_1(qb)}{r^2qK_0(qb)} + \frac{K_0(qr)}{K_0(qb)}\right]. \tag{5.48}$$

The axial stress is

$$\sigma_{zz} = \frac{\nu}{1+\nu}\Phi + \frac{3\nu_u\mu_w}{BV_w(1+\nu_u)} \quad , \quad \overline{\sigma}_{zz} = -\frac{2\eta\mu_{wb}K_0(qr)}{V_w sK_0(qb)}. \tag{5.49}$$

The stress and displacement due to σ^w_{rr} do not vary with time:

$$u = -\frac{b^2}{2Gr}\sigma^w_{rr} \tag{5.50}$$

$$\sigma_{rr} = -\sigma_{\theta\theta} = \frac{b^2}{r^2}\sigma^w_{rr} \tag{5.51}$$

and the deviatoric stress is

$$\sigma_{rr} - \sigma_{\theta\theta} = \frac{2b^2}{r^2}\sigma^w_{rr}. \tag{5.52}$$

This is Mode 1 loading, in the notation of Detournay & Cheng (1988).

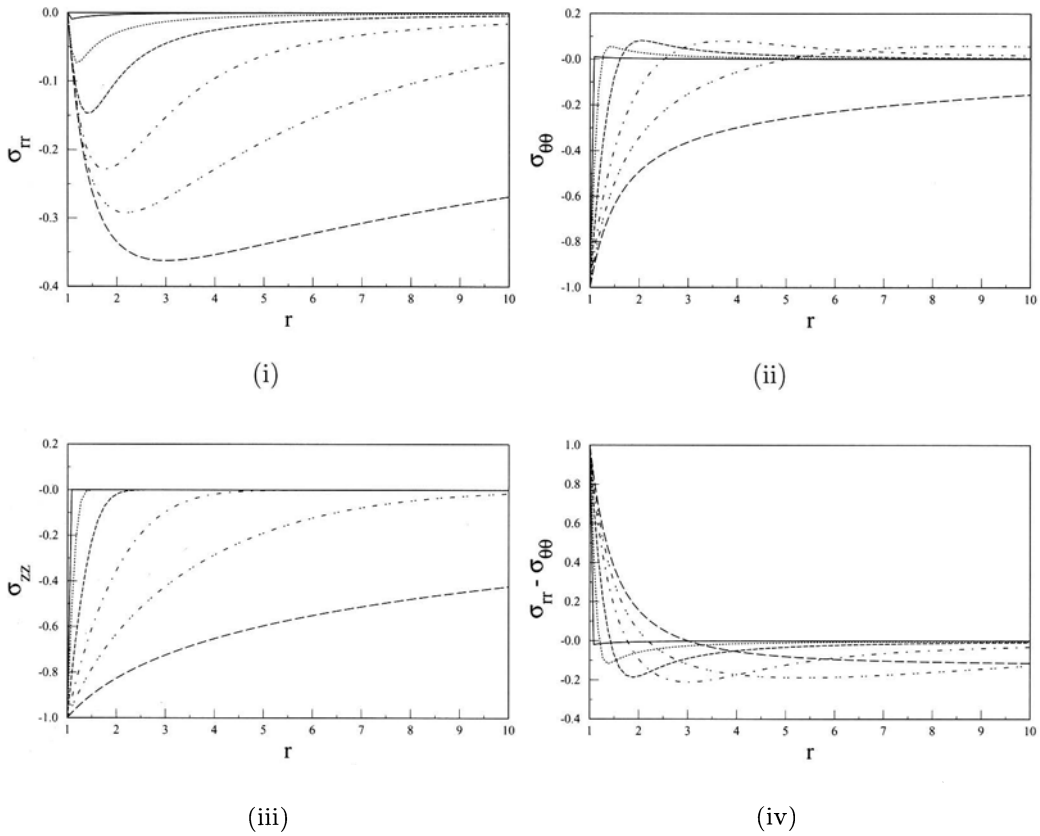

Figure 12. The non-dimensional wellbore stresses due solely to mode 2 loading ($\sigma_{rr}^{w} = 0$), as a function of the non-dimensional radial position $\hat{r} = r/b$. Non-dimensional times: ——— $\hat{t} = tc/b^2 = 10^{-4}$; ····· $\hat{t} = 0.01$; – – – – – $\hat{t} = 0.1$; —·—·—·— $\hat{t} = 1.0$; —··—··—··— $\hat{t} = 10.0$; — — — — — $\hat{t} = 10^3$. (i) radial stress $\hat{\sigma}_{rr} = \sigma_{rr}/2\eta\mu_{wb}$; (ii) tangential stress $\hat{\sigma}_{\theta\theta}$; (iii) axial stress $\hat{\sigma}_{zz}$; (iv) deviatoric stress $\hat{\sigma}_{rr} - \hat{\sigma}_{\theta\theta}$.

Fluid invasion occurs if $\mu_{wb} > 0$, and draining occurs if $\mu_{wb} < 0$. Setting $\sigma_{rr}^{w} = 0$, we obtain Mode 2 Loading. Asymptotic results for the behaviour at small times have been given by Detournay & Cheng, who also give long-time asymptotes for the radial displacement u and stresses σ_{rr}, $\sigma_{\theta\theta}$:

$$\lim_{t\to\infty} u = \frac{\eta\mu_{wb}}{2GV_w}\left(r - \frac{b^2}{r}\right) \tag{5.53}$$

$$\lim_{t\to\infty} \sigma_{rr} = -\frac{\eta\mu_{wb}}{V_w}\left(1 - \frac{b^2}{r^2}\right) \tag{5.54}$$

$$\lim_{t\to\infty} \sigma_{\theta\theta} = -\frac{\eta\mu_{wb}}{V_w}\left(1+\frac{b^2}{r^2}\right). \tag{5.55}$$

The radial displacement u at the wellbore due to Mode 2 loading is always zero. Combining modes 1 and 2, the deviatoric stress at the wellbore wall is

$$\sigma_{rr}-\sigma_{\theta\theta} = 2\sigma^w_{rr}+2\frac{\eta\mu_{wb}}{V_w} \tag{5.56}$$

$$= -2(1-\eta)p_{\rm mud}+\frac{2\eta RT}{V_w}\ln a_{\rm mud}-2\sigma^\infty_{rr}-\frac{2\eta\mu^\infty_w}{V_w}+2\eta g z\rho_w, \tag{5.57}$$

which does not vary with time.

We now set $\sigma^w_{rr}=0$, and consider the time-dependent stresses within the rock (i.e. $r>b$) due to mode 2 loading. We non-dimensionalise stress by $2\eta\mu_{wb}/V_w$, radial position by b and time by b^2/c, and denote non-dimensional quantities by a caret $\hat{}$. The Laplace transforms may be inverted numerically, using the Stehfest algorithm (Stehfest 1970), and we assume $B=1$, $\nu_u=0.5$ and $\nu=0$. Figure 12 shows the radial dependence of $\hat\sigma_{\theta\theta}$, $\hat\sigma_{rr}$ and $\hat\sigma_{zz}$. The shale will initially be under a state of compression, and the figures represent the modification to the compressive stresses. The deviatoric stress $\hat\sigma_{rr}-\hat\sigma_{\theta\theta}$ in the horizontal plane is shown in figure 12(iv). This must be combined with the time-independent Mode 1 deviatoric stress, given by (5.52). The resulting stress difference $|\sigma_{rr}-\sigma_{\theta\theta}|$ always has maximum magnitude at $r=b$. Detournay & Cheng showed that this is not necessarily so if the initial stress in the plane perpendicular to the wellbore is anisotropic. The effect of borehole inclination has been studied by Cui *et al.* (1997) and by Abousleiman *et al.* (1999).

Field tests of osmotic transport into or out of boreholes have been reported by Neuzil (2000).

5.2 Swelling of a finite shale sample

We now discuss experiments performed on cylindrical shale samples of length $h=195$ mm and diameter $2a=150$ mm. A cylindrical hole of nominal diameter $2b=25.4$ mm was drilled along the axis of the sample, and represented a scaled-down wellbore. The measured diameter was typically 25.9 mm: a realistic oilfield wellbore diameter would be typically between 75 mm (modern slimhole technology) and 310 mm. A Biot poroelastic analysis similar to that of §5.1 is reported for this geometry by Sherwood & Bailey (1994), where full details of the experiments can be found. Finite element computations have been made for a similar geometry by Onaisi *et al.* (1993), but with boundary conditions which differ from those in our experiments.

The wellbore simulator in which the experiments were performed is depicted in figure 13. It is similar to, though somewhat smaller than, the downhole simulation cell (DSC) described by Simpson *et al.* (1989), and works at stresses up to 31.5 MPa, with temperatures up to 80 °C. It has proved sufficiently successful to be used as the basis for a wellbore simulator suitable for X-ray tomography (Cook *et al.* 1993). The major difference between the simulator used here, and the DSC of Simpson *et al.*, is that in the latter the shale can be drilled (under stress), and exposed to drilling fluid, in the course of a single experiment. This is closer to actual field conditions. In the experiments

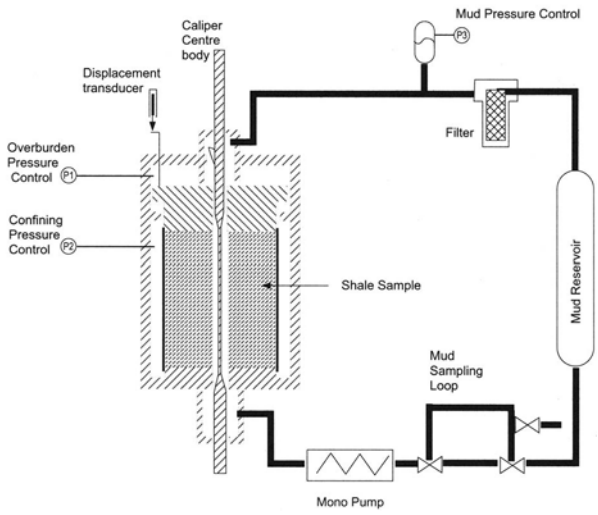

Figure 13. The wellbore simulator.

presented here, the drilling and subsequent swelling tests have been separated, in order to simplify both the experimental equipment and the test procedure. A full description of the wellbore simulator is given by Sherwood & Bailey (1994) and by Bailey *et al.* (1994b).

A radial confining stress σ^a_{rr} can be applied to the outer cylindrical surface $r = a$, and an axial load F_z is applied by means of a piston. In the experiments it is usual to control the overburden pressure σ^a_{zz}, defined by the average

$$F_z = \pi(a^2 - b^2)\sigma^a_{zz} = 2\pi \int_b^a r\sigma_{zz} \mathrm{d}r, \tag{5.58}$$

and our boundary condition during swelling will be that F_z and σ^a_{zz} are constant (the radial distribution of stress $\sigma_{zz}(r)$ varies with time). The wellbore can be filled with drilling fluid at pressure p_{mud}, and the fluid can be pumped along the wellbore to represent the fluid flow within a well. We assume that deformation and stresses are uniform in the axial (z) direction. This requires that slip can occur at the outer boundaries at which the external loads are applied.

The experiments reported here were performed upon a Pierre I shale supplied by Terratek Inc. (Utah). The shale is an outcrop of a Cretaceous formation, and in its native state is water saturated, with a water activity of 1.0 and a porosity of 24%. The water content w, defined by $w =$ (weight of water)/(weight of dry shale), with the shale dried at a temperature 105°C, was initially $w = 0.12$. The mineralogy of a typical sample, obtained from XRD analysis, is carbonate 15%, quartz+feldspar 32%, montmorillonite 10%, illite 30% and kaolinite 11%, with traces of pyrite. The shale has a Cation Exchange Capacity of 0.2 ± 0.02 meq per gram of dry shale, determined by tetramethylammonium displacement of the counterions (Denis *et al.* 1991). The displaced counterions were

present in the (equivalent) proportions 64% Ca, 32% Mg, 3% K and 1% Na. A detailed description of the chemistry of Pierre shale is given by Schultz (1978).

In all the experiments reported here the normal to the bedding planes within the shale was aligned at approximately 60° to the wellbore axis.

The shale was first drained, usually by applying a stress $\sigma_{zz}^{(1)} = 15$ MPa to the sample, with the cylindrical hole temporarily filled by a sandstone core to prevent collapse. The volume of pore fluid squeezed from the shale initially increased as $t^{1/2}$, and full drainage took 5 days: even so, it is possible that insufficient time was allowed for pore fluid within the shale to come into equilibrium with the fluid removed during drainage. The water content within the core was by now reduced to $w = 0.09$. The applied stress was then reduced to zero and the central sandstone core removed. The net effect of this procedure is to reduce the chemical potential of water within the stressed shale. If we assume that the shale behaves as a perfect ion-exclusion membrane and that water in its pores comes into equilibrium with an external reservoir at atmospheric pressure during drainage, we expect that when the drainage stresses $\sigma_{kk}^{(1)}$ are removed the chemical potential of water within the unstressed shale should be

$$\frac{\mu_w}{V_w} = p + \frac{RT}{V_w} \ln a_w = \tfrac{1}{3} B \sigma_{kk}^{(1)}. \tag{5.59}$$

Any cavitation of the pore fluid is likely to render (5.59) invalid.

At this point the water activity in the drained shale was measured by means of a Novasima Humidat-TH2 humidity meter at 20 °C. The wellbore simulator was then loaded with wellbore fluid.

The shale was subjected to a radial confining stress $\sigma_{rr}^{(2a)} = -26$ MPa, axial stress $\sigma_{zz}^{(2a)} = -27.3$ MPa and fluid pressure $p_{\text{mud}}^{(2)} = 25$ MPa within the wellbore: the stresses and wellbore pressure were increased to their final values in steps of 1 MPa over a period of 30 minutes. The axial compressive strengths for Pierre shale given by Hale *et al.* (1992) suggest that the unswollen shale can withstand this small deviatoric stress. Indeed, Cook *et al.* (1993) found that failure (at similar stress levels) occurred only when the wellbore pressure p_{mud} was more than 4 MPa below the radial confining stress $|\sigma_{rr}^{(2a)}|$.

The subsequent swelling experiments were performed at ambient temperature (20 ± 5 °C) and continued for 48 h. The wellbore, axial and confining pressures were then reduced to zero over a 2 hour period, rather than instantaneously, in order to avoid fractures caused by pore pressures higher than the total stress. At the end of the experiment, the shale cores were cut in half along the axis of cylindrical symmetry, and samples of shale were removed for chemical analysis. The 20 mm closest to the wellbore wall was divided into 4 sections each of 5 mm; the outer region was divided into 10 mm sections. The near-wellbore region was sampled in duplicate, and at least 2 g of material was removed from each section.

During the swelling test the piston applying the axial force F_z was allowed to move in order to keep F_z constant. Swelling could therefore be monitored. Figure 14(i) shows the displacement u_z of the piston, relative to some arbitrary origin, for a shale sample swelling in deionised water. The change in u_z of 0.3 mm corresponds to a strain $e_{zz} = 1.5 \times 10^{-3}$.

We first consider the effect of drainage pressure upon the swelling. Three shale samples were drained at 25 MPa, 15 MPa and 0 MPa (i.e. the last sample was not drained). The

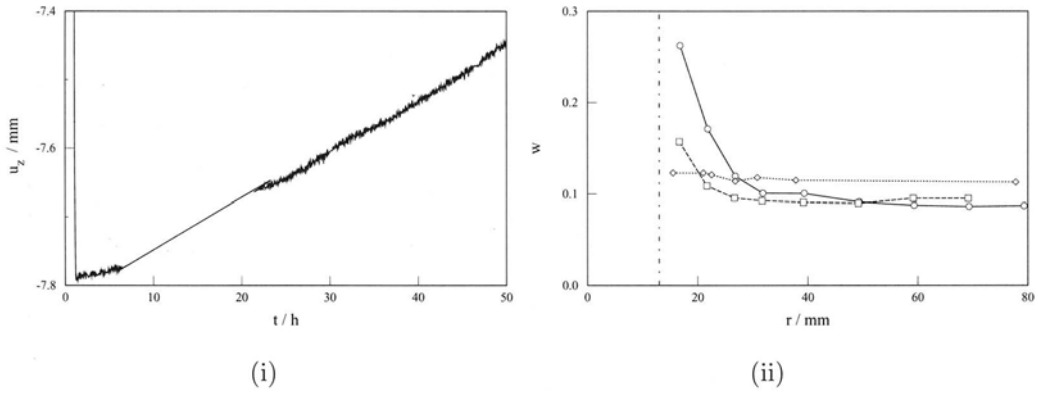

Figure 14. (i) Axial displacement u_z of the piston applying the axial force F_z, relative to some arbitrary origin. Drainage at 15 MPa, swelling in deionised water with 10 g l^{-1} Xanthan. (ii) Final water content w as a function of radial position r. The shales were drained at (a) —○— 25 MPa, (b) – –□– – 15 MPa and (c) ·····◇····· 0 MPa (i.e. undrained), and allowed to swell for 48 h in deionised water with 10 g l^{-1} Xanthan. The broken vertical line indicates the initial position of the wellbore wall.

initial water content of all 3 shales before drainage was $w = 0.12$. After drainage, the water contents were $w = 0.086$, 0.091 and 0.12, and the water activities (after removal of the drainage stress) were 0.85 ± 0.02, 0.90 ± 0.02 and 1.0. Taking $V_w = 1.80 \times 10^{-5}$ m^3, $R = 8.31$ J K^{-1}mol^{-1} and $T = 293$ K we find $RT/V_w = 135$ MPa. Assuming (5.59) holds with $B = 1$, the (isotropic) drainage stresses required to produce these values of μ_w were 22 MPa, 14 MPa and 0 MPa, in fair agreement with the stresses which were actually applied. The three samples were then subjected to a 48 h test using a wellbore fluid consisting of 10 g l^{-1} Xanthan gum in deionised water (water activity $a_w = 1$).

Figure 14(ii) shows the final water contents of the three shales. The data points are positioned at the centre of each 5 mm (or 10 mm) sampling section, and the vertical broken line indicates the initial position of the wellbore surface. The undrained sample has not been affected by exposure to deionised water. The drained samples have swollen, with a final water content which depends upon the drainage pressure, and which is higher than that before draining. Thus the drainage-swelling cycle is not reversible, contrary to the assumptions of the Biot analysis in §4. In soil mechanics, the irreversibility of compaction followed by subsequent swelling is well-known, and can be due, *inter alia*, to rearrangement of the particles and frictional losses. The degree of swelling is usually smaller than the initial compaction: here the opposite behaviour is observed. One possibility is that the process of draining the sample has destroyed some of the cementation between clay particles.

Figure 15 shows the effect of using, as the wellbore fluid, a 240 g l^{-1} (3.2 molar) KCl solution thickened by 8 g l^{-1} Xanthan gum. The water activity is reduced to 0.88 in the wellbore fluid. This is slightly lower than the water activity of shale drained at

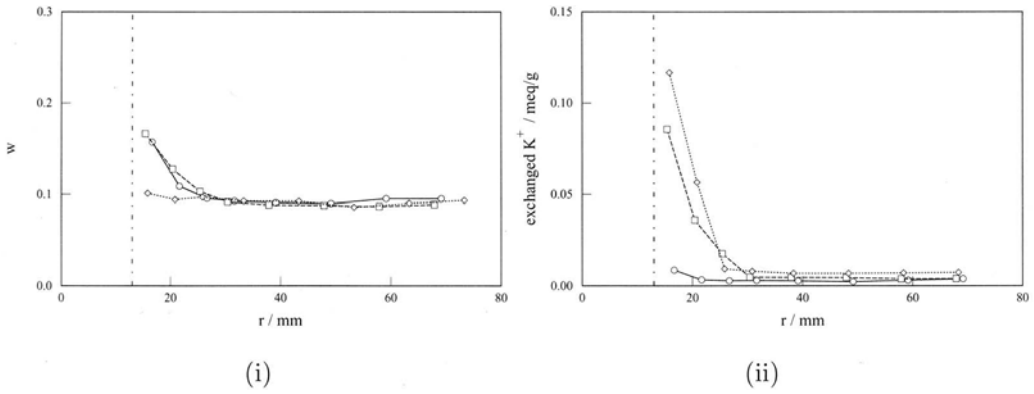

Figure 15. Measured final values of (i) water content w and (ii) concentration of K^+, as as a function of radial position r. The shales were drained at 15 MPa and allowed to swell for 48 h in (a) —○— deionised water with 10 $g\,l^{-1}$ Xanthan, (b) – –□– – 49 $g\,l^{-1}$ KCl solution, with 9 $g\,l^{-1}$ Xanthan, (c) ·····◇····· 240 $g\,l^{-1}$ KCl solution, with 8 $g\,l^{-1}$ Xanthan. The broken vertical line indicates the initial position of the wellbore wall.

15 MPa (0.90 ± 0.02), as measured in the unstressed core after drainage. The stresses applied to the core prior to the swelling experiment raise the chemical potential of water within the core, by an amount which depends on Skempton's parameter B. If $B = 1$, the chemical potential of water within the stressed shale will be slightly lower than that within the pressurised wellbore fluid (ignoring the slight differences between $p^{(2)}_{\rm mud}$ and the radial and confining stresses $|\sigma^{(2a)}_{rr}|$ and $|\sigma^{(2a)}_{zz}|$ applied to the core). Thus we expect no movement of water into the shale. Figure 15(i) indeed shows that the water content of the shale remained almost at its initial value. However the ionic transport was not reduced to zero. Figure 15(ii) shows the profile of the K^+ counterions after the test, as determined by tetramethylammonium displacement. Potassium entered the shale, and exchanged onto the clay.

Figure 15 also shows results obtained using a 49 $g\,l^{-1}$ (0.66 molar) KCl solution, with 9 $g\,l^{-1}$ Xanthan. The water activity of the fluid was 0.98, and the shale was invaded by both water (figure 15(i)) and potassium (figure 15(ii)). Results of tests using NaCl in the drilling fluid were reported by Sherwood & Bailey (1994). The choice of salt is important. Swelling of Na-smectite is known to be greater than that of Ca-montmorillonite (Mesri & Olson 1971). Similarly, swelling of Na-montmorillonite is reduced by the presence of potassium (Lubetkin *et al.* 1984, Denis *et al.* 1991). Thus ion-exchange can influence the final degree of swelling.

During the course of each experiment, the profile of the swollen wellbore could be determined by a spring-loaded caliper which was run along the wellbore. The caliper exerted a pressure of order 0.1 MPa on the weak surface of the swollen shale, and caused additional erosion. The caliper measurements were therefore made sparingly: non-invasive

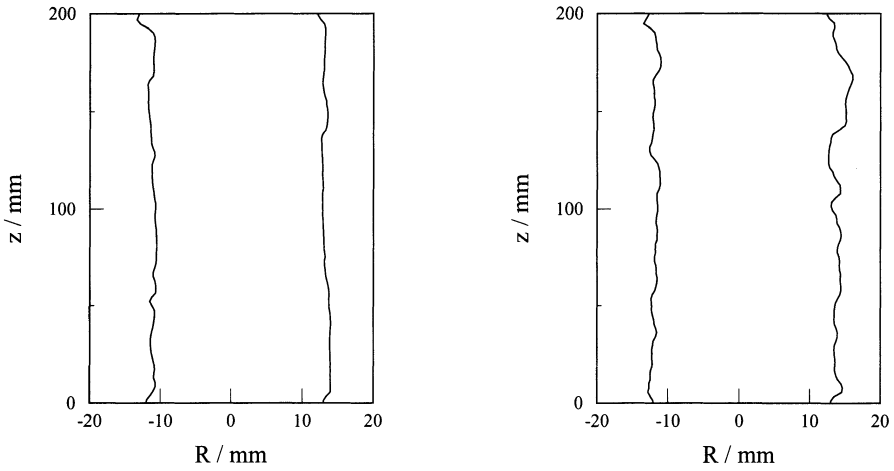

Figure 16. Profile $R(z)$ of the wellbore. Drainage at 15 MPa. (i) initial profile (ii) after swelling for 48 h in deionised water with 10 g l^{-1} Xanthan.

techniques, such as X-ray tomography (Onaisi *et al.* 1993, Cook *et al.* 1993) avoid this problem.

The profile was determined in two mutually perpendicular cross-sections. Swelling (and erosion) was far from uniform, and figure 16 shows profiles obtained before and after swelling in deionised water. We choose here to reduce these profiles of the wellbore diameter $D(z) = 2R(z)$ to a mean D_0 and standard deviation ΔD. The values of $D_0 \pm \Delta D$ may be plotted as a function of time. Figure 17(i) shows such plots for shale samples drained at (a) 25 MPa (b) 15 MPa and (c) 0 MPa. The wellbore was initially uniform, with $\Delta D \simeq 0.2$ mm. The radius of the undrained sample remained unchanged during the course of the experiment. That of the drained sample increased somewhat, and became much less uniform: the increase in ΔD is represented by a widening of the gap between the two lines $D_0 \pm \Delta D$ of figure 17(i). It is evident from the figure that the caliper tended to enlarge the wellbore in the shale drained at 25 MPa, which swelled most and was therefore softest. During the overnight lulls in the scanning activity the swelling reduced the diameter of the wellbore. The effect was slightly less marked in the shale drained at 15 MPa.

Figure 17(ii) shows similar results for experiments using KCl solutions. The 240 g l^{-1} KCl solution prevented imbibition of water into the shale and so almost eliminated swelling and erosion. This was also found when using 300 g l^{-1} NaCl solution as the wellbore fluid. With the 49 g l^{-1} KCl solution the wellbore diameter initially decreased, indicating swelling, and the degree of roughening (ΔD) was markedly larger than with

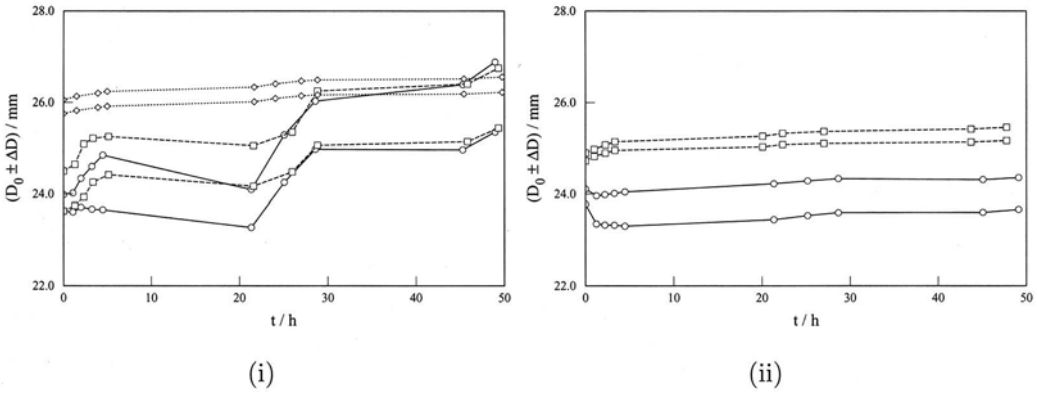

Figure 17. The wellbore diameter $D_0 \pm \Delta D$ (mean $\pm$ standard deviation) as a function of time t. (i) Shales drained at (a) —○— 25 MPa, (b) – –□– – 15 MPa and (c) ·····◇····· 0 MPa (i.e. undrained), swelling in deionised water with 10 g l^{-1} Xanthan. (ii) Shales drained at 15 MPa and swelling in (a) —○— 49 g l^{-1} KCl solution, 9 g l^{-1} Xanthan, (b) – –□– – 240 g l^{-1} KCl solution, with 8 g l^{-1} Xanthan.

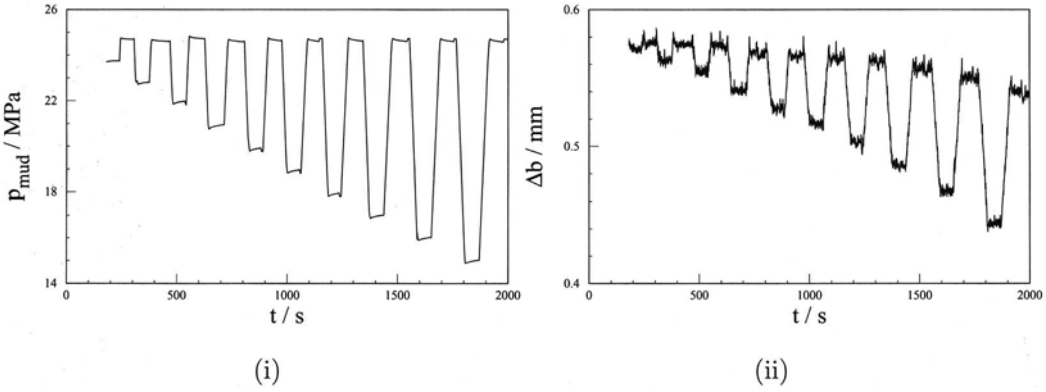

Figure 18. (i) The oscillating borehole pressure p_{mud} plotted against time t. (ii) The corresponding change in the borehole radius Δb.

the more concentrated solution.

The mean diameter D_0 of the wellbore in the drained shale sample appears to increase with time in deionised water (figure 17). This agrees with the predictions of poroelasticity for a finite sample with fixed stress imposed on the outer boundary (Sherwood & Bailey, 1994). However, the experimental results represent a combination of both swelling and erosion: significant amounts of shale (typically more than 40 g) were recovered from a

400 μm filter placed in the flow loop. Thus swelling has led to fracture and dispersion of the rock. Some of the erosion would have been due to the flow of fluid within the wellbore.

The response of the shale sample to changes in stress imposed by the experimental cell can be used to determine mechanical properties (Bailey *et al.*, 1994b). Figure 18 shows the change in the wellbore diameter, as measured by the caliper, when the drilling fluid pressure oscillates in the borehole. The KCl polymer fluid was designed to minimize swelling. Towards the end of the test the shale no longer behaves elastically, and the borehole does not return to its initial dimensions when the pressure reverts to 24.7 MPa.

In the analysis of §5.1 the motion of water into the shale was assumed to be determined solely by the chemical potential of water μ_w. The experiments of §5.2 show that swelling can indeed be inhibited by reducing μ_w within the wellbore. However, ion-exchange occured. Such ion exchange modifies the relationship between water content and μ_w within the shale (see, for example, Keren & Shainberg, 1979). Thus even when μ_w within the wellbore fluid was equal to the initial value of μ_w within the shale, exchange of Na^+ onto the shale was accompanied by considerable swelling. Exchange of K^+, on the other hand, did not adversely affect the uptake of water into the shale.

At the end of the experiments any swollen shale close to the wellbore was soft and mushy. A linear analysis based upon constant material coefficients cannot hope to describe the behaviour of a material which is significantly altered during the experiment, nor can it be expected to make predictions about deformation after the rock has failed. There is a clear need to take into account the large changes in material properties which occur if swelling is not inhibited by correct formulation of the wellbore fluid. Further progress is likely to require numerical computation, and we refer the reader to the work of Heidug & Wong (1996). Similarly, a complete analysis of the swelling process, and its inhibition, should include the effect of ion exchange upon the chemical and mechanical properties of the rock.

5.3 A bench-top swelling test

Large-scale experiments, such as those described in §5.2, are time-consuming and expensive, and it is natural to seek smaller, bench-top tests. One such test device is depicted in figure 19. In the absence of any imposed stress, the swelling of the sample can be detected by means of a displacement transducer, and typical results are shown in figure 20. Figure 20(i) shows swelling of a shale core, prepared in a controlled humidity environment so that its pore water is at activity $a_w = 0.9$. Oil based drilling fluid consists of a suspension of brine droplets in oil. If we vary the salt concentration within the brine, we can control whether water tends to flow from the brine droplets into the shale, or vice-versa, as shown in figure 20(i). Figure 20(ii) shows swelling in ionic solutions of various salts.

We can again use Biot poroelasticity to predict the response of the shale sample, and as in §5.1 a useful first approximation is to assume that only water enters the shale. The problem is axisymmetric, but if the shale is unconfined and allowed to expand there will be end effects. However, when the shale is confined axially between platens at which slip can occur, the stresses are independent of the axial coordinate. We shall not enter

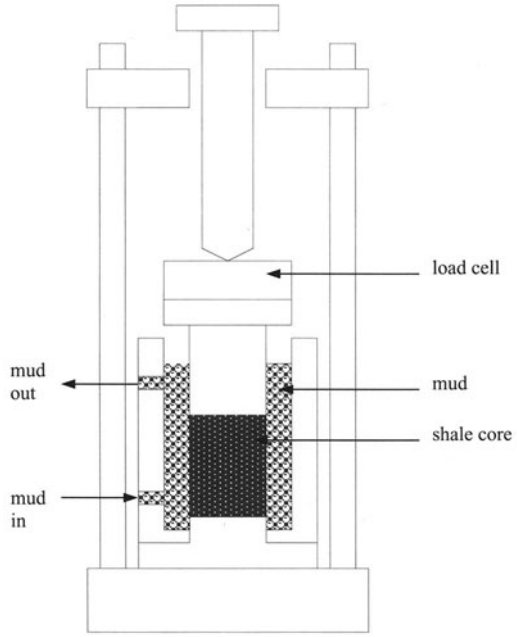

Figure 19. A bench-top shale swelling test. The device can measure either the change in length of an unconfined shale sample, or the stress developed by a confined sample.

into details here, since the analysis proceeds in a manner similar to that presented by Sherwood & Bailey (1994) for the wellbore simulator. However, it is of interest to note that the initial swelling at the outer surface of the shale causes this region to expand. The inner part of the core, close to the axis, is then under radial tension and tends to contract in the axial direction.

5.4 Chemical potential μ_w in a column of drilling fluid

The chemical potential of water within the drilling fluid can be determined at atmospheric pressure and temperature by means of a humidity measurement. The downhole pressure will be higher, both because of hydrostatic pressure, and because of viscous pressure drops which occur during circulation of the drilling fluid. However, the chemical potential must now include a gravitational term (Guggenheim 1967), and hence

$$\mu_w = pV_w + RT \ln a_w + M_w g z + \mu_w^{\ominus} \tag{5.60}$$

where M_w is the mass of one mole of water, gz is the gravitational potential, and $\mu_w^{\ominus}$ is the chemical potential in the reference state. In a static column of pure water, the pressure at position z will be

$$p = p^{\ominus} - gz\rho_w = p^{\ominus} - gzM_w/V_w, \tag{5.61}$$

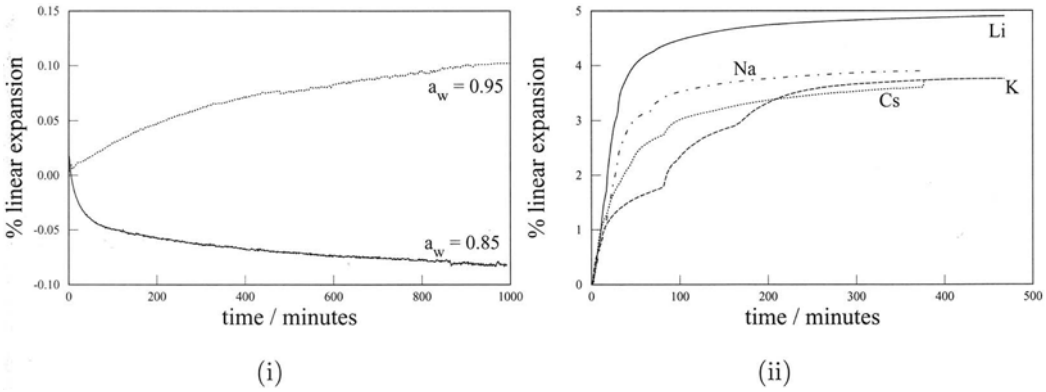

Figure 20. Small-scale strain test of Pierre I shale with pore water activity $a_w = 0.9$. (i) Oil based drilling fluid at (a) $a_w = 0.95$ and (b) $a_w = 0.85$. (ii) 1 molar solutions of (a) LiCl, (b) CsCl, (c) KCl, (d) NaCl.

where $p^{\ominus}$ is some reference pressure. The sum $pV_w + M_w gz$ in (5.60) is therefore independent of z, and the chemical potential μ_w is uniform over the height of the column. If the water contains sedimenting particles (e.g. barite), the density of the fluid will be higher than that of pure water, and μ_w will increase with depth. The gradient in chemical potential drives water upwards, allowing the water to replace the particles which have sedimented downwards. In drilling fluid, sedimentation is sometimes prevented by the gel of bentonite particles. In this case, the weight of the barite is taken by the gel, and the pressure within the liquid is that of a column of water. We shall assume that the fluid is circulating during drilling. The gel is disrupted, and is unable to prevent sedimentation. The hydrostatic pressure within the drilling fluid therefore depends on the bulk (weighted) density. Hence

$$p = p^{\ominus} - gz\rho_{\text{mud}} \tag{5.62}$$

and

$$\mu_w = (p^{\ominus} - gz\rho_{\text{mud}})V_w + RT \ln a_w + M_w gz + \mu_w^{\ominus}. \tag{5.63}$$

We choose $p^{\ominus}V_w + \mu_w^{\ominus} = 0$, and hence

$$\mu_w = (\rho_w - \rho_{\text{mud}})gzV_w + RT \ln a_w. \tag{5.64}$$

Thus one can vary the pressure within the drilling fluid by varying the amount of barite within the mud, and thereby control the mechanical stability of the rock. The water activity can be independently varied (within limits) by addition of salt. However, as seen in the experiments of §5.2, shales do not behave as perfect ion exclusion membranes. Invasion and swelling can be reduced, but not entirely eliminated.

We have emphasised the effect of salt in reducing the chemical potential of water within the wellbore, thereby improving wellbore stability, because of recent advances in

our understanding of this topic. Drilling fluid engineers make use of a much wider range of chemicals, the action of which is not always well understood. For recent examples of drilling fluids which inhibit shale swelling we refer the reader to papers by Bailey *et al.* (1998), Brady *et al.* (1998) and Schlemmer *et al.* (2002).

6 Transport of water and ions through a clay membrane

We have seen that one way to improve wellbore stability is to reduce the chemical potential of water within the drilling fluid. This reduces the final equilibrium amount of swelling. An alternative route might be to ignore equilibrium, and instead aim to decrease the *rate* of swelling. Once drilling has finished, a steel casing pipe is slid into the wellbore and the annulus between casing and rock is filled with cement. If this can be achieved before shale has had time to swell, equilibrium swelling is no longer a concern.

Transport of water and ions through compacted clay is difficult to characterise: the permeability of the clay is very low, and osmotic properties of the clay must also be determined. Compacted clay can behave as an imperfect osmotic membrane (Kemper & Rollins 1966, Shainberg & Kemper 1972, Kharaka & Berry 1973). Transport of salt is hindered compared to that of water, but is nevertheless non-zero. There can be additional effects due to ion exchange, which we shall not consider here.

Theories for the flow of solutions through osmotic membranes are well developed, but it is general easier to write down such theories than to determine the corresponding transport properties experimentally. Sherwood & Craster (2000) report a simple experimental technique, based on a cell which operates at low pressure. We shall first describe the cell and give a summary of the analysis. Then we present experimental results. The cell has the advantage of simplicity and low cost, and can provide rapid screening of potential additives to drilling fluids used within the petroleum industry (Bailey *et al.* 1994a). However, it offers less control of the experimental conditions than can be achieved in a more sophisticated experiment (Malusis *et al.* 2001, Malusis & Shackelford 2002).

Figure 21 shows a cell divided by a clay membrane to form two reservoirs. Inserted into each reservoir is a capillary tube of cross sectional area A_c which is open to the atmosphere. The reservoirs are filled with salt solutions, and molecules of salt and water move from one reservoir to the other through the membrane, driven by any imbalance of the chemical potentials on the two sides of the membrane. Changes in the volumes of fluid on each side of the membrane are easily determined by changes in the height of fluid within the capillary tubes, and if the density of the fluid is known the pressures p^1, p^2 in reservoirs 1 and 2 and the pressure difference $\Delta p = p^1 - p^2$ across the membrane are easily determined from the height of fluid within the capillaries.

Initially the fluid levels in the two reservoirs are equal (or nearly so). Osmotic effects drive fluid into the reservoir with the higher salt concentration. However, salt can cross the membrane, albeit less easily than water. The final steady state of the symmetric cell is therefore one in which each reservoir contains the same volume V_0 of fluid at salt concentration c_0 and density ρ_0.

The fluxes of salt and water through the clay membrane (of area S) can be made larger (and therefore more easily measured) either by increasing the difference in pressure and concentration across the clay, or by decreasing the thickness h of the sample. High

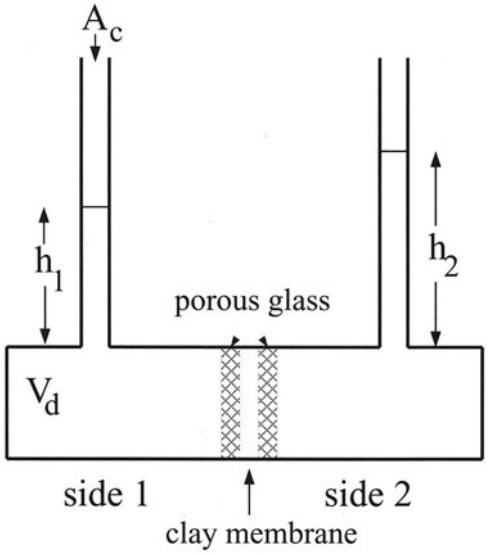

Figure 21. Schematic of the clay membrane cell cell. The fluid reservoirs each have volume V_d and the capillary cross-sectional area is A_c.

pressures complicate the apparatus, and salt concentration profiles within the clay need to be taken into account if the total change in concentration across the sample is large. We therefore sought to make h small. However, thin shale samples are fragile. We therefore used clay membranes re-constituted by filtration of an aqueous suspension of clay. The disadvantage of such an approach is that reconstitution of argillaceous material changes the pore structure and thereby affects transport properties.

6.1 Theory

Sherwood & Craster (2000) considered a salt which in solution dissociates into ν^+ cations of valence z^+, and ν^- anions of valence z^-, where $\nu^+ z^+ + \nu^- z^- = 0$. Linear transport relations for the flux f_w of water, measured in moles, from side 1 to side 2, and fluxes $f_s^\pm$ of ions may be written in the form (Staverman & Smit, 1975)

$$f_w = \lambda_{11}\Delta\mu_w + \lambda_{12}(\Delta\mu_s^+ + z^+F\Delta\phi) + \lambda_{13}(\Delta\mu_s^- + z^-F\Delta\phi) \quad (6.1)$$

$$f_s^+ = \lambda_{21}\Delta\mu_w + \lambda_{22}(\Delta\mu_s^+ + z^+F\Delta\phi) + \lambda_{23}(\Delta\mu_s^- + z^-F\Delta\phi) \quad (6.2)$$

$$f_s^- = \lambda_{31}\Delta\mu_w + \lambda_{32}(\Delta\mu_s^+ + z^+F\Delta\phi) + \lambda_{33}(\Delta\mu_s^- + z^-F\Delta\phi) \quad (6.3)$$

where $\Delta\mu_w, \Delta\mu_s^\pm$ are the differences in chemical potential of the water and salt ions due to concentration and pressure differences across the membrane. Electrical contributions to the electrochemical potentials have been shown explicitly in terms of the change in electrical potential $\Delta\phi$ and the Faraday F.

We assume that all solutions are ideal. The molar volumes of water and ions are $V_w, V_s^\pm$, and that of the salt is $V_s = \nu^+V_s^+ + \nu^-V_s^-$. Changes in the chemical potentials

of water and ions may be written in the form

$$\Delta\mu_w = V_w\Delta p + RT\Delta(\ln x_w) \tag{6.4}$$
$$\Delta\mu_s^{\pm} = V_s^{\pm}\Delta p + RT\Delta(\ln x_s^{\pm}), \tag{6.5}$$

where R is the gas constant, T the absolute temperature and x_w, $x_s^{\pm}$ are the mole fractions of water and ions in the solution. If n_s^i and n_w^i are the number of moles of salt and water on side i of the membrane, we define the mole fraction of salt

$$x_s^i = \frac{n_s^i}{n_w^i + n_s^i} \tag{6.6}$$

and write the change in chemical potential of the salt across the membrane in the form

$$\begin{aligned}\Delta\mu_s &= \left(\nu^+V_s^+ + \nu^-V_s^-\right)\Delta p + RT\left[\nu^+\Delta(\ln x_s^+) + \nu^-\Delta(\ln x_s^-)\right] \\ &\approx V_s\Delta p + (\nu^+ + \nu^-)RT\frac{\Delta x_s}{x_s},\end{aligned} \tag{6.7}$$

where we have assumed that $x_s \ll 1$. Thus we can re-write (6.4),(6.7) in the form

$$\Delta\mu_s = V_s\Delta p + \Delta\pi_s/c_s \tag{6.8}$$
$$\Delta\mu_w = V_w\left(\Delta p - \Delta\pi_s\right), \tag{6.9}$$

where

$$c_s = \frac{n_s}{V_w n_w + V_s n_s} \approx \frac{x_s}{V_w} \tag{6.10}$$

and

$$\pi_s = (\nu^+ + \nu^-)\frac{RT}{V_w}x_s \approx (\nu^+ + \nu^-)RTc_s \tag{6.11}$$

is the osmotic pressure.

If no current is allowed to flow across the membrane, an electrical potential $\Delta\phi$ will be set up rapidly across the membrane such that the total current $I = z^+f_s^+ + z^-f_s^- = 0$ (e.g. Lomba *et al*, 2000), and we may take the flux of salt to be $f_s = f_s^-/\nu^- = f_s^+/\nu^+$. In consequence we may re-write the transport relations (6.1)–(6.3) as

$$f_w = \lambda_{ww}\Delta\mu_w + \lambda_{ws}\Delta\mu_s \tag{6.12}$$
$$f_s = \lambda_{sw}\Delta\mu_w + \lambda_{ss}\Delta\mu_s \tag{6.13}$$

where $\lambda_{sw} = \lambda_{ws}$, and then, by (6.4) and (6.7),

$$f_w = (1 - x_s)k\Delta p - V_w^{-1}\left[(1-\lambda)(\nu^+ + \nu^-)RTk + \lambda V_s D\right]\Delta x_s \tag{6.14}$$
$$f_s = \lambda x_s k\Delta p + \lambda D\Delta x_s, \tag{6.15}$$

where k is a Darcy transmission coefficient, D a diffusivity, and λ is a transmission coefficient such that $\lambda = 1$ corresponds to unimpeded flow of salt and $\lambda = 0$ corresponds to a perfect ion-exclusion membrane (Sherwood 1994b). Thus $1 - \lambda$ is a reflection coefficient. If the liquid viscosity is μ, then $k = k_d/(V_w\mu h)$, where k_d is the standard Darcy permeability of the clay membrane.

An approach more frequently adopted (e.g. van Oort *et al.*, 1996) follows that of Katchalsky & Curran (1965) who write the total volumetric flux $J_v = V_w f_w + V_s f_s$ and the salt flux $J_s = f_s$ using three transport coefficients L_p, σ and ω:

$$J_v = L_p\left(\Delta p - \sigma\Delta\pi_s\right) \tag{6.16}$$

$$J_s = c_s(1-\sigma)J_v + \omega\Delta\pi_s. \tag{6.17}$$

Comparing (6.12)–(6.13) and (6.16)–(6.17), and noting that $x_s \ll 1$, we conclude

$$L_p = kV_w \tag{6.18}$$

$$\sigma = 1-\lambda \tag{6.19}$$

$$\omega = \frac{\lambda D V_w}{(\nu^+ + \nu^-)RT} + x_s\lambda(1-\lambda)k. \tag{6.20}$$

Changes in the density of liquid within the capillary tubes typically have negligible effect upon Δp compared with changes in the height of liquid within the capillaries (Sherwood & Craster, 2000), so we take the fluid density ρ_0 to be constant. If a volume δV of fluid moves across the membrane the level of liquid in each capillary will change by an amount $\delta h = \delta V/A_c$. Hence the rate of change of pressure with time t is

$$\begin{aligned}\frac{\mathrm{d}(\Delta p)}{\mathrm{d}t} &= -2S\rho_0 g J_v/A_c = -2S\rho_0 g L_p\left(\Delta p - \sigma\Delta\pi_s\right)/A_c \\ &= A\Delta p + B\Delta x_s,\end{aligned} \tag{6.21}$$

where g is the acceleration due to gravity, and

$$A = -2Sg\rho_0 kV_w/A_c \tag{6.22}$$

$$B = 2Sg\rho_0(1-\lambda)(\nu^+ + \nu^-)RTk/A_c. \tag{6.23}$$

The rate of change of salt concentration is

$$\begin{aligned}\frac{\mathrm{d}(\Delta x_s)}{\mathrm{d}t} &= -\frac{2S}{n_w^0}(J_s - c_0 J_v) = \frac{2S}{n_w^0}\left[\sigma c_0 L_p\Delta p - (\omega + L_p\sigma^2 c_0)\pi_s\right] \\ &= C\Delta p + E\Delta x_s,\end{aligned} \tag{6.24}$$

where n_w^0 is the number of moles of water in one reservoir at equilibrium, x_s^0 is the corresponding mole fraction of salt and

$$C = 2Skx_s^0(1-\lambda)/n_w^0 \tag{6.25}$$

$$E = -\frac{2S}{n_w^0}\left\{\lambda D + \frac{x_s^0(1-\lambda)(\nu^+ + \nu^-)RTk}{V_w}\right\}. \tag{6.26}$$

Equations (6.21) and (6.24) have solution

$$\Delta p = \Delta p_0\frac{(\lambda_2 e^{-k_1 t} - \lambda_1 e^{-k_2 t})}{\lambda_2 - \lambda_1} + \lambda_1\lambda_2\Delta x_s^0\frac{(e^{-k_1 t} - e^{-k_2 t})}{\lambda_2 - \lambda_1} \tag{6.27}$$

$$\Delta x_s = \Delta p_0\frac{(e^{-k_1 t} - e^{-k_2 t})}{\lambda_1 - \lambda_2} + \Delta x_s^0\frac{(\lambda_1 e^{-k_1 t} - \lambda_2 e^{-k_2 t})}{\lambda_1 - \lambda_2}, \tag{6.28}$$

where $\Delta p_0, \Delta x_s^0$ are the initial values of $\Delta p, \Delta x_s$ at $t = 0$, and

$$\lambda_i = \frac{E - A \pm \left[(E-A)^2 + 4CB\right]^{1/2}}{2C} \tag{6.29}$$

$$-k_i = \frac{E + A \pm \left[(E-A)^2 + 4CB\right]^{1/2}}{2}. \tag{6.30}$$

In the limit $\lambda \to 1$ both B and C become small. Hence, assuming $(E-A)^2 \gg 4CB$,

$$\lambda_1 \simeq (E-A)/C \quad , \quad \lambda_2 \simeq B/(A-E) \tag{6.31}$$

with $|\lambda_1| \gg |\lambda_2|$, and

$$k_1 \simeq -E \quad , \quad k_2 \simeq -A. \tag{6.32}$$

Analysis of the experimental results then becomes straightforward. However, $k_1 \approx k_2$ for some of the experimental results presented in §6.3, so that $E \approx A$. The above approximations for λ_1, λ_2 break down, but can be circumvented since when $\Delta p_0 = 0$, (6.27) simplifies to

$$\begin{aligned} \Delta p &= \frac{\lambda_1 \lambda_2 \Delta x_s^0}{\lambda_2 - \lambda_1}(e^{-k_1 t} - e^{-k_2 t}) = \frac{B \Delta x_s^0 (e^{-k_1 t} - e^{-k_2 t})}{[(E-A)^2 + 4CB]^{1/2}} \\ &= \frac{B \Delta x_s^0 (e^{-k_1 t} - e^{-k_2 t})}{k_2 - k_1}. \end{aligned} \tag{6.33}$$

If experimental results for Δp can be represented by an expression of the form

$$\Delta p = a_1 \left[\exp(-a_2 t) - \exp(-a_3 t)\right], \tag{6.34}$$

with $a_2 < a_3$, then for reasons discussed by Sherwood & Craster (2000) we identify a_2 with k_2, a_3 with k_1. From (6.33)

$$B = a_1(a_3 - a_2)/\Delta x_s^0 \tag{6.35}$$

and by (6.23), (6.25),

$$C = \frac{A_c x_s^0 B}{n_w^0(\nu^+ + \nu^-) g \rho_0 RT}. \tag{6.36}$$

Hence by (6.30), (6.35) and (6.36)

$$\begin{aligned} (E-A)^2 &= (k_2 - k_1)^2 - 4CB \\ &= (a_3 - a_2)^2 \left[1 - \frac{4 a_1^2 x_s^0 A_c}{n_w^0(\nu^+ + \nu^-) g \rho_0 RT}\right]. \end{aligned} \tag{6.37}$$

For the experiments reported in §6.3, a_1 is sufficiently small that $(E-A)^2 \approx (a_3 - a_2)^2$, and so even when $a_2 \approx a_3$ we take $a_2 = -A$, $a_3 = -E$.

Further insight can be obtained by considering the limits $k_1 \gg k_2$, and $k_2 \gg k_1$. As a preliminary, we first estimate the relative magnitudes of D and k.

The flux of salt due to a pressure difference $\Delta p = RT\Delta x_s/(V_s x_s^0)$ is, by (6.15), $f_s = \lambda kRT\Delta x_s/V_s$ and we assume for the moment that this is of similar magnitude to the flux of salt $f_s = \lambda D\Delta x_s$ due to a concentration difference Δx_s. This implies that $D \sim kRT/V_s \sim kRT/V_w$ and hence, by (6.26), that $E \sim -2S\lambda D/n_w^0$. The ratio of the two rate constants k_1, k_2 (6.32) can now be estimated. When $1-\lambda \ll 1$,

$$\frac{k_1}{k_2} = \frac{E}{A} = \frac{DA_c}{n_w^0 V_w g\rho_0 k} \sim \left(\frac{RT}{V_w}\right)\left(V_w n_w^0 g\rho_0/A_c\right)^{-1}. \tag{6.38}$$

The term RT/V_w in (6.38) is typically 138 MPa. The term $V_w n_w^0 g\rho_0/A_c$is the hydrostatic pressure which would be generated if all the n_w^0 moles of water molecules occupied the capillary of cross section A_c. Thus k_1/k_2 depends upon geometrical effects. If the reservoirs were doubled in volume the change in concentration caused by the transfer of 1 mole of salt across the membrane would be halved, so that the relaxation rate would be halved. However, the corresponding change in fluid level within the capillary would be unaffected. If on the other hand the cross-sectional area A_c of the capillaries is halved, the rate at which pressure returns to zero will be doubled, but the relaxation rate of salt concentration will be unaffected.

The volume of water in each reservoir is $V_w n_w^0 \approx 1.4 \times 10^{-5}$ m^3 and $A_c = 9.1$ mm^2. Taking $g = 9.8\ \mathrm{m\,s^{-2}}$ and $\rho_0 = 1000\ \mathrm{kg\,m^{-3}}$, the hydrostatic pressure $V_w n_w^0 g\rho_0/A_c$ is typically 10^4 Pa. We conclude that $E \gg A$ and $k_1 \gg k_2$. We first study this case and then, for completeness, study the opposite limit $k_1 \ll k_2$.

The case $k_1 \gg k_2$

If $1-\lambda \ll 1$, both B and C are small and hence $|\lambda_1| \gg |\lambda_2|$ with

$$\lambda_1 = \frac{E}{C} = -\frac{D}{kx_s^0(1-\lambda)}, \tag{6.39}$$

$$\lambda_2 = -\frac{B}{E} = \frac{g\rho_0(\nu^+ + \nu^-)RTkn_w^0}{A_c D}. \tag{6.40}$$

At the end of the rapid phase we have

$$\Delta p = \Delta p_0 + \lambda_2 \Delta x_s^0 \tag{6.41}$$

and

$$\Delta x_s = -\frac{\Delta p_0}{\lambda_1} - \frac{\lambda_2 \Delta x_s^0}{\lambda_1} = -\frac{\Delta p}{\lambda_1} \simeq -\frac{C\Delta p}{E}. \tag{6.42}$$

We see from (6.42) and (6.24) that the rapid phase comes to an end when the diffusive flux of salt has come into equilibrium with the flux generated by the weak osmotic pressure. The difference in salt concentration is small at the end of the rapid phase, and subsequent changes in concentration will be difficult to observe.

The case $k_2 \gg k_1$

If $V_w n_w^0 g\rho_0/A_c \gg RT/V_w$, then $k_2 \gg k_1$ and $A \gg E$, so that

$$\lambda_1 \simeq -A/C \tag{6.43}$$

$$\lambda_2 \simeq B/A = -(1-\lambda)(\nu^+ + \nu^-)RT/V_w. \tag{6.44}$$

When the fast (k_2) process has ended, the jump in salt mole fraction is

$$\Delta x_s \simeq \frac{\Delta p_0}{\lambda_1 - \lambda_2} + \frac{\lambda_1 \Delta x_s^0}{\lambda_1 - \lambda_2} \simeq -\left(\frac{C}{A}\right)\Delta p_0 + \Delta x_s^0$$

$$\simeq \frac{x_s^0(1-\lambda)A_c}{n_w^0 \rho_0 g V_w}\Delta p_0 + \Delta x_s^0. \tag{6.45}$$

The first term of (6.45) represents the amount of salt transferred by the rapid Darcy flow driven by Δp_0. The jump pressure has become

$$\Delta p \simeq \frac{\lambda_2 \Delta p_0}{\lambda_2 - \lambda_1} + \frac{\lambda_1 \lambda_2 \Delta x_s^0}{\lambda_2 - \lambda_1} \simeq -\left(\frac{\lambda_2}{\lambda_1}\right)\Delta p_0 - \lambda_2 \Delta x_s^0$$

$$\simeq \frac{(1-\lambda)^2(\nu^+ + \nu^-)RT x_s^0 A_c}{n_w^0 g \rho_0 V_w^2}\Delta p_0 + \frac{(1-\lambda)(\nu^+ + \nu^-)RT\Delta x_s^0}{V_w}$$

$$= \frac{(1-\lambda)(\nu^+ + \nu^-)RT}{V_w}\Delta x_s \tag{6.46}$$

which is merely the Van t'Hoff pressure multiplied by the reflection coefficient $1 - \lambda$.

6.2 Experimental procedure

The results presented here were obtained using montmorillonite SWy-1 (Wyoming) supplied by the Clay Minerals Repository, Missouri. The CEC was measured and found to be 79.9 meq/100 g, similar to the value 76.4 meq/100 g given by van Olphen & Fripiat (1979). Samples were prepared following the procedure of Denis *et al.* (1991). Clay particles of size smaller than 2 μm were selected by sedimentation (Brindley & Brown 1984). The clay was washed, exchanged to the Na form by the addition of Na-EDTA, dialysed with de-ionised water and concentrated by centrifugation.

The results presented by Sherwood *et al.* (2002) were obtained on membranes prepared from suspensions of clay alone. The membranes of Sherwood & Craster (2000), which we discuss in §6.3, also contained spherical glass beads with mean diameter 2 μm, with a solids mass fraction 0.3 of beads.

After dilution to approximately 0.9 wt% solids, 40 g of the suspension was weighed into an API filtration cell (American Petroleum Institute 1988) containing a polyvinylidene fluoride filter paper (Durapore) with an average pore diameter of 0.45 μm. After filtration at a pressure of 2.0 bar for 2 hr, only a solid film remained. To condition the clay film, 20.0 g of salt solution, identical to the lower concentration fluid subsequently used in the cell test, was forced through the clay. The clay film was then removed from the filtration cell and its thickness h measured by means of a micrometer. The void ratio within the cake was found to be $e = 2.96$.

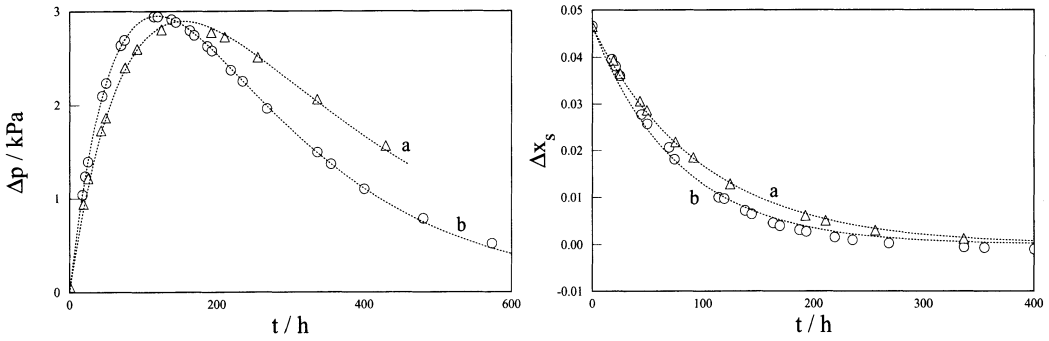

(i) (ii)

Figure 22. Results for reservoirs initially containing (a) 0.5 & 3.0 molar NaCl; (b) 0.5 & 3.0 molar KCl. Fits (indicated by dotted lines) are based on both the pressure and concentration data. (i) The differential pressure Δp as a function of time t. (ii) The corresponding difference in salt mole fraction Δx_s, derived from the fluid conductivity.

The clay film was then placed within the cell, as shown schematically in figure 21 and described by Sherwood & Craster (2000). The film was supported on each side by a porous glass filter of thickness 3.0 mm and pore size between 1.0 and 1.5 μm, and by filter paper. Nitrile O-rings prevented fluid flow between the two sides of the cell except through the clay membrane.

The reservoirs were filled with the two test fluids, and glass capillary tubes of length 1.52 m and cross-sectional area $A_c = 9.1$ mm^2 were then inserted into the cell body. The liquid level in the tubes was adjusted to 730 mm by means of a hypodermic syringe. The cell was then placed in a water bath thermostatted at 25.0 ± 0.5 °C, with the capillary tubes vertical.

The concentration of salt in one reservoir was monitored by means of a conductivity probe. However, it was shown by Sherwood & Craster (2000) that the three transport coefficients (permeability, diffusivity and reflection coefficient) can be determined from measurements of pressure alone.

6.3 Experimental results

During each test the liquid levels in the two capillary tubes were noted. At the end of the test the salt concentrations on the two sides of the cell were identical, and the difference in liquid levels was converted to a pressure difference using the final density ρ_0 of the solution. Results from Sherwood & Craster (2000) are shown in figure 22, with reservoir concentrations initially 0.5 molar (NaCl or KCl) on one side of the membrane and 3.0 molar on the other. Other tests are reported by Sherwood *et al.* (2002).

The differences in salt concentration across the clay membrane were too large for the linear analysis of §6.1 to be valid. Nevertheless, the experimental pressure difference Δp

could be well represented by the expression (6.34). The difference in salt concentration dropped to zero at the rapid relaxation rate, as predicted above when $k_1 \gg k_2$. The data for Δp and Δx_s were fitted simultaneously to (6.28) and (6.27) to obtain the dotted curves seen in figure 22. For NaCl this gave $a_1 = 8.33 \times 10^3$ Pa, $a_2 = 3.82 \times 10^{-3}$ h^{-1}, $a_3 = 1.02 \times 10^{-2}$ h^{-1}, whereas for KCl we obtained $a_1 = 9.01 \times 10^3$ Pa, $a_2 = 5.13 \times 10^{-3}$ h^{-1}, $a_3 = 1.29 \times 10^{-2}$ h^{-1} Note that the sign convention for a_2, a_3 used here differs from that adopted by Sherwood & Craster (2000).

Membrane permeability k

We interpret the results for NaCl. The rate constants for KCl are similar to those for NaCl, and the transport coefficients for the two salts were found by Sherwood & Craster to be similar.

We know that the reflection coefficient is close to zero (i.e. $1 - \lambda \ll 1$), since the osmotic pressures generated are small. By (6.22) and (6.32b)

$$2Sg\rho_0 kV_w/A_c = a_2. \tag{6.47}$$

We take $S = 7.55 \times 10^{-4}$ m^2, $A_c = 9.1$ mm^2, $V_w = 1.8 \times 10^{-5}$ m^3 mol^{-1}, $g = 9.81$ m^2 s^{-1}, and the density of the final 1.75 molar solution is $\rho_0 = 1147$ kg m^{-3} (Lide, 1996). Equation (6.47) then gives

$$k = 3.4 \times 10^{-8} \text{ mol m}^{-2}\,\text{Pa}^{-1}\text{s}^{-1}. \tag{6.48}$$

The film thickness $h = 120$ μm and solution viscosity $\mu = 10^{-3}$ Pa s (water) so that (6.48) corresponds to a Darcy permeability

$$k_d = \mu V_w hk = 7.3 \times 10^{-20} \text{ m}^2 = 7.3 \times 10^{-8} \text{ Darcy}. \tag{6.49}$$

Such a low permeability is typical for compacted clay (Meeten & Sherwood 1994, Bailey *et al.* 1994b, Dewhurst *et al.* 1999), and is similar to the results of figure 3(ii) at void ratio $e = 2.96$. The permeability is likely to be anisotropic (Clennell *et al.* 1999): the value obtained here is for flow perpendicular to the bedding plane. Transport through a packed bed of plate-like particles is slow (Sherwood 1992, Eitzman *et al.* 1996) because of the highly tortuous pore space.

The permeability of the glass filters to water was approximately 10^{-11} m^2, and so we may ignore the hydraulic resistance of the filters compared to that of the clay film.

Transmission coefficient λ

We now estimate the transmission coefficient λ. The inital molarities on the two sides of the film are 3 and 0.5 molar, corresponding to an initial jump in salt mole fraction $\Delta x_s^0 \approx 2.5/55.6 = 0.045$. The final concentration, 1.75 M, corresponds to a salt mole fraction $x_s^0 \approx 0.032$. From (6.35) and (6.23)

$$1 - \lambda = \frac{a_1(a_3 - a_2)A_c}{2Sg\rho_0(\nu^+ + \nu^-)RTk\,\Delta x_s^0} \tag{6.50}$$

so that, taking $T = 300$ K and $R = 8.31$ J K^{-1}mol^{-1},

$$1 - \lambda = 0.0011\ . \tag{6.51}$$

Reflection coefficients for real (rather than re-constituted) shale are small, though the values reported by Bailey *et al.* (1998) are somewhat larger than those obtained here.

Salt diffusivity D

The total volume of water on one side of the membrane (excluding the capillaries) is approximately $V_w n_w^0 \approx V_d = 1.4 \times 10^{-5}$ m^3, so that $n_w^0 = 0.78$. By (6.26) and (6.32a)

$$\lambda D + \frac{x_s^0(1-\lambda)(\nu^+ + \nu^-)RTk}{V_w} = \frac{n_w^0 a_3}{2S}. \tag{6.52}$$

The second term on the left-hand side of (6.52) is usually small, but not always negligible. However, both k and $1-\lambda$ have already been estimated and we find from (6.52)

$$D = 1.1 \times 10^{-3} \text{ mol m}^{-2}\text{s}^{-1}, \tag{6.53}$$

somewhat smaller than the value reported by Sherwood & Craster (2000) because of their neglect of the second term on the left-hand side of (6.52). If we seek a traditional salt diffusivity D_s such that the flux of salt across a membrane of thickness h is

$$f_s = D_s \Delta c_s / h, \tag{6.54}$$

then since $\Delta x_s \approx V_w \Delta c_s$ (6.10) we find

$$D_s = h V_w D = 2.4 \times 10^{-13} \text{ m}^2\text{s}^{-1}. \tag{6.55}$$

Diffusivities reported elsewhere (e.g. Mokady & Low, 1968) at similar clay concentrations are considerably larger, of order 5×10^{-10}m^{2}s^{-1}. A comparable diffusion coefficient for NaCl in water is $D_{s0} = 1.6 \times 10^{-9}$ m^{2}s^{-1} (Robinson & Stokes, 1959), and we would expect diffusion to be smaller in a low permeability membrane.

Ion exchange is not an issue when, as here, the cations in solution are the same as the exchangeable ions on the surface of the clay. We shall not attempt to discuss ion exchange during transport of pore fluid, which clearly occurred in the wellbore simulator experiments of §5.3. However, ion exchange chromatography has been well studied (e.g. Helfferich & Klein, 1970), and models for ion exchange on clays are available (e.g. Fletcher & Sposito, 1989).

Finally we note that the model for ionic transport through a clay membrane, discussed above, can also be applied to transport through other membranes. The application to swelling of a capsule is discussed by Sherwood *et al.* (2003).

My interest in electrical double layers dates back to my studies under Professor E.J. Hinch, and a lecture by Professor J. Rice stimulated my interest in Biot poroelasticity. The work presented in these lectures was performed in collaboration with many colleagues, and I acknowledge in particular the contributions of L. Bailey, B. Craster, J. Crawshaw, G. Goldsmith and G. Meeten.

Bibliography

Abousleiman, Y., Ekbote, S., Cui, L., Mody, F., Roegiers, J.-C. and Zaman, M. 1999 Time-dependent coupled processes in wellbore design and stability: PBORE-3D. In *Proc. SPE Annual Technical Conf.*, Houston, 3–6 October, paper 56759. Richardson, Texas: Society of Petroleum Engineers.

American Petroleum Institute, 1988 Recommended practice standard procedure for field testing drilling fluids. API Recommended Practice 13B, 12th edition. API, Washington DC.

Anandarajah, A. 2000 Numerical simulation of one-dimensional behaviour of a kaolinite. *Géotechnique* **50**, 509–519.

Appelo, C.A.J. 1977 Chemistry of water expelled from compacting clay layers: a model based on Donnan equilibrium. *Chem. Geol.* **19**, 91–98.

Atkinson, J.H. and Bransby, P.L. 1978 *The mechanics of soils. An introduction to critical state soil mechanics.* Maidenhead: McGraw Hill.

Bailey, L., Denis, J.H. and Maitland, G.C. 1991 Drilling Fluids and wellbore stability — current performance and future challenges. In *Chemicals in the Oil Industry: developments and applications*, ed. P.H. Ogden, pp. 53–70. Cambridge: R. Soc. Chem. Special publication No 97.

Bailey, L., Reid, P.I. and Sherwood, J.D. 1994a Mechanisms and solutions for chemical inhibition of shale swelling and failure. In *Recent Advances in Oilfield Chemistry*, ed. P.H. Ogden, pp. 13–27. Cambridge: R. Soc. Chem. Special publication No 159.

Bailey, L., Denis, J., Goldsmith, G., Hall, P.L. and Sherwood, J.D. 1994b A wellbore simulator for mud-shale interaction studies. *J. Petrol. Sci. Engng* **11**, 195–211.

Bailey, L., Craster, B., Sawdon, C., Brady, M. and Cliffe, S. 1998. New insight into the mechanisms of shale inhibition using water based silicate drilling fluids. In *Proc. 1998 IADC/SPE Drilling Conf.*, Dallas, Texas, March 3–6, paper 39401. Richardson, Texas: Soc. Petrol. Engineers.

Biot, M.A. 1941 General theory of three-dimensional consolidation. *J. Appl. Phys.* **12**, 155–164.

Biot, M.A. 1956a Thermoelasticity and irreversible thermodynamics. *J. Appl. Phys.* **27**, 240–253.

Biot, M.A. 1956b Theory of deformation of a porous viscoelastic anisotropic solid. *J. Appl. Phys.* **27**, 459–467.

Biot, M.A. 1973 Nonlinear and semilinear rheology of porous solids. *J. Geophys. Res.* **78**, 4924–4937.

Bol, G.M. 1986 The effect of various polymers and salts on borehole and cutting stability in water-base shale drilling fluids. In *Proc. IADC/SPE Drilling Conf.*, Dallas, Texas, 10–12 February, paper 14802. Richardson, Texas: Society of Petroleum Engineers.

Bol, G.M., Wong, S.-W., Davidson, C.J. and Woodland, D.C. 1992 Borehole stability in shales. In *Proc. European Petroleum Conf.* Cannes, France, 16–18 November, paper 24975. Richardson, Texas: Society of Petroleum Engineers.

Bolt, G.H. 1961a The pressure filtrate of colloidal suspensions. I Theoretical considerations. *Kolloid Z.*, **175**, 33–39.

Bolt, G.H. 1961b The pressure filtrate of colloidal suspensions. II Experimental data on homoionic clays. *Kolloid Z.*, **175**, 144–150.

Brady, M.E., Craster, B., Getliff, J.M. and Reid, P.I. 1998 Highly inhibitive, low-salinity glycol water-base drilling fluid for shale drilling in environmentally sensitive locations. In *Proc. SPE Int. Conf. Health, Safety Environment*, Caracas, 7–10 June, paper 46618. Richardson, Texas: Society of Petroleum Engineers.

Brindley, G.W. and Brown, G. 1984 *Crystal structures of clay minerals and their identification.* London: Mineral. Soc.

Carrier, W.D. and Beckman, J.F. 1984 Correlations between index tests and the properties of remoulded clays. *Géotechnique* **34**, 211–228.

Chan, D.Y.C., Pashley, R.M. and Quirk, J.P. 1984 Surface potentials derived from co-ion exclusion measurements on homoionic montmorillonite and illite. *Clays Clay Miner.* **32**, 131–138.

Chang, F-R.C., Skipper, N.T. and Sposito, G. 1998 Monte Carlo and molecular dynamics simulations of electrical double layer structure in Potassium-Montmorillonite hydrates. *Langmuir* **14**, 1201–1207.

Chenevert, M.E. 1970 Shale alteration by water adsorption. *J. Pet. Tech.* **22**, 1141–1148.

Chenevert, M.E. and Osisanya, S.O. 1992 Shale swelling at elevated temperature and pressure. In *Rock Mechanics, Proc. 33rd U.S. Symposium*, Santa Fe, New Mexico, 3–5 June, ed. J.R. Tiller and W.R. Wawersik, pp. 869–878. Rotterdam: Balkema.

Clennell, M.B., Dewhurst, D.N., Brown, K.M. and Westbrook, G.K. 1999. Permeability anisotropy of consolidated clays. In *Muds and Mudstones: physical and fluid flow properties*, ed. A.C. Aplin, A.J. Fleet and J.H.S. Macquaker, pp. 79–96. London: Geological Society, Special publications 158.

Cook, J.M., Goldsmith, G, Geehan, T., Audibert, A., Bieber, M.-T. and Lecourtier, J. 1993 Mud/shale interaction: model wellbore studies using X-ray tomography. In *Proc. SPE/IADC Drilling Conf.*, Amsterdam, February 22–25, paper 25729. Richardson, Texas: Society of Petroleum Engineers.

Cui, L., Cheng, A.H.-D. and Abousleiman, Y. 1997 Poroelastic solution for an inclined borehole. *ASME J. Appl. Mech.* **64**, 32–38.

de Kretser, R.G., Boger, D.V. and Scales, P.J. 2003 Compressive rheology: an overview. In *Rheology Reviews 2003*, ed. D.M. Binding and K. Walters, pp. 125–165. Aberystwyth: British Society of Rheology.

Den Haan E.J., 1992 The formulation of virgin compression of soils. *Géotechnique,* **42**, 465–483.

Denis, J.H. 1991 Compaction and swelling of Ca-smectite in water and in $CaCl_2$ solutions: water activity measurements and matrix resistance to compaction. *Clays Clay Miner.* **39**, 35–42.

Denis, J.H., Keall, M.J., Hall, P.L. and Meeten, G.H. 1991 Influence of potassium concentration on the swelling and compaction of mixed (Na, K) ion-exchanged montmorillonite. *Clay Minerals* **26**, 255–268.

Detournay, E. and Cheng, A.H.-D. 1988 Poroelastic response of a borehole in a non-hydrostatic stress field. *Int. J. Rock Mech. Min. Sci. & Geomech. Abstr.* **25**, 171–182.

Dewhurst, D.N., Yang, Y. and Aplin, A.C. 1999 Permeability and fluid flow in natural mudstones. In *Muds and Mudstones: physical and fluid flow properties*, ed. A.C. Aplin, A.J. Fleet and J.H.S. Macquaker, pp. 23–43. London: Geological Society, Special publications 158.

Dormieux, L., Barboux, P., Coussy, O. and Dangla, P. 1995 A macroscopic model of the swelling phenomenon of a saturated clay. *Eur. J. Mech. A/Solids* **14**, 981–1004.

Durand, C., Forsans, T., Ruffet, C., Onaisi, A. and Audibert, A. 1995a Influence of clays on borehole stability: a literature survey. Part one: occurrence of drilling problems. Physico-chemical description of clays and their interaction with fluids. *Rev. Inst. Français Pétrole* **50**, 187–218.

Durand, C., Forsans, T., Ruffet, C., Onaisi, A. and Audibert, A. 1995b Influence of clays on borehole stability: a literature survey. Part two: mechanical description and modelling of clays and shales. Drilling practice versus laboratory simulations. *Rev. Inst. Français Pétrole* **50**, 353–370.

Eitzman, D.M., Melkote, R.R. and Cussler, E.L. 1996 Barrier membranes with tipped impermeable flakes. *AIChE J.* **42**, 2–9.

Elrick, D.E., Smiles, D.E. and Wooding, R.A. 1972 Double membrane diaphragm technique for absolute measurements of diffusion coefficients. *J. Chem. Soc. Faraday Trans.* **68**, 591–599.

Engelhardt, W. v. and Gaida, K.H. 1963 Concentration changes of pore solutions during the compaction of clay sediments. *J. Sedimentary Petrol.* **33**, 919–930.

Everett, D.H. 1959 *An introduction to the study of Chemical Thermodynamics.* London: Longmans.

Fletcher, P. and Sposito, G. 1989 The chemical modelling of clay/electrolyte interactions for Montmorillonite. *Clay Minerals* **24**, 375–391.

Ghassemi, A. and Diek, A. 2002 Porothermoelasticity for swelling shales. *J. Petrol. Sci. Engng* **34**, 123–135.

Gross, R.J. and Osterle, J.F. 1968 Membrane transport characteristics of ultrafine capillaries. *J. Chem. Phys.* **49**, 228–234.

Guggenheim, E.A. 1967 *Thermodynamics* 5th edition. Amsterdam: North Holland.

Hale, A.H., Mody, F.K. and Salisbury, D.P. 1992 Experimental investigation of the influence of chemical potential on wellbore stability. In *Proc. SPE/IADC Drilling Conf.*, New Orleans, Louisiana, Feb 18–21, paper 23885. Richardson, Texas: Society of Petroleum Engineers.

Heidug, W.K. and Wong, S.W. 1996 Hydration swelling of water-absorbing rocks: a constitutive model. *Int. J. Num. Anal. Method Geomech.* **20**, 403–430.

Helfferich F.G. and Klein, G. 1970 *Multicomponent Chromatography.* New York: Marcel Dekker.

Hunter, R.J. 1981 *Zeta potential in colloid science.* London: Academic.

Huyghe, J.M. and Janssen, J.J. 1997 Quadriphasic mechanics of swelling incompressible porous media. *Int. J. Eng. Sci.* **35**, 793–802.

Israelachvili, J. 1992 *Intermolecular and surface forces.* 2nd edn, London: Academic.

Jacazio, G., Probstein, R.F., Sonin, A.A. and Yung, D. 1972 Electrokinetic salt rejection in hyperfiltration through porous materials. Theory and experiment. *J. Phys. Chem.* **76**, 4015–4023.

Katchalsky A. and Curran, P.F. 1965. *Nonequilibrium thermodynamics in biophysics.* Cambridge Ma.: Harvard University Press.

Kedem, O. and Katchalsky, A. 1963 Permeability of composite membranes. Part 1. — electric current, volume flow and flow of solute through membranes. *Trans. Faraday Soc.* **59**, 1918–1930.

Kemper, W.D. and Rollins, J.B. 1966 Osmotic efficiency coefficients across compacted clays. *Soil Sci. Soc. Am. Proc.* **30**, 529–534.

Kemper, W.D. and Quirk, J.P. 1972 Ion mobilities and electric charge of external clay surfaces inferred from potential differences and osmotic flow. *Soil Sci. Soc. Am. J.* **36**, 426–433.

Keren, R. and Shainberg, I. 1979 Water vapour isotherms and heat of immersion of Na/Ca-montmorillonite systems II: mixed systems. *Clays Clay Miner.* **27**, 145–151.

Kharaka, Y.K. and Berry, F.A.F. 1973 Simultaneous flow of water and solutes through geological membranes — I. Experimental investigation. *Geochim. Cosmochim. Acta* **37**, 2577–2603.

Leote de Carvalho, R.J.F., Trizac, E. and Hansen, J.-P. 2000 Nonlinear Poisson-Boltzmann theory of a Wigner-Seitz model for swollen clays. *Phys. Rev.* E **61**, 1634–1647.

Lide, D.R. (ed.) 1996 *CRC Handbook of Chemistry and Physics,* 77th edn. Boca Raton, Florida: CRC Press.

Lomba, R.F.T., Chenevert, M.E. and Sharma, M.M. 2000 The ion-selective membrane behaviour of native shales. *J. Petrol. Sci. Engng* **25**, 9–23.

Lubetkin, S.D., Middleton, S.R and Ottewill, R.H. 1984 Some properties of clay-water dispersions. *Phil. Trans. R. Soc. Lond.* A **311**, 353–368.

McKelvey, J.G. and Milne, I.H. 1962 The flow of salt solutions through compacted clay. *Clays Clay Miner.* **9**, 248–259.

Malusis, M.A., Shackelford, C.D. and Olsen, H.W. 2001 A laboratory apparatus to measure chemico-osmotic efficiency coefficients for clay soils. *Geotechnical Testing J. ASTM* **24**, 229–242.

Malusis, M.A. and Shackelford, C.D. 2002 Chemico-osmotic efficiency of a geosynthetic clay liner. *J. Geotech. Geoenvironmental Eng.* **128**, 97–106.

Meeten, G.H. 1994 Shear and compressive yield in the filtration of a bentonite suspension. *Colloids and Surfaces* **82**, 77–83.

Meeten, G.H. and Sherwood, J.D. 1994 The hydraulic permeability of bentonite suspensions with granular inclusions. *Chem. Engng Sci.* **49**, 3249–3256.

Mesri, G. and Olson, R.E. 1971 Consolidation characteristics of montmorillonite. *Géotechnique* **21**, 341–352.

Mody, F.K. and Hale, A.H. 1993 A borehole model to couple the mechanics and chemistry of drilling fluid shale interaction. In *Proc. SPE/IADC Drilling Conf.*, Amsterdam, February 22–25, paper 25728. Richardson, Texas: Society of Petroleum Engineers.

Mody, F.K., Tare, U.A., Tan, C.P., Drummond, C.J. and Wu, B. 2002 Development of novel membrane efficient water-based drilling fluids through fundamental understanding of osmotic membrane generation in shales. In *Proc. SPE Annual Technical Conf.*, San Antonio, October, paper 77447. Richardson, Texas: Society of Petroleum Engineers.

Mokady, R.S. and Low, P.F. 1968 Simultaneous transport of water and salt through clays: I. Transport mechanisms. *Soil Sci.* **105**, 112–131.

Molenaar, M.M. and Huyghe, J.M. 2002 An electro-chemo-mechanical mixture formulation of shale. In *Chemo-Mechanical coupling in clays; from nano-scale to engineering applications*, ed. C. Di Maio, T. Hueckel and B. Loret, pp. 247–260. Lisse: Balkema.

Moyne, C. and Murad, M.A. 2002 Micromechanical computational modeling of hydration swelling of montmorillonite. In *Chemo-Mechanical coupling in clays; from nano-scale to engineering applications*, ed. C. Di Maio, T. Hueckel and B. Loret, pp. 121–133. Lisse: Balkema.

Neuzil, C.E. 2000 Osmotic generation of 'anomalous' fluid pressures in geological environments. *Nature* **403**, 182–184.

Norrish, K. and Rausell-Colom, J.A. 1963 Low-angle X-ray diffraction studies of the swelling of montmorillonite and vermiculite. *Clays Clay Miner.* **10**, 123–149.

Onaisi A., Audibert, A., Bieber, M.T., Bailey, L., Denis, J. and Hammond, P.S. 1993 X-ray tomography vizualization and mechanical modelling of swelling shale. *J. Petrol. Sci. Engng.* **9**, 313–339.

Overbeek, J.Th.G. 1956 The Donnan Equilibrium. *Prog. Biophys.* **6**, 57–84.

Philip, J.R. and Smiles, D.E. 1982 Macroscopic analysis of the behaviour of colloidal suspensions. *Adv. Colloid Interface Sci.* **17**, 83–103.

Posner, A.M. and Quirk, J.P. 1964 The adsorption of water from concentrated electrolyte solutions by montmorillonite and illite. *Proc. R. Soc. Lond.* A **278**, 35–56.

Powell, D.H., Fischer, H.E. and Skipper, N.T. 1998 The structure of interlayer water in Li-Montmorillonite studied by neutron diffraction with isotopic substitution. *J. Phys. Chem.* B **102**, 10899-10905.

Rice, J.R. and Cleary, M.P. 1976 Some basic stress diffusion solutions for fluid-saturated elastic porous media with compressible constituents. *Rev. Geophys. Space Phys.* **14**, 227–241.

Rieke, H.H. and Chilingarian, G.V. 1974 *Compaction of argillaceous sediments* Ch. 5. Amsterdam: Elsevier.

Robinson, R.A. and Stokes, R.H. 1959 *Electrolyte Solutions.* London: Butterworths.

Rolfe, P.F. and Aylmore, L.A.G. 1981 Water and salt flow through compacted clays. II Electrokinetics and salt sieving. *J. Colloid Interface Sci.* **79**, 301–307.

Rowan, D.G. and Hansen, J.-P. 2002 Salt-induced ordering in lamellar colloids. *Langmuir* **18**, 2063–2068.

Russel, W.B., Saville, D.A. and Schowalter, W.R. 1989 *Colloidal Dispersions.* Cambridge University Press.

Salisbury, D.P., Ramos, G.G. and Wilton, B.S. 1991 Wellbore instability of shales using a downhole simulation test cell. In *Rock Mechanics as a multidisciplinary science, Proc. 32rd U.S. Symposium*, Norman Oklahoma, 10–12 July, ed. J.-C. Roegiers, pp. 1015–1024. Rotterdam: Balkema.

Savage, W.Z. and Braddock, W.A. 1991 A model for hydrostatic consolidation of Pierre shale. *Int. J. Rock Mech. Min. Sci. & Geomech. Abstr.* **28**, 345–354.

Schlemmer, R., Friedheim, J.E., Growcock, F.B., Bloys, J.B., Headley, J.A. and Polnaszek, S.C. 2002 Membrane efficiency in shale — an empirical evaluation of drilling fluid chemistries and implications for fluid design. In *Proc. IADC/SPE Drilling Conf.*, Dallas, February 26–28, paper 74557. Richardson, Texas: Society of Petroleum Engineers.

Schultz, L.G. 1978 Mixed-layer clay in the Pierre shale and equivalent rocks, Northern Great Plains Region. US Geological survey professional paper 1064-A. Washington: US Government Printing Office.

Shainberg, I., Bresler, E. and Klausner, Y. 1971 Studies on Na/Ca montmorillonite systems 1. The swelling pressure. *Soil Sci.* **111**, 214–219.

Shainberg, I. and Kemper, W.D. 1972 Transport numbers and mobilities of ions in bentonite membranes. *Soil Sci. Soc. Am. Proc.* **36**, 577–582.

Sherwood, J.D. 1992 Ionic motion in a compacting clay filtercake. *Proc. R. Soc. Lond.* A **437**, 607–627.

Sherwood, J.D. 1993 Biot poroelasticity of a chemically active shale. *Proc. R. Soc. Lond.* A **440**, 365–377.

Sherwood, J.D. 1994a A model for the flow of water and ions into swelling shale. *Langmuir* **10**, 2480–2486.

Sherwood, J.D. 1994b A model for hindered transport of solute in poroelastic shale. *Proc. R. Soc. Lond.* A **445**, 679–692.

Sherwood, J.D. 1997 The initial and final stages of compressible filtercake compaction. *AIChE J.* **43**, 1488–1493.

Sherwood, J.D. and Bailey, L. 1994 Swelling of shale around a cylindrical wellbore. *Proc. R. Soc. Lond.* A **444**, 161–184.

Sherwood, J.D. and Craster, B. 2000 Transport of water and ions through a clay membrane. *J. Colloid Interface Sci.* **230**, 349–358.

Sherwood, J.D. and Meeten, G.H. 1997 The filtration properties of compressible mud filtercakes. *J. Petrol. Sci. Engng* **18**, 73–81.

Sherwood, J.D. and Stone, H.A. 1995 Electrophoresis of a thin charged disc. *Phys. Fluids* **7**, 697–705.

Sherwood, J.D. and Van Damme, H. 1994 Non-linear compaction of an assembly of highly deformable plate-like particles. *Phys. Rev. E* **50**, 3834–3840.

Sherwood, J.D., Meeten, G.H., Farrow, C.A. and Alderman, N.J. 1991 The concentration profile within non-uniform mudcakes. *J. Chem. Soc. Faraday Trans.* **87**, 611–618.

Sherwood, J.D., Craster, B., Bailey, L. and Baigazin, K. 2002 Osmotic transport through a clay membrane. In *Chemo-Mechanical coupling in clays; from nano-scale to engineering applications*, ed. C. Di Maio, T. Hueckel and B. Loret, pp. 317–323. Lisse: Balkema.

Sherwood, J.D., Risso, F., Collé-Paillot, F., Edwards-Lévy, F. and Lévy, M.-C. 2003 Transport rates through a capsule membrane to attain Donnan equilibrium. *J. Colloid Interface Sci.* **263**, 202–212.

Simpson, J.P. and Dearing, H.L. 2000 Diffusion Osmosis — An unrecognised cause of shale instability. In *Proc. SPE/IADC Drilling Conf.*, New Orleans, February 23–25, paper 59190. Richardson, Texas: Society of Petroleum Engineers.

Simpson, J.P., Dearing, H.L. and Salisbury, C.K. 1989 Downhole simulation cell shows unexpected effects of shale hydration on borehole wall. *SPE Drilling Engng* **4**, 24–30.

Slade, P.G., Quirk, J.P. and Norrish, K. 1991 Crystalline swelling of smectite samples in concentrated NaCl solutions in relation to layer charge. *Clays Clay Miner.* **39**, 234–238.

Smiles, D.E. and Harvey, E.G. 1973 Measurement of moisture diffusivity of wet swelling systems. *Soil Sci.* **116**, 391–399.

Smith, J.E. 1977 Thermodynamics of salinity changes accompanying compaction of shaly rocks. Paper SPE 6329, *Soc. Petrol. Engin. J.*, October 377–386.

Staverman, A.J. 1952 Non-equilibrium thermodynamics of membrane processes. *Trans. Faraday Soc.* **48**, 176–185.

Staverman, A.J. and Smit, J.A.M. 1975 Thermodynamics of irreversible processes. Membrane theory: osmosis, electrokinetics, membrane potentials. In *Physical Chemistry: Enriching topics from colloid and surface science*, ed. H. van Olphen and K.J. Mysels, Ch. 22, pp. 343–384. La Jolla, California: Theorex

Stehfest, H. 1970 Numerical inversion of Laplace transforms. CACM **13**, 47–49 and 624.

Swolfs, H.S. and Nichols, T.C. Jr 1987 Anisotropic characterization of Pierre shale — preliminary results. U.S. Geological Survey Open file report 87-417.

van Olphen, H. 1977 *An introduction to clay colloid chemistry.* 2nd edn. New York: Wiley.

van Olphen, H. and Fripiat, J.J. (eds.) 1979 *Data handbook for clay materials and other non-metallic minerals.* Oxford: Pergamon Press.
See also http://web.missouri.edu/ geoscjy/SourceClay/

van Oort, E., Hale, A.H., Mody, F.K. and Roy, S. 1996 Transport in shales and the design of improved water-based shale drilling fluids. *SPE Drilling & Completion* **11**, 137–146.

Wyllie, M.R.J. 1951 An investigation of the electrokinetic component of the self potential curve. *Trans. AIME* **192**, 1–18.

Yew, C.H., Chenevert, M.E., Wang, C.L. and Osisanya, S.O. 1990 Wellbore stress distribution produced by moisture adsorption. *SPE Drilling Engng.* **5**, 311–316.

Molecular Modelling of Pore Fluids in Clays

Neal Skipper[1]

[1] Department of Physics and Astronomy, University College London,
Gower Street, London WC1E 6BT, UK.
Email: n.skipper@ucl.ac.uk
http://www.cmmp.ucl.ac.uk/~nts

Abstract. Recent advances in statistical mechanical molecular modelling of clay-fluid interactions will be discussed, with emphasis on empirical potential based Monte Carlo and molecular dynamics simulations. These methods will be illustrated by reference to the structure and dynamics of ions and solvent at hydrated clay surfaces. The aim of this research is to provide molecular scale insight into fluid dependent processes, for example; clay swelling, solute transport through clays, and clay compaction during burial. Models for the interparticle interactions will be reviewed, with particular reference to the various strategies used to represent clay-fluid systems. The general principles of Monte Carlo and molecular dynamics computer simulation will then be described. A number of specific issues arise when these techniques are applied to the properties of confined fluids: long-range interactions, system size limitations, boundary conditions, choice of thermodynamic ensemble, and statistical sampling. Throughout, we will compare and contrast recent computer simulations of clay-fluid systems with experimental data, and draw general lessons from these examples.

1 Introduction

The swelling clay minerals, for example smectite and vermiculite, are layer-type aluminosilicates that are widespread in geologic deposits, soils, and sedimentary rocks (Brindley & Brown, 1980). They are comprised of stacks of negatively charged mica-like sheets, which are held together by charge balancing interlayer counterions, for example sodium or calcium. Since these counterions have a strong tendency to hydrate, water molecules and other polar molecules can be intercalated between the clay layers. This creates an interlayer ionic solution, which causes the clay to swell. Typically, the expanding clay passes through three discrete hydration states, and is then governed by longer-range electrical double layer interactions (Sposito 1982, Newman 1987).

Detailed knowledge of clay swelling and interlayer fluids is essential if we are to understand many important natural and industrial processes. For example, clay hydration/dehydration plays a key role in subsurface fluid migration, damage to buildings, and oil-well collapse (North, 1990). In addition, the interlayer region of clays provides an ideal environment in which to study the fundamental properties of 2-dimensional pore-fluids.

Statistical mechanical computer simulations provide a direct link between the microscopic properties of particles, such as their masses and interactions, and the observable properties of

macroscopic systems, such as the energetics, average structure, and transport coefficients (figure 1; Allen and Tildesley, 1987; Frenkel and Smit, 1996). Such computational techniques have been particularly effective in providing detailed microscopic understanding of aqueous solutions and clay-fluid systems, and have helped to resolve many fundamental questions in these fields.

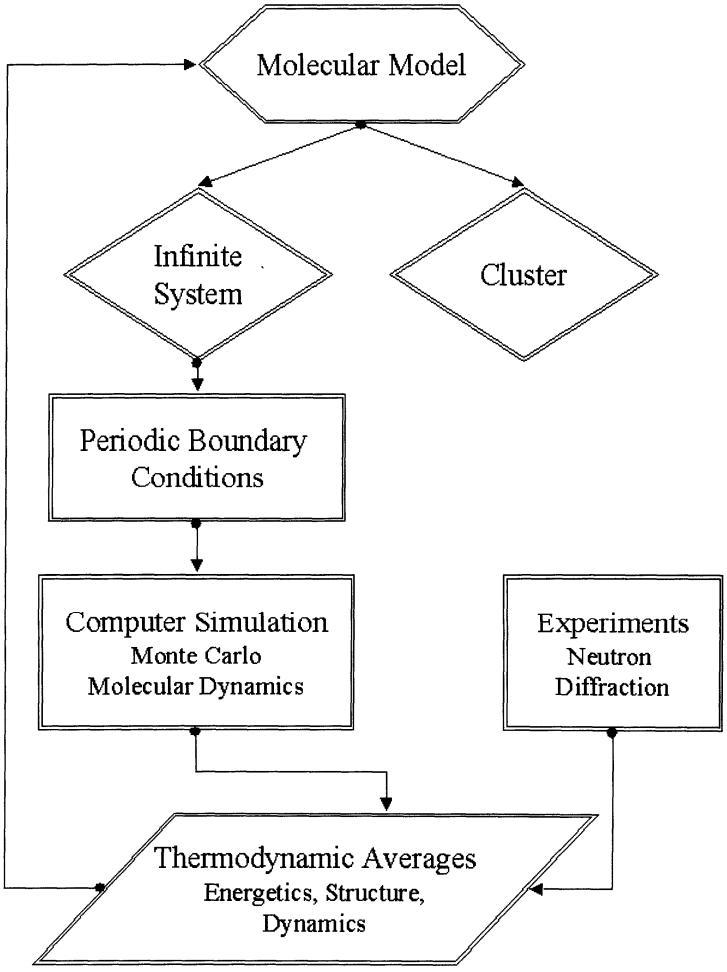

Figure 1. The general role of computer simulations in studies of condensed matter systems, showing the cycle for refinement of the molecular model via comparison with experimental data.

The aim of these lectures is to describe the general principles of both Monte Carlo and molecular dynamics simulations, and to discuss the application of these techniques to interlayer fluids in clay minerals. Many of these techniques have been reviewed by Kubicki and Bleam

(1998). The main focus here will be on the properties of water and aqueous solutions in swelling clays such as smectites and vermiculites. We therefore begin with a brief review of clay minerals and clay swelling, before turning to the potential role of computer modeling as a predictive tool and a complement to experimental techniques. After this general introduction, we address the specific questions relating to molecular modeling of clay-fluid systems.

The first technical issue is that of interparticle interactions, and in particular the molecular models that are currently available for use in computer simulations of interlayer fluids in clays. This is followed by a general discussion of the two methods of molecular simulation; Monte Carlo and molecular dynamics. Next, we introduce some of the specific issues that need to be addressed when we study clay-fluid systems: treatment of long-range interactions, simulation cell size limitations, boundary conditions, choice of thermodynamic ensemble, and statistical sampling. Finally, we examine the current status of molecular modeling in this field, and discuss how studies of idealised model systems can be incorporated into studies of real materials.

At this point we comment that simulations of the types described in these notes are routinely conducted on desktop or laptop PC's, and that suitable simulation codes are available for most platforms. For example;

- *Monte* (http://www.cmmp.ucl.ac.uk/~nts/monte.html),
- *Moldy* (http://www.ccp5.ac.uk/moldy/moldy.html),
- *DL_POLY* (http://www.cse.clrc.ac.uk/msi/software/DL_POLY/index.shtml).

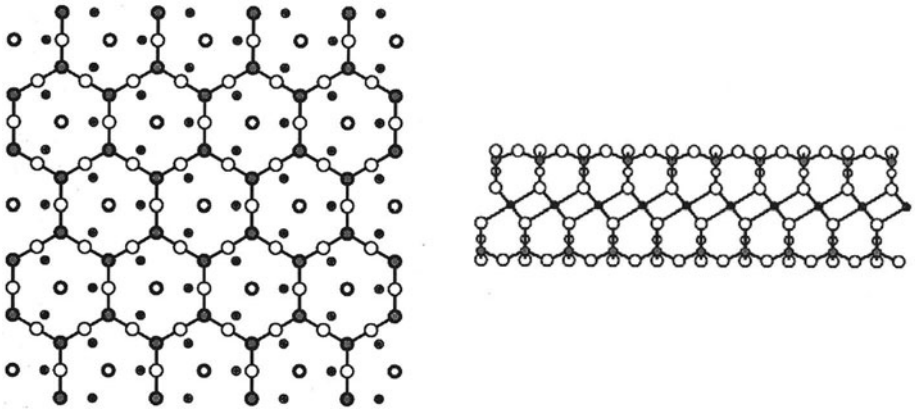

Figure 2. The structure of an uncharged talc sheet, showing projections in the *ab*- and *ca*-planes. Octahedral magnesium ions are small dark spheres, tetrahedral silicon ions are large grey spheres, oxygen atoms are large feint spheres, and hydroxyl groups are the large bold spheres recessed into the hexagonal cavity sites. The dimensions of the clay sheet shown here are 18.24Å×21.12Å×6.54Å: this is typical of the slabs used in computer simulation unit cells and contains sixteen $Mg_3Si_4O_{10}(OH)_2$ units. For convenience, the *ab*-projection shows only the opt half of the layer.

1.1 Swelling Clays and their Interaction with Water

Clay minerals are layered aluminosilicates (Brindley and Brown, 1980; Newman, 1987). They are made up of sheets of octahedrally coordinated cations, such as Mg^{2+} or Fe^{3+}, and tetrahedrally coordinated cations, such as Si^{4+} or Al^{3+} (figure 2). Unsaturated oxygen atoms, which lie on the clay surface or in recessed hexagonal cavity sites, form hydroxyl groups. The broadest classification of clay structure is in terms of the number of the octahedral and tetrahedral sheets. This gives us 1:1 clays, such as kaolin and serpentine, and 2:1 clays, such as talc, smectite, vermiculite and mica.

Within the family of 2:1 clay minerals there are a number of further subdivisions of minerals, that recognise different possible valences and substitutions of the octahedral and tetrahedral cations (Newman, 1987). If the majority of octahedral cations are divalent, then all three possible cation sites must be occupied to maintain charge neutrality, and the clay is referred to as "trioctahedral". If, on the other hand, the octahedral cations are trivalent, then only two of the three sites are occupied, and the clay is "dioctahedral". The two charge-neutral clays are called talc (trioctahedral) and pyropyllite (dioactahedral), with structural units $Mg_3Si_4O_{10}(OH)_2$ and $Al_2Si_4O_{10}(OH)_2$ respectively. Both of these minerals are hydrophobic, and do not swell spontaneously in water.

Clay sheets can acquire negative charge when either the octahedral or tetrahedral cations are substituted by species of lower valence. For example: Li^+ for Mg^{2+}, or Al^{3+} for Si^{4+}. This isomorphic replacement leads to a rich variety in the location and density of layer charges in clay minerals. If we use generic tri- and dio-ctahedral structural formulae, $[T_{3-x}M_x][Si_{4-z}Al_z]O_{10}(OH)_2$ and $[D_{2-x}M_x][Si_{4-z}Al_z]O_{10}(OH)_2$, we can then identify some general classes of clay particles based on the total layer charge, $Q = x + z$:

- **Talcs & pyrophyllites**: $Q \sim 0.0$. Non-swelling hydrophobic clays.
- **Smectites:** $0.2 < Q < 0.6$. Swelling clays with small platelet size (~μm^2).
- **Vermiculites**: $0.6 < Q < 0.9$. Swelling clays with macroscopic platelet sizes (~mm^2).
- **Illites & Micas**: $0.9 < Q < 1.0$. Non-swelling hydrophilic clays.

The smectites and vermiculites are therefore the swelling clays. Examples of the former include: saponite, hectorite and laponite (trioctahedral), and; montmorillonite and beidelite (dioctahedral).

Clay Layer charge is balanced by interlayer counterions, such as Na^+, K^+, or Ca^{2+}. These ions have a strong affinity for water and other polar solutes, and it is these that cause the clays to expand in the presence of water and other polar solvents. In the first instance this expansion takes the form of a series of disrete steps, known as crystalline swelling (figure 3a). Crystalline swelling is loosely associated with the formation of molecular layers of interlayer water, but is in fact more closely associated with solvation of the interlayer cations. In certain cases, crystalline swelling is followed by longer-range colloidal, or osmotic, swelling (figure 3b). In this regime the interparticle interactions are typically governed by continuum electrostatic forces (Norrish, 1954; Glaeser and Méring, 1968; Brindley and Brown, 1980; Sposito and Prost, 1982; Newman, 1987).

Within the two broad regimes of clay swelling there is in fact great complexity of hydration behaviour, reflecting the subtle balance between the various interparticle forces. For a given fluid, the precise nature of clay-fluid interactions is mainly determined by: (i) the valence,

radius and number density of the interlayer counterions, and; (ii) the number density and origin (octahedral or tetrahedral substitution) of the clay layer charges (Brindley and Brown, 1980; Newman, 1987). If anything, the former is generally regarded as the most important factor. For example: Na- and Li-smectites expand infinitely in water; Ca-smectites and Na- and Ca-vermiculites absorb two molecular layers of water; K-smectites and K-vermiculites absorb only one molecular layer of water, and; K-micas do not swell at all.

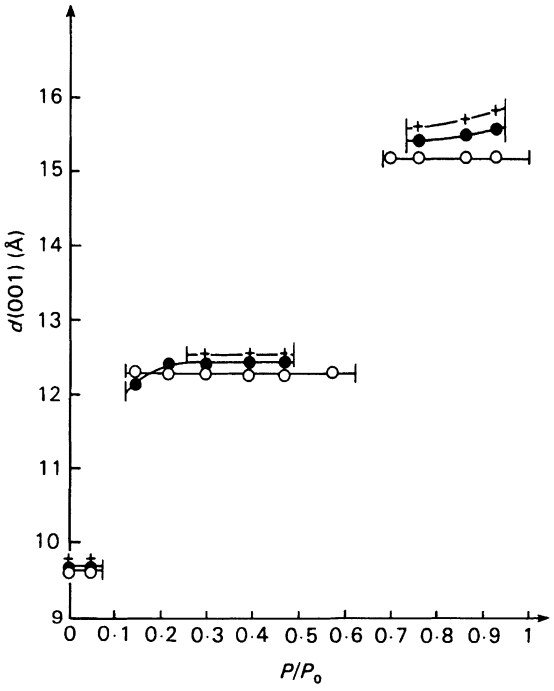

Figure 3a. The crystalline swelling of Na-smectites as a function of water vapour pressure, P/P_0. Solid circles – Na-montmorillonite, open circles – Na-beidelite, and crosses – Na-hectorite. The data show the step-wise expansion from dry clay to a two-layer hydrate. (after Glaeser and Méring, 1968).

Here, we note that when we attempt to model clay-fluid systems there are in fact six sets of interactions to be considered: water-water, water-cation, water-clay, cation-cation, cation-clay, and clay-clay. It is the ability to unravel the effects of these competing and finely balanced interests that makes molecular scale computer simulation such a powerful approach. We also point out that the dependence of clay hydration on the interlayer cation valence and surface charge density is mirrored in many other fields where solid-solution interfaces are present. Most notably, one can point to the numerous biochemical processes that depend on ion-selectivity in pores and at surfaces (Kuyucak et al, 2001).

1.2 The Role of Molecular Modelling in Studies of Clay-Fluid Systems

Statistical mechanical molecular modelling of condensed matter aims to calculate the observable properties of systems in which the particles interact through a specified set of potential energy functions (Allen and Tildesley, 1987; Frenkel and Smit, 1996). Generically, these interaction potentials can be broadly classified according to the level of approximation they involve:

- **Ab Initio:** the properties of the system are calculated by solving the Schrödinger equation for all electrons and atomic nuclei (Bleam, 1993; Tossell, 1995). Computationally, quantum mechanical solution of the all electron problem is extremely demanding, and is only feasible for systems containing fewer than ten or so atoms. For example, the interaction energy of a water dimer as a function of its geometry (Matsouka et al, 1976), or simple molecules adsorbed onto small clay-like clusters (Delville, 1991; Bleam, 1993).
- **Semi-empirical:** to reduce the computational cost of *ab initio* calculations, some knowledge of the electronic properties of the system can be used to simplify solution of the Schrödinger equation. For example, many important properties depend on the nature of the valence, rather than core, electrons. To economise, the nucleus plus core electrons can therefore be represented by a *pseudopotential,* which then acts on the valence electrons. At this level we can calculate the energy surfaces of systems containing more than a hundred atoms, and can study the thermodynamic properties of systems containing tens of atoms (Car and Parinello, 1985; Payne et al, 1992; Lee et al, 1992; Bleam, 1993; Tossell, 1995; Boek and Sprik, 2003).
- **Empirical:** to further increase the size of system that can be treated, a potential energy function can be chosen to represent the effective interactions between atoms and molecules. These effective interaction potentials will involve pair-wise terms, and may also include higher order effects such as polarisation. In any case, the potential energy of a particular configuration is calculated from a set of empirical parameters. Examples include the Lennard-Jones model for interactions between noble gas atoms. Using empirical potential models the thermodynamic properties of systems containing thousands of atoms are routinely studied (Allen and Tildesley, 1987; Frenkel and Smit, 1996). This number of particles is sufficient to mimic the properties of liquids, such as water and aqueous solutions, in both the bulk phase (Enderby and Neilson, 1981; Finney et al, 1986; Ohtaki and Radnai, 1993), and in clay pores (Guven, 1992; Bleam, 1993).
- **Continuum:** certain aspects of some solutions are insensitive to the detailed molecular structure of the solvent. In this case the solvent can be represented as a structureless dielectric continuum; the so-called primitive model (Enderby and Neilson, 1981). This approach is currently used in studies of colloidal systems, including hydrated clays, where long-range electrostatic interactions are thought to be dominant (Guldbrand et al, 1983; Israelachvili and Wennerström, 1996).

Ab initio and semi-empirical interaction potentials will provide electronic structure/energy, through quantum mechanical solution of the Schrödinger equation. They can therefore be used to study chemical reactions of particular species at mineral surfaces (Bleam, 1993; Tossell, 1995). In this article, however, we are concerned with the statistical mechanical properties of

liquids, particularly water and aqueous solutions, at clay surfaces. For a practical reason (current computer power) we must therefore concentrate on empirical potential models of the empirical type. We note, however, that quantum statistical mechanical simulations of clay-water systems, using semi-empirical functions of type (ii) are on the horizon (Car and Parrinello, 1985; Remler and Madden, 1990; Bridgeman et al, 1996, Boek and Sprik 2003).

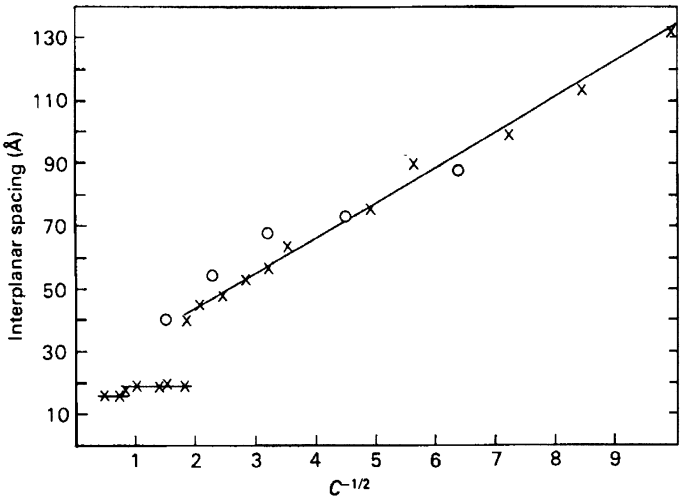

Figure 3b. The colloidal swelling of Na-montmorillonite immersed in NaCl (crosses) or Na_2SO_4 (circles) solution, showing the linear dependence on reciprocal square root of concentration (after Norrish, 1954)

2 Empirical Molecular Models for Clay-Fluid Interactions

If we consider a system of N atoms, then, in the absence of an external field, the potential energy can be divided into terms involving the coordinates of pairs, triplets, quadruplets and so on (Allen and Tildesley, 1987). The pair-wise terms depend only on the separation of particles, and are dominant. However, at liquid densities the terms for triplets and above are not negligible, and must be included. To avoid the crippling increase in computation time that would accompany explicit calculation of all three-body terms, we dress-up our pair-potentials as "effective pair potentials". Perhaps the best way to explain and justify this approach is to take a specific example: liquid water.

One of the most successful empirical models of liquid water is known as TIP4P (Jorgensen et al, 1983; Vlot et al, 1999; Mahoney and Jorgensen, 2000). This model places four interaction sites on each molecule, corresponding to the oxygen (O) and hydrogen (H) atoms, and a charge site (M) located on the C_2 axis of the molecule (figure 4). The interaction energy between two sites on different molecules then takes the form:

$$v_{ij}(r_{ij}) = \frac{q_i q_j}{r_{ij}} + 4\varepsilon_{ij}\left[\left(\frac{\sigma_{ij}}{r_{ij}}\right)^{12} - \left(\frac{\sigma_{ij}}{r_{ij}}\right)^{6}\right], \quad (2.1)$$

where r_{ij} is the separation between sites i and j. q_i, ε_{ij}, and σ_{ij} are empirical parameters representing the partial charges, binding energy and contact separation respectively. The total interaction energy between two molecules is then the sum over all different intermolecular pairs of sites.

We see that the TIP4P functional form is a Coulombic (electrostatic) interaction with a Lennard-Jones potential. In the TIP4P molecule the HOH bond angle is 104.52°, r_{OH} = 0.09572nm and r_{OM} = 0.015nm. The "partial charge", q_H, on each hydrogen atom is 0.52e, and q_M = -1.04e, ε_{oo}= 0.6487 kJmol^{-1} and σ_{oo}= 0.3154 nm. The effective nature of these pair-wise terms becomes clear when one notes that the dipole moment of a TIP4P molecule is 2.18D, compared with 1.85D for an isolated water molecule.

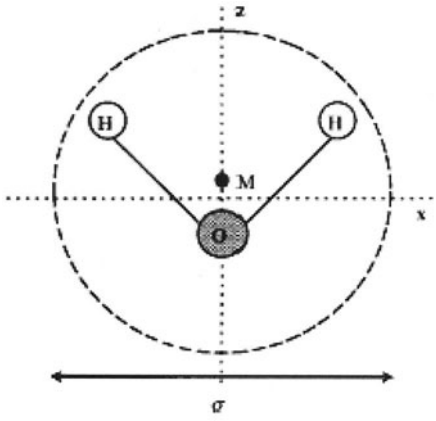

Figure 4. A schematic of the TIP4P model of water, showing the geometry of the interaction sites (after Vlot et al, 1999).

The intermolecular interactions shown in equation 1 are known as "non-bonding" terms. In fact, the TIP4P model assumes that each molecule is a rigid entity. If one wanted to include "bonding" intramolecular terms, such as bond-bending or stretching, then these would appear as a sum over sites on the same molecule (Allen and Tildesley, 1987; Frenkel and Smit, 1996).

To model a clay-fluid system we require three complete sets of interaction potential functions: fluid-fluid, fluid-clay and clay-clay (for the purposes of this section, we will assign interlayer counterions to the fluid, rather than the clay). The most popular starting point is to exploit the models developed for studies of water and aqueous solutions, and then to build fluid-clay and clay-clay potentials of the same functional form either empirically, or by fitting to *ab initio* energy surfaces.

2.1 Fluid-Fluid Interactions

A number of potential models have been proposed for the interaction between two water molecules (Jorgensen et al, 1983; Finney et al, 1986; Watanabe and Klein, 1989; Mahoney and Jorgensen, 2000). Of these, the two that are currently most popular for studies of clay-fluid systems are the MCY and TIP4P models, due to Matsouka et al, (1976) and Jorgensen et al, (1983) respectively.

Both the MCY and TIP4P models represent a water molecule as a rigid entity comprised of four interaction sites. Three of these sites are placed on the atomic oxygen and hydrogen. The fourth site is a (negative) charge that lies on the C_2 axis of the molecule. Both the MCY and TIP4P "molecules" meet the demands of relatively simple functional form, and accurate representation of the energetics, hydrogen bonded structure, and dynamics of bulk water (Finney et al, 1986; Watanabe and Klein, 1989).

The MCY model of Matsouka et al, (1976) was obtained by fitting the total potential energy, V, for a wide range of configurations of the water dimer to *ab initio* potential energy data (Lie et al, 1976). For the MCY model site-site interactions are represented by;

$$v_{ij}(r_{ij}) = \frac{q_i q_j}{r_{ij}} + A_{ij}\exp\left(-B_{ij}r_{ij}\right) - C_{ij}\exp\left(-D_{ij}r_{ij}\right). \tag{2.2}$$

In this function q_i is the partial charge in site i, and A_{ij}, B_{ij}, C_{ij} and D_{ij} are fitted constants. The first term therefore again represents Coulomb interactions the second term short range Pauli repulsion, and the third term van der Waals attraction. Interaction sites (A_{ij} *and* $C_{ij} \neq 0$) are placed on the O and H sites. A partial charge of 0.71748e is placed on each hydrogen atom, and a balancing charge of –1.4349e on the site located 0.2677Å down the C_2 axis (figure 2). The dipole moment of the molecule is therefore 2.19D. At this point we again note that the dipole moment of an isolated water molecule is 1.85D. The difference is attributed to the polarisation of a molecule in the liquid by its neighbours (three- and four-body effects). MCY endeavours to capture these many-body effects within the sum of pair-wise terms, and is therefore another example of an effective pair potential.

The strength of the MCY model is the fact that it is based on *ab initio* energy data for a wide range of configurations. It is therefore likely to be accurate for water in non-tetrahedral environments, such as clays. The main disadvantage is that a large pressure is required to maintain the liquid at a density of $1 gcm^{-3}$ at 298K (Lie et al, 1976).

The TIP4P model, on the other hand, was obtained by refining the parameters in equation 1 by reference to thermodynamic and X-ray data for liquid water at STP. Importantly, the TIP4P model reproduces the density of bulk water, at STP (Jorgensen et al, 1983) and beyond (Brodholt and Wood, 1993; Siqueira et al, 1997). However, because the parameters were fitted to data for bulk water at STP, it might be expected to be less apposite in confined, non-tetrahedral, environments.

There are numerous potential functions available to describe the interactions of ions with MCY and TIP4P water. These models have been collated and compared with experimental data by Enderby and Neilson (1981), Neilson and Enderby (1989) and Ohtaki and Radnai (1993). The general conclusion is that the hydration of monovalent ions (such as Li^+, Na^+, and K^+) can be well represented by rigid molecule effective pair potential models. Small di- and

trivalent cations (such as Mg^{2+} and Al^{3+}) are more problematic (Bounds, 1985). These ions are strongly polarising, and may therefore require flexible/polarisable model of the solvent molecules (Lybrand and Kollmann, 1985; Smith and Haymet, 1992).

In this article we will focus on interlayer aqueous fluids. However, there is increasing demand for accurate modelling of clay-water-organic systems. For example, to predict hydrocarbon and pollutant migration. There is now a realistic prospect that computer simulation will provide an important contribution to these fields. To illustrate this, the TIP4P model forms part of a complete set of models for studying aqueous-organic fluids, the so-called OPLS potential parameters (Jorgensen, 1981, 1984; Jorgensen et al, 1983). This set of potentials is obtained by using the combination rules for Lennard-Jones parameters (equation 1);

$$\varepsilon_{ij} = \left[\varepsilon_{ii}\varepsilon_{jj}\right]^{1/2} \text{ and } \sigma_{ij} = \frac{1}{2}\left[\sigma_{ii} + \sigma_{jj}\right]. \tag{2.3}$$

This set of potentials is eminently suitable for incorporation into model clay-fluid systems (Boek et al, 1995a, 1995b; Titiloye and Skipper, 2001).

2.2 Fluid-Clay Interactions

Within the realm of atomistic empirical models there are two common routes to fluid-clay interaction potential functions (Bleam, 1993), (i) fitting to *ab initio* potential energy surface calculations (Delville, 1991, 1992), and (ii) direct transfer of parameters from fluid-fluid potential functions (Skipper et al, 1991, 1995a). In either case, the functional form should be consistent with the choice of fluid-fluid interactions, and be able to represent octahedral and/or tetrahedral substitution within the clay sheet.

To date the clays sheets themselves have been treated as rigid entities, with a structure based on atomic co-ordinates derived from X-ray diffraction (Brindley and Brown, 1980). The main weakness of this procedure is that the orientation of clay surface hydroxyl groups is poorly resolved, and is also assumed to be independent of the hydration-state of the clay. A priority for future work is therefore to allow rotational freedom among the hydroxyl groups on the clay surface.

2.3 Clay-Clay Interactions

The final piece in the jigsaw is clay-clay interactions. In the current context this is a simple matter: when we choose parameters, such as partial charges, to describe clay-fluid interactions we have necessarily chosen clay-clay parameters as well. Studies of dry clays and monolayer hydrates have shown that this description of the clay sheets can capture clay-clay interactions rather well (Table 1; Skipper et al,1995b).

To complete this section we look at a system that will be used as an example in these lectures: sodium substituted Wyoming montmorillonite. The unit cell frequently used in computer simulations has the composition (figure 5):

$$Na_{0.75}nH_2O\ [Al_{3.5}Mg_{0.5}][Si_{7.75}Al_{0.25}]O_{20}(OH)_4. \tag{2.4}$$

This system is illustrated in figure 5. If we work with potentials of the TIP4P form, then we can use the combination rules for the interaction Lennard-Jones function given in equation 2.3, to obtain the parameters given in table 1. We note from this that the only sites with Lennard-Jones parameters are oxygen and sodium, and that other species in the clay layer are represented a charge sites.

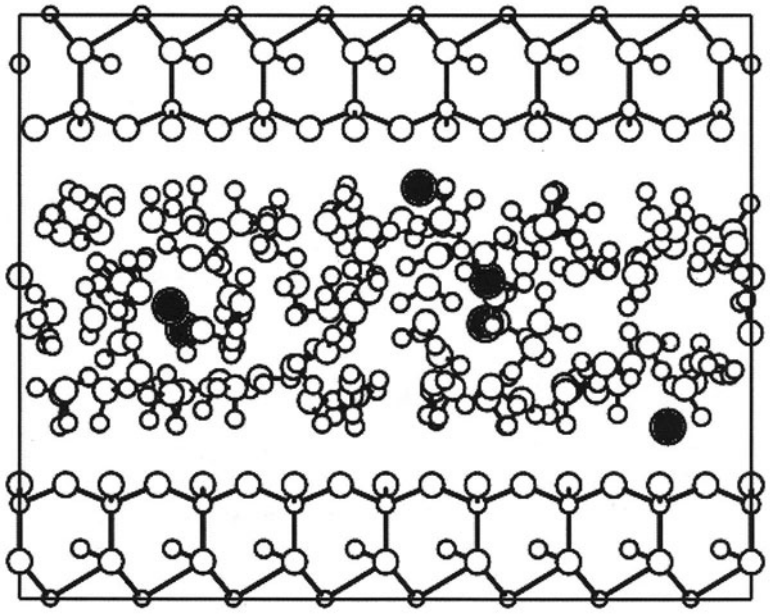

Figure 5. Simulation cell for a three layer hydrate sodium smectite. The simulation cell contains a 20Å×20Å×6.56Å clay sheet, 6 Na cations and 96 water molecules (see equation 2.4). The sodium counterions are shown in black. We see that two ions form inner sphere complexes – these are bound to sites of tetrahedral substitution in the clay layer. Notice also that the interfacial water molecules are hydrogen-bonded to the clay platelet – with one proton directed towards the surface.

Table 1. TIP4P-type interaction parameters for use in computer simulations of sodium substituted clays, of the type given in equation 2.4 (Boek et al, 1995a)

	q/e	σ_{ii}/nm	ε_{ii}/kJmol^{-1}
O (interlayer H_2O)	0.0	0.3154	0.6487
M (interlayer H_2O)	-1.04	0.0	0.0
H (interlayer H_2O)	0.52	0.0	0.0
Na (interlayer)	1.0	0.1897	6.7243
O (clay surface)	-0.8	0.3154	0.6487
O (clay apical)	-1.0	0.3154	0.6487
O (clay OH)	-1.52	0.3154	0.6487
H (clay OH)	0.52	0.0	0.0
Si (clay tetrahedral)	1.2	0.0	0.0
Al (clay tetrahedral)	0.2	0.0	0.0
Al (clay octahedral)	3.0	0.0	0.0
Mg (clay octahedral)	2.0	0.0	0.0

3 Molecular Modeling: Generic Issues

Molecular modelling aims to calculate equilibrium thermodynamic averages for a macroscopic system in which the particles interact via a set of potential energy functions. Practically, this will require us to calculate the total energy of a relatively small system, and/or forces on the individual particles, and to sample from a statistically significant set of configuration. We will consider some of the generic issues that have to be addressed to achieve this.

3.1 Mimicking an Infinite System: Periodic Boundary Conditions

With modern computers, used in conjunction with empirical interaction functions, it is possible to calculate the energy of simulation cells containing up to a few thousand particles. In the case of a clay-water-cation system, the cell might contain a 20Å×20Å section of clay sheet, 6 cations, and 64 water molecules. If such a system were to be studied in isolation edge effects would, of course, dominate. Before we hand the cell to our computer we must therefore disguise the small simulation cell so that it looks like an infinite system. To do this we normally repeat the simulation cell infinitely in all three directions, using so-called periodic boundary conditions (Allen and Tildesley, 1987; Frenkel and Smit, 1996). By casting the system as an infinite number of repeats of a finite cell we have created two potentially embarrassing problems (figure 6).

First, we have, in principle, to sum energy over an infinite number of pairwise terms to obtain the total potential energy of the system: each molecule interacts with the others in the unit cell, but also with all their images. To reduce this summation to manageable proportions we

only consider particles in our simulation unit cell, and apply two protocols depending on the range of the interactions being considered.

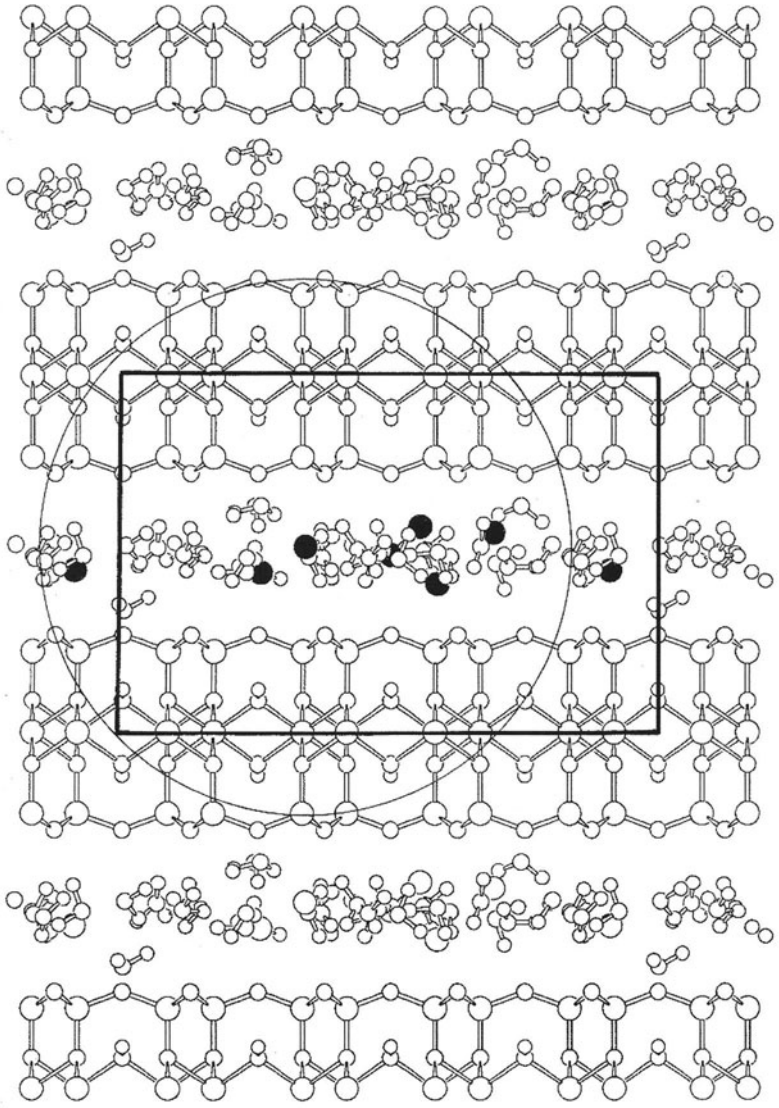

Figure 6. Computer-eye view of a two layer Na-smectite hydrate. The simulation cell is shown as the bold box, with the 10Å cut-off radius centred on one of the black interlayer cations being shown as the circle. The simulation cell contains a 20Å×20Å×6.56Å clay sheet, 6 Na cations and 64 water molecules (see equation 2.4). In this case the long-range interactions were evaluated in an all-image convention (Skipper, 1995a)

– Short-range interactions, such as van der Waals and Pauli repulsion, are cut-off at an appropriate distance, r_c, typically 1nm. Outside this cut-off we approximate the total interaction by integrating a mean-field background based on the average particle density (Allen and Tildesley, 1987).

$$\partial U_{sr} = 2\pi N\rho \int_{r_c}^{\infty} r^2 v(r) dr \tag{2.5}$$

where ∂U_{sr} is the correction to the short-range energy, ρ is the number density of particles, and $v(r)$ is the short-range pair potential function.

– Long-range Coulombic interactions (term 1 in equations 2 and 3) do not converge under a cut-off scheme. An Ewald sum or reaction field is therefore used to evaluate charge-charge interactions in our periodic system (Allen and Tildesley, 1987; Skipper et al, 1995a; Frenkel and Smit, 1996). In the Ewald sum, Coulombic interactions are evaluated as the sum of a short-range real space series, and a long-range reciprocal-space series. The Ewald sum is rather time-consuming, and makes no attempt to hide the periodic nature of the model system. However, it is relatively easy to quantify effects due to simulation cell size. For this reason the Ewald sum is generally first choice, and has been applied to 3-dimensional systems (Skipper, 1995a). An alternative method based on the mean-field approximation has been applied to 2-dimensional systems (Delville, 1993a, 1993b).

The second problem lies in the periodic system itself, and in particular whether periodicity manifests itself in the data generated. One must therefore vary the size of the simulation cell, and check for unwanted size dependent effects. In practice, a simulation cell such as that shown in figure 1 is generally found to be sufficiently large for most practical purposes (Skipper et al. 1995a).

3.2 Orientation of Molecules: Quaternions

The orientations of a rigid molecule can be defined by three Euler angles, calculated relative to some reference. However, this leads to instability in the equations of motion as one approaches poles of the orientation sphere. An elegant solution involves the use of a set, $\boldsymbol{Q}$, of four scalar quaternions;

$$\boldsymbol{Q} = (q_0, q_1, q_2, q_3), \tag{3.1}$$

with normalisation.

$$q_o^2 + q_1^2 + q_2^2 + q_3^2 = 1 \tag{3.2}$$

Referring to the Euler angles, the quaternions can be defined;

$$q_0 = \cos\frac{1}{2}\theta \cos\frac{1}{2}(\phi + \psi), \tag{3.3a}$$

$$q_1 = \sin\frac{1}{2}\theta \cos\frac{1}{2}(\phi - \psi), \tag{3.3b}$$

$$q_2 = \sin\frac{1}{2}\theta \sin\frac{1}{2}(\phi - \psi), \tag{3.3c}$$

$$q_3 = \cos\frac{1}{2}\theta \sin\frac{1}{2}(\phi + \psi). \tag{3.3d}$$

3.3 Thermodynamic Averaging

The classical equilibrium average of any experimentally observable macroscopic quantity, A, can be expressed either as a time or ensemble average (Allen and Tildesley, 1987; Frenkel and Smit, 1996). If we sample the system over τ regular time-intervals, ∂t, for a total time t, then our average quantities are given by;

$$\langle A(t) \rangle = \frac{1}{\tau}\sum_{n=1}^{\tau} A(n). \tag{3.4}$$

Ensemble averages will be taken over Γ different configurations, each of which is sampled according to the probability distribution function P;

$$\langle A(\Gamma) \rangle = \frac{\sum_{m=1}^{\Gamma} P(m) \times A(m)}{\sum_{m=1}^{\Gamma} P(m)} = \langle A(t) \rangle. \tag{3.5}$$

As an example, if our system is in the Canonical (N,V,T) ensemble then we would sample from the Boltzmann distribution:

$$P = \exp\left(\frac{-U}{kT}\right), \tag{3.6}$$

where U is the total potential energy. For example, if we refer to our pair-wise potential energy functions from equations 2.1 and 2.2, then;

$$U = \sum_{i=1}^{N}\sum_{j>i}^{N} v_{ij}(r_{ij}). \tag{3.7}$$

We note here that we have been required to evaluate the partition function explicitly, and that we therefore cannot apply the above principles to evaluate the absolute free energy, $F(N,V,T)$, or related quantities such as the entropy (Mezei, 1982; Allen and Tildesley, 1987; Bash et al, 1987). These quantities depend directly on the partition function. They are therefore not observable in a single experiment, but appear as a derivative to give, for example, the pressure:

$$\left(\frac{\partial F(N,V,T)}{\partial V}\right)_{NT} = -p \,. \tag{3.8}$$

More generally, we can calculate free energy differences between two states by following a reversible path in some quantity, λ, by using (Bash et al, 1987);

$$\left(\frac{\partial F(N,V,T,\lambda)}{\partial \lambda}\right)_{NVT\lambda} = \left\langle \frac{\partial U(N,V,T,\lambda)}{\partial \lambda} \right\rangle_{NVT\lambda} . \tag{3.9}$$

Relevant examples include the creation/annihilation of a particle to calculate chemical potential, or the change of their separation to calculate a potential of mean force for association/dissociation of particles.

Another question that is highly relevant to studies of fluids in clays and porous media is the determination of the average number of particles absorbed into the system when chemical potential is fixed. This requires sampling of the Grand Canonical (μ,V,T) ensemble (Shroll and Smith, 1999; Chavez-Paez et al, 2001a, 2001b). The particular problem here in is the fact that in dense media, instantaneous creation or annihilation of particles is extremely unlikely. Equilibration of the number of particles is therefore extremely problematic (Karaborni et al, 1996) Strategies for dealing with this issue will be discussed in section 5.

3.4 Equilibration and Statistically Significant Sampling

If averages obtained from equation 3.1 or 3.2 are to have any significance for our understanding of the systems in question, we must first be satisfied that the system has reached equilibrium before sampling has started. Typically, our system will start in a random configuration of high potential energy, U. The initial stages of the simulation will be dedicated to relaxation of the system, with equilibrium being conceded when quantities such as U, V and T fluctuate normally about a constant value.

Once sampling has commenced the question is then: how should the simulation be run to obtain statistically reliable averages? The answer to this question may depend on what quantity is being sought. In the context of clay-fluid systems, for example, one can obtain a stable figure for the equilibrium layer spacing long before a reliable value emerges for the diffusion constant of the counterions. The rule here should be to compare at least two runs of equal duration to eliminate the possibility of any systematic errors. In the case that a system becomes stuck in a low energy configuration, it may be necessary to "force" the system to wander through phase space more efficiently by applying a smart algorithm, such as Umbrella sampling (Allen and Tildesley, 1987; Frenkel and Smit, 1996).

Here, it is also important to be clear about the role system size. It is quite possible to obtain statistically significant averages for systems containing a small number of a particular species. For example, the solvation structure of many ions has been calculated for systems at infinite dilution, where only one ion is present. The undesirable effects of small *overall* system size must, however, be resolved as described in section 3.1.

4 Molecular Modeling: General Methods

Two methods of computer simulation are currently available to calculate the equilibrium thermodynamic properties of a system in which the particles interact through a set of potential energy functions: Monte Carlo and molecular dynamics (figure 3; Allen and Tildesley, 1987; Frenkel and Smit, 1996). Both methods can be used to calculate time-averaged quantities, such as the structure and density. Molecular dynamics, though more time consuming, can also give time-dependent quantities, such as diffusion coefficients.

4.1 Monte Carlo

Monte Carlo simulations obtain ensemble averages by importance sampling of configurations, which allows the evaluation of thermodynamic functions to be concentrated around the regions of phase space that make the greatest weighted contribution. The commonly adopted procedure is to follow a finite Markov chain of states, in which the outcome of each attempt to generate a new trial configuration depends only on the outcome of the previous trial. The most widely used scheme to generate the transitions between states is due to Metropolis et al, and is known as the asymmetrical solution.

For a Metropolis Monte Carlo simulation in the Canonical ensemble, consider a system in a configuration 1, with potential energy U_1. A particle is then moved, to give a new configuration 2, with new potential energy U_2. The change in energy is then;

$$\Delta U = U_2 - U_1 . \tag{4.1}$$

In the (N,V,T) Canonical ensemble, acceptance of this new configuration is then decided as follows.

– If $\Delta U > 0$, then the new configuration is accepted with probability;

$$P \propto \exp\left(\frac{-\Delta H}{kT}\right), \text{ where } \Delta H = \Delta U . \tag{4.2}$$

– If $\Delta U \leq 0$, then the new configuration is accepted.

New moves are then attempted until; (i) the system has reached satisfactory equilibrium, and following this; (ii) statistically significant thermodynamic averages have been obtained. In practice, the system shown in figure 1 might require 1,000,000 attempted moves for equilibration, and 2,000,000 for sampling of energetic and structural properties. Inadequate equilibration sampling is a common pitfall of computer simulations, and can best be avoided by comparing data obtained from different starting configurations and different length runs (Skipper *et al.*, 1995a).

Using the Metropolis scheme, other ensembles can be accessed. For example, in the isobaric (N,p,T) ensemble, ΔH in equation 4.2 is given by;

$$\Delta H = \Delta U + p\Delta V - NkT \ln\left(\frac{V_2}{V_1}\right) \tag{4.3}$$

The Grand Canonical (μ,V,T) ensemble requires us to change the total number of particles, via particle insertion or deletion. In the Metropolis scheme these events are accepted according to the following probabilities (Porion et al, 2003);

– Particle insertion is accepted with probability;

$$P \propto \frac{\exp(B)\exp\left(\frac{-\Delta U}{kT}\right)}{N+1}, \tag{4.4a}$$

– Particle deletion is accepted with probability;

$$P \propto \frac{N\exp\left(\frac{-\Delta U}{kT}\right)}{\exp(B)}, \tag{4.4b}$$

where $B = \frac{\mu}{kT} + \ln\left(\frac{V}{\Lambda^3}\right)$ and Λ is the thermal wavelength of particles. Moves that do not involve particle creation or removal are accepted according to equation 4.2. In practice changes in the number of particles are very unlikely, and it is necessary to apply a biasing scheme to seek out the most favourable sites/orientations for these events (Chavez-Paez et al, 2001a).

4.2 Molecular Dynamics

Molecular dynamics simulations solve the classical equations of motion for all the particles in the system, under the force field of interactions with the other particles (Allen and Tildesley, 1987; Frenkel and Smit, 1996). Exact solution of this problem is not practical, but numerical solution of the required accuracy can be achieved by extrapolating the position, velocity and acceleration of each particle from a record of the past. The extrapolation time, ∂t, known also as the timestep, is chosen so that the changes to the state of the system are small. A typical value for the timestep is 0.25×10^{-15}s, with the simulation itself extending over 200×10^{-12}s. The predicted trajectories of the individual particles can then, in principle, be obtained via Taylor expansion of the position, velocity and acceleration;

$$r(t+\partial t) = r(t) + \partial t \times v(t) + \frac{1}{2}\partial t^2 \times a(t) ..... \tag{4.5a}$$

$$v(t+\partial t) = v(t) + \partial t \times a(t) + \frac{1}{2}\partial t^2 \times a'(t) ..... \tag{4.5b}$$

$$a(t+\partial t) = a(t) + \partial t \times a'(t) + \frac{1}{2}\partial t^2 \times a''(t) ..... \tag{4.5c}$$

However, these predictor equations need to be corrected for Newton's equations of motion, which moderate the acceleration via the forces on the particles. This gives us a so-called corrector step in the algorithm.

Molecular dynamics integration techniques are discussed in the texts by Allen and Tildesley (1987) and Frenkel and Smit (1996). Perhaps the most widely used are those based on the one Verlet algorithm;

$$r(t+\partial t) = 2r(t) - r(t-\partial t) + \partial t^2 \times a(t) \tag{4.6a}$$

$$v(t) = \frac{r(t+\partial t) - r(t-\partial t)}{2\partial t}. \tag{4.6b}$$

Whichever algorithm is chosen, it should satisfy the known conservation laws for energy and momentum, and be time reversible. In addition, it should allow the use of relatively large integration timesteps.

The condition that energy is conserved during the simulation implies that one is working in the microcanonical (N,V,E) ensemble. In this case temperature is calculated from the average kinetic energy of the particles. Canonical (N,V,T) or (N,V,p) ensemble molecular dynamics requires the equations of motion to be coupled to a thermostat or barostat (Andersen, 1980; Nosé, 1986).

Thermodynamic quantities can be calculated from molecular dynamics simulations by averaging over instantaneous values for many timesteps. Time-dependent quantities can be calculated directly from the trajectories of the particles. In the current context, an important example relates to the diffusion (mobilities) of the interlayer species. If we consider motion in n-dimensions, diffusion coefficients can be obtained directly from the velocity autocorrelation function;

$$D = \frac{1}{n}\int_0^\infty dt \langle v(t) \cdot v(0) \rangle . \tag{4.7}$$

The corresponding Einstein relation, valid at long times, relates the self-diffusion constant to the mean square displacement of each particle as a function of time;

$$2tD = \frac{1}{n}\left\langle |r(t) - r(0)|^2 \right\rangle . \tag{4.8}$$

Current molecular dynamics simulations of clay-water-cation systems have extended to about 200×10^{-12}s (Refson et al 1994; Chang et al, 1995, 1997), providing a lower calculable limit of $D=1\times10^{-11}$m^{2}s^{-1}. For reference, the calculated self-diffusion coefficients for water molecules and sodium counterions in a two-layer smectite hydrate are about 1.4×10^{-9}m^{2}s^{-1} and 5.1×10^{-11}m^{2}s^{-1} respectively (Chang et al, 1995).

We conclude with a brief note about non-equilibrium molecular dynamics. These simulations couple the equations of motion of the particles with an external perturbation, and allow us to study phenomena such as a shear or heat flow (Allen and Tildesley, 1987).

5 Molecular Modeling: Clay-Fluid Systems

In this section we discuss some recent computer simulations of clay-water-cation systems. The broad aim is to compare and contrast simulation and experimental data, thereby highlighting the successes and failures of the modelling studies. We will therefore begin by discussing the options for, and implications of, the statistical sampling ensemble. We then describe the current state of affairs concerning simulation of aqueous fluids in smectites. We are particularly concerned with establishing the current consensus and future challenges. To illustrate the power of molecular modelling for studies we will focus on studies of the archetypal swelling clay: Wyoming montmorillonite. The hydration of this clay has been the subject of many Monte Carlo and molecular dynamics computer simulations, covering interlayer cations Li, Na, K, Cs, Mg and Ca. This research samples from several different ensembles, and exploits several different molecular models. By comparison with experiments, these simulations have demonstrated that empirical models can provide an accurate representation of the interlayer region, and have provided new insight into the molecular mechanisms underlying clay swelling.

5.1 Choice of Statistical Ensemble

The equilibrium thermodynamic state of the system is usually defined by a small set of state parameters. For example, in the canonical ensemble these are the number of particles, N, volume, V, and temperature, T. Before we start a lengthy simulation we must therefore decide which parameters are relevant to the system and conditions of interest.

For a clay-water-cation system in contact with an external bath of fluid, held at temperature T, equilibrium occurs when the chemical potential of the interlayer fluid, μ, is equal to that of the external fluid. Since the clay can, in general, expand or contract to accommodate the interlayer fluid the final state depends also on the applied pressure, p. In this usage the pressure refers to the state within the external fluid (Delville and Sokolwoski, 1993). Within an inhomogenous system, such as a clay-fluid system, one has to distinguish between the normal and tangential components of the pressure tensor (Frenkel and Smit, 1996). We will therefore use the stress tensor, σ_{ij}, to refer to the state within the clay itself. In particular, σ_{zz} will define the stress normal to the clay sheets.

In principle, therefore, the preferred statistical ensembles are constant (μpT) or $(\mu\sigma_{zz}T)$. In practice, however, the computational cost of sampling this ensemble is prohibitive. The main reasons are that setting μ requires us to create/destroy water molecules, and sampling of both N and V is therefore very slow (Allen and Tildesley, 1987; Delville, 1991, 1992; Frenkel and Smit, 1996; Karaborni *et al.*, 1996). For this reason we look for a less time consuming alternative.

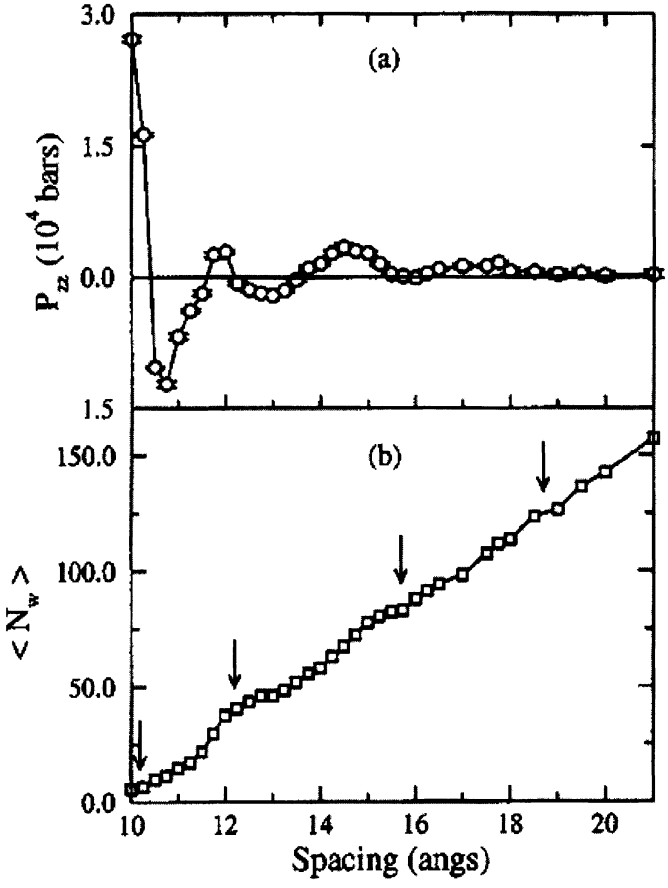

Figure 7. Calculated swelling pressure (a), and average number of molecules (b), in stable states of Na-montmorillite hydrate, obtained from Grand Canonical computer simulation (Chávez-Páez et al (2001). The arrowed spacings are mechanically stable, and should be compared with the plateaus in figure 3a.

Most recently, Schroll and Smith (1999), Chávez-Páez et al (2001a, 2001b) and Porion et al (2003) have opted for a series of simulations in grand canonical (μVT) ensembles, covering a range of volumes, V, relevant to hydrated clays. This approach has the important advantage that it can predict water content for a given clay-layer spacing (figure 7). The drawback is that sampling of the number of water molecules, N, is still extremely slow. However, these most recent simulations have produced swelling data that are consistent with experiments and earlier simulations (Chang et al. 1995, Boek et al. 1995b).

To side-step the problems inherent to constant μ sampling, Skipper et al. (1991, 1995a) have conducted a series of simulations in the ($N\sigma_{zz}$ T) ensemble, covering a suitable range of water contents, N. In these simulations, pressure is applied normal to the clay surfaces to produce σ_{zz}. This choice provides contact with experiment by predicting the clay-layer spacing as a function of water content (figure 8, 9), but has the disadvantage that it cannot predict water content *a priori*.

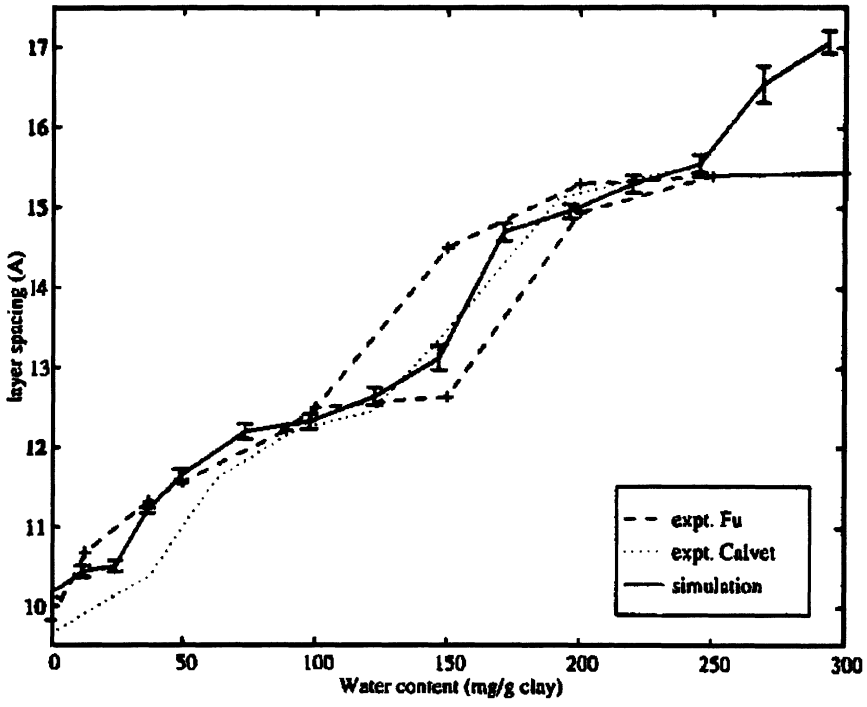

Figure 8. Calculated swelling curve for Na-montmorillite hydrates, showing layer spacing as a function of water content, obtained through simulations in the ($N\sigma_{zz}$ T) ensemble (Boek et al, 1995a). The simulated data (solid line) pass through the experimental adsorption (lower dashed) and desorption (upper dashed) data, illustrating that the simulations are sampling equilibrium. Copyright 1995 American Chemical Society.

A third option is sampling in *(NpT)* ensembles over a range of both N and p. This choice has applications when water is absorbed onto exposed clay surfaces, but is not ideal for studies of clay swelling, except when used to follow (μVT) equilibration (Delville and Sokolwoski, 1993).

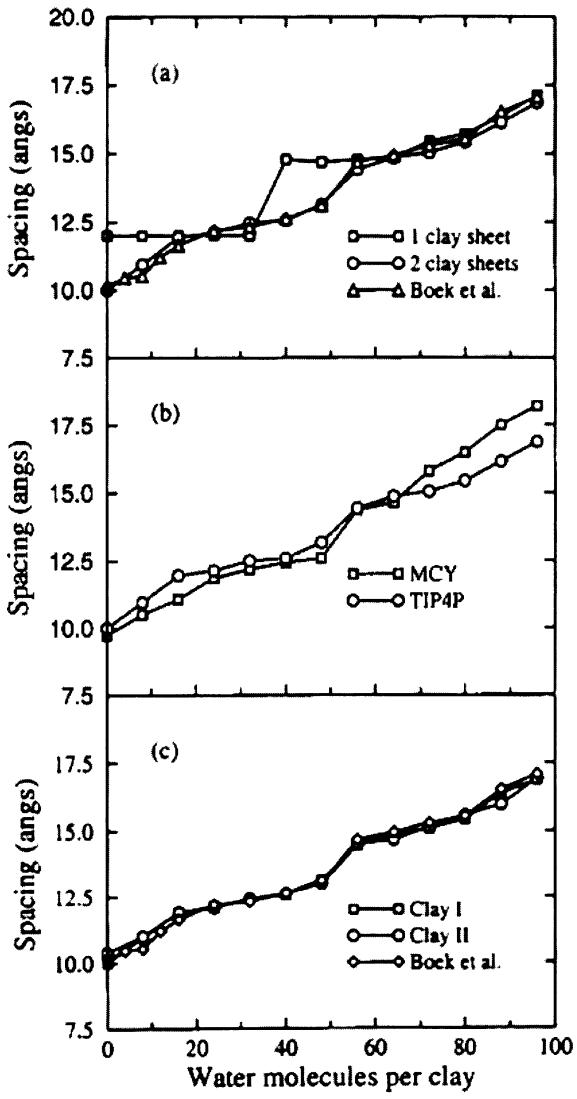

Figure 9. Calculated layer spacings in the ($N\sigma_{zz}$ T) ensemble for Na-montmorillonite as a function of water content, showing comparisons between (a) simulation cells of 1 and 2 layer repeats, (b) MCY and TIP4P water models, and (c) clays with different locations for isomorphic charge substitution (Chávez-Páez et al (2001a). Copyright 2001 American Institute of Physics

5.2 Thermodynamics

In principle computer simulations can provide statistical averages of all thermodynamic properties of the system. For clay hydrates, the relevant quantities include the clay-layer spacing as a function of water content (and therefore interlayer water density), enthalpy/heat of immersion, swelling pressure as a function of layer spacing or external water chemical potential. If we compare a clay system containing N water molecules with a dry system ($N=0$), and define ensemble averages of potential energy, U, and volume, V:

$$\Delta U(N) = U(N) - U(0) \tag{5.1}$$

and,

$$\Delta V(N) = V(N) - V(0), \tag{5.2}$$

then the heat of immersion of the simulation cell is given by;

$$\Delta H_{im}(N) = \Delta U(N) + p\Delta V(N) \tag{5.3}$$

and the interlayer water density by;

$$\rho(N) = \frac{N m_{H_2O}}{\Delta V(N)} \tag{5.4}$$

where m_{H_2O} is the molecular mass of water. For these quantities, the data calculated from simulations are in excellent agreement with experiment (Skipper et al. 1995a, 1995b; Smith, 1998; Boek et al 1995a, 1995b; Delville, 1993a). These data are summarized in table 2.

More recently, Hensen and Smit (2002), Chávez-Páez et al (2001a and 2001b) and Shroll and Smith (1999) have used Grand Canonical ensemble calculations to study Na-, Ca- and Cs-substituted Wyoming montmorillonites. They are then able to calculate the clay swelling disjoining pressure (and equilibrium water content) and free energy as a function of clay layer spacing. The mechanically stable hydrates are those for whom the swelling pressure intersect, with negative slope, corresponds to the applied pressure (1 bar). In sodium Wyoming montmorillonite, for example, stable distances are predicted to be 10.2, 12.2, 15.7 and 18.7Å: in excellent agreement with experiment (figure 7).

Table 2. Summary of thermodynamics and diffusion data for water molecules and cations in hydrated montmorillonite clays, obtained by computer simulation. Data in parentheses are experimental values (Boek et al, 1995a; Chang et al, 1997; Sposito et al, 1999).

Hydrate	Cation	$D_{Water}/10^{-9}$ m^2 s^{-1}		$D_{cation}/10^{-9}$ m^2 s^{-1}		$\Delta U(N)$/kJmol^{-1}	$\rho(N)$/gcm^{-3}
1-layer	Li^+	0.13	(0.05-0.4)	0.011		64.5	0.95
	Na^+	0.10		0.015	(0.001)	59.0	1.15
	K^+	0.13		0.12		60.0	1.30
2-layer	Li^+	0.45	(0.26-0.70)	0.067		52.6	0.96
	Na^+	0.79	(1.0)	0.25	(0.10)	49.0	1.04
	K^+	0.85		0.25		51.7	1.30
3-layer	Li^+	1.40	(1.0)	0.43		49.9	0.99
	Na^+	0.72		0.11		47.9	1.08
	K^+	0.99		0.50		49.2	1.31
Bulk	Li^+			1.0			
	Na^+			1.4			
	K^+			2.0			
	None	2.3	(2.3)			42.7	1.0

5.3 Structure

The structural properties of the interlayer region are traditionally visualised in terms of the particle density profiles normal to the clay surfaces, $\rho_\alpha(z)$, and the radial distribution functions, $g_{\alpha\beta}(r)$.

$$\rho_\alpha(z) = \frac{c_Z}{N_\alpha}\frac{dn_\alpha}{dz} \tag{5.5}$$

where c_Z is the clay layer-layer spacing, and dn_α is the average number of particles of type α lying between z and $z+dz$, and;

$$g_{\alpha\beta}(r) = \frac{1}{4\pi\rho_\beta r^2}\frac{dn_{\alpha\beta}}{dr} \tag{5.6}$$

where ρ_β is the number density of species β ,and $dn_{\alpha\beta}$ is the average number of particles of type β lying at distances r to $r+dr$ from a particle of type α.

Sampling of the counterion distribution is rather challenging, as one must overcome relatively large potential energy barriers to travel between the various hydration states. One can best account for these states by approaching equilibrium from several different start points, and averaging over long, independent, production runs (Skipper et al 1995a; Chang et al, 1995, 1997, de Carvalho & Skipper 2001).

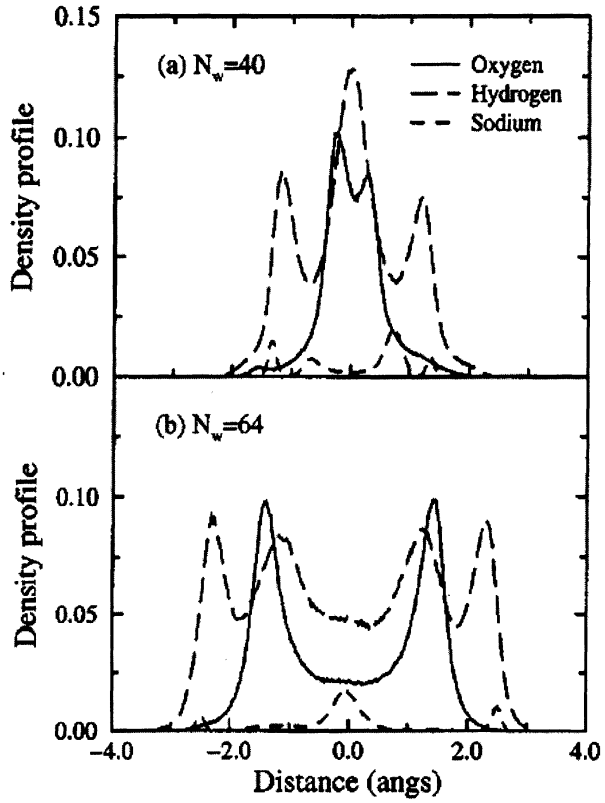

Figure 10. Interlayer particle density profiles for Na-montmorillonite (a) 1-layer hydrate, and (b) 2-layer hydrate. The plots show the layering of water molecules in the interlayer region, and the tendency for the water molecules to form hydrogen bonds to the negative clay surface (Chavez-Paez et al, 2001a). Copyright 2001 American Institute of Physics.

Once the counterions have been hydrated, the interlayer water molecules attempt to reproduce the hydrogen-bonded network that they enjoy in the bulk. In fact simultaneous satisfaction of the two (counterion hydration and hydrogen bonding) is not possible, and so the weakest is sacrificed. For this reason one observes distortion and breaking of hydrogen bonds (Sposito et al 1999, Chang *et al* 1999). The interlayer water density profiles show that the oxygen atoms form broad layers at intervals of approximately 2.5-3.0Å from the clay surface.

Where possible hydrogen atoms are directed towards the clay sheets, to form hydrogen bonds to the oxygen atoms of the clay surface (see also figures 10, 11).

At a fully hydrated (colloidal) hectorite surface the counterion profiles demonstrate the strong tendency to form inner sphere complexes on the clay surface (figure 11). However, there is evidence of diffuse ionic atmosphere at larger distances. When present, chloride co-ions appear to be excluded from the inner sphere region. Each clay surface is associated with at least two distinct layers of water molecules. It is interesting to note that the orientation of these molecules assists rapid charge balance over the interface.

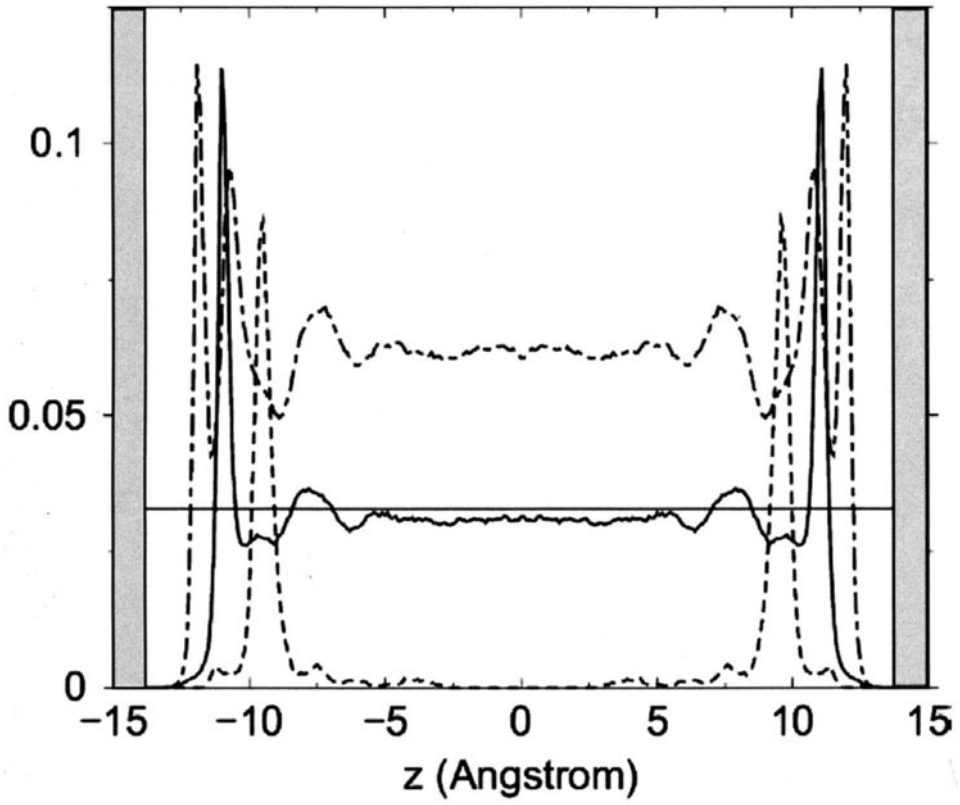

Figure 11. Interlayer particle density profiles for Na-hectorite hydrate, of layer spacing 34Å. The profiles are oxygen – solid line, hydrogen – dot/dash line, and sodium – dash line. Note that the counterions are concentrated near the clay surface, as hydrated complexes, and that there is evidence for three structured layers of water at the interface. Even at the center of the interlayer region the water density has not recovered to its bulk value, shown as the horizontal line (de Carvalho and Skipper, 2000). Copyright 2000 American Institute of Physics

Nearest neighbour coordination of the counterions is extremely similar to that in bulk solutions, namely; six oxygen atoms occur at an equilibrium distance of about 2.4Å (figure 12). If there are insufficient water molecules, or if the counterion is bound to a surface charge site, then this sphere is completed by oxygen atoms from the clay surface. Observation of events at the clay surface points to an important distinction between isomorphic substitution among (i) octahedral and (ii) tetrahedral layer cations. The latter are located at the clay surface, and therefore interact more strongly with interlayer counterions (Chang et al. 1995, 1997). The ratio of inner to outer sphere complexes is therefore related closely to the ratio of tetrahedral to octahedral charge sites.

Comparison between Li^+, Na^+ and K^+ counterions show that the smaller counterions prefer to hydrate in the presence of water, rather than remain attached to the clay surface. K^+, on the other hand, is rather weakly hydrated, and is therefore reluctant to leave the charged clay surfaces (Boek et al, 1995b: Chang et al, 1995, 1997: Delville, 1991, 1992, 1993). This behaviour can be linked to the role of K^+ as a clay swelling inhibitor (Boek et al, 1995b).

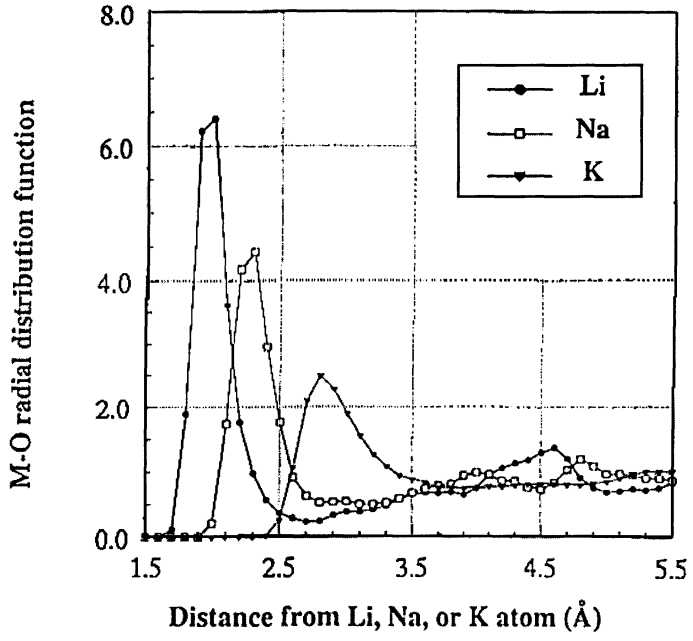

Figure 12. Calculated cation-water radial distribution functions in 2-layer montmorillonite hydrates. (Chang et al 1998). These distributions show that the counterion hydration is very similar to that in the bulk. Copyright 1998 American Chemical Society.

5.4 Dynamics

Time-dependent quantities can be calculated directly from the trajectories of the particles in molecular dynamics simulations. In the current context, an important example is the mobilities of interlayer species. These can be obtained directly from the 2-dimensional Fick's Law, which relates the self-diffusion constant, D, to the mean square displacement of each particle as a function of time as given in equation 4.5.

Current molecular dynamics simulations of clay-water-cation systems have extended to about 200×10^{-12}s (Refson et al 1994; Chang et al, 1995, 1997; Sposito et al; 1999), providing a lower calculable limit of $D=1\times10^{-12}m^2s^{-1}$. For reference, the calculated self-diffusion coefficients for water molecules and sodium counterions in a two-layer smectite hydrate are about $1.4\times10^{-9}m^2s^{-1}$ and $5.1\times10^{-11}m^2s^{-1}$ respectively (Table 2; Chang et al, 1995).

In a recent development, Porion et al (2003) have used multiscale statistical analysis to model the data from ^{1}H pulsed gradient spin-echo in NMR measurements. Over the picosecond timescale they have used analysis of the velocity autocorrelation function to determine the diffusion coefficient, see equation 4.5. This was followed by Brownian dynamics (Allen and Tildesley, 1987) to extend the timescale to several μs.

6 Conclusions and Future Challenges

Monte Carlo and molecular dynamics computer simulations are proving to be powerful techniques in the study of clay-fluid interactions and clay swelling. Using molecular models developed originally for studies of water and aqueous solutions these methods have provided detailed molecular insight into processes occurring at the clay-fluid interface. In many cases simulations have suggested new experiments, and a healthy synergistic relationship is developing between modelling and experiment. Future challenges include the development of polarisable and flexible models, implementation of (μpT) ensemble algorithms, studies of non-aqueous fluids and solutes, and systematic investigation of clay-fluid interactions at elevated pressures and temperatures.

In this workshop we also seek links between the microscopic and macroscopic properties of swelling clays. In this context, bulk properties such as the liquid limit of clays can be related directly to the extent of the solid-liquid interface. One can also use diffusion coefficients such as those given in table 1 as input to macroscopic modelling of the visco-elastic mechanical properties and long-time diffusion properties of clay-rich materials (Ichikawa et al, 1999, 2001; Porion et al, 2003).

References

Allen M.P and Tildesley D.J. (1987) *Computer Simulation of Liquids*. Clarendon Press, Oxford, UK.

Andersen H.C. (1980) Molecular dynamics simualtions at constant pressure and/or temperature. *J. Chem. Phys.* **72**, 2384-2393.

Bash P.A., Singh U.G., Langridge R. and Kollman P.A. (1987) Free energy calculation by computer simulation. *Science* **49**, 564-568.

Bleam W.F (1993) Atomic Theories of Phyllosilicates: Quantum Chemistry, Statistical Mechanics, Electrostatic Theory, and Crystal Chemistry. *Rev.Geophysics*, **31**, 51-73.

Boek E.S., Coveney P.V. and Skipper N.T. (1995a) Molecular Modelling of Clay Hydration: A Study of Hysteresis Loops in the Swelling Curves of Sodium Montmorillonites. *Langmuir*, **11**, 4629-4631.

Boek E.S., Coveney P.V. and Skipper N.T. (1995b) Monte Carlo Molecular Modelling Studies of Hydrated Li-, Na-, and K-smectites: Understanding the Role of Potassium as a Clay Swelling Inhibitor. *J.Am.Chem.Soc.*, **117**, 12608-12617.

Boek E.S. and Sprik M. (2003) Ab initio molecular dynamics study of the hydration of a sodium smectite clay. *J. Phys. Chem. B* **107**, 3251-3256.

Bounds D.G. (1985) A molecular dynamics study of the structure of water around the ions Li^+, Na^+, K^+, Ca^{2+}, Ni^{2+} and Cl^-. *Mol.Phys.* **54**, 1335-1355.

Bridgeman C.H., Buckingham A.D., Skipper N.T. and Payne M.C. (1996) Ab initio total energy study of uncharged clays and their interaction with water. *Mol.Phys.*, **89**, 879-888.

Brindley G.W and Brown G. (1980) Crystal Structures of Clay Minerals and their X-ray Identification. Mineralogical Society, London, UK.

Brodholt J. and Wood B. (1993) Simulations of the structure and thermodynamic properties of water at elevated pressures and temperatures. *J.Geophys.Res: Solid Earth*, **98**, 513-536.

Car R. and Parrinello M. (1985) Unified Approach for Molecular Dynamics and Density Functional Theory. *Phys.Rev.Lett.*, **55**, 2471-2474.

Chandrasekhar J., Spellmeyer D.C. and Jorgensen W.L. (1984) Energy Component Analysis for Dilute Aqueous Solutions of Li^+, Na^+, F^- and Cl^- ions. *J.Am.Chem.Soc.*, **106**, 903-910.

Chang F-R.C., Skipper N.T. and Sposito G. (1995) Computer Simulation of Interlayer Molecular Structure in Sodium Montmorillonite Hydrates. *Langmuir*, **11**, 2734-2741.

Chang F-R.C., Skipper N.T. and Sposito G. (1997) Monte Carlo and molecular dynamics simulations of interfacial structure in lithium montmorillonite hydrates. *Langmuir*, **13**, 2074-2082.

Chavez-Paez M, de Pablo L and de Pablo J.J (2001a) Monte Carlo simulations of Ca-montmorillonite hydrates. *J.Chem.Phys.*, **114**, 10948-10953.

Chavez-Paez M, van Workum K, de Pablo L and de Pablo J.J (2001b) Monte Carlo simulations of Wyoming sodium montmorillonite hydrates. *J.Chem.Phys.*, **114**, 1405-1413.

De Carvalho RJFL and Skipper NT (2001) Atomistic computer simulation of the clay-fluid interface in colloidal laponite. *J.Chem.Phys.* **114**, 3727-3733.

Delville A. (1991) Modelling the Clay-Water Interface. *Langmuir*, **7**, 547-555.

Delville A. (1992) Structure of Liquids at a Solid Interface: An Application to the Swelling of Clay by Water. *Langmuir*, **8**, 1796-1805.

Delville A. (1993a) Structure and Properties of Confined Liquids: A Molecular Model of the Clay-Water Inteface. *J.Phys.Chem.*, **97**, 9703-9712.

Delville A. and Sokolowski S. (1993b) Adsorption of Vapour at a Solid Interface: A Molecular Model of Clay Wetting. *J.Phys.Chem.*, **97**, 6261-6271.

Enderby J.E. and Neilson G.W. (1981) The structure of electrolyte solutions. *Rep. Prog.Phys.*, **44**, 593-643.

Finney J.L., Quinn J.E., and Baum J.O. (1986) The water dimer potential surface. *Water Science Reviews*, **1**, 93.

Frenkel D. and Smit B. (1996) *Understanding Molecular Simulation*. Academic Press, San Diego, USA.

Glaeser R. et Méring J. (1968) Domaines d'hydration homogène des smectites. *C. r. hebd. Séan. Acad. Sci. Paris* **267**, 463-466.

Guldbrand L., Jonsson B., Wennerstrom H. and Linse P (1983) Electrical double layer forces. A Monte Carlo study. *J.Chem.Phys*., **80**, 2221-2228.

Guven N. (1992) Molecular Aspects of Clay-Water Interactions. *Clay Water Interface and its Rheological Implication, e*ditors N.Guven and R.M.Pollastro, Volume 4, CMS Workshop Lectures, The Clay Minerals Society, Boulder, Colorado, USA.

Hensen E.J.M and Smit B. (2002) Why Clays Swell. *J. Phys. Chem*. B, **106**, 12664-12667.

Ichikawa Y., Kawamura K., Nakano M., Kitayama K. and Kawamura H. (1999). Unified molecular dynamics and homogenization analysis for bentonite behaviour: current results and future possibilities. *Eng. Geology,* **54**, 21-31.

Ichikawa Y., Kawamura K., Nakano M., Kitayama K., Seiki T. and Theramast N. (2001). Seepage and consolidation of bentonite saturated with pure- and salt-water by the method of unified molecular dynamics and homogenization analysis. *Eng. Geology,* **60**, 127-138.

Jorgensen W.L., Chandrasekhar J., Madura J., Impey R.W. and Klein M.L. (1983) Comparison of simple potential functions for modelling water. *J.Chem.Phys*., **79**, 926-935.

Israelachvili J.N. and Wennerstrom H. (1996) The Role of Hydration and Water Structure in Biological and Colloidal Systems. *Nature*, **379**, 219-225.

Jorgensen W.L. (1981) Transferable intermolecular potential functions for water, alcohols and ethers. Application to liquid water. *J.Am.Chem.Soc*., **103**, 335-340.

Jorgensen W.L., Chandrasekhar J., Madura J., Impey R.W. and Klein M.L. (1983) Comparison of simple potential functions for modelling water. *J.Chem.Phys*., **79**, 926-935.

Jorgensen W.L. (1984) Optimised Intermolecular Potential Functions for liquid hydrocarbons. *J.Am.Chem.Soc*., **106**, 6638-6646.

Karaborni S., Smit B., Heidug W., Urai J. and van Oort E. (1996) The Swelling of Clays: Molecular of the Hydration of Montmorillonite. *Science*, **271**, 1102-1104.

Kubicki J.D. and Bleam W.F. (1998). *Molecular modeling of clays and mineral surfaces: a short course.* CMS Workshop 12. Clay Minerals Society, Boulder, USA**.**

Kuyucak S., Andersen O.S. and Chung S-H. (2001) Models of permeation in ion channels. *Rep. Prog. Phys.* **64**, 1427–1472.

Lee C., Vanderbilt D., Laasonen K., Car R. and Parrinello M. (1992) Ab initio Studies on High Pressure Phases of Ice. *Phys.Rev.Lett*., **69**, 462-465.

Lie G.C., Clementi E. and Yoshimine O. (1976) Study of the structure of molecular complexes. XIII. Monte Carlo simulation of liquid water with a configuration interaction pair potential. *J.Chem.Phys*., **64**, 2314-2323.

Lybrand T.P and Kollman P.A. (1985) Water-water and water-ion potential functions including terms for many body effects. *J.Chem.Phys*., **83**, 2923-2933.

Mahoney M.W. and Jorgensen W.L. (2000) A five-site model for liquid water and the reporduction of the density anomaly by rigid, nonpolarizable potential functions. *J. Chem. Phys.* **112**, 8910-8922.

Matsouka O., Clementi E. and Yoshimine M. (1976) CI study of the water dimer potential surface. *J.Phys.Chem*., **64**, 1351-1361.

Mezei M. (1982) Excess free energy of different water models computed by Monte Carlo methods. *Mol. Phys.* **47**, 1307-1315.

Neilson G.W. and Enderby J.E. (1989) Co-ordination of metal aquaions. *Adv. Inorg. Chem*., **34**, 196-218.

Newman A.C.D. (1987) *Chemistry of Clays and Clay Minerals*. Wiley, New York, USA.

Norrish K. (1954) The swelling of montmorillonite. *Discuss Faraday Soc*. **18**, 120-132.

North F.K. (1990) *Petroleum Geology*. Unwin-Hyman, Boston, USA.

Nosé S. (1986) An extension of the canonical ensemble molecular dynamics method. *Mol. Phys.* **57**, 187-191.

Ohtaki H. and Radnai T. (1993). Structure and dynamics of hydrated ions. *Chem. Rev.*, **93**, 1157-1204.

Park S-H. and Sposito G. (2000) Monte Carlo simulation of total radial distribution functions for interlayer water in Li-, Na-, and K-montmorillonite hydrates. *J. Phys. Chem. B* **104**, 4642-4648.

Payne M.C., Teter M.P., Allan D.C., Arias T.A. and Joannopoulos J.D. (1992) Iterative minimization techniques for ab initio total-energy calculations: molecular dynamics and conjugate gradients. Rev.Mod.Phys., 64, 1045-1097.

Porion P., Al Mukhtar M., Faugére A.M., Pellenq R.J.M., Meyer S. and Delville A. (2003) Water self diffusion within nematic dispersions of nanocomposites: a multiscale analysis of ^{1}H pulsed gradient spin-echo NMR measurements. *J. Phys. Chem. B* **107**, 4012-4023.

Refson K. Skipper N.T. and McConnell J.D.C. (1993), Molecular dynamics simulation of water mobility in smectites. In *Geochemistry of Clay-Pore fluid interactions*, editors D.A.C.Manning and P.L.Hall, Mineralogical Society, Chapman and Hall, London, UK.

Remler D.K. and Madden P.A. (1990) Molecular dynamics without effective pair potentials via the Car-Parrinello approach. *Mol.Phys.*, **70**, 921-966.

Shroll R.M. and Smith D.E. (1999) Molecular dynamics simulations in the grand canonical ensemble: application to clay mineral swelling. *J.Chem.Phys.*, **111**, 9025-9033.

Siqueira A. de, Skipper N.T., Coveney P.V and Boek E.S. (1997) Computer Simulation Evidence for Enthalpy driven Dehydration of Clays Under Sedimentary Basin Conditions. *Mol.Phys.*, **92**, 1-6.

Skipper N.T., Refson K. and McConnell J.D.C. (1991) Computer simulation of interlayer water in 2:1 clays. *J.Chem.Phys.*, **94**, 7434-7445.

Skipper N.T., Chang F-R.C. and Sposito G. (1995a) Monte Carlo simulation of interlayer molecular structure in swelling clay minerals. 1. Methodology. *Clays Clay Miner.*, **43**, 285-293.

Skipper N.T., Chang F-R.C. and Sposito G. (1995b) Monte Carlo simulation of interlayer molecular structure in swelling clay minerals. 2. Monolayer Hydrates. *Clays Clay Miner.*, **43**, 294-303.

Smith D.E. (1998) Molecular computer simulation of the swelling properties and interlayer structure of cesium montmorillonite. *Langmuir* **14**, 5959-5967.

Smith D.E. and Haymet A.D.J. (1992) Structure and dynamics of water and aqueous solutions: the role of flexibility. *J.Chem.Phys.*, **96**, 8450-8459.

Sposito G. and Prost R. (1982) Structure of water adsorbed on smectites. *Chem.Rev.*, **82**, 553-573.

Sposito G., Skipper N.T., Sutton R., Park S-H., Chang F-R, Soper A.K. and Greathouse J.A. (1999) Surface Geochemistry of the clay minerals. *Proc. Natl. Acad. Sci. USA,* **96**, 3358-3364.

Titiloye J.O. and Skipper N.T. (2001) Molecular dynamics simulation of methane in sodium montmorillonite clay hydrates at elevated pressures and temperatures. *Mol. Phys.* **99**, 899-906.

Tossell J.A. (1995) *Mineral Surfaces: Theoretical Approaches.* Edited by D.J.Vaughan and R.A.D.Pattrick. Chapman and Hall, London, UK.

Vlot M.J., Huinink J. and van der Eerden J.P. (1999) Free energy calculations on systems of rigid molecules: an application to the TIP4P model of H_2O. *J. Chem. Phys.* **110**, 55-61.

Watanabe K. and Klein M.L. (1989) Effective pair potentials and the properties of water. *Chem.Phys.*, **131**, 157-167

POLYELECTROLYTE GELS
Basics, Modelling and Simulation

Thomas Wallmersperger [*] , Bernd Kröplin [*], and Rainer W. Gülch[†]

[*] Institut für Statik und Dynamik der Luft- und Raumfahrtkonstruktionen
Universität Stuttgart, 70569 Stuttgart, Germany

[†] Physiologisches Institut II, Universität Tübingen, 72076 Tübingen, Germany

Abstract

The increasing precision of shapes and displacements required by structures in both, aerospace and precision mechanics, as well as the desire of health monitoring of damaged components, lead to the concept of structures with actuatoric and sensoric capabilities. The basis for the adaptive structures are multi-functional materials.

A very promising representative of these materials are electroactive polymers (EAP). In the first section of this paper we give a short overview on this group of materials. In the following we focus our interest on polyelectrolyte gels which is one key material of EAP. These gels - consisting of a polymer network with fixed ionizable groups and a liquid phase with mobile ions - are distinguished by enormous swelling capabilities under the influence of external physical or chemical stimuli. These properties make them very attractive for a new generation of "pseudomuscular" actuators.

In the present work we investigate chemically and electrically stimulated polymer gels. At first we give a model based on the theory of "swelling of network structures" by Flory (1953). In the third section we present a coupled chemo-electro-mechanical multi-field formulation which is capable to describe the phenomena occurring in the different fields. Then, an overview over the space-time finite element discretization method is given. These unconditionally stable finite elements give the possibility to treat the phenomena in space and time equally.

In the last section, chemical as well as electrical stimulation is considered. The numerical simulation is computed for all the fields involved. The numerical results of the electric potential show a promising correlation with experiments in which the Donnan potential has been registered in PAAm/PAA gels with a new microelectrode technique. For anionic gels, in both theory and experiment "hyperpolarisation", i.e. increased negativity, can be found on the anode-side of the gel and "depolarisation" on the cathode-side. These changes in the electric potential, which are supposed to affect swelling or deswelling of polyelectrolyte gels, lead to bending deformations of the gel.

1 INTRODUCTION

1.1 Adaptive Structures

The desire of a high precision for structures in both, aerospace and precision mechanics, as well as the demand of health monitoring of damaged components, lead to the concept of structures with actuatoric and sensoric capabilities.

While uncontrolled structures simply react to external influences (such as forces, temperature, etc.) with a passive response (like deformation, vibration, etc.), stuctures incorporating actuators and sensors are able to produce an active behavior. The sensors measure the displacement and the actuators produce an active displacement. If both components are - in the optimal case - embedded in the structure and having load-carrying function as well and are linked together with an external controller, the structure is called adaptive, see Fig. 1.

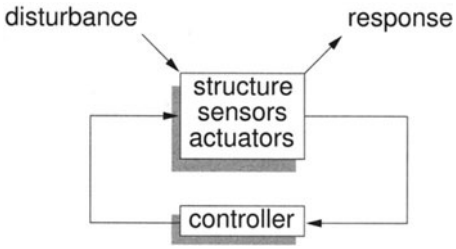

Figure 1. Definition of adaptive structures

1.2 Adaptive Materials

The basis of adaptive structures are multi-functional materials which - apart from their load-carrying-capability - possess actuatoric and/or sensoric capabilities. Materials which exhibit a change in non-mechanical (e.g. thermal, electrical, chemical, optical) properties as a reaction to a given mechanical excitation can be used as sensors. When responding to a non-mechanical stimulus by a change of their mechanical properties (e.g. Young's modulus, viscosity) they can be employed as actuators.

The most important materials used in adaptronics are

- piezoelectric and electrostrictive ceramics
- magnetostrictive materials
- shape memory alloys
- electro- and magnetorheological fluids
- electroactive materials

In Tab. 1 (Grohmann et al., 1998), a classification, special characteristics and the application areas (Banks et al., 1996) of adaptive materials are given.

Materials which can be used as actuators should provide e.g. large displacements while sensors should provide e.g. large electrical voltages at a given small displacement. Concluding, this means the demand for an efficient energy transfer.

Typical characteristics for smart materials are "active strain" and "frequency". The range of these values is given in Fig. 2 for different adaptive materials.

Table 1. Classification of adaptive materials

ADAPTIVE MATERIAL	CONTROL	CHARACTERISTICS	APPLICATION AREA
polymer gels	absorption/delivery of solvent in the gel leads to a change in volume, stimulated by change of the electric field or PH-value $\Rightarrow$ contraction/relaxation	very large deformations, $\epsilon_{max} \approx 300\%$ small stiffness, change of viscosity	electro-chemical-mechanical actuators, artificial muscles
piezoelectric materials: piezoceramics e.g. lead zirconate-titanates (PZT) piezopolymers e.g. polyvinylidene fluorides (PVDF)	direct and converse piezoelectric effect	small deformations, PZT: $\epsilon_{max} \approx 0,1\%$, TRS: $\epsilon_{max} \approx 0,5\%$ (at 3000 V/mm), low power-specific mass	force, pressure and acceleration sensors, actuators in structures, structural acoustics and fluid/structure systems
electrostrictive materials e.g. Pb-Mg-alloy	electrostrictive law, direct and converse effect	small strains, temperature dependence	sensors and actuators in structural systems
magnetostrictive materials e.g. Terfenol-D	magnetostrictive effect magnetoelastic effect	small strains, $\epsilon_{max} \approx 0.2\%$ highly nonlinear	sensors and actuators in structural systems,
electrorheological fluids	change of viscosity as a function of applied electric field	fast (> 1000Hz) temperature dependence	actuators in large load-bearing structures, active damping, tailoring (rotor blades)
shape memory alloys	temperature-controlled transformation from the austenite to martensite phase	large deformations, $\epsilon_{max} \approx 5\%$, slow ($< 10$Hz) active displacement not exactly controllable	structural conform embedded actuators, mechanical or electrical switch-gears

Applications requiring high frequencies (e.g. helicopter rotor blades, structural acoustics) are often realized with piezo ceramics. For applications which require larger displacements, electroactive polymers can be a quite good alternative. We should however keep in mind that some of these materials are up to now still in a "research state".

1.3 Electroactive Polymers

Electroactive polymers (EAP) are a particularly attractive class of actuation materials with great similarity to biological contractile tissues (Chiarelli et al., 1992). They consist of polymers in various composition and in variable form. They can be classified according to Bar-Cohen (2001) in

- Electronic EAP and
- Ionic EAP

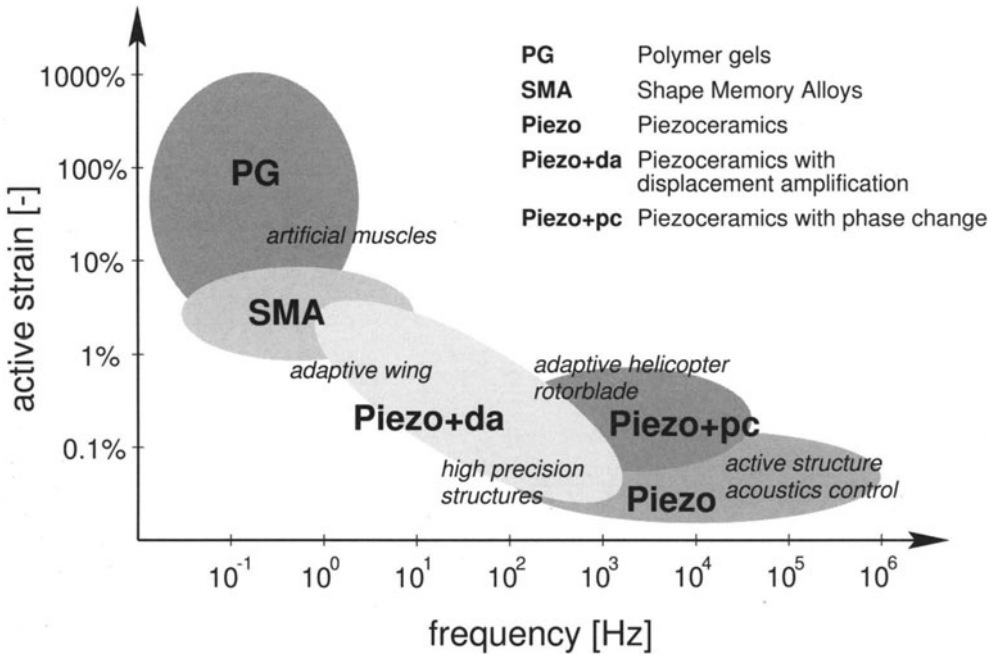

Figure 2. Active strain and frequency of typical adaptive materials

1.3.1 Electronic EAP

Electronic EAP comprise e.g. Ferroelectric EAP, Dielectric EAP, Electrostrictive Graft Elastomers, Electrostrictive Paper and Liquid Crystal Elastomer Materials.

Ferroelectric polymers - a common material is PVDF (polyvinylidene fluoride) - are partly crystalline, with an inactive amorphous phase (Bar-Cohen, 2001). A short comparison of the characteristics and material parameters of PVDF and PZT are given in Tab. 2.

Dielectric Polymers have a low elastic stiffness and a high dielectric constant. They can produce large actuation strains when applying an electrostatic field. More details about dielectric EAP can be found e.g. in Pelrine et al. (2000).

Electrostrictive Paper can be composed of a multitude of discrete particles - e.g. fibers - which form a network structure. An EAP actuator has been prepared by bonding two silver laminated papers with silver electrodes placed on the outside surface by Kim et al. (2000). Applying an electric voltage produces a bending deformation: this effect is characterized by electrostatic forces and an intermolecular interaction of the adhesive.

Liquid Crystal Elastomer (LCE) Materials can be used to form actuators having piezoelectric characteristics. They are electrically activatible by inducing Joule heating. LCEs are composite materials that consist of monodomain nematic liquid crystal elastomers and conductive polymers that are distributed within their network structure (Shahinpoor, 2000). The actuation mechanism involves phase transition between nematic and isotropic phases over a period of less than a second. The inverse process is much slower (approx. 10s). The mechanical properties of LCE

Table 2. Material properties of PVDF and PZT

material producer			PVDF Kynar	PZT-5A Morgan Matroc
elastic modulus	E_{11}	$[GPa]$	2	69
	E_{33}	$[GPa]$	2	106
density	ρ	$[kg/m^3]$	1800	7700
relative permittivity	K_{33}	$[-]$	12	1700
$(\widetilde{\epsilon}_{ik} = K_{ik} \cdot 8.85 \cdot 10^{-12} \frac{As}{Vm})$	K_{11}	$[-]$	12	1730
piezoelectric coefficient	d_{33}	$[m/V]$	$-33 \cdot 10^{-12}$	$374 \cdot 10^{-12}$
	d_{31}	$[m/V]$	$23 \cdot 10^{-12}$	$-171 \cdot 10^{-12}$
pyroelectric coefficient	p_1	$[As/(m^2K)]$	$-25 \cdot 10^{-6}$	$-0.02 \cdot 10^{-6}$
Curie-temperature	T_C	$[°C]$	–	365
operation temperature	T_{max}	$[°C]$	$-40 \cdots +80$	< 250
max. electric field strength	$\widetilde{E}_{3,max}$	$[kV/mm]$	30	0.7
ultimate tensile strength	σ_{max}	$[MPa]$	200	76
ultimate compression strength	σ_{min}	$[MPa]$	-60	-520

can be controlled and optimized by effective selection of the liquid crystalline phase, density of cross-linking, flexibility of the polymer backbone, the coupling between the backbone and the liquid crystal group, and the coupling between the liquid crystal group and the external stimuli (Bar-Cohen, 2001). The first LCEs have been synthesized by Finkelmann et al. (1981).

1.3.2 Ionic EAP

Ionic EAP comprise (ionic) polymer gels, ionic polymer-metal composites, carbon nanotubes and bucky paper.

A relatively low voltage is required to stimulate bending in ionic polymer-metal composites (IPMC), where the base polymer provides channels for mobility of positive ions in a fixed network of negative ions on interconnected clusters. Two types of base polymers are used to form IPMC: Nafion® and Flemion® (Bar-Cohen, 2001). The chemical structure is given in Fig. 3.

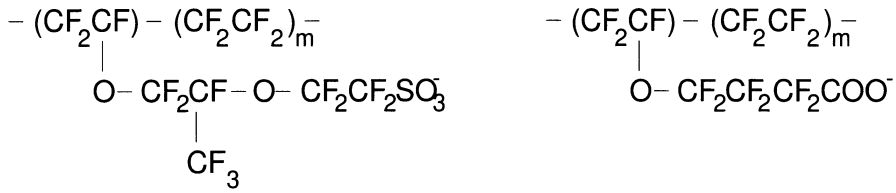

Figure 3. Chemical structure of Nafion® (left) and Flemion® (right)

IPMCs have been realized e.g. Oguro et al. (1992), Bar-Cohen et al. (2000), Nemat-Nasser and Li (2000).

Carbon nanotubes are cylindrical molecules 1 nm in diameter and 1-100 microns in length. They are constituted of carbon atoms only, and can be thought of as a layer of graphite rolled-up

into a cylinder. Most of these tubular fullerene molecules consist of multiple shells, where many tubes are arranged coaxially, see Fig. 4.

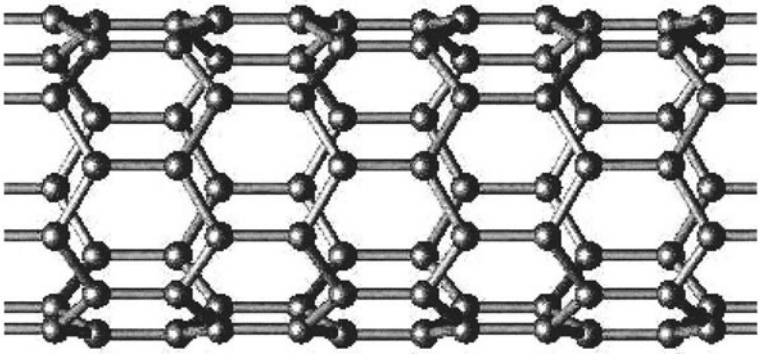

Figure 4. Carbon Nanotube consisting of graphite rolled up into a cylinder

2 POLYMER GELS

Electrolyte polymer gels are ductile-elastic adaptive materials.

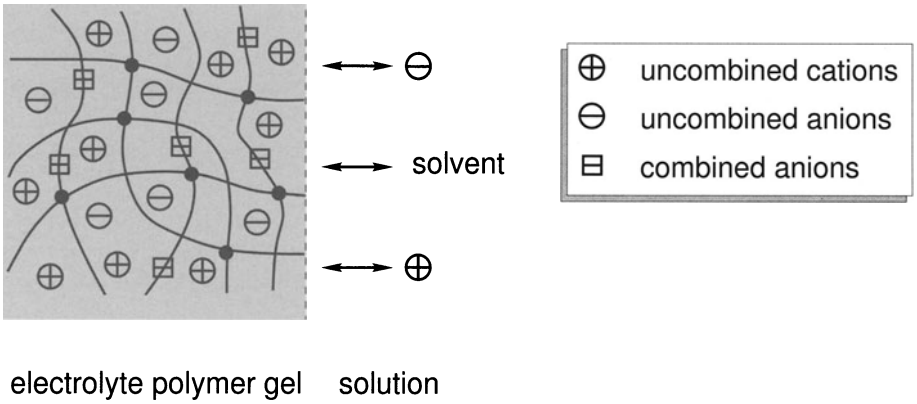

Figure 5. Anionic polymer gel network with bound anionic groups and mobile ions in solution

They consist of a polymer network with ionizable groups and a liquid phase with mobile ions, see Fig. 5. Absorption and delivery of solvent lead to a considerably large change of volume. This mechanism can be induced by different stimuli such as change of temperature, of pH-value or salt concentration in the solution (chemical stimulation) or by an applied electric field (electric stimulation). Due to this capability, they can be used as actuators for technical applications where large swelling and shrinkage is desired, e.g. for artificial muscles or other chemo-electro-mechanical actuators (Gülch et al., 2000).

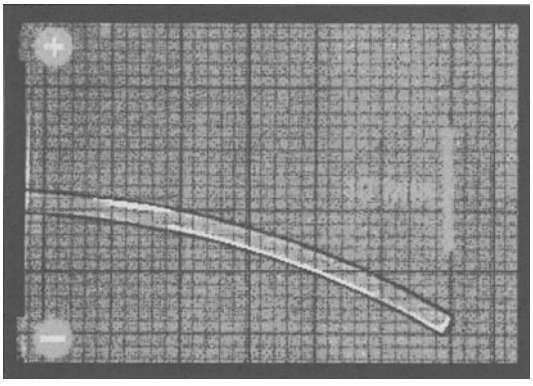

Figure 6. Anionic polymer gel fiber in a solution bath with applied electric field

In Fig. 6, the experimental plot of an anionic polymer gel fiber in a solution bath with applied electric field is given.

2.1 Statistical Theory

In order to learn more about the fundamental transition process in electroactive polymers, a closer look at the effect of changes in the chemical environment surrounding the gel should be taken.

Based on the theory of "swelling of network structures" by Flory (1953) and the extension for large swelling ratios by Treloar (1958), the change of the gel surrounding condition can be described by a change of the Gibbs free energy ΔF. The total free energy is the sum of the free energies of mixing ΔF_M, of elastic deformation ΔF_{el} and of the one depending on the mobile ions, i.e. the different concentrations inside and outside the gel, ΔF_{ion}, see Rička and Tanaka (1984), Ohmine and Tanaka (1982) and Schröder and Oppermann (1996).

The equilibrium state is characterized by a minimum of the total free energy difference ΔF between the solution and the gel phase. This means, the chemical potentials μ_1 in both corresponding phases are identical. This can be formulated by

$$\begin{aligned}\Delta\mu_1 &= \left(\frac{\partial\Delta F_M}{\partial n_1}\right)_{T,V} + \left(\frac{\partial\Delta F_{el}}{\partial n_1}\right)_{T,V} + \left(\frac{\partial\Delta F_{ion}}{\partial n_1}\right)_{T,V} \\ &= \left(\frac{\partial\Delta G_M}{\partial n_1}\right)_{p,T} + \left(\frac{\partial\Delta G_{el}}{\partial n_1}\right)_{p,T} + \left(\frac{\partial\Delta G_{ion}}{\partial n_1}\right)_{p,T} \\ &= \Delta\mu_{1,M} + \Delta\mu_{1,el} + \Delta\mu_{1,ion} = 0 \end{aligned} \tag{2.1}$$

2.1.1 Mixture Potential

In the unswollen state, the polymer network and the solvent are completely separated. In all swollen states, a "mixture" is obtained by a migration of the solvent in the gel phase. The mixture term of the Gibbs free energy is obtained as

$$\Delta F_M = RT\,(n_1 \ln\phi_1 + n_2 \ln\phi_2 + \chi n_1 \phi_2) \tag{2.2}$$

Two different mechanisms are contributing to the mixture potential:
the combinatoric part

$$\Delta F_{M,comb} = RT\,(n_1 \ln\phi_1 + n_2 \ln\phi_2) \tag{2.3}$$

being able to describe the different conformations of the amorphous polymer,
and the contact part between polymer and solution

$$\Delta F_{M,cont} = RT\,\chi n_1 \phi_2 \tag{2.4}$$

due to the interaction between the molecules.

$\phi_2 = \phi_p$ is the volumetric content of the polymer and $\phi_1 = \phi_s$ of the solvent in the equilibrium state; n_1 and n_2 are the appropriate molar fractions. The volume fractions ϕ_1 and ϕ_2 are defined as follows

$$\phi_1 = \frac{n_1}{n_1 + s n_2} \quad \text{and} \quad \phi_2 = \frac{s n_2}{n_1 + s n_2} \tag{2.5}$$

Note, the sum of the volume fractions ϕ_1 and ϕ_2 equals 1. This means, there is no matter-free region in the mixture. The number of moles of the polymer n_2 in the gel is constant and does not change over the whole swelling process.

χ represents the Flory-Huggins polymer-solution interaction parameter, i.e. the contact between gel and solution. s is the number of chain segments of a polymer molecule, where the volume of the polymer molecules is identical the product of s with the volume of the solvent molecules V_s, i.e. $V_p = s \cdot V_s$.

The mixture potential

$$\Delta\mu_{1,M} = \left(\frac{\partial \Delta G_M}{\partial n_s}\right)_{T,p} = RT\left(\ln\phi_1 + \phi_2 - \frac{n_2}{n_1 + s n_2} + \chi\phi_2^2\right) \tag{2.6}$$

may be derived from the free energy due to mixture. Neglecting the third term of Eq. (2.6), which is very small compared to the other terms, we obtain

$$\Delta\mu_{1,M} = RT\left(\ln(1-\phi_p) + \phi_p + \chi\phi_p^2\right). \tag{2.7}$$

The total swelling ratio q is the product of the cross-linking swelling, the so-called pre-swelling q_v, and the relative swelling q_r

$$q = q_v \cdot q_r = \phi_p^{-1} \tag{2.8}$$

Due to the increased number of possible states of the polymer-solution system, this results in the swollen state in an increase of entropy due to the mixture.

2.1.2 Elastic Potential

The elastic deformation of the polymer gel network comprises the extension due to free swelling and the strain at constant volume under keeping the enthalpy of the whole gel system constant. The elongation of the network when swelling leads to a decrease of the network chain-entropy. In the equilibrium state, the sum of the entropy changes due to the elastic term and the mixture term as well as the mobile ion contribution is again identical zero.

The free energy resulting from the elastic deformation can be given according to Flory (1953) by

$$\Delta F_{el} = \frac{RT\nu_e}{2}\left[\alpha_x^2 + \alpha_y^2 + \alpha_z^2 - 3 - \ln(\alpha_x \cdot \alpha_y \cdot \alpha_z)\right] \tag{2.9}$$

where $\alpha_i = 1 + \varepsilon_i$ is the one-dimensional swelling in i-direction.

2.1.2.1 Isotropic Swelling

If an isotropic swelling behavior $\alpha_s = \alpha_x = \alpha_y = \alpha_z$ is assumed, we can set

$$\alpha_s^3 = \frac{V}{V_0} = \frac{V_0 + n_1 v_1}{V_0} = \frac{1}{\phi_p} \tag{2.10}$$

where V is the actual volume, V_0 the volume in reference state, v_1 the molar volume of the solvent in the reference state and ν_e is the effective molar number of polymer chains in the gel. For this case we obtain

$$\Delta F_{el} = \frac{RT\nu_e}{2}\left[3\alpha_s^2 - 3 - \ln\alpha_s^3\right] \tag{2.11}$$

Using Eq. (2.5) and (2.10), we obtain from Eq. (2.11) the chemical potential due to elastic deformation as

$$\Delta\mu_{1,el} = v_1 RT\frac{\nu_e}{V_0}\left(\phi_p^{1/3} - \frac{\phi_p}{2}\right) \tag{2.12}$$

Comparing this term to the result obtained by Schröder (1994), when Gaussian theory is applied

$$\Delta\mu_{1,el} = \nu^* RTV_1\eta A q_v^{-1} q_r^{-1/3} \tag{2.13}$$

a nearly identical behavior can be observed: The Eqs. (2.12) and (2.13) for the elastic potential provide the same results for large swelling ratios due to the larger contribution of the ϕ_p-term compared to the $\phi_p^{1/3}$-term in Eq. (2.12). For obtaining identical results, the other parameters have to be chosen as

$$A\eta\nu^* q_v^{-1} = \frac{\nu_e}{V_0} q_v^{-1/3}$$

where A is a structural factor, η the dilatation factor and ν^* represents the number of effective network chains per volume of the dry polymer network.

For a very large dilatation, the Gaussian theory is no longer valid without restrictions. Therefore, the Non-Gaussian theory has to be applied (Schröder, 1994; Schröder and Oppermann, 1996). This theory considers the change of the entropy from the unswollen to the swollen state. The chain energy and the free energy can be formulated by using the Langevin function $\mathcal{L}$

$$\mathcal{L}(\beta) = coth\beta - \frac{1}{\beta} = \frac{r}{nl} \qquad \text{where} \quad \beta = \mathcal{L}^{-1}\left(\frac{r}{nl}\right) \tag{2.14}$$

see e.g. Treloar (1958). The entropy S of one single polymer chain can be given according to Treloar (1958) by

$$S = c_2 - kn\left[\frac{r}{nl}\beta + \ln\left(\frac{\beta}{sinh\beta}\right)\right] \qquad \text{where} \quad \beta = \mathcal{L}^{-1}\left(\frac{r}{nl}\right) \tag{2.15}$$

where k is the Boltzmann constant, n the number of static segments per chain, l the mean length of one segment and r is the distance between the chains.

The chemical potential related to the elastic deformation (Non-Gaussian Theory) can be given as (Schröder, 1994)

$$\Delta\mu_{1,el} = \nu^* RTv_1\eta A q_v^{-1} q_r^{-2/3} n^{1/2}\mathcal{L}^{-1}\left(\frac{q_r^{1/3}}{n^{1/2}}\right) \tag{2.16}$$

2.1.2.2 Directional Swelling

For $\alpha_i \neq \alpha_j$, we obtain a directional swelling. We define $q = V/V_0$ where q is the swelling ratio and V and V_0 are the actual and the initial volume. If x is the preferred direction, we can set

$$\alpha_x = L/L_0 \tag{2.17}$$

Assuming identical elongations in y- and z-direction, we obtain from $\alpha_y \cdot \alpha_z \cdot L/L_0 = q$

$$\alpha_y = \alpha_z = \sqrt{\left(q \cdot \left(\frac{L}{L_0}\right)^{-1}\right)} \tag{2.18}$$

Substituting the direction depending parameter α_i in Eq. (2.9) we obtain - see also Turrin (2003) -

$$\Delta F_{el} = \frac{RT\nu_e}{2}\left[(L/L_0)^2 + 2 \cdot q \cdot \left(\frac{L}{L_0}\right)^{-1} - 3 - \ln\left(L/L_0 \cdot q \cdot \left(\frac{L}{L_0}\right)^{-1}\right)\right] \tag{2.19}$$

According to Flory (1953) and Lee (1996), another possibility to describe the 3D swelling is

$$\alpha_x = \alpha\left(\frac{V}{V_P}\right)^{1/3} = \alpha \cdot \phi_P^{-1/3} \tag{2.20}$$

$$\alpha_y = \alpha_z = \left(\alpha^{1/2} \cdot \phi_P^{1/3}\right)^{-1} \tag{2.21}$$

where $\phi_P = V_P/V$ is the volume fraction of polymer and α represents the quotient of the swollen to the unstretched length since the swelling is isotropic. Using Eqs. (2.20) and (2.21), Lee has obtained

$$\Delta F_{el} = \frac{RT\nu_e}{2}\left[\left(\frac{\alpha^2}{\phi_P^{2/3}}\right) + \left(\frac{2}{\alpha\phi_P^{2/3}}\right) - 3 - \ln\phi_P\right] \tag{2.22}$$

for the Gibbs free energy change.

2.1.3 Mobile ion potential

For ionic polymer gels, additionally to the elastic and the mixture term, the mobile ion potential has to be considered. This term results from the differences in the charge density between the solvent in the polymer and the solution and leads to an increase in the swelling ratio compared to uncharged gels.

The chemical potential based on the charge differences can be formulated by

$$\Delta\mu_{1,ion} = -RT\nu_1 \sum_{\alpha=1}^{N_f}\left(c_\alpha^{(g)} - c_\alpha^{(g)}\right) \tag{2.23}$$

where $c_\alpha^{(g)}$ and $c_\alpha^{(s)}$ are the concentrations in the gel and the solution. ν_1 is the molar volume of the solvent and N_f is the total number of freely movable (unbound) ions. Note, Eq. (2.23) is

formulated in terms of the concentrations instead of for the activities $a_\alpha = f_\alpha c_\alpha$, because the activity coefficient is approx. 1 due to the small concentrations.

To obtain the ion concentrations in the gel and in the solution, the condition of neutrality

$$\sum_{\alpha=1}^{N_f+N_b} (z_\alpha c_\alpha) = 0 \tag{2.24}$$

has to be fulfilled. z_α is the charge number of the species α and N_b is the number of species bound to the polymer.

Note, in literature this equation is often given by

$$\sum_\beta (z_\beta c_\beta) + \sum_m (z_m c_m) = 0 \tag{2.25}$$

where c_m is the concentration of the bound species in the gel and z_m is the corresponding charge number. c_β are the concentrations of the mobile species.

For a *NaCl* solution surrounding the gel leads to

$$+1\, c^{(s)}_{Na^+} + 1\, c^{(s)}_{H^+} - 1\, c^{(s)}_{Cl^-} - 1\, c^{(s)}_{OH^-} = 0 \tag{2.26}$$

in the solution. For anionic gels

$$+1\, c^{(g)}_{Na^+} + 1\, c^{(g)}_{H^+} - 1\, c^{(g)}_{Cl^-} - 1\, c^{(g)}_{OH^-} - 1\, c^{(g)}_{A^-} = 0 \tag{2.27}$$

and for cationic ones

$$+1\, c^{(g)}_{Na^+} + 1\, c^{(g)}_{H^+} - 1\, c^{(g)}_{Cl^-} - 1\, c^{(g)}_{OH^-} + 1\, c^{(g)}_{cat^-} = 0 \tag{2.28}$$

is obtained.

For cationic gels with carboxylic groups A^- as fixed charges, the dissociation can be formulated as

$$c_{M,0} = q \cdot \left(c^{(g)}_{HA} + c^{(g)}_{A^-} \right) \tag{2.29}$$

with the dissociation coefficient

$$K_a = \frac{c^{(g)}_{H^+} \cdot c^{(g)}_{A^-}}{c^{(g)}_{HA}} \tag{2.30}$$

where $c_{M,0}$ denotes the concentration of the polyelectrolyte in the xerostate and $c^{(g)}_{HA}$ the concentration of the acrylic acid compound of the gel.

Using Eqs. (2.29) and (2.30), $c^{(g)}_{A^-}$ may be obtained from

$$c^{(g)}_{A^-} = \frac{c_{M,0}}{q} \cdot \left(1 + \frac{c_{H^+}}{K_a} \right)^{-1} \tag{2.31}$$

For completely dissociated gels, it follows

$$c^{(g)}_{A^-} = \frac{c_{M,0}}{q} \tag{2.32}$$

2.1.3.1 Electrochemical Potential

In order to calculate the concentrations, identical electrochemical potential μ_α^*

$$\mu_\alpha^* = \mu_\alpha + z_\alpha F \Psi = \mu_\alpha^0 + RT \ln a_\alpha + z_\alpha F \Psi \tag{2.33}$$

in the gel and in the solution

$$\mu_\alpha^{(g)} + z_\alpha F \Psi^{(g)} = \mu_\alpha^{(s)} + z_\alpha F \Psi^{(s)} \tag{2.34}$$

has to be fulfilled, where μ_α is the chemical potential and Ψ is the electric potential in the gel or in the solution.

Due to the identical zero-potential in gel and solution,

$$RT \ln a_\alpha^{(g)} + z_\alpha F \Psi^{(g)} = RT \ln a_\alpha^{(s)} + z_\alpha F \Psi^{(s)} \tag{2.35}$$

is obtained for all the species. This results in the Donnan equation - the activity coefficients are considered identical -

$$\frac{c_\alpha^{(g)}}{c_\alpha^{(s)}} = exp\left(- z_\alpha \frac{F}{RT} (\Psi^{(g)} - \Psi^{(s)}) \right) \tag{2.36}$$

from which the quotient of the concentrations between gel and solution can be obtained.

Obtaining the resulting concentrations by using Eqs. (2.24) and (2.36), the mobile ion potential $\Delta\mu_{1,ion}$ can be determined by Eq. (2.23).

In literature, the contribution due to the charged groups in the polymer is often given by a term depending on the number of bound ions f.

2.2 Thermal Stimulation

In this section, we focus our interest on the temperature dependency of the swelling ratio q.

The chemical potential $\Delta\mu$ consisting of the elastic term, mixture potential and mobile ion potential

$$\begin{aligned} \Delta\mu &= RT \left[ln(1-\phi_p) + \phi_p + \chi\phi_p^2 + \frac{v_1 \nu_e}{V_0} \left(\phi_p^{1/3} - \frac{1}{2}\phi_p \right) \right] \\ &+ RT \left[2 v_1 \left(c_s - \sqrt{c_s^2 + \left(\frac{c_{M,0}}{2} \phi_p \right)^2} \right) \right] = 0 \end{aligned} \tag{2.37}$$

is given for an anionic gel with completely dissociated groups in a solution constisting of a monovalent salt of the concentration c_s. Due to the small number of H^+- and OH^--ions, this contribution is neglected.

The temperature dependency of the swelling ratio $q = 1/\phi_p$ is obtained from the temperature-dependent Flory-Huggins interaction parameter $\chi = \chi(T)$.

A general expression for χ is

$$\chi = \chi(T) = \frac{\Delta e}{2 k_B T} \tag{2.38}$$

where Δe is the difference between two states of the polymer chain[1].

From Eq. (2.37) we can obtain

$$\tau = 1-2\chi = 1+2\frac{ln(1-\phi_p)}{\phi_p^2}+\frac{2}{\phi_p}+2\frac{\nu_1\,\nu_e}{V_0}\left(\phi_p^{-\frac{5}{3}}-\frac{1}{2\phi_p}\right) + \frac{4}{\phi_p^2}\nu_1\left(c_s-\sqrt{c_s^2+\left(\frac{c_{M,0}}{2}\phi_p\right)^2}\right) \tag{2.39}$$

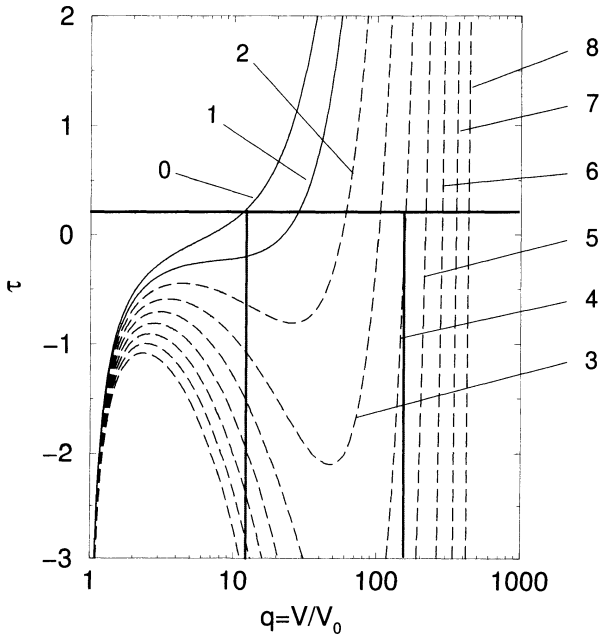

Figure 7. Swelling ratio q versus variable reduced temperatures $\tau = 1-2\chi$ for variable concentrations of fixed charges $c_{M,0} = 0, 1, \ldots, 8\,mol/l$ where $c_s = 10^{-4}\,mol/l$, $\nu_e/V_0 = 0.14\,mol/l$ and $\nu_1 = 0.018\,l/mol$

For the practical use of electroactive polymers as actuators, the temperature dependency is normally not of main interest. For some applications, where the length of the material should be kept constant over a wide temperature range, this dependency is even undesired.

2.3 Chemical Stimulation

For polymer gels, chemical stimulation (variation of the salt concentration or variation of pH) is a very promising actuation method. It is very attractive for medical applications.

[1]For more details see Shibayama and Tanaka (1993)

2.3.1 Variation of Salt Concentration

In this section, the various ion concentrations are calculated for the different salt concentrations in the gel-surrounding solution. In the first testcase, the concentration distribution without consideration of the change of the gel swelling ratio is investigated. Subsequently, the swelling and the resulting concentrations in the gel are solved simultaneously by a Newton-Raphson method.

2.3.1.1 Ion concentrations without change of the swelling ratio

In this testcase, the anionic gel is placed in a $NaCl$-solution, H^+ and OH^--ions are also considered and their concentration in the solution is $c^{(s)}_{H^+} = c^{(s)}_{OH^-} = 10^{-7}\,mol/l$.

The requirement of identical electro-chemical potential in gel and solution results in

$$\frac{c^{(g)}_{Na^+}}{c^{(s)}_{Na^+}} = \frac{c^{(g)}_{H^+}}{c^{(s)}_{H^+}} = \frac{c^{(s)}_{Cl^-}}{c^{(g)}_{Cl^-}} = \frac{c^{(s)}_{OH^-}}{c^{(g)}_{OH^-}} \tag{2.40}$$

Additionally, the condition of electroneutrality in gel and solution reads

$$c^{(g)}_{Na^+} + c^{(g)}_{H^+} = c^{(g)}_{Cl^-} + c^{(g)}_{OH^-} + c^{(g)}_{A^-} \tag{2.41}$$

$$c^{(s)}_{Na^+} + c^{(s)}_{H^+} = c^{(s)}_{Cl^-} + c^{(s)}_{OH^-} \tag{2.42}$$

From (2.40)-(2.42) we obtain

$$\left(1 + \frac{c^{(s)}_{H^+}}{c^{(g)}_{Na^+}}\right)\left(c^{(g)}_{Na^+}\right)^2 - c_{A^-} \cdot c^{(g)}_{Na^+} - c^{(s)}_{Na^+}\left(c^{(s)}_{Cl^-} + c^{(s)}_{OH^-}\right) = 0 \tag{2.43}$$

From this equation follows

$$z_\alpha\, c^{(g)}_\alpha > z_\alpha\, c^{(s)}_\alpha$$

This means, the concentration of positive charged ions is larger in the gel than in the solution; for negative charged ions, the concentration in the gel is smaller than in the solution.

In Fig. 8 are plotted the concentration differences

$$\Delta c_\alpha = c^{(g)}_\alpha - c^{(s)}_\alpha \tag{2.44}$$

between gel and solution for different salt concentration in the solution. For small salt concentrations, the concentration of H^+ in the gel is considerably larger than in the solution. Increasing the salt concentration leads to a decrease of the H^+ ions for the benefit of the Na^+ ions. At $c_s = 10^{-7}\,mol/l$, the concentration of the mobile Na^+ and H^+ ions is identical. Increasing c_s, the concentration of Na^+ in the gel is significant larger in the gel than in the solution; the other mobile ions play a minor role. For $c_s > 10^{-4}\,mol/l$, Δc_{Na^+} as well as Δc_{Cl^-} are decreasing and reaching the limiting values

$$\Delta c_{Na^+} = \frac{c_{A^-}}{2} \quad \text{and} \quad \Delta c_{Cl^-} = -\frac{c_{A^-}}{2} \tag{2.45}$$

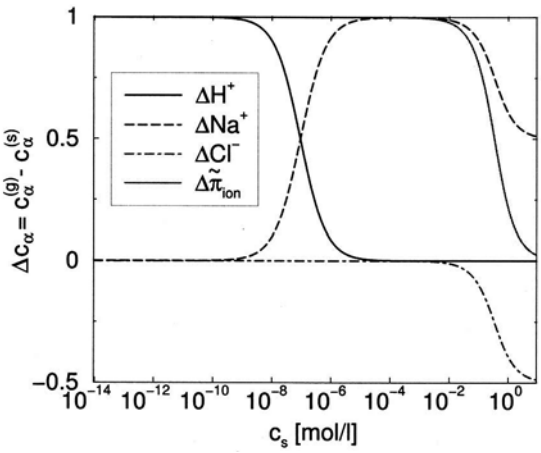

Figure 8. Concentration differences Δc_α between gel and solution versus the salt concentration c_s for an anionic gel ($c_{A^-} = 1\,mol/l$)

The whole behavior confirms the investigations by Ohmine and Tanaka (1982).

With the computed concentrations, the normalized differential osmotic pressure in Fig. 8 given by

$$\Delta\tilde{\pi}_{ion} = \tilde{\pi}_{ion}^{(g)} - \tilde{\pi}_{ion}^{(s)} = \sum_\alpha \left(c_\alpha^{(g)} - c_\alpha^{(s)} \right) \tag{2.46}$$

is maximal for $c_s < 10^{-4}\,mol/l$. A further increase of the salt concentration leads to a decrease of $\Delta\tilde{\pi}_{ion}$; for high c_s the osmotic pressure is reaching the value zero.

2.3.1.2 Ion concentrations with change of swelling ratio

In this section, the change of the ion concentrations with the variation of the swelling ratio is investigated. In order to obtain the desired results, the statistical theory with the elastic potential Eq. (2.12), mixture potential Eq. (2.6) and the mobile ion potential Eq. (2.23) as well as the Donnan equation and the condition of neutrality where

$$c_{A^-}^{(g)} = \frac{c_{M,0}}{q} \tag{2.47}$$

have been used.

In order to describe the behavior of PAAm/PAMPS-gels realistically, the parameters for the numerical simulation have been chosen as $\nu_e/V_0 = 0.233\,mol/l$, $\nu_1 = 0.018\,l/mol$, $\chi = 0.4$ and $c_{M,0} = 4\,mol/l$.

The swelling ratio $q = V/V_0$ versus the salt concentration c_s is plotted in Fig. 9 (top right). It can be seen that for small salt concentrations a maximal swelling of $q \approx 76$ is obtained. The increase of c_s leads to a decrease of the swelling ratio and also of the osmotic pressure. The

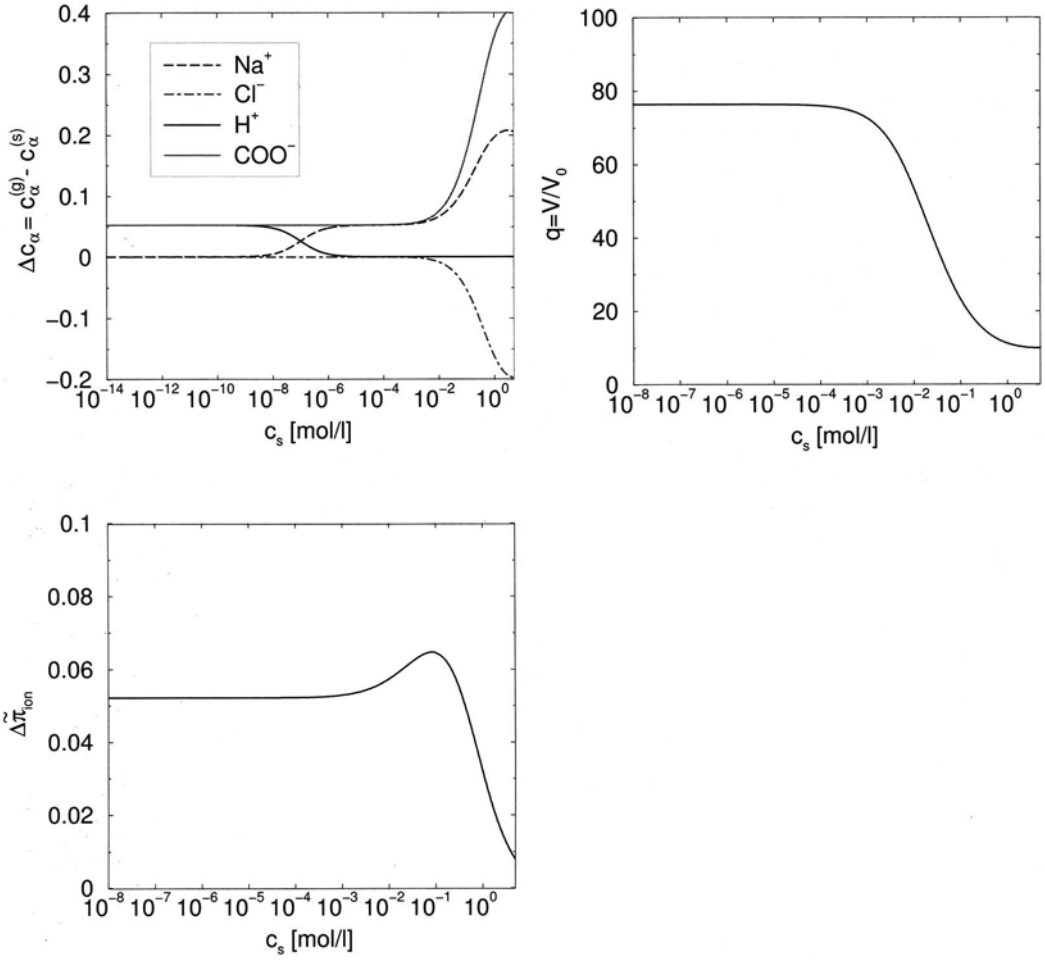

Figure 9. Difference of the ion concentrations between gel and solution (top left); swelling ratio (top right); normalized differential osmotic pressure (bottom)

minimal value of the swelling ratio for large salt concentrations is $q = 12$ which can be regarded as the value of the preswelling of the gel.

Taking account of the swelling, the ion concentrations are depicted in Fig. 9 (top left). For small salt concentrations c_s we obtain the same behavior as in Fig. 8. Due to the decrease of the swelling for large c_s we obtain an increase of the bound anionic groups and this results in an increase of the other (cationic) concentrations in the gel.

The differential osmotic pressure, depicted in Fig. 9 (bottom), shows the same (qualitative) behavior as in Fig. 8.

2.3.1.3 Ion concentrations with change of swelling ratio and variable dissociation

In this testcase, the swelling ratio of polymer gels with variable dissociation of the anionic groups is investigated. The underlying equations are the same as in the last subsection. Additionally, the dissociation with given dissociation constant K_a

$$K_a = \frac{c^{(g)}_{H^+} c^{(g)}_{A^-}}{c^{(g)}_{HA}} \qquad \text{where:} \qquad \frac{c_{M,0}}{q} = c^{(g)}_{HA} + c^{(g)}_{A^-}$$

has been used. This testcase is used in order to describe some experimental results, e.g. a smaller swelling for minimal salt concentration, which could not be explained up to now. Therefore, a fixed number of bound groups $c_{M,0} = q \cdot (c^{(g)}_{HA} + c^{(g)}_{A^-}) = 4 mol/l$ as well as the dissociation constant $K_a = 10^{-5} mol/l$ have been given.

In Fig. 10 (top), the concentration differences between gel and solution are given: The result depends on the actual ratio of dissociated rest groups (see Fig. 10 (middle left)) $\widetilde{c}_{A^-} = c_{A^-}/(c_{A^-} + c_{HA})$ which is dependent on K_a and was $1 = const$ in the last testcase. For $c_s < 10^{-7} mol/l$ the normalized dissociation $\widetilde{c}_{A^-}$ is smaller than 1%. Increasing c_s leads to an increase of the normalized dissociation; for $c_s \approx 10^{-2} mol/l$, $\widetilde{c}_{A^-}$ is approx. 1, i.e. nearly complete dissociation. The run of the curve can be explained by a small number of H^+ ions for small c_s. Since

$$K_a = \frac{c^{(g)}_{H^+} c^{(g)}_{A^-}}{c^{(g)}_{HA}} \tag{2.48}$$

a small $c^{(g)}_{A^-}/c^{(g)}_{HA}$ number is obtained and this results in a reduced swelling ratio compared to the last testcase.

The swelling ratio, depicted in Fig. 10 (middle right), can be seen as superposition of the swelling ratio in the last testcase, Fig. 9 and the dissociation ratio; i.e. for small salt concentrations, only for a normalized dissociation $\widetilde{c}_{A^-} > 10\%$, a relevant increase of the swelling ratio can be seen. For complete dissociation, the swelling ratio reaches the same value as in the last testcase.

The ion concentrations can be interpreted as a superposition of the concentrations (testcase Sec. 2.3.1.1) multiplied with the run of the curve for the dissociation and the inverse of the swelling.

2.3.2 Comparison between theory and experiments

In this section we present a comparison between experimental results and the ones calculated by the theory described in this chapter.

The swelling behavior is investigated for two different gel species:

- Polyacrylamid-Polyacrylmethylsulfid-acid (PAAm/PAAMPS)-gel consisting of strong acid, i.e. nearly complete dissociated anionic groups, see Fig. 11 (left)
- Polyacrylamid-Polyacrylacid (PAAm/PAA)-gel consisting of weak acid, Fig. 11 (right)

The parameters used for the numerical simulation are given in Tab. 3.

As we can see in Fig. 11, the numerical and experimental results match quite well for PAAm/-PAMPS as well as for PAAm/PAA-gels.

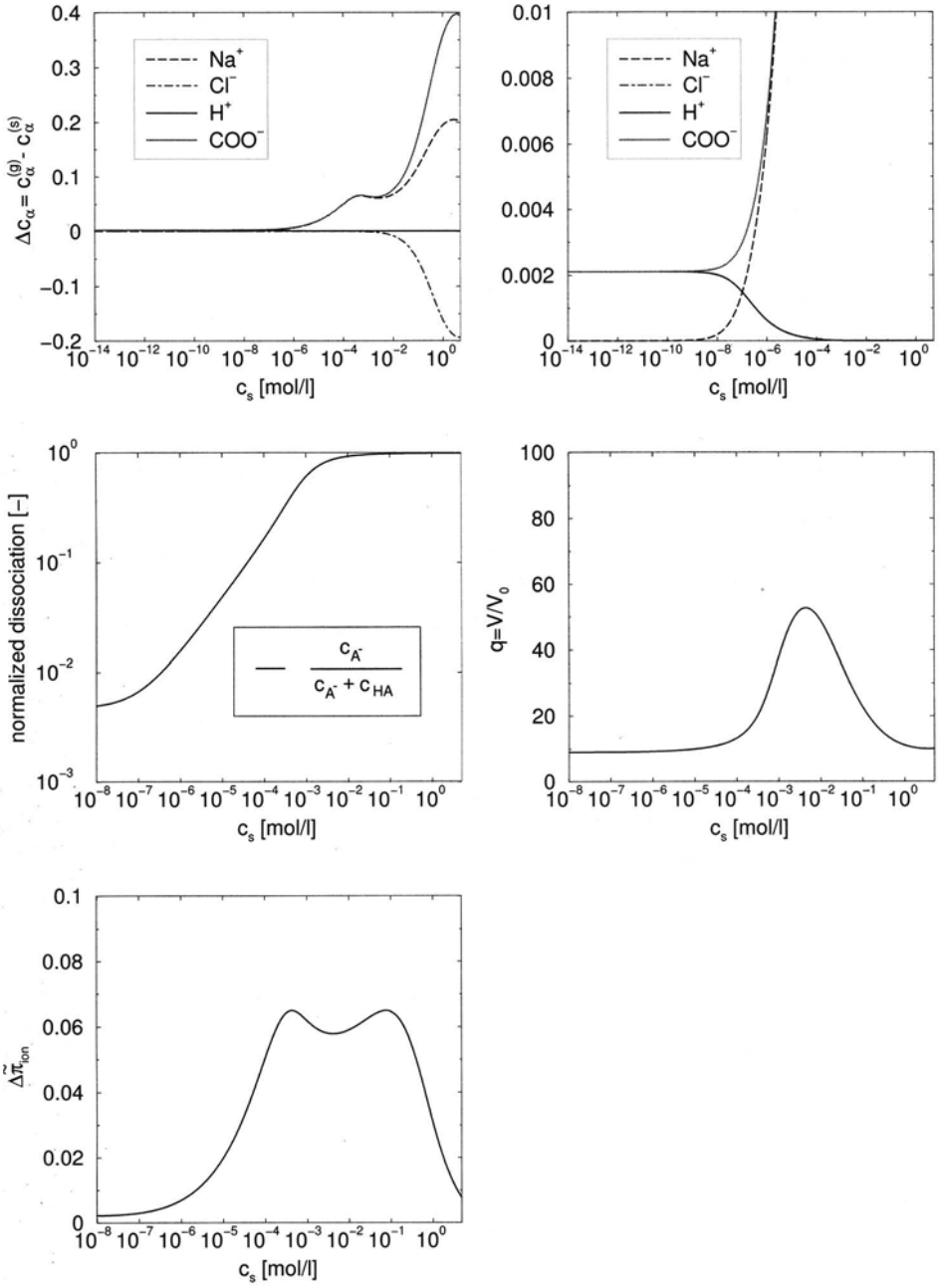

Figure 10. Difference of the ion concentrations between gel and solution (top left), in detail (top right); dissociated ratio of the fixed charges (middle left); swelling ratio (middle right); normalized differential osmotic pressure (bottom)

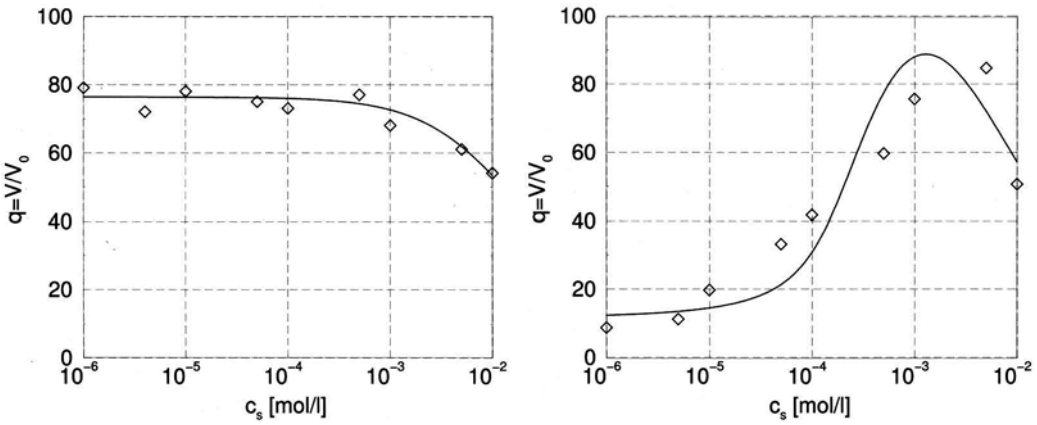

Figure 11. Comparison of measured ($\diamond$) and calculated ($-$) stationary swelling ratio q of PAAm/-PAMPS- (left) and PAAm/PAA gel (right) at variable salt concentration c_s. The experimental measured swelling ratios have been published by Gülch et al. (2000)

Table 3. Material parameters for the simulation of PAAm/PAMPS- and PAAm/PAA-gel

			PAAm/PAMPS-Gel	PAAm/PAA-Gel
molar volume of the solvent	v_1	$[l/mol]$	0.018	0.018
anionic rest groups in the reference state	$c_{M,0}$	$[mol/l]$	4	2
normalized material parameter	$\frac{\nu_e}{V_0}$	$[mol/l]$	0.2330	0.080
Flory-Huggins parameter	χ	$[-]$	0.4	0.44
dissociation constant	K_a	$[mol/l]$	∞	10^{-5}

2.3.3 Variation of pH

The pH-value is defined by the negative logarithm of the concentration of protons per $1\,mol/l$:

$$pH = -\lg \frac{[H^+]}{1\,mol/l} \tag{2.49}$$

This means, that a proton concentration of $10^{-7}\,mol/l$ equals $pH = 7$. In an acidic solution, c_{H^+} is larger than $10^{-7}\,mol/l$, i.e. $pH < 7$; in an alkaline solution, pH is lager than 7. Note,

$$pH + pOH = 14 \tag{2.50}$$

In this section, the theoretical and experimental swelling behavior of PAN (polyacrylnitrile) gels are compared. PAN gels are ampholytic gels, i.e. they have anionic and cationic fixed groups. Due to the very small number of cationic groups, in the numerical simulation they are neglected.

In the experiment, the different pH values have been made by dilution of a 1-molar HCl-solution and for $pH > 7$ of a $NaOH$-solution. In the numerical simulation, the prescribed concentrations in the gel-surrounding solution have been chosen as

$$[H^+] = [Cl^-] = 10^{-pH}\, mol/l$$
$$[OH^-] = [Na^+] = 10^{-(14-pH)}\, mol/l \tag{2.51}$$

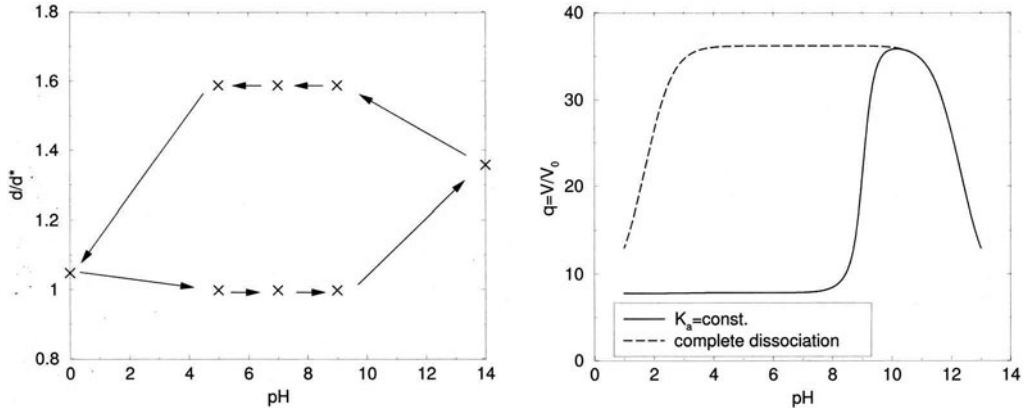

Figure 12. Experimentally measured isotonic elongation of a PAN fiber (left) and numerically obtained swelling (right) for various pH

In Fig. 12 (left), a representative cycle of the experimentally measured isotonic elongation of a PAN fiber is plotted. A numerical simulation using the presented model gives the result plotted in Fig. 12 (right).

The simulation has been performed with $K_a = \infty$ for complete dissociation and with $K_a = 10^{-5}\, mol/l$. In the testcase with complete dissociation a symmetry to $pH = 7$ is obtained. Increasing or decreasing of pH leads to an increase of the ion concentration in the solution, see Eq. (2.51). For large concentrations in the solution bath, the number of fixed charged groups does not play an important role; the differential osmotic pressure is decreasing and a reduced swelling ratio is obtained.

For the testcase where $K_a = 10^{-5}\, \frac{mol}{l}$, a small concentration of COO^- ions is obtained according to

$$[COO^-] = K_a \frac{[COOH]}{[H^+]} \tag{2.52}$$

for small pH due to the large number of protons in gel and solution. This results in a decreased swelling ratio. For large pH, the concentration of H^+ ions is reduced, i.e. the anionic rest groups are almost completely dissociated. Therefore, the same swelling ratio as in the testcase with complete dissociation is obtained.

3 Coupled Chemo-electro-mechanical Multi-Field Formulation

Although there are various chemical and physical kinds of stimulation, due to simplicity, the electrical stimulation plays a central role in technical applications.

The dynamic behavior of ionic polymer gels in electric fields has been investigated quasi-statically by Doi et al. (1992), Shiga and Kurauchi (1990) and Shahinpoor (1995). Brock et al. (1994) have given a coupled formulation for the ion-dynamics and a theory for large displacements. Nemat-Nasser and Li (2000) have presented an electro-mechanical model for ionic polymer metal composites, while Neubrand (1999), Grimshaw et al. (1990), deGennes et al. (2000) and Wallmersperger et al. (2001) have published electro-chemical and electro-mechanical formulations for ion-exchange membranes and ionic gels.

In this section, a coupled chemo-electro-mechanical multi-field formulation will be presented to obtain a more precise insight into the phenomena occurring in polyelectrolyte gels, see also Wallmersperger (2003). The ion concentrations and the electric field can be calculated by the chemical and electrical field equations. Based on the concentration differences, the swelling behavior of the polymer gels can be described by the mechanical field equation.

3.1 Chemical Field

The chemical field is described by the convection-diffusion equation for all the species α

$$\dot{c}_\alpha = \left[D_\alpha c_{\alpha,i} + z_\alpha c_\alpha \mu_\alpha \Psi_{,i} \right]_{,i} - (c_\alpha v_i)_{,i} + r_\alpha(c_\alpha) \tag{3.1}$$

where:
- c_α : concentration of the species α
- D_α : diffusion constant
- μ_α : unsigned mobility
- z_α : valence of the ions
- Ψ : electric potential
- $\mathbf{v}$: convective velocity
- r_α : source term resulting from the chemical conversion

The equation consists of

- a diffusive term resulting from the concentration gradients
- a migrative term which stems from the gradient in the electric potential
- a convective term which originates from an applied convection of the solvent
- and a source term.

The convection-diffusion equation (3.1) is an elliptic PDE of first order in time representing the conservation of mass and charge.

3.2 Electric Field

The electric field is described by the Poisson equation

$$\Psi_{,ii} = -\frac{F}{\epsilon_r \epsilon_0} \sum_{\alpha=1}^{N_f+N_b} (z_\alpha c_\alpha) \tag{3.2}$$

where:
- ϵ_0 : permittivity of free space; $\epsilon_0 = 8.8542 \cdot 10^{-12} As/(Vm)$
- ϵ_r : dielectric constant
- F : Faraday constant; $F = N_A \cdot e = 96487 C/mol$
- N_f : number of freely movable species
- N_b : number of bound species

The electric field equation (3.2) is an elliptic PDE in space. The velocity of wave-propagation is much higher in the electric field than in the chemical field. Hence, the quasi-static form of the Poisson equation is sufficient. Equation (3.2) is based on the second and fourth Maxwell equation.

The condition of neutrality

$$\sum_{\alpha=1}^{N_f+N_b} (z_\alpha c_\alpha) = 0 \tag{3.3}$$

is obtained when $\Psi_{,ii}$ in Eq. (3.2) is identical to zero. This condition is satisfied in the whole domain (gel and solution) outside the small region of the boundary layer.

3.3 Mechanical Field

Usually, dynamic processes are described by partial differential equations of second order in time. Due to the relatively slow swelling process, the influence of the inertia term is very small; the term of second order in time is therefore neglected. Hence, the mechanical field is described by a PDE of first order in time.

$$f \dot{u}_i = \sigma_{ij,j} + \rho b_i \tag{3.4}$$

$$\sigma_{ij} = C_{ijkl} \cdot (\epsilon_{kl} - \bar{\epsilon}_{kl}) \tag{3.5}$$

where:
- $\boldsymbol{\sigma}$: stress tensor
- $\boldsymbol{\epsilon}$: strain tensor
- $\bar{\boldsymbol{\epsilon}}$: prescribed strain
- $\mathbf{u}$: displacement unknowns
- $\mathbf{C}$: elasticity tensor
- f : friction coefficient
- $\mathbf{b}$: body forces

3.4 Coupling

The force equilibrium in the gel network can be given by the electrostatic forces, the osmotic forces, the cohesion between polymer and solvent and the viscoelastic restoring forces. All these forces can be seen as contributions to a prescribed strain $\bar{\epsilon}$.

In our model we restrict to the concentration differences between gel and solution resulting in an osmotic pressure difference. This differential osmotic pressure can be given as

$$\Delta\pi = RT \sum_{\alpha=1}^{N_f} (c_\alpha^{(s)} - c_\alpha^{(g)}) \tag{3.6}$$

The normalized form as a measure for the local swelling can be expressed by

$$\Delta\widetilde{\pi} = -\frac{\Delta\pi}{RT} = \sum_{\alpha=1}^{N_f} \left(c_\alpha^{(g)} - c_\alpha^{(s)}\right) \tag{3.7}$$

From Eq. (3.5) follows

$$\sigma_{ij} = C_{ijkl}\,(\epsilon_{kl} - \bar{\epsilon}_{kl}) \qquad \text{where} \qquad \bar{\epsilon}_{kl} = \widetilde{const}_{kl}\,\Delta\widetilde{\pi} \tag{3.8}$$

So, the prescribed strain $\bar{\epsilon}$ can be given by the normalized osmotic pressure $\Delta\widetilde{\pi}$ multiplied by the material parameters $\widetilde{\mathbf{const}}$.

3.5 Coupling Strategy

The chemo-electro-mechanical multi-field formulation consists of a system of coupled PDEs:

- the convection-diffusion equation (3.1) for the concentrations c_α of all species α,
- the Poisson equation (3.2) for the electric potential Ψ,
- and the equation of motion (3.4) for the displacement unknowns u.

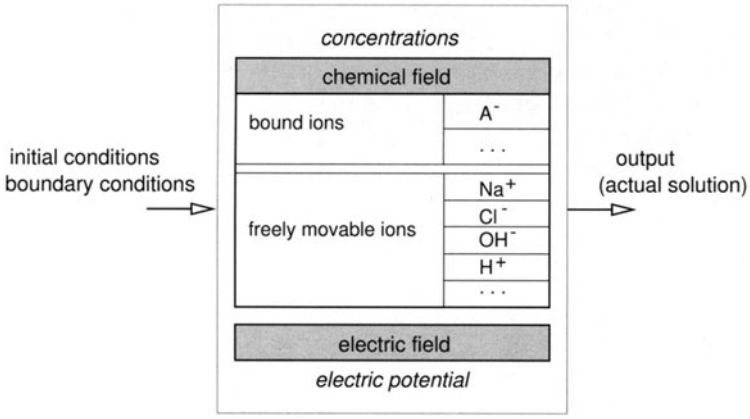

Figure 13. Chemo-electric coupling scheme

Considering the coupled chemo-electric field only, for the $(N_f + N_b)$ concentration unknowns and for the unknown electric potential, the $(N_f + N_b)$ convection-diffusion equations and the Poisson equation are solved simultaneously, see Fig. 13. The characteristics of the coupled formulation are given in Tab. 4.

Table 4. Characteristics of the coupled chemo-electric formulation

unknowns/equations		*Number*	*Eq.no.*
concentration	c_α	$N_f + N_b$	
electric potential	Ψ	1	
electric current density	j	(1) postprocessing	
convection-diffusion equation		$N_f + N_b$	Eq. (3.1)
neutrality condition		0	Eq. (3.3)
Poisson equation		1	Eq. (3.2)
Faraday equation		(1) postprocessing	Eq. (5.1)
transition conditions			
concentration gel-solution		no	
electric potential		no	
features		one integration domain for gel and solution	

In order to obtain the deformation of the gel, the equation of motion has to be solved subsequently to the chemo-electric field, see Fig. 14. The differential osmotic pressure, resulting from the concentration differences of the mobile ions at the gel-solution interface has to be used as an input for the equation of motion. This pressure difference can be regarded as an external force or as a kind of prescribed strain inside the gel.

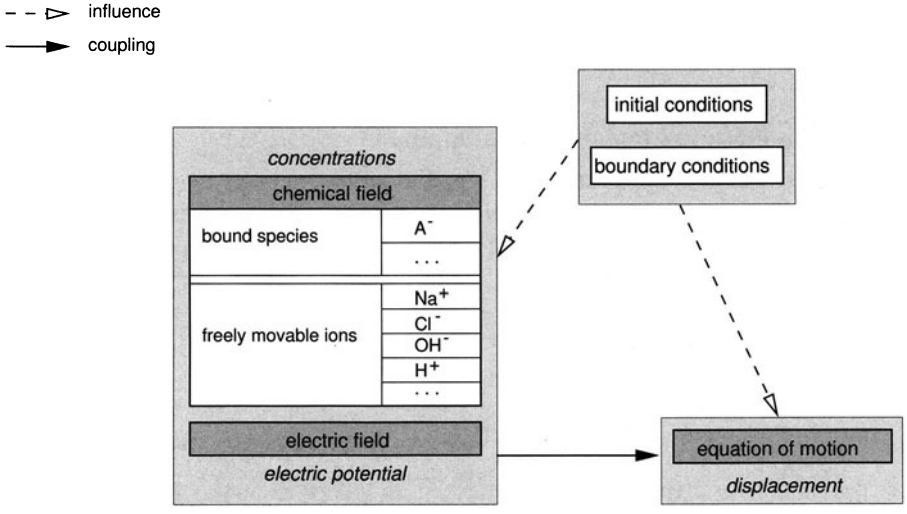

Figure 14. Chemo-electro-mechanical coupling scheme

4 DISCRETIZATION

The finite element method (FEM) has been used for elliptic problems in space since many years. Nevertheless, for transient computations semi-discrete methods using FEM in space and independent time-stepping schemes are most commonly applied. A more natural approach applies finite element discretization for both space and time. The methodology has been investigated for elastodynamics (Hughes and Hulbert, 1988), structural dynamics (Hulbert, 1992) and general second order hyperbolic problems (Johnson, 1993). They employ time-discontinuous Galerkin (TDG) finite elements which yield implicit and unconditionally stable and higher order accurate discretization. Furthermore, in recent years much progress has been made in the computation of fluid flow using stabilized finite elements (Hughes et al., 1994; Johnson, 1985). While the Galerkin/least-squares stabilization has originally been developed for flow problems (Hughes et al., 1989), it has been also applied to elastodynamics (Hughes and Hulbert, 1988), structural dynamics (Hulbert, 1992) and general sets of Hamilton-Jacobi and level set equations (Barth and Sethian, 1997). Thompson (1995) has applied the stabilized TDG approach for structural acoustics problems in infinite domains and has successfully conducted the stability and convergence analysis of the coupled problem. Stabilized space-time finite elements have also been applied to aeroelasticity (Grohmann, 2002) employing the deforming-spatial-domain/space-time (DSD/ST) procedure in order to handle the deforming fluid domains (Tezduyar and Behr, 1992).

The scope of the present paper is the development of a general framework of space-time discretization schemes for the treatment of multi-physics problems involving PDEs of different order in time which cover a wide class of relevant problems in physics and engineering. The general formulations including error analysis for PDEs of first and second order in time are introduced in section 4.2 and 4.3, respectively. A new single-field formulation for PDEs of second order in time is developed in section 4.3.3.

Note, parts of this chapter have been taken from the paper "Time-Discontinuous Stabilized Space-Time Finite Elements for PDEs of First- and Second-Order in Time" presented by Wallmersperger et al. (1999) at the ECCM'99

4.1 Space-Time Finite Element Formulation

For the discretization in space and time of partial differential equations (PDEs) of first and second order in time, the implicit, unconditionally stable time-discontinuous Galerkin (TDG) method is applied. For this purpose, both the trial solutions $\mathbf{U}_h$ and the weighting functions $\mathbf{W}_h$ are approximated by kth-order polynomials $\mathcal{P}_k$. These are assumed to be H^1 functions and C^0 continuous within each space-time slab $Q_N = I_N \times \Omega(t)$ where $I_N = \{t | t_n \leq t \leq t_{n+1}\}$, but may be discontinuous in time between adjacent time slabs, see Fig. 15. Thus, $\mathbf{U}_h \in \mathcal{U}_h$ and $\mathbf{W}_h \in \mathcal{W}_h$ belong to the Sobolev spaces

$$\mathcal{U}_h = \left\{ \mathbf{U}_h | \mathbf{U}_h \in [C^0(Q_N)]^{n_{\text{dof}}}, \mathbf{U}_h|_{Q_N^e} \in [\mathcal{P}_k(Q_N^e)]^{n_{\text{dof}}}, \mathbf{U}_h = \mathbf{g}(t) \text{ on } P_{g_h} \right\}$$

$$\mathcal{W}_h = \left\{ \mathbf{W}_h | \mathbf{W}_h \in [C^0(Q_N)]^{n_{\text{dof}}}, \mathbf{W}_h|_{Q_N^e} \in [\mathcal{P}_k(Q_N^e)]^{n_{\text{dof}}}, \mathbf{W}_h = \mathbf{0} \text{ on } P_{g_h} \right\}$$

with the number of degrees of freedom n_{dof}. Dirichlet boundary conditions $\mathbf{U} = \mathbf{g}(t)$ are imposed on the boundary $P_{g_h} = I_N \times \Gamma_{g_h}(t)$. In order to deal with problems including deforming domains, space-time interpolations may also be used for the finite element geometry. In this case, the

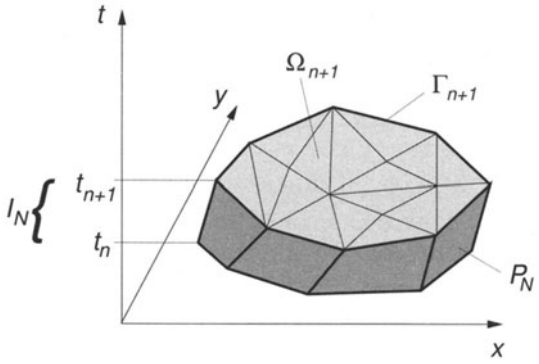

Figure 15. Space-Time Domain

space-time finite element method gives a natural framework to treat the domain deformation (Tezduyar and Behr, 1992) without the formal complexity of an arbitrary Lagrange-Euler (ALE) formulation.

4.2 PDEs of First Order in Time

Typical physical problems involving PDEs of first order in time deal with the conservation of mass, momentum or energy. These conservation laws may be written as

$$\widetilde{\mathbf{U}}_{,t} + \mathbf{F}^{conv}_{i,i} - \mathbf{F}^{diff}_{i,i} - \mathcal{S} = \mathbf{0} \tag{4.1}$$

$$\widetilde{\mathbf{U}}_{,t} + \mathbf{A}^{conv}_{i}\widetilde{\mathbf{U}}_{,i} - (\mathbf{A}^{diff}_{ij}\widetilde{\mathbf{U}}_{,j})_{,i} - \mathcal{S} = \mathbf{0} \tag{4.2}$$

where $\widetilde{\mathbf{U}}$ denotes the vector of conserved quantities, $\mathbf{F}^{conv}_{i}$ the convective flux, $\mathbf{F}^{diff}_{i}$ the diffusive flux with the corresponding Jacobians $\mathbf{A}^{conv}_{i}$ and $\mathbf{A}^{diff}_{ij}$ and $\mathcal{S}$ the source vector. On the domain boundaries appropriate boundary conditions have to be applied. If the convection-diffusion equation Eq. (4.2) is written in terms of variables $\mathbf{U}$ differing from the conservation variables $\widetilde{\mathbf{U}}$ the differential form

$$\mathbf{B}_0\mathbf{U}_{,t} + \mathbf{B}^{conv}_{i}\mathbf{U}_{,i} - (\mathbf{B}^{diff}_{ij}\mathbf{U}_{,j})_{,i} - \mathcal{S} = \mathbf{0} \tag{4.3}$$

is obtained, where $B_0 = \frac{\partial\widetilde{\mathbf{U}}}{\partial\mathbf{U}}$. Note, generally the matrices $\mathbf{A}^{conv}_{i}$, $\mathbf{A}^{diff}_{ij}$, $\mathbf{B}_0$, $\mathbf{B}^{conv}_{i}$ and $\mathbf{B}^{diff}_{ij}$ are non-symmetric. In order to investigate the characteristics of the TDG timestepping scheme, the system of ordinary differential equations (ODEs) in time

$$\mathbf{C}\dot{\mathbf{u}} + \mathbf{K}\mathbf{u} - \mathbf{f} = \mathbf{0}, \tag{4.4}$$

which is obtained by integration of Eq. (4.3) in space, is introduced.

4.2.1 Time-Discontinuous Galerkin Method

The time-discontinuous Galerkin (TDG)-formulation of Eq. (4.4) is given as

$$\int_{I_N} \mathbf{w}^T \cdot \{\mathbf{C}\dot{\mathbf{u}} + \mathbf{K}\mathbf{u} - \mathbf{f}\}\, dt + \mathbf{w}^T|_n^+ \{\mathbf{C}\mathbf{u}|_n^+ - \mathbf{u}|_n^-\} = \mathbf{0}. \tag{4.5}$$

The first term represents the weak form in time of the differential equation, the second term - the temporal jump term or temporal jump residuum (TJR) - enforces the continuity of the unknowns **u** between subsequent time slabs. Generally, a TJR-term appears for every time-derivative in the underlying differential equation.

4.2.1.1 TDG-Error Analysis

For the error analysis of the system of ODEs Eq. (4.4), the scalar equation

$$c\dot{u} + ku = 0 \tag{4.6}$$

using the initial condition $u(t=0) = u_0$ is considered.

Table 5. PDE of 1st-Order in Time: Comparison of the TDG with different interpolations

method	interpolation of u	error		unknowns
		u	$\dot{u}$	
TDG-P0	constant	$\sim \Delta t$		1
TDG-P1	linear	$\sim \Delta t^3$	$\sim \Delta t$	2
TDG-P2	quadratic	$\sim \Delta t^5$	$\sim \Delta t^2$	3

In Fig. 16, the error of the displacement u and the velocity $\dot{u}$ of the TDG-solution with respect to the exact solution after $t = 10\frac{c}{k}$ is plotted. Different interpolations are used, where Pi denotes the TDG formulation employing i-th order polynomials $\mathcal{P}^i$ in time for the displacement u. In Tab. 5, it can be seen that the error for the displacement u is $\sim \Delta t^{2i+1}$ and for the velocity $\dot{u}$ is $\sim \Delta t^i$. It should be noted that considering PDEs of first-order in time, usually only displacement-unknowns are of interest and for this reason the decrease of accuracy of the velocities is irrelevant.

4.2.2 Galerkin/Least-Squares Stabilization

In order to stabilize the formulation, especially in the case of non-symmetric coefficient matrices, e.g. resulting from convection dominated problems, an additional Galerkin/least-squares (GLS) operator is introduced. When added to the standard TDG Eq. (4.5), this operator minimizes the square of the residual and for this reason spurious oscillations are suppressed.

The GLS-formulation of the differential equation of first order in time Eq. (4.4) is given as

$$\int_{I_N} \mathbf{w}^T \{\mathbf{C}\dot{\mathbf{u}} + \mathbf{K}\mathbf{u} - \mathbf{f}\} + \{\tau \mathcal{L}^T \mathbf{w}\}^T \{\mathcal{L}\mathbf{u} - \mathbf{f}\}\, dt + \mathbf{w}^T|_n^+ \{\mathbf{C}\mathbf{u}|_n^+ - \mathbf{C}\mathbf{u}|_n^-\} = \mathbf{0} \tag{4.7}$$

where

$$\mathcal{L}\mathbf{u} := \mathbf{C}\dot{\mathbf{u}} + \bar{\mathbf{K}}\mathbf{u}. \tag{4.8}$$

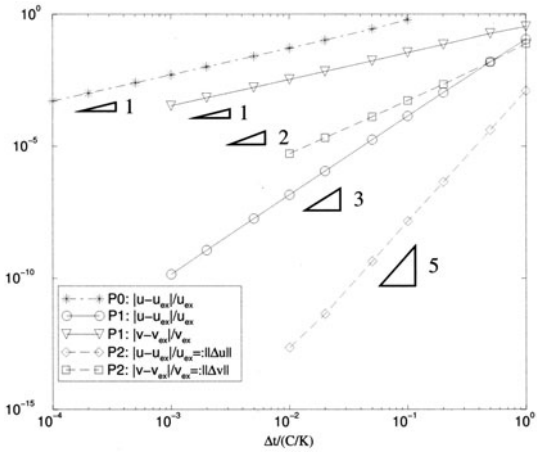

Figure 16. PDE of 1st-Order in Time: Error of displacement u and velocity $v = \dot{u}$ of the TDG method with different interpolations at $t = 10\frac{c}{k}$

Both $\mathbf{K}$ and $\bar{\mathbf{K}}$ represent the spatial operators of the underlying PDE integrated in space. Note, $\mathbf{K}$ has been integrated by parts and the resulting boundary terms have been dropped for conciseness. The definition of the matrix of intrinsic time scales $\boldsymbol{\tau}$ can be taken from Shakib (1988), Soulaimani and Fortin (1994)

$$\boldsymbol{\tau} = \left\{ \left\| \frac{\partial \tau}{\partial t} \mathbf{C} \right\|^m + \|\mathbf{K}\|^m \right\}^{-\frac{1}{m}} \tag{4.9}$$

In the case of hyperbolic partial differential equations where the solution may contain discontinuities or sharp gradients, a nonlinear discontinuity capturing operator may be added to the formulation in order to suppress spurious oscillations (Shakib, 1988).

4.2.2.1 GLS-Error Analysis

In order to investigate the accuracy of the GLS-formulation, the same scalar ODE Eq. (4.6) as for the TDG is considered. The intrinsic time scale $\tau = \frac{1}{c\frac{2}{\Delta t}+k}$ is used. The resulting GLS-formulation is obtained

$$\begin{aligned} &\int_{I_N} w^T \{c\dot{u} + ku\}\, dt + w^T|_n^+ \{cu|_n^+ - cu_n|^-\} \\ &+ \int_{I_N} \{c\dot{w} + kw\}^T \cdot \left(\frac{1}{c\frac{2}{\Delta t}+k} \right) \cdot \{c\dot{u} + ku\}\, dt \end{aligned} \tag{4.10}$$

In Fig. 17, the error of the displacement u after $t = 10\frac{c}{k}$ using different interpolations for the *TDG*- and *GLS*-formulation is plotted. The error of the displacement u of the TDG using i-th

order polynomials $\mathcal{P}^i$ is $\sim \Delta t^{2i+1}$ and of the GLS the order of convergence is one order lower, i.e. the error is $\sim \Delta t^{2i}$.

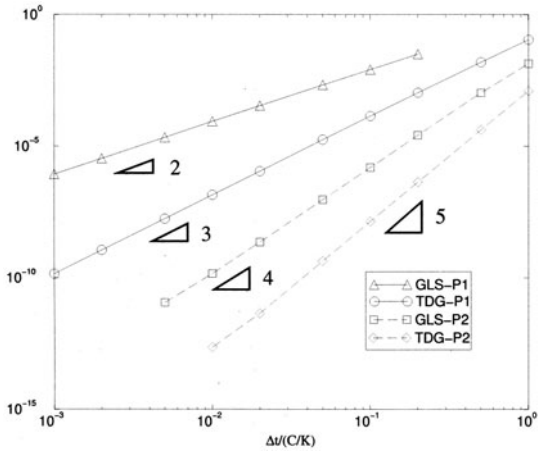

Figure 17. PDE of 1st-Order in Time: Error of displacement u of the TDG- and GLS-method with different interpolations at $t = 10\frac{c}{k}$

4.3 PDEs of Second Order in Time

In structural dynamics and elastodynamics typical problems are governed by partial differential equations of second order in time like the momentum equation

$$\rho\ddot{\mathbf{U}} - \nabla \cdot \boldsymbol{\sigma}(\nabla \mathbf{U}) - \mathbf{f} = \mathbf{0} \tag{4.11}$$

with the displacements $\mathbf{U}$, the stress $\boldsymbol{\sigma}(\nabla \mathbf{U})$ as well as the forcing-term $\mathbf{f}$ and appropriate boundary conditions. Discretization of Eq. (4.11) in space and including structural damping yields the equation of motion in the semi-discrete matrix form

$$\mathbf{M}\ddot{\mathbf{u}} + \mathbf{C}\dot{\mathbf{u}} + \mathbf{K}(\mathbf{u})\mathbf{u} - \mathbf{f} = \mathbf{0}. \tag{4.12}$$

4.3.1 Two-Field-Formulation

Introducing independent variables for the displacement and velocity unknowns $\mathbf{u}$ and $\mathbf{v}$, the system of differential equations of second order in time Eq.(4.12) may be transformed into a system of differential equations of first order in time

$$\dot{\mathbf{u}} - \mathbf{v} = \mathbf{0} \tag{4.13}$$

$$\mathbf{M}\dot{\mathbf{v}} + \mathbf{C}\mathbf{v} + \mathbf{K}\mathbf{u} - \mathbf{f} = \mathbf{0}. \tag{4.14}$$

Now, the TDG methodology Eq. (4.5) for first order PDEs in time

$$\int_{I_N} \widetilde{\mathbf{w}}^T \cdot \{\widetilde{\mathbf{C}}\dot{\widetilde{\mathbf{u}}} + \widetilde{\mathbf{K}}\widetilde{\mathbf{u}} - \widetilde{\mathbf{f}}\}\, dt + \widetilde{\mathbf{w}}^T|_n^+ \{\widetilde{\mathbf{C}}\widetilde{\mathbf{u}}|_n^+ - \widetilde{\mathbf{C}}\widetilde{\mathbf{u}}|_n^-\} = \mathbf{0} \tag{4.15}$$

may be applied using the definitions

$$\widetilde{\mathbf{u}} =: \begin{bmatrix} \mathbf{u} \\ \mathbf{v} \end{bmatrix}; \quad \widetilde{\mathbf{w}} =: \begin{bmatrix} \mathbf{w}_1 \\ \mathbf{w}_2 \end{bmatrix}; \quad \widetilde{\mathbf{C}} =: \begin{bmatrix} \mathbf{K} & \mathbf{0} \\ \mathbf{0} & \mathbf{M} \end{bmatrix}; \quad \widetilde{\mathbf{K}} =: \begin{bmatrix} \mathbf{0} & -\mathbf{K} \\ \mathbf{K} & \mathbf{C} \end{bmatrix}; \quad \widetilde{\mathbf{f}} =: \begin{bmatrix} \mathbf{0} \\ \mathbf{f} \end{bmatrix}.$$

This yields the two-field TDG-formulation for PDEs of second order in time

$$\begin{aligned} \int_{I_N} [\mathbf{w}_1, \mathbf{w}_2]^T \cdot \left\{ \begin{bmatrix} \mathbf{K} & \mathbf{0} \\ \mathbf{0} & \mathbf{M} \end{bmatrix} \begin{bmatrix} \dot{\mathbf{u}} \\ \dot{\mathbf{v}} \end{bmatrix} + \begin{bmatrix} \mathbf{0} & -\mathbf{K} \\ \mathbf{K} & \mathbf{C} \end{bmatrix} \begin{bmatrix} \mathbf{u} \\ \mathbf{v} \end{bmatrix} - \begin{bmatrix} \mathbf{0} \\ \mathbf{f} \end{bmatrix} \right\} dt \\ + [\mathbf{w}_1, \mathbf{w}_2]^T|_n^+ \left\{ \begin{bmatrix} \mathbf{Ku} \\ \mathbf{Mv} \end{bmatrix}_n^+ - \begin{bmatrix} \mathbf{Ku} \\ \mathbf{Mv} \end{bmatrix}_n^- \right\} = \mathbf{0} \end{aligned} \tag{4.16}$$

The second hyper row of the domain integral represents the equation of motion Eq. (4.14) whereas the first hyper row enforces Eq. (4.13) in weak sense. The last term, the TJR, enforces the continuity for the displacement $\mathbf{u}$ and the velocity $\mathbf{v}$ between subsequent time slabs. It can also be interpreted as continuity of kinetic and potential energy between subsequent time slabs.

4.3.2 Previously Developed Single-Field Formulation

The single-field time-discontinuous Galerkin formulation for structural dynamics (Hulbert, 1989, 1992) is based on the principle of virtual power

$$\begin{aligned} \int_{I_n} \dot{\mathbf{w}}^T \cdot \{\mathbf{M}\ddot{\mathbf{u}} + \mathbf{C}\dot{\mathbf{u}} + \mathbf{K}\mathbf{u} - \mathbf{f}\}\, dt \\ + \mathbf{w}^T|_n^+ \{\mathbf{Ku}|_n^+ - \mathbf{Ku}|_n^-\} + \dot{\mathbf{w}}^T|_n^+ \{\mathbf{M}\dot{\mathbf{u}}|_n^+ - \mathbf{M}\dot{\mathbf{u}}|_n^-\} = \mathbf{0} \end{aligned} \tag{4.17}$$

The integral represents the weak form of the equation of motion inside the time slab, whereas the second and third terms, the temporal jump terms or temporal jump residua, enforce the continuity of the potential and kinetic energy between subsequent time slabs.

4.3.3 New Single-Field Formulation

The new single field formulation may be derived from the two-field formulation Eq. (4.16) by setting $\dot{\mathbf{u}} - \mathbf{v} = \mathbf{0}$ in strong sense. The first hyper row of Eq. (4.16)

$$\int_{I_n} \mathbf{w}_1^T \mathbf{K} \underbrace{\{\dot{\mathbf{u}} - \mathbf{v}\}}_{=0}\, dt + \mathbf{w}_1^T|_n^+ \underbrace{\{\mathbf{Ku}|_n^+ - \mathbf{Ku}|_n^-\}}_{\Rightarrow \quad =0} = \mathbf{0} \tag{4.18}$$

shows that this requirement enforces the continuity of the potential energy between subsequent time slabs. In the linear case, this leads to the equivalence of $\mathbf{u}|_n^+$ and $\mathbf{u}|_n^-$.

By setting $\mathbf{w}_2 =: \dot{\mathbf{w}}$ and $\mathbf{v} =: \dot{\mathbf{u}}$ the new single-field formulation

$$\int_{I_n} \dot{\mathbf{w}}^T \cdot \{\mathbf{M}\ddot{\mathbf{u}} + \mathbf{C}\dot{\mathbf{u}} + \mathbf{K}\mathbf{u} - \mathbf{f}\}\, dt + \dot{\mathbf{w}}^T|_n^+ \{\mathbf{M}\dot{\mathbf{u}}|_n^+ - \mathbf{M}\dot{\mathbf{u}}|_n^-\} = \mathbf{0} \tag{4.19}$$

is obtained. The TJR enforces the continuity of momentum between subsequent time slabs.

Note, if weighting-functions $\mathbf{w}^T$ instead of $\dot{\mathbf{w}}^T$ were used in Eq. (4.19), this would lead to dropping out of the TJR $\mathbf{M}\dot{\mathbf{u}}|_n^+ - \mathbf{M}\dot{\mathbf{u}}|_n^-$ and for that reason the formulation would lose the characteristics of a TDG.

Using the single-field formulation developed by Hulbert (1989, 1992), the interpolations are continuous in space but discontinuous in time between adjacent time slabs for all unknowns. The new formulation is discontinuous in time for the velocity, but continuous in time for the displacement. This way, a reduction of unknowns can be achieved without loss of stability and accuracy of displacement and velocity.

4.3.4 TDG-Error Analysis

In order to investigate the amplitude errors for the displacement u and the velocity v and to analyze the damping characteristics of the previously developed formulations, the following scalar differential equation of 2nd order in time

$$m\ddot{u} + ku = 0 \tag{4.20}$$

representing an undamped spring-mass-oscillator is considered. The initial conditions are imposed to be $u(t=0) = u_0$ and $\dot{u}(t=0) = \dot{u}_0 = 0$.

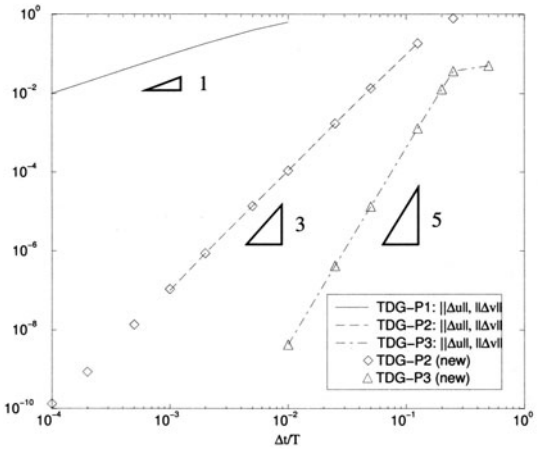

Figure 18. PDE of 2nd-Order in Time: Error of displacement u and velocity $\dot{u}$ of the single-field TDG-method with different interpolations

In Fig. 18, the error of the displacement u and the velocity $\dot{u}$ after respectively $t = 10T$ and $t = 9.75T$ $\left(T = 2\pi\sqrt{\frac{m}{k}}\right)$ for different non-dimensional timesteps $\frac{\Delta t}{T}$ is shown. Pi denotes the

Table 6. PDE of 2nd-Order in Time: Single-field and two-field formulation

method	interpolation of u	amplitude error			unknowns	
		u	$\dot{u}$	$\ddot{u}$	formulation (Hulbert, 1989, 1992)	NEW formulation
P1	linear	$\sim \Delta t$	$\sim \Delta t$		2	1
P2	quadratic	$\sim \Delta t^3$	$\sim \Delta t^3$	$\sim \Delta t$	3	2
P3	cubic	$\sim \Delta t^5$	$\sim \Delta t^5$	$\sim \Delta t^2$	4	3
P0-P0	constant	$\sim \Delta t$	$\sim \Delta t$		2	-
P1-P1	linear	$\sim \Delta t^3$	$\sim \Delta t^3$		4	-
P2-P2	quadratic	$\sim \Delta t^5$	$\sim \Delta t^5$		6	-

TDG single-field formulation employing i-th order polynomials $\mathcal{P}^i$ in time for the displacement u. It can be seen that the amplitude error for both u and $\dot{u}$ is $\sim \Delta t^{2i-1}$.

In Tab. 6 a comparison between the single-field formulation (Hulbert, 1989, 1992), the new single-field formulation and the two-field formulation is given. Pi-Pj represents the two-field formulation employing $\mathcal{P}^i$ for the displacement u and $\mathcal{P}^j$ for the velocity v.

4.3.5 Galerkin/Least-Squares Formulation

For problems involving a large scale of frequencies and wave numbers, it is advisable to stabilize the numerical scheme by adding a least-squares operator to the TDG formulation. While the standard (Bubnov-)Galerkin method minimizes the residual of the underlying partial differential equation in a weak sense, the additional term of the Galerkin/least-squares (GLS) method minimizes the square of the residual. For this reason, high frequency/short wave length spurious oscillations are suppressed.

In the case of the two-field formulation the differential operators

$$\mathcal{L}_1\mathbf{U} := \mathbf{M}\dot{\mathbf{v}} + \mathbf{C}\mathbf{v} + \bar{\mathbf{K}}\mathbf{u} \tag{4.21a}$$

$$\mathcal{L}_2\mathbf{U} := \dot{\mathbf{u}} - \mathbf{v} \tag{4.21b}$$

are introduced and the time-discontinuous Galerkin/least-squares (GLS) method

$$\begin{aligned} &\int_{I_N} \mathbf{w}_2^T \{\mathbf{M}\dot{\mathbf{v}} + \mathbf{C}\mathbf{v} + \mathbf{K}\mathbf{u} - \mathbf{f}\} + \mathbf{w}_1^T \mathbf{K}\mathcal{L}_2\mathbf{U} \\ &+ \{\tau_1 \mathcal{L}_1\mathbf{W}\}^T \{\mathcal{L}_1\mathbf{U} - \mathbf{f}\} + \{\tau_2 \mathcal{L}_2\mathbf{W}\}^T \mathbf{K}\mathcal{L}_2\mathbf{U} \quad dt \\ &+ \mathbf{w}_1^T|_n^+ \{\mathbf{K}\mathbf{u}|_n^+ - \mathbf{K}\mathbf{u}|_n^-\} + \mathbf{w}_2^T|_n^+ \{\mathbf{M}\mathbf{v}|_n^+ - \mathbf{M}\mathbf{v}|_n^-\} = \mathbf{0} \end{aligned} \tag{4.22}$$

is given where the boundary terms resulting from the integration by parts of the stiffness matrix have been dropped for conciseness. Note that the GLS stabilization of the equation of motion Eq. (4.14) leads to additional terms in both hyper rows, i.e. affects the weak form of both the equation of motion itself and the identity $\dot{\mathbf{u}} - \mathbf{v} = \mathbf{0}$. The least-squares of Eq. (4.13) also modifies both rows.

From the generalization to structural dynamics of the definition for τ developed in the framework of compressible flows by Shakib (1988) the intrinsic time scales

$$\tau_1 = \frac{\partial \tau}{\partial t}\left\{\left\|\left(\frac{\partial \tau}{\partial t}\right)^2 \mathbf{M}\right\|^m + \left\|\frac{\partial \tau}{\partial t}\mathbf{C}\right\|^m + \|\mathbf{K}\|^m\right\}^{-\frac{1}{m}} \tag{4.23a}$$

$$\tau_2 = \left\{\frac{\partial \tau}{\partial t}\right\}^{-1}\mathbf{I} \tag{4.23b}$$

are obtained where the generalized norm $\|\ \|^m$ and $m \in \{1,2,\infty\}$ has been introduced according to Soulaimani and Fortin (1994). Note the leading factor $\frac{\partial \tau}{\partial t}$ in Eq. (4.23a) which stems from the principle of virtual power.

The stabilized single-field formulation

$$\int_{I_N} \dot{\mathbf{w}}^T\{\mathbf{M}\ddot{\mathbf{u}} + \mathbf{C}\dot{\mathbf{u}} + \mathbf{K}\mathbf{u} - \mathbf{f}\} + \{\tau_1 \mathcal{L}\mathbf{w}\}^T\{\mathcal{L}\mathbf{u} - \mathbf{f}\} \quad dt \tag{4.24}$$
$$+\mathbf{w}^T|_n^+\{\mathbf{K}\mathbf{u}|_n^+ - \mathbf{K}\mathbf{u}|_n^-\} + \dot{\mathbf{w}}^T|_n^+\{\mathbf{M}\dot{\mathbf{u}}|_n^+ - \mathbf{M}\dot{\mathbf{u}}|_n^-\} = \mathbf{0}$$

where

$$\mathcal{L}\mathbf{u} := \mathbf{M}\ddot{\mathbf{u}} + \mathbf{C}\dot{\mathbf{u}} + \bar{\mathbf{K}}\mathbf{u} \tag{4.25}$$

may be obtained by choosing the interpolations for the displacements $\mathbf{u}, \mathbf{w}_1$ one order higher in time than the interpolations for the velocities $\mathbf{v}, \mathbf{w}_2$ and by explicitly setting $\mathcal{L}_2\mathbf{U} = \mathbf{0}$. Note, for the new single-field GLS-formulation, the $\{\mathbf{K}\mathbf{u}|_n^+ - \mathbf{K}\mathbf{u}|_n^-\}$-term is exactly satisfied.

4.3.6 Error Analysis and Filtering Characteristics

In order to compare the numerical properties of the various methods discussed previously, the same scalar model problem as in section 4.3.4 is considered. In contrary to the PDEs of first order in time, the addition of the GLS-stabilization does not reduce the order of convergence of the underlying TDG-methods for PDEs of second order in time.

Figure 19 depicts the temporal filtering characteristics of several single-field and two-field schemes. The matrix of intrinsic time scales for the GLS formulations has been chosen $\tau_1 = \Delta t/(2m)$ and $\tau_2 = \Delta t/2$.

Expressing the discrete unknowns $\mathbf{u}|_{n+1}^-$ and $\mathbf{v}|_{n+1}^-$ at the end of time slab I_N in terms of the corresponding initial conditions $\mathbf{u}|_n^-$ and $\mathbf{v}|_n^-$ yields

$$\begin{bmatrix} \mathbf{u}|_{n+1}^- \\ \Delta t\mathbf{v}|_{n+1}^- \end{bmatrix} = \mathbf{A}\begin{bmatrix} \mathbf{u}|_n^- \\ \Delta t\mathbf{v}|_n^- \end{bmatrix} \tag{4.26}$$

where $\mathbf{A}$ is the amplification matrix. The spectral radius ρ of $\mathbf{A}$ is defined as

$$\rho(\mathbf{A}) = \max_i(|\lambda_i(\mathbf{A})|) \tag{4.27}$$

where λ_i are the eigenvalues of $\mathbf{A}$. The spectral radius is a measure for the artificial, numerical damping. Since all schemes are unconditionally stable, the numerically computed amplitude is

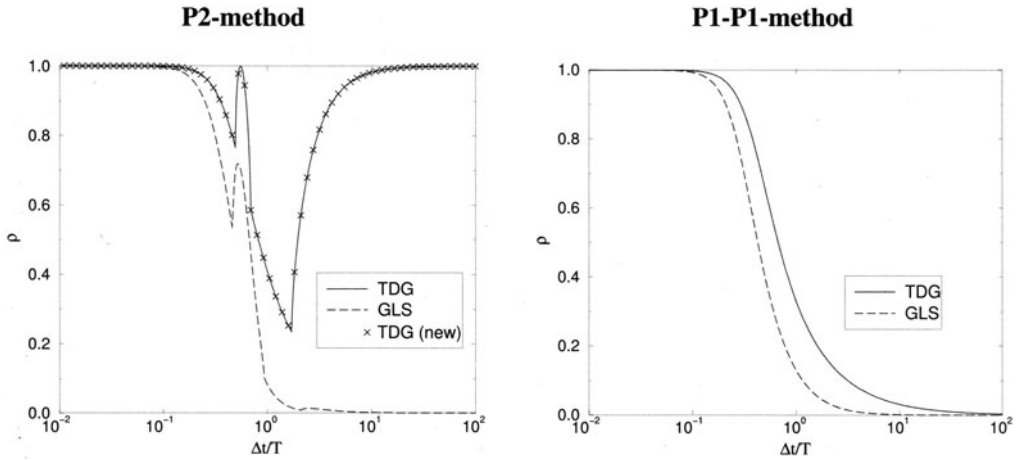

Figure 19. Filtering Characteristics

always less than or equal the exact amplitude, i.e. $\rho \leq 1$. For sufficient resolution $\Delta t/T \ll 1$ the amplitude error approaches zero and $\rho \to 1$. For resolutions with less than 10 time steps per period ($\Delta t/T > 0.1$) the numerical damping becomes significant. For less than approximately 4 time steps per period the physical oscillations are not adequately resolved. For $\Delta t/T \gg 1$ the two-field and single-field formulations show completely different damping characteristics: while the two-field TDG methods annihilate the underresolved scales ($\lim_{\Delta t/T \to \infty} \rho(\Delta t/T) = 0$), the single-field TDG methods preserve their amplitudes, i.e. $\lim_{\Delta t/T \to \infty} \rho(\Delta t/T) = 1$, see also Hulbert (1992, 1994). It is well-known that underresolved scales may spoil the overall solution if they are not dampened (Hughes, 1987). For this reason, the high frequency filtering characteristics of the two-field formulations are desirable and may justify their use despite of the larger number of unknowns compared to the single-field TDG-methods. Note that the GLS formulations for both P1-P1 and P2 are asymptotically annihilating underresolved scales.

4.4 Discretization of The Chemo-Electro-Mechanical Field

In this section, the discretization is applied on the differential equations given in the previous sections. For this reason, in the following sections,

- the convection-diffusion equation
- the electric field equation
- and the equation of motion

are given in the form used for the numerical simulation.

4.4.1 Discretization of the convection-diffusion equation

The convection-diffusion equation is a partial differential equation (PDE) of first order in time and represents the conservation of mass and charge. Formulating the time-continuous form in space and time we obtain

$$\int_{I_n}\int_{\Omega_n} \delta c_\alpha^T \left(\dot{c}_\alpha - \sum_\beta (D_{\alpha\beta}\, c_{\beta,i} + z_\beta\, c_\beta\, \mu_{\alpha\beta}\, \Psi_{,i})_{,i} - r_\alpha\right) d\Omega\, dt = 0 \tag{4.28}$$

where δc_α is the weighting function or the variation of the unknown c_α.

The time-discontinuous Galerkin formulation of Eq. (4.28)

$$\begin{aligned}
&-\int_{I_N}\int_{\Gamma(t)} \delta c_\alpha^T \sum_\beta (D_{\alpha\beta}\, c_{\beta,i} + z_\beta\, c_\beta\, \mu_{\alpha\beta}\, \Psi_{,i})\cdot n_i\, d\Gamma\, dt - \int_{I_N}\int_{\Omega(t)} \delta \dot{c}_\alpha^T\, c_\alpha\, d\Omega\, dt \\
&+\int_{I_N}\int_{\Omega(t)} \delta c_{\alpha,i}^T \sum_\beta (D_{\alpha\beta}\, c_{\beta,i} + z_\beta\, c_\beta\, \mu_{\alpha\beta}\, \Psi_{,i})\, d\Omega\, dt - \int_{I_N}\int_{\Omega(t)} \delta c_\alpha^T\, r_\alpha\, d\Omega\, dt \\
&+\int_{\Omega(t_{n+1})} \delta c_\alpha^T|^-\, c_\alpha|^-\, d\Omega - \int_{\Omega(t_n)} \delta c_\alpha^T|^+\, c_\alpha|^-\, d\Omega = 0
\end{aligned} \tag{4.29}$$

enforces the initial conditions in weak form. For each time derivative, a "jump term" is introduced. The given equation is integrated by parts in space and time; therefore the conservation of the flux is fulfilled and the flux boundary conditions can be implemented easily.

4.4.2 Discretization of the electric field equation

The electric field equation is represented by an elliptic PDE in space. Due to higher velocity of propagation of the electric compared to the characteristic velocities of the other fields, the numerical simulation is performed quasi-statical, i.e. no derivative in time in Eq. (3.2) is formulated. Deriving the weak form in space and time of the electric field equation, we obtain

$$\int_{I_N}\int_{\Omega(t)} \delta\Psi^T \left(\Psi_{,ii} + \frac{F}{\epsilon_r\, \epsilon_0} \sum_\alpha (z_\alpha\, c_\alpha)\right) d\Omega\, dt = 0 \tag{4.30}$$

Integration by parts leads to

$$\begin{aligned}
&-\int_{I_N}\int_{\Omega(t)} \delta\Psi_{,i}^T\, \Psi_{,i}\, d\Omega\, dt + \int_{I_N}\int_{\Omega(t)} \delta\Psi^T\, \frac{F}{\epsilon_r\, \epsilon_0} \sum_\alpha (z_\alpha\, c_\alpha)\, d\Omega\, dt \\
&+\int_{I_N}\int_{\Gamma(t)} \delta\Psi^T\, \Psi_{,i}\cdot n_i\, d\Gamma\, dt = 0
\end{aligned} \tag{4.31}$$

4.4.3 Discretization of the equation of motion

For the PDE of second order in time, the principle of virtual work is applied, while the variation of the velocity $\delta\dot{u}$ is used as weighting function - as given in Sec. 4.3.2 - in order to employ the jump for the variable u. For the time-continuous principle of virtual work

$$\int_{I_N}\int_{\Omega(t)} \delta u_i^T \left(\rho\ddot{u}_i + f\dot{u}_i - \sigma_{ij,j} - \rho b_i\right) d\Omega\, dt = 0 \tag{4.32}$$

is obtained.

Applying the time-discontinuous Galerkin followed by an integration by parts in space and time, we get

$$\begin{aligned}
&-\int_{I_N}\int_{\Omega(t)} \delta\dot{u}_i^T\, \rho\dot{u}_i\, d\Omega\, dt + \int_{I_N}\int_{\Omega(t)} \delta\dot{u}_i^T\, f\dot{u}_i\, d\Omega\, dt \\
&-\int_{I_N}\int_{\Gamma(t)} \delta\dot{u}_i^T\, \sigma_{ij}\cdot n_j\, d\Gamma\, dt + \int_{I_N}\int_{\Omega(t)} \delta\dot{u}_{i,j}^T\, \sigma_{ij}\, d\Omega\, dt \\
&-\int_{I_N}\int_{\Omega(t)} \delta\dot{u}_i^T\, \rho b_i\, d\Omega\, dt \\
&+\int_{\Omega(t_{n+1})} \delta\dot{u}_i^T|^-\, \rho\dot{u}_i|^-\, d\Omega - \int_{\Omega(t_n)} \delta\dot{u}_i^T|^+\, \rho\dot{u}_i|^-\, d\Omega \;=\; 0
\end{aligned} \tag{4.33}$$

5 NUMERICAL SIMULATION

In this section, chemical and electrical stimulation of electrolyte polymer gels are investigated. The testcases are conducted on a fixed gel placed in the middle of a solution bath.

5.1 Chemical Stimulation

In this testcase, a gel film ($10 \times 10 mm^2$) with a concentration $c_{A^-} = 5 mM$ is placed in a solution bath ($30 \times 30 mm^2$) with a concentration of $c^{(s)}_{Na^+} = c^{(s)}_{Cl^-} = 1 mM$, see Fig. 20.

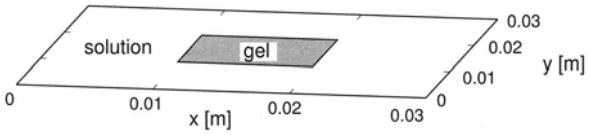

Figure 20. Polymer gel in a solution bath without applied electric field

The boundary conditions for the Na^+ and Cl^- ions at the whole boundary of the solution are set to $1 mM$. Since the concentrations of H^+ and OH^- ions are very small, they can be neglected.

Since the gel domain is fixed, only the coupled chemo-electric field is considered. The convective velocity of the solvent v equals zero and dissociation effects are neglected. Due to the large number of unknowns, a multigrid (MG) method using 96×96 elements in space on 5 MG levels has been applied for the computations. To obtain a good resolution even in the small region of the boundary layer at the gel-solution interface, an adaptive mesh-refinement has been applied.

In Fig. 21, the stationary solution of the ion concentrations and of the electric potential in the gel and in the solution is depicted. The concentrations of Na^+ and Cl^- in the whole gel region are $c^{(g)}_{Na^+} = 5.193 mM$ and $c^{(g)}_{Cl^-} = 0.193 mM$. In the solution near the gel-solution boundary, the concentrations are $c^{(s)}_{Cl^-} = c^{(s)}_{Na^+} = 1 mM = const$. From Eq. (3.7), a normalized differential osmotic pressure $\Delta\tilde{\pi} = 3.386 mM$ between gel and solution is obtained at the complete interface. It should be noted that for chemical stimulation the same results can be obtained by using Eqs. (3.3) and (2.36).

5.2 Electrical Stimulation

In this section, electrical stimulation of the electrolyte polymer gel is investigated.

In this testcase, the gel fiber ($10 \times 10 mm^2$) with a concentration of bound anionic groups $c_{A^-} = 5 mM$ is placed between two electrodes in a solution bath ($30 \times 30 mm^2$) having a concentration of $c^{(s)}_{Na^+} = c^{(s)}_{Cl^-} = 1 mM$, see Fig. 22. The boundary conditions for Na^+ and Cl^- in the solution near the electrodes are set to $c_{Na^+} = c_{Cl^-} = 1 mM$. Since the concentrations of H^+ and OH^- ions are very small, they can be neglected. In the solution an electric potential of $-100 mV$ near to the cathode and of $+100 mV$ near to the anode is prescribed.

As the gel domain is fixed, only the coupled chemo-electric field is considered. The convective velocity of the solvent v equals zero and changes in dissociation are neglected. In this

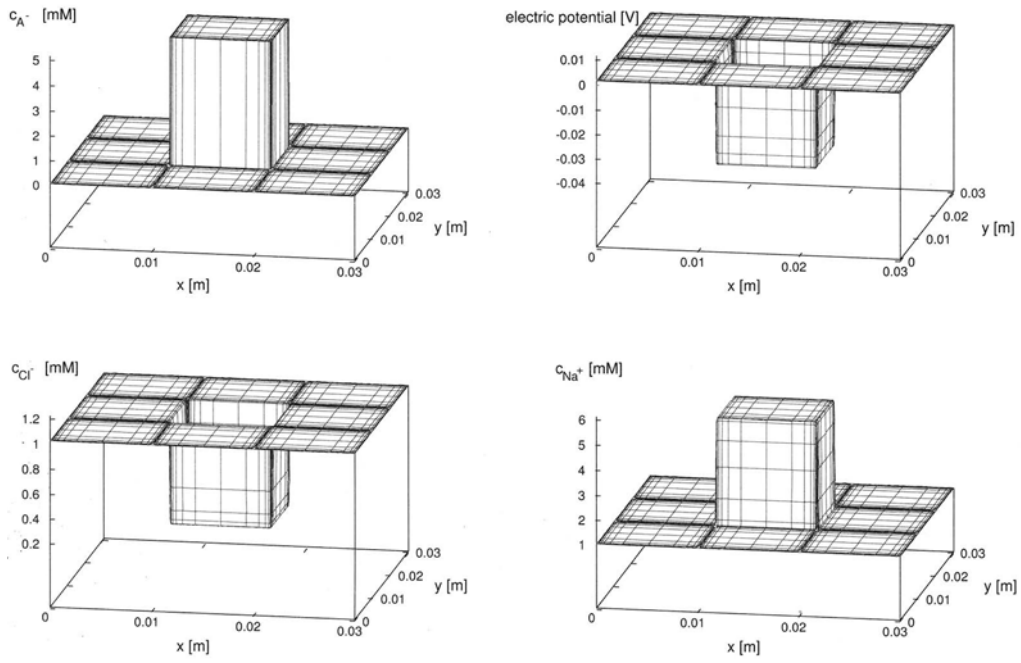

Figure 21. 2D-calculation of the ion concentrations (A^- (top left), Cl^- (bottom left), Na^+ (bottom right)) and electric potential Ψ (top right) in the gel and the solution without applied external electric field

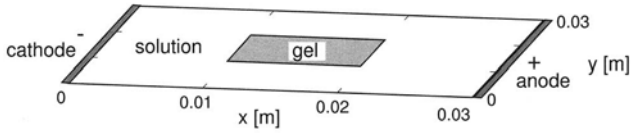

Figure 22. Polymer gel in a solution bath under an applied electric field

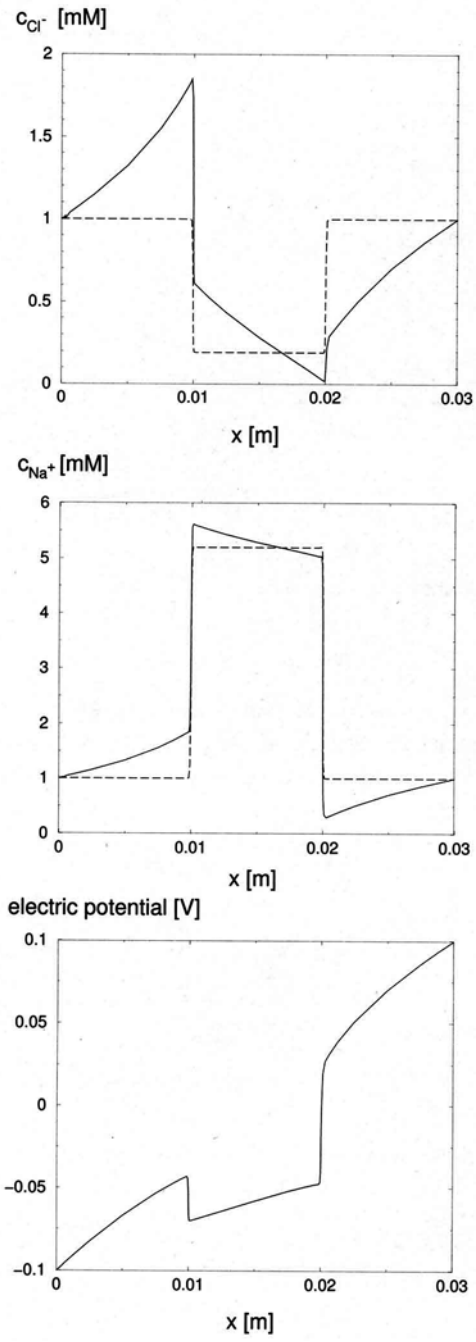

Figure 23. Initial conditions (dashed line) and stationary solution (solid line) of the concentrations and the electric potential at $y = 0.015\,m$

testcase, a multigrid method has been also applied for the computations. An adaptive refined mesh has been used to obtain a high resolution in the whole domain.

The stationary solution of the testcase without applied external electric field (see Sec. 5.1) has been taken as initial condition for this testcase, i.e. the concentrations of Na^+ and Cl^- in the whole gel region were given for $t = 0$ as: $c^{(g)}_{Na^+} = 5.193\,mM$ and $c^{(g)}_{Cl^-} = 0.193\,mM$.

In Fig. 23, the initial conditions (dashed line) and the stationary solution (solid line) of the testcase with applied external electric field are plotted for the cross-section placed at $y = 0.015\,m$.

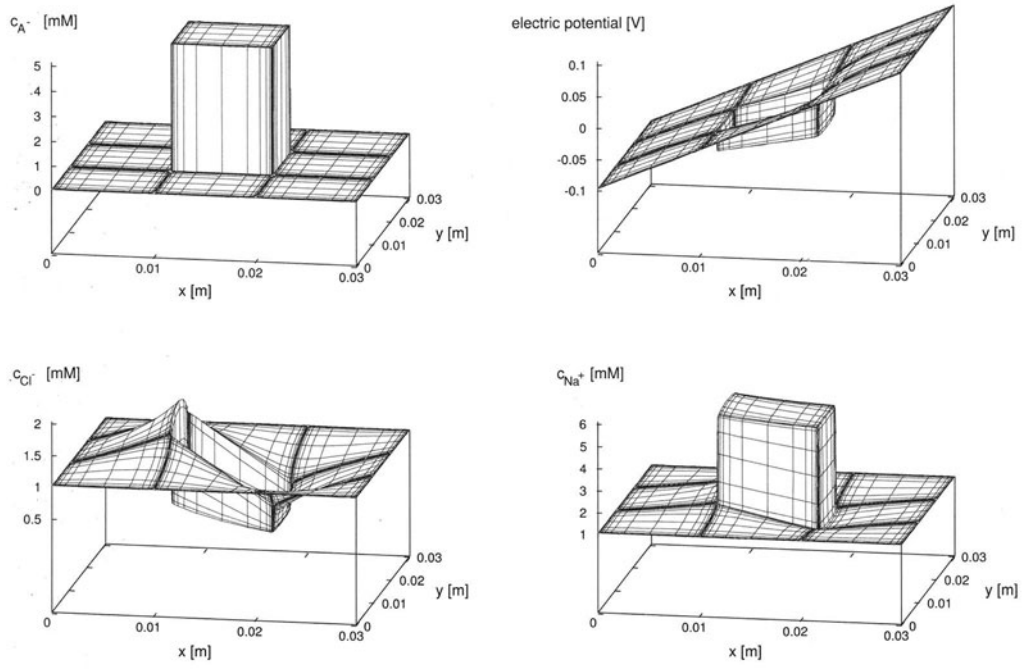

Figure 24. 2D-plot of the ion concentrations (A^- (top left), Cl^- (bottom left), Na^+ (bottom right)) and electric potential Ψ (top right) in the gel and the solution under an applied external electric field

The stationary solution of the ion concentrations and the electric potential in the gel and in the solution bath with applied electric field is depicted in Fig. 24. The concentrations of the cations and anions are higher on the cathode side and lower on the anode side of the gel compared to the initial conditions. Near the gel-solution interface, the ion concentrations in the solution are also increased at the cathode side and decreased at the anode side. It has to be mentioned that the condition of electroneutrality Eq. (3.3) is fulfilled in the whole domain - gel and solution - outside the small boundary layer at the interface.

The electric potential behaves nearly linear in x-direction and constant in y-direction in the solution. The increase over x in the gel is smaller than in the solution. This is compensated by a smaller step at the cathode side and a larger one at the anode side of the gel compared to the initial values without applied electric field.

5.2.1 Differential osmotic pressure

In this subsection, the differential osmotic pressure resulting from the concentration differences between gel and solution at the interface outside the small boundary layer is investigated in detail.

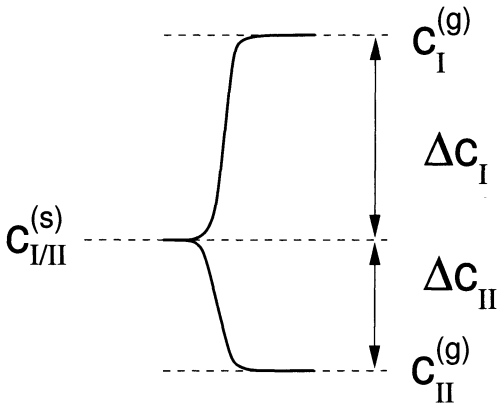

Figure 25. Concentrations in the gel and in the solution at the interface

The normalized pressure difference $\Delta\widetilde{\pi} = \sum_{\alpha=1}^{N_f}(c_\alpha^{(g)} - c_\alpha^{(s)})$ for the stationary solution as well as for the initial conditions of the electrically stimulated case is depicted in Fig. 26. It should be noted that the concentrations in the gel and the solution have been taken at the interface outside the boundary layer, see Fig. 25. Without applied electric field, the pressure difference at the interface at all edges is $\Delta\widetilde{\pi}_0 \approx 3.39\,mM$, independent of the x- or y-position. The stationary solution of the differential osmotic pressure with applied electric field shows the following behavior: at the edges perpendicular to the electrodes, the course is nearly linear. The pressure difference $\Delta\widetilde{\pi}_{cathode}$ is approx. $2.51\,mM$ at $x = 0.01\,m$, at $x = 0.02\,m$ $\Delta\widetilde{\pi}_{anode}$ is approx. $4.51\,mM$. This behavior is also depicted in Fig. 27 in detail.

At the edges parallel to the electrodes, a different behavior can be determined: The normalized osmotic pressure at the boundary $x = 0.01\,m$ has a nearly quadratic behavior; in the middle of this edge (at $y = 0.015\,m$), it is minimal, i.e. the difference between the values with and without applied electric field is maximal. At the boundary $x = 0.02\,m$, $\Delta\widetilde{\pi}$ at $y = 0.015\,m$ is maximal, i.e. the difference between the differential osmotic pressures is also maximal.

The differences over the y-coordinate are smaller than the ones over x, hence in the following they are neglected. Summarizing, a depolarisation (smaller normalized osmotic pressure difference compared to the initial conditions) on the cathode sides and a hyperpolarisation on the anode side of the gel are obtained as a result of the applied electric field.

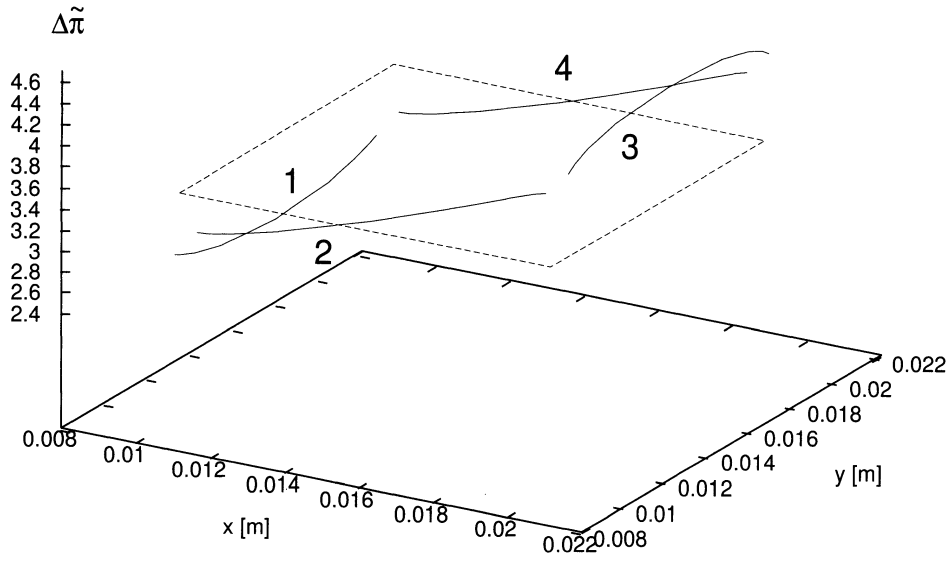

Figure 26. Normalized differential osmotic pressure $\Delta\tilde{\pi}$

5.2.2 Electric current

The electric current density j_i in i-direction can be calculated by the Faraday equation

$$j_i = F \sum_{\alpha=1}^{N_f} \left(z_\alpha (-D_\alpha \frac{\partial c_\alpha}{\partial x_i} - z_\alpha \mu_\alpha c_\alpha \frac{\partial \Psi}{\partial x_i} + v_i c_\alpha) \right) \tag{5.1}$$

The computation of the current density is performed by a postprocessing using the nodal values and the local gradients of the unknowns.

The electric current density j_x in x-direction for this testcase is depicted qualitatively in Fig. 28. These fluxes are normalized by a mean value of the diffusion constants $\bar{D}$ of all species. This allows to compare the fluxes of salt solutions containing different ions. Due to the second term of Eq. (5.1), a flux in negative x-direction can be determined. At the edge of the gel parallel to the electrodes at $x = 0.02\,m$, a minimal current density is obtained. Inside the gel, this value is larger, i.e. an additional flux enters the gel at the boundaries perpendicular to the electrodes. The electric current density in the solution far away from the gel is nearly constant over the whole domain. In this region, assuming $c_\alpha^{(s)} \approx const$, i.e. the gradients of the concentrations in x-direction

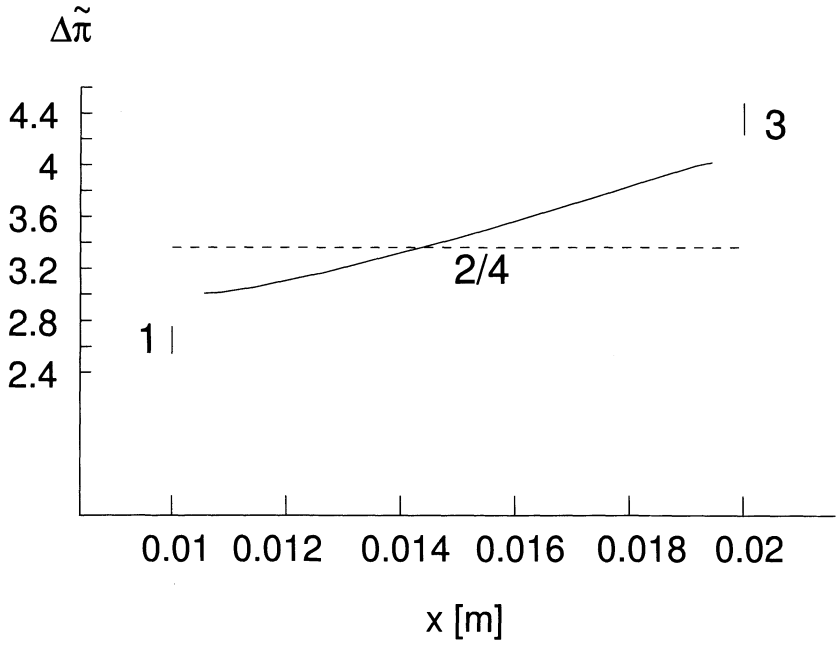

Figure 27. Normalized differential osmotic pressure $\Delta\tilde{\pi}$

are vanishing, the (mean) value of the current density can be estimated by

$$j_x^* = \frac{1}{\bar{D}} j_x = \frac{1}{\bar{D}} F \sum_{\alpha=1}^{N_f=2} \left(z_\alpha \left(-D_\alpha \frac{\partial c_\alpha}{\partial x} - z_\alpha \mu_\alpha c_\alpha \frac{\partial \Psi}{\partial x} \right) \right) \tag{5.2}$$

$$\approx -\frac{1}{\bar{D}} F \sum_{\alpha=1}^{N_f=2} \left(z_\alpha^2 \mu_\alpha c_\alpha \frac{\partial \Psi}{\partial x} \right) = -\frac{2}{\bar{D}} F \bar{\mu} \bar{c} \frac{\Delta \Psi}{\Delta x} \tag{5.3}$$

where $\bar{c} \approx c_1 \approx c_2$

5.2.3 Deformation of the gel fiber

Due to the different concentrations at the interface, different differential osmotic pressures at the anode and cathode side of the gel are obtained:

$$\Delta\tilde{\pi}_{cathode} = 2.51\,mM$$
$$\Delta\tilde{\pi}_{anode} = 4.51\,mM$$

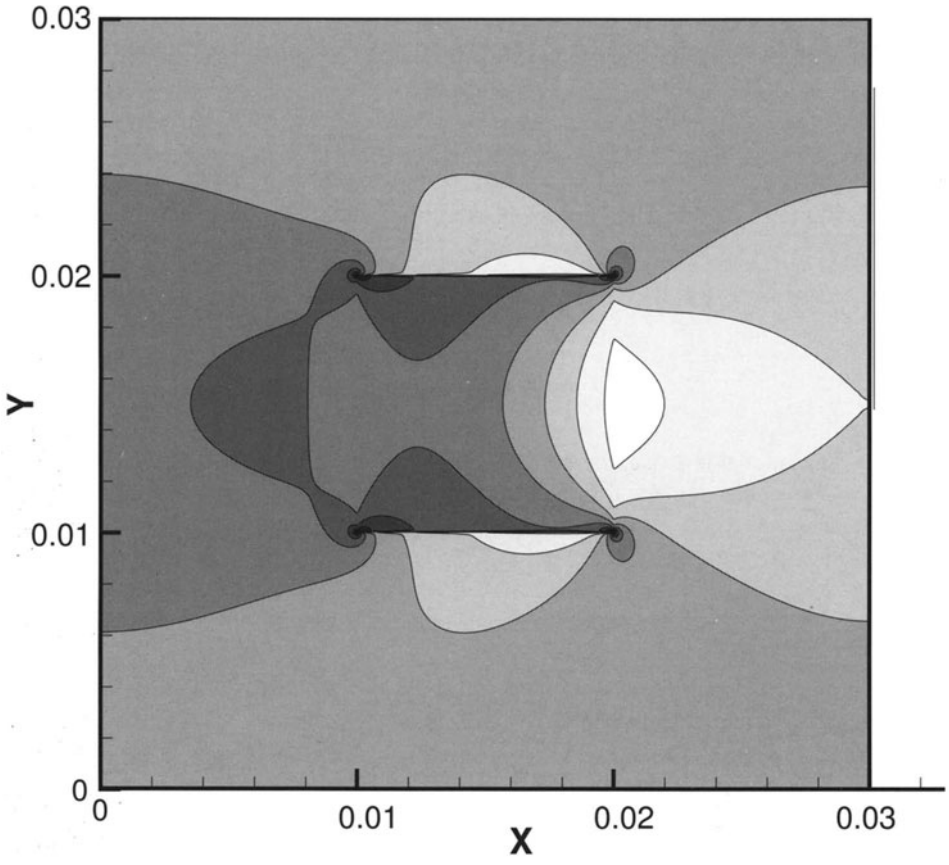

Figure 28. Normalized electric current density j_x^* (qualitative plot)

Based on the different osmotic pressures, see Sec. 5.2.1, a prescribed strain $\bar{\epsilon}_{ij}$ according to

$$\begin{aligned} \bar{\epsilon}_{ij} = \epsilon^{[1]} - \epsilon^{[0]} &= \widetilde{const}_{ij} \left[(\Delta\widetilde{\pi}_{cathode} - \Delta\widetilde{\pi}_0) + (\Delta\widetilde{\pi}_{anode} - \Delta\widetilde{\pi}_{cathode}) \frac{x - x_0}{l_{gel}} \right] \\ &= \widetilde{const}_{ij} \left[-0.88 + (1.12 - (-0.88)) \frac{x - x_0}{l_{gel}} \right] mM \end{aligned} \tag{5.4}$$

where: $l_{gel} = x_1 - x_0\,; \quad x_0 = 0.01\,m\,; \quad x_1 = 0.02\,m$

can be given. The superscript [0] denotes the state of the initial conditions, [1] the stationary solution of this testcase. The constant $\widetilde{const}_{ij}$ depends on the type of gel, the crosslink density,

the affinity between gel and solution and the number of anionic/cationic groups bound to the polymer. To give a qualitative solution of the deformation of the gel film, this constant is chosen as

$$\widetilde{const}_{ij} = 0.1\,\delta_{ij}/mM$$

From the equations given above, the following prescribed strains for the mechanical testcase are attained:

$$\begin{aligned} \bar{\epsilon}_{11} &= -0.088 + 0.2\,\frac{x - x_0}{l_x} \\ \bar{\epsilon}_{22} &= -0.088 + 0.2\,\frac{x - x_0}{l_x} \end{aligned}$$

For this two-dimensional testcase, the gel is fixed in y-direction at $y_0 = 0.02m$ and fixed in x-direction at $x = \frac{x_0+x_1}{2}$. The numerical simulation is conducted on a three-level multigrid using 24×24 shell elements.

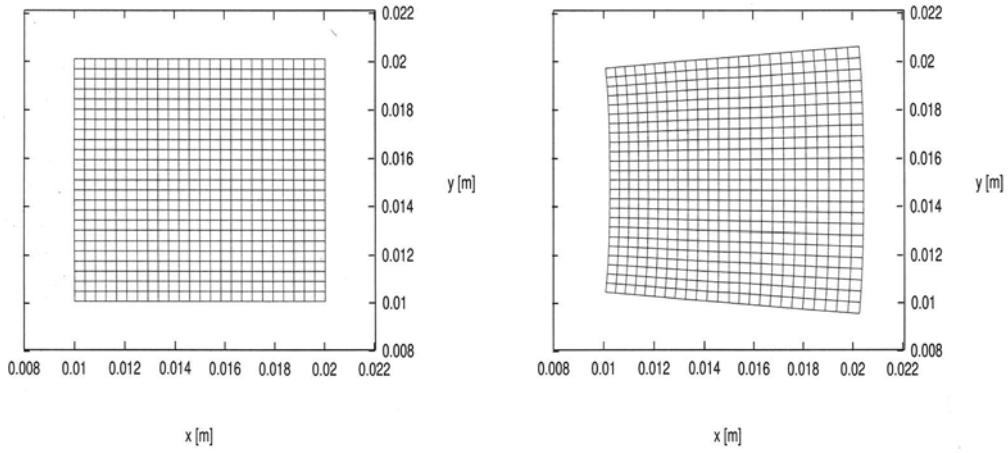

Figure 29. Undeformed (left) and deformed gel film (right)

Fig. 29 (left) depicts the undeformed gel and Fig. 29 (right) the stationary solution of the deformed gel film.

A deswelling on the left (=cathode) side and an additional swelling on the anode side can be determined. The gel contour is nearly linear on the edges perpendicular to the electrodes and parabolic on the edges parallel to the electrodes. This swelling/deswelling phenomenon is in good agreement with the experimental results by Gülch et al. (2000).

This shows the validity and the potential of the employed coupled chemo-electro-mechanical model.

ACKNOWLEDGEMENTS

The authors want to thank Dr.-Ing. Boris Grohmann for his contributions in the field of "Stabilized Space-Time Finite Elements" and Dipl-Ing. Michele D'Ottavio for his help by preparing the manuscript.

Parts of this manuscript have been taken from Wallmersperger (2003). These parts have been reprinted with kind permission of the VDI-Verlag, Düsseldorf.

Bibliography

Banks, H. T., Smith, R. C., Wang, Y., 1996. Smart Material Structures: Modeling, Estimation and Control. John Wiley and Sons Ltd, Ch. Smart Materials Technology and Control Application.

Bar-Cohen, Y., 2001. Electroactive Polymer (EAP) Actuators as Artificial Muscles - Reality, Potential, and Challenges. Vol. PM 98. SPIE Press, Bellingham, WA, USA, Ch. EAP History, Current Status, and Infrastructure, pp. 4–44.

Bar-Cohen, Y., Leary, S., Yavrouian, A., Oguro, K., Tadokoro, S., Harrison, J., Smith, J., Su, J., 2000. Challenges to the application of IPMC as actuators of planetary mechanisms. In: Bar-Cohen, Y. (Ed.), 7th International Symposium on Smart Structures and Materials. Electroactive Polymer Actuators and Devices. SPIE, pp. 140–146, newport Beach, 2000.

Barth, T. J., Sethian, J. A., 1997. Numerical schemes for the Hamilton-Jacobi and level set equations on triangulated domains. NAS report NAS-97-022, NASA Ames Research Center.

Brock, D., Lee, W., Segalman, D., Witkowski, W., 1994. A dynamic model of a linear actuator based on polymer hydrogel. J. Intelligent Material Systems and Structures 5, 764–771.

Chiarelli, P., Basser, P. J., Rossi, D. D., Goldstein, S., 1992. The dynamics of a hydrogel strip. Biorheology , 383–398.

deGennes, P. G., Okumura, K., Shahinpoor, M., Kim, K. J., 2000. Mechanoelectric effects in ionic gels. Europhysics Letters 50 (4), 513–518.

Doi, M., Matsumoto, M., Hirose, Y., 1992. Deformation of ionic polymer gels by electric fields. Macromolecules 25, 5504–5511.

Finkelmann, H., Kock, H. J., Rehage, G., 1981. Investigations on liquid crystalline silozanes: 3.liquid crystalline elastomer - a new type of liquid crystalline material. Makromolecular Chemistry 2, 317.

Flory, P. J., 1953. Principles of Polymer Chemistry. Cornell University Press, Ithaca, NY.

Grimshaw, P. E., Nussbaum, J. H., Grodzinsky, A. J., Yarmush, M. L., 1990. Kinetics of electrically and chemically induced swelling in polyelectrolyte gels. J. Chem. Phys. 93 (6), 4462–4472.

Grohmann, B., Konstanzer, P., Lay, A., Wallmersperger, T., Kröplin, B., 11.-12. November 1998. On the principle of adaptive structure systems. In: NAFEMS Seminar "FEM-Anwendungen für adaptive Struktursysteme". NAFEMS, Magdeburg.

Grohmann, B. A., 2002. Stabilized space-time finite elements for transonic aeroelasticity. Ph.D. thesis, ISD, Universität Stuttgart, shaker Verlag, Aachen.

Gülch, R. W., Holdenried, J., Weible, A., Wallmersperger, T., Kröplin, B., 2000. Polyelectrolyte gels in electric fields: A theoretical and experimental approach. In: Bar-Cohen, Y. (Ed.), 7th International Symposium on Smart Structures and Materials. Vol. 3987 of Electroactive Polymer Actuators and Devices. SPIE, pp. 193–202, newport Beach, 2000.

Hughes, T. J. R., 1987. The Finite Element Method – Linear Static and Dynamic Finite Element Analysis. Prentice-Hall.

Hughes, T. J. R., Franca, L. P., Hulbert, G. M., 1989. A new finite element formulation for computational fluid dynamics: VIII. The Galerkin/least-squares method for advective-diffusive equations. Comput. Methods Appl. Mech. Engrg. 75, 173–189.

Hughes, T. J. R., Hauke, G., Jansen, K., Johan, Z., 1994. Stabilized finite element methods in fluids: Inspirations, origins, status and recent developments. In: Hughes, T. J. R., Onate,

E., Zienkiewicz, O. C. (Eds.), Recent Developments in Finite Element Analysis – A Book dedicated to Robert L. Taylor. CIMNE, Barcelona.

Hughes, T. J. R., Hulbert, G. M., 1988. Space-time finite element methods for elastodynamics: formulations and error estimates. Comput. Methods Appl. Mech. Engrg. 66, 339–363.

Hulbert, G. M., 1989. Space-Time Finite Element Methods for Second-Order Hyperbolic Equations. Ph.D. thesis, Stanford University.

Hulbert, G. M., 1992. Time finite element methods for structural dynamics. Int. J. Numer. Meth. Eng. 33, 307–331.

Hulbert, G. M., 1994. A unified set of single-step asymptotic annihilation algorithms for structural dynamics. Comput. Methods Appl. Mech. Engrg. 113, 1–9.

Johnson, C., 1985. Finite Elements in Fluids. John Wiley & Sons.

Johnson, C., 1993. Discontinuous Galerkin finite element methods for second order hyperbolic problems. Comput. Methods Appl. Mech. Engrg. 107, 117–129.

Kim, J., Kim, J.-Y., Choe, S. J., 2000. Electro-active papers: its possibility as actuators. In: Bar-Cohen, Y. (Ed.), 7th International Symposium on Smart Structures and Materials. Vol. 3987 of Electroactive Polymer Actuators and Devices. SPIE, newport Beach, 2000.

Lee, W., 1996. Polymer gel based actuator: Dynamic model of gel for real time control. Ph.D. thesis, Massachusetts Institute of Technology, Boston, USA.

Nemat-Nasser, S., Li, J. Y., 2000. Electromechanical response of ionic polymer-metal composites. Journal of Applied Physics 87 (7), 3321–3331.

Neubrand, W., 1999. Modellbildung und Simulation von Elektromembranverfahren. Ph.D. thesis, Universität Stuttgart.

Oguro, K., Kawami, Y., Takenaka, H., 1992. Bending of an ion-conducting polymer film-electrode composite by an electric stimulus at low voltage. Trans. Journal of Micromachine Society 5, 27–30.

Ohmine, I., Tanaka, T., 1982. Salt effects on the phase transition of ionic gels. Journal of Chemical Physics 77(11), 5725–5729.

Pelrine, R., Kornbluh, R., Pei, Q., Joseph, J., 2000. High speed electrically actuated elastomers with strain greater than 100%. Science 287, 836–839.

Rička, J., Tanaka, T., 1984. Swelling of ionic gels: Quantitative performance of the donnan theory. Macromolecules 17, 2917–2921.

Schröder, U., Oppermann, W., 1996. Physical Properties of Polymeric Gels. John Wiley and Sons, Ch. Properties of Polyelectrolyte Gels, pp. 19–38.

Schröder, U. P., 1994. Experimentelle und theoretische Untersuchungen an hochgequollenen hydrogelen. Ph.D. thesis, Institut für Textil und Faserchemie der Universität Stuttgart.

Shahinpoor, M., 1995. Micro-electro-mechanics of ionic polymeric gels as electrically controllable artificial muscles. J. Intelligent Material Systems and Structures 6, 307–314.

Shahinpoor, M., 2000. Elastically-activated artificial muscles made with liquid crystal elastomers. In: Bar-Cohen, Y. (Ed.), 7th International Symposium on Smart Structures and Materials. Vol. 3987 of Electroactive Polymer Actuators and Devices. SPIE, pp. 187–192, newport Beach, 2000.

Shakib, F., 1988. Finite element analysis of the compressible euler and navier-stokes equations. Ph.D. thesis, Stanford University.

Shibayama, M., Tanaka, T., 1993. Volume phase transition and related phenomena of polymer gels. In: Responsive Gels: Volume Transitions I. Vol. 109 of Advances in Polymer Science. Springer-Verlag, pp. 1–62.

Shiga, T., Kurauchi, T., 1990. Deformation of polyelectrolyte gels under the influence of electric field. J. of Applied Polymer Science 39, 2305–2320.

Soulaimani, A., Fortin, M., 1994. Finite element solution of compressible viscous flow using conservative variables. Comput. Methods Appl. Mech. Engrg. 118, 319–350.

Tezduyar, T. E., Behr, M., 1992. A new strategy for finite element computations involving moving boundaries and interfaces – The deforming-spatial-domain/space-time procedure: I. The concept and the preliminary numerical tests. Comput. Methods Appl. Mech. Engrg. 94, 339–351.

Thompson, L. L., Sept. 1995. A multi-field space-time finite element method for structural acoustics. In: Design Engineering Technical Conferences. Vol. 3 – Part B. ASME, Boston, pp. 49–64.

Treloar, L. R. G., 1958. The Physics of Rubber Elasticity. Oxford University Press.

Turrin, S., 2003. Protein-based polymers as pseudo-muscular actuators. Master's thesis, Institut für Statik und Dynamik der Luft- und Raumfahrtkonstruktionen (ISD), Universität Stuttgart.

Wallmersperger, T., 2003. Modellierung und Simulation stimulierbarer polyelektrolytischer Gele. Ph.D. thesis, ISD, Universität Stuttgart, Fortschritt-Berichte VDI Reihe 5, VDI-Verlag, Düsseldorf.

Wallmersperger, T., Grohmann, B., Kröplin, B., 1999. Time-discontinuous stabilized space-time finite elements for PDEs of first- and second-order in time. In: European Conference on Computational Mechanics ECCM '99. GACM, München, Germany.

Wallmersperger, T., Kröplin, B., Gülch, R. W., 2001. Electroactive Polymer (EAP) Actuators as Artificial Muscles - Reality, Potential, and Challenges. Vol. PM 98. SPIE Press, Bellingham, WA, USA, Ch. Modelling and Analysis of Chemistry and Electromechanics, pp. 285–308.